Asian Electromagnetics Conference 2019

ASIAEM 2019

September 15-20,2019

Xi'an, China

Wyndham Grand Xi'an South

Organizers and Co-organizers

Organizers

西安交通大学
XI'AN JIAOTONG UNIVERSITY

电力设备电气绝缘国家重点实验室
STATE KEY LABORATORY OF ELECTRICAL INSULATION AND POWER EQUIPMENT

瞬态电磁环境与应用国家级国际联合研究中心
National Center for International Research on Transient Electromagnetics and Applications (TEA)

Co-organizers

Institute of Science & Technology, Xi'an Jiaotong University

Department of International Cooperation & Exchanges，Xi'an Jiaotong University

Technical Sponsor

SUMMA
FOUNDATION

Committee

General Chair

Yan-zhao Xie *Xi'an Jiaotong University, China*

Technical Program Committee

TPC Chair:

William Radasky *Metatech, USA*

TPC Co-Chairs:

Lihua Shi *E3OE Laboratory, China*

Chang-Su Huh *Inha University, South Korea*

Advisors:

D. V. Giri *Pro-Tech, USA*

Edl Schamileglu *University of New Mexico, USA*

Richard Hoad *QinetiQ, UK*

Lars Ole Fichte *Helmut Schmidt University, Germany*

International Scientific Committee

W.-J. Chen,
Y.-Z. Chen,
S.-T. Li,
Y.-D. Li,
Kasmi Chaouki,
M. Bäckström,
S. W. Choi,
J.-H. Deng,
E. Farr,
R. Gardner,
J. Guo,
T.-H. Jang,
S. B. Jeon,
A. Kaelin,
A. Wraight,
Jin Soo Choi,
A. Bhattacharya,
A. -X. Zhang,
J.-S. Luo,
H.-G. Ma,
C. Meng,
K. Mittal,
L. Palisek,
W. Prather,
F. Rachidi,
J.-G. Rhee,
F. Sabath,
Y.-J. Yoon,
D. C. Pande,
M. Nyffeler,
M. Rubinstein ,
Chang-Su Huh,
Woochul Park,
J.-P. Parmantier,
H.-J. Zhou,
H.-L.Yang
S.-H. Wang,
S.-Q. Zheng,
A. Wraight,
Janet O'Neill,
Jaimin Lee,
J.-G. Wang,
J. Lee,
P. Smith,
Dong-Ho Kim,
Shi Qiu,
P. Zwamborn,
Q. Liu,
Nicolas Mora,
F. Vega,
Dhiraj K. Singh,
Jong-Gwan Yook,
S. Umbarkar,

Contents

F

G

H

J

K

L

M

N

T

V

W

X

Y

Z

Application of the FDTD Method to the Surge Analysis of a Transmission Line Tower with a Power Cable

Akiyoshi Tatematsu
Electric Power Engineering Research Lab.
Central Research Institute of Electric Power Industry
Kanagawa, Japan
akiyoshi@criepi.denken.or.jp

***Abstract*—A direct lightning strike to a transmission line tower may cause overvoltages and insulation failures, and to avoid unexpected insulation failures and protect power equipment, it is necessary to install effective lightning protection measures. To design effective countermeasures, it is necessary to predict lightning surge phenomena. The finite-difference time-domain (FDTD) method, which is one of the full-wave numerical approaches not requiring the assumption of the transversal electromagnetic (TEM) mode, has been an effective tool for accurately predicting electromagnetic transient phenomena in three-dimensional structures such as transmission line towers and grounding systems. In this study, using a technique for representing coaxial cables, we simulate a reduced-scale model of a transmission line tower with a power cable, calculate the surge phenomena in the tower model when a surge current is injected into the top of the tower, and compare the FDTD results with the measured results for validation.**

Keywords—FDTD method, lightning, transmission line towers, power cables

I. Introduction

A direct lightning strike to a transmission line tower may cause overvoltages and insulation failures, and to avoid unexpected insulation failures and protect power equipment, it is necessary to install effective lightning protection measures. To design effective countermeasures, it is necessary to predict lightning surge phenomena. Conventionally, transmission-line (TL) based simulation techniques have been used for the analysis of lightning surge phenomena in structures such as substations, transmission lines, and distribution lines. On the other hand, full-wave numerical approaches such as the finite-difference time-domain (FDTD) method [1], which do not require the assumption of the transverse electromagnetic (TEM) mode, can be used to solve electromagnetic transient phenomena in three-dimensional structures such as transmission line towers and grounding systems more accurately, and have been widely employed for predicting electromagnetic transient phenomena [2].

Compared with the other computation methods, the FDTD method presents a number of advantages such as its capabilities of (i) handling inhomogeneous electrical parameters of the soil, (ii) handling nonhorizontal ground surfaces, (iii) modeling nonstraight lightning channels, and (iv) solving transient phenomena in a time domain, which makes it easy to incorporate nonlinear effects. To apply the FDTD method to surge analysis, several techniques, for example, for representing thin wires such as electrical wires and earth electrodes [3], [4], the lossy effects of thin wires [5], [6], and coaxial cables [5]-[7], have been developed. With the development of such useful simulation techniques, the FDTD method has been used to analyze lightning and switching surge phenomena in a practical configuration (e.g., [8]-[13]).

In this study, using a technique for representing coaxial cables, we simulate a reduced-scale model of a transmission line tower with a power cable, calculate the electromagnetic transient phenomena when a surge current is injected into the top of the tower, and compare the FDTD results with the measured results for validation.

II. FDTD-based Lightning Surge Simulations

A. Technique for Representing Coaxial Cables

In [7], we proposed a technique for representing a coaxial cable in FDTD-based surge simulations. The metallic sheath of a coaxial cable is directly represented in the FDTD method using the thin-wire representation technique [3]. In this technique, the metallic sheath is placed along the sections of cells in an analysis space simulated by the FDTD method, and the tangential electric fields on the sheath are set to zero by ignoring the finite conductivity of the metallic sheath. As shown in Fig. 1, the radius of the metallic sheath r_s is represented by modifying the permittivity ε and permeability μ in the update of the four radial electric fields and four rotational magnetic fields adjacent to the metallic sheath. The constant value m is obtained from the relationship between the specified radius r_s and the size of the cells surrounding the sheath. On the other hand, the surge phenomena inside the metallic sheath are simulated by solving telegrapher's equations using one-dimensional TL theory on the basis of the assumption of the TEM mode. In this technique, as shown in Fig. 2, a thin wire connected to the core of the coaxial cable can also be taken into account by incorporating the voltage between the core and the

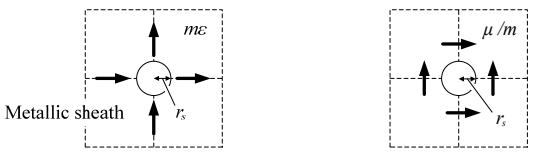

(a) Electric fields (b) Magnetic fields

Fig. 1. Modification of electrical parameters to represent the radius of the metallic sheath (adapted from [7]).

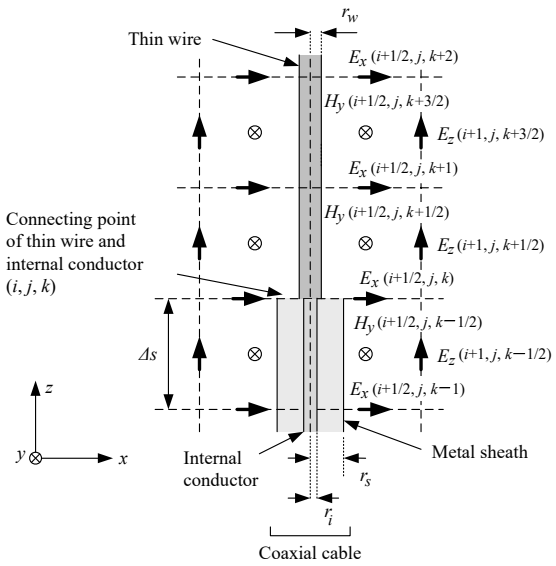

Fig. 2. Electric and magnetic fields surrounding a thin wire and a coaxial cable (adapted from [7]).

metallic sheath at the end of the cable in the update of the four rotational magnetic fields, for example, $H_y(i+1/2, j, k+1/2)$ in Fig. 2.

In this study, the effect of the conductor internal impedances of a core and a metallic sheath and that of the surface transfer impedance through the metallic sheath are not important factors. Both effects are ignored for simplicity, although these effects can also be simulated using improved cable-modeling techniques [5], [6].

B. FDTD-based Surge Simulation Code

In this study, we carried out FDTD simulations using a surge simulation code developed by Central Research Institute of Electric Power Industry (CRIEPI) on the basis of the three-dimensional FDTD method, which is called Virtual Surge Test Lab. Restructured and Extended Version (VSTL REV) [14], [15]. This simulation code can be executed on a GPU-based parallel computer using the CUDA (compute unified device architecture) [16] and MPI (message passing interface), which can reduce computation time dramatically.

III. Measured and Calculated Results

A. Reduced-scale Model of a Transmission Line Tower

Fig. 3 shows an experimental setup of a reduced-scale model of a TL tower with a power cable. The TL tower model with a height of 2 m is composed of cylindrical conductors with a radius of 5 mm, and it is placed on a large copper plate. To simulate the effect of a grounding resistance, a resistance of 30 Ω is inserted between each tower foot and the copper plate. As shown in Fig. 3, the coaxial cable (3D-2W) used to simulate a power cable is fixed at the cross arm with a height of 0.95 m. The coaxial cable is placed vertically inside the TL tower model and the horizontal part of the cable at the bottom of the tower model is placed 5 cm away from the copper plate. The upper end of the coaxial cable is treated as an open end, whereas the lower end of the coaxial cable is grounded with its matching resistance of 50 Ω. The metallic sheath of the cable is electrically connected to the cross arm at the upper end, whereas it is connected to the copper plate at its lower end. A wire with a diameter of

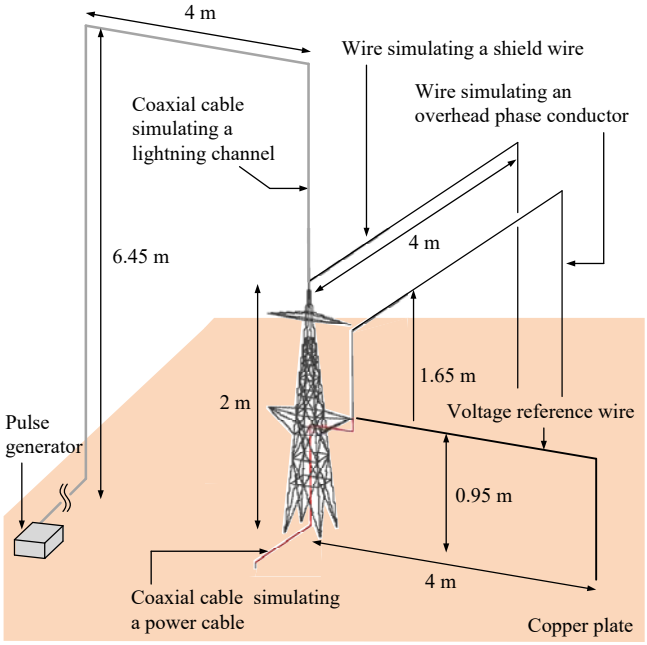

Fig. 3. Experimental setup of a reduced-scale TL model.

0.55 mm used to simulate a shield wire is connected to the top of the tower model. The height of the shield wire is 2 m, and its far end is connected to the copper plate. A wire with a diameter of 0.55 mm used to simulate an overhead phase conductor is connected to the core of the coaxial cable. The wire is placed vertically, and it is bent horizontally 5 cm below the upper cross arm with a height of 1.7 m. The wire used to simulate an overhead phase conductor is also connected to the copper plate at its far end.

To inject a surge current into the tower model, as shown in Fig. 3, another coaxial cable (3D-2W) is placed vertically above the tower model, and the core of the coaxial cable is electrically connected to the top of the tower model via a resistance of 510 Ω. The far end of the coaxial cable is connected to a pulse generator mounted on the copper plate.

Using the above-explained TL tower model, we measured the following items: (i) the current injected into the top of the tower model, (ii) the current flowing into the shield wire, (iii) the currents flowing through the grounding wires of the metallic sheath of the coaxial cable at both ends, (vi) the potential rise of the cross arm supporting the coaxial cable, and (v) the voltage between the cable core and the metallic sheath at both ends. As shown in Fig. 3, the potential rise of the cross arm was measured using a horizontal voltage reference wire with a cross section of 2 mm^2, of which far end is connected to the copper plate.

B. Calculation Model for FDTD Simulations

The dimensions of the analysis space simulated by the FDTD method are 6 m × 6 m × 6.45 m. The bottom surface of the analysis space is treated as a perfectly conducting ground plane, whereas the absorbing boundary condition of Liao's formulation of the second order [17] is applied to the other five external surfaces. In the TL tower model, the wires used to simulate a shield wire and a phase conductor, and the voltage reference wire are represented by the thin-wire representation technique [3]. The resistances connected to the tower foot are modeled by lumped parameter resistances [18]. The coaxial cable used to simulate a power cable is

represented using the technique described in Sec. II.A. To inject a surge current into the top of the tower, a voltage source with an internal resistance of 50 Ω is connected to the top of the tower via a lumped parameter resistance of 510 Ω. The output waveform of the voltage source is simulated on the basis of the measured results of the voltage at the open end of the coaxial cable when it is disconnected from the tower model. A thin wire used to simulate the metallic sheath of the coaxial cable is attached to the top of the voltage source, and the upper end of the thin wire is attached to the upper surface of the analysis space. The analysis space is divided uniformly into cubic cells with a size of 1 cm. The time discretization is set to 9.63 ps. The FDTD simulations are carried out using 24 GPUs, and the calculation time is about 1.5 min when the observation time is 40 ns.

C. Comparison between Measured and Calculated Results

Figs. 4(a) and (b) show the measured and calculated waveforms of the currents injected into the top of the tower model and flowing into the shield wire, respectively. Figs. 5(a) and (b) show the measured and calculated waveforms of the potential rise of the cross arm supporting the coaxial cable and the voltages between the core and the metallic sheath at both ends of the coaxial cable, respectively. From the above results, the calculated injected current, the current distribution in the tower model, and the transient potential rise of the tower model agree well with the measured results obtained by taking into account the electromagnetic coupling of the structure of the tower, the thin wires used to simulate a shield wire and an overhead phase conductor, and the vertical metallic sheath representing a lightning channel. Furthermore, we found good agreement between the calculated and measured voltages inside the coaxial cable, which validates the applicability of the technique for representing coaxial cables to the surge analysis of a TL tower with power cables.

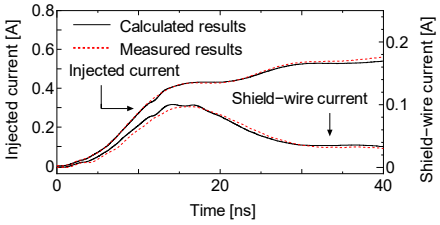

(a) Currents injected into the tower model and flowing into the shield wire

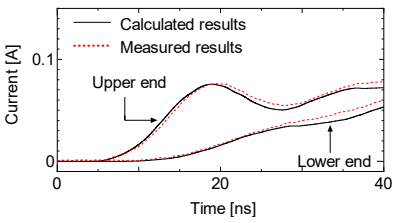

(b) Currents flowing into the grounding wires of the metallic sheath

Fig. 4. Measured and calculated waveforms of the currents.

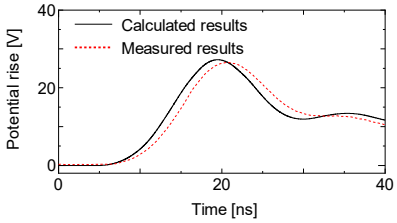

(a) Potential rise of the cross-arm to support the coaxial cable

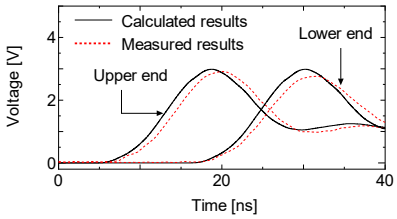

(b) Voltages between the core and sheath of the coaxial cable

Fig. 5. Measured and calculated waveforms of the voltages.

REFERENCES

[1] K. S. Yee, "Numerical solution of initial boundary value problems involving Maxwell's equations in isotropic media," *IEEE Trans. Antennas Propag.*, vol. AP-14, no. 3, pp. 302-307, May 1966.

[2] Working Group C4.501, "Guideline for numerical electromagnetic analysis method and its application to surge phenomena," *Cigre report*, no. 543, Jun. 2013.

[3] T. Noda and S. Yokoyama, "Thin wire representation in finite difference time domain surge simulation," *IEEE Trans. Power Del.*, vol. 17, no. 3, pp. 840-847, Jul. 2002.

[4] Y. Baba, N. Nagaoka, and A. Ametani, "Modeling of thin wires in a lossy medium for FDTD simulations," *IEEE Trans. Electromagn. Compat.*, vol. 47, no. 1, pp. 54-60, Feb. 2005.

[5] A. Tatematsu, "A technique for representing lossy thin wires and coaxial cables for FDTD-based surge simulations," *IEEE Trans. Electromagn. Compat.*, vol. 60, no. 3, pp. 705-715, Jun. 2018.

[6] Y. Du, B. Li, and M. Chen, "The extended thin wire model of lossy round wire structures for FDTD simulations," *IEEE Trans. Power Del.*, vol. 32, no. 6, pp. 2472-2480, Dec. 2017.

[7] A. Tatematsu, "A technique for representing coaxial cables for FDTD based surge simulations," *IEEE Trans. Electromagn. Compat.*, vol. 57, no. 3, pp. 488-495, Jun. 2015.

[8] Y. Baba and V. A. Rakov, "Applications of the FDTD Method to lightning electromagnetic pulse and surge simulations," *IEEE Trans. Electromagn. Compat.*, vol. 56, no. 6, pp.1506-1521, Dec. 2014.

[9] A. Tatematsu, Y. Baba, M. Ishii, S. Okabe, T. Ueda, and N. Itamoto, "Development of surge simulation techniques based on the finite difference time domain method and its application to surge analysis," *Cigre Session 2016*, no. C4-302, 2016.

[10] A. Tatematsu, F. Rachidi, and M. Rubinstein, "Analysis of electromagnetic fields inside a reinforced concrete building with layered reinforcing bar due to direct and indirect lightning strikes using the FDTD method," *IEEE Trans. Electromagn. Compat.*, vol. 57, no. 3, pp. 405-417, Jun. 2015.

[11] A. Tatematsu, K. Yamazaki, and H. Matsumoto, "Lightning surge analysis of a microwave relay station using the FDTD method," *IEEE Trans. Electromagn. Compat.*, vol. 57, no. 6, pp. 1616-1626, 2015.

[12] J. Takami, T. Tsuboi, K. Yamamoto, S. Okabe, and Y. Baba, "FDTD simulation considering an AC operating voltage for air-insulation substation in terms of lightning protection level," *IEEE Trans. Dielectr. Electr. Insul.*, vol. 22, no. 2, pp. 806-814, Apr. 2015.

[13] A. Tatematsu, S. Moriguchi, and T. Ueda, "Switching surge analysis of an EHV air-insulated substation using the 3D FDTD method," *IEEE Trans. Power Del.*, vol. 33, no. 5, pp. 2323-2334, Oct. 2018.

[14] A. Tatematsu, "Development of a surge simulation code VSTL REV based on the 3D FDTD method," in *Proc. Joint IEEE Int. Symp. EMC and EMC Europe*, pp. 1111-1116, 2015.

[15] A. Tatematsu, "Overview of the three-dimensional FDTD-based surge simulation code VSTL REV," in *Proc. 2016 Asia-Pacific Int. Symp. on Electromagn. Compat.*, no. SS04-02, 2016.

[16] CUDA Zone: https://developer.nvidia.com/cuda-zone (Apr. 9th, 2019)

[17] Z. P. Liao, H. L. Wong, B. P. Yang, and Y. F. Yuan, "A transmitting boundary for transient wave analysis," *Scientia Sinica*, Series A, vol. 27, no. 10, pp. 1063-1076, 1984.

[18] M. P.-May, A. Taflove, and J. Baron, "FD-TD modeling of digital signal propagation in 3-D circuits with passive and active loads," *IEEE Trans. Microw. Theory. Techn.*, vol. 42, no. 8, pp. 1514-1523, Aug. 1994.

Coupling Characteristics Analysis of Low-altitude Targets over Half Space under HPEM Environments

Aote Zhang
College of Communication and Information Engineering
Xi'an University of Science and Technology
Xi'an, China
aotezhangunique@163.com

Le Cao
College of Electric and Control Engineering
Xi'an University of Science and Technology
Xi'an, China
caole@xust.edu.cn

Yuanguo Zhou
College of Communication and Information Engineering
Xi'an University of Science and Technology
Xi'an, China
zyg@xust.edu.cn

***Abstract*—Since the reflection effect of half-space, the interaction between high power electromagnetic (HPEM) environment and low-altitude targets is different from the free space case. The reflected wave of half-space would lead a second time energy burst when the target is located near ground. The electromagnetic field coupling into low-altitude targets over lossy half space is computed by Finite Difference Time Domain (FDTD) method. The bidirectional incident wave of the FDTD region is introduced by the Fresnel formula, Fourier Transform and the Equivalence Principle. The numerical results show that this method can provide a reliable technique for estimating the electromagnetic coupling effects on targets over half space under HPEM environments.**

Keywords—Electromagnetic coupling, half-space, low-attitude targets, FDTD

I. INTRODUCTION

HPEM susceptibility estimation of electronic devices is extremely important in electromagnetic compatibility (EMC). Damage or failures in electronic devices could lead to technical or financial disasters as well as injuries or the loss of life. The previous works about coupling characteristics analysis of targets under HPEM environment are carried out in free space [1-4], but the reflection effects cannot be ignored for low-altitude targets. For strong reflective medium, the reflected wave can be comparable to incident wave and it will produce a stronger coupling effect on target In this paper, the time domain waveform of the singly reflected wave can be obtained by Fourier and Inverse Fourier Transform method. Then both of the incident and reflected wave are introduced into Finite Difference Time Domain (FDTD) calculation region. Finally, the electromagnetic coupling energy is computed by the use of FDTD method. The numerical results show that this method can be used for the computation of electromagnetic field and energy coupling of low-altitude targets over half space under HPEM environments.

II. THE INTRODUCTION OF TOTAL INCIDENT WAVEFORM

The computational region of traditional FDTD approach is shown in Fig. 1. It contains target (Region I), part of half space interface (Region III) and the region between them (Region II).It can be seen that the requirement of time and memory will be greatly raised with the increase of the height of the target from the half space interface.

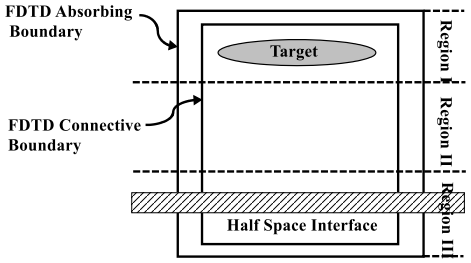

Fig. 1. The traditional FDTD computational domain

To decrease the memory requirement, a new computational region partitioning is proposed in Fig.2. This new computational region only contains the target, hence, the memory size and time consume are much smaller.

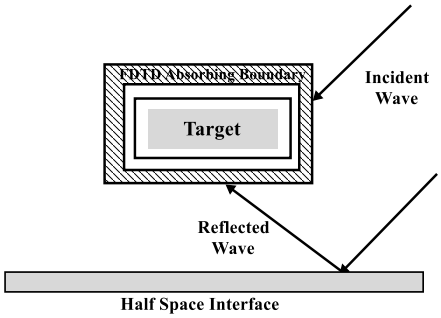

Fig. 2. The proposed FDTD computational domain

A. The introduction of directly incident wave

The incident wave is introduced by Total Field/Scattered Field (TF/SF) method [5]. The TF/SF formulation is based on the linearity of Maxwell's equations.The computation region can be zoned into two distinct regions: total fields region and scattered fields region. These two regions are separated by a virtual surface that serves to connect the fields in the two regions, and thereby generates the incident wave.

If the incident wave is only in total fields region, the equivalent surface electric and magnetic current on the connecting surface are defined as

$$\boldsymbol{J} = -\boldsymbol{e}_n \times \boldsymbol{H}_i \qquad \boldsymbol{J}_m = \boldsymbol{e}_n \times \boldsymbol{E}_i$$

where $\boldsymbol{e}_n$ is the outer normal vector of the virtual surface, $\boldsymbol{H}_i$ and $\boldsymbol{E}_i$ are the field values of incident wave.

B. *The introduction of reflected wave*

In this paper, the time domain waveform of reflected wave is obtained by Fourier Transform (FT) and Inverse Fourier Transform (IFT). First, frequency spectrum of incident wave can be acquired by FT. As we know frequency spectrum of the reflected wave is the product of the direct incident frequency spectrum and the reflection coefficient of the corresponding frequency. Then, the waveform of reflected wave can be obtained by IFT. The reflection coefficient is computed by Fresnel formula[6]. After obtaining both the direct incident wave and singly reflected wave, we can introduce them into the FDTD calculation region by TF/SF method. As shown in Fig.3 a bidirectional incident wave can be introduced into FDTD calculation region by setting two one-dimensional FDTD iterative expressions [7].

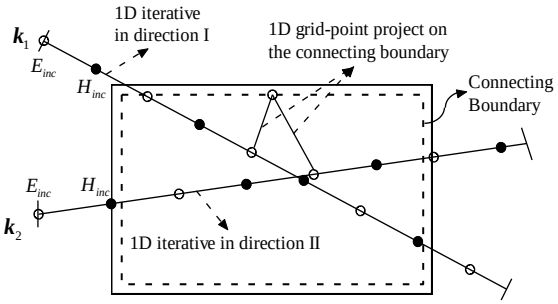

Fig. 3. Introduction of multi-direction incident wave

III. NUMERICAL RESULTS

To demonstrate the correctness of proposed method, we consider the reflected wave of a lossless medium ($\varepsilon_r = 4, \sigma = 0S/m$). The results of one-dimensional Maxwell's equation method [7] and proposed method are shown in Fig.4. It can be seen that they are in good agreement.

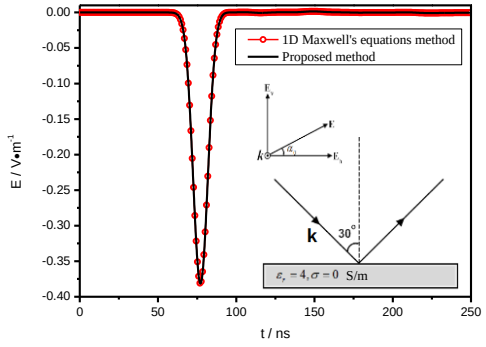

Fig. 4. The waveform of reflected wave

A. *Computer case with gap over lossy half-space*

A computer case with a small gap is shown in Fig.5. The incident wave is UWB pulse. The incident angle is $\theta_i = 30°, \varphi_i = 0°$ and the polarizing angle is $\alpha_0 = 0°$. The discrete grid in FDTD calculation is $\delta = 0.4cm$ and the time step is $\Delta t = 0.005ns$. The CPML absorbing boundary is employed in FDTD calculation. The two dimensional near field distribution patterns with different time step are shown in Fig.6.

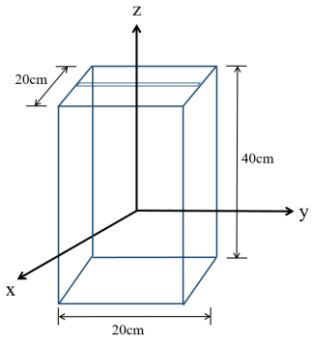

Fig. 5. Computer case with gap

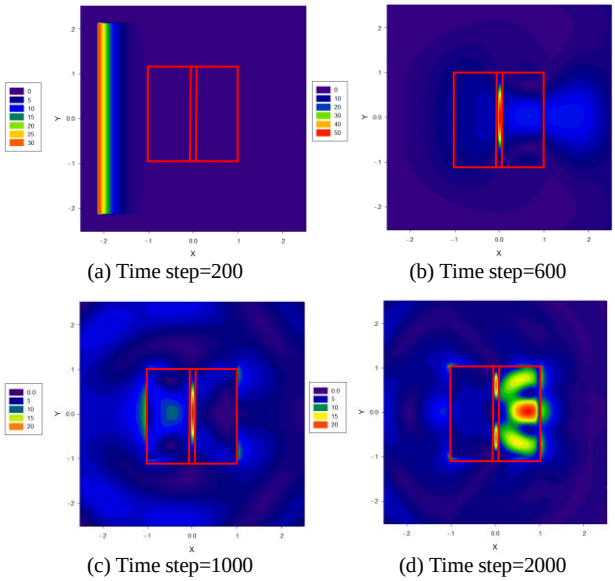

Fig. 6. Near field distribution pattern of *xoy* plane

B. *Radome over lossy half-space*

A three-dimensional radome is shown in Fig. 7. This shape of radome whose body is a super ellipsoid geometry can reduce the backward RCS caused by missile warheads. The structure behind the parabolic antenna is a circle metal plane has a radius of 0.52m. The radome is located 20m above the ground with the subsurface characterized by $\varepsilon_r = 10, \sigma = 0.01S/m$. The incident wave is UWB pulse, the incident angle is $\theta_i = 225°, \varphi_i = 90°$ and the polarizing angle is $\alpha_0 = 0°$. The discrete grid in FDTD calculation is $\delta = 0.4cm$ and the time step is $\Delta t = 0.005ns$. The CPML absorbing boundary is employed in FDTD calculation. The two dimensional near field distribution patterns with different time step are shown in Fig.8.

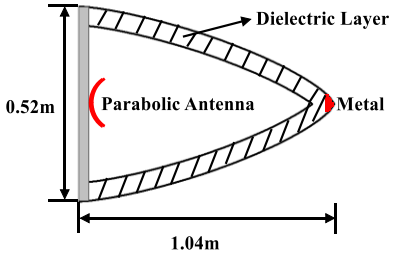

Fig. 7. Three-dimensional radome

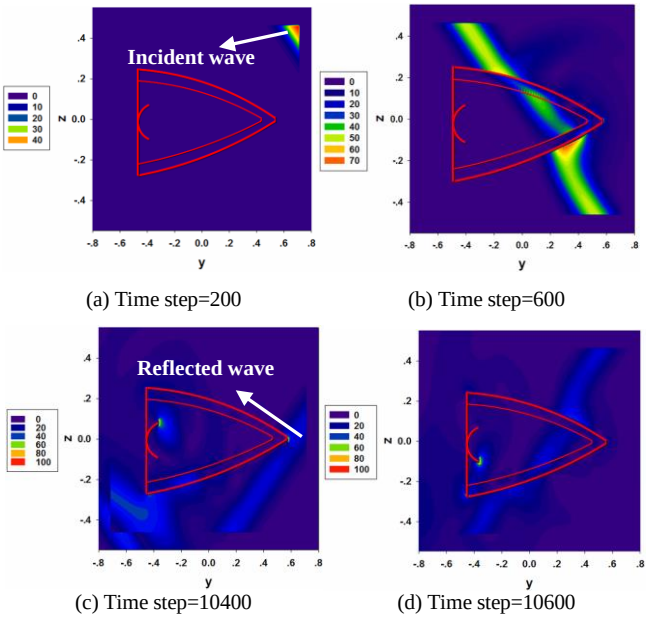

(a) Time step=200 (b) Time step=600

(c) Time step=10400 (d) Time step=10600

Fig. 8. Near field distribution pattern of *yoz* plane

IV. ACCURACY VERIFICATION

In order to prove the correctness of the proposed method, the traditional half-space FDTD method and the proposed method are used to calculate the field strength near the target. Target is a dielectric cube with a side length of 0.16m($\varepsilon_r = 4$),The lower half space is a lossy medium, and three observation points are set inside the calculation area. Two methods are used to calculate the field value of the observation point.

The splitting grid of FDTD is $\delta_x = \delta_y = \delta_z = 8mm$, and the time interval is $\Delta t = 0.005ns$ .The absorption boundary nodes of CPML are: -53:53 (x direction), -53:53 (y direction), -93:93 (z direction), and the connection boundary nodes are: -43:43(x direction), -43:43 (y direction), -83:83 (z direction). The coordinates of the three observation points are respectively $E_{P1}(0\text{m}, 0.16\text{m}, 0.16\text{m})$, $E_{P2}(0\text{m}, -0.16\text{m}, 0.16\text{m})$, $E_{P3}(0\text{m}, 0\text{m}, 0.16\text{m})$. It can be seen from the Fig.9. That the results of the proposed method agree well with the results of the traditional half-space FDTD method, which proves the correctness of the proposed method.

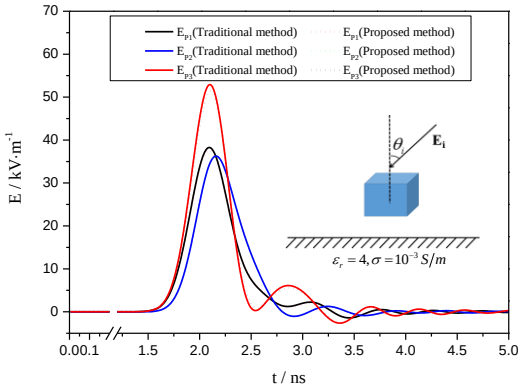

Fig. 9. Near field value of a dielectric cube above a half space

V. CONCLUSION

In this paper, a new method which has a combination of FDTD algorithm and semi-analytic method of introduction of incident wave is proposed. The near field of low-altitude targets over lossy half space under HPEM environment are computed.

REFERENCES

[1] Liang Zhou, Wen-Yan Yin, Weifeng Zhou, and Liang Lin, "Experimental Investigation and Analysis of the LDMOS FET Breakdown under HPM Pulses," *IEEE Trans. Electromagn. Compat.* , vol. 55, no. 5, pp. 909-916, Oct. 2013.

[2] Marco Leone, "Radiated Susceptibility on the Printer-Circuit-Board Level: Simulation and Measurement," *IEEE Trans. Electromagn. Compat.* , vol. 47, no. 3, pp. 471-478, Oct. 2005.

[3] Song Shu-Ting, Jiang Hong, and Huang Yu-Lan, "Simulation and Analysis of HEMP Coupling Effect on a Wire Inside an Apertured Cylindrical Shielding Cavity," *Appl. Comput. Electrom.* , vol. 27, no. 6, pp. 505-515, Jun 2012.

[4] Mats G. Backstrom, and Karl Gunnar Lovstrand, "Suceptibility of Electronic Sytems to High-Power Microwaves: Summary of Test Exprience," *IEEE Trans. Electromagn. Compat.* , vol. 46, no. 3, pp. 396-403, Aug. 2004.

[5] Y.N.Jiang, D. B. Ge, and S. J. Ding, "Analysis of TF/SF Boundary for 2D-FDTD with Plane P-Wave Propogation in Layered Dispersive and Lossy Media" *Prog. Electromagn Res*,vol. 83, pp. 157-172, 2008.

[6] Jin Au Kong, *Electromagnetic Wave Theory*. New York: John Wiley, 1986.

[7] Allen Taflove, and Susan C. Hagness, *Computational Electrodynamics: The Finite-Difference Time-Domain Method*. Norwood, MA: Artech House, 2005.

Medium-Voltage Transformers under EMP-Conditions

Armin W. Kaelin
EMProtec AG
CH-8450 Andelfingen, Switzerland
armin.kaelin@emprotec.ch

Markus Nyffeler
Armasuisse Science and Technology
CH-3602 Thun / Switzerland
markus.nyffeler@armasuisse.ch

Carlos Romero
Armasuisse Science and Technology
CH-3602 Thun / Switzerland
carlos.romero@armasuisse.ch

***Abstract*—This paper describes experiments to investigate the behavior of medium-voltage transformers in the case of early-time (E1) and intermediate-time (E2) HEMP. In order to consider also the worst case, both common-mode and differential-mode pulses were injected into the high-voltage side of two typical medium-voltage transformers having a transmission ratio of 70:1.**

Keywords—HEMP, medium-voltage transformer

I. Introduction

The electric power grid is one of the most critical parts of all critical infrastructures. No wonder, that there is an increasing interest in the resilience of the power grid against Electromagnetic effects such as High-altitude Electro-Magnetic Pulse (HEMP) [1].

Depending on the transmission distances the power grid uses different voltage levels: The high voltage grid (50 kV up to 1 MV or higher) is preferably used for very long distances (hundreds to thousands of km), the medium voltage grid (typically 10 to 50 kV) is used for medium distances, and the low voltage grid (typically 400/230 VAC) is used to branch the distribution into customer premises. The adaption between the voltage levels is accomplished by transformers.

Nowadays most HEMP-protected facilities are protected on the low voltage side only. Since the power grid can involve very long line length we have to consider all components of HEMP [2], namely the early-time (E1), the intermediate time (E2) and the late time (E3) component of HEMP. According to Table I on the low voltage side the E1 and the E2 components of HEMP are important, while E3 coupling is negligible. This raises an important question: what is the role of transformers between different voltage levels in terms of HEMP survivability and HEMP transmission to the lower voltage side? Table II gives some preliminary estimation how HEMP might threaten high-voltage transformers or medium-voltage transformers. On the high-voltage side E3 may be the biggest threat due to the length of high-voltage lines. Medium-voltage transformers seem to be more in danger by the high voltages expected by E1, which might exceed the dielectric strength of the transformers insulation.

In the recent years we observe a considerable increase in decentralized electric power production. This fact together with emerging smart-grid technologies increases the importance of the medium voltage part of electric power grids. So far HEMP-protection is mostly realized on low voltage level. However, for the resilience of the power grid it is important to know, how medium-voltage transformers behave under HEMP-conditions. Some results of experiments with Steep Front-Short Duration (SFSD) Surges on single-phase 25 kVA transformers are published [3]. In this work we investigate the behavior of typical three-phase medium-voltage transformers when E1 and E2 pulses of conducted [4] HEMP currents hit a transformer either in common or in differential mode.

TABLE I. HEMP-Coupling into different Grid levels

HEMP-Component	Electric Power Grid Levels		
	High Voltage	*Medium Voltage*	*Low Voltage*
E1	++	++	++
E2	++	++	- to +
E3	++	-	--

++ very strong coupling; + strong coupling; - some coupling; -- coupling negligible

TABLE II. HEMP-Threats Estimation for Transformers

HEMP-Component	Transformer Type	
	High to Medium Voltage	*Medium to Low Voltage*
E1	-	++
E2	+	- to +
E3	++	-

++ dangerous threat; + possibly dangerous; - low threat; -- negligible threat

II. DUT's and Test Setup

A. Devices Under Test (DUT)

Fig. 1. DUT's: Oil-insulated medium-voltage transformer T1 (left) and resin-insulated medium-voltage transformer T2 (right)

Two medium-voltage three-phase transformers, each for 16 kV to 400/230 V transformations, as they are commonly used in Switzerland, are the DUT's for our experiments: T1 is an oil-insulated 65 kVA transformer, whereas T2 is a resin-insulated 250 kVA transformer (see Fig. 1).

Both transformers have a winding ratio of approximately 70:1 and have Dyn5 windings. This means that the primary side has Delta windings (D) and the secondary has y-windings (y) with a neutral (n) that is usually locally grounded. The number 5 means that the lower voltage has a phase lag of 5 times 30° with respect to the primary voltage.

The transformers are not new, but fully functional. Their behavior has been tested by the so-called FRA-method (Frequency Response Analysis) [5], which shows that the windings of the transformers are OK and that such transformers are capable to transmit frequencies up to several MHz.

B. *Test Setup*

Before we describe the test setup let's have a look at the equivalent circuit of a transformer. An ideal transformer just changes the voltage ratio by a:1, a typical real transformer has an equivalent circuit that consist of a real transformer a:1 and some lumped elements shown in Fig. 2.

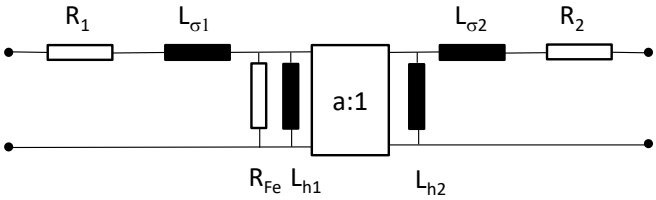

Fig. 2. Equivalent circuit of a typical transformer with ratio a:1

For the purpose of our HEMP experiments, where E1 is a high frequency phenomenon, we have to consider also the stray capacitances between primary and secondary windings $C_{21} = C_{12}$ and the capacitances between primary winding and the iron core C_{10} and between secondary winding and the iron core C_{20}. This results in the equivalent circuit shown in Fig. 3.

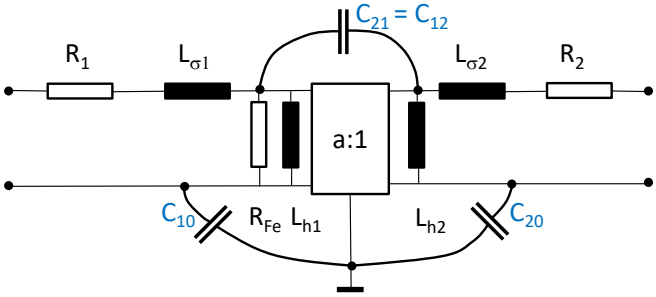

Fig. 3. Equivalent circuit of a transformer with stray capacitances between windings and between windings and iron core

To investigate the transmission of a pulsed signal from the high-voltage side to the low-voltage side we inject pulses between two points of the primary windings both in common mode and in differential mode. During all experiments the transformers were unpowered. Although HEMP disturbances are primarily coupled as common-mode currents in reality it could happen, that due to asymmetries or due to flash-overs the common mode currents are converted into a differential mode pulse. Therefore we investigate both common mode (Fig. 4) and differential mode (Fig. 5) pulses.

As test pulses three different pulse shapes are used: 1) 5/50 ns pulse (EFT electric fast transient), 2) 8/20 µs pulse (lightning surge) and 3) 1.5/5000 µs (E2) pulse. These pulses represent typical transients expected for medium-voltage transformers.

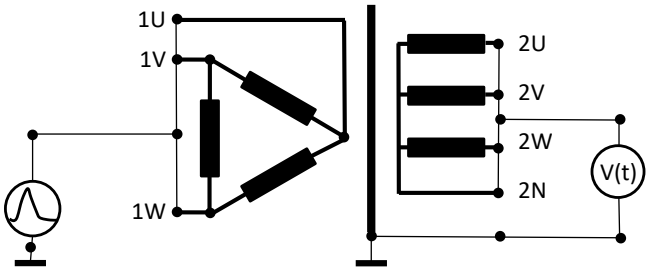

Fig. 4. Principle of common-mode injection into the primary winding of the transformer and measurement on the secondary side

In common mode an ideal transformer would not couple anything onto the secondary winding. However, real transformers have stray capacitances as shown in Fig. 3 and therefore we expect some coupling especially for high frequencies or fast pulses.

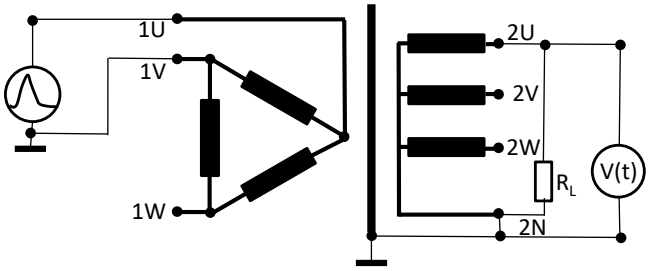

Fig. 5. Principle of differential-mode injection into the primary winding of the transformer and measurement on the secondary side

In differential mode we expect both capacitive coupling and coupling according to the winding ratio of the transformer, which is expected to be frequency dependent.

III. Measurement Results

A. *Effect of capacitive coupling*

In a first step the capacitances between the windings and between a winding and the iron core are measured by using a LRC-Meter, which can measure the capacitance at different frequencies, namely 100 Hz, 1 kHz, 10 kHz and 100 kHz. In this frequency range the values are relatively stable and are in the range of 1 nF for T1 for the inter-winding capacitance and the capacitance of the high-voltage side to the iron core. The capacitance between the low-voltage winding to the iron core is around 2 nF, which is approximately twice as high as the other values. This is due to the geometry of the transformer, because the low-voltage winding is located closer to the iron core. The capacitances of transformer T2 are similar as for T1, but the values are between 400 pF and 1200 pF and therefore lower by a factor of two compared to T1. The reasons are likely to be the geometry and the different dielectric constant of the insulation material.

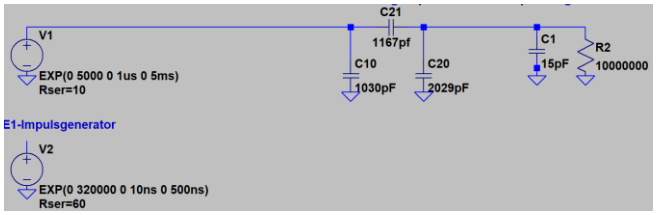

Fig. 6. LTSpice simulation of the capacitive divider formed by the winding capacitances and the voltage probe.

Fig. 6 shows the schematic of the capacitive divider formed by the winding capacitances in a LTSpice simulation The ratio is approx. 2.8:1, which means that nearly one third of the fast E1 HEMP amplitude will be transmitted onto the secondary side even in the common mode.

B. Common Mode Injection Results

About one third of the peak amplitude of fast common-mode pulses such as E1 is transmitted to the secondary side (Fig. 7), which is in good agreement with the expectations from the capacitive divider (Fig. 6).

Fig. 7. Fast Input pulse (green) and voltage on secondary side (purple)

Common-mode E2 pulses are differentiated by the capacitive divider. This blocks the relatively long E2 pulse. However, the peak during the rising portion of the pulse is transmitted by the ratio of the capacitive divider.

C. Differential Mode Injection Results

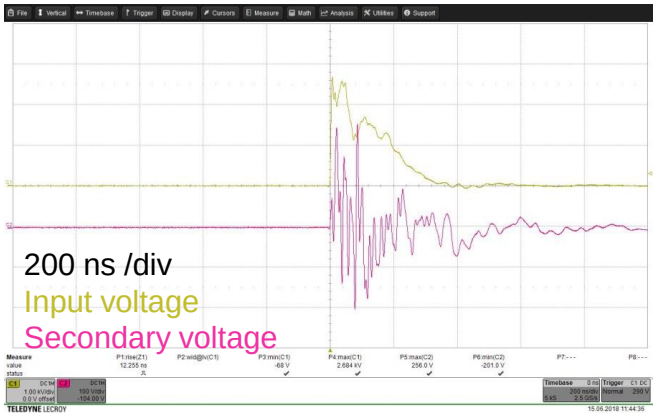

Fig. 8. The Differential-mode transmission of fast pulses is dominated by capacitive coupling and is much higher than would be expected by the transformers winding ratio.

In differential mode we expect a transmission by the transformers ratio of 70:1. In reality we found that much more, approximately one third of the input amplitude, is transmitted to the secondary side of the transformer. Again this is due to the capacitive effects.

The good news is that the relatively slow and long duration E2 pulse is transmitted by the transformer ratio 70:1 as expected. The E2 pulse is differentiated by the capacitive divider and the long duration pulse is truncated. This makes the medium-voltage transformer a useful part of protection against E2 pulses.

IV. Summary of the Results

Medium-voltage transformers transmit up to one third of the amplitude and the pulse energy of fast pulses such as an early-time HEMP E1 to the secondary side. This is true regardless whether E1 is coupled in common-mode or in differential-mode. This coupling is due to the effects of stray capacitances and is considerably higher than would be expected by the transformer winding ratio of 70:1 in differential mode. However, the slower but energy-rich E2 pulses are widely blocked in common-mode. In differential mode the E2 pulse voltage is transmitted by the winding ratio of the transformer. Thus the E2 residual voltage on the secondary side of a medium-voltage transformer is reduced by 70:1. The E2 residual voltage on the secondary side is lower than the operating voltage and therefore safe even for sensitive equipment. This is a very important feature, since HEMP-filters on the low-voltage side cannot block E2 pulses to sufficiently low levels because of the high in-band energy.

V. Conclusions

Medium-voltage transformers cannot block fast E1 pulses due to capacitive coupling between primary and secondary side. However, medium-voltage transformers play an important role to protect the low-voltage power supply against E2. Currently not sufficiently investigated is whether the insulation of a medium-voltage transformer can survive the relatively high voltage pulses of an early-time HEMP E1. In order to investigate this we will have to take into account the effect of the medium-voltage varistors often used to protect underground cables and transformers against lightning.

References

[1] U.S. Department of Energy, «Joint Electromagnetic Pulse Resilience Strategy», July 2016, https://www.energy.gov

[2] IEC 61000-2-9, «Part 2 Environment – Description of HEMP environment – Radiated disturbance», IEC International Electro-technical Commission, Geneva, Switzerland, https://www.iec.ch

[3] C.H. Eichler ; J.R. Legro; P.R. Barnes, «Experimental determination of the effects of steep front-short duration surges on 25 kVA pole mounted distribution transformers», April 1989, IEEE Transactions on Power Delivery (Volume: 4, Issue 2)

[4] MIL-STD-188-125-1, «High-Altitude Electromagnetic Pulse (HEMP) Protection for Ground-Based C4I Facilities Performing Critical, Time-Urgent Missions», Department of Defense Interface Standard, 17 July 1998, USA.

[5] René Martin Wimmer, «Die Ermittlung der Übertragungsfunktion von Grosstransformatoren mittels On- und Offline-Messungen», Institut für Energieübertragung und Hochspannungstechnik, Universität Stuttgart, 02.11.2009

Design and simulation of a 300kV Pulse Generator for a Bounded-wave Simulator

ZHANG Beizhen
Science and Technology on High Power Microwave Laboratory
Institute of Applied Electronics, CAEP
Mianyang, China
99477228@qq.com

SONG Falun
Science and Technology on High Power Microwave Laboratory
Institute of Applied Electronics, CAEP
Mianyang, China
emplasma@ustc.edu

Gan Yanqing
Science and Technology on High Power Microwave Laboratory
Institute of Applied Electronics, CAEP
Mianyang, China
1014939772@qq.com

XIE Ping
Science and Technology on High Power Microwave Laboratory
Institute of Applied Electronics, CAEP
Mianyang, China
269094848@qq.com

QIN Fen
Science and Technology on High Power Microwave Laboratory
Institute of Applied Electronics, CAEP
Mianyang, China
qinfen791@163.com

***Abstract*—A high voltage pulse generator for a bounded-wave simulator was established. The principles, basic structures and design methods were elaborated, and a simulation was conducted, the results of which showed that a output voltage of no less than 300 kV could be attained, and the rising edge, pulse width meet the standards. Subsequently, the electric field waveform in the radiator was also simulated, the results consistent with the measured waveform were obtained through simulation, and the accuracy of the simulation was confirmed. The simulation results and design methods in this paper can provide useful help for the design of bounded-wave simulator.**

Keywords—NEMP, bounded-wave simulator, peaking circuit, high-voltage pulse generator

I. INTRODUCTION

In nuclear explosion, lots of shock waves, heat radiation, nuclear radiation and electromagnetic pulses are generated. When a nuclear explosion occurs at a high altitude (above 30 km), the electromagnetic pulse is almost the only nuclear explosion effect. For electronic systems with anti-nuclear requirements, to assess their survivability, the bounded wave EMP simulator is one of the basic tools.

US Department of Defense in 1999 issued a military standard MIL-STD-461E, in which the standard waveform of nuclear electromagnetic pulse was defined as double exponential waveform with a rise time of 2.3ns ±0.5ns, and a FWHM of 23ns ±5ns, of which the field strength is no less than 50kV/m. The specific expression is:

$$E(t) = E_0 k(e^{-\alpha t} - e^{-\beta t}) \quad (1)$$

Where E_0 is the peak field strength, no less than 50kV/m; k the correction coefficient, k=1.3, α, β, the parameters characterizing the rising and falling edges of the pulse, $\alpha=4\times10^7$, $\beta=6\times10^8$.

The bounded-wave simulator can be roughly divided into a pulse source, a radiator, and a terminal load. The radiator is usually composed of a front transition section, a parallel section, and a rear transition section (some radiators do not include parallel sections), and the test equipment is placed in a parallel section for testing. The electric field waveform of the working area must meet the standard. The actual generated waveform, is affected by many factors, such as the form of the terminal load, the rising transition section, the inclination of the falling transition section, and the environment around the radiator. [1-4]

In order to provide a high-voltage pulse generator capable of generating the above standard waveform to the bounded-wave EMP simulator, and to obtain a standard waveform in the radiator, the pulse source design and waveform simulation research were carried out.

II. DESIGN OF THE PULSE GENERATOR

A. Working principles

The pulse generator for the bounded-wave simulator consists of three main components, a Marx generator, a peaking capacitor, and a main switch (peaking switch). The high voltage output of the pulse generator is connected to the radiator and the terminal load. The equivalent circuit of the entire bounded-wave simulator with load is shown in Fig. 1.

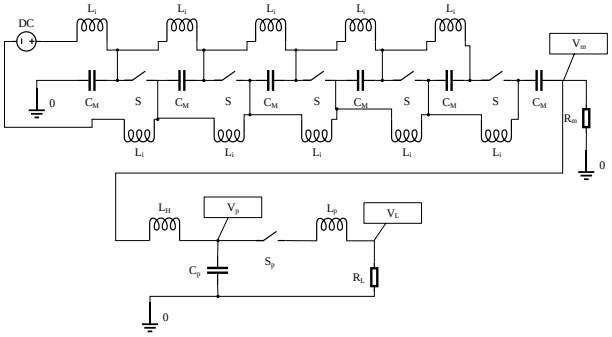

Fig. 1. Circuit of the pulse generator

In Fig.1, C_M is the stage capacitance of the Marx generator, L_i, the isolated inductance, S, the Marx stage switch, R_m, the ground (measurement) resistance, L_H, the resonant inductance, C_p, the peaking capacitance, S_p, the peaking switch, L_p, the peaking loop inductance, and R_L, the matching load. Entire circuit can be divided into two parts, Marx circuit and peaking circuit. The peaking circuit contains a peaking capacitor, a main switch, an inductance of the peaking circuit, and a matching load. The standard waveform is mainly generated by the peaking capacitor.

B. *Design of the peaking circuit*

For a double exponential pulse, its waveform parameters α and β are actually related to the eigenvalues of the RCL second-order circuit. For the standard waveform of nuclear electromagnetic pulse, the values of α and β has been clearly defined. If the matching impedance is determined, the value of the peaking capacitor and the inductance can be precisely expressed.

$$C_p = \frac{\alpha+\beta}{\alpha\beta} R^{-1} \tag{2}$$

$$L_p = (\alpha+\beta)^{-1} R \tag{3}$$

For the standard waveform, $\alpha = 4 \times 10^7$, $\beta = 6 \times 10^8$; In our bounded wave simulator, the matching load R = 160 Ω, then, C_p = 167pF, Lp = 250 nH.

C. *Design of the Marx generator*

The Marx generator is designed to 5 stages, with isolate inductance, using positive and negative bilateral charging simultaneously. After the Marx generator is erected, the Marx generator charges the peaking capacitor before the peaking switch is closed. According to preliminary estimates, the Marx generator's stage capacitance needs to greater than 1nF. Because of the existence of isolation inductance, capacitance leakage current, grounding resistance (measuring resistance) and other factors, better to simulate the circuit during design.

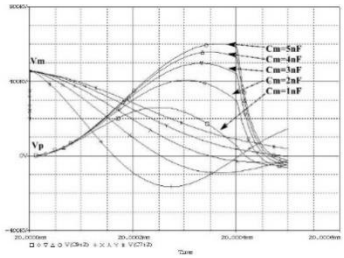

Fig. 2. Charging efficiencies under different values of stage capacitance in Marx

In simulation, select the isolation inductance L_i = 50uH, the grounding resistance R_m = 2kΩ, the peaking capacitance C_p = 167pF, the Marx generator stage capacitor C_M varies from 1nF to 5nF, and the voltage monitoring point is located on the V_m and V_p in Fig. 1. The simulation results are shown in Fig. 2, and the charging efficiency of the peak capacitor can be seen. It can be seen that when the stage capacitor is around 3nF, the charging efficiency of Marx to the peaking capacitor is greater than 1.

In design, a peaking capacitor of 180 pF, a stage capacitance of 5 nF in Marx generator were chosen. In simulation, the waveform obtained on the load is shown in Figure 3. In Fig. 3, the peak time $t_2 - t_0$ =5.0 ns; the FWHM $t_3 - t_1$ =24 ns. It can be seen that our parameter selection is feasible.

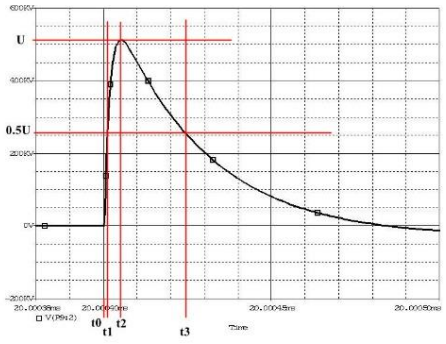

Fig. 3. Output wave of simulation

D. *Final construction*

The complete set of pulse generator we developed is shown in Figure 4. The peaking switch we designed worked in SF_6, the working pressure of it is about 5 atm. The breakdown voltage can be adjusted by both the working pressure and the electrode gap.

The working process of the whole set of equipment is as follows: 1. The DC power source charges the Marx generator to reach a predetermined voltage; 2. Trigger source Working, Marx erected; 3. The Marx generator begins to charge the peaking capacitor. 4. When the maximum charging voltage is reached, the peaking switch occurs self-breakdown.

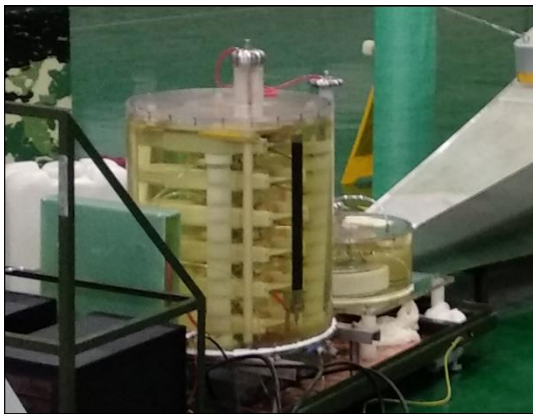

Fig. 4. Pulse generator

III. SIMULATION OF WAVEFORM IN RADIATOR

A. *model of bounded-wave simulator [5-8]*

Our radiator is constructed of metal plates. The approximate dimensions are shown in Figure 5. The equivalent impedance is about 160 Ω. The terminal load is connected in parallel by three 480 Ω resistors.

Model the radiator according to dimensions in Fig. 5, and some field strength detection points are arranged in the parallel section of the radiator, in the middle section, as shown in Fig.6. Set the peak time of the feed waveform to about 1.2ns, and the leading edge is about 800ps. See Fig. 7.

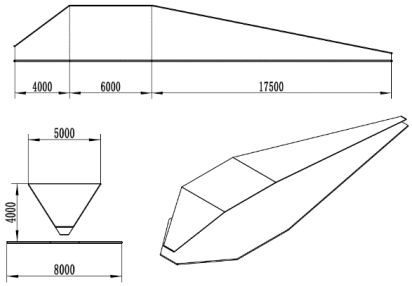

Fig. 5. Dimensions of the radiator

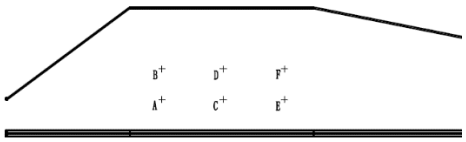

Fig. 6. Setup of probes

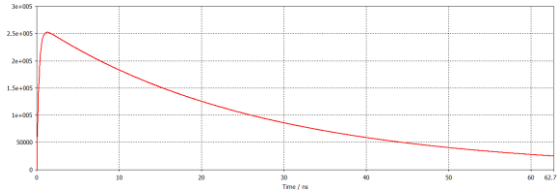

Fig. 7. Feed wave with 1.2ns peaking time

B. *Simulation results*

Focus on the waveforms of monitoring points A, C, and E, as shown in Figure 8. It can be seen that the rising edge of the waveform is a little bit slower than feed wave and the oscillation is induced. As for point E, rise time is about 2.5ns. Therefore, it can be seen that the peaking loop inductance should be strictly controlled in the design.

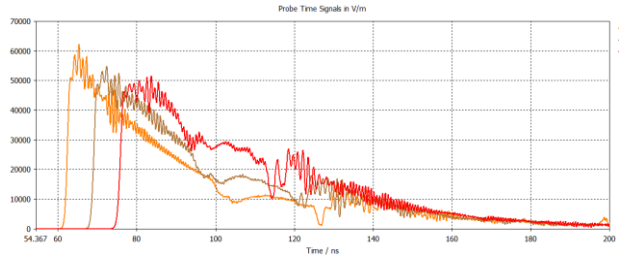

Fig. 8. Waveform on probes

Fig.9 is the actual waveform measured in radiator. In Fig 9, automatically read by oscilloscope, the rising edge of the pulse is 2.037ns, FWHM, 20.45 ns. It can be seen that the simulated waveform has a certain degree of accuracy. In the simulation, more accurate simulation results can be obtained by considering the surrounding environment of the laboratory, such as walls and floors.

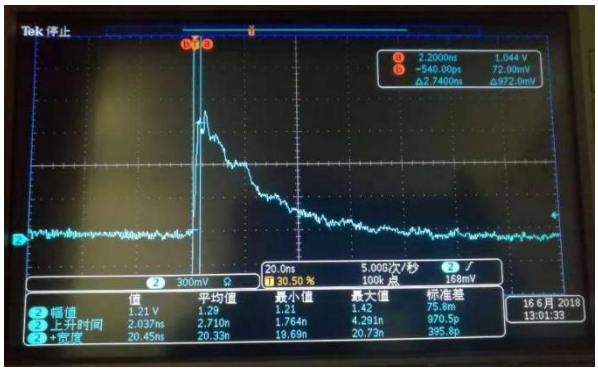

Fig. 9. Measurement of Electric field

IV. CONCLUSION

A 300kV high-voltage pulse generator used in a boundary-wave EMP simulator was designed. Theoretical analysis, simulation and experimental research, were conducted. Result shows, a double exponential waveform with a leading edge of about 2 ns and FWHM of 20.45 ns could be attained. The peaking loop inductance should be reduced so that the pulse generator is able to produce a waveform with short rise time.

REFERENCES

[1] BI Xiaoliang. Inveistigation on Electromagnetic Pulse Simulator and Its Control. Harbin: Harbin University of Science and Technology, 2009.毕晓亮. 电磁脉冲模拟器及其控制研究. 哈尔滨：哈尔滨理工大学，2009.

[2] SONG Changqi. Correlate Components Design and Experimental Features Research for Electromagnetic Pulse Simulator. Harbin: Harbin University of Science and Technology, 2014.宋长奇. 电磁脉冲模拟器相关部件设计及实验特性研究. 哈尔滨：哈尔滨理工大学，2014.

[3] SUN Beiyun, ZHOU Yan, ZHENG Zhenxing, ZHU Min, LIANG Jian, CAO Peng. The Development of High Voltage Pulse Generator for Bounded-wave EMP Simulator. High Power Laser and Particle Beams, 2000, 12(4): 505-508.孙蓓云，周晏，郑振兴，祝敏，梁坚，曹鹏. 有界波 EMP 模拟器脉冲高压源. 强激光与粒子束， 2000, 12(4): 505-508

[4] XIE Linshen, JIA Wei, GUO Fan, CHEN Weiqing, ZHANG Guowei, WANG Haiyang, et al. High Power pulse generator for bounded-wave EMP simulator. Journal of Terahertz Science and Electronic Information Technology, 2016, 14(6): 982-984.谢林燊，贾伟，郭帆，陈维青, 张国伟, 王海洋, 等. 用于有界波模拟装置的高功率窄脉冲源研制. 太赫兹科学与电子信息学报，2016, 14(6): 982-984.

[5] PAN Xiaodong, WEI Guanghui. Research on Terminal Load of Bounded-wave Simulator. Journal of Microwaves: 2007, 23(2):63-66. 潘晓东，魏光辉. 有界波模拟器终端负载设计研究. 微波学报，2007, 23(2):63-66.

[6] HONG Rentang, MA Rupo, CHEN Hailin, SHI Lihua. Simulation of Large Bounded Wave Simulator for Wire Grating. EMC Simulation: 2017, 2:59-63.洪仁堂，马如坡，陈海林，石立华. 大型线栅有界波模拟器仿真研究. 电磁仿真，2017, 2:59-63.

[7] DUAN Zemin, HAO Fengzhu, ZHANG Song, ZHU Bo, YAO Zhicheng. Waveform simulation and experimental study of bounded-wave simulator. Transducer and Microsystem Technologies, 2018, 37(2): 76-79.段泽民，郝凤柱，张松，朱博，姚志成. 有界波模拟器波形仿真与实验研究. 传感器与微系统，2018, 37(2): 76-79

[8] DU Leiming, XIE Yanzhao, WANG Shaofei. Simulation computation and analytic modification of characteristic impedance of parallel-plate transmission line. High Power Laser and Particle Beams, 2015, 27(8): 83201.杜雷鸣， 谢彦召， 王绍飞. 平行板传输线特性阻抗仿真计算及解析修正. 强激光与粒子束， 2015, 27(8): 83201.

Effects of GIC on Winding Currents of Single Phase UHV Autotransformer with Load

Bing Li
State Key Laboratory of Alternate Electrical Supply System with Renewable Energy Sources
North China Electric Power University
Beijing, China
102206

Zezhong Wang
State Key Laboratory of Alternate Electrical Supply System with Renewable Energy Sources
North China Electric Power University
Beijing, China
102206

Mingyang Li
State Key Laboratory of Alternate Electrical Supply System with Renewable Energy Sources
North China Electric Power University
Beijing, China
102206

Ke Liu
State Key Laboratory of Alternate Electrical Supply System with Renewable Energy Sources
North China Electric Power University
Beijing, China
102206

Mengzhen Xuan
State Key Laboratory of Alternate Electrical Supply System with Renewable Energy Sources
North China Electric Power University
Beijing, China
102206

Suxin Guo
State Key Laboratory of Alternate Electrical Supply System with Renewable Energy Sources
North China Electric Power University
Beijing, China
102206

***Abstract*—DC bias occurs when GIC flows into transformer windings. Time-domain field-circuit coupled finite element model has been widely used to calculate the electromagnetic quantities of transformers under DC bias. The long process of transformer inrush is extremely time consuming, especially when comes to UHV transformer, which has less resistance and larger inductance. Besides, miscalculations usually occur as the component of DC bias can be easily neglected by the extra high AC voltage in the simulation. In this paper, a fast solution by series resistance and voltage compensation method (SRVCM) is utilized, by which method, precise winding current of UHV autotransformer with load are obtained under various DC bias. The correctness of the model is verified by experiment data of a scale-reduced transformer.**

Keywords—DC bias, time-domain field-circuit coupling, SRVCM, UHV autotransformer, load, scale-reduced transformer model.

I. INTRODUCTION

Ultra-high voltage (UHV) autotransformer is one of the key equipment of UHV transmission system, their safe and stable operation is directly related to the safety of UHV transmission system. UHV transformers mostly use self-coupling structure, and the transformer group composed of the single-phase autotransformer has less tolerance to the dc-bias current[1-2]. The main effect of a dc-bias current flowing into a transformer is the asymmetric magnetic core saturation during a sinusoidal half-period (half-cycle saturation), as a result, a series of problems occur, such as the serious distortion of excitation current, increased reactive power absorption, partial overheating and increase of vibration and noise [3-4]. Thus, precise and in-depth analysis of dc-bias for UHV autotransformers is necessary for the safe operation of equipment and transmission system.

Nowadays, many in-depth research and analysis have been studied on the transformer dc-bias problem by simulation [5-6]. Finite Element Method (FEM) are widely used in the analysis of simulations. However, a FEM for the simulation can be extremely time-consuming with the massive mesh and long transient state [7], especially in the calculation of UHV autotransformer, consists of large inductance and small resistance, which means a long transient process.

Due to the large inductance to small resistance as well as the large 1000 kV AC voltage to small dc components in UHV autotransformer, a long transient process of minimal time step and error criterion is required for avoiding data inundation by conventional calculation [8]. This paper proposes a new fast solution of excitation current in UHV autotransformer, by making good use of series resistance and voltage compensation method (SRVCM), the proposed method can shorten the transient process and obtain the precise value with acceptable time and memory consumption.

II. FIELD-CIRCUIT MODEL OF UHV AUTOTRANSFORMER

The time-domain field-circuit coupling finite element model is wildly used to calculate electromagnetic quantities of transformer. The dynamic inductance and current can be obtained by magnetic field and circuit model, respectively [9].

A. Magnetic field model

The capacity of UHV autotransformer has reached 1000 MVA, in order to reduce the capacity of each column, single-phase four-limb or single-phase five-limb are mainly adopted. This paper focus on single-phase four-limb UHV autotransformer, which consists of two main limbs and two side limbs, the two main limbs are in parallel. There are low voltage winding, public winding and series winding from inside to outside, respectively. It has to be noted that the tank, the tie bars and the clamping plate which are made of massive steel and carry eddy currents are neglected. The core and the tank shielding are laminated and are assumed to be free of eddy currents. The eighth magnetic model is shown in Fig. 1 (a).

The magnetic field solution based on the edge finite element method is utilized for its good accuracy of

boundary problem of high permeability material [8]. The edge finite element method uses vector magnetic potential A and field equation according to Maxwell can be obtained

$$\nabla\times\frac{1}{\mu}\nabla\times\boldsymbol{A}=\boldsymbol{J} \tag{1}$$

Where, μ is permeability of magnetic material, J is current density.

Edge element interpolation function is followed

$$A=\sum_{k=1}^{n}M_n(\mathrm{x},\mathrm{y},\mathrm{z})A_n \tag{2}$$

Where, $\{M_\mathrm{n}, \mathrm{k}=1, 2, \dots, n\}$ is basis sequences, n is the total number of edge.

Applying the Green theorem, the Galerkin weighted residual equation is obtained as follows

$$\iiint_V\frac{1}{\mu}(\nabla\times M_m)(\nabla\times M_n)A_n\mathrm{d}V=\iiint_V M_nJ\ \mathrm{d}V \tag{3}$$

Where, M_m is basis sequences of the same weight and basis function, with the known current density J, which is supposed be obtained by circuit model, magnetic vector A can be calculated by substituting the weight function in equation (3).

B. Circuit model

According to the connection mode, the circuit diagram of UHV transformer is shown in Fig. 1 (b).

Flux linkage equation based on the circuit as follows

$$\psi=L_s(t,i)i \tag{4}$$

Where, ψ is flux linkage, i is winding current, L_s is static inductance.

Derivation of transient differential equations of the circuit is

$$u=(\mathrm{d}\frac{L_\mathrm{s}}{\mathrm{d}i}i+L_s)\frac{\mathrm{d}i}{\mathrm{d}t}=L_D(i)\frac{\mathrm{d}i}{\mathrm{d}t} \tag{5}$$

Where, u is voltage source, L_D is dynamic inductance, which is supposed obtained by magnetic field model.

The equation of the circuit is shown as follows

$$u_i=\sum_{ij}(R+r_i)i_i+L_{ii}\frac{\mathrm{d}i_1}{\mathrm{d}t}+M_{ij}(\frac{\mathrm{d}i_i}{\mathrm{d}t}+\frac{\mathrm{d}i_j}{\mathrm{d}t}) \tag{6}$$

Then the differential equation matrix with imposed DC-bias current is obtained as

$$\begin{bmatrix}L_1+M_{12} & L_2+M_{12} & M_{13}+M_{23}\\ M_{12} & L_2 & M_{23}\\ M_{13} & M_{23} & L_3\end{bmatrix}\begin{bmatrix}\frac{\mathrm{d}i_1}{\mathrm{d}t}\\ \frac{\mathrm{d}i_2}{\mathrm{d}t}\\ \frac{\mathrm{d}i_3}{\mathrm{d}t}\end{bmatrix}+\begin{bmatrix}r_1+R & r_2 & 0\\ -R_{L2} & r_2+Z_{L2} & 0\\ 0 & 0 & r_3+Z_{L3}\end{bmatrix}\begin{bmatrix}i_1\\ i_2\\ i_3\end{bmatrix}=\begin{bmatrix}U_\mathrm{m}\cos(\omega t)+U_\mathrm{DC}\\ 0\\ 0\end{bmatrix} \tag{7}$$

Where, U_m is AC voltage source, U_dc is imposed dc voltage source, L_1, L_2, L_3 presents the equivalent inductance of series winding, public winding and low voltage winding, respectively. M is the mutual inductance, Z_L is load impedance.

III. INTRODUCTION OF SRVCM

Unlike with the general transformer, the resistance of the UHV autotransformer is extremely small compared to its large inductance, especially when inductive load imposed at low voltage side. The long transient process can be a disaster, which requires a huge CPU time and memory consumption. Beyond that, this characteristic of large inductance and small resistance could also easily lead to the miscalculations as the component of DC bias can be easily neglected by the extra high AC voltage in the simulation.

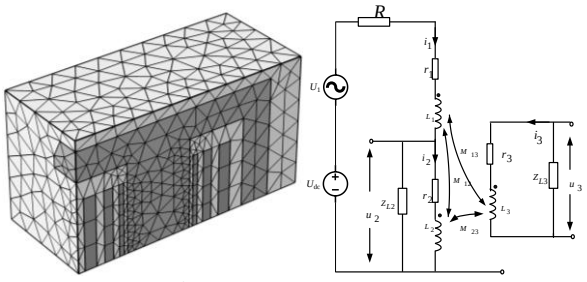

(a) Eighth magnetic field model (b) Circuit model

Fig. 1. Field-circuit coupling model of UHV autotransformer.

In order to solve these problems, series resistance is used to reduce the transient process as well as to make sure the imposed dc voltage will not be neglected.

The amplitude of the calculated current is changed due to the series resistance as well as the wave offset. The reason is that the voltage shared by the series resistance increases with the series resistance, and the voltage of the rest in the circuit model is smaller than the original voltage. Thus, in order to revise the error caused by series resistance, voltage compensation is required, which is expressed as follows.

$$\max\left|u^{'}-U_\mathrm{m}\cos\left(\omega t\right)\right|\le 1\%U_\mathrm{m} \tag{8}$$

Where, U_m is the amplitude of the rated AC voltage on the original side, u' is the voltage after k+1 compensation.

When the above criteria are satisfied, the iterative calculation of voltage compensation is stopped.

The final compensated voltage $u_{\mathrm{k}+1}$ can be obtained by

$$u_{k+1}=U_\mathrm{m}\cos(\omega t)+U_\mathrm{dc}+R(i_k-I_{kdc})\quad k=1,2... \tag{9}$$

Where, U_dc is the imposed dc voltage, i_k is k_th current in steady state, i_kdc is dc components in steady state.

IV. CALCULATION WITH LOAD UNDER DC-BIAS

The SRVCM presented above has been applied to the UHV autotransformer. The values of the imposed DC bias current have been chosen to be 20A, 50A, 80A and 100A. As an example, 20A and 100A DC bias effects on winding currents at rated operation are show in Fig.2 (a) and (b), respectively. The dash line presents rated current without DC bias, whereas, the solid line with symbol present the winding currents under DC bias. As can be seen from the figure, big distortion occurs when the DC bias current flows into the windings, mainly concentrated in the first half of the cycle. And the distortions increase as the DC bias increase.

The excitation current under various DC bias are calculated, which are shown in Fig. 3 (a). Besides, Fast Fourier transform (FFT) is performed in a steady state cycle and the harmonics amplitudes under various DC bias are shown in Fig. 3 (b). The amplitude of excitation current is about 1.6 A without DC bias, and the waveform is symmetrical in positive and negative cycle. With the increase of DC bias current, the amplitude of the excitation current increases gradually and the waveform is seriously distorted. The excitation current reaches the peak at the

center of the positive cycle, the excitation current is close to 660 A when DC bias reaches 100A. From the harmonic spectrum of excitation current, it can be seen that the even harmonics occur under DC bias, the main harmonics appear on 2nd, 3rd and 4th. Especially the 2nd harmonic, almost with the increase DC bias current linearly.

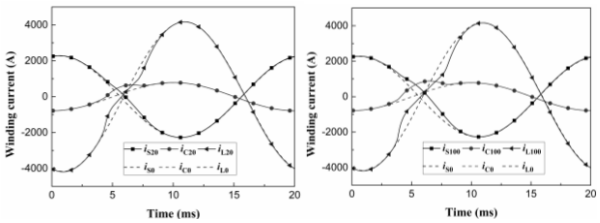

(a) 20A DC bias (b) 100A DC bias

Fig. 2. Various DC bias effects on winding current.

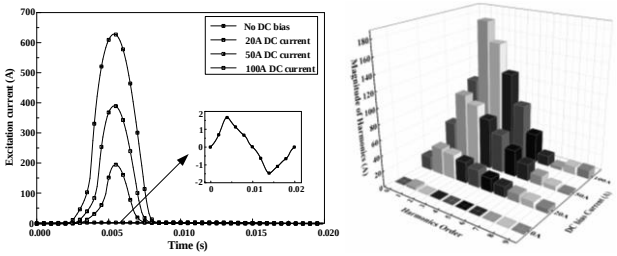

(a) Excitation current waveform (b) Harmonics of excitation current

Fig. 3. Various DC bias effects on excitation current.

V. Experiment Setups

The DC bias test rig is established to verify the proposed model, as shown in Fig. 4 (a). A single-phase four-column scale-reduced autotransformer with rated capacity of 5 kVA and rated voltage of 360V is used as the transformer under test, as shown in Fig. 4 (b). Its core structure and connection are consistent with that of UHV transformers, and its size of core and window is 1/12 of that of UHV transformer, which is 661 mm*100 mm*356 mm.

The calculated and measured high-voltage current under 3A DC bias current are shown in Fig. 5. As can be seen from the picture, the correctness of proposed model can be verified by the good agreement of the calculated and measured waveform.

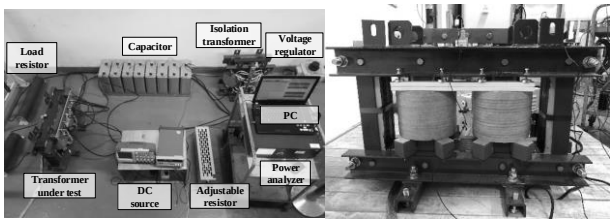

(a) Test rig (b) Scale-reduced transformer

Fig. 4. Experiment setups of DC bias effects on transformer.

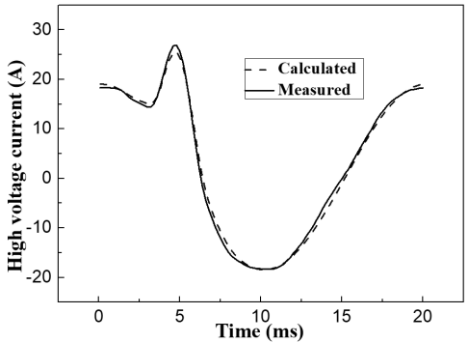

Fig. 5. High voltage current under 3A DC bias current.

VI. Conclusion

By utilizing the SRVCM, the electromagnetic quantities of UHV autotransformer with load under DC bias are analyzed, and the conclusions are obtained.

1) By means of SRVCM, the CPU time and memory consumption can be reduced for shorten the transient process with acceptable accuracy.
2) The winding current distorted severely under DC bias, almost concentrated on the first half cycle, which is consistent with excitation current.
3) Even harmonics occur under DC bias, the main harmonics appear on 2nd, 3rd and 4th. The effects of DC bias on higher harmonics is insignificant.

References

[1] Biro O, Koczka G, Leber G, et al. Finite Element Analysis of Three-Phase Three-Limb Power Transformers Under DC Bias[J]. IEEE Transactions on Magnetics, 2014, 50(2):565-568.

[2] Zhongdong D U, Dong X, Wang J, et al. "Test and Analysis on Restraining Transformer DC Bias by Changing Electric Potential of Grounding Grid[J]. " High Voltage Engineering, 2006, 32(8):69-72.

[3] Zheng, Kuan, et al. "Effects of System Characteristics on Geomagnetically Induced Currents." IEEE Transactions on Power Delivery 29.2(2014):890-898.

[4] G.Buticchi, “Detection Method of the DC Bias in Distribution,” Trans. Ind. Elec., vol.60, no.8, Aug. 2013.

[5] Wang, Jun, et al. "Investigation of the Influence of Direct Current Bias on Transformer Vibration." International Journal of Emerging Electric Power Systems 19(2018).

[6] Monteiro, Thiago Costa, et al. "Transformer Operation at Deep Saturation: Model and Parameter Determination." IEEE Transactions on Industry Applications 48.3(2012):1054-1063.

[7] Zhao, Xiaojun, et al. "Characteristics Analysis of the Square Laminated Core under dc-biased Magnetization by the Fixed-point Harmonic-balanced FEM." IEEE Transactions on Magnetics 48.2(2012):747-750.

[8] Pan, Zhuohong, et al. "Potential Compensation Method for Restraining the DC Bias of Transformers During HVDC Monopolar Operation." IEEE Transactions on Power Delivery 31.1(2016):103-111.

Enhanced Data Analysis for the Microwave Power Spectroscopy Method

Carl Friedrich Rädel
Faculty of Electrical Engineering
Helmut Schmidt University
Hamburg, Germany
raedelc@hsu-hh.de

Marcus Stiemer
Faculty of Electrical Engineering
Helmut Schmidt University
Hamburg, Germany
m.stiemer@hsu-hh.de

Tomas Hurtig
Division of Defence & Security
Systems and Technology
FOI - Swedish Defence
Research Agency
Norra Sorunda, Sweden
tomas.hurtig@foi.se

***Abstract*—In microwave power spectroscopy critical coupling frequencies for electromagnetic interference are detected from an increase in power absorption measured in an electrical reverberation chamber. At a much higher power level the same environment can be used to validate the identified frequencies by destructive testing. In this work the power spectroscopy method is applied to different sets of real world targets: light emitting diodes (LED) and radio frequency identification devices (RFID). Precise identification of critical frequencies requires however a suitable data processing to extract the characteristic target response from the chamber background and antenna noise. To this end, a symmetrizing transformation of the measured frequency data into time domain and adequate filtering techniques including time gating are applied. The analysis is based on a linear time invariant system model of the chamber. The frequency dependent damping behavior over time can, hence, be visualized by an absorbed power spectrogram giving important information on the targets. Extending measured data along the time axis turns out useful for the identification of coupling frequencies and the characterization of the target. The methods are compared and validated at two different test sites.**

Keywords—electromagnetic reverberation chamber, spectrogram, time gating

I. Introduction

Electromagnetic waves interact with active or passive electrical devices leading to a more or less intricate net of currents inside the device, that in turn can radiate electromagnetic energy. If the device is triggered at one of its natural frequencies the power transfer and, hence, the excited currents become maximal. The triggered currents exhibit a damped sinusoidal behavior in time domain or possess the form of a rational function with complex singularities in frequency domain. The same applies to the scattered electromagnetic field, which superposes the triggering field, at any spatial point. For the particular context relevant for this work, this physical principle is excellently explained by Carl Baum in his famous Note 88 [1], which has been the starting point for a long and fruitful scientific discussion ever since. It is exactly the phenomenon described above that is exploited in microwave power spectroscopy: The natural frequencies of the damped oscillating system represented by the device under test (DUT) are identified by monitoring the superposed scattered and applied triggering fields. In its simplest form, power spectroscopy is just based on considering the power consumed in the DUT, which must be at maximum at natural frequencies since the optimum power transfer of the forced oscillation at a natural frequency maximizes excited currents and, hence, Joule heating in the DUT. However, more sophisticated observation methods may lead to more accurate and further leading information about the DUT, such as, e.g., its damping behavior, the phase shift between triggering and scattered field, up to the transfer function of a linear model of the DUT obtained by linearization in a small frequency interval about a natural frequency.

An ideal environment to exhibit a DUT to an appropriately dosed electromagnetic field and to measure the field scattered by the DUT is given by an electric reverberation chamber (ERC). This is a metal enclosure with some stirring device, i.e., a device to alter the applied electromagnetic fields stochastically, and at least one antenna. Mechanical stirrers as used in this work to provide field modulation via geometry changes are only one of many possible methods. As soon as critical coupling frequencies have been detected, the vulnerability of the DUT can be tested by drastically increasing the applied field strength, where small ERCs profit from the high fields that can be excited with relatively small energy. The group around Tomas Hurtig published first results on spectroscopic properties of real world devices such as LEDs or RFIDs obtained with the help of an ERC, e.g. [2] or [3]. Earlier, Lars Ole Fichte et al. [4] proposed a method that was later validated by generic targets in [5]. In both approaches, the frequency depending power consumption of the device under test is determined by subtracting the power consumed by the empty chamber from that consumed by the loaded one.

The purpose of this work is to present an enhanced method for data analysis of spectroscopic data and to compare the results to those earlier obtained, cf. [3]. To this end, new measurements have been carried out in another ERC.

II. Equipment and Targets

As targets for the analysis reported on in this work, two relatively simple electronic devices are employed:

- passive ultra high frequency (UHF) RFID tags with specified working frequencies in the band 860–960 MHz manufactured by Confidex Ironside and based on the Impinj Monza 4 Q integrated circuit
- LEDs of type RND 135-00029 with the following specifications: 1.8-2.4 V forward voltage and 5.5 cm combined wire length (spread)

Radio frequency identification devices (RFID) exhibit unique natural resonances (usually one according to the American and one according to the European standard) and can in addition harness radio wave power to drive a circuit, usually by combining an antenna with some form of rectification. The current development of circuits consuming increasingly less power and the rise of ambient electromagnetic power being available on ever more frequencies will probably lead to more devices able to operate on ambient radio wave energy. The study of such devices for optimization, impairment, detection

or safe destruction can be performed with small reverberation chambers.

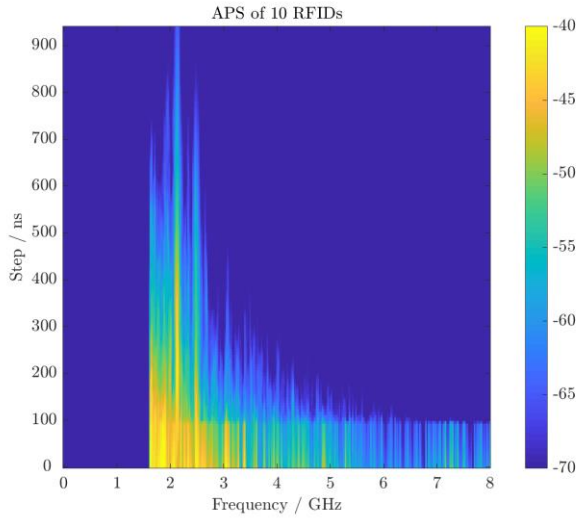

Fig. 1: Absorbed power spectrogram for 10 RFIDs in an ERC.

While the reference measurements at the FOI have been carried out using an ERC with an internal volume of 1.24 x 0.98 x 0.82 m^3 and an identified working volume of 0.72 x 0.56 x 0.4 m^3 for a lowest usable frequency of 1 GHz, the results here presented have been determined with an ERC with an internal volume of 98 x 78 x 69 m^3. For all presented results obtained by single antenna measurements (see below), a tapered horn antenna with a free space voltage standing wave ratio smaller 2 for 0.5-8 GHz was used. It has been shown that the employed ERC provides samples of Rayleigh distributed electrical field strength values for frequencies above 1.6 GHz. Due to these restrictions only off band measurements of the RFID are possible.

III. Theory and Methods

Most of the theory concerning reverberation chambers relies on a two antenna approach. This is both true for the analysis of spectroscopic data and the system theoretic understanding of the information flow inside the device, that is best explained by the antenna power wave theory of Everett Farr [6], which also includes scattering at objects. In such a setting the properties of the empty or loaded chamber can be described by the S-parameters of the corresponding two port model. However, all relevant information can also be extracted from the input reflection coefficient of a single antenna measurement. The data acquisition time of the employed network analyzer (NWA) has to be adjusted to meet the inverse of the minimal frequency step so that the scattered wave of the target can be taken into account. In this case early and late time response can be separated. To do so, a symmetric inverse discrete Fourier transform (SIDFT) is applied to the spectral reflection coefficient to create a real time signal, which represents the complete system response to a virtual Dirac pulse. Via time gating, the obtained real time signal can be cut in pieces corresponding to particular time intervals, which are then subjected to a forward symmetric discrete Fourier transform (SDFT) each [7]. The obtained data set shows the temporal change of the spectrum of the excited loaded ERC and can be represented in a spectrogram. If the DUT's power absorption and storage is the interesting quantity, this figure can be determined for each time segment via the formula

$$P_{\mathrm{DUT}}(t)/P_0 = 1 - |S_{11}(t)|^2 \qquad (1)$$

with reference power P_0, the power absorbed by the DUT $P_{\mathrm{DUT}}(t)$ in a time interval about *t*, and the input reflection parameter $S_{11}(t)$ for the corresponding time interval trimmed as indicated above. As usual in ERC measurements, the SIDFT-SDFT transformation procedure and the trimming to the short time intervals is performed for each stirrer position yielding an according number of $P_{\mathrm{DUT}}(t)/P_0$ values, whose average will be determined to rule out all directional or polarization effects. In Fig. 1 this process has exemplarily been performed for the case of 10 RFIDs put in an ERC at the same time. The horizontal axis depicts the exciting frequencies, while the vertical axis represents time. The different colors indicate the power stored in the DUT after a particular time and for a particular frequency in dB. The whole diagram is called absorbed power spectrogram (APS). In the case presented here, for each considered time interval the difference between loaded and empty chamber has been computed, although reference to the unloaded case may not be essential in this method (see below). The APS shown in Fig. 1 is an additionally filtered low resolution version, where two stronger tones (natural frequencies) can clearly be seen of roughly the same quality, but difference in amplitude. The second frequency possesses lower destructive coupling [8].

The APS offers much more information than a simple determination of the absorbed power. It provides information of the damping behavior of individual modes. Particularly, the small coherence time of different natural frequencies allows for separating the target signal from the back ground signal of the ERC. Moreover, frequency depending quality factors can be studied. The implementation of this finding in further measurement processes will potentially avoid the necessity to determine the chamber background by a determination of the power absorption of the empty ERC for the sake of simpler and more accurate measurement procedures. In addition to the RFID results, also a plot obtained from 20 LEDs measured in the ERC is given in Fig. 2, which has been determined by the same method. The wire length of 5.5 cm correspond to a dipole resonance of 2.7 GHz, but the bulk of the power absorption appears at a lower frequencies due to the load, which could vary due to manufacturing. In fact multiple isolated long lasting tones are visible in the figure. It is not clear if they correspond to variations in the forward voltage yet.

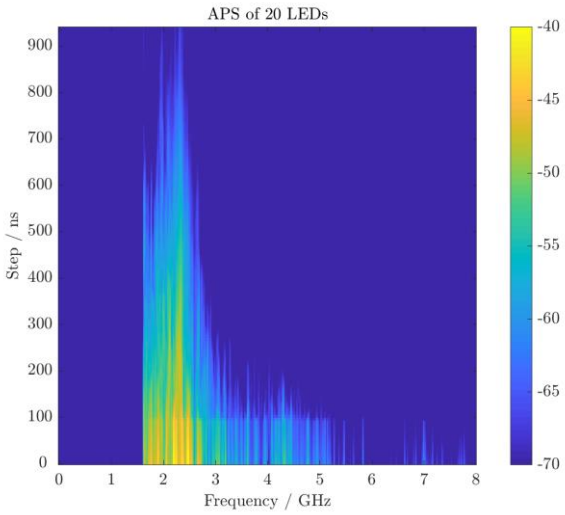

Fig. 2: Absorbed power spectrogram for 20 LEDs in an ERC.

IV. Data Comparizon

The results presented above have been compared with the data obtained at the FOI that have been analyzed without Fourier methods, see e.g. [3]. Validation under various aspects has been carried out. With high confidence, the same basic results could be recovered from the same consumer devices analyzed in different test setups. However, the new methods promise a deeper inside in the DUTs electric properties and a higher accuracy. In addition, the greater susceptibility of the devices at natural frequencies could be proven by a destructive test, see [8]. This indicates that there could be a correlation between the ability of a target to absorb power over time at a certain frequency and destructive pathways.

V. Conclusion and Outlook

As an extension of the microwave power absorption method, an enhanced data analysis based on Fourier transforms and filtering techniques has been proposed and positively validated. In addition to information about mere power absorption maxima, the frequency depending damping of the system "ERC - DUT" can be visualized. This does not only indicate critical frequencies clearer, but also avoids a reference measurement with an empty chamber, since the target signal can be separated from the chamber signal due to a small coherence time. Further, the different energy storage time of different natural frequencies can be applied as a filter, since the long term signal does only contain those frequencies whose energy is stored for a longer time. The presented results can be enhanced by choosing an appropriate measurement time, that corresponds to signal length in the time domain and by employing a NWA with a high dynamic range.

The next step will now be to implement further filtering strategies. Moreover, it has become clear that the whole analysis process can favorably be represented in the context of the powerful mathematical apparatus provided by Frame theory [9], which shall be applied to the random data of reverberation chambers. In this theory, the measured data are mapped by an analysis operator leading to a dimension reduction and subsequently after application of suitable filtering techniques recovered with a synthesis operator. This is exactly the procedure for creating a spectrogram, but presented in a broader context.

Also of great interests are applications of sets of involuntary matrices, where synthesis and analysis operation are represented by the same operator, such as, e.g., in case of the discrete Hankel transformation (DHT), which could be used for modal reduction of the data. For comparison, also simple techniques such as moving average filters are used.

References

[1] C. E. Baum, "On the Singularity Expansion Method for the Solution of Electromagnetic Interaction Problems," Interaction Notes, Note 88, 1971. (available for download at www.ece.unm.edu/summa/notes/In/0088.pdf).

[2] T. Hurtig, L. Adelw, M. Akyuz, M. Elfsberg, A. Larsson, and S. E. Nyholm, "Destructive high-power microwave testing of simple electronic circuit in reverberation chamber," in 2015 IEEE International Symposium on Electromagnetic Compatibility (EMC), pp. 1133-1135, August 2015.

[3] N. Wellander, M. Elfsberg and T. Hurtig, "Finding frequencies of enhanced electromagnetic coupling to electronic devices by the use of mode stirred reverberation chambers," in 2017 International Symposium on Electromagnetic Compatibility - EMC EUROPE, Angers, pp. 1-6, 2017.

[4] L. O. Fichte, S. Potthast, and K. U. Wendt, "Modenverwirbelungskammer zur Prüfung elektronischer Schaltungen," 2014, German Patent DE102012024373 A1.

[5] M. Stiemer, L. O. Fichte, C. H. Schlie, C. Vierck, S. Potthast, M. Schaarschmidt, F. Sabath, and K. U. Wendt, "Power spectroscopy with electrical reverberation chambers for EMC," in proc. 19eme Colloque International et Exposition sur la Compatibilité Électro- Magntique (CEM), 2018.

[6] E. G. Farr, "A power wave theory of antennas," in 2013 IEEE International Conference on Ultra-Wideband (ICUWB), pp. 7-12, September 2013.

[7] Yu-Ting Hsiao, Yo-Yi Lin, Yu-Cheng Lu, and His Tseng Chou, "Applications of time-gating method to improve the measurement accuracy of antenna radiation inside an anechoic chamber," in IEEE Antennas and Propagation Society International Symposium. Digest, vol. 3, pp. 794-79, June 2003.

[8] T. Hurtig, M. Elfsberg, H. Sundberg, and N. Wellander, "Comparison of electromagnetic coupling measurements and the energy needed for destruction of electronic systems," in Proc. AMEREM 2018, Santa Barbara, 2018.

[9] R. J. Duffin and A. Ch. Schaeffer, "A class of nonharmonic Fourier series," Trans. Amer. Math. Soc., vol. 72, pp. 341-366, 1952.

EM Failures Analysis of Analogue and Digital Sensors from a Safety and Security perspective

Chaouki Kasmi
Mobile and Telecom Lab
xen1thLabs
DarkMatter Group
Abu Dhabi, United Arab Emirates
chaouki.kasmi@darkmatter.ae

Fahad Al Yafei
Tawazun
Abu Dhabi, United Arab Emirates
fharhara@tawazun.ae

***Abstract*—The trend in society is to develop a safe and digital world based on the integration of smart and connected devices. Cyber-physical systems and connected cars are good example of the integration of analogue and digital sensors for information gathering about the environment and the status of specific physical observables. The reliability and the confidence of reported data collected by these electronic functions is obviously fundamental. We propose to the audience to go through the evolution of challenges regarding the integration of analogue and digital sensors beyond the safety requirements by highlighting the common needs between safety and security when dealing with intentional manipulation based on electromagnetic interference**

Keywords—IEMI, Safety, Security, Smart Devices

I. Introduction

From cyber-physical systems to autonomous cars, the trend in society is to augment the daily activities by digitalizing redundant operations prone to human failure [1]. This can be obtained by the integration of multiple sensors [2] and actuators [3] into electronics and infrastructures [4]. In many domains, possible failures of these electronic functions were already hardened [5] with pre-conditioning or post-processing functions as well as duplicating the source of data collection.

During the last decades, many studies have demonstrated how analogue and digital sensors can be affected by parasitic fields emitted by electronic devices in the vicinity of the electronics. Post-processing, conditioning techniques and software counter-measures have been added in the design as well as the duplication of elementary functions for safety purpose. Recently, the information security has shown a high interest in analyzing the threats of electromagnetic attacks against sensors to manipulate the connected actuators leading to malicious actions. We propose hereafter a short summary of what an attacker could target on smart sensor and smart devices, the related scenarios and the results if attacks are successful.

II. Read, Process and Execute

In a classical smart device, the sensor will gather the physical observable and convert it a voltage/current value by the mean of a transduction process. A controller will either get a digital value from an analogue to digital converter either with an embedded function or from a discrete component placed between the sensor and the controller. The controller will then process the value and execute a specific action. The controller could implement a proportional-integral-derivative (PID) function in order to optimize the process and execution phases if a specific value of the sensor has a predefined setpoint (SP).

III. Analysis of Threats

From a threat analysis, the attacker would try to reach a remote manipulation that could lead to the compromising of smart device as follows:

- Manipulation of the data [6] reported by the sensors: the attacker will send a specifically crafted signal to induce the reading of a specific value that will lead to a specific action of the controller.
- Corruption of the process: the attacker will try to create a software or hardware failure of processing phase. For example, the reading of value that will lead to erroneous calculation [7]. For example a division by 0 that could induce the propagation of software error;
- Manipulating the actuator [6, 8]: the attacker will send a specifically crafted signal that could lead to the manipulation of the actuator part.
- Creating cascading effects [9]: when the smart sensor is part of a large and stable electronic system, the manipulation of one sensor operation. As an example and for simplicity, this could lead to a higher power consumption, which may have an effect on power network stable state. This could result in the shutdown of the power system.

IV. Summary

While the EMC/EMI communities have been working on hardening solution to avoid sensors failure, the information security community is currently reviewing the design of electronic function and the hardening techniques from the attack scenarios perspective. Many papers, highlighting the interest of the information security experts to low-level attacks, have been published. Especially SCADA/ICS devices represent interesting targets as many sensors and actuators are exposed due to the lack of security of measures at the electric signal level.

During the plenary talk at ASIAEM 2019, the attendees will have a better understanding of the efficiency of hardening

techniques applied in EMC and how these could be challenge from information security perspective.

REFERENCES

[1] General Motors, 2018 Self-driving Safety Report, 2018, online

[2] M. Glesner and F. Philipp, "Embedded systems design for smart system integration," 2013 IEEE Computer Society Annual Symposium on VLSI (ISVLSI), Natal, 2013, pp. 32-33.

[3] A. F. Taha, N. Gatsis, T. Summers and S. Nugroho, "Actuator selection for cyber-physical systems," 2017 American Control Conference (ACC), Seattle, WA, 2017, pp. 5300-5305.

[4] M. Bajer, "IoT for Smart Buildings - Long Awaited Revolution or Lean Evolution," 2018 IEEE 6th International Conference on Future Internet of Things and Cloud (FiCloud), Barcelona, 2018, pp. 149-154.

[5] Baleani, Massimo, Ferrari, Alberto, Mangeruca, Leonardo, Peri, Maurizio, Pezzini, Saverio, Fault-Tolerant Platforms for Automotive Safety-Critical, CASES '03 Proceedings of the 2003 international conference on Compilers, architecture and synthesis for embedded systems, Pages 170-177 San Jose, California, USA — October 30 - November 01, 2003.

[6] E. Al Shahhi, M. Bluhm, A. Garipov, C. Kasmi, Susceptibility Testing of COTS Sensors to RF Pulses with Focus on Widespread Electronics for Information Security Risks Management and Mitigation. URSI AT-RASC 2018.

[7] V. Houchouas, J. L. Esteves, E. Cottais, C. Kasmi and K. Armstrong, "Immunity assessment of a servomotor exposed to an intentional train of RF pulses," 2017 International Symposium on Electromagnetic Compatibility - EMC EUROPE, Angers, 2017, pp. 1-5.

[8] J. Selvara, Intentional Electromagnetic Interference Attack on Sensors and Actuators, Graduate Theses and Dissertation, Iowa State University, 2018, online.

[9] B. Jager, A. Preinerstorfer, G. Neubauer, Awareness of the vulnerability of critical infrastructures to IEMI threats: lessons from Austria, Proceedings of the 10 International Conference on Risk Analysis (RISK 2016)

Improvement of Double-Frequency Test Technique for Nonlinear Characteristics

PANG Chen
Rocket Force University of Engineering
Xi'an, China
2024199880@qq.com

YU Zhiyong
Rocket Force University of Engineering
Xi'an, China

DU Wenzhan
Rocket Force University of Engineering
Xi'an, China

***Abstract*—The automated double-frequency test technique can comprehensively detect and identify all nonlinear responses (including intermodulation, cross-modulation and spurious response,etc) of nonlinear devices or systems through one test, which has important application value for nonlinear characteristics acquisition and evaluation of devices. In the improved development of double-frequency test technique, the problem that needs to be solved first is still the problem of testing efficiency. In this paper, under the premise of ensuring the integrity of the double-frequency test data, the frequency sweeping method is improved, and the fast identification method of the nonlinear response type in the double-frequency diagram is proposed based on the frequency condition equation, which greatly shortens the test and identification time, and is more in line with the requirements of the system field test, and is more practical.**

Keywords—automated double-frequency test technique, nonlinear characteristic, double frequency diagram, frequency condition equation

I. INTRODUCTION

As the core device of information technology equipment such as communication, detection and electronic warfare, when the receiver is exposed to the high-intensity, wide-band, multi-standard battlefield complex electromagnetic environment, the undesired radio frequency (RF) interference energy will be received by the antenna or transmission line and enter the RF receiving system, which result in failure or serious performance degradation of the RF receiving system due to nonlinear effects, thereby reduce the operational effectiveness of the entire electronic information system. The testing technology for studying the nonlinear effects of receivers has become an urgent problem to be solved in the construction of weapons and equipment.

At present, the most advanced nonlinear test technology in the world is the automated double-frequency test technique (ADFTT)[1],[2] proposed by the Electromagnetic Compatibility Research and Development Laboratory of Belarusian State University of Informatics and Radioelectronics (BSUIR). The technology uses two signal sources to perform fast sweep and slow sweep in the test frequency band respectively, which can generate a frequency combination covering all double-frequency signals in the test frequency band to test the tested receiving system, without missing excitation signal used in frequency combination. Theoretically, all nonlinear responses of the receiver under test can be excited. ADFTT has been introduced to China in recent years, but there are still many key problems to be solved in the process of digestion, absorption and re-innovation[3],[4], in which the primary trouble is the test efficiency problem. In this paper, the efficiency of double-frequency testing is improved by optimizing the double-frequency test sweeping strategy and improving the data processing method.

II. PRINCIPLE AND SYSTEM COMPOSITION OF ADFTT

The presence of nonlinear devices such as amplifiers and mixers inside the receiver causes the output-input characteristics of the receiver to exhibit the following power-level relationship[3]:

$$u_{out} = k_1 u_{in} + k_2 u_{in}^2 + k_3 u_{in}^3 + \cdots + k_n u_{in}^n \qquad (1)$$

where u_{in} and u_{out} represent the input signal and output signal levels, respectively, and k_i represents the receiver nonlinear characteristic parameters.

When the input signal is a two-tone signal, i.e., $u_{in} = U_1 \cos 2\pi f_1 t + U_2 \cos 2\pi f_2 t$, it can be seen from (1) that due to the existence of nonlinearity, the output of the receiver produces a series of combined frequency components in addition to the fundamental and direct current (DC) components. Normally the frequency of harmonics is much higher than that of useful signals, so it is easy to filter out through filters. Therefore, the receiver nonlinear interference mainly manifests as: two or more external interference signals generate new interference frequency components near the receiver tuning frequency due to the frequency conversion effect of receiver front-end nonlinear characteristics. The nonlinear interference of receiver mainly includes intermodulation, cross-modulation, desensitization and spurious response, etc[5].

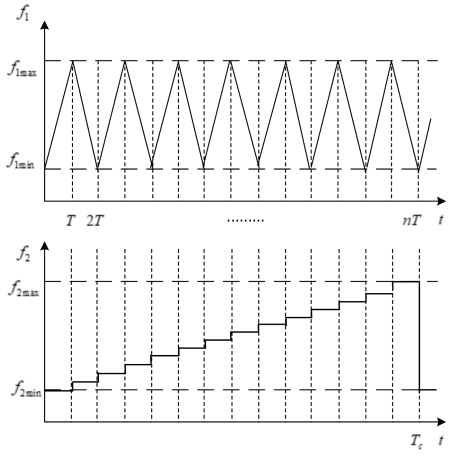

Fig. 1. Double-frequency signal scanning mode

Double-frequency test technique uses a combiner to synthesize the output signals of two signal sources into double-frequency signals, one of which is a fast scanning mode with a scanning range of $f_{1\min} \sim f_{1\max}$, a total of n

scans are performed, and the other is a slow scanning mode with a scanning range of $f_{2\min} \sim f_{2\max}$ and only one scanning, as shown in Fig. 1. Generally, the sweep range of the two signal sources is the same, and the input signal level remains unchanged during the sweep process. By this scanning method, all double-frequency signal combinations (f_1, f_2) in the test band can be generated, and then input into the device under test, recording the output response which can be described by the following formula[3],[4]:

$$H(f_1, f_2) = U_{out}(f_1, f_2 \mid_{U_{2in=const}}^{U_{1in=const}}) \tag{2}$$

where U_{out} is the output signal level when two test signals at frequencies f_1 and f_2 with levels U_{1in}, U_{2in} correspondingly are applied to the receiver input; as a rule, $U_{1in} = U_{2in}$.

Intercepting the three-dimensional double-frequency map at different output power thresholds, i.e.

$$W_i(f_1, f_2 \mid U_{ti}) = \mathrm{sgn}\{H(f_1, f_2) - U_{ti}\} \tag{3}$$

where $U_{ti}(i = 1,2,\cdots)$ is the specified threshold; sgn( ) is sign function. Two-dimensional double-frequency images can be obtained at different interception threshold levels.

The double-frequency automated test system consists of signal generators, device under test (DUT), combiner, spectrum analyzer, computer and cable hardware,etc. The system architecture principle is shown in Fig.2.

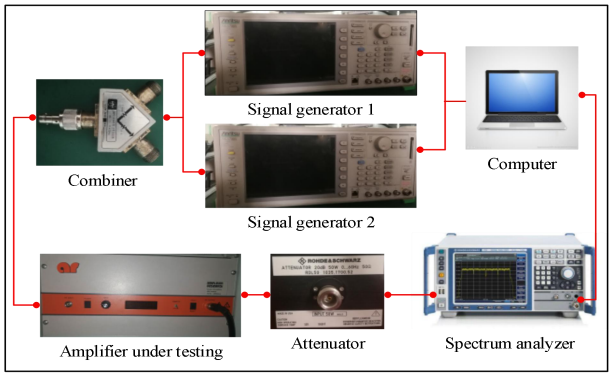

Fig. 2. Architecture schematic diagram of double-frequency automated test system

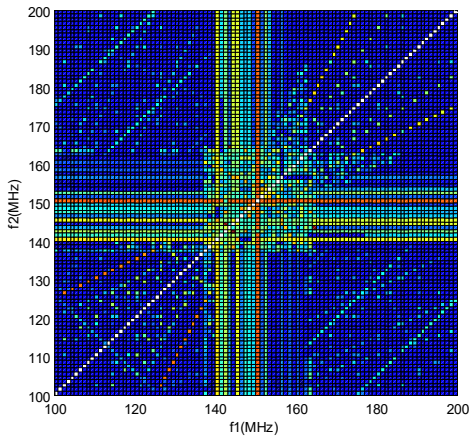

Fig. 3. Two-Dimensional double-frequency map

Taking the Amplifier research 100A250A as an example, a nonlinear double-frequency test is performed. Set the sweep range of the double-frequency test signal to 100 MHz-200MHz, the signal amplitude is -33 dBm, and the source sweep step is 1 MHz, which includes 101 × 101 frequency combinations. When the threshold is -85 dBm, the two-dimensional double-frequency diagram is shown in Fig. 3.

III. Improvement of Frequency Sweep Strategy for ADFTT

The traditional ADFTT is theoretically feasible by testing in a large sweep range and small steps, but it takes a long time and cannot fully meet the current experimental test requirements. Therefore, improving the test speed without sacrificing the integrity of the test data is a primary problem to be solved[4],[5],[6].

According to the principle of double-frequency automated test, the sweep range of the two input signals is the same, and the two frequencies are non-primary. In the traditional ADFTT, two signal sources are set to perform full-band scanning in the working frequency band respectively, which causes a large amount of redundancy in the double-frequency test combination, resulting in waste of resources and long test period. Thus, since the double-frequency diagram is theoretically symmetric about the diagonal, by properly removing the redundant frequency combination, the total test frequency combination can be reduced by nearly half, greatly improving the test efficiency. The test process is shown in Fig. 4.

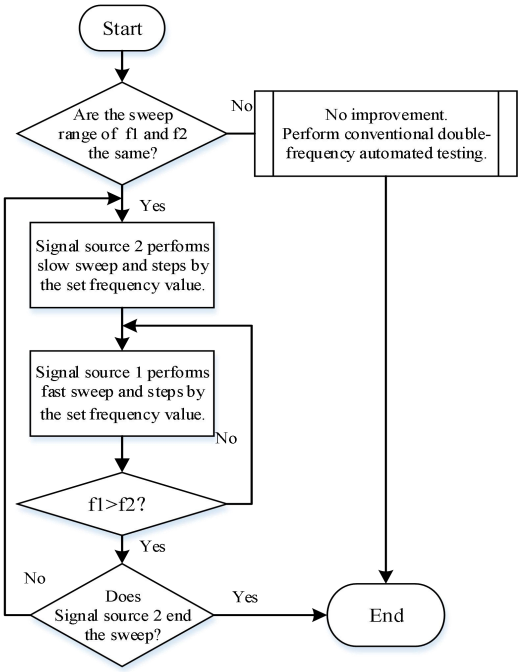

Fig. 4. Optimized ADFTT flow char

IV. Identification of Nonlinear Response Types in Double-Frequency Diagrams

Only when the frequency conditional equation is connected with the double-frequency diagram, the nonlinear characteristics of the devices under test can be obtained by the double-frequency diagram. The known frequency condition equation of power amplifier is:

$$k_1 f_1 + k_2 f_2 = f_c \tag{4}$$

where $k_1, k_2 = 0, \pm1, \pm2, \cdots$ represent the order of f_1 and f_2, respectively; f_c is the fixed measurement center frequency. In order to identify the non-linear types of lines on double-frequency maps, it is necessary to establish a line library corresponding to the frequency conditional equation. If the frequency conditional equation is analyzed to order n, the established line library will contain $(3n^2+n)/2$ lines, including receiving channels, intermodulation and spurious response paths, as shown in Fig. 5. Then, the double-frequency diagram is identified by using the established frequency conditional equation, as shown in Fig. 6. And all the intermodulation response types are obtained, as shown in TABLE I.

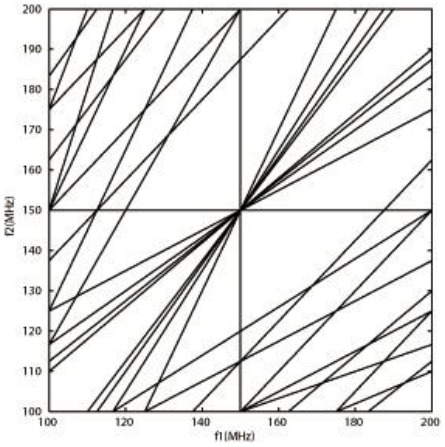

Fig. 5. Linear library of order 9

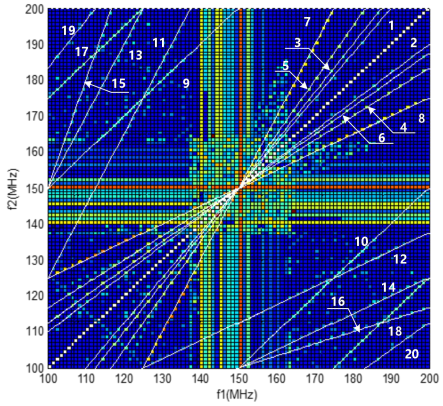

Fig. 6. Identification of double frequency graph

TABLE I. TYPES OF NONLINEAR RESPONSE OF AMPLIFIER OUTPUT

Number	Intermodulation type	Order
1	$5f_1-4f_2=f_c$	9
2	$-4f_1+5f_2=f_c$	9
3	$4f_1-3f_2=f_c$	7
4	$-3f_1+4f_2=f_c$	7
5	$3f_1-2f_2=f_c$	5
6	$-2f_1+3f_2=f_c$	5
7	$2f_1-f_2=f_c$	3
8	$-f_1+2f_2=f_c$	3
9	$3f_1-3f_2=f_c$	6
10	$-3f_1+3f_2=f_c$	6
11	$4f_1-2f_2=f_c$	6
12	$-2f_1+4f_2=f_c$	6
13	$6f_1-3f_2=f_c$	9
14	$-3f_1+6f_2=f_c$	9
15	$3f_1-f_2=f_c$	4
16	$-f_1+3f_2=f_c$	4
17	$2f_1-2f_2=f_c$	4
18	$-2f_1+2f_2=f_c$	4
19	$3f_1-4f_2=f_c$	7
20	$-4f_1+3f_2=f_c$	7

V. CONCLUSION

In this paper, the improvement of ADFTT is studied . Firstly, the ADFTT is improved by halving the combination of the scan frequency, and the sweep time is shortened by nearly half, which greatly improves the test efficiency. Then, based on the frequency condition equation, the nonlinear type in the double-frequency diagram is identified, and all the nonlinear characteristics of the device under test in the scanning frequency band are obtained. The test results have important reference value for evaluating the electromagnetic sensitivity and environmental adaptability of the device, and have certain guiding significance in the electromagnetic compatibility analysis in the design stage[3],[7].

REFERENCES

[1] Mordachev V.I. Automated double frequency test system. Vth Int. Conf. Electromagn. Interference Compat. (INCEMIC),1997,P.99-104.

[2] Mordachev V.I. Automated Double-Frequency Testing Technique for Mapping Receiver Interference Responses. IEEE Transactions on Electromagnetic Compatibility, May 2000, Vol.42(2), pp. 213-225.

[3] LIU Peiguo, TAN Yujian, LU Zhonghao, et al. Technology of in-situ electromagnetic compatibility measurement and analysis[M]. Beijing:National Defense Industry Press, 2013.

[4] XING Kui, XUE Menglin, WANG Yawei. Application of wireless receiver's EMC fast testing technique in complicated electromagnetic environment[J]. Journal of Astronautic Metrology and Measurement, 2015,35(5):21-26.

[5] MA Chen, ZHOU Dongming, LIU Peiguo. A new test method to quickly acquire non-linear characteristics of receiving system[J]. Modern Electronics Technique, 2013,36(21):145-151

[6] E. Sinkevich, "Universal technique for interference response recognition from results of radio receiver's double-frequency testing," IX-th Int. Symp. On EMC and Electromagnetic Ecology, Saint-Petersburg, Russia, Sept 13-16,2011, pp. 308-311.

[7] V.I. Mordachev, E.V. Sinkevich, "Experimental analysis of radio receiver susceptibility to out-of-band interference by means of double-frequency test system," 10-th Int. Symp. On EMC "EMC Europe 2011", UK, York, Sept. 26-30, 2011, pp.405-411.

A Non-Contact Approach for Lightning Strike and Fault Location of Transmission Lines by Broadband Electro-Optic Field Sensors

Chijie Zhuang
D*ept. of Electrical Engineering,*
Tsinghua University
Beijing, China
chijie@tsinghua.edu.cn

Huaiyuan Yang
D*ept. of Electrical Engineering,*
Tsinghua University
Beijing, China
306630716@qq.com

Rong Zeng
D*ept. of Electrical Engineering,*
Tsinghua University
Beijing, China
zengrong@tsinghua.edu.cn

Shijun Xie
State Grid Sichuan Electric Power
Research Institute,
Chengdu, China
sj-xie@163.com

Hao Yu
D*ept. of Electrical Engineering,*
Tsinghua University
Beijing, China
yuhao16@mails.tsinghua.edu.cn

She Wang
D*ept. of Electrical Engineering,*
Tsinghua University
Beijing, China
wangshethu@qq.com

***Abstract*—Lightning strike and fault location of transmission lines is important for the safety and continuous operation of power systems. The existing fault location methods based on traveling waves mostly use current transformer to obtain the transient signals, which can hardly exactly capture signals exceeding 200 kHz, and needs to connect with the live lines and therefore brings inconvenience to the installation, debugging and maintenance. In this paper, we propose a non-contact approach for lightning strike and fault location of transmission lines based on broadband electro-optic field sensors, which is easier for the devices to be installed, debugged, and maintained. The method was validated and tested by both simulation experiment and artificial fault experiment of a real 500 kV transmission line. The artificial fault experiment shows a location error of 200 m for the 177-km-long 500 kV power transmission line.**

Keywords—non-contact approach, lightning strike, fault location, transmission line, electro-optic field sensor

I. INTRODUCTION

Quick location of lightning strike and fault in transmission lines is important for the safety and continuous operation of power systems. Considering that many power lines are in the mountain areas which results in inefficient patrol of human workers, quickly locating the lightning strike and fault position becomes an urgent demand.

The fault location methods based on traveling waves are widely used (see Fig. 1). It uses the time difference of arrival (TDOA) of the traveling waves at both ends of the line to measure the distance directly:

$$\mathrm{D} = \frac{1}{2}[L \pm v(t_M - t_N)]$$

where L is the total length of the line, t_M-t_N is the time difference between the arrivals of the traveling waves at two ends of the line, v is the wave velocity.

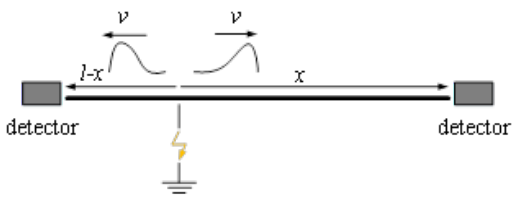

Fig. 1. Schematic diagram of two-end location method.

Traveling electromagnetic wave signals can be detected by voltage transformer or current transformer (CT). However, the high frequency response of capacitive voltage transformer is poor. Alternatively, CTs can measure the traveling current waves better, so the existing fault location methods based on traveling waves mostly use CT to obtain the signals. However, CTs used for fault location can hardly exactly capture signals exceeding 200 kHz, and need connecting with the live lines, which brings inconvenience to the installation, debugging and maintenance of the devices.

The transient voltage is proportional to the electric field in power systems (except the VFTO in GIS system). By measuring the transient electric field by non-contact field sensors [1,2], the time of arrival can also be obtained. In [3], a non-contact method to measure the transient voltage is proposed based on electro-optic field sensors.

In this paper, we propose and test a non-contact approach for lightning strike and fault location of transmission lines based on broadband electro-optic field sensors, which is easier for the devices to be installed, debugged, and maintained.

II. METHOD

The fundamental characteristics of the proposed method is that it uses broadband, metal-free and contactless electric field sensors to detect the transients [3].

The integrated electro-optic field (IEOS) is based on the Pockels effect. The sensor is shown in Fig. 2. The waveguide is fabricated on a $LiNbO_3$ substrate by titanium diffusion.

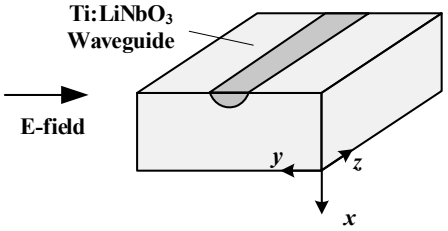

(a) a diagram of the sensor

(b) an implemented IOES

Fig. 2. Diagram and a picture of the IEOS

III. SIMULATION EXPERIMENTS

As shown in Fig. 3, a 1900-m-long conductor supported on the brackets was used to simulate the overhead transmission line in laboratory. Sensors were installed at both ends of the conductor, and were connected to the data acquisition device through two polarization maintaining fibers of equal length. An impulse voltage generator (EMC Pro) was used to apply voltage impulse at different positions of the conductor to simulate the lightning strikes. Note the wave forms of these impulses differ from real faults or lightning strikes, however, the principle of the proposed method remains the same.

The impulse voltages were first applied at one end of the conductor to calibrate the velocity of the traveling wave. The location of the "strike point" was then calculated by TDOA of the waves measured at two terminals.

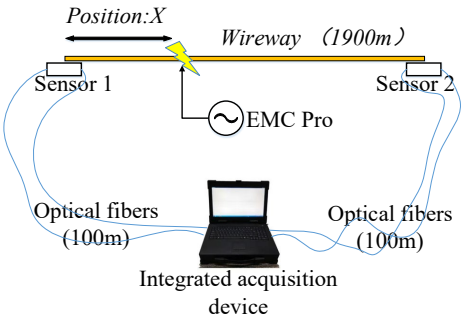

Fig. 3. Schematic diagram of simulation experiments.

The measured waveforms consisted of the applied voltage signals and the noise. Therefore, how to determine the arrival time of different waveforms is a problem that needs to be solved firstly. In this paper, the method shown in Fig. 4 is used. The average amplitude of signals before the arrival of the wave is taken as the reference. Assuming the amplitude of the noise is ΔV, and the intersection of the 2ΔV and 3ΔV within the waveform is made as an oblique line. The intersection of the oblique line and the reference is defined as the beginning of the wave, i.e., the arrival of the wave.

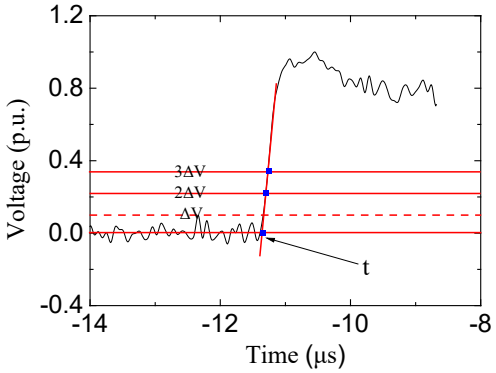

Fig. 4. Diagram of how to determine the start of the wave.

When the impulse voltages are applied at x=0, the TDOA of the two traveling waves measured at the two ends of the line is the largest, and hence the calculated speed is more accurate. Therefore, the impulse voltages were applied at x = 0 for 7 times, and the average TDOA $\overline{\Delta t} = 6.76 \pm 0.08$ μs. Considering L=1900 m, the wave velocity through the wire was $(2.811 \pm 0.034) \times 10^8$ m/s. Then impulse voltages were applied at different positions of the conductor, 5 times per point. The "lightning strike" positions can be calculated accordingly (shown in Tab.1), which shows that the average location error is about 20 m.

TABLE I. LOCATION RESULTS OF STRIKES AT DIFFERENT PLACES

x/m	average TDOA (μs)	$\overline{x'}/m$	average error /m
0	6.76	——	——
200	5.36	196	-4
600	2.66	580	-20
1000	-0.45	1013	13
1400	-3.23	1404	4
1800	-6.27	1822	22

IV. PRACTICAL EXAMPLE OF NON-CONTACT LOCATION

The non-contact approach for lightning strike and fault location of transmission lines was also tested by an artificial fault of a 500 kV transmission line between Linzhi and Langxian substations in Tibet, which is 177 km long in total (excluding the effect of sag). The field layout is shown in Fig. 5. The sensors were placed several meters below the line in the substations, near the position of CVTs, and had no connection to the power systems.

The short-circuit (fault) point was set at the first tower outside Linzhi substation, about 300 m away from CVT. After the short-circuit (artificial fault), the circuit breakers of Linzhi substation reclosed about 1 second later.

The transient voltage waveforms of the short-circuit and reclosing of the breaker at both ends of the line were measured using the non-contact transient voltage measuring device with GPS synchronization, which are shown in Fig. 6.

Therefore, the wave velocity can be calculated from the TDOA of the reclosing transients measured at the two ends (see Tab. 2), and $v = 2.854 \times 10^8$ m/s. The position of the fault was then located as D=100 m, which is about 200 m away from the real fault position.

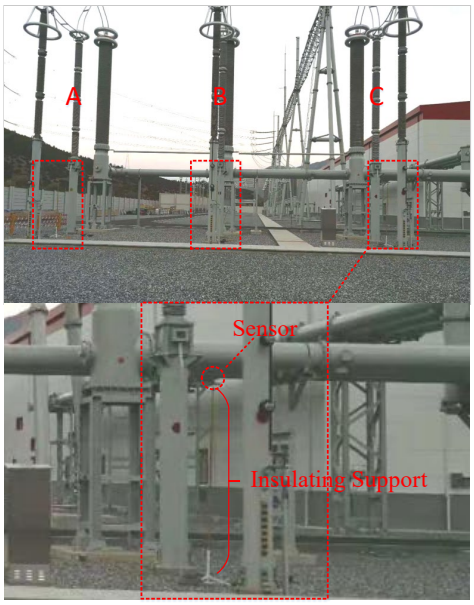

Fig. 5. A photo of the field installation in Linzhi 500 kV AC substation

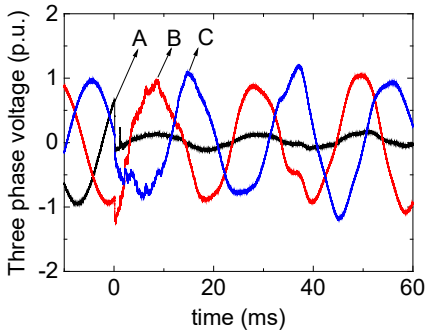

(a) Fault transient waveforms measured in Linzhi substation

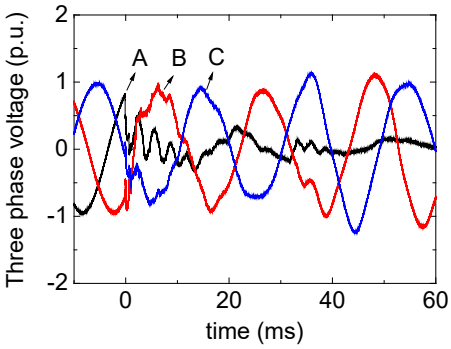

(b) Fault transient waveforms measured in Langxian substation

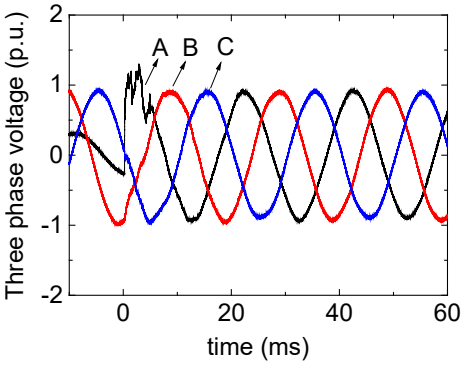

(c) Voltage waveforms of reclosing measured in Linzhi substation

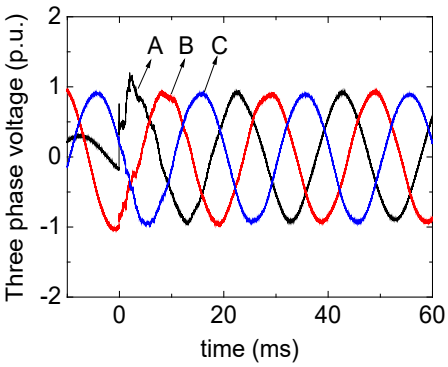

(d)Voltage waveforms of reclosing measured in Langxian substation

Fig. 6. Voltage waveforms of single-phase short-circuit and breaker-reclosing measured at Linzhi and Langxian substations

TABLE II. STATISTICS OF WAVE ARRIVAL TIME

Action	Measuring point	Time of arrival (hour:minute:second)	TDOA
Reclosing	Linzhi	18:48:04.5487465	620.1μs
Reclosing	Langxian	18:48:04.5481264	
Short-circuit	Linzhi	18:48:03.6087441	619.4μs
Short-circuit	Langxian	18:48:03.6093635	

V. CONCLUSIONS

In this paper, we proposed a non-contact approach for lightning strike and fault location of transmission lines by broadband electro-optic field sensors. The transient voltage signals are captured by broadband electric field sensors which can be placed near the ground and have no connections to the power system.

The method was validated and tested by both simulation experiments in lab and an artificial fault experiment of a real 500 kV transmission line. The artificial fault experiment shows a location error of 200 m for the 177-km-long line.

ACKNOWLEDGMENT

This work is supported by State Grid Corporation of China under project 52199916024K.

REFERENCES

[1] Rong Zeng, Bo Wang, Ben Niu and Zhanqing Yu, “Development and Application of Integrated Optical Sensors for Intense E-Field Measurement,” Sensors, 2012, 12(8): 11406-11434.

[2] Hai Wang, Rong Zeng, Chijie Zhuang. Thermal variation of electric field sensor bias caused by anisotropy of $LiNbO_3$. Applied Physics Letters. 2019,114(14): 143501.

[3] Hai Wang, Chijie Zhuang, Rong Zeng, et al. Transient voltage measurements for overhead transmission lines and substations by metal free and contactless integrated electro-optic field sensors. IEEE Transactions on Industrial Electronics. 2019, 66(1):571-579.

Electrostatic Characteristics of Two Conducting Spheres in a Grounded Cylinder

D. V. Giri
Pro-Tech, Wellesley, MA USA
Dept. of ECE, University of New Mexico
Albuquerque, NM, USA
Giri@DVGiri.com

S. Banerjee
Department of Physics
Rhodes College
Memphis, TN, USA
banerjees@rhodes.edu

***Abstract*— An understanding of the electrostatic interaction between charged electrical conductors embedded in a grounded cylinder is quite useful in the design of compact pulse generators. We get the capacitance between the two spheres and the capacitance between the sphere and the grounded cylinder, in closed form. The dependence of these capacitances on various geometrical parameters is very useful in the design phase of a Marx generators where the stray capacitances play crucial roles.**

Keywords— electrostatic interaction, conducting spheres, capacitances, Marx generators

I. INTRODUCTION

It is very common to have spherical conductors which form a spark-gap switch inside a grounded cylinder in high-power transient generators. One popular example of such a machine is the Marx generator [1] wherein many identical capacitors are charged in parallel from a single DC source and then these charged capacitors are connected in series to multiply the voltage. However, the stray capacitances across the switch conductors and the capacitance between one of the switch conductors and the grounded cylindrical tube in a compact Marx, affects the performance resulting in some erratic behavior in switching. Figure 1 illustrates a 4-stage Marx generator. The corresponding electrostatic problem can be formulated as shown in Figure 2. The three geometrical parameters *a, R* and *H* are shown, and we seek the capacitance C_{11} between the spheres and C_{12} between the sphere and the cylinder.

II. MOTIVATION AND SOLUTION APPROACH

Our literature search has revealed that a problem of this type was first solved by R. C. Knight [2] in 1935 where he addressed the case of one sphere in a grounded cylinder. W. R. Smythe [3] offered an alternate solution. Chang and Chang [4] also analyzed this problem in 1967. Furthermore, the electrostatic characteristics of two isolated spheres was considered by many researchers [5,6]. We were motivated to tackle this problem analytically for three reasons; a) it is somewhat puzzling that such an elegant problem has not been analyzed, b) our solution clearly demonstrates the dependence of the capacitances on various geometrical parameters in the problem and c) the analysis serves as a test case to check the accuracy numerical results.

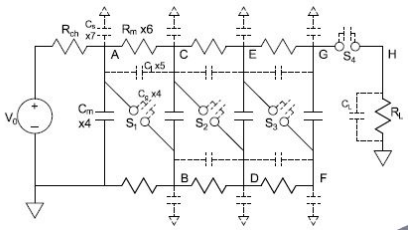

Figure 1. Four stage Marx generator showing the stray capacitances of interest

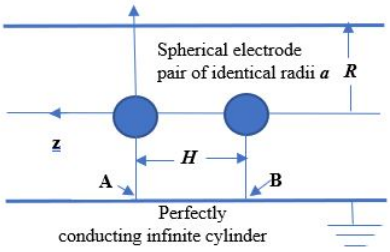

Figure 2. Two spherical electrodes inside a grounded cylinder

We extend the solution of Laplace equation of Chang and Chang [4] to the present case. The solution of Laplace equation is written out everywhere in the grounded cylinder and boundary conditions on the conducting spheres and the and infinitely long cylinder are satisfied. The gradient of the potential gives the electric field everywhere. The normal component of the electric field on the spheres result in the charge distribution (C/m^2) written as a multipole expansion. Integrating the charge distribution on the spheres leads to the total charge on the sphere. Knowing the total charge and voltages on the sphere finally leads to the capacitance estimates which is the goal of the problem.

III GENERAL POTENTIAL FORMULATION FOR A SINGLE SPHERE

Rederiving and generalizing the Chang and Chang [5]formulation gives equations (1) and (2). The radial distance from the sphere is r and θ is the polar angle. For any fixed n, the quantity inside the two square brackets above go to zero at any point on the cylinder, $r = R/\sin\theta$. For top down symmetric case of Chang and Chang [5] the odd part goes to zero, $A_{2l+1} = 0$.

$$V(r,\theta) = \sum_{n=0}^{\infty} A_{2n}\left[\frac{P_{2n}(\cos\theta)}{r^{2n+1}} - \sum_{m=0}^{\infty}\frac{C_{nm}r^{2m}P_{2m}(\cos\theta)}{R^{2n+2m+1}}\right] + \sum_{l=0}^{\infty} A_{2l+1}\left[\frac{P_{2l+1}(\cos\theta)}{r^{2l+2}} - \sum_{k=0}^{\infty}\frac{D_{lk}r^{2k+1}P_{2k+1}(\cos\theta)}{R^{2l+2k+3}}\right] \quad (1)$$

where

$$C_{nm} = \frac{2}{\pi}\frac{(-1)^{n+m}}{(2n)!(2m)!}\int_0^{\infty}\frac{\lambda^{2(n+m)}K_0(\lambda)}{I_0(\lambda)}d\lambda$$
$$D_{lk} = \frac{2}{\pi}\frac{(-1)^{l+k}}{(2l+1)!(2k+1)!}\int_0^{\infty}\frac{\lambda^{2(l+k+1)}K_0(\lambda)}{I_0(\lambda)}d\lambda. \quad (2)$$

The first sphere is at the origin and r,θ are the coordinates of any point from the center of this sphere. The center of the second sphere is at a distance $z=-2h=-H$ from the origin. The coordinates of any point r,θ from the first sphere, as measured from the second sphere are given by

$$r_b = \sqrt{r^2+H^2+2rH\cos\theta} \quad (3)$$

$$\theta_b = \cos^{-1}\left(\frac{H+r\cos\theta}{r_b}\right). \quad (4)$$

For the symmetric +V / -V Case both spheres are held a potential $V=+1$ volt. The general form of the potential for this case can be written as

$$V_+(r,\theta) = V(r,\theta)+V'(r_b,\theta_b). \quad (5)$$

where the coefficients for $V'(r_b,\theta_b)$ are $A_{2n}^{+\prime} = A_{2n}^{+}$ $A_{2l+1}^{+\prime} = -A_{2l+1}^{+}$ to make the potential top down symmetric. The boundary conditions to determine these constants are

$$V_+(a,\theta) = 1, \quad (6)$$

for all angles θ. This yields the infinite equations needed to be solved to uniquely determine all A's. It is not clear if a general solution for this problem exists. However, we may construct approximate solutions by limiting ourselves to a small number of A's and assuming that the contribution from the higher order multipole terms is small. That is, let only, $A_0^+, A_1^+, \ldots A_{N-1}^+$ be non-zero, where N is the number of non-zero multipoles and all higher multipoles be zero. The equations that determine these N multipole moments can be obtained by fixing the potential at P evenly spaced points on the sphere.

$$M^+ A^+ = \mathbf{1} \quad (7)$$

where A^+ and $\mathbf{1}$ are N x 1 column vectors with entries $A_0^+, A_1^+, \ldots A_{N-1}^+$ and $1,1,1\ldots\ldots1$ respectively and the $N \times N$ matrix M^+.

On the other hand, for the antisymmetric +V / -V case the first sphere is held at + 1 Volt and the second sphere is held at potential $V=-1$ volt instead. The general form of the potential for this case can be written as

$$V_-(r,\theta) = V(r,\theta)+V'(r_b,\theta_b), \quad (8)$$

Where the coefficients of V' are $A_{2n}^{-\prime} = -A_{2n}^{-}$ and $A_{2l+1}^{-\prime} = A_{2l+1}^{-}$ to make the potential anti-symmetric.

The boundary conditions to determine the constants are

$$V_-(a,\theta) = 1, \quad (9)$$

for all angles θ. Similar to symmetric case, we may construct approximate solutions by limiting ourselves to a finite number of multi-pole coefficients and assuming that the contribution from the higher order multipole terms is negligibly small. That is let only, $A_0^-, A_1^- \ldots\ldots A_{N-1}^-$ be non-zero, where N is the number of non-zero multipoles and all higher multi-poles be zero. The equations that determine these N multipole moments can be obtained by fixing the potential at P evenly spaced points on the sphere.

$$M^- A^- = \mathbf{1} \quad (10)$$

where A^- and $\mathbf{1}$ are N x 1 column vectors with entries $A_0^-, A_1^- \ldots\ldots A_{N-1}^-$ and $1,1,1\ldots\ldots1$ respectively and the $N \times N$ matrix M^-.

VI. QUADRUPOLE APPROXIMATION

For the quadrupole approximation (N = 3), we impose three boundary conditions on the sphere at $\theta = 0, \pi/2$ and π. For the symmetric case, expanding the solutions to order of $(a/H)^4$ gives the following approximate but relatively simple form.

$$\frac{A_0^+}{a} \approx 1 - \frac{a}{H}\left[1 - 1.74138\frac{H}{R} + 0.205911\frac{H^2}{R^2}\right] + \frac{a^2}{H^2}\left[1 - 3.48276\frac{H}{R} + 3.03241\frac{H^2}{R^2} + 0.411822\frac{H^3}{R^3} - 0.71714\frac{H^4}{R^4}\right] - \frac{a^3}{H^3}\left[1 - 5.22414\frac{H}{R} + 9.09722\frac{H^2}{R^2} - 4.66284\frac{H^3}{R^3} - 2.15142\frac{H^4}{R^4} + 1.87322\frac{H^5}{R^5}\right] + \frac{a^4}{H^4}\left[2 - 6.96552\frac{H}{R} + 18.1944\frac{H^2}{R^2} - 21.1223\frac{H^3}{R^3} + 4.89264\frac{H^4}{R^4} + 7.49288\frac{H^5}{R^5}\right] \quad (11)$$

$$\frac{A_1^+}{a^2} \approx + \frac{a^2}{H^2}\left[1 - 0.411822\frac{H^3}{R^3}\right] - \frac{a^3}{H^3}\left[1 - 1.74138\frac{H}{R} - 0.205911\frac{H^3}{R^3} + 0.71714\frac{H^4}{R^4}\right] + \frac{a^4}{H^4}\left[2 - 3.48276\frac{H}{R} + 3.03241\frac{H^2}{R^2} + 0.71714\frac{H^4}{R^4} - 1.24881\frac{H^5}{R^5}\right] \quad (12)$$

$$\frac{A_2^+}{a^3} \approx - \frac{a^3}{H^3}\left[1 + 0.411822\frac{H^3}{R^3}\right] + \frac{a^4}{H^4}\left[1 - 1.74138\frac{H}{R} + 0.617734\frac{H^3}{R^3} - 0.71714\frac{H^4}{R^4} + 0.0847989\frac{H^6}{R^6}\right] \quad (13)$$

VII. CAPACITANCE CALCULATIONS

The capacitance coefficients are simply related to the charges on the spheres for specific choice of voltages on the sphere. If both spheres are held at +1 volt then the charge on each sphere is

$$C_+ = C_{11} + C_{12}, \quad (14)$$

and if one sphere is held at 1 volt and the other sphere is held at -1 volt then the charge on the first sphere is

$$C_- = C_{11} - C_{12}. \quad (15)$$

The coefficients C_+ and C_- can be calculated from the solution to Laplace's equation for $V_+(r,\theta)$ and $V_-(r,\theta)$ in the following manner. The charge density on the first sphere is given by

$$\sigma_\pm(\theta) = -\epsilon\left.\frac{\partial V_\pm(r,\theta)}{\partial r}\right|_{r=a}, \quad (16)$$

where ϵ is the permittivity of the medium surrounding the spheres. The capacitance coefficients can be calculated by integrating the charge density over the surface of the sphere

$$C_\pm = \int_0^{2\pi}\int_0^{\pi}\sigma_\pm(\theta)a^2\sin\theta d\theta d\phi = 2\pi a^2\int_0^{\pi}\sigma_\pm(\theta)\sin\theta d\theta. \quad (17)$$

To a good approximation of order $(a/H)^5$ the charge on the sphere is given by the A_0 term in the voltage. Using this approximation of only considering A_0 for capacitance calculations we get

$$\frac{C_{\pm}}{4\pi\epsilon a} \approx A_0^{\pm}\left(1 \mp \frac{2f^3}{1-f^2}\right), \qquad (18)$$

where $f = a/H$, and A_0^+ , A_0^- are the monopole coefficients from the +/+ and +/- cases respectively. From the above calculation we get

$$\frac{C_{11}}{4\pi\epsilon a} = \frac{1}{2}\left[\frac{C_+ + C_-}{4\pi\epsilon a}\right] \quad (19) \quad \text{and} \quad \frac{C_{12}}{4\pi\epsilon a} = \frac{1}{2}\left[\frac{C_+ - C_-}{4\pi\epsilon a}\right] \qquad (20)$$

In previous sections we calculated pretty good closed-form approximations for the monopole term $A_0^{\pm}$. By substituting those expressions in the two equations above we generate C_{11} and C_{12} and ``exact" results in these plots are computed by using 8 multipole terms (A_0 , ..., A_7) and $m = k = 10$ cylinder terms.

VII. COMPARISON OF NUMERICAL AND ANALYTICAL SOLUTIONS

The computation of capacitances from analytical expressions developed in this paper may also be compared to a numerical simulation using the commercial CST code. The results of such comparisons are shown in Figures 3 and 4. We consider an illustrative case of a / R = 0.1 as a function of (a/H).

Next, we compare the capacitance calculations.

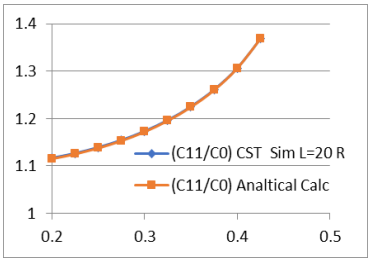

(a/H) →

Figure 3. Comparison of analytical and numerical results of Capacitance between spheres f or a/R = 0.1, as a function of (a.H)

It is noted that the capacitances shown in Figures 3 and 4 are normalized to the capacitance of the isolated sphere given by $C_0 = 4\pi\varepsilon_0 a$. It is emphasized that the capacitances are given in this paper by the leading monopole term Ao. The higher order terms do not contribute to the total charge on the sphere and hence do not contribute to the capacitances.

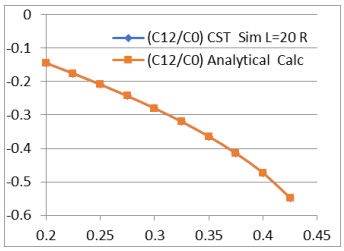

(a/H) →

Figure 4. Comparison of analytical and numerical results of Capacitance between either sphere and the grounded cylinder for a/R = 0.1 as a function of (a/H)

However, the value of the monopole term is dependent on how many multipoles are considered. The coefficient Ao has been obtained in close form for the monopole, dipole and quadrupole expansions.

Once again, the comparison of the capacitances calculated by CST simulation and the analysis presented in this paper are seen to be very good, when we use the octupole expansions.

VI. SUMMARY

This problem arose in the context of trying to enhance our understanding of the compact Marx generators. . Analytical formulation clearly shows the dependence of the capacitances on various geometrical parameters of the problem, As in many mathematical physics problems, one needs to be aware of the valid ranges of the parameters of the multipole expansion.

Acknowledgement

The authors are thankful to Prof. Jane M. Lehr and Mr. J. Cameron Pouncey of Dept. of ECE, University of New Mexico, Albuquerque, NM for suggesting this problem that came up during their research on compact Marx generators.

References

[1] J.C.Pouncey, J.M.Lehr and D.V. Giri, “Triggering of Compact Marx Generators”, Presented at AMEREM 2018 held at University of Santa Barbara, August 2018.

[2]R.C.Knight, “The Potential of a Sphere inside an Infinite Circular Cylinder”, Quarterly Journal of Mathematics, Oxford University Press, November 1935.

[3]W.R.Smythe, “Charged Sphere in a Cylinder”, Journal of Applied Physics, Volume 31, Number 3, March 1960, pp 553-556.

[4] I.C.Chang and I.D.Chang, “Potential of a Charged Sphere inside a Grounded Cylindrical Tube”, Studies in Applied Mathematics, Volume 47, Issue 1-4 , 1967, pp 360-367.

[5] A.Morrison, “Potential and Electric Fields of a Conducting Sphere in the Presence of a Charged Conducting Plane”, U. S. Army, HDL Report Number, HDL-TR-2161, Approved for Public Release, Distribution Unlimited, August-Nov 1988.

[6] S. Banerjee, et al., “Exact and Approximate Capacitance and Force Expressions for the Electrostatic Interaction Between Two Equal-Sized Charged Conducting Spheres”, IEEE Transactions on Industry Applications, Volume 53, Number 3, May-June 2017, pp 2455-2460.

Singularity Expansion Method as Applied to a Linear Antennas in Conducting Media

D. V. Giri
Pro-Tech, Wellesley, MA USA
Dept. of ECE, University of New Mexico
Albuquerque, NM, USA
Giri@DVGiri.com

F. M. Tesche
EM Consultant (Retired)

***Abstract*— This presentation is based on a paper published by the two authors in the Journal of Electromagnetics [1]. Singularity Expansion Method (SEM) [2] has been applied to antennas and scatterers in free space where the pole contributions dominate. We have explored the SEM considerations of a linear antenna in a conductive medium which result in branch cut contributions, in addition to the pole contributions. In some cases, the branch cut contributions can be negligible, but nevertheless present.**

Keywords—Singularity Expansion Method, linear antenna, SEM poles and branch cuts, conductive medium

Introduction

The application of the singularity expansion method (SEM) to the analysis of antennas and electromagnetic scatterers has usually been applied to simple, isolated bodies in free space or to simple bodies near a perfectly conducting groundplane.. In analytically investigating the behavior or antennas in a lossy medium, it is known that in addition to simple pole singularities, there is a branch cut linking two branch points in the complex frequency representation of the antenna response. While significant information regarding the nature of the branch cut and its effect on the antenna response can be obtained by purely analytical methods, a numerical study of this can also provide useful results.

I. Motivation and Solution Approach

SEM is a useful analytical tool for transmission lines, scatterers and antennas in free space. This has motivated us to investigate SEM of antennas and scatterers in conducting media. Our first example is a 2-wire transmission line with arbitrary loads at the two ends, as shown in Figure 1. Let us say the transmission line is of length ℓ and the loads at the two ends are respectively Z_1 and Z_2. The characteristic impedance of the line is Z_c. We immediately know that the line will resonate when the length ℓ becomes an integral multiple of half wavelength. Moving to the complex frequency or the complex s-plane (Ω+j ω), we can show that the complex natural frequencies are given by equation (1) where ρ_1 and ρ_2 are the reflection coefficients at the two ends. Our second example is a wire scatterer of length L shown in Figure 2.

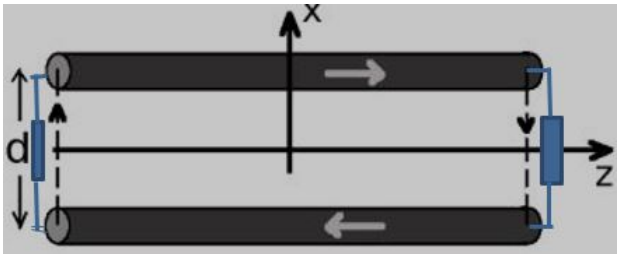

Figure 1. Two-wire transmission line with arbitrary terminations

$$\Omega = \ln\left(\frac{1}{\rho_1\rho_2}\right)\frac{c}{2\ell}; \qquad \omega_n = 2\pi n\frac{c}{2\ell} \tag{1}$$

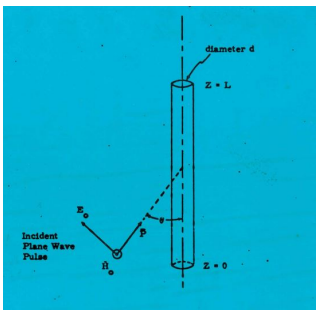

.

Figure 2. A thin wire scatterer of length L in free space

The complex natural frequencies of the wire scatterer has been investigated in detail by many researchers [3-6]. The complex natural frequencies occur in layers in the upper left half of the complex s-plane (Figure 3). It is interesting to note that the Meyers, et al. solution [6] provides only the resonances for the first layer (ℓ = 1). This is likely due to the use of only the first layer current distributions in their variational calculations. It is speculated that if the higher layer modal current distributions were to be used in the calculation, this method might provide the ℓ = 2 and 3 resonances as well.

III SEM OF AN ANTENNA/SCATTERER IN A CONDUCTING MEDIUM

We now consider the problem of an antenna (or a wire scatterer) in a conducting medium shown in Figure 4.

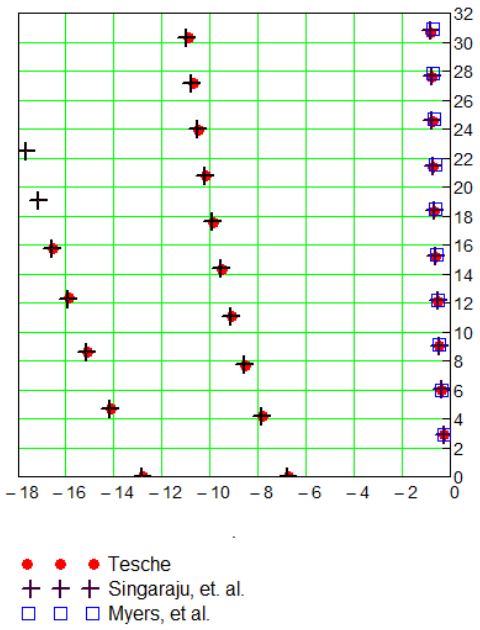

Figure 1. Overlay plots of the normalized resonant frequencies reported in [4, 5 and 6]

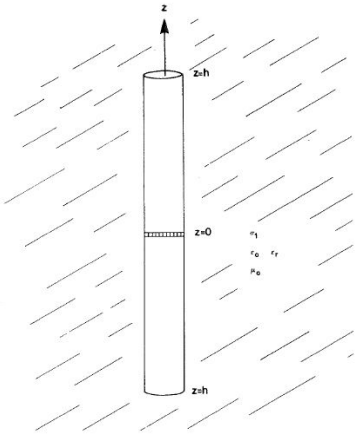

Figure 4. Antenna of length L= 2h and radius a immersed in a conducting medium

The length of the antenna is L = 2h and the radius is a. The constituent parameters of the surrounding medium is indicated in Figure 4. The Pocklington form of the integral equation for the current distribution in this case is like the free space case, with 2 differences. The propagation constant of the current waveform is different and there is conduction current in the surrounding medium. The Electric Field Integral equation EFIE is given by equ ation (2). In the Kernel function K (z, z',s) of the EFIE, the exponent $\gamma_1 R$ is the source of occurrence of branch points., since the distance R(z, z') is frequency independent, we need to examine γ_1.

$$\left(\frac{\partial^2}{\partial z^2} - \gamma_1^2\right) \int_{-h}^{h} I(z',s)\, K(z,z';s)\, dz' = -(s\varepsilon + \sigma_1) E_z^{inc}(z,s)$$

where

$$K(z,z';s) = \frac{e^{-\gamma_1 R(z,z')}}{4\pi R(z,z')}$$

$$\gamma_1 \equiv \text{complex propagation constant} = \frac{s}{c}\sqrt{\varepsilon_r + \frac{\sigma_1}{s\varepsilon_0}} = \sqrt{s\mu_0}\sqrt{s\varepsilon + \sigma_1}$$

and $R(z,z') = [(z-z')^2 + a^2]$.

(2)

This leads to branch points at s = 0, and s = $-\sigma_1/(\varepsilon_0 \varepsilon_r)$. We proceed by first matricizing the EFIE, and obtaining the input admittance Y_{in} and the short circuit current I_{sc} from a solution of the current distribution I (z,s).One can also get the input impedance of the antenna Z_{in} from these calculations. It is important to note that the change from antenna in free space is like making a change of variable from

$$s \text{ to } s\sqrt{\varepsilon_r + (\sigma_1/s\varepsilon_0)}. \qquad (3)$$

This observation leads to the following relationship

$$p_{\alpha 1} = \frac{-\sigma_1}{2\varepsilon_0\varepsilon_r} + \frac{1}{2\varepsilon_r}\sqrt{\left(\frac{\sigma_1}{\varepsilon_0}\right)^2 + 4\varepsilon_r p_{\alpha 0}^2} \qquad (4)$$

Where $p_{\alpha 1}$ and $p_{\alpha o}$ are the poles in conducting medium and free space respectively. We have computed the poles and zeroes of the antenna's input impedance for the case of L = 1m and (L/a) = 200.

We show the first few numerically computed poles and zeros for the free space situation. Note that the origin is an impedance pole when the conductivity = 0. But as soon as some finite conductivity is introduced, the origin turns into a branchpointandpolesand zerosasymptoticallymovetoward-$_{00}$ on the negative real axis. The pole-zero trajectories are plotted in Figure 5, where the conductivity is gradually increased fromOmhos/m toabout0.05 mhos/m.

Once the pole-zero structure in the upper left half s-plane is known, it is straightforward to compute the corresponding pole-zero locations for the antenna input quantity, when the antenna is surrounded by aconducting medium. The determination of the singularity structure is complete, once thebranchcut is added to the knowledge of the pole-zero locations. The occurrence of the finite branch cut along the negative real axis of the complex s-plane also contributes to the pole series of antenna input quantity say F(s). F(s) can represent either Z_{in} or Y_{in} of the antenna in a conducting medium. Let us now determine the branch cut contribution to F(s), Consider the contour integral shown in Figure 6. From Cauchy's residue theorem, we have

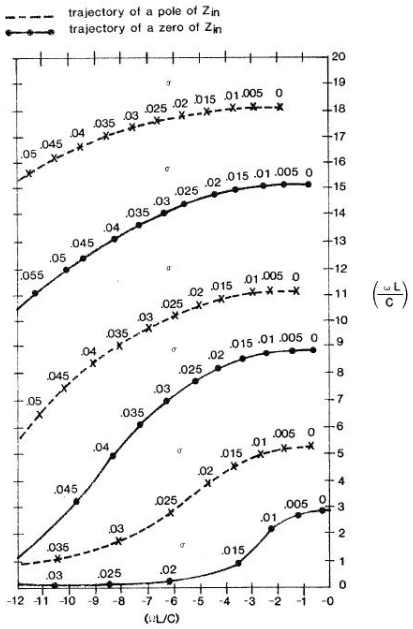

Figure 5. Trajectories of poles and zeros of the input impedance

$$\int \frac{F(s)}{s_0 - s}\, ds = 2\pi j \left[F(s_0) + \sum_{\alpha} \frac{R_\alpha}{s_\alpha - s_0} \right]. \quad (5)$$

If we assume that the contour integral on the big circle does not contribute, equation (5) can be approximated by

$$F(s) = \sum_{\alpha} \frac{R_\alpha}{s - s_\alpha} + \frac{1}{2\pi j} \int_{0}^{-\Omega_b} \frac{\Delta F(\Omega)}{s - \Omega}\, d\Omega \quad (6)$$

Where $\Delta F(\Omega)$ is the discontinuity across the branch cut on the negative real axis. The summation term in equation (6) is the pole contribution and the integral term is the branch cut contribution arising out of the fact that the antenna is immersed in a conducting medium. It is now possible to compare the two separate contributions. We have estimated the input impedance of the antenna for the case of L = 1m and L/a = 200, for many values of conductivity and shown in in Figure 7.

IV SUMMARY

In this paper, we have extended the SEM analysis of an antenna in free space to the case of antenna in a conducting medium. SEM is a mature subject, but past analyses have not accounted for branch cut contributions which arise if the antenna is in a conducting medium or if the antenna is near a half space. We have observed that if we know the complex poles of the antenna in free space, we can derive these poles for the antenna in a conducting medium by a simple change of variable method. Branch points and hence branch cut contribution to the response function occur in this case of antenna in a conducting medium. It is possible to evaluate the relative contributions of the pole series and the branch cut portion. The occurrence of the branch cut and its finite extent was also numerically validated,

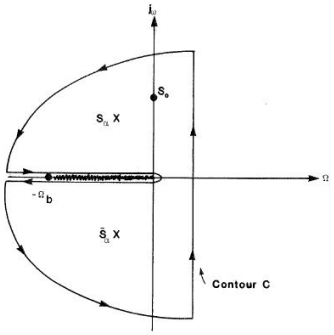

Figure 6. Estimating the branch cut contribution

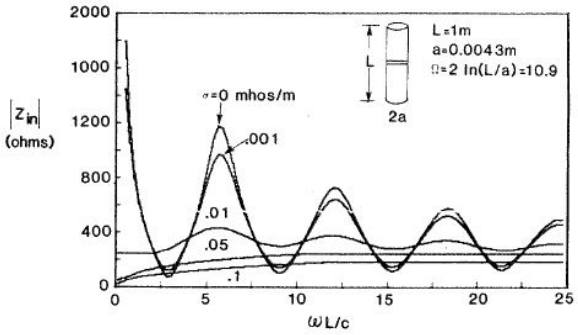

Figure 7. Antenna input impedance for varying conductivities

It turned out that for the cases of geometry and the conductivities we considered in this study, the branch cut contribution was not important, but in general this cannot be neglected and should be included,

References

[1] D. V. Giri and F. M. Tesche, "On the Use of Singularity Expansion Method of an Antenna in a Conducting Medium", **Electromagnetics,** 1981. pp 455-471.

[2] C. E. Baum, "The Singularity Expansion Method: Background and Developments", IEEE APS Newsletter,Vol28, Issue 4, pp 14-23, Aug 1986.

[3] F. M. Tesche and D. V. Giri, "An Overview of the Natural Frequencies of a Straight Wire by Various Methods", IEEE Transactions on Antennas and Propagation, Volume 60, Issue 12, pp 5859-5866.

[4] F. M. Tesche, "On the Analysis of Scattering and Antenna Problems Using the Singularity Expansion Technique," IEEE Transactions on AP, vol. AP-21, pp. 53–62, January 1973.

{5] B. K. Singaraju, D. V. Giri, and C. E. Baum, "Further Developments in the Application of Contour Integration to the Evaluation of the Zeros of Analytic Functions and Relevant Computer Programs", Mathematics Notes, Note 42, March 1976. Available for download at http://www.ece.unm.edu/summa/notes/Mathematics/0042.pdf

[6] J. M. Meyers, S. S. Sandler and T. T. Wu, "Electromagnetic Resonances in a Straight Wire", IEEE Trans AP, vol. 59, No. 1, Jan. 2011.

HF Radio E1 HEMP Protection Using Gas Discharge Tube Surge Protectors

Edward B Savage
Metatech Corporation
Goleta, California, USA
savagee@cox.net

William A Radasky
Metatech Corporation
Goleta, California, USA
wradasky@aol.com

***Abstract*—Radios are designed to receive weak RF signals from their antennas, and typically have sensitive components on their front ends. However if an E1 HEMP is incident on the antenna, then the signal brought in can be very large, and potentially damage the receiver. This situation is similar to large transients from nearby lightning, although E1 HEMP is a faster, higher frequency, assault. Tests were performed to see how well lightning protectors for HF radios would work for E1 HEMP protection.**

Keywords—gas discharge tubes, surge protectors, HF radio protection

I. Introduction

A high level EM disturbance, such as E1 HEMP or nearby lightning, will be picked up by an HF antenna and result in a high level pulse going down the cable and into the receiver. This can easily destroy the receiver front end, and protection devices should be used to prevent this[1]. The devices tested were simple surge protectors, connected into the cabling from the antenna to the radio. Fig. 1 shows one of the tested sample devices. These are nonlinear devices that are essentially "invisible" to the normal operation of the system until the voltage gets too high, when they quickly then turn into a short circuit, connecting the coaxial center wire to the inside of the cable shield. There are several questions of interest for such protectors: How good is the short circuit? At what voltage does the protection get triggered? How does this vary with very fast pulses (fast rise rates)?[2] Can the protector itself get damaged, and if so, what is its damage state? It is also important to recognize that under normal conditions there is no feedback that indicates if it is OK – that it will work as planned when a high level destructive pulse comes down the cable towards the radio. Samples of such surge protectors were tested with high level pulses to investigate these issues for E1 HEMP like pulses. The protection in the sample of Fig 1 used a shunt gas tube – under high enough voltage the gas was ionized and became a short circuit.

Fig. 1. Example of a GDT surge protector (taken apart).

II. Test Setup

The test setup consisted of a pulser feeding into the surge protector on one side, and an oscilloscope on the other side, recording how much of the pulse gets through. The test equipment and cabling were all matched 50Ω. The point of the test was to evaluate the protection for the very fast E1 HEMP pulses – typically such devices are meant for the slower-rising (but more energetic) lightning pulses.

III. Test Results

Fig. 2 shows oscilloscope recordings for three pulses, at incident peak levels as given in the legend. The lowest level pulse (0.8 kV, green line) does not trigger the protection; for the 0.9 kV pulse (blue line), the protection is triggered well after the peak; and for the 2.5 kV (red line) the short turns on just before the peak, but the leakage peak is about 1.9 kV. Fig. 3 shows the leakage pulse peaks versus incident peak level for all the measured test shots on another sample.

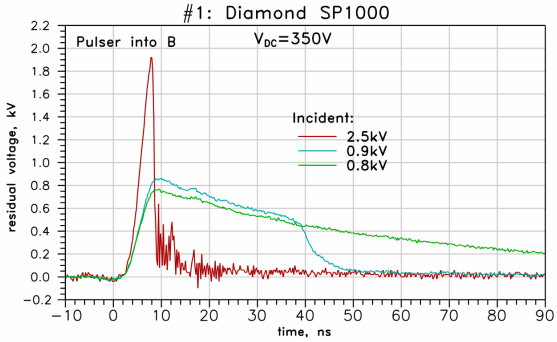

Fig. 2. Sample residuals.

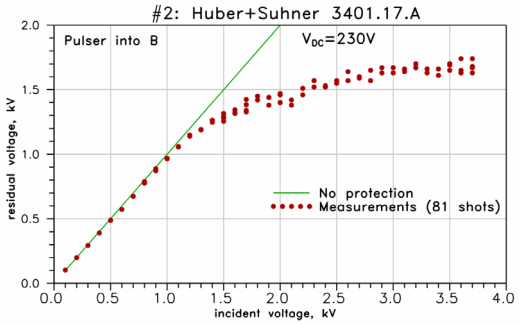

Fig. 3. Peak residuals for all shots for one device.

IV. Conclusions

There was some variation in all the test samples, but a general conclusion is that the leakage pulse peak for E1 HEMP pulses is much higher than the device spec protection level, which is given for much slower pulses. For further work it would be useful to test these devices under active transceiver conditions – with the transmitter sending out RF energy.

References

[1] Steven Karty, N5SK, "Lightning (and EMP) Surge Protection for HF Radios", CQ magazine, July 2018, pg. 18-23.

[2] M. A. Messier, K. S. Smith, W. A. Radasky, and M. J. Madrid, "Response of Telecom Protection to Three IEC Waveforms", Zurich EMC Symposium, February 18, 2003

Geomagnetic Storms and Electric Power Grid Issues

Edward B Savage
Metatech Corporation
Goleta, California, USA
savagee@cox.net

William A Radasky
Metatech Corporation
Goleta, California, USA
wradasky@aol.com

***Abstract*—Geomagnetic disturbances (or storms), GMDs, interact with electric power grids, and can cause blackouts and damage. The mechanism is generation of quasi-DC currents in the lines – GIC (geomagnetically induced currents). In an upcoming Cigre technical bulletin typical GMDs, and resulting GICs, are presented to help predict their effects, and plan protection. Here we will present typical results for three types of GMDs, and discuss some possible misunderstandings.**

Keywords—geomagnetic storm, GMD, power grid vulnerability, electrojet, coronal hole, sudden impulse

I. Introduction

Past experience has shown that GMDs can be an issue for the power grid, and have caused blackouts and damage [1]. A major issue is that the grid evolves at a fast rate compared to the tie scale of the occurrences of, and variations in, very large GMDs. To plan for, and lessen the impact of, very large storms, an upcoming Cigre technical bulletin will present typical GMDs of three types: electrojet, coronal holes, and sudden impulse – which will be summarized in this presentation. We will also point out some possible misunderstandings.

II. Electric Power Grid Circuit

The important part of a GMD is the horizontal vector disturbance to the geomagnetic magnetic (B) field, such as might be measured by magnetometer sites. Through ground conductivity profiles (down to deep depths), these produce electric fields (E) [2], and the resulting ground currents. Some of the ground current will flow through power lines, if grounded at two separate points. These effects are slow enough to be quasi-DC, and only governed by resistances (wires, transformers windings, and grounds).

III. Some Results

It is sometimes believed that the B disturbance is predominately just a north/south effect (here we use geomagnetic directions), and so the resulting E field is only in the east/west direction – thus north/south power lines are not at risk. This is not true – Fig. 1 shows a typical auroral electrojet example of the E field vector direction over time for four locations. We see that at some times there are also significant north/south extents to the E field.

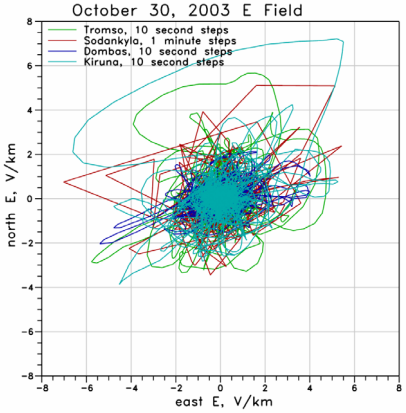

Fig. 1. Rotation plots of E fields for sample electrojet.

Coronal Hole High Speed Stream (CHHSS) is similar to electrojet, but a significant difference is that the coronal hole can repeat night after night for months, as shown in the example of Fig. 2.

Electrojet and coronal hole are known to be worse at higher latitudes. Sudden impulse, however, occurs simultaneously and at similar levels throughout the world, as shown by the example in Fig. 3, which has a worldwide distributions of measurement points.

IV. Conclusions

More work is needed in fully understanding and characterizing the various types of GMDs. The coupling to the eletric grid is understood in principle, although the modeling parameters may not always be well known. It is important to avoid misunderstandings, such as thinking GICs are only an issue for higher latitudes or only for east/west power lines.

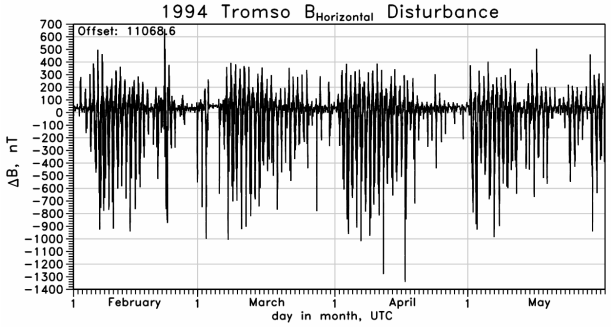

Fig. 2. Coronal hole B disturbance magnitude for four months.

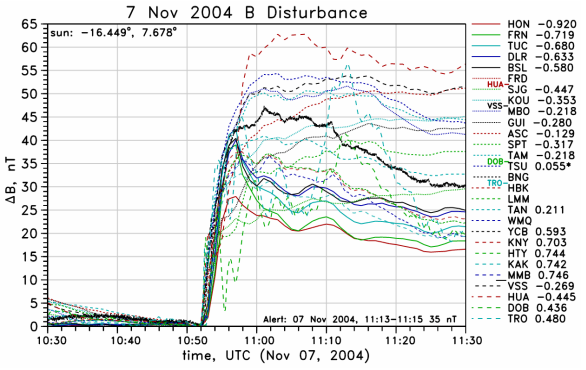

Fig. 3. SI B disturbance magnitudes for November 7, 2004.

References

[1] W. A. Radasky, "Overview of the impact of intense geomagnetic Storms on the U.S. high voltage power grid," 2011 IEEE International Symposium on EMC, Long Beach, August 2011, pp. 300-305.

[2] J. L. Gilbert, W.A. Radasky, E. B. Savage, "A technique for calculating the currents induced by geomagnetic storms on large high voltage power grids," 2012 IEEE International Symposium on EMC, Pittsburgh, August 2012.

The Self-breakdown Characteristics of the Output Switch for EMP Simulator

Fan Guo, Yanzhao Xie, Wei Jia, Zhiqiang Chen, Shi He
State Key Laboratory of Electrical Insulation and Power Equipment
Xi'an Jiaotong University
Xi'an, China

Wei Wu, Xiaoping He, Linshen Xie
State Key Laboratory of Intense Pulsed Radiation Simulation and Effect
Northwest Institute of Nuclear Technology
Xi'an, China

***Abstract*—The self-breakdown characteristics of the output switch for different electrode configurations, materials and the slopes of pulsed voltage-d*u*/d*t* under high electric field of hundreds of kV/cm in SF_6 have been investigated. The influences of hemisphere, cone and annulus electrode configurations for stainless steel electrode material have been compared. Four types of electrode materials for annulus electrode configuration have also been considered in the experiment, including stainless steel, brass, W-Cu alloy and graphite. The output switch was pressurized from 0.1 to 0.5 MPa with SF_6 and operated from 170 to 550 kV with the maximum breakdown electric field up to 700 kV/cm. The effects of electrode configuration, material and d*u*/d*t* on the breakdown voltage and time delay of the output switch have been presented. To estimate the relationship between breakdown electric field and d*u*/d*t*, a novel empirical fitting formula has been proposed. We have also analyzed the breakdown time delay under high electric field of hundreds of kV/cm. The experimental results can provide data supports for designing the optimal conditions and improving the performance of self-breakdown pulsed gas switch.**

Keywords—Pulsed gas switch, high electric field, SF_6, breakdown voltage, breakdown time delay, electrode configuration, electrode material, d*u*/d*t*

I. INTRODUCTION

Electromagnetic pulse (EMP) simulator is the key equipment for the EMP research [1-2]. The radiation performance of EMP simulator depends on the characteristics, in particular, on the breakdown deviation or jitter of the output switch as pulse compression device. Designing the optimal conditions of the output switch is critical to obtain appropriate pulse shaping [3-5]. In the high power pulsed equipments, to achieve low breakdown deviation or jitter, the trigger system or trigger circuits, such as laser trigger system [6-10], external electrical trigger circuit and UV-illuminated circuit [11-14] are needed. For gas switch that require nanosecond or sub-nanosecond jitter, the laser triggering is the best method. However, the complicated optical path and high cost limit the wide use of laser triggering. If there is no limitation on the peripheral space, external electrical triggering or UV pre-ionization method can be utilized.

In order to meet IEC 61000-2-9 standard of HEMP environment [15], with the rise time of ~2.3±0.5 ns and the standard waveform, the output switch of EMP simulator must be very low inductance with the gap distance of ~cm in high pressure SF_6 and can hold off the pulsed voltage up to 2 MV. Hence, the output switch is operated in the high electric field from hundreds of kV/cm to MV/cm and in the charge time of several tens of nanoseconds. Meanwhile, the output switch is in three separate pressure vessels. Due to the limitation of space, it is difficult to trigger or UV illuminate the output switch. Therefore, the output switch is operated in self-breakdown mode, which brings a big challenge to achieve the low jitter.

Microsecond or hundreds of nanoseconds pulsed switches with the breakdown electric field of 100~200 kV/(cm·atm) had been investigated [10-14,16-17]. But few literatures have been reported about the effect of fast pulse and high electric field on breakdown deviation or jitter. For fast rise-time pulse or high electric field condition, a point of view different from the classical streamer model should be taken [18]. Various researchers had studied the influence of electrode configuration [19-21], electrode material and surface conditions [22-26], gap distance [27] and rise rate of pulse [28] on the breakdown characteristics of pulsed discharge. However, it is difficult to systematically compare with the effect of these factors on deviation and jitter due to different experimental conditions.

Based on the theory of pulsed gas discharge, electrode material and configuration may affect the initial electron emission while electric field distribution may affect the formation path of streamer and the development of plasma channel. To improve the performance of pulsed gas switch in self-breakdown mode, we have carried out the research about the impact of electrode configuration, material and d*u*/d*t* on the breakdown characteristics under the electric field from 210 to 700 kV/cm and 50 ns pulsed charge time in SF_6.

II. EXPERIMENTAL SETUP

A. Experimental Circuit

The experimental equivalent circuit is shown in Fig. 1. The Marx bank, which has an erected capacitance of 3.3 nF, pulse-charges a 450 pF transfer capacitor. The transfer switch closes to rapidly discharge into a 150 pF peaking capacitance. The breakdown time of the output switch is from 20 ns to 50 ns. The load resistance is 166 Ω, which is parallel connected with six high power resistances of 1 kΩ.

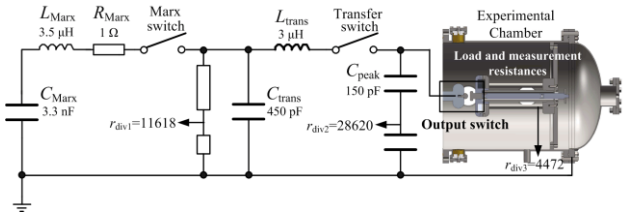

Fig. 1 The schematic of experimental equivalent circuit

The experimental parameters are measured by the resistive dividers and capacitive divider. The ratios of resistive divider for Marx voltage and output voltage are

11618 and 4472, respectively. The ratio of capacitor divider for breakdown voltage of output switch is 28620, which is designed as a kind of self-integral mode.

To investigate the self-breakdown characteristics of the output switch, electrode configuration, electrode material and d*u*/d*t* as the influence factors have been considered. Three types of configurations including hemisphere, cone and annulus electrode have been designed. The diameters of all electrodes are both 30 mm and the chamfer radii of hemisphere, cone and annulus are 15, 7.5 and 4 mm, respectively. The electric field distributions for three types of electrodes are shown in Fig. 2.

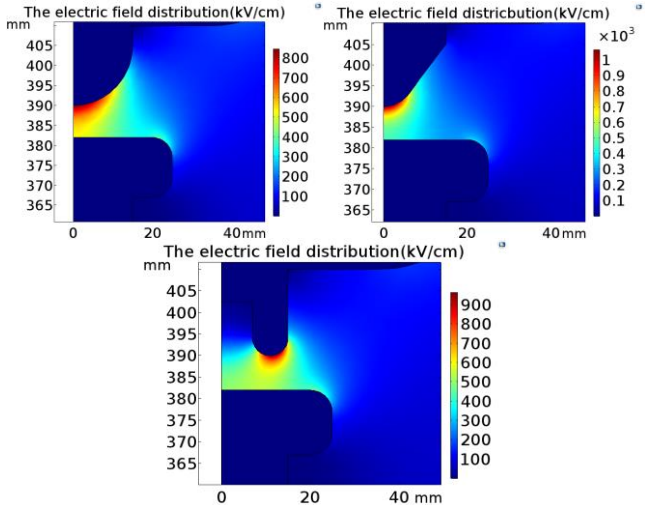

Fig. 2 The electric field distributions for three types of electrodes

From the electric field distributions, the electric field enhance factors can be calculated as 1.35, 1.71 and 1.54 under 8 mm gap, respectively. Four types of electrode materials including stainless steel, brass, W-Cu alloy and graphite are used in the experiment. By adjusting the input voltage of Marx, the effect of d*u*/d*t* on the breakdown characteristics can be compared. The input voltages of Marx are set as 16, 20, 25 and 30 kV, respectively. The output switch is pressurized with SF_6 and the pressure is set from 0.1 to 0.5 MPa.

B. *Experimental method*

The Marx capacitors are firstly charged to a voltage of 16 kV and then discharges to the transfer capacitor. When the pulsed voltage of transfer capacitor excesses the breakdown voltage of transfer switch with UV illumination, the energy is transferred to the peaking capacitor. The stainless steel and hemisphere electrode, SF_6 insulated output switch at a pressure of 0.1 MPa finally transfers the energy to the load resistance within 50 ns. For the same experimental condition, 20 shots data will be obtained including Marx output voltage, switch breakdown voltage and load voltage. Fig. 3 shows the typical waveforms. Because of pre-pulse of peaking capacitor, the breakdown time delay is defined as the time from the point of intersection between the prolong line of d*u*/d*t* and X axis to the breakdown point. The slope of pulsed voltage is determined by the point of 40% peak value and the point of peak value.

The breakdown characteristics have been investigated by increasing the input voltage of Marx from 16 to 30 kV and the pressure of pulsed gas switch from 0.1 to 0.5 MPa. The output switch hardly discharges with low input voltage for 0.4 and 0.5 MPa, hence, the input voltage of Marx is only set as 25 and 30 kV. After the experiment, SF_6 will be recycled and the electrode configuration and material will be exchanged into the other types. It is difficult to process the data by manual method since the numbers of total experimental data are relatively large. The data acquisition can be firstly obtained by Tek DPO4104 oscillograph automatically and then the data of breakdown voltage and time delay can be processed by using Matlab self-programming after the experiment.

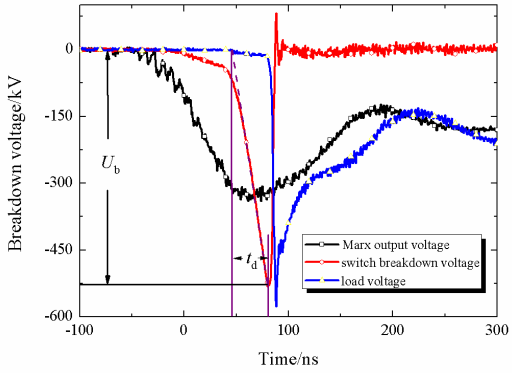

Fig. 3 The typical experimental waveforms

III. EXPERIMENTAL RESULTS

A. *Effect of the slope of pulsed voltage*

In order to estimate the effect of the slope of pulsed voltage, the distributions of breakdown points of stainless steel electrode for hemisphere, cone and annulus electrodes under three values of d*u*/d*t* are shown in Fig. 4, 5 and 6, respectively.

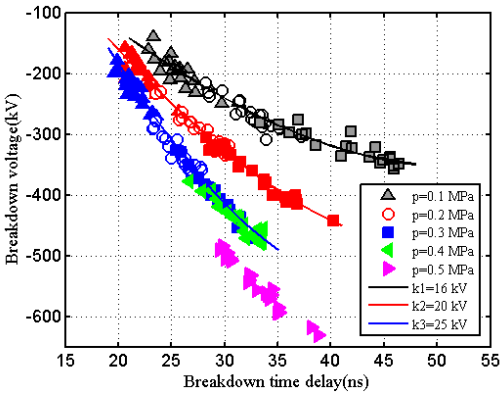

Fig. 4 The breakdown distributions for hemisphere electrode

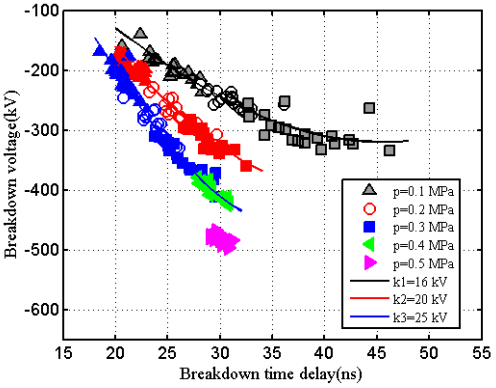

Fig. 5 The breakdown distributions for cone electrode

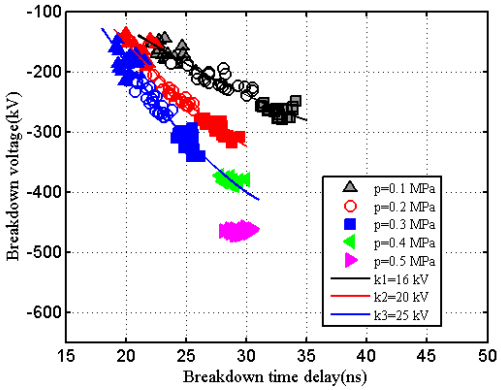

Fig. 6 The breakdown distributions for annulus electrode

As the value of d*u*/d*t* increased, the breakdown voltage will be increased while the breakdown time delay will be short. Thus, the way of comparing the percentage of deviation is better. In general, there are no distinct differences of breakdown voltage for three values of d*u*/d*t*. The absolute values of variation are both less than 2%, so there are no need to reduce the deviation by increasing the value of d*u*/d*t*. However, to improve the reliability, it is can be utilized by increasing the value of d*u*/d*t* and decreasing the pressure at the same time. For example, when the breakdown voltage is 300 kV, the breakdown deviation percentage is 9.9% under 8 kV/ns of d*u*/d*t* at a pressure of 0.3 MPa, but the breakdown deviation percentage will be decreased below 5.2% under 13 kV/ns of d*u*/d*t* at a pressure of 0.2 MPa. In addition, when the value of d*u*/d*t* is 8 kV/ns, the trend between breakdown voltage deviation and jitter is different, while the jitter is larger than the deviation of breakdown voltage. Because the breakdown points are focus on the region of peaking pulse, the breakdown time delay will be more dispersive.

B. *Effect of electrode configuration*

In order to estimate the relationship between breakdown voltage and time delay, the absolute values of breakdown voltage are present in the below figures. The deviations of breakdown voltage and time delay of stainless steel electrode for different configurations with 8 mm of gap distance are shown in Fig. 7.

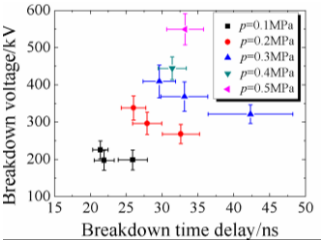

(a) Hemisphere electrode

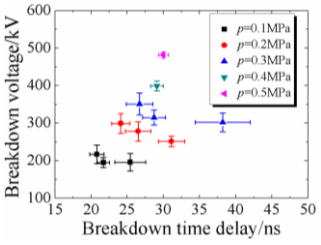

(b) Cone electrode

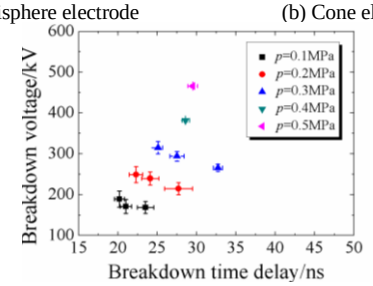

(c) Annulus electrode

Fig. 7 The breakdown voltage and time delay for different configurations

From Fig. 7, it can be noted that the breakdown voltage deviation and time delay jitter of annulus electrode are both lower than those of other electrode configurations at the same experimental condition. The jitters for hemisphere electrode are both more than 5%. On the contrary, the jitters for annulus electrode are both less than 5% in the whole range of experimental conditions, in particularly, less than 2% at the pressure of 0.4 and 0.5 MPa. However, the breakdown voltage is lower 10~15% than that of hemisphere electrode.

C. *Effect of electrode material*

The breakdown voltage and time delay of annulus electrode for four types of electrode materials with 10 mm of gap distance are shown in Fig. 8.

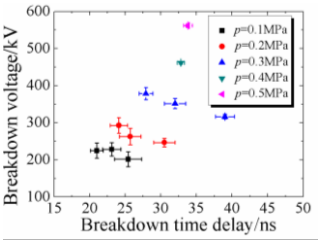

(a) Stainless steel electrode

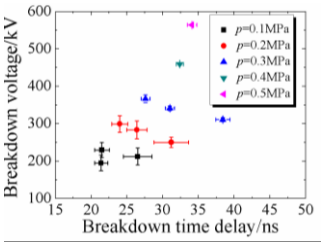

(b) Brass electrode

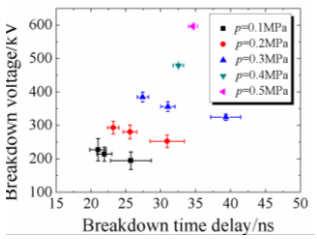

(c) W-Cu alloy electrode

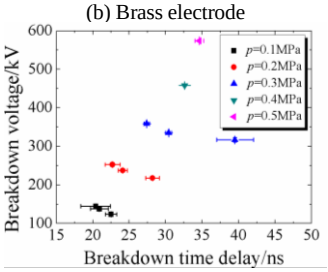

(d) Graphite electrode

Fig. 8 The breakdown voltage and time delay for different materials

It can be seen that there are no distinct differences for the breakdown voltage deviation and time delay jitter of three metallic electrodes. Besides, the breakdown voltage of graphite electrode is lower than those of three metallic electrodes at the pressure of 0.1 and 0.2 MPa, especially less than 30% at a pressure of 0.1 MPa. Except for this, the breakdown performance of graphite electrode is better than those of three metallic electrodes.

D. *The empirical fitting of breakdown voltage*

The experimental results show that even if electrode configuration, gas pressure and gap distance are the same, the breakdown voltage and time delay will simultaneously change by varying the values of d*u*/d*t*. In another word, the breakdown voltage and time delay are correlated. At present, the estimation of breakdown electric field is based on J. C. Martin formula and the effective time should be determined. However, Martin formula is summarized under the experimental conditions of non-uniform field in the range of 5 to 100 kV/ns and with an effective time of 9 ns, which brings some limitations to the estimation of breakdown electric field for different d*u*/d*t*. To compare with the experimental data for different d*u*/d*t*, the value of breakdown voltage should be normalized. We consider the format of J.C. Martin formula and the relationship of the parameters can be described by the following equations:

$$E = A \cdot p^{a} \cdot (t_{\text{eff}})^{b} \qquad (1)$$

$$t_{eff} = 0.11 \cdot t_d \quad (2)$$

$$t_d = E/k \quad (3)$$

where E is the breakdown electric field, kV/cm; A is the linear influence factor, which is depended on the gas dielectric and electrode configuration; p is the gas pressure, MPa; t_{eff} is the efficient breakdown time delay; a is the coefficient of pressure; b is the coefficient of efficient time delay; t_d is the breakdown time delay; k is the slope of electric field.

From equation (1)~(3), equation (4) can be derived by taking logarithm from both sides as follow:

$$\ln E = \frac{\ln A}{1-b} + \frac{a}{1-b} \cdot \ln p + \frac{b}{1-b} \cdot \ln\left(\frac{0.11}{k}\right) \quad (4)$$

According to the experimental data of cone electrode, the breakdown electric field, pressure and the slope of electric field as the known quantities, the linear influence factor A, the coefficients a and b can be fitted by Matlab. Martin formula fitting curve, pressure-time fitting curve, pressure-slope fitting curves and experimental results for cone electrode with 30 ns of t_{eff} are shown in Fig. 9.

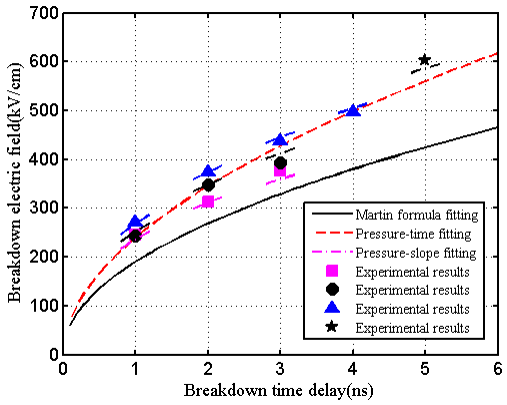

Fig. 9 The fitting curves and experimental results for cone electrode

From Fig. 9, the experimental values of breakdown electric field are higher than the calculated values of Martin formula. It is not suitable to estimate the breakdown electric field as the pressure is increased by utilizing Martin formula for fast pulsed charge and quasi-uniform electric field. The fitting values are relatively close to the experimental results by using pressure-time formula, however, it's difficult to fit for different du/dt. The pressure-slope fitting as a novel fitting formula has been proposed, which is helpful to estimate the breakdown electric field for different du/dt. It can be obviously seen that the fitting values are closer to the experimental results by utilizing the new fitting formula for different du/dt.

IV. Discussion

The breakdown process and mechanism of pulsed gas discharge are actually very complicated and have not been completely investigated. However, it has been noted that the electric field emission, electric field distribution and initial electron development as the influence factors have played very significant roles in the discharge process for the high electric field. To illuminate the effect of electric field distribution and electrode materials on the electric field emission, effective electron and plasma channel development, the distributions of the breakdown points for different electrode configurations and materials and the distributions of axis electric field for different electrode configurations are present as the following paragraphs.

A. Breakdown characteristics

The distributions of the breakdown points for different electrode configurations are shown in Fig. 10.

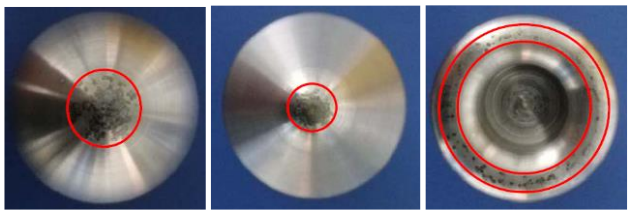

(a) Hemisphere electrode (b) Cone electrode (c) Annulus electrode

Fig. 10 The breakdown points distributions for different configurations

The breakdown distributions of three types of electrode configurations are different and the breakdown points are basically focused on the high electric field region, comparing with the distributions of electric field from Fig. 2. Based on the distributions of the breakdown points and electric field, we can find that the minimum electric field of the breakdown points for hemisphere, cone and annulus electrode are 745, 935 and 875 kV/cm, respectively. The minimum electric field of hemisphere electrode is lower 15% and the distribution area of the breakdown points is larger than those of other configurations, which leads larger deviation for the electric field emission and effective electron development. The minimum breakdown electric field of cone electrode is the maximum value in the three types of electrode configurations, but at the same time the breakdown points are too concentrated in the center, which would cause more erosion of electrode and change the microstructure of electrode. Thus, the characteristics of electric field emission would be also changed. However, the annulus electrode can produce the initial electrons of electric field emission at more spots, hence, the erosion would be less and the breakdown points of the annulus electrode are all round of electrode.

The distributions of the breakdown points for different electrode materials are shown in Fig. 11.

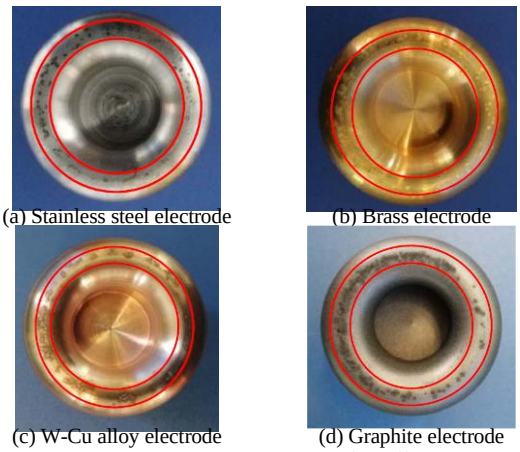

(a) Stainless steel electrode (b) Brass electrode

(c) W-Cu alloy electrode (d) Graphite electrode

Fig. 11 The breakdown points distributions for different materials

From the distributions of breakdown points, stainless steel and brass electrodes are similar, showing scattered distribution. W-Cu alloy electrode is clustered distribution and graphite electrode appears to be a succession of points. It can be concluded that the surface microstructure of electrode would affect the characteristics of electric field

emission and the process of discharge [29]. For stainless steel and brass electrode, the surface microstructures are similar. Tungsten composition can form protrusions around the breakdown point for W-Cu alloy electrode. There are many whiskers on the surface of graphite electrode, which could easily emit electrons. Hence, the breakdown voltage of graphite is relatively lower at the pressure of 0.1 and 0.2 MPa. When the pressure is more than 0.3 MPa, as the electric field increased to a certain threshold value, there are no obvious differences for the characteristics of electric field emission between graphite and metallic electrodes.

B. Analysis for breakdown time delay

The process of the pulsed gas discharge can be described as follows: the initial electrons are produced from the protrusions or whiskers on the surface of electrode in the high electric field and developed to the effective electrons with a certain probability. Those effective electrons multiply in a Townsend avalanche process. When the electric field of the space charge begins to dominate over the applied field, the streamer starts to speed up. After the avalanche and streamer process have completed, a weak ionized column will bridge the electrodes gap. While the energy being deposited in the gap would take some time to heat the plasma, the resistance of gas switch will fall down with the gap being breakdown. According to the process, the breakdown time delay can be divided into five parts: the static breakdown voltage time, t_0; the effective electron time, t_e; the electron avalanche time, t_a; the formative time, t_f and the channel heating time, t_h, as shown in Fig. 12.

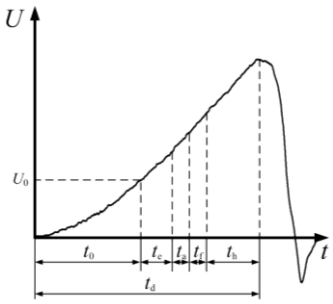

Fig. 12 The definition of breakdown time delay

For pulse breakdown in gases under high electric field of hundreds of kV/cm, there are two effects to consider. One is the surface microstructure of electrode. From the breakdown characteristics of different materials, it can be noted that the electric field emission ability caused by the microstructure of electrode has a significant influence on the breakdown time delay. The second one is the electric field distribution of electrode. The distributions of the axis electric field for different configurations are shown in Fig. 13.

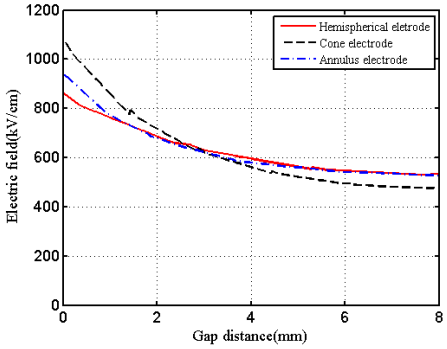

Fig. 13 The axis electric field distributions for different configurations

From the electric field distributions of three types of electrode configurations, the average electric fields near anode electrode are basically the same between hemisphere and annulus electrode. If the formative time and the channel heating time have greater influence on the breakdown time delay, this is not consistent with the experimental results. In addition, according to the relationship between breakdown time delay and voltage from Fig. 7, with the increase of pulse voltage slope, the breakdown time delay decreases more than the breakdown voltage. Therefore, it can be inferred that the proportion of the initial phase time over the entire breakdown time delay is greater. In another word, the characteristics and time of electric field emission have significant influence on the whole breakdown time delay.

V. Conclusion

The self-breakdown characteristics of the output switch for EMP simulator have been investigated. It can been noted that the configuration and the surface microstructure of electrode will significantly influence the breakdown voltage deviation and time delay jitter from the experimental data. The electric field emission property and average electric field distribution of annulus electrode are better than those of two electrode configurations. There are no obvious differences for three types of metallic electrodes in the annulus configuration. The breakdown property of graphite electrode is better than those of metallic electrodes except for lower breakdown voltage for 0.1 and 0.2 MPa.

References

[1] C. E Baum, “Reminiscences of high-power electromagnetics,” IEEE Trans. Electromagn. Compat., vol. 49, no. 2, pp. 211–218, May. 2007.

[2] I. D. Smith and H. Aslin, “Pulsed Power for EMP Simulators,” IEEE Trans. Electromagn. Compat., vol. 10, no. 3, pp. 53–59, Feb. 1978.

[3] H. Schilling, J. Schluter and M. Peters, “High voltage generator with fast risetime for EMP simulation,” IEEE Pulsed Power Conference, pp. 1359-1364, July. 1995.

[4] C. Gilman, S.K. Lam, J. T. Naff, et al, “Design and performance of the FEMP-2000 a fast risetime 2 MV EMP pulser,” IEEE Pulsed Power Conference, pp. 1437-1440, June. 1999.

[5] V. Bailey, V. Carboni, C. Eichenberger, et al, “A 6-MV Pulser to Drive Horizontally Polarized EMP Simulators,” IEEE Trans. Plas. Sci., vol. 38, no. 10, pp. 2554–2558, Oct. 2010.

[6] W. R. Rapoport, J. Goldhar and J. R. Murray. "KrF Larser-Triggered SF6 Spark Gap for Low Jitter Timing," IEEE Trans. Plas. Sci., vol. PS-8, no. 3, pp. 167–170, Sept. 1980.

[7] H. C. Harjes, K. H. Schonbach, M. Kristiansen, et al, "Laser Triggering Through Fiber Optics of a Low Jitter Spark Gap," IEEE Trans. Plas. Sci., vol. PS-8, no. 3, pp. 170–176, Sept. 1980.

[8] J. R. Woodworth, R. G. Adams and C. A. Frost. "UV-Laser Triggering of 2.8-Megaovolt Gas Switches," IEEE Trans. Plas. Sci., vol. PS-10, no. 4, pp. 257–261, Dec. 1982.

[9] R. G. Adams, D. L. Smith and J. R. Woodworth. "Simultaneous ultraviolet laser triggering of two multimegavolt gas swtiches," Appl. Phys. Lett. 43(2), pp. 163-165, July, 1983.

[10] F. Hegeler, M. C. Myers, M. F. Wolford, et al. "Low Jitter, High Voltage, Repetitive Laser Triggered Gas Switches," IEEE Trans. DEI, vol. 20, no. 4, pp. 1168–1188, Aug. 2013.

[11] J. Li, W. Jia, J. Tang, et al, “A 3MV Low Jitter UV Illumination Switch,” IEEE Trans. Plas. Sci., vol. 41, no. 2, pp. 360–364, Feb. 2013.

[12] J. Li, W. Chen, Z. Chen, et al. "Effects of Optical Pulse Parameters on a Pulsed UV-Illuminated Switch and Their Adjusting Methods," IEEE Trans. Plas. Sci., vol. 43, no. 9, pp. 3293–3297, Sept. 2015.

[13] J. Yin, F. Sun, A. Qiu, et al, “2.8-MV Low-Inductance Low-Jitter Electrical-Triggered Gas Switch,” IEEE Trans. Plas. Sci., vol. 44, no. 10, pp. 2045–20524, Oct. 2016.

[14] J. Yin, F. Sun, X. Jiang, et al. "Novel trigger pulse feed method for mega-volt gas switch," Rev. Sci. Instrum. 88,076102-1-3, 2017.

[15] *IEC 61000-2-9*, 1996. "Description of HEMP environment-Radiated disturbance."

[16] M. S. Dicapua, E. K. Freytag, W. R. Dixon, et al. "A Simple Self-breaking 2 MV Gas Switch," IEEE Pulsed Power Conference, June. 2013.

[17] M. A. Kemp, R. D. Curry and S.D. Kovaleski, "Experimental Study of the Multichanneling 3 MV Rimfire Gas Switch in the Self Breakdown Mode," IEEE Pulsed Power Conference, pp. 746-750, June. 2005.

[18] S. J. Levinson, E. E. Kunhardt, "Investigation of the Statistical and Formative Time Lags Associated with the Breakdown of a Gas in a Gap at High Overvoltage," IEEE Trans. Plas. Sci., vol. PS-10, no. 4, pp. 266–270, Dec. 1982.

[19] E. Puetz, I. Molina, S. Portillo, et al. "RITS-3 Self-break Water Switch Studies," IEEE Pulsed Power Conference, pp. 899-901, June. 2003.

[20] F. Wan, D. Pommerenke, H. Shumiya, et al, "Effect of spark gap shape on time lag," Electronics Letters, vol. 49, no. 13, June. 2013.

[21] J. Li, W. Chen, Z. Chen, et al, "Influences of electric field on the jitter of ultraviolent illuminated switch under pulsed voltages," Phys. Plasmas, vol. 21, 033509, pp. 1–7. 2014.

[22] P. E. Wakeland, J. P. Corley, K. C. Hodge, et al. "Material Testing on High Voltage Laser Triggered Gas Switches for ZR," IEEE Pulsed Power Conference, pp. 428-431, June. 2007.

[23] J. J. Ramirez. "Effect of electrode surface conditions on the self-breakdown strength and jitter of a high pressre pulsed gas swtich," Jour. App. Phys. vol. 47, no. 5, pp:1925-1928, May, 1976.

[24] A. L. Donaldson, R. Ness, M. Hagler, et al, "Modeling of spark gaps performance," IEEE Pulsed Power Conference, pp. 525-529, July. 1983.

[25] M. Hikita, S. Ohtsuka, N. Yokoyama, et al. "Effect of electrode surface roughness and dielectric coating on breakdown characteristics of high pressure CO2 and N2 in a quasi-uniform electric field," IEEE Trans. DEI, vol. 15, no. 1, pp. 243-250, Feb. 2008.

[26] C. Yeckel and R. D. Curry. "Effect of Electrode Surface Roughness on the Breakdown Jitter of a Nanoparticle-Infused Dielectric Oil Spark Gap Switch," IEEE Pulsed Power Conference, July. 2011.

[27] Y. Kamada, S. Shamoto and T. Hosokawa, "Nanosecond pulse breakdown of gas insulated gaps," J. Appl. Phys. vol. 63, no. 6, pp. 1877-1881, Mar. 1988.

[28] L. M. Vasiyak, S. P. Vetchinin and D. N. Polyakov, "Effect of the rise rate of nanosecond high-voltage pulses on the breakdown of air gaps," Tech. Phys. Let. vol. 25, no. 9, pp. 749-751, Sep. 1999.

[29] F. Guo, S. He, W. Luo, et al. "The breakdown time delay and jitter of different cathode materials under nanosecond pulse in N2," 2017 1st International Conference on Electrical Materials and Power Equipment, May, 2017.

Effects of Control Algorithms on Electromagnetics Transient Process in UHVDC Transmission System

Fang Yu
School of Electrical Engineering
Xi'an Jiaotong University
Xi'an, China
megpet@stu.xjtu.edu.cn

Jie Guo
School of Electrical Engineering
Xi'an Jiaotong University
Xi'an, China
jguo0510@mail.xjtu.edu.cn

Yuying Wu
School of Electrical Engineering
Xi'an Jiaotong University
Xi'an, China
393817703@qq.com

***Abstract*—To improve the dynamic recovery characteristic of Ultra High Voltage DC (UHVDC) transmission system, this paper focuses on effects of nonlinear optimal control and PI control in electromagnetics transient process. Control systems in UHVDC based on state feedback exact linearization method and PI controllers are respectively established. The rationality and validity of UHVDC transmission system on resisting disturbances are verified by simulation results using PSCAD/EMTDC software. Compared with PI controllers, nonlinear optimal control can keep constant current and voltage more accurately, shorten system recovery time about 50%, realize the decoupling control, are more useful for system stability of UHVDC and ac networks.**

Keywords—dynamic recovery characteristic, UHVDC, nonlinear optimal control, state feedback exact linearization, PI controllers

I. INTRODUCTION

Presently, ±1100kV UHVDC transmission system is under testing and debugging in China, which has the highest voltage level, the longest transmission line and the greatest transmission capacity of dc power systems in the whole world [1], [2]. For avoiding the stability problems of multi-infeed mode, UHVDC hierarchically connected to 500kV and 1000kV ac grid, has the advantages of greater transmission capacity, stronger voltage support capability of ac system and more reasonable distribution of power flow.

In the existing UHVDC and HVDC projects in China, control systems mostly consist of PI or PD controllers. The recovery time of UHVDC transmission system after AC system fault should be less then 120ms in the rectifier and 140ms in the inverter [3]. To improve dynamic characteristics, nonlinear control methods such as differential geometry method [4], inverse system method [5], output-tracked method [6], sliding-mode control method [7], and so on, have been applied in control system.

In this paper, two kinds of control systems based state feedback exact linearization method (SFEL) and PI controllers are respectively established in UHVDC transmission system. The validities of control systems are verified by simulation results using PSCAD/ EMTDC software. Based on simulation results during ac fault, dynamic characteristics of two control algorithms in UHVDC during a dynamic turbulence are summarized.

II. CONTROL ALGORITHM BASED ON PI CONTROLLERS

A schematic diagram based PI controllers is shown in

This work was supported by the National Key Research and Development Program of China (Project No.2016YFB0900801).

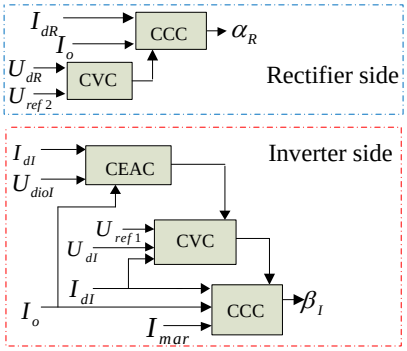

Fig. 1. Control algorithm schematic diagram

Fig.1. The outputs of constant extinction angle control (CEAC) and constant voltage control (CVC) are sent as the limitation of PI controller in sequence. U_{dR} and I_{dR}, U_{dI} and I_{dI} stand for dc voltage and current of the rectifier and inverter, respectively. In the rectifier, the output of CVC is set as the minimum of PI controller in constant current control (CCC). In the inverter, the output of CEAC is sent to be the maximum of PI controller in CVC and the output of CVC is set as the maximum of PI controller in CCC. The parameters of PI controllers can be regulated according to the range and derivative of input. CVC and CCC are composed of PI controllers whereas CEAC is not. CEAC is a predictive extinction angle control, which is used to calculate the firing angle. Because the voltage references U_{ref1} and U_{ref2} are different and higher than the rated voltage U_{dN}, CVC are used to limit overvoltage in UHVDC system and should not disturb normal voltage regulation of transformer tap changer control. In steady state, due to the margin I_{mar} in CCC of inverter, CCC of rectifier and CEAC actually work.

When an earth fault occurs at 500kV ac line, 500kV ac bus voltage U_{500} and the ideal no-load dc voltage of inverter U_{dioI} decrease rapidly. Then I_{dI} increases quickly. The commutation overlap angles increase, therefore the extinction angles γ_H and γ_L reduce quickly. The reduction of U_{500} will trigger the output of linkage commutation failure prediction (CFP) increasing after a response time delay. In that way, β_I will increase and there is no commutation failure in lower valve units (LVU), hence restraining commutation failure of the normal converter when one ac grid suffered a fault comes true.

III. CONTROL ALGORITHM BASED ON STATE FEEDBACK EXACT LINEARIZATION

According to the nonlinear control theory [7], when the system relation degree is equal to the dimension of state vector x, SFEL can be used to design nonlinear optimal control system. State feedback and appropriate coordinate

conversion can make nonlinear system actualize exact linearization and possess excellent dynamic quality. The control algorithm schematic diagram based on SFEL is shown as Fig.2.

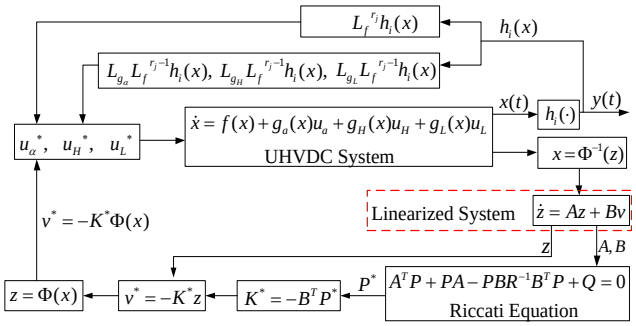

Fig. 2. Control algorithm schematic diagram based on SFEL

q_i (i=1, 2, 3, and 4) and r_i (i=1, 2, and 3) are the diagonal elements of weight matrix Q and R, respectively.

$$J=\int_0^\infty (q_1\Delta I_d^2+q_2\Delta \dot{I}_d^2+q_3\Delta\gamma_H^2+q_4\Delta\gamma_L^2+r_1\Delta\ddot{I}_d^2+r_2\Delta\dot{\gamma}_H^2+r_3\Delta\dot{\gamma}_L^2)dt \quad (1)$$

Under the optimal control rules, the index J can reach the minimum value when the square, the fluctuation speed, and the acceleration of dc current deviation, the square and fluctuation speed of extinction angle deviation, are the entire minimums. The optimal control embodies CCC and CEAC and reflects the demands of system dynamic quality.

IV. Simulation Result

In order to verify the aforementioned control algorithms used in hierarchical connected ±1100kV UHVDC transmission system, simulation is carried out using PSCAD. The parameters in the simulation are given in Table I. For obtaining transient performances and automatic recovery ability of UHVDC, a single-phase grounding fault is applied in 500kV ac system. The fault occurs at t = 0.8s and is cleared at t = 0.81s. The grounding resistance R_g is 11 Ω.

TABLE I. PARAMETERS

Quantity	Values
Rated dc bus voltage	±1100kV
Rated dc power per polar	6000MW
Rated dc current	5.455kA
Reactance of smoothing reactors	300mH
Resistance of dc line	9.41Ω
ideal no-load dc voltage of inverter	308.33kV
Rated firing angle of rectifier	15°
Steady state control range	±2.5°
Lower limit of firing angle	5°
Rated extinction angle of inverter	17°

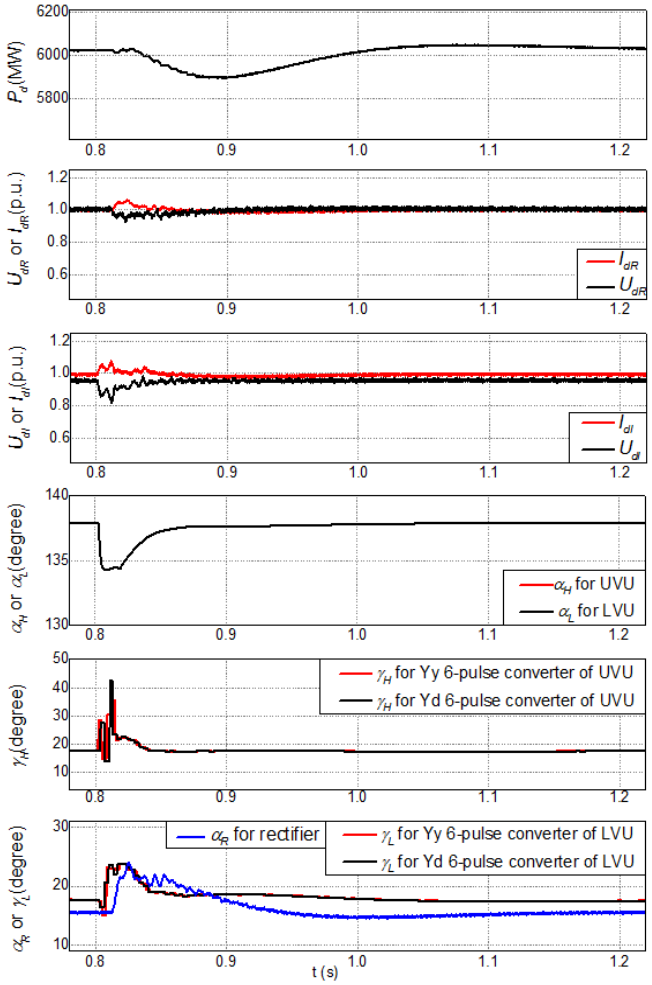

Fig. 3. Dynamic responses based on PI controllers

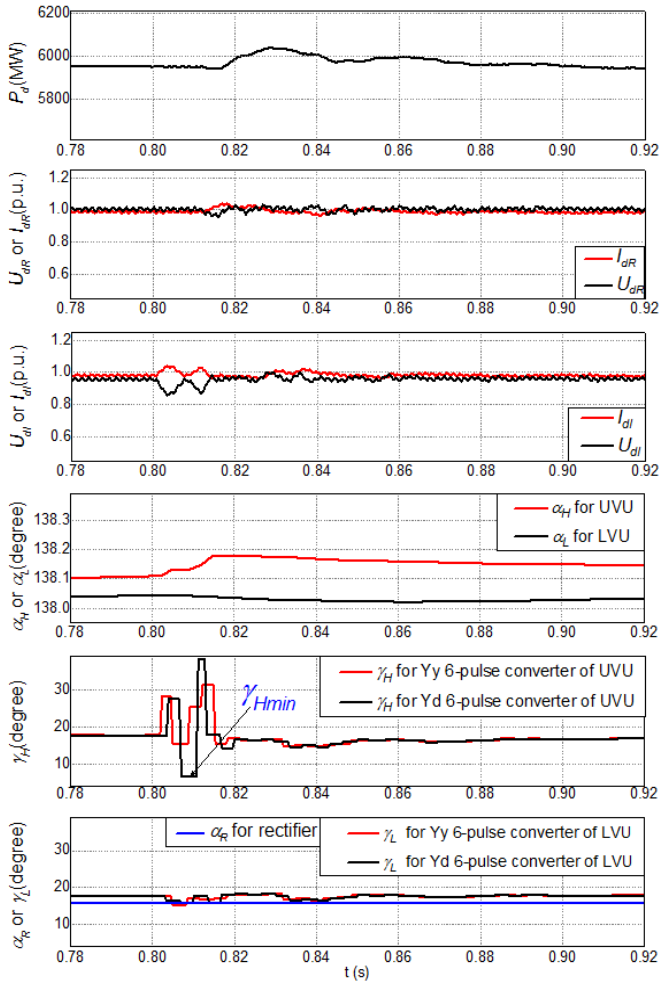

Fig. 4. Dynamic responses based on SFEL

A. *Dynamic Responses based on PI controllers*

The dynamic responses based on PI controllers are shown in Fig.3. After 0.8s, U_{500} reduces, U_{dI} declines and I_{dI} increases immediately, that leads to the rapid decrease of γ_H and γ_L. The firing angles α_H and α_L of upper valve units (UVU) and LVU are quickly regulated by CEAC and the linkage CFP. The firing angle of rectifier α_R is regulated by CCC to limit current. The minimum of γ_H and γ_L are respectively 13.9° and 15.1°. UVU and LVU work normally. In system recovery process, the ranges of dc voltage, current, and active power P_d are small and the recovery time after ac fault being cleared is short. When R_g is 0.05Ω and the fault lasting time is 50ms, there is a transient commutation failure in UVU whereas LVU works normally. The control system can successfully restrain commutation failure of the normal converter when one ac grid has a fault. After the fault is cleared, the system can return to steady state automatically and the recovery time is less than 140ms.

B. *Dynamic Responses based on SFEL*

Fig.4 shows the dynamic responses based on SFEL. After 0.8s, α_H and α_L are regulated to restrain changes of γ_L and γ_H, respectively. Hence, γ_H in Yy 6-pulse converter of UVU returns automatically. LVU work normally and the undulate range of its extinction angles is extremely small, which means that nonlinear control system realizes the decoupling control of UVU and LVU. As the disturbance is resisted quickly by α_H and α_L and the electrical signal transmission time from the inverter to rectifier is about 11ms, α_R is not yet to be changed. In the system recovery process, the undulate ranges of voltage, current and active power are quite small and system recovery time after the fault being cleared is very short. The minimum γ_{Hmin} of extinction angle in Yd 6-pulse converter of UVU is 7°. When R_g varies from 100 Ω to 9.5 Ω, V_{500} reduces from 0.997 p.u. to 0.812 p.u. and γ_{Hmin} reduces from 17.1° to 0°. Once there is a dynamic commutation failure, the dynamic equation is changed and an auxiliary module similar to CFP is needed to escape from commutation failure for a short time. Then the system can return to steady state automatically.

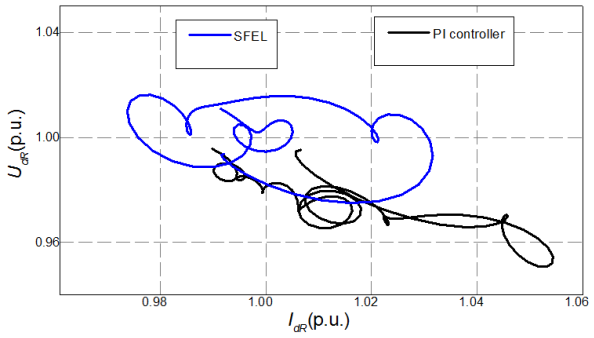

Fig. 5. Dynamic trajectories of U_{dR}-I_{dR}

TABLE II. DYNAMIC RESPONSES

Control algorithm	Description	
PI	Range of U_{dR} (p.u.)	0.93-1.03
	Range of I_{dR} (p.u.)	0.98-1.06
	γ_{Hmin} (°)	13.9
	Recovery time (ms)	135
SFEL	Range of U_{dR} (p.u.)	0.96-1.03
	Range of I_{dR} (p.u.)	0.96-1.04
	γ_{Hmin} (°)	7
	Recovery time (ms)	68

C. *Comparisons of Dynamic Responses*

Fig.5 shows dynamic trajectories of U_{dR} - I_{dR} based on PI from 0.81s to 0.88s and dynamic trajectories of U_{dR} - I_{dR} based on SFEL from 0.81s to 0.86s. Table II shows the comparative results of dynamic responses. From Fig.5, dc voltage and dc current fluctuate in a smaller range in the nonlinear control. Compared with PI controllers, the system recovery times in nonlinear control are reduced 50%; γ_{Hmin} in nonlinear control are lower and the auxiliary module is needed to restraining commutation failure. Therefore, the dynamic performances and recovery characteristics of nonlinear control based on SFEL is better than that in PI controllers.

V. CONCLUSION

This paper proposes control algorithms based on conventional PI controllers and SEFL in hierarchical connected UHVDC system and compares the dynamic recovery characteristics between two control algorithms. Compared with PI controllers, control systems based on SFEL have higher respond speeds and lower fluctuation of dc voltage, dc current and active power during a dynamic turbulence; can keep constant current and voltage more accurately, reduce the system recovery times about 50%, improve the rapid recovery of dc transmission power, and realize the decoupling control of UVU and LVU. Dynamic characteristics of nonlinear control based on SFEL are more useful for the system stability of UHVDC and ac networks.

REFERENCES

[1] D. J. Wang, H. Zhou, and X. Deng, "Switching overvoltage characteristics of ±1100-kV UHVDC converter Station," IEEE Trans. Power Del., vol. 30, no. 3, pp. 1205-1212, June. 2015.

[2] Z. H. Liu, J. Yu, X. S. Guo, T. Sun，and J Zhang, "Survey of technologies of line commutated converter based high voltage direct current transmission in China," CSEE J. Power Energy Syst., vol. 1, no. 2, pp. 1-8, June. 2015.

[3] HVDC Standardization Technical Committee for the Electric Power Industry, "System design standard for ±800kV HVDC system", Bejing, China, China electric power press, 2009, pp.29-31.

[4] Q. Lu, S. W. Mei, and Y. Z. Sun, Nonlinear Control of Electric Power Systems. Bejing, China: Tsinghua University Press, 2008, pp.148-167, 241-245, 373-385.

[5] X. D. Sun, Z. Shi, L. Chen, and Z. B. Yang, "Internal model control for a bearingless permanent magnet synchronous motor based on inverse system method," IEEE Trans. Energy Convers., vol. 31, no. 4, pp. 1539-1548, Dec. 2016.

[6] Z. L. Zhao and B. Z. Guo, "A novel extended state observer for output tracking of MIMO systems with mismatched uncertainty," IEEE Trans. Automat. Control, vol. 63, no. 1, pp. 211-212, Jan. 2018.

[7] A. Musa, L. R. S. Jr, and A. Monti, "Robust predictive sliding mode control for multiterminal HVDC grids," IEEE Trans. Power Del., vol. 33, no. 4, pp. 1545-1555, Aug. 2018.

Singularity Expansion Method (SEM) for Open-Circuited Wires Above Ground

Felix Middelstaedt
Chair of Electromagnetic Compatibility
Otto von Guericke University
Magdeburg, Germany
felix.middelstaedt@ovgu.de

Sergey V. Tkachenko
Chair of Electromagnetic Compatibility
Otto von Guericke University
Magdeburg, Germany
sergey.tkachenko@ovgu.de

Ralf Vick
Chair of Electromagnetic Compatibility
Otto von Guericke University
Magdeburg, Germany
ralf.vick@ovgu.de

***Abstract*—This paper deals with the analytic approximation of the natural frequencies for two parallel thin wires above ground. The wires are terminated with an open circuit. In previous publications the approximation of the natural frequencies for two wires were non-physical, meaning their real part was positive instead of negative. The goal is to minimize this unphysical behavior of the analytic approximation.**

***Index Terms*—Multiconductor Transmission Lines, Singularity Expansion Method (SEM)**

I. Introduction

Recently, the natural frequencies of multiple parallel wires above ground were approximated analytically using a combination of an asymptotic approach with an iterative method [1], [2]. The key of this approach is an accurate approximation of the reflection coefficient. This way high frequency effects, that appear at the wire terminals, can be included in the solution. The used methods work very well for single wires above ground [3], [4]. It was shown that the approximation of the natural frequencies using the iterative method is much more accurate than the solution from classical transmission line theory.

But somehow, the iterative method yields an unphysical solution if no ohmic losses are present. This was pointed out in [2]. Then the real part of the first few resulting natural frequencies is positive. This means that the passive system (the MTL) had actually an active part [5]. This problem is investigated here for the example of two parallel wires above ground terminated with an open circuit as shown in Fig. 1.

II. Methods and Results

Instead of working with the total currents on the two wires, the currents are represented as a linear combination of common and differential mode currents I_+ and I_-. This way, two decoupled currents, that do not influence each other, are considered separately and a more direct solution for the reflection coefficient is possible.

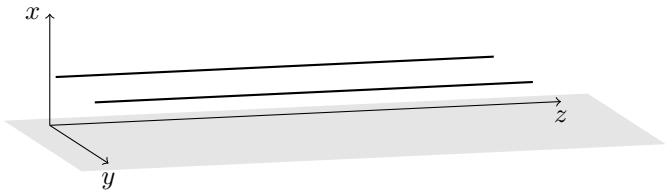

Fig. 1. Two parallel open-circuited wires above ground.

In [4] it is shown that the natural frequencies $s_{m,\pm}$ of the currents can be determined by using the fixed point iteration

$$\frac{s_{m,\pm}^{(0)} L}{\pi c} = \mathrm{j}\, m \tag{1}$$

$$\frac{s_{m,\pm}^{(n+1)} L}{\pi c} = \mathrm{j}\, m + \frac{\mathrm{j} \arg\{\Gamma_\pm(s_m^{(n)})\}}{\pi} + \frac{\ln|\Gamma_\pm(s_m^{(n)})|}{\pi} \tag{2}$$

where L denotes the wire length, c is the speed on light and $\Gamma_\pm$ is the frequency dependent reflection coefficient of the common or differential mode current. This fixed point iteration converges already after two to three iterations. The initialization $s_{m,\pm}^{(0)}$ coincides with the classical transmission line solution.

In (2) it can be seen that the real part of the natural frequencies depends only on the absolute value of the reflection coefficient. If the absolute value of $\Gamma_\pm$ is smaller than one, the real part of $s_{m,\pm}^{(0)}$ is negative, otherwise it is positive.

Using the iterative approach as described in [4] to analytically approximate $\Gamma_\pm$ results in

$$\Gamma_\pm \approx \Gamma_\pm^{(1)} \tag{3}$$

$$\Gamma_\pm^{(1)} = \frac{E_1\left(\frac{2sh}{c}\right) - E_1\left(\frac{sa}{c}\right) \pm \left[E_1\left(\frac{s}{c}\sqrt{d^2+4h^2}\right) - E_1\left(\frac{sd}{c}\right)\right]}{\ln\left(\frac{2h}{a}\right) \pm \frac{1}{2}\ln\left(1+\frac{4h^2}{d^2}\right)} \tag{4}$$

with the radius a, the wire height above ground h and the distance between the wires d. The exponential integral function is denoted by E_1 (see [6]). The $^{(1)}$ means that the iterative approach was terminated after the first iteration.

Using the first iteration reflection coefficient to determine the natural frequencies results in the exact same (unphysical)

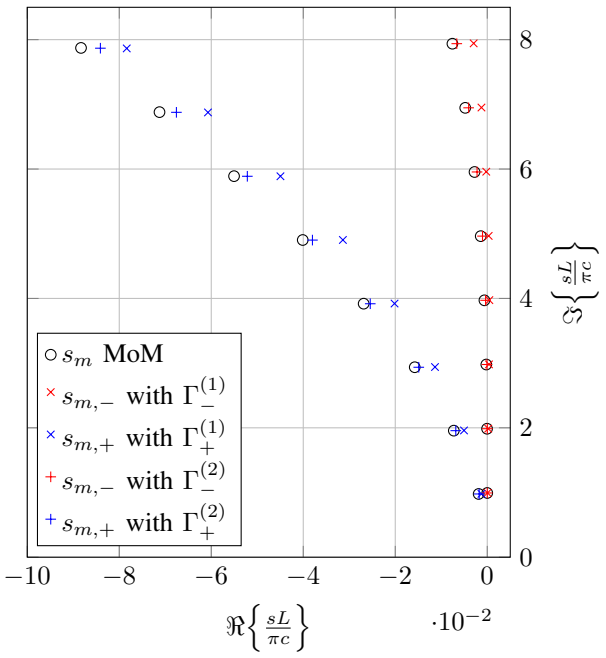

Fig. 2. Normalized natural frequencies for $L = 10\,\mathrm{m}$, $h = 0.5\,\mathrm{m}$, $a = 1\,\mathrm{mm}$ and $d = 0.5\,\mathrm{m}$.

solution as the one presented in [1], [2] without the decoupled currents.

To increase the accuracy of the approximation the second order iteration is used for the reflection coefficients. The results are compared in Fig. 2 with a numerical reference. The numerical reference is obtained by contour integration of the determinant of the system matrix of a method of moments (MoM) solver [7].

It can be seen that the solution is greatly improved by the second order approximation. But closer inspection shows that the real part of the first two differential mode natural frequencies is extremely small but still positive. Nevertheless, this is yet another example (see [8]) that the iterative approach converges towards the correct solution (numerical reference).

III. Conclusions

For multiple parallel wires above ground an iterative method results in an unphysical solution for the differential mode reflection coefficient. Its absolute value is slightly larger than 1 for low frequencies. By considering the second order approximation the approximation of the reflection coefficient and thus the approximation of the natural frequencies is improved. However, the problem of the positive real part still exists for very low frequencies.

The second order approximation can also be used for a single wire above ground by taking the limit $d \to \infty$.

The detailed analysis of common and differential mode currents allows a limitation of the error to the differential mode. In [2] common and differential mode are not analytically distinguishable.

In a future project the exact source of the problem will be sought in the iterative method.

References

[1] S. Tkachenko, F. Middelstaedt, J. Nitsch, and R. Vick, "Application of the singularity expansion method (SEM) for multiconductor transmission lines," in *AMEREM 2018*, Santa Barbara, CA, 2018.

[2] F. Middelstaedt, S. V. Tkachenko, and R. Vick, "Natural frequencies of long symmetric multiconductor transmission lines," *IEEE Transactions on Antennas and Propagation*, pp. 1–1, 2019.

[3] F. Middelstaedt, S. Tkachenko, R. Vick, and R. Rambousky, "Analytic approximation of natural frequencies of bent wire structures above ground," in *2015 IEEE International Symposium on Electromagnetic Compatibility (EMC)*, Aug. 2015, pp. 812–817.

[4] F. Middelstaedt, S. V. Tkachenko, and R. Vick, "Transmission line reflection coefficient including high-frequency effects," *IEEE Transactions on Antennas and Propagation*, vol. 66, no. 8, pp. 4115–4122, Aug 2018.

[5] C. E. Baum, "On the singularity expansion method for the solution of electromagnetic interaction problems," Air Force Weapons Laboratory, Kirtland Air Force Base, Albuquerque, NM, USA, Interaction Note 88, Dec. 1971. [Online]. Available: http://ece-research.unm.edu/summa/notes/In/0088.pdf

[6] M. Abramowitz and I. A. Stegun, Eds., *Handbook of Mathematical Functions, With Formulas, Graphs and Mathematical Tables*, 10th ed. National Bureau of Standards, 1972.

[7] B. K. Singaraju, D. V. Giri, and C. E. Baum, "Further development in the application of contour integration to the evaluation of the zeros of analytic functions and relevant computer programs," Air Force Weapons Laboratory, Kirtland Air Force Base, Albuquerque, NM, USA, Mathematics Note 42, Mar. 1976. [Online]. Available: http://ece-research.unm.edu/summa/notes/Mathematics/0042.pdf

[8] F. Middelstaedt, S. V. Tkachenko, and R. Vick, "Analysis of an iterative approach to determine the current on the straight infinite wire above ground," *Advances in Radio Science*, 2019, accepted.

Investigation of Frequency Selective Surfaces in HPEM Applications

Felix Vega, Fernando Albarracin-Vargas
Electrical and Electronic Engineering Department
National University of Colombia
Bogota, Colombia
jfvegas@unal.edu.co

Chaouki Kasmi
Mobile and Telecom Lab
xen1thLabs, DarkMatter
Abu Dhabi, UAE
chaouki,kasmi@darkmatter.ae

Lars Ole Fichte
Faculty of Electrical Engineering
Helmut Schmidt University
Hamburg, Germany
lo.fichte@hsu-hh.de

***Abstract*—This paper presents a new type of resonant radiator obtained as a combination of a Frequency Selective Surface and an Impulse Radiating Antenna. The effects of different FSS is studied and compared using simulation. The main outcomes of this paper are linked with the possibility of modifying the waveform emitted by radiator for specific applications as well as designing hardening modules that could be integrated into buildings.**

Keywords—Frequency Selective Surface, Impulse Radiating Antenna, Complementary Split Ring Resonator

I. INTRODUCTION

Electromagnetic attacks against critical infrastructure represent a non-negligible risk for the resilience of services provided by a facility. Control and command centers responsible for handling a facility and the related processes needs to be harden in a way that the electromagnetic fields do not affect the security of the operations. Concrete walls [1] have already shown when prepared appropriately that it has interesting properties to block electromagnetic fields. Thus, when windows are present, they represent a point of entry for electromagnetic fields. Covering the windows with metallic grids have shown to be interesting to block part of the field at specific frequencies related to the mesh behaving as a Frequency Selective Surface (FSS).

In related studies, it has been shown that the grid itself expose interesting properties when illuminated with a radiator. Giri et al. [2] have been working on analyzing the possibility of damping the emitted pulse signal by chaining a set of metallic screens placed in front of the antenna. These serve to transform the fast-pseudo-impulse from the antenna into a damped sinusoidal waveform.

We propose in this paper to investigate the application of FSS for modifying the waveform of a radiator in flexible way by adding different metallic grids at several location of the source. Moreover, the FSS are analyzed for hardening applications that could be a quick protective measure to be added in existing facilities.

A. Impulse Radiating Antenna

The Impulse Radiating Antenna (IRA) has been proposed as a hyperband, high-power radiator in several applications related to the study of Intentional Electromagnetic Interference (IEMI) [3]. The combined antenna and its pulser radiate an impulse-like signal, whose electric field in boresight is given as:

$$E_i(t,r) = f_i \frac{1}{2\pi f_g} \left(\begin{array}{l} \frac{V(t-r/c)}{r} \frac{\sin(\beta)}{1+\cos(\beta)} - \frac{V(t-l/c-R_2/c)}{R_2} \frac{\sin(\beta)+\sin(\gamma)}{1+\cos(\beta-\gamma)} \\ -\frac{4}{D} V(t-2F/c-r/c) + (2+2\cos(\gamma)) \frac{V(t-l/c-R_2/c)}{D} \end{array} \right) (V/m)$$

Where: $V(t)$ is the feeding voltage c is the speed of light and r the distance between the focal point and the measurement point. The term $f_g = Z_{IRA}/120\pi$, where Z_{IRA} is the input impedance of the antenna. For D, F, l, β, γ, R_2, see Figure 1.

B. Frequency Selective Surface

Frequency Selective Surfaces (FSS) are two-dimensional structures, formed by unitary conductive patterns, printed on a dielectric surface, forming a periodic array or matrix. When illuminated by an electromagnetic field, the FSS can behave either as a bandpass or a band-stop filter of the incident electromagnetic field. The behavior of the FSS, its Q and central frequency depend on the unitary pattern, its dimensions and the dielectric constant of the substrate.

FSS of different patterns have been proposed in the literature. Some typical structures are outlined in [4].

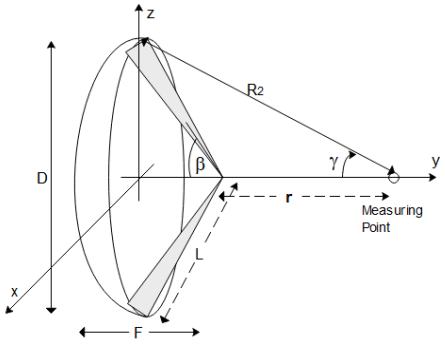

Figure 1 Geometry of the IRA

II. SIMULATION SETUP

The IRA has the following parameters:

D= 1(m), F/D=0.4, Z_{IRA}=400 (Ω)

The excitation voltage is an ERFC double-exponential like signal, with the following parameters:

V_{peak}= 50 (kV), r_t=100 ps, FWHM=2 ns

Fig 2 shows the radiated electric field in time domain at distances of r= 5 (m) and 10(m) from the focal point.

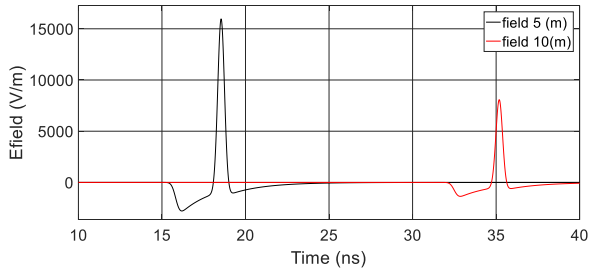

Figure 2 Field radiated by the IRA in time domain

The design here presented aims at producing a mesoband radiator using an IRA [3] as hyperband excitation, illuminating a bandpass Frequency Selective Surface (FSS) [4]. The bandwidth and central frequency of the resulting radiator can be easily changed by changing the FSS characteristics.

The effect of the FSS will be considered as the resulting spectrum of the E-field in the far-field zone, after the excitation pulse passes through the FSS. A Complementary Split Ring Resonator (CSRR)-based FSS is considered and designed to act as a high-Q band pass filter at f_0= 1.5 GHz.

The FSS will be placed at 0.1 m from the focal point. The electric field will be measured at 5 m, and 10 m from the focal point in broadside.

III. Design of the FSS

Since the main idea in this approach is to retrieve a narrow-band signal (ideally a single frequency one) after the signal radiated by the IRA passes through certain FSS, a high-quality factor unit cell shall be used. As mentioned above, we have designed a Complementary Split Ring Resonator (CSRR) first proposed in [5], as the one depicted in Fig. 3.

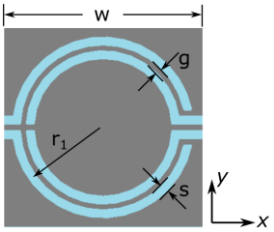

Figure 3 Geometry of the CSRR (FSS-unit-cell). w =3.9; r_1 = 13.5; g =1; s = 1.2. All the dimensions are in mm. The substrate (blue colored background) is 1 mm thick, with ε_r = 1.

The transmission and reflection parameters of the simulated CSRR-based FSS are shown in Fig. 4. It an be seen the narrow-band response of the FSS, and its suitability to be used as a high-Q band-pass filter. The unit cell has been simulated as an infinite periodic structure.

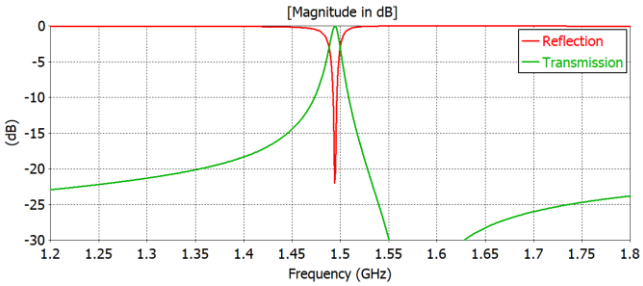

Figure 4 Transmission and reflection parameters of the CSRR-based FSS.

Once the FSS is tuned, and the IRA is optimized to generate the intended mesoband pulse, the complete antenna system (IRA + FSS) is simulated in a full-wave time-domain solver suite. Nevertheless, the finite size condition of a realistic FSS for a potential implementation, as well as the near-field interaction between the IRA and the FSS, imposes a significant limitation on the frequency selectivity response of the complete system. The authors expect to present the complete system results at the time of the conference.

References

[1] G. Antonini, A. Orlandi and S. D'elia, "Shielding effects of reinforced concrete structures to electromagnetic fields due to GSM and UMTS systems," in *IEEE Transactions on Magnetics*, vol. 39, no. 3, pp. 1582-1585, May 2003.

[2] F. M. Tesche and D. V. Giri, "Modification of Impulse-Radiating Antenna Waveforms for Infrastructure Element Testing", Sensor and Simulation Note 572, 22 October 2015.

[3] F. Vega, N. Mora, F. Rachidi et al, Design, Construction and Test of a Half Impulse Radiating Antenna (HIRA), AMEREM 2010, Ottawa, Canada, 2010.

[4] R. Yahya, A. Nakamura and M. Itami, "3D UWB band-pass frequency selective surface," 2016 IEEE International Symposium on Antennas and Propagation (APSURSI), Fajardo, 2016, pp. 959-960, 2016.

[5] J. D. Ortiz, J. D. Baena, V. Losada, F. Medina, and J. L. Araque, "Spatial Angular Filtering by FSSs Made of Chains of Interconnected SRRs and CSRRs," *IEEE Microwave and Wireless Components Letters*, vol. 23, no. 9, pp. 477–479, Sep. 2013.

A frequency-agile relativistic magnetron with axial tuning*

Fen Qin
Key Laboratory on High Power Microwave Technology
Institute of Applied Electronics, China Academy of Engineering Physics
Mianyang, China

Yong Zhang
Key Laboratory on High Power Microwave Technology
Institute of Applied Electronics, China Academy of Engineering Physics
Mianyang, China

Sha Xu
Key Laboratory on High Power Microwave Technology
Institute of Applied Electronics, China Academy of Engineering Physics
Mianyang, China

Lu-rong Lei
Key Laboratory on High Power Microwave Technology
Institute of Applied Electronics, China Academy of Engineering Physics
Mianyang, China

Dong Wang
Key Laboratory on High Power Microwave Technology
Institute of Applied Electronics, China Academy of Engineering Physics
Mianyang, China
mr20001@sina.com

***Abstract*—A frequency-agile relativistic magnetron with axial tuning is presented. In this configuration, each sectorial cavity in most traditional RM is replaced by reentrant cavity to achieve axial tuning. Each reentrant cavity has two radial parts connected by a coupling hole. Resonant frequency of this cavity chain can be tuned by adjusting the axial length of each coupling hole without any variation of other parameters. Multi-antenna output technique had been integrated with the reentrant cavity chain to obtain high conversion efficiency in the whole tuning range. Simulation results validated that this tube had a tuning range between 1.23 GHz to 1.70 GHz, corresponding to relative bandwidth of 32% about a center frequency of 1.465 GHz. In this tuning range, the maximum output power is 1.81 GW at 1.605 GHz, corresponding to an efficiency of 54.5%. This axial tuning RM is a promising compact high power microwave source with wide tuning range.**

Keywords—High power microwave, relativistic magnetron, axial tuning, reentrant cavity, multi-antenna output

I. INTRODUCTION

The relativistic magnetron (RM) is a robust, relatively compact high power microwave source which has applications in various fields [1-3]. One of the most attracting merits for RM is that it has a wide frequency tuning range in a single tube. The operating frequency of conventional frequency-agile RM is tuned by variation on the radius of anode block which had been verified with a wide tuning range [4-5]. However, the tuning structure is relatively complex to adjust all the anode blocks in the radial direction. Besides, this tuning structure is difficult to be integrated with axial extraction technique such as diffraction output [6-7] and all cavity output [8-9], which brings relatively low power conversion efficiency.

Axial tuning for RM has many advantages. First, it tunes the resonant frequency without extension of cavity radius which brings a relative compact inducing magnet, i.e. a relative compact tube configuration. Second, axial extraction technique is easy to be integrated with this type of tuning RM which brings a higher conversion efficiency. Axial tuning method such as inserting metal rod tuner or solid dielectric material into the cavities had been proposed in previous literature [10-11]. However, power capacity is limited when metal rods or solid dielectric material exist in the resonant cavity.

In this paper, a frequency-agile relativistic magnetron with axial tuning is presented for the first time. Reentrant cavity is introduced instead of traditional sectorial cavity. Each reentrant cavity has two radial parts which are connected by a coupling hole. Frequency tuning is realized by adjusting the axial length of each coupling hole. When this anode structure is combined with multi-antenna output technique [12], the frequency-agile RM will have both merits of wide frequency tuning range and high power conversion efficiency. Simulation results reveals that this tube have a tuning range between 1.23 GHz to 1.70 GHz,

This work was supported by the National Natural Science Foundation of China under Grant 61701460.

corresponding to relative bandwidth of 32% about a center frequency of 1.465 GHz. In this tuning range, the maximum output power is 1.81 GW at 1.605 GHz, corresponding to a magnetron efficiency of 54.5%.

II. TUNING MODEL

The schematic of reentrant cavity is shown in figure 1. In this configuration, each sectorial cavity in traditional RM is replaced by a reentrant cavity which comprises a outer cavity, a coupling hole and a inner cavity. Altering the dimensions of each coupling hole will tune the resonant frequency of each cavity when the radial dimensions of the cavities remains unchanged. Based on this idea, a novel tuning model is presented in which the axial length of each coupling hole is adjusted simultaneously to achieve axial tuning.

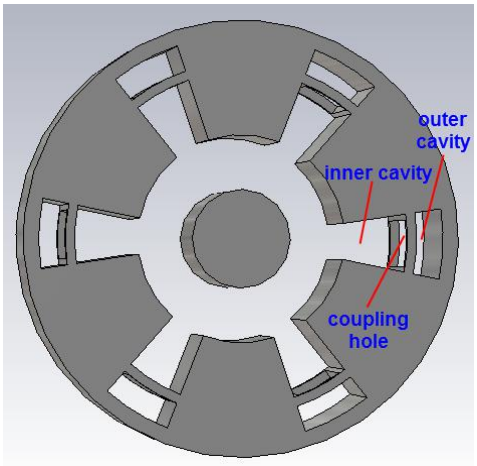

Fig. 1. Schematic of reentrant cavity of RM.

To validate the tuning model, an L-band RM anode block with reentrant cavities had been proposed based on the L-band RM in Ref [12]. To obtain the tuning character of this configuration, π mode oscillation frequencies had been obtained by high frequency analysis. The results is illustrated in Figure 2. When axial length of each coupling hole is adjusted, π mode frequency decreases with the length of each coupling hole. The tuning range is about 500 MHz for this anode block configuration with reentrant cavities.

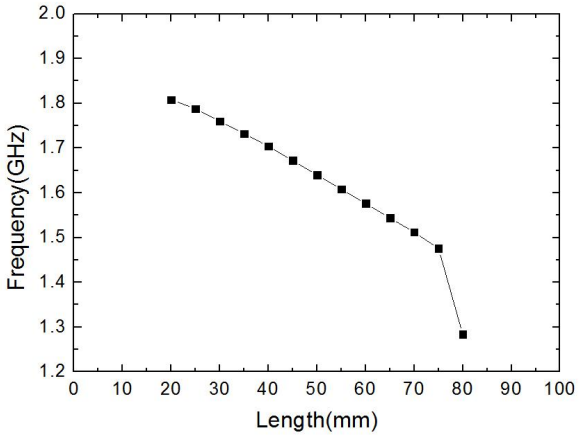

Fig. 2. π mode oscillation frequency vs axial length of each coupling hole.

III. PIC SIMULATION

The high frequency analysis results shows that the proposed anode block has a wide tuning range. When this anode structure is combined with multi-antenna output technique [12], a frequency-agile RM with axial tuning is put forward. Figure 3 illustrates the schematic of the axial tuning RM with multi-antenna output structure. A metal tuner with six tuning plates had been inserted in the reentrant cavities of the anode block. Three conducting rods were arranged and connected to the right end of the anode block to act as extraction antennas which extract π mode in the anode area to cylindrical TM_{01} mode in the output waveguide. Transparent cathode [13] had been adopted to ensure rapid startup of microwave and higher power conversion efficiency.

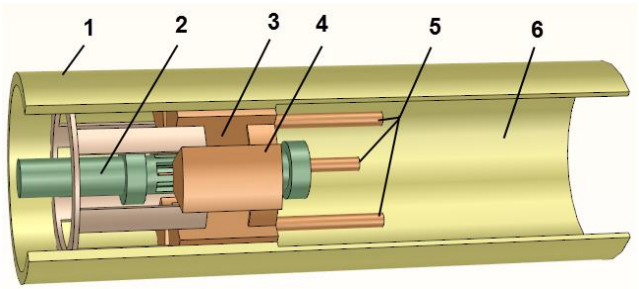

Fig. 3. Schematic of axial tunable RM with multi-antenna output. 1-anode shell; 2-cathode; 3-coupling hole; 4-anode block; 5-extracting antenna; 6-output waveguide.

PIC simulation had been carried out to validate previous prediction. Figure 4 shows the Simulation results. This tube have a tuning range between 1.23 GHz to 1.70 GHz, corresponding to relative bandwidth of 32% about a center frequency of 1.465 GHz, which is in accordance with previous high frequency analysis results. In this tuning range,

the maximum output power is 1.81 GW at 1.605 GHz, corresponding to an efficiency of 54.5%. The minimum power in this tuning range is 1.2 GW at 1.23 GHz, corresponding to an efficiency of 36.2%.

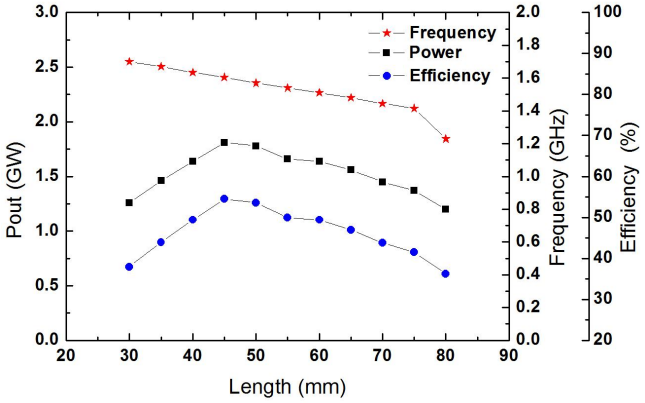

Fig. 4. PIC simulation results for axial tunable RM with multi-antenna output.

IV. CONCLUSION

A frequency-agile relativistic magnetron with axial tuning is proposed in this paper for the first time. Reentrant cavity is introduced to achieve wide tuning frequency range in the axial direction. High frequency analysis revealed that RM anode with reentrant cavity configuration has a tuning range of about 500 MHz at L-band. PIC simulation had been carried out for the tuning RM integrated with multi-antenna output configuration. Simulation results validated that the presented frequency-agile relativistic magnetron with axial tuning has a tuning range of over 32% about its central frequency of 1.465 GHz. These results reveals that the presented frequency-agile RM has a wide tuning range. The axial tuning structure is simple thus the presented frequency-agile RM in this paper is easy to be implemented in experiment. Combined with other merits such as compact and high efficiency, this tube is a promising high power microwave source with wide tuning range.

REFERENCES

[1] J. Benford, J. A. Swegle, and E. Schamiloglu, High Power Microwaves, 2nd ed., Chap. 3, New York, Taylor and Francis, 2007, pp. 43–108.

[2] R. J. Barker, E. Schamiloglu, High-Power Microwave Sources and Technology, Beijing, China, TsingHua University Press, 2005, (in Chinese), pp283.

[3] J. Benford, "History and future of the relativistic magnetron," Origins and Evolution of the Cavity Magnetron, IEEE, 2010:40-45.

[4] J. Levine, B. Harteneck, and D. Price, Proc. SPIE, 2557, 74, (1995).

[5] Tianming Li, Jiayin Li, and Biao Hu, IEEE Trans. Plasma Sci., VOL. 40, NO. 5, MAY 2012

[6] M. I. Fuks, N. F. Kovalev, A. V. Andreev, and E. Schamiloglu, "Mode conversion in a magnetron with axial extraction of radiation", IEEE Trans. Plasma Sci., vol. 34, no. 3, pp. 620–626, Jun. 2006.

[7] M. Daimon, and W. Jiang, "Modified configuration of relativistic magnetron with diffraction output for efficiency improvement", Applied Physics Letters, vol. 91, no. 19, pp. 191503-1 – 191503-3, 2007.

[8] B. W. Hoff, A. D. Greenwood, P. J. Mardahl, and M. D. Haworth, "All Cavity-Magnetron Axial Extraction Technique", IEEE Trans. Plasma Sci., 40, 3046, 2012.

[9] Sha Xu, Lurong Lei, Fen Qin, and Dong Wang, "Compact, high power and high efficiency relativistic magnetron with L-band all cavity axial extraction", Physics of Plasmas, 25, 083301 (2018).

[10] Hae Jin Kim and Jin Joo Choi, "Three-dimensional Particle-in-cell Simulation Study of a Frequency Tunable Relativistic Magnetron", IEEE Transactions on Dielectrics and Electrical Insulation, 14, 1045(2007)

[11] Li Wei and Liu Yong-Gui, "Simulation investigation of the 2 π mode operating tunable relativistic magnetron with axial radiation", Acta Phys. Sin. Vol. 60, No. 12 (2011) 128403.

[12] Fen Qin, Sha Xu, Lu-rong Lei, Bin-quan Ju, and Dong Wang, "A compact relativistic magnetron with lower output mode", IEEE Transactions on Electron Devices, vol. 66, pp. 1960–1964, April 2019.

[13] M. Fuks and E. Schamiloglu, "Rapid start of oscillations in a magnetron with a "transparent" cathode", Phys. Rev. Lett. vol. 95, 205101, 2005.

Correlation Between Time and Frequency Domain Shielding Effectiveness of Metallic Enclosures with Apertures

Gang Wu, Peng Chen, Linshen Xie, and Wei Wang

State Key Laboratory of Intense Pulsed Radiation Simulation and Effect (Northwest Institute of Nuclear Technology), Xi'an, China, 710024

***Abstract*—An analytical correlation between time domain shielding effectiveness of metallic enclosures with apertures against EMP excitation, and their frequency domain forms, has been proposed. With the assumption that the first resonance, typically TE_{101} mode for rectangular enclosures, dominates the long term behavior of the coupled electric field, it is derived that time domain definitions can be roughly estimated, via spectral data near (with a factor of ~0.6) the resonant frequency substituting a correction factor. Several numerical and experimental cases have been checked to confirm the applicability. Through the simple formulas, one may not only directly estimate values through frequency domain measurements, but also predict quantitatively their variation with parameters of the exciting pulse.**

***Keywords*—shielding effectiveness, electromagnetic pulse, time-domain analysis, metallic enclosures, apertures**

I. Introduction

Shielding effectiveness of metallic enclosures are traditionally defined and measured in frequency domain [1-2]. As high power electromagnetics has attracted more and more attention of the scientific community, both time domain definitions and measurement methods have been proposed and developed in many literatures [3-4]. There is also doubt that frequency domain characterization may not address the nature of the transient coupling process completely. And that electric engineers have much concern about the amplitude of the residual electric field inside the enclosure.

Both time and frequency domain shielding effectiveness can be evaluated by numerical simulation [5]. However, calculated results are just for given models with specific parameters, usually unable to reveal laws behind the numeric variations with those parameters. Results based on analytical formulations may be more helpful for designers and test engineers. For frequency domain shielding effectiveness, some simple but useful models, such as the equivalent circuit analysis based on transmission line theory, have been developed and further improved [6-7]. Though minimum phase algorithms is well known to be used for reconstructing time domain responses through spectral transfer function data [8], the relation between them is indirect, and generally not so applicable to make clear predictions.

Time domain concerns often relate to EMP excitations, which have been addressed both in waveforms and spectra. Additionally, the coupling nature of metallic enclosures with apertures are also well analyzed [9]. These make it possible to derive some explicit correlations between temporal and spectral descriptions, with a few reasonable approximations.

II. Simplification and Derivation

The electric field intensity of the incident EMP plane wave is usually described by a double exponential (DEXP) function:

$$E(t) = k_0 E_0 (\mathrm{e}^{-\alpha t} - \mathrm{e}^{-\beta t}) \tag{1}$$

which has a spectral content characterized as

$$\bar{E}(\omega) = k_0 E_0 (\beta - \alpha) / [(\omega - \mathrm{j}\alpha)(\omega - \mathrm{j}\beta)] \tag{2}$$

where k_0 is a scale factor, E_0 is the field intensity constant, α and β are the decay and rise time constants respectively. According to the well-known standards, we choose E_0=5×10^4 V/m, k_0 =1.3, α =4×10^7 s^{-1} and β=6×10^8 s^{-1} typically, referring to a pulse with a rise time of 2.5 ns and an FWHM of 23 ns. In some cases, α =4×10^8 s^{-1} and β=6×10^9 s^{-1} are also chosen for a comparison, which refer to a pulse with a rise time of 0.25 ns and an FWHM of 2.3 ns very close to an ultra-wideband (UWB) excitation.

The electric field intensity at a specified observation point inside the enclosure can be expressed by sum of a series of resonant components, each corresponding to a damped sinusoidal wave, as follows:

$$E_{\mathrm{in}}(t) = \sum_i E_i \mathrm{e}^{-a_i t} \sin(\omega_i t + \varphi_i) \tag{3}$$

where E_i is the amplitude, a_i is the decay constant, ω_i is the resonant angular frequency, and φ_i is the shifting phase of the i component.

Since high-order resonant components are excited by high frequency content of the DEXP pulse, with a limit of a f^{-1} or f^{-2} law, one can expect that the coupled electric field intensity are often dominated by a few low-order resonances. Especially for enclosures with a relatively large apertures, the coupled electric field intensity can be approximated roughly by the first resonant component, e.g., the TE_{101} mode of a cubic enclosure. Fig. 1 shows a typical case for this. Then (3) can be rewritten as

$$E_{\mathrm{in}}(t) \approx k_1 E_1 \mathrm{e}^{-at} \sin(\omega_0 t) \tag{4}$$

where E_1 is the amplitude of the coupled electric field intensity, ω_0 is the angular frequency of the lowest resonance, k_1 is a scale factor to characterize the amplitude of this component, and a is the decay constant. Spectral content of (4) is

$$\bar{E}_{\mathrm{in}}(\omega) = k_1 E_1 \frac{\omega_0}{a^2 + \omega_0^2 - \omega^2 + \mathrm{j}2a\omega} \tag{5}$$

Through this assumption, one can derive readily as follows:

$$SE_{\omega} = 20\lg \frac{\left|\bar{E}(\omega)\right|}{\left|\bar{E}_{\mathrm{in}}(\omega)\right|} = 20\lg\left(\frac{kE_0}{k_1 E_1} s\right) \tag{6}$$

$$SE_{\mathrm{tp}} = 20\lg(E_0 / E_1) \tag{7}$$

$$SE_{\omega} - SE_{\mathrm{tp}} - \delta = 20\lg(s) \tag{8}$$

$$\delta = 20\lg(k_0 / k_1) \tag{9}$$

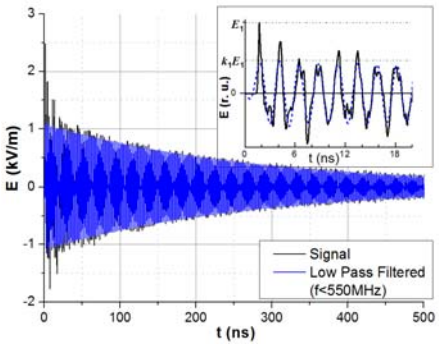

Fig. 1. An example waveform of coupled electric fields inside a metallic enclosure, illustrating the domination feature of a damped sinusoidal wave.

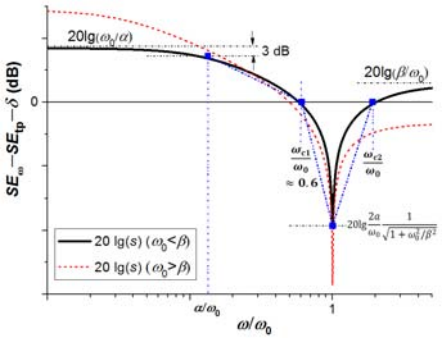

Fig. 2. Analytical correlation between time and frequency domain shielding effectiveness of metallic enclosures with apertures defined by (8) -(10).

$$s = \frac{\beta - \alpha}{\omega_0}\sqrt{\frac{(a^2+\omega_0^2-\omega^2)^2+4a^2\omega^2}{(\omega^2+\alpha^2)(\omega^2+\beta^2)}} \qquad (10)$$

Since both SE_{tp} and δ are constants rather than frequency domain functions, (8) means that variation of SE_ω with ω is determined analytically by s, defined in (10). Fig. 2 illustrates this frequency dependence. A meaningful inference is to set s=1, which then defines a critical angular frequency $\omega_{c1}<\omega_0$, and another one $\omega_{c2}>\omega_0$ just for $\omega_0<\beta$ cases. Generally, the parameters satisfy the relations as $\alpha<<\beta$, $a<<\omega_0$, $\alpha<<\omega_0$, so that a simple expression may be found as:

$$\omega_{c1,2}/\omega_0 \approx \sqrt{(3 \mp \sqrt{5+4\omega_0^2/\beta^2})/2(1-\omega_0^2/\beta^2)} \qquad (11)$$

ω_{c1}/ω_0 varies quite slowly as ω_0/β changes, as shown in Fig. 3(b), that $\omega_{c1}/\omega_0 \approx 0.6$ for $\omega_0 \le \beta$, and $0.4 \le \omega_{c1}/\omega_0 \le 0.6$ for $\beta \le \omega_0 \le 5\beta$. Substituting this inference to (8), we get

$$SE_{tp} = SE(\omega=\omega_{c1}) - \delta \cong SE(\omega=0.6\omega_0) - \delta \qquad (12)$$

(12) means that one can estimate SE_{tp} for a given EMP excitation directly from a specified frequency domain data, just with subtraction of a correction factor δ, which is found to vary in the range of a few dB to about 20 dB for different scale apertures or excitation EMP signal. A further discussion will be given in Sec. III.

III. Validation and Discussion

A. A Small Enclosure with A Relatively Large aperture

Fig. 3 shows frequency domain comparisons of electric field *SE* (a) and amplitude spectrum (b) for simulated and analytically approximated results at center of a 50 cm × 50 cm × 50 cm enclosure with a Φ20 cm aperture. The simulation are carried out via CST MICROWAVE STUDIO soft, setting the incident wave vector normal to the front side with the aperture.

When excited by a DEXP pulse of 2.5/23 ns, it has been determined that the amplitude of the electric field at center is E_1=2.5 kV/m, while the first resonant component (TE_{101} mode) at f_0=427 MHz contributes an amplitude of k_1E_1=1.15 kV/m, found by a low-pass filter processing. Then we get SE_{tp}=26 dB, δ=9 dB for this case. Substituting the parameters to (10) and (8), it is shown in Fig. 3(a) that the approximated formula SE_ω fits the simulation result quite well in a wide band of 1-700 MHz. As revealed in Fig. 3(b), the approximation of a damped sinusoidal wave at the first resonance may characterizes nearly precisely the amplitude spectrum within the wide band.

When excited by a DEXP pulse of 0.25/2.3 ns, with much less low frequency content but more high frequency content, it is found that E_1=15.6 kV/m, k_1E_1=4.9 kV/m, SE_{tp}=10 dB, δ=12 dB. Although with an obvious departure in the frequency range below 200 MHz, the approximated formula (8) still agrees reasonably well with the simulation result in the higher frequency range up to about 700 MHz. Further checking that $SE(f=0.6f_0)-\delta$ =14 dB, about 4 dB larger than SE_{tp} (10 dB), we validate that formula (12) may give out a reasonable estimation, even for a UWB-like excitation in this case. Fig. 3(b) indicates that the real amplitude spectrum for this case has a f^{-1} dependence in the range of $f<\alpha/\pi$, while the approximated damped sinusoidal wave at the first resonant frequency has a nearly constant low frequency content. This results in the discrepancy of (8) with the simulated data in low frequency range.

B. A Large Enclosure with A Relatively Small Aperture

Fig. 4 shows a frequency domain comparison of electric field *SE* (a) and waveform data (b) for simulated and analytically

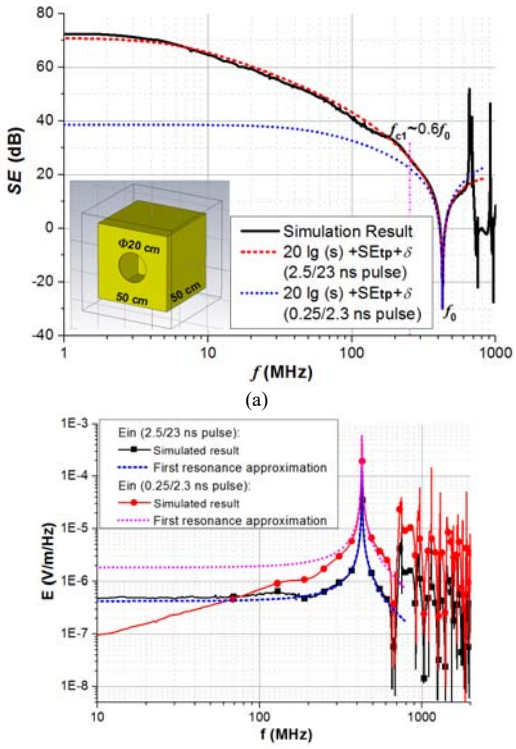

Fig. 3. Simulated and analytically approximated electric field *SE* (a) and amplitude spectrum (b), at center of a 50 cm × 50 cm × 50 cm enclosure with a Φ20 cm aperture.

approximated results at center of a 2 m × 2 m × 2 m enclosure with a 20 cm × 20 cm aperture. One may expect that a large enclosure with a relatively small aperture should have a much lower first resonant component in the transient coupling. As excited by a DEXP pulse of 2.5/23 ns, it has been determined that SE_{tp}=37 dB, k_1=0.1, δ=22 dB, really larger than those of two cases mentioned above.

We can see in Fig. 4(a) that the approximated formula (8) also shows a reasonable good agreement with the simulation data in a wide frequency range, and that (12) may also be validated again. The early time waveforms illustrated in Fig. 4(b), for three observation points, all exhibit a spike-like feature, with the amplitudes of the spikes about ten times greater than the first resonant component (TE_{101} mode), implying that they are dominated by higher order resonances. However, the long term behavior still translates close to the first resonant component ultimately, since higher frequency resonances may also leak out through the aperture or dissipate through resistive loss much sooner.

C. Application to Experimental Cases

Fig. 5 shows both measured and analytically approximated electric field *SE* at center of a 2 m × 2 m × 2 m steel cabinet with a double door. The experiments are conducted on a vertically polarized guided-wave simulator, with a test volume height of 5m, and a nominal excitation waveform of 2.5/23 ns. The cabinet has been rotated 90 degrees to make the central slit (1.8-m long) illuminated by electric field in both two normal polarization directions. For the electric field parallel to the central slit, we get SE_{tp}=29 dB, k_1=0.6, δ=7 dB, and those for the perpendicular case are SE_{tp}=16 dB, k_1≈1, δ=2 dB. The variance with above cases is that the correction factors δ tend to be smaller, especially for the electric field perpendicular to the central slit. Since the slit is so long, that a large amount of

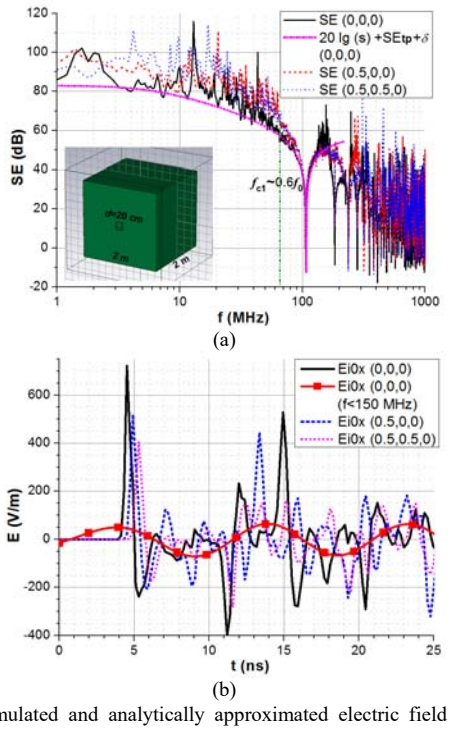

Fig. 4. Simulated and analytically approximated electric field *SE* (a) and amplitude spectrum (b), at center of a 2 m × 2 m × 2 m enclosure with a 20 cm × 20 cm aperture. The coordinate (0,0,0) denotes center of the enclosure.

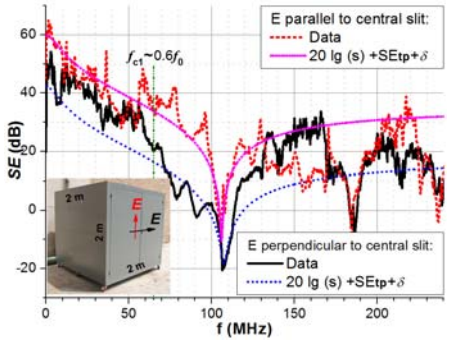

Fig. 5. Measured and analytically approximated electric field *SE* at center of a 2 m × 2 m × 2 m steel cabinet with a double door, forming a central slit and four long slits (1.8m) on the edges.

electromagnetic energy penetrates through the slit, then converts to the TE_{101} mode resonance, which greatly dominates the coupled electric field at the center. Besides, formula (8) still gives out an approximated description quite close to measured data in a wide frequency range, and that (12) also works out reasonable estimations with deviations less than 5 dB.

IV. Conclusion

Time domain shielding effectiveness, SE_{tp}, of metallic enclosures with apertures against EMP excitation, has been explicitly correlated to their frequency domain characterization SE_{ω}. With the assumption that the first resonance, typically TE_{101} mode for rectangular enclosures, dominates the long term behavior of the coupled electric field, it is derived that SE_{tp} can be roughly estimated via $SE(\omega\approx 0.6\omega_0)$ substituting a correction factor δ in a range of a few dB to about 20 dB. Several numerical and experimental cases have been checked to confirm the applicability. Through the simple formulas, one may not only directly estimate SE_{tp} based on SE_{ω}, which can be easily done in most EMC laboratories, but also get a knowledge about the variation of SE_{tp} with parameters of the exciting pulse.

References

[1] *IEEE Standard Method for Measuring the Effectiveness of Electromagnetic Shielding Enclosures*, IEEE Standard 299-2006, 2006.

[2] *High-Altitude electromagnetic pulse (HEMP) protection for ground-based C^4I facilities performing critical, time-urgent missions, part 2 transportable systems*, *MIL-STD-188-125-2*, 1999.

[3] S. Celozzi, R. Araneo, "Alternative Definitions for the Time-Domain Shielding Effectiveness of Enclosures". *IEEE Trans. Electromagn. Compat.*, vol. 56, pp. 482-485, 2014.

[4] L. G. G. Perez, A. J. L. Guerrero, J. M. B. Ruiz, et al, "Time-Domain Shielding Effectiveness of Enclosures Against a Plane Wave Excitation". *IEEE Trans. Electromagn. Compat.*, vol. 59, pp. 789-796, 2017.

[5] M. F. Xue, W. Y. Yin, Q. F. Liu, et al, "Wideband Pulse Responses of Metallic Rectangular Multistage Cascaded Enclosures Illuminated by an EMP". *IEEE Trans. Electromagn. Compat.*, vol. 50, pp. 928-939, 2008.

[6] M. P. Robinson, T. M. Benson, C. Christopoulos, et al, "Analytical Formulation for the Shielding Effectiveness of Enclosures with Apertures". *IEEE Trans. Electromagn. Compat.*, vol. 40, pp. 240-248, 1998.

[7] M. C. Yin, P. A. Du, "An Improved Circuit Model for the Prediction of the Shielding Effectiveness and Resonances of an Enclosure With Apertures". *IEEE Trans. Electromagn. Compat.*, vol. 58, pp. 448-456, 2016.

[8] F. M. Tesche, "On the Use of the Hilbert Transform for Processing Measured CW Data". *IEEE Trans. Electromagn. Compat.,* vol. 34, pp. 259-266, 1992.

[9] L. Klinkenbusch, "On the Shielding Effectiveness of Enclosures". *IEEE Trans. Electromagn. Compat.,* vol. 47, pp. 589-601,2005.

Achieving deep transcranial magnetic stimulation by activating a white matter fiber tract*

Guanghao Zhang
Beijing Key Laboratory of Bioelectromagnetism
Institute of Electrical Engineering, Chinese Academy of Sciences
Beijing, China
zhangguanghao@mail.iee.ac.cn

Xiaolin Huo
Beijing Key Laboratory of Bioelectromagnetism
Institute of Electrical Engineering, Chinese Academy of Sciences
Beijing, China
huoxl@mail.iee.ac.cn

Chanzhe Wu
Beijing Key Laboratory of Bioelectromagnetism
Institute of Electrical Engineering, Chinese Academy of Sciences
Beijing, China
wuzhe@mail.iee.ac.cn

Cheng Zhang
Beijing Key Laboratory of Bioelectromagnetism
Institute of Electrical Engineering, Chinese Academy of Sciences
Beijing, China
zhangchengcc@mail.iee.ac.cn

***Abstract*—Transcranial magnetic stimulation (TMS) is a safe and powerful diagnostic tool for exploring brain functions. However, the depth of widely used figure 8 coil is usually 2 to 3 cm, without reaching the deep brain areas. Although the H coil increased the depth of stimulation, the complicated shape, expensive cost and large focal area impede its application. This study presents a new method to indirectly activate the deep brain by choosing a white matter fiber tract as a stimulation target. The electric field induced by a figure 8 coil at arbitrary initial position was first computed using the finite element method and a personalized head model. The coil position was then optimized using the Nelder-Mead method to calculate a reasonable value of the objective function for the targeted fibers corresponding to different coil places and coil orientations. The result confirms that the proposed optimization method worked well in nonaffected neighboring fiber tracts. Thus, excitation can propagate to the terminal of the target fibers and activate the neighboring neurons at the deep brain areas.**

Keywords—component, formatting, style, styling, insert

I. INTRODUCTION

Transcranial magnetic stimulation (TMS) is a powerful tool for exploring brain functions [1]. Although TMS is widely used in clinical practice, the coil position parameters, such as coil position and coil orientation, for effective TMS administration have not been optimized [2]. Specifically, current approaches for determining coil position and orientation when targeting white matter fiber tracts on an individual basis remain suboptimal. Therefore, excitation could not reach the deep brain regions. Many psychological and clinical studies that have employed TMS reported that limited changes to the TMS coil stimulation parameters lead to drastic changes in psychological or clinical outcomes [3, 4].

Here, we propose an optimization method for precise TMS treatment planning when targeting a white matter fiber tract. TMS coil stimulation parameters includes coil position, coil orientation and coil current amplitude. The electric field induced by TMS was computed by the finite element method (FEM) using a personalized head model including realistic head geometry and tissue anisotropy, allowing clinicians and researchers to target a white matter fiber tract.

II. MATERIALS AND METHODS

A. Data acquisition

The realistic head model and fiber trajectories were derived from MRI and DTI data of one healthy, right-handed human subject.

B. Tissue segmentation

To create a realistic head model, Statistical Parametric Mapping 12.0 software was implemented to segment the structural MRI images into 5 tissue regions, including scalp, skull, cerebrospinal fluid (CSF), gray matter and white matter.

C. Brain tractography

For practical targeting of a given white matter fiber tract, we used the tractography tool of the Brainsuite software [28] to reconstruct the fiber trajectories. First, the DTI dataset was used to estimate the diffusion tensors. The diffusion tensor volumes were further coregistered to the same subject's T1-weighted MRI volumes. Then, the coregistered diffusion tensors were used to reconstruct the whole neural fiber trajectories with a track seeding of 0.5 voxel, a step size of 0.25 mm, a maximum step of 500, a bending angle threshold of 30°, an anisotropy threshold of 0.05, an orientation distribution function (ODF) sampling of 20 and a generalized fractional anisotropy (GFA) threshold of 0.01. Subsequently, we applied the region of interest (ROI) method in TrackVis software to extract the relevant white matter fiber tracts, which included targeted neural fiber tract. To obtain fiber trajectories of interest, we defined an ROI sphere with a diameter of 5 mm.

D. Tissue electrical properties

Electrical properties of tissues vary with the frequency of the coil stimulation current. Values of electrical properties can be calculated as explained in [5, 6].

E. Computer simulation

The commercial software COMSOL Multiphysics (COMSOL Inc., Palo Alto, CA) was used to simulate the induced electric field generated in the subject's head and brain. First, a volume conductor head model was built based

on reconstructed 3D tissue models and electrical properties. We built a figure-of-eight coil model with a winding external diameter of 88 mm, a winding aperture diameter of 56 mm, a winding thickness of 4 mm and 9 turns. The initial amplitude of the current injected into the coil was 3 200 A, and the current waveform frequency was 3 kHz. These applied parameters were adopted from an in-house TMS device.

We calculated the effective electric field E_l=$\mathbf{E}\cdot\mathbf{l}_l$, which is the component of the electric field $\mathbf{E}$ tangent to the fiber trajectory $\mathbf{l}$=$l\cdot\mathbf{l}_l$ ($\mathbf{l}_l$ can be obtained from the diffusion tensors) and which effectively contributes to neuronal stimulation. It was assumed that the directional derivative of the effective electric field could depolarize or hyperpolarize the membrane and was most likely to evoke an action potential at the minimum [7-9]. The directional derivative of the effective electric field can be described by the equation

$$-\lambda^2 \frac{\partial E_l}{\partial l} \quad (1)$$

Here, λ denotes the membrane space constant, which is approximately 1 mm.

F. Design of the optimization method

The distribution of the effective electric field on the targeted neural fiber E_l is dependent on coil position, coil orientation, coil current amplitude. If all these factors need to be considered during the optimization of coil stimulation parameters, the whole problem will become exceedingly difficult. To reduce the complexity of the optimization problem, the entire optimization problem is divided into two simple problems. First, the coil position and orientation are optimized to maximize the value of $-\lambda^2\partial E_l/\partial l$ for a given coil stimulation current. Second, the optimal current flow through the coil can be obtained by adjusting the value of $-\lambda^2\partial E_l/\partial l$ such that it activates only the targeted fiber tract. The Nelder-Mead algorithm in COMSOL was adopted to optimize the stimulation parameters of the TMS coil.

III. Result

The optimization method of TMS coil stimulation parameters was investigated using personalized head and realistic fiber tracts. When targeting Fiber 1, we chose mean values of the x and y coordinates of the targeted fiber tract, which were 149.25 mm and 141.87 mm, respectively, as the initial position of the center of the bottom plane of the coil. The initial coil orientation was 0 degrees, as shown in Fig. 3A (left panel). After solving the first optimization problem, we obtained the optimal position and orientation of the TMS coil, as shown in Fig. 1A (right panel). The x and y coordinates of the optimal coil position were 158.93 mm and 141.59 mm, and the optimal rotation angle was 74.99 degrees. The value of the objective function F was 60.02 mV, which was larger than the activation threshold P_{th}. By solving the second optimization problem, we obtained the optimal coil current amplitude, which was 2 772.50 A, and the value of the objective function H was 1.50e-03 mV. Because we were mainly interested in the electric field distribution within the cerebral tissues, only the gray matter (left panel) and the white matter (right panel) were imaged in Fig. 1B. The electric field amplitude $|\mathbf{E}|$ (left panel), the effective electric field $\mathbf{E}_l$ (meddle panel) and the value of $-\lambda^2\partial E_l/\partial l$ (right panel) along the targeted fiber tract (Fiber 1) and the neighboring fiber tract (Fiber 2) were presented in Fig. 1C. As shown in Fig. 1C, the value of $-\lambda^2\partial E_l/\partial l$ differed from the electric field amplitude and the effective electric field along the targeted fiber tract.

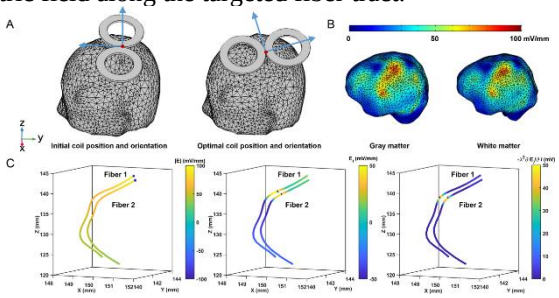

Fig. 1. Results of the optimization problem targeting Fiber 1. (A) The initial (left panel) and optimal (right panel) coil positions and orientations. (B) The electrical field strength distributions on the surface of the gray matter (left panel) and the white matter (right panel). (C) The electric field amplitude $|\mathbf{E}|$ (left panel), the effective electric field $\mathbf{E}_l$ (middle panel), and the value of $-\lambda^2\partial E_l/\partial l$ (right panel) along the targeted fiber tract (Fiber 1) and the neighboring fiber tract (Fiber 2).

The variation in the effective electric field $\mathbf{E}_l$ with the distance along the fiber tracts and the estimated activation site on the targeted fiber are presented in Fig. 2. The activation site was estimated by choosing the tract point with the maximum value of $-\lambda^2\partial E_l/\partial l$ under the optimal coil stimulation parameters. As demonstrated in Fig. 2, the estimated activation site on Fiber 1 at $l = 6.75\ mm$ with the maximum value of $-\lambda^2\partial E_l/\partial l$ was 52.00 15 mV, and the maximum value on Fiber 2 at $l = 5.14\ mm$ was 47.1622 mV. The distance between the estimated activation site on Fiber 1 and the nearest tract point on Fiber 2 to the estimated activation site was 0.81 mm. The activation site corresponded to neither the maximum effective electric field nor the closest tract point to scalp.

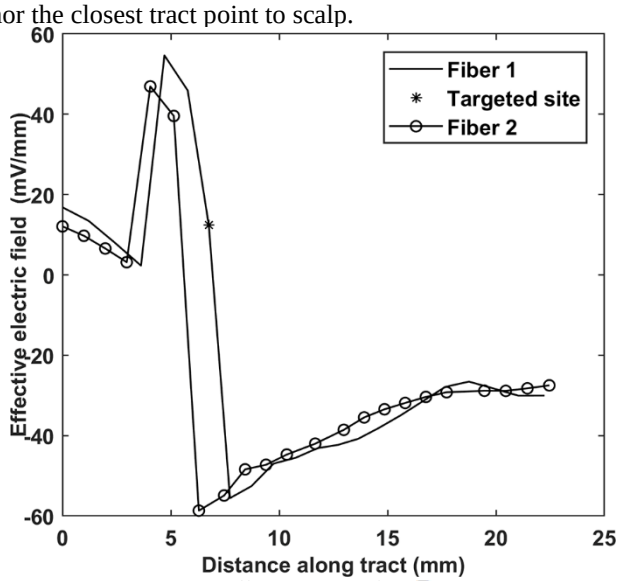

Fig. 2. Variation in the effective electric field $\mathbf{E}_l$ with distance along the fiber tracts targeting Fiber 1; the estimated activation site is plotted by an asterisk (∗).

IV. Conclusion

This study presents a new method to calculate the optimal TMS coil stimulation parameters by computing the electric field along a realistic targeted fiber tract in individual heads. The result confirms that the proposed optimization method worked well in nonaffected neighboring fiber tracts, and the activated accuracy reached a millimeter size because

the nearest distance between the fiber tracts is below 1 mm. Additionally, the result demonstrates that considering the stimulation target along a fiber tract is essential given the sensitivity of fiber tract direction to coil orientation. The optimized coil stimulation parameters reported here are quantitatively more accurate than the coil stimulation parameters estimated by researchers using navigation systems. The proposed method is much easier to use in precise TMS treatment planning and may reduce the number of MEP recordings or other measurements compared with previously used protocols. In the future, the optimization method for calculating the optimal TMS coil stimulation parameters will be integrated into neuronavigation systems. This integration can be used to guide clinicians and researchers in determining the precise coil stimulation parameters for TMS procedures.

REFERENCES

[1] T. Takakura, Y. Muragaki, M. Tamura, T. Maruyama, M. Nitta, C. Niki, T. Kawamata, Navigated transcranial magnetic stimulation for glioma removal: prognostic value in motor function recovery from postsurgical neurological deficits, Journal of Neurosurgery, 127 (2017) 1.

[2] E.M. Wassermann, T. Zimmermann, Transcranial Magnetic Brain Stimulation: Therapeutic Promises and Scientific Gaps, Pharmacol Ther, 133 (2012) 98-107.

[3] S. Kayser, B.H. Bewernick, C. Grubert, B.L. Hadrysiewicz, N. Axmacher, T.E. Schlaepfer, Antidepressant effects, of magnetic seizure therapy and electroconvulsive therapy, in treatment-resistant depression, Journal of Psychiatric Research, 45 (2011) 569-576.

[4] Z. Gangliang, Z. Guanghao, R. Yanping, Z. Cheng, W. Changzhe, J. Wei, H. Xiaolin, Electric field simulation and analysis of modified electroconvulsive therapy and magnetic seizure therapy in a realistic human head model, Journal of Biomedical Engineering, 35 (2018.08).

[5] K.S. Cole, R.H. Cole, Dispersion and Absorption in Dielectrics I. Alternating Current Characteristics, Journal of Chemical Physics, 9 (1941) 341-351.

[6] S. Gabriel, R.W. Lau, C. Gabriel, The dielectric properties of biological tissues: III. Parametric models for the dielectric spectrum of tissues, Physics in Medicine & Biology, 41 (1996) 2271.

[7] B.J. Roth, Mechanisms for electrical stimulation of excitable tissue, Crit Rev Biomed Eng, 22 (1994) 253-305.

[8] B.J. Roth, P.J. Basser, A model of the stimulation of a nerve fiber by electromagnetic induction, IEEE transactions on bio-medical engineering, 37 (1990) 588-597.

[9] S. Silva, P.J. Basser, P.C. Miranda, Elucidating the mechanisms and loci of neuronal excitation by Transcranial Magnetic Stimulation using a finite element model of a cortical sulcus, Clinical Neurophysiology, 119 (2008) 2405-2413.

Influence of foilless diode parameters on radial beam oscillation

Guangshuai Zhang
Science and Technology on High Power Microwave Laboratory
Northwest Institute of Nuclear Technology
Xi'an, China
zhangguangshuai@nint.ac.cn

Jun Sun
Science and Technology on High Power Microwave Laboratory
Northwest Institute of Nuclear Technology
Xi'an, China
sunjun@nint.ac.cn

Ping Wu
Science and Technology on High Power Microwave Laboratory
Northwest Institute of Nuclear Technology
Xi'an, China
wuping@nint.ac.cn

Yibing Cao
Science and Technology on High Power Microwave Laboratory
Northwest Institute of Nuclear Technology
Xi'an, China
caoyibing@nint.ac.cn

Zhimin Song
Science and Technology on High Power Microwave Laboratory
Northwest Institute of Nuclear Technology
Xi'an, China
songzhimin@nint.ac.cn

Meng Zhu
Science and Technology on High Power Microwave Laboratory
Northwest Institute of Nuclear Technology
Xi'an, China
zhumeng@nint.ac.cn

Zhiqiang Fan
Science and Technology on High Power Microwave Laboratory
Northwest Institute of Nuclear Technology
Xi'an, China
fanzhiqiang@nint.ac.cn

***Abstract*—The radial beam oscillation will be larger in foilless diodes with low guiding magnetic field, which may cause low efficiency and instability of high power microwave (HPM) generators. This paper focuses on the effects of the magnetic field intensity, the diode voltage, the anode radius and the cathode-anode gap on radial beam oscillation. The amplitude and spatial period of the radial beam oscillation increase significantly with a low magnetic field. The spatial period of the radial beam oscillation increases linearly with the diode voltage rising, but the amplitude of the radial beam oscillation fluctuates affected by the enhanced radial electric field near the drift tube head. Increasing the anode radius can reduce the amplitude of the radial beam oscillation, when the anode-cathode gap is large, the suppression of the radial beam oscillation will be better. In addition, the spatial period of the radial beam oscillation will be slightly lengthened. With the cathode-anode gap enlarging, the amplitude of the radial beam oscillation fluctuates and decreases as a whole. When the beam passes through the drift tube head with enhanced radial electric field, if the electrons are moving from the peak of the radial beam oscillation to the valley, the negative work done by the radial electric field makes the amplitude of the radial beam oscillation smaller, and the spatial period of the radial beam oscillation lengthens first and then remains basically unchanged. The radial beam oscillation can be suppressed by optimizing diode parameters, which establishes foundation for stable operation of O-type HPM devices with low guiding magnetic field.**

Keywords—high power microwave, foilless diode, radial beam oscillation, low magnetic field

I. INTRODUCTION

The O-type high power microwave device packaged with permanent magnets is an important research direction [1-6]. This kind of devices usually adopts foilless diodes which are well capable of high power density, long pulse, and repetitive operation. With an axial guiding magnetic field, the intense relativistic electron beam (IREB) generated by an annular explosive emission cathode interacts with electromagnetic field in the high-frequency structures to generate microwave. When the guiding magnetic field is strong, the high-quality electron beam can ensure high beam-wave interaction efficiency, but the magnet is so large and heavy that the applications of HPM systems are limited. Thus, reducing the guiding magnetic field is conductive to realize the miniaturization of HPM systems. Constrained by a low magnetic field, the angular nonuniformity of the electron beam is obvious [7-8], even causes undesirable mode competition [9-11]. Meanwhile, the radial beam oscillation is too large to reduce the beam-wave interaction efficiency. Some stray electrons with larger radial displacement may bombard the drift tube and cause vacuum breakdowns [12-14]. Therefore, it is a great challenge to improve efficiency and stability of low-magnetic-field O-type HPM devices.

The electron beam transmission characteristics in low-magnetic-field foilless diodes have been researched for many years. The transverse motion of the electron beam in a drift tube can be theoretically decomposed into fast and slow cyclotron modes [13]. It is also verified that the radial motion of the electron beam has spatial periodicity by particle-in-cell (PIC) simulations and experiments, which is in good agreement with the theoretical results without considering the space charge effect [14]. The guiding magnetic field intensity and the structure of foilless diodes play important roles in the generation and transmission of annular electron beams. In this paper, the effects of foilless diode parameters on the radial beam oscillation are further studied, focusing on the amplitude and spatial period of the radial beam oscillation. It provides a basis for choosing appropriate foilless diode parameters and suppressing the radial beam oscillation. It is of positive significance for improving efficiency and stability of HPM devices.

II. MODEL

Fig. 1 gives the foilless diode structure which includes a cathode, an anode, a drift tube and a magnet. The main parameters are the cathode radius R_c, the thickness of the cathode blade w, the anode radius R_a, the cathode-anode gap L_{ac}, and the drift tube radius R_d. Without the special explanation, R_a = 39 mm, R_c = 19.5 mm, w = 0.5 mm, R_d = 25 mm, L_{ac} = 14 mm, and the magnetic field strength is 0.5 T.

Due to the strong correlation of the foilless diode parameters, it is too difficult to decouple them independently, and thus a self-consistent explosive emission model is adopted in PIC simulations, the electron beam current satisfies the space charge limiting current. The radial beam oscillation has a spatial period P_e. The amplitude T_e of the radial beam oscillation is defined as the difference between the maximum radial position of the outer beam envelope and the minimum radial position of the inner beam envelope.

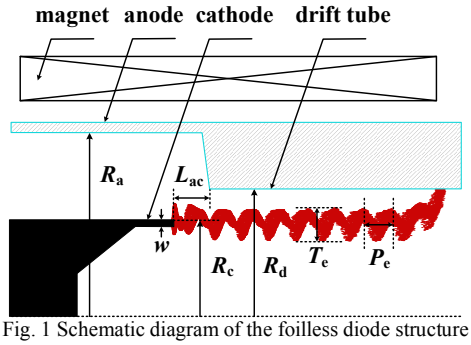

Fig. 1 Schematic diagram of the foilless diode structure

III. RESULTS AND DISCUSSION

A. Magnetic Field Intensity

Strong guiding magnetic field is conductive to restrain the electron emission from the cathode rod and prevent the electron beam from refluxing to bombard the insulator structure, effectively improving the beam quality. In the design of foilless diodes, the magnetic field intensity should ensure stable transmission of the electron beam through the high-frequency structures. The effect of magnetic field intensity on the radial beam oscillation is shown in Fig. 2. Under the default diode parameters, the same voltage waves are injected from the left port of the diode, the reflected voltage waves are slightly changed with different magnetic field intensities. the lower the magnetic field is, the smaller the Larmor radii of electrons become, the larger the amplitude T_e will be. With a stronger magnetic field, the electron cyclotron frequency is higher, the axial velocities of electrons are almost unchanged, and thus the spatial period P_e is smaller.

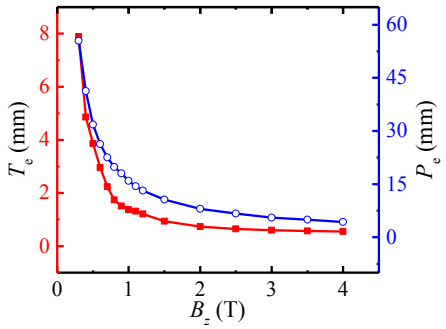

Fig. 2 The effect of the guiding magnetic field intensity

B. The diode voltage

The annular electron beam emitted by the explosive emission cathode is accelerated by the electric field in the cathode-anode gap. The strong radial electric field is a main reason for the radial beam oscillation. Under a certain diode structure, the radial electric field is proportional to the diode voltage. Therefore, the effect of the diode voltage on the radial beam oscillation is studied by PIC simulations, as shown in Fig. 3. When the diode voltage is rising, the electric field between the anode and the cathode is enhanced linearly, which accelerates the electron beam to obtain more transverse and axial momentum, thus the spatial period P_e increases approximately linearly, and the amplitude increases as a whole, but fluctuates locally. This fluctuation is not only affected by the enhanced radial electric field near the drift tube head, but also related to the motion of the electron beam through the region of the enhanced radial electric field under different diode voltages. Further researches will be done later.

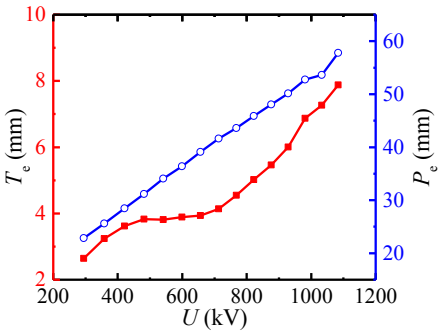

Fig. 3 The effect of the diode voltage

C. The anode radius

The radial electric field affected by the anode radius in the cathode-anode gap results in the radial beam oscillation. Fig. 4 gives the effect of the anode radius on the radial beam oscillation, the foilless diode remains the default settings except the anode radius. In PIC simulation, Increasing the anode radius can reduce the radial electric field, and then the electron beam gets less transverse momentum, which makes the amplitude T_e smaller. When the anode radius is large or the cathode-anode gap is small, the radial electric field in the cathode-anode gap is mainly determined by the cathode and drift tube head, and the anode radius has little effect on the radial beam oscillation. The PIC simulations are performed with the same diode injection voltage, the diode voltage rises with the anode radius increasing, the electron beam gets more axial momentum, thus the spatial period P_e becomes larger.

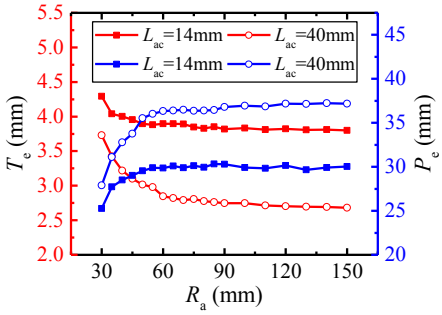

Fig. 4 The effect of the anode radius

D. The cathode-anode gap

Fig. 5 shows the variation of the radial beam oscillation with the cathode-anode gap L_{ac}. In the process of increasing Lac, affected by the match between the motion of electrons and enhanced radial electric field near the drift tube head, the amplitude T_e shows a large fluctuation which decreases slightly. The phase space of the electron beam in PIC simulation is given in Fig. 5(b), The results show that if the electron beam is moving from the peak of the radial beam

oscillation to the valley near the drift tube head, the negative work done by the radial electric field to the electron beam makes the amplitude T_e smaller. On the contrary, if the electron beam is moving from the valley to the peak, the radial electric field does positive work to the electron beam, so that the amplitude T_e becomes larger. When L_{ac} is small, the diode voltage is rising with L_{ac} increasing, the electron beam gets more axial momentum, and as a result, the spatial period increases. At the same time, the current decreases and the impedance increases. When L_{ac} is large, and the spatial period P_e basically remains unchanged due to the almost unaffected electrical parameters.

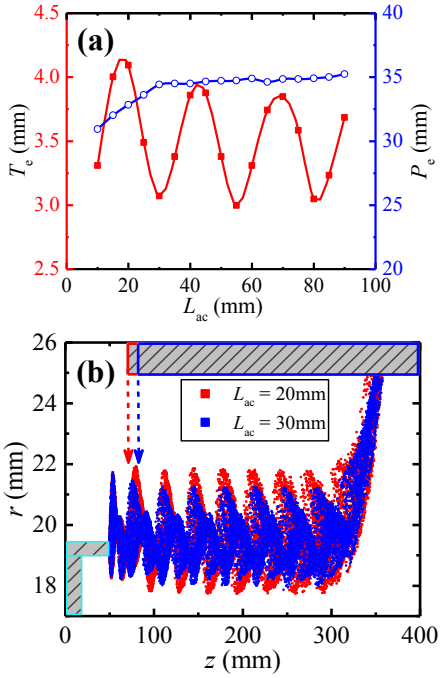

Fig. 5 The effect of the cathode-anode gap, (a) the PIC simulation results, (b) the phase space of the electron beam

IV. Conclusion

The radial beam oscillation has a close influence on the efficiency and stability of low-magnetic-field HPM generators. The PIC simulations are performed by using full-electromagnetic code UNIPIC. This paper researches the effects of magnetic field intensity, diode voltage, anode radius and cathode-anode gap on the radial beam oscillation. With a low magnetic field, the amplitude and spatial period of the radial beam oscillation are greatly increased due to the larger Larmor radii and the lower cyclotron frequency of electrons. Increasing the diode voltage linearly enhances the electric field between the cathode and the anode, and the electron beam gets more transverse and axial momentum, thus the spatial period of the radial beam oscillation becomes larger. However, affected by the enhanced radial electric field near the drift tube head, the amplitude of the radial beam oscillation increases as a whole, but fluctuates locally. Increasing the anode radius can reduce the radial electric field in the cathode-anode gap, and thus reduce the amplitude of the radial beam oscillation. When the cathode-anode gap is large, a better suppression of the radial beam oscillation can be obtained. In addition, with the same injection diode voltage, increasing the anode radius will slightly increase the spatial period of the radial beam oscillation. With the cathode-anode gap increasing, the amplitude of radial beam oscillation shows a large fluctuation which decreases slightly, the spatial period increases first and then remains basically unchanged. By comparing the phase space of the electron beam, it is found that if the electron beam is moving from the peak of the radial beam oscillation to the valley near the drift tube head with an enhanced radial electric field, the negative work done by the radial electric field on the electron beam makes the radial oscillation amplitude smaller, and conversely, the amplitude of the radial beam oscillation increases. The research results in this paper have guiding significance for suppressing the radial beam oscillation and improving the stability of low-magnetic-field O-type HPM devices.

References

[1] Chen Changhua, Liu Guozhi, Huang Wenhua, et al. A Repetitive X-Band Relativistic Backward-Wave Oscillator [J]. IEEE Trans Plasma Sci, 2002, 30(3): 1108-1111.

[2] Zhang Jun, Jin Zhenxing, Yang Jianhua, et al. Recent advance in long-pulse HPM sources with repetitive operation in S-, C-, and X-bands[J]. IEEE Trans Plasma Sci, 2011, 39(6): 1438-1445.

[3] Totmeninov E M, Gunin A V, Klimov A I, et al. X-band relativistic BWO-RR with controlled microwave pulse duration[J]. IEEE Trans Plasma Sci, 2012, 40(6): 1590-1593.

[4] Zhang Dian, Zhang Jun, Zhong Huihuang, et al. Ananlysis of the power capacity of overmoded slow wave structures[J]. Phys Plasmas, 2013, 20(7): 073111.

[5] Xiao Renzhen, Chen Changhua, Wu Ping, et al. Role of dc space charge field in the optimization of microwave conversion efficiency from a modulated intense relativistic electron beam[J]. J Appl Phys, 2013, 114(21): 214503.

[6] Teng Yan, Chen Changhua, Sun Jun, et al. Effect of end reflections on conversion efficiency of coaxial relativistic backward wave oscillator[J]. J Appl Phys, 2015, 118(17): 173103.

[7] Korovin S D, Rostov V V, Polevin S D, et al. Pulsed power-driven high-power microwave sources[J]. Proc IEEE, 2004, 92(7): 1082-1095.

[8] Korovin S D, Litvinov E A, Mesyats G A, et al. Degradation and recovery of the emission from a graphite cathode in relation to the repetition frequency of nanosecond accelerating pulses[J]. IEEE Trans Plasma Sci, 2006, 34(5): 1771-1776.

[9] Chen Changhua, Liu Guozhi, Song Zhimin, et al. Effects of axial guiding magnetic field on microwave power of relativistic backwave oscillators[J]. High Power Laser and Particle Beams, 2000, 12(6):745-748.

[10] Zhai X, Garate E, Proh aska R, et al. Experimental study of plasma-filled backward wave oscillator[J]. IEEE Trans Plasma Sci,1993, 21(1): 142-149.

[11] Vlasov A. N., Ilyin A. S., Carmel Y. Cyclotron effects in relativistic backward-wave oscillators operating at low magn etic fields[J]. IEEE Trans Plasma Sci, 1998, 26(3): 605～614.

[12] Xiao Renzhen, Tan Weibing, Li Xiaoze, et al. A high-efficiency overmoded klystron-like relativistic backward wave oscillator with low guiding magnetic field[J]. Phys Plasmas, 2012, 19(9): 093102.

[13] Teng Yan, Cao Yibing, Song Zhimin, et al. A Ka-band TM02 mode relativistic backward wave oscillator with cascaded resonators[J]. Phys Plasmas, 2014, 21(12): 123108.

[14] Wu Ping, Tan Weibing, Sun Jun, et al. Electron motion of an annular beam in a low-magnetic-field drift tube[J]. Phys Plasmas, 2014, 21(12): 123111.

Simulation evaluation of the coupling effect of cables crossing cabins in frequency domain

Guoshuai Zhen
Aviation Key Laboratory of Science and Technology on Electromagnetic Environmental Effects
Shenyang Aircraft Design and Research Institute, AVIC
ShenYang, China
lanyun0@163.com

Jiazuo Zang
Aviation Key Laboratory of Science and Technology on Electromagnetic Environmental Effects
Shenyang Aircraft Design and Research Institute, AVIC
ShenYang, China
llyp8@163.com

Xuefeng Qi
Aviation Key Laboratory of Science and Technology on Electromagnetic Environmental Effects
Shenyang Aircraft Design and Research Institute, AVIC
ShenYang, China
qixuefeng08@sina.com

Yan Wang
Aviation Key Laboratory of Science and Technology on Electromagnetic Environmental Effects
Shenyang Aircraft Design and Research Institute, AVIC
ShenYang, China
sy601wangyan@163.com

Abstract: **To analyze the coupling effect of cables, the model of cabins and cables are established. The influence of cables on the electromagnetic shielding effectiveness of cabins is simulated in the frequency below 1GHz by changing cable length, cable radius and the radius of the crossing hole. Through the comparison of electromagnetic shielding effectiveness, it is found that the coupling effect of cables is a common phenomenon in the frequency below 600MHz. When cable length is larger than 2m and the gap between cabin and cable is larger than 2mm, the coupling effect of cables is strong and no longer affected by cable length, cable radius and the radius of crossing hole.**

Keywords Cables, coupling effect, electromagnetic shielding effectiveness, frequency domain

I. INTRODUCTION

There are a large number of cables in the military aircraft equipment cabins. Under the external strong electromagnetic environment, electromagnetic energy enters equipment cabins through the gaps or holes on the airframe. Some electromagnetic energy is coupled to the cables and then transmitted to the inside of airborne equipments, which may be a threat to the normal operation of airborne equipments. In high-field electromagnetic environment such as lightning [1], strong electromagnetic pulse [2] and high-power microwave, the researches of cables coupling effect are the foundation of aircraft electromagnetic protection researches.

In the electromagnetic compatibility test of national military standard, the influence of electromagnetic signal transmitted by the cable

itself on the airborne equipment is investigated. Most of airborne cables are shielded and the coupling of cables is about the external electromagnetic energy coupled by the shielding layer to a great extent. Most of researches on the coupling effect of cables are limited to several parallel cables or cables with some certain arrangement rules [3-4]. However, there are various and intricate cables in the equipment cabin with no certain arrangement rules. On the other hand, most of researches are limited to the time domain waveform of the transmission signal by cables. The coupling effect of cabled is not considered as a whole in the frequency domain.

In this paper, cabin and cable models are constructed. The influence of cable length, cable radius and the radius of crossing hole on the coupling effect of cable are evaluated from the view of frequency domain. It is confirmed that the cable coupling is a common phenomenon in the frequency below 600MHz and cables longer than 2m can introduce most of the external electromagnetic energy into the airborne equipment.

II. CABLE AND CABIN MODELS

Cabin and cable models are shown in Figure 1 and the material both of them are defined as ideal metal. The cabin is defined as a cube with the size of 2m*1m*1.4m. There is a hatch cover on one side of cabin and electromagnetic energy can enter the interior through gaps. The cable with length *l* is located in the red circle shown in Figure 1, and the top view of crossing position is shown in the enlarged Figure 1. The radius of cable is *r*1 and he radius of crossing hole is *r*2. There is electromagnetic wave incident directly in front of model and the direction of electric field is parallel to the axial direction of cable.

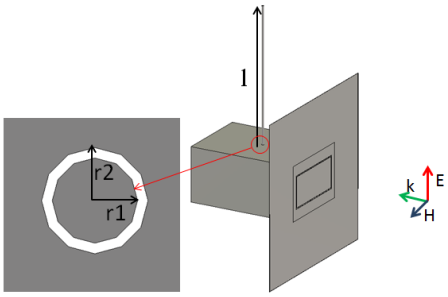

Figure 1 Cabin and cable models. The red circle zone is enlarged. Electromagnetic wave is incident from front. *r*1 is cable radius, *r*2 is crossing hole radius, *l* is cable length.

III. THE COUPLING EFFECT OF CABLES

When *r*2 equals *r*1, the cabin is closed at the crossing position of cable. Electromagnetic wave can only enter the interior of cabin from the gaps of hatch cover. When *r*2 is larger than *r*1, there is a gap between cabin and cable, through which electromagnetic wave can enter the interior of cabin. Comparing the electromagnetic shielding effectiveness (SE) distribution of cabin under two conditions can reflect the influence of cable coupling. In this paper, the influence of cable length, cable radius and the radius of crossing hole are mainly considered.

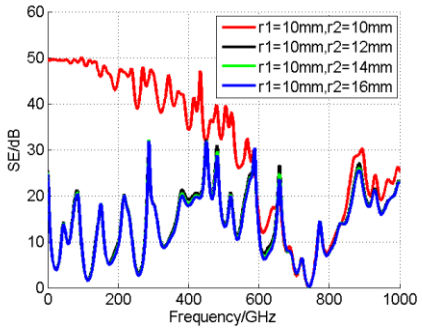

Figure 2 The SE distribution of cabin below 1GHz with different *r*2. The red line corresponds to *r*1=*r*2. The other lines correspond to *r*2>*r*1.

Figure2 shows the SE distribution in the frequency below 1GHz when cable radius is fixed at 10mm. The red line is the SE distribution of cabin when *r*2 equals *r*1. As a whole, the SE decreases with the increase of frequency. There is electromagnetic resonance at the gap of hatch cover around 750MHz, which

leads to the decrease of SE of cabin.

When *r*2 is larger than *r*1, the electromagnetic wave can enter the cabin along cable or through the gaps between cabin and cable. In Figure 2, the SE distribution of cabin decreases significantly in the frequency below 600MHz and is 5dB in some frequency bands, which means that more than half of electromagnetic energy can enter the cabin. With the increase of *r*2, the SE distribution of cabin is basically the same, indicating that the electromagnetic energy is mainly transmitted into the cabin along cable. The gap width of 2mm is enough for electromagnetic wave to enter the cabin, while the gap between cabins and cables is generally lager than 2mm inside the aircraft. Once electromagnetic wave is coupled to cables, electromagnetic wave can conduct inside aircrafts along cables.

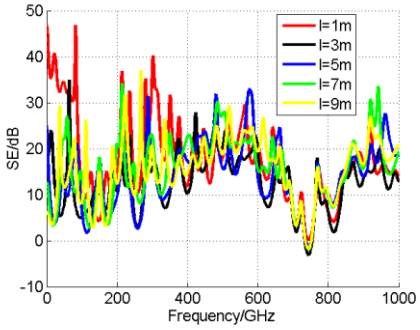

Figure 3 The SE distribution of cabin below 1GHz with different *l*.

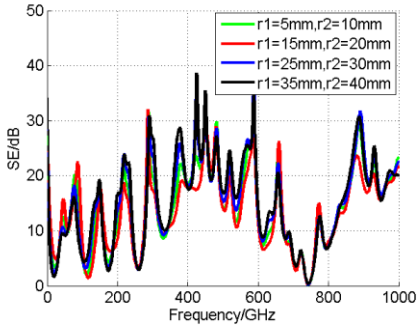

Figure 4 The SE distribution of cabin below 1GHz with different *r*1.

Figure 3 shows the SE of cabin with the changing of cable length. When cable length is 1m, the SE is about 35dB below 100MHz, which is smaller than the SE of 50dB without cable coupling effect and larger than the SE of 15dB with other cable length. It means that there is cable coupling effect but the coupling effect is weak. When the frequency is above 100MHz or the cable length is larger than 2m, the change of cable length has no influence on the SE distribution of cabin. And the change of the cable radius has no influence on the SE distribution of cabin as well in Figure 4. It means that the cable coupling is strong with no limit on the cable radius once the cable is longer than 2m.

IV. Conclusion

Through the comparison of electromagnetic shielding effectiveness distribution of the cabin, it is found that the coupling effect of cables is a common phenomenon in the frequency below 600MHz. When the cable length is larger than 2m and the gap width between cabins and cables is larger than 2mm, the coupling effect of cables is strong and no longer affected by cable length, cable radius and the radius of the crossing hole. This conclusion is helpful to guide the design of aircraft protection under strong electromagnetic environment. In the design and test of electromagnetic compatibility, attention should be paid to the coupling effect of cables in the frequency below 600MHz.

References

[1] F. Zhang and Y. Liu, “Analysis and protection of lighting damage in pumped storage power station hillside cable,” 2017 international conference on robots &intelligent system, pp. 36–41, 2017.

[2] B. Y. Sun, Z. Hui and X. Yanzhao, “Comparison of the cable coupling effects under two kinds of HEMP environment” High power laser & Particle beams, 2002.

[3] J.P. Parmantier, M. Ridel and S. Bertuol “Modeling of HIRF coupling on complex cable architectures” International conference on electromagnetic in advanced applications, 2011.

[4] P. Kirawanich, N.E. Islam, and J. Yakura “Electromagnetic topology simulations for cable coupling with a radiating dipole at an aperture” IEEE international symposium on electromagnetic compatibility, 2006.

Acute hepatic effects of Ka-HPM pulses exposure on KM mouse

Haihui Yang,
Key Laboratory of Biomedical Information Engineering of Ministry of Education, School of Life Science and Technology
Xi'an Jiaotong University
Xi'an, China
yanghaihui0710@126.com

Fan Fan
Key Laboratory of Biomedical Information Engineering of Ministry of Education, School of Life Science and Technology
Xi'an Jiaotong University
Xi'an, China
casdial@163.com

Xiaoyun Lu*
Key Laboratory of Biomedical Information Engineering of Ministry of Education, School of Life Science and Technology
Xi'an Jiaotong University
Xi'an, China
luxy05@xjtu.edu.cn

Yi Zhou
State Key Laboratory of Electrical Insulation and Power Equipment, School of Electrical Engineering
Xi'an Jiaotong University
Xi'an, China
zhouyi107@126.com

Yangxin Qiu
State Key Laboratory of Electrical Insulation and Power Equipment, School of Electrical Engineering
Xi'an Jiaotong University
Xi'an, China
yxinqiu@163.com

Yanzhao Xie
State Key Laboratory of Electrical Insulation and Power Equipment, School of Electrical Engineering
Xi'an Jiaotong University
Xi'an, China
yzxie@xjtu.edu.cn

***Abstract*—Km mice were exposed to Ka-band high-power microwave (Ka-HPM) pulse with average power density of 50 kW/cm^2, pulse width of 300 ps, central frequency of 37 GHz and repetition rate of 10 Hz for 30 seconds. The acute exposure to Ka-HPM resulted in the increase of plasma AST level and alternation of hepatocytes ultrastructure. The hepatic metabonomics analysis indicated that several metabolic pathways including ascorbate/aldarate metabolism pathway, glycine/serine/threonine metabolism pathway and fatty acid biosynthesis pathway were affected by Ka-HPM pulses radiation and stearic acid was most dramatically up-regulated metabolite. These results implied the potential health risk of Ka-HPM pulses exposure and limited exposure duration might resulted in the stress of hepatocytes and change of hepatic metabolic activities.**

Keywords — Ka-HPM pulses, hepatocyte ultrastructure, hepatic metabonomics, stearic acid

I. Introduction

Narrow-band high-power microwave (HPM) has the characteristics of high frequency, short pulse (tens of nanoseconds) and high power, which is widely used in various fields such as the application for radar, navigation, and communication [1-2]. Although a large number of experiments have been done in an attempt to provide an insight into the biological effects of microwave electromagnetic (EM) fields [3-5], there was still some gap in the relative study concerning some given microwave frequencies. In this study, we specifically investigated the effect of Ka-band high-power microwave (Ka-HPM) acute exposure on mice. The blood biochemical examination, histological characterization and hepatic metabonomic analysis were used to reveal the potential bioeffects of Ka-HPM pulses exposure.

II. Materials and Methods

A. Animals and Ka-HPM pulses exposure procedure

The Ka-HPM pulses radiation system was installed in the National Center for International Research on Transient Electromagnetics and Applications (TEA), School of Electrical Engineering, Xi'an Jiaotong University. The Ka-HPM in the testing volume with average peak power density of 50 kW/cm^2, repetition rate of 10 Hz and pulse width of 300 ps were generated by a RADAN-based Ka-band BWO system and the central frequency of the pulses was 37 GHz. 25g-30g Kunming mice were used and randomly divided into two groups. The treating group was exposed to Ka-HPM for 30 seconds with the total pulse number of 300. The sham group was placed in the same environment but without Ka-HPM radiation.

B. Histological, TEM and metabonomics analysis

Mice were sacrificed at 24h after exposure. The blood samples and tissue samples were prepared according to the corresponding standard protocols. The hepatic and rental functions were analyzed by blood biochemical examination. Histological characteristics were analyzed with the paraffin-embedded tissue slices combined with conventional Hematoxylin-Eosin staining method. The uranium acetate-lead nitrate double staining was used for preparing samples for transmission electron microscope (TEM) observation. The hepatic metabonomics was analyzed by GC-TOF-MS.

III. Results

A. The effect of Ka-HPM pulsse exposure on the hepatic and rentl functions of KM mice

The blood biochemical examination results revealed that only aspartate aminotransferase (AST) was increased after Ka-HPM pulses exposure. No other parameters implied the change of hepatic and rental functions.

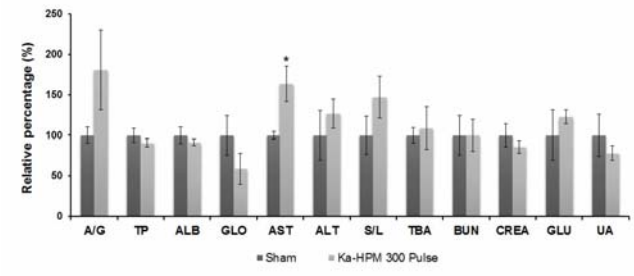

Fig. 1. Effects of Ka-HPM pulses on blood biochemical parameters of mice

B. *Histological characterization and TEM observation of hepatic tissue after Ka-HPM pulses exposure*

The hepatic tissue paraffin-embedded slices were prepared and stained with Hematoxylin-Eosin. As shown in Fig. 2, histological analysis did not revealed significant difference between sham and Ka-HPM exposure groups. While the TEM observe results indicated the ultrastructure difference of hepatocytes between the sham and Ka-HPM exposure groups. The mitochondria in hepatocytes were swelled and lipid droplets could be seen in the cytoplasm (Fig. 3). This implied the possible dysfunction of hepatic metabolism, especially the disorder of fatty acid metabolism after Ka-HPM pulses exposure.

C. *Non-target hepatic metabonomic analysis of liver after Ka-HPM pulses exposure*

Based on the hepatocytes ultrastructure alternation revealed by TEM observation, the hepatic metabonomics were further analyzed by GC-TOF-MS. There were 10 up-regulated metabolites and 16 down-regulated metabolites identified in Ka-HPM pulses exposure group. The metabolic pathway enrichment analysis indicated that ascorbate/ aldarate metabolism pathway and glycine/serine/threonine metabolism pathway were significantly influenced. Among those altered metabolites, stearic acid was the most dramatically changed metabolite which might explain the droplets observed under TEM. These results suggest that Ka-HPM with 50 kW/cm^2 average power density for 30 seconds exposure may lead to lipid metabolism disorder.

IV. Conclusion

The acute short-term exposure to Ka-HPM resulted in the increase of plasma AST level and alternation of hepatocytes ultrastructure. The mitochondria in hepatocytes were swelled and lipid droplets could be seen in the hepatycytes cytoplasm. of mice exposed to Ka-HPM for just 30 seconds. Ka-HPM pulses radiation also affected the amino acid and fatty acid metabolism of mice and Stearic acid was most dramatically up-regulated metabolite. These results implied the potential health risk of Ka-HPM pulses exposure and short-term exposure to Ka-HPM pulses might already be able to result in the stress of hepatocytes.

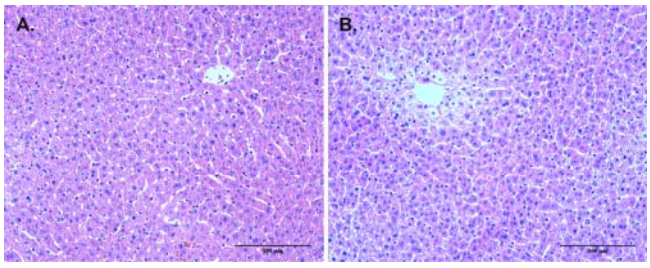

Fig. 2. HE staining of the hepatic tissue. A: Sham; B: Ka-HPM (40×)

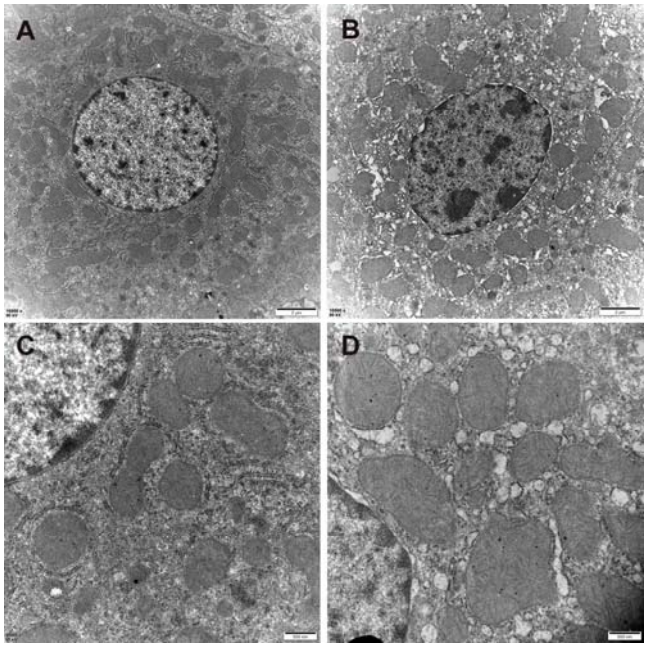

Fig. 3. TEM observation of hepatocytes ultrastructure. A&C: Sham group; B&D: Ka-HPM

References

[1] E. Schamiloglu, "High Power Microwave Sources and Applications," IEEE MTTS, Fort Worth, Texas, 2004.

[2] P.D. Smith, S.R. Cloude, "Ultra-Wideband, Short-Pulse Electro-magnetics 5", New York: Kluwer Academic/Plenum Publishers, 2002.

[3] R. L. Seaman, "Review of Literature on High Power Microwave Pulse Biological Effects". AFRLRH-BR-TR-2009-0068. Brooks City-Base, TX: Air Force Research Laboratory, Human Effectiveness Directorate, 2009.

[4] J. R. Jauchem, "Effects of low-level radio-frequency (3kHz to 300GHz) energy on human cardiovascular, reproductive, immune, and other systems: a review of the recent literature". Int J Hyg Environ Health, 2008, pp:1-29.

[5] J. A. D'Andrea, C. K. Chou, S. A. Johnston, E. R. Adair, "Microwave effects on the nervous system". Bioelectromagnetics, 2003, pp: S107-147.

Prediction of Radio Frequency in a Large Structure from External Electromagnetic Source

Han-Hee Lee
Korea Aerospace University
Goyang, Republic of Korea
lhanniii@gmail.com

J.W. Lee
Korea Aerospace University
Goyang, Republic of Korea
jwlee1@kau.ac.kr

J.H.Lim
Korea Aerospace University
Goyang, Republic of Korea
1357dla@naver.com

J.H. Kwon
Electronics and Telecommunications Research Institute(ETRI)
Daejeon, Republic of Korea
hjkwon@etri.re.kr

J.H. Hwang
Electronics and Telecommunications Research Institute(ETRI)
Daejeon, Republic of Korea
jhhwang@etri.re.kr

C.H. Hyoung
Electronics and Telecommunications Research Institute(ETRI)
Daejeon, Republic of Korea
hyoung@etri.re.kr

***Abstract*—The IEMI effect problem in a large structure is predicted by using theoretical model developed from our own programming code and this result is compared with measurement and simulation to verify its validity. For measurements, the targeted large structure built with common building materials has been selected and a measurement was carried out at the 0.6-6GHz band. The received power was measured inside the building for the electromagnetic waves radiated from outside the structure. In order to predict the level of the received power, we developed the performance-Enhanced PWB method(PEPWB) which overcomes the limitation of the previously studied PWB method. In order to verify the validity of the theoretical model, Wireless Insite, the commercially available simulation tool, was also used.**

Keywords—Electromagnetic Interference(EMI), Electromagntic Compatibility(EMC), Topological Analysis, PWB method, PEPWB method.

I. INTRODUCTION

Various types of electronic devices are being developed due to communication technologies in modern society and the most ICT (Information & Communication Technology) is being used in almost all fields of life. Therefore, the influences of intentional and non-intentional electromagnetic waves on the system may lead to major problems. For this reason, the study of Electromagnetic Compatibility(EMC) and Electromagnetic Interference(EMI) has been performed. Studies on EMC/EMI techniques have been based on numerical analysis techniques such as finite difference method (FDTD) and moment method (MoM), which usually solve Maxwell's equations by using computer resources. However, it requires a considerably long time and a large amount of data in large scaled structures. In order to overcome these limitations of numerical methods, a topological analysis method and a PWB method (PoWer Balance method) have been proposed for electromagnetic field analysis in large-scaled structures[1][2]. Since the PWB method is basically based on probability theory assuming uniform field distribution inside the building in a relatively high frequency regime, it is possible to analyze for electromagnetic environment in large scaled structures. Recently, the Performance-Enhanced PWB method(PEPWB method) has been proposed to overcome the limitations of the conventional PWB method. Therefore, in this paper, we will install transmitting/receiving system and measure electromagnetic waves in the large structure. In addition, PEPWB method is used to predict the electromagnetic environment inside the targeted large structure. Also, For the cross check of the validity of our analysis, we use the Wireless Insite, commercially available simulation tool with the predicted results from our analysis and measured results.

Electronics and Telecommunications Research Institute(ETRI)

II. THE TARGET SITE AND MEASUREMENT SET-UP

A. Target structure

The target building is characterized by many rooms and long hallway. The structure to be analyzed is a building made of general building materials such as doors and windows. There are three kinds of spaces that are located inside the structure. The three spaces are called Room1, Hallway and Room2. The sizes of Room1, Hallway and Room2 are $6.8\times7.3\times2.6m^2$, $20.4\times3.2\times2.6m^3$, $13.6\times79\times2.6m^3$, respectively. Each space is composed of windows, columns of a building, and so on.

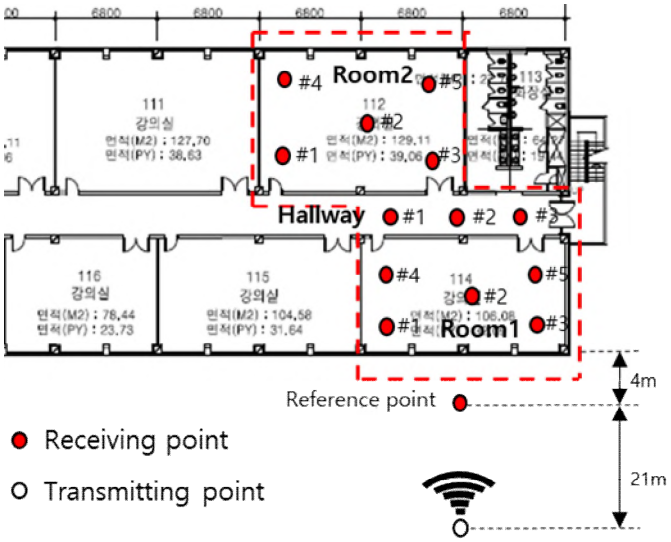

Fig. 1. Description of measurement situation

B. Measurement Set-Ups

In order to make the far-field conditions, the transmitting point was located at 25 m away from the target building as shown in Fig. 1. The transmitting system consists of a signal generator, a power amplifier, a coupler, and a directional antenna. There are five receiving points in Room1 and Room2, and three in Hallway. The receiving system consists of a directional antenna and a spectrum analyzer. At all receiving points, the measurement is performed by rotating

the receiving antenna at 0^o, 90^o, 180^o, and 270^o with respect to the direction of looking at the transmitting antenna. In the derivation method, an average value according to the direction of the receiving antenna is obtained and an average value for each space is obtained again.

III. THEORETICAL METHOD AND SIMULATION

A. *The theoretical method*

$$<\sigma_{wall}>= T_w \cdot \frac{16}{9\pi}(\frac{2\pi}{\lambda})^4 \cdot {a_{wall}}^4, (f \le \frac{1.3c}{12\pi a_{wall}}) = T_w \cdot \frac{\pi {a_{wall}}^2}{2}(f \le \frac{1.3c}{12\pi a_{wall}}) \quad (1)$$

$$<\sigma_{ap}>= \frac{16}{9\pi}(\frac{2\pi}{\lambda})^4 \cdot {a_{ap}}^4, (f \le \frac{1.3c}{12\pi a_{ap}}) = \frac{\pi {a_{ap}}^2}{2}(f \le \frac{1.3c}{12\pi a_{ap}}) \quad (2)$$

$$<\sigma_{ant}>= \frac{\lambda^2}{8\pi}(1-|S_{11}|^2) \quad (3)$$

$$<\sigma_{obj}>= \frac{\lambda Q_{obj}}{2\pi V} \quad (4)$$

$$Q_X = \frac{\lambda <\sigma_X>}{2\pi V}(X = wall, ap, ant, obj) \quad (5)$$

The PEPWB method, which enhances the performance of the conventional PWB method is used to efficiently perform the electromagnetic effect analysis within an electrically large structure[3]. In general, The PWB method performs the analysis based on the assumption that the electromagnetic field is uniformly distributed inside an electrically large structure compared to the wavelength of the target frequency. However, the conventional PWB method has a limited range of structures which are only made of conductors. In contrast to the PWB method, the PEPWB method overcomes the disadvantages of the PWB method and maintains its merits since the range of the structure to be analyzed is extended to a structure with a general medium as well as conductor. This method defines the elements causing the loss in the analysis structure and calculates the mean coupling cross section and the Q-factor for the loss factor. In the large structures, losses due to wall, apertures, antennas and objects are common. In PEPWB method, the mean coupling cross section of these elements can be calculated using (1)-(4), where a_{wall} and a_{ap} is a radius of wall area and aperture, T_w is transmission coefficient of a concrete, c is the speed of light, S_{11} is a return loss of the antenna, V is a volume of the structure[3]. The relationship between the Q-factor and the mean coupling cross section can be expressed as (5). After defining these loss factors, we can derive the result of the PEPWB method by setting the propagation multipath of the electromagnetic wave inside the large structure. In this paper, we derive the received power in each space.

B. *Simulation*

The Wireless Insite is mainly used for a wide range of propagation path analysis problems by modeling the physical characteristics of terrain and urban buildings and tracking the light rays to calculate the interaction of rays including reflection, diffraction, and transmission of the shaped surface[4]. By using this simulation tool, 3-D model of the targeted large structures was constructed and a simulation environment which is similar to the measurement environment was set. Considering the physical phenomena such as reflection, diffraction, and transmission, it gives accurate results but time consumption increases infinitely.

IV. RESULT

In Fig. 2, it is the result of comparing the received power in Room2 predicted by the PEPWB method to the result of measurement and simulation. In the actual measurement environment, there are factors that can affect the wave propagation phenomenon such as weather, surrounding environment, and so on. Simulation and PEPWB method do not perfectly consider these factors. However, as shown in Fig. 2, the results of the simulation and the PEPWB method show similar tendencies regardless of considering these factors.

As shown in Table 1, the computational time of the PEPWB method is only 18 seconds, but the analysis time of Wireless Insite is 223,310 seconds. Therefore, the PEPWB method, which is the theoretical model proposed in this paper, is more efficient than the commercially available simulation tool.

V. CONCLUSION

This study was carried out to efficiently analyze, using the PEPWB Method, the electromagnetic effects in the targeted large structure from the external electromagnetic source. To verify its accuracy and efficiency, measurement had been performed on actual large structures. In addition, we used Wireless Insite, a commercially simulation tool, for cross validation. Comparing all the results, the PEPWB method shows a similar tendency to the actual measurement method and shows more efficient analysis results than those of the commercially available simulation tool for the large structure. Therefore, it is expected that the electromagnetic environment can be predicted for large structures under construction or already constructed.

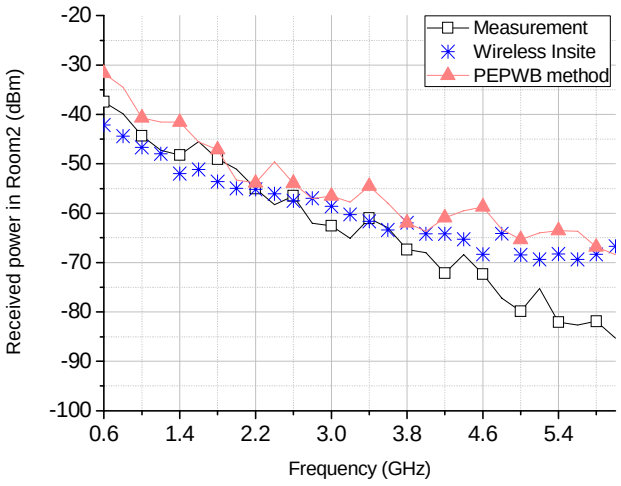

Fig 2. Comparison of the received powers in Room2

Table 1. The comparison the Wireless Insite and PEPWB method in time consumption

	Wireless Insite	PEPWB method
Analysis time	223,310 seconds (62h 1m 50s)	18.331 seconds

REFERENCES

[1] I. Junqua, P. Parmantierm F. Issac, “A network formulation of the PWB method for high frequency EM coupling applications”, Interaction Notes 576, 2002.

[2] I. Junqua, F. Isssac, J.P. Parmantier, “A network formulation of the power balance method for high frequency coupling”, Electromagnetics, vol. 25, no. 7, pp. 603.-622, Oct, 2005.

[3] Han-Hee Lee, Jae-Wook Lee, “Analysis of Electromagnetic Effect inside Large Buildings by External Electromagnetic waves Uisng Performance-Enhanced PWB Method," The Journal of Korean Institute of Electromagnetic Engineering and Science, Vol. 30, No. 1, pp. 12~22, 2019.

[4] Wireless Insite 3.3.0 User's Guide.

PCI Test on Power Line Filter against HEMP

Hanming Cui
Field Engineering College, Army Engineering University
Nanjing, China
877454053@qq.com

Zhewen Xu
Field Engineering College, Army Engineering University
Nanjing, China
905421370@qq.com

Yantao Duan
National Key Laboratory on Electromagnetic Environment Effects and Electro-Optical Engineering
Nanjing, China
dcmchdyt@126.com(Corresponding author)

Lihua Shi
National Key Laboratory on Electromagnetic Environment Effects and Electro-Optical Engineering
Nanjing, China
shilih@tom.com

Ke Wang
National Key Laboratory on Electromagnetic Environment Effects and Electro-Optical Engineering
Nanjing, China
1363611280@qq.com

***Abstract*—In order to test the protection performance of power line filter to suppress conducted interference from high-altitude nuclear electromagnetic pulse (HEMP), this paper uses PCI method to test a one-phase power line filter. By calculating the current suppression ratio, the conduction interference suppression of the filter is judged. The experimental results show that when the input current pulse peak is 1.0kA, 1.5kA, 2.0kA, 2.5kA, the current suppression ratio of the filter is less than 30dB, and with the increase of the input current peak, the residual current peak is increased, the maximum value reaches to 267.2A. The test results laid the foundation for improving the power line filter to against HEMP.**

Keywords—Power Line Filter, HEMP, PCI method.

I. INTRODUCTION

Conducting interference has attracted more and more attention. In the research on electromagnetic compatibility of switching power supply, conducting interference is a common technical problem. Generally, a power line filter is installed on the input port of the power supply to suppress the electromagnetic interference entering the equipment or system through the power line. Special tests are needed to verify whether these power line filters can effectively suppress the conduction interference generated by HEMP.

Pulse Current Injection (PCI) is an effective EMC test method, which has always been used as a basic method of anti-interference test or sensitivity test in electromagnetic compatibility. Because of its good repeatability and simple utility, it has been widely recognized in commercial, aviation and military electromagnetic compatibility testing fields as a proven effective technology in the field of EMC problem area diagnosis and evaluation hardware reinforcement technology

MIL-STD-188-125-1 and -2 gives line-to-ground current injection or common mode current injection to verify the suppression effect of cable back-end protection devices (such as power line filter) on HEMP conduction interference [1-2]. They define three PCI pulse types for testing the protective effect on the protection system. Relevant tests have been reported in [3].

In the paper, according to the relevant requirements of the standard and the configuration of line-to-ground current injection test in PCI test method, pulse current with different amplifications is injected into the phase line of the filter to measure the residual current after filtering, so as to test the protection effect of a single-phase power line filter for HEMP.

II. PCI TEST CONFIGURATION

The PCI test method has two test configurations: line-to-ground current injection test configuration and common mode current injection test configuration. The former requires relatively simple test equipment, as shown in Fig.1 [1]. The double exponential pulse source and the current coupling device inject the pulse current which meets the standard requirements into the phase line under test. The POE protection device is the device under test. The injection current measurement sensor and residual current sensor are generally Rokowski coils, which are used to measure the current on the front and rear phase lines of the device under test. Internal load for filter protection equipment, etc., can be used to replace the dummy load. If the device under test has an external load, it needs to be protected by an isolating device to prevent damage caused by the pulse current. Residual current measurement or current suppression ratio calculation (injection current/residual current) can be used to test the power line filter's nuclear electromagnetic pulse protection capability.

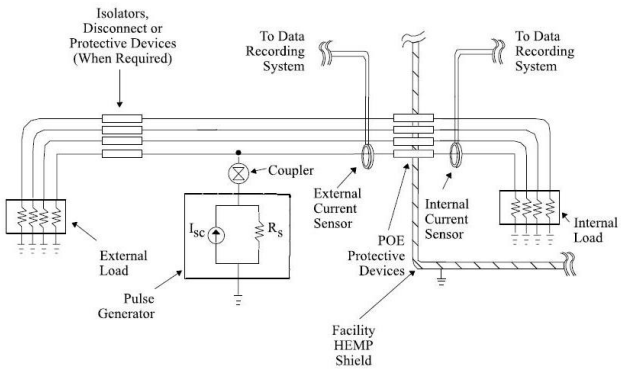

Fig. 1. Wire-to-ground current injection test configuration [1]

III. INJECTION TEST

Before the test, it is necessary to calibrate the output waveform of the pulse current source. Short-circuit the output end of the source, and use the current probe to measure the current waveform. The waveform of injection current requires the rise time to be less than 20ns, and the pulse half-width is 500ns ~ 550ns. The typical waveform after calibration is shown in Fig. 2, and it can be seen that its parameters meet the requirements.

The injection current was divided into four grades: 1.0kA, 1.5kA, 2.0kA and 2.5kA, and three tests were conducted for each grade. For each injection of current, an oscilloscope is used to record the residual current waveform and read the maximum residual current. During the test, the residual current should be continuously observed and the residual current in the next level should be estimated to prevent damage to the filter caused by high current. At the end of the test, the maximum residual current of the three tests in each injection grade was taken as the residual current of that grade.

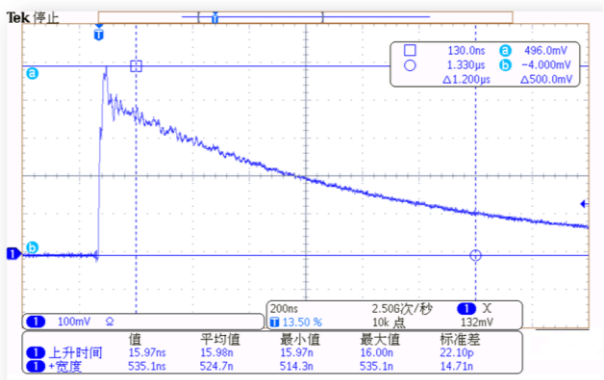

Fig. 2. Typical waveform of pulse injection current

IV. TEST RESULTS

Pulse currents of different grades are injected to measure the residual current peak on the output phase line of the power filter, and the current suppression is calculated as

$$SE_v = 20\log_{10}(I_{peak}//I_{residual}) \quad (1)$$

Where, SE_V is the current suppression ratio, I_{peak} is the peak of injection current for calibration, and $I_{resdual}$ is the measured residual current peak. The test data are shown in TABLE I. It can be seen that the current suppression ratios are all less than 20dB at different injection levels. In addition, with the increase of the peak value of the injection current, the peak value of the residual current increases to 267.2A, which is far greater than the 10A value required by MIL-STD-188-125-1 and -2. Therefore, it can be judged that the power line filter of this type needs to be strengthened and improved to improve the protection effect on HEMP.

Fig. 3 shows the typical residual current test waveform. As can be seen that the rise time of the residual current waveform becomes slower, and the pulse half-width increases, compared with the injection current waveform. And there is oscillation phenomenon in the later period of the waveform.

TABLE I. TEST DATA

Injection current/kA	residual current/A	current suppression ratio /dB
1	133.6	17.48
1.5	184.8	18.18
2	232.8	18.68
2.5	267.2	19.42

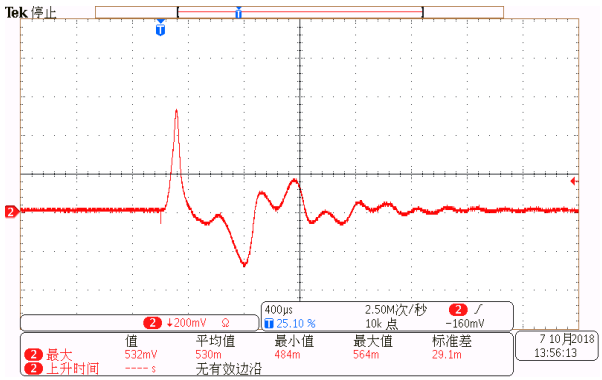

Fig. 3. Typical waveform of residual current

V. CONCLUSION

In this paper, PCI method is used to test the protection performance of a single-phase power line filter. The results show that the PCI method can effectively detect the electromagnetic pulse protection capability of the power filter. Under different impulse current injection levels, the current suppression ratio of the tested power line filter is all less than 20dB, and with the increase of the peak value of injection current, the residual current peak value increases to A maximum value of 267.2 A, which does not meet the requirements of relevant standards. The experimental results give a foundation for the improvement of the anti-nuclear electromagnetic pulse filter.

References

[1] Nalborczyk A J. HEMP filter design to meet MIL-STD-188-125 PCI test requirements [C]. International Conference on Electromagnetic Interference & Compatibility. IEEE, 2008.

[2] MIL-STD-188-125-1. High-Altitude Electromagnetic Pulse(HEMP) Protection for Fixed Ground-Based Facilities[S]. Department of Defense Interface Standard, 1998.

[3] MIL-STD-188-125-2. High-Altitude Electromagnetic Pulse (HEMP) Protection for Transportable System[S]. Department of Defense Interface Standard, 1999.

Study on Shielding Effectiveness Measurement Method of Concrete for RF Shield

Hong-Je Jang
S.M.A.R.T Industry Division
Korea Testing Laboratory
Ansan city, South Korea
jahoje@ktl.re.kr

Tae-Seung Song
S.M.A.R.T Industry Division
Korea Testing Laboratory
Ansan city, South Korea
tssong@ktl.re.kr

Hyo-Sik Choi
S.M.A.R.T Industry Division
Korea Testing Laboratory
Ansan city, South Korea
chs3040@ktl.re.kr

Sung-Wook Kim
Department of Infrastructure safety research
Korea Institute of Civil engineering and building Technology
Goyang city, South Korea
swkim@kict.re.kr

Nam-Kon Lee
Department of Infrastructure safety research
Korea Institute of Civil engineering and building Technology
Goyang city, South Korea
nklee@kict.re.kr

***Abstract*— In this paper, shielding effectiveness measurement method is studied for concrete used in buildings. Recently, the electromagnetic shielding characteristic of concrete is studied for EMP, and a method of measuring the shielding effectiveness of that concrete is needed. The standard samples made for conventional material shielding methods(ASTM 4935) are difficult to produce with concrete. And the materials, such as steel fibers, added for shielding properties is more difficult to make conventional standard samples. Therefore, the measurement method for the shielding effectiveness from 600 ㎒ to 1.5 ㎓ were studied, and simple measurement device is developed to cover from 300 ㎒ to 1.5 ㎓**

Keywords—Shielding effectiveness, EMP, RF, Test method

I. INTRODUCTION (*HEADING 1*)

Recently, problems related to electromagnetic interference have been raised with the development of wireless technology. Many protecting methods are being studied to prevent the main equipment (servers, data storage devices and etc.) of information and communication from lightning or electromagnetic attack. IEC 61000-2-13 provides an analysis of the IEMI (Intentional Electromagnetic Interference) environment which can harm the information communication equipment from various signal sources. In the case of PHASER (Pulsed High-Amplitude Sinusoidal Electromagnetic Radiation), it generates the maximum electric power of 1,800 MW and the electric field of 2.3 kW / m at 3 km at 1.1 GHz. High-power electromagnetic (HPEM) waves can cause problems such as data loss, power reset, power-off, connection failure, components destroyed [1]. Information and communication technology is deeply related within our lives, it is likely to cause a big problem.

In order to prevent such that problems, a shielding room, a shielding rack, a filter have been mainly used. In recent years, studies have been conducted to improve the shielding effectiveness (SE) with the concrete constituting the building and to protect the equipment and facilities installed therein.

Concrete for RF shield can be manufactured by blending various materials. In order to measure the shielding effectiveness of the developed concrete, it tried to apply measurement method in ASTM D 4935. However, it is difficult to make concrete sample by drilling four holes with a diameter of about 133 mm and a thickness of 5 mm (25 μm and average 5% error rate) [2, 3]. Thin concrete is fragile, and it is more difficult to make sample for measurements when shielding materials such as steel fiber are added. A practically applicable shielding effectiveness measurement method is required to construct and develop a concrete block for shielding. And it is necessary to be able to measure 600 MHz to 1.5 GHz including 1 GHz which is the main use frequency.

Therefore, in this paper, it is studied the criterion for the concrete block applicable to the shielding effectiveness measurement. Shielding effectiveness measurement standard MIL-STD-188-125 and IEEE-STD-299 were used to study measurement system and equipment. In addition, a simplified test system was developed to easily measure the characteristics of large structures by pre-test.

II. SHIELDING EFFECTIVENESS MEASUREMENT SYSTEM

A. Selection of concrete block for Shielding Effectiveness

The size of the concrete block is an important factor in measuring the shielding effectiveness, because it affects the shielding effectiveness according to the wavelength. The block size should be selected to cover with the purpose bandwidth of 600 MHz to 1.5 GHz. Also, in order to independently check the shielding characteristic of the concrete, except the structure of the building, a cell between the reinforcing bars can be used as a reference in the reinforced concrete. This is a criterion for measuring the shielding effectiveness of concrete, because the interval of the reinforcing bars makes resonant frequency, which occurs the shielding effectiveness by the reinforcing bars installed in the building.

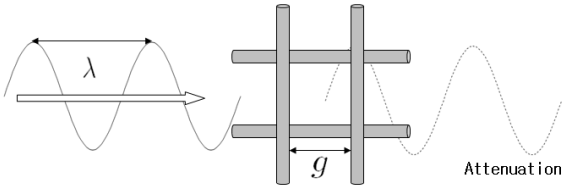

Fig. 1. Shielding effectiveness of gap of reinforcements

This research was supported by a grant (18SCIP-B146646-01) from Construction Technology Research Project funded by the Ministry of Land, Infrastructure and Transport of Korea government.

$$SE_{dB} \approx 20 \log (\lambda / 2g) \quad (1)$$

$$\lambda = c / f \quad (2)$$

The shielding effectiveness on the interval of reinforcing bar can be expressed above equation (1) [4]. The shielding effectiveness according to frequency is related with the wavelength and the reinforcing bar. It calculate with 1 GHz according to the equation (2) that the distance between the reinforcing bars is 15 cm. This is the distance between the electromagnetic waves and the reinforcing bars is the same, so that the shielding effectiveness does not occur.

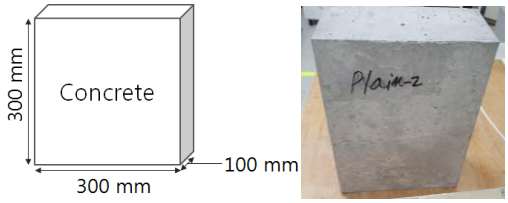

Fig. 2. Concrete block for shielding effectiveness measurement

B. *Shielding Effectiveness Measurement Jig*

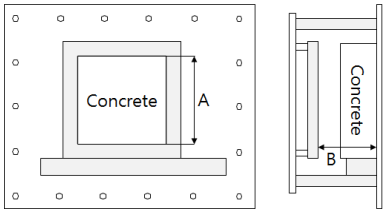

Fig. 3. Shielding effectiveness measurement jig

The shielding effectiveness measuring jig must be designed to be compatible with the concrete block. Therefore, the length of A in Fig. 3 should be 25 cm and the length of B should be 10 cm or more. This jig is a device for mounting and fixing concrete blocks and is designed to be connected to a metal plate and attached to the wall. Also, there is an air compressor on the front so that the concrete can be completely adhered to the metal wall.

C. *RF Shielding Effectiveness Measurement System*

There are MIL-STD-188-125 and IEEE-STD-299 standards on how to measure the shielding effectiveness. Most of the standard measurement methods have similar parts, but there are differences in details such as the distance between the antennas and the size of one cell to be measured. In this paper, military standard MIL-STD-188-125 is mainly referred for concrete block shielding effectiveness measurement methods [5-8].

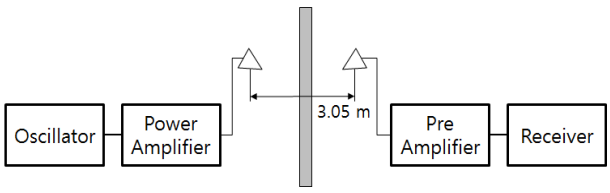

Fig. 4. Configuration of shielding effectiveness measurement equipment in MIL-STD-188-125

There is the measurement configuration by the MIL-STD-188-125 shows in Fig. 4. The oscillator in Fig. 5 can be a signal generator and the receiver can be a RF receiver, a network analyzer, or a spectrum analyzer. In addition, the above standard uses a power amplifier and a preamplifier to ensure the dynamic range (DR) because the reference shielding effectiveness is very high at 80 dB for military use. On the other hand, since the shielding effectiveness of concrete block is not high enough, it is possible to measure sufficiently with dynamic range of 50 dB, and a shielding effectiveness measuring system is constructed without using each amplifier.

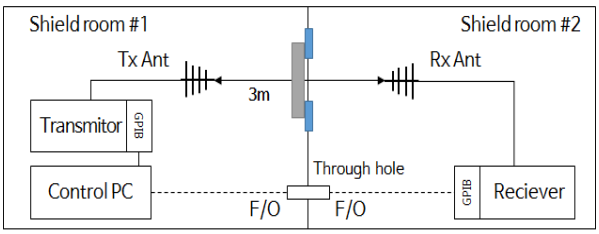

Fig. 5. Shielding effectiveness measurement system configuration

The block diagram for measuring the shielding effectiveness of the concrete block can be presented as shown in Fig 5. The measurement location is isolated by a metal wall between the two shield rooms as shown in Fig. 5. In order to minimize the electromagnetic waves flowing into the receiver, the receiving antenna and the receiver are placed in the shield room # 2, and the other electronic equipment is installed in the shield room # 1 where the transmitting antenna is located.

Two antennas used for transmission and reception are a log-periodic antenna and have a measurement bandwidth of 290 MHz to 2 GHz. And those antennas are placed in LOS through the aperture of the measuring jig on the metal wall. The distance between the antennas is 3 m. The height was 1.2 m, which is the same as the center of the aperture

The transmitter used a signal generator and the receiver used a RF receiver. The NI GPIB is used to connect each device and between the PC and the receiver between the isolated shield rooms by the optical fiber. Shielding effectiveness measurement system in Fig. 5 can control the whole system using a PC.

III. Experiment and Result

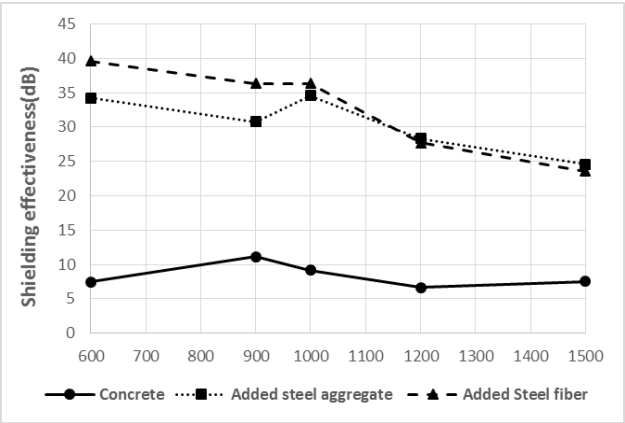

Fig. 6. Result of shielding effectiveness measurement of concrete block

The shielding effectiveness of concrete blocks with each added steel aggregate and steel fiber is shown in Fig 6. It can be seen that the shielding effectiveness is not large with simple concrete. It can be seen that the shielding effectiveness is significantly increased when steel aggregate or steel fiber is added.

As the frequency increases, the shielding effectiveness tends to decrease. This phenomenon is analyzed that the shielding effectiveness is reduced by the half-wavelength of 1.5 GHz at the concrete block thickness of 10 cm. Further added steel aggregate and steel fiber all increase shielding effectiveness. The effects of the materials show differences at frequencies below 1 GHz. In the case of steel fiber, the shielding effectiveness change is a little, but concrete block containing steel aggregate shows a tendency to change to 1 GHz peak

IV. Simplified Test Equipment

It has developed a simplified test device that can easily verify the shielding effect tendency without installing the existing test jig. It is possible to measure from 300 MHz to 1.5 GHz with 50 MHz steps. The output signal strength is 20 dBm, and the input signal can be received from 20 to -80 dBm. The antenna is a spiral antenna having a bandwidth of 300 MHz to 3 GHz. The system configuration of the simplified test system is as follows in Fig. 7, and it is controlled using Art Mega 128A.

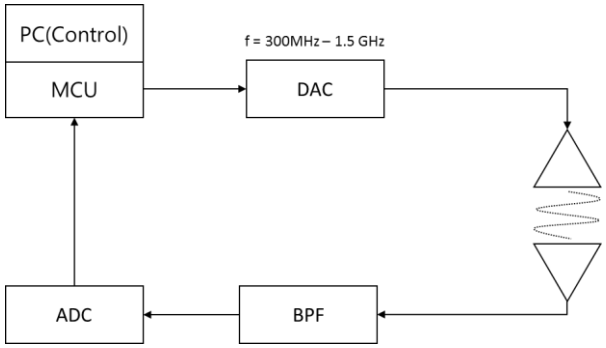

Fig. 7. Simplified test equipment block diagram

The measurement result for the transmitted signal is as shown in the Fig. 8, and it is confirmed that 25 signals are generated by 50 MHz step. The output power of transmitted signal is 19.04 dBm (expectation 20 dBm) at the marker, but it is generating a signal power within ± 1dBm.

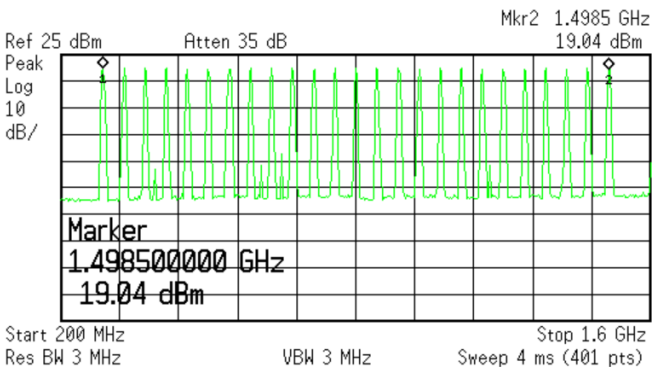

Fig. 8. Transmission signal from simplified test equipment

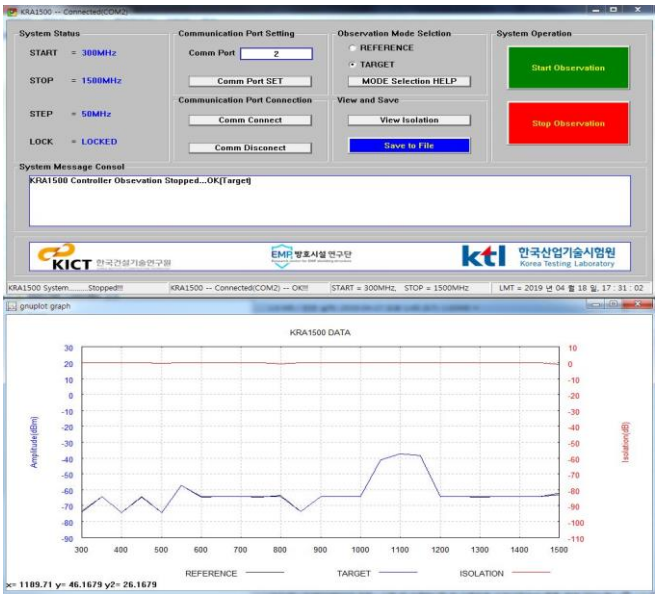

Fig. 9. Simplified test equipment block diagram

Software for driving the simple testing device was also developed. As shown in Fig. 9, the shielding rate can be measured by comparing the reference and shielding block pass values. Because the number of frequencies is small, the total sweep time is about 4-5 seconds, which is easy to use at the laboratory level.

V. Conclusion

A size of concrete blocks were determined to measure the shielding effectiveness of concrete. The shielding test method was developed considering that size. As expected, the shielding effectiveness was confirmed in the concrete with the shielding material.

A simplified test device was developed that can be used in the same form as the previous test method. We will compare the two test methods and verify the results through the actual test with the concrete blocks.

References

[1] G. Eason, B. Noble, and I. N. Sneddon, “On certain integrals of Lipschitz-Hankel type involving products of Bessel functions,” Phil. Trans. Roy. Soc. London, vol. A247, pp. 529–551, April 1955. *(references)*

[2] J. Clerk Maxwell, A Treatise on Electricity and Magnetism, 3rd ed., vol. 2. Oxford: Clarendon, 1892, pp.68–73.

[3] I. S. Jacobs and C. P. Bean, “Fine particles, thin films and exchange anisotropy,” in Magnetism, vol. III, G. T. Rado and H. Suhl, Eds. New York: Academic, 1963, pp. 271–350.

[4] K. Elissa, “Title of paper if known,” unpublished.

[5] R. Nicole, “Title of paper with only first word capitalized,” J. Name Stand. Abbrev., in press.

[6] Y. Yorozu, M. Hirano, K. Oka, and Y. Tagawa, “Electron spectroscopy studies on magneto-optical media and plastic substrate interface,” IEEE Transl. J. Magn. Japan, vol. 2, pp. 740–741, August 1987 [Digests 9th Annual Conf. Magnetics Japan, p. 301, 1982].

[7] M. Young, The Technical Writer’s Handbook. Mill Valley, CA: University Science, 1989.

[8] H. J. Choi, H. K. Choi, S. W. Lim, H. S. Lee, A Literature Review and Experimental Study of Basic Physical Properties about Electromagnetic Shielding Concrete Development, KIC, Vol. 16 Issue 1, p41-42. May 2016

Simulation on Lightning Electromagnetic Environment of CFRP

Hongzhi Ouyang
State Key Laboratory of Electrical Insulation and Power Equipment
Xi'an Jiaotong University
Xi'an , China
Email: oyhz1982@163.com

Xueling Yao
State Key Laboratory of Electrical Insulation and Power Equipment
Xi'an Jiaotong University
Xi'an , China
xlyao@mail.xjtu.edu.cn

Jingliang Chen
State Key Laboratory of Electrical Insulation and Power Equipment
Xi'an Jiaotong University
Xi'an , China
cjl@mail.xjtu.edu.cn

***Abstract*—Carbon fiber reinforced polymer(CFRP) are widely used in many fields, especially in the aerospace industry. In order to study the electromagnetic environment of lightning for this material, using CST software with TLM (Transmission Line Matrix) solver to simulate the carbon fiber panel and the cubic model with gaps. The surface current distribution, the spatial electromagnetic field distribution and the electromagnetic coupling law of the three cables are obtained under the action of the lightning current component A wave and H wave. The results show that the shielding effectiveness of carbon fiber material is smaller than that of a metal material. The magnitude of induction current in cables is significantly affected by lightning current parameters. Narrowing the gap width, twisting and shielding can effectively reduce electromagnetic interference. These results can provide a reference for lightning indirect effect on aircraft.**

Keywords—electromagnetic environment of lightning;CFRP;TLM;cable coupling

I. INTRODUCTION

Lightning is a common discharge phenomenon in nature and has a great impact on aircraft. The impact of lightning on aircraft can be divided into direct effects and indirect effects. CFRP is a new composite material with epoxy resin as the matrix and carbon fiber as the reinforcement. It has many advantages such as high specific strength, high specific modulus and easy integral forming, which can meet the requirements of lightweight and stability. Compared with traditional aluminum alloy and other metal materials, the composite material has poor electrical conductivity, which leads to a decrease in the electromagnetic shielding performance of the aircraft skin, which maybe make aircraft vulnerable to damage in extreme weather such as lightning and may cause catastrophic accidents. Domestic research on lightning effects is mainly focused on direct effects. The study of indirect effects is still in its infancy. Most of the standards and experiments are used for reference from abroad, and most of studies are aimed at aircraft with metal material skins. The study of indirect effects is almost rare [1]. Electromagnetic simulation software for indirect effects of lightning are EMA3D, FEKO, CST, etc. The CST Studio Kit is a professional simulation software designed for 3D electromagnetic fields, circuits, temperature and structural stress. Its unique transmission line matrix (TLM) algorithm is especially suitable for the calculation of large structures. Using the CST2017 cable studio, current density distribution after the lightning strike, the electromagnetic field transient distribution of the main parts and the electromagnetic coupling of the internal cables were analyzed and calculated by different skin materials, carbon fiber sheets with different waveform excitations and cubic models with gaps. The article provides a certain theoretical basis for the aircraft lightning electromagnetic environment.

II. TLM METHOD

TLM is a numerical method for time-domain differentiation. It is based on Huygens' optical propagation model and equivalent transmission line theory, and is now commonly used for electromagnetic field simulation of three-dimensional structures. In this method, the engineering problem is first replaced by a continuous transmission line network, using a lumped parameter component to represent a node in the network, the physical parameters correspond to the parameters of the actual problem, thus it can discretize the space; The numerous nodes formed by the transmission line simulate the lumped parameter components, so it discretize the time [2]. As shown in Figure 1, in a symmetric condensed node (SCN) algorithm, each node is connected by a pair of orthogonally polarized transmission lines. Typically, the dielectric load is represented by a reactive short-line load node. A lossy medium can introduce losses on the transmission line or add a lossy short line to the load node. The propagation process can be described by equation (1) and (2):

$$V_r = SV_i \quad (1)$$

$$V_{r,\ k+1} = CV_k \quad (2)$$

Where, V_i is the excitation voltage matrix; Vr is the reflected voltage matrix; S is the pulse scattering matrix of the node; C is the connection matrix describing the network topology.

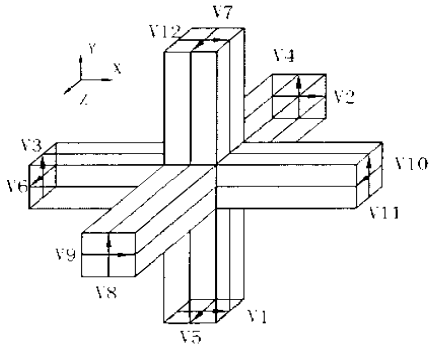

Fig.1 Symmetric condensed node

The advantages of the TLM are flexibility and versatility. It combines the electromagnetic field, the boundary and the dielectric properties of its materials. Many parameters can be simply considered in the program, it is suitable for dealing

with complex nonlinear characteristic media, and can simulate the propagation of waves in the time domain, avoiding the calculations of massive equations.

III. SIMULATION RESULTS AND DISCUSSION

The material is set to homogeneous isotropic with a conductivity of 1×10^4 S/m and the dielectric constant is 3. The test waveforms are A wave and H wave(double-exponential waveform), the peak time is 6.4 μs, the half peak time is 69 μs for the former wave;the peak time is 0.245 μs, the half peak time is 4 μs for the later wave,the current peak is all 100 A. Lightning current is blown in from the CFRP board and cube face to face. Three cables of single wire, coaxial cable and two-core twisted pair are placed at a distance of 100 mm from the bottom surface of cube, and the length is 1 m.

A. CFRP board simulation results

1) Surface electromagnetic field distribution

The field monitor was used to observe the distribution law of the electromagnetic field on the surface of the sheet. Figure 2 shows the electromagnetic field distribution at 7 μs. It can be seen that the amplitude of the electromagnetic field at the point of impact, the current of the lightning current and the point of the strike is large, and the amplitude of the electromagnetic field on both sides and corners is small, and the gradient of the electric field is larger than that of the magnetic field.

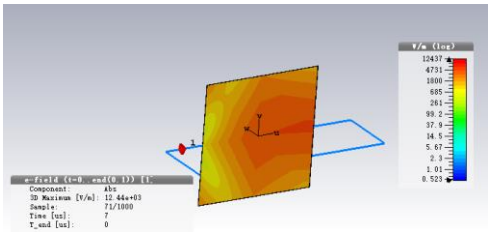

（a）Electric field intensity distribution

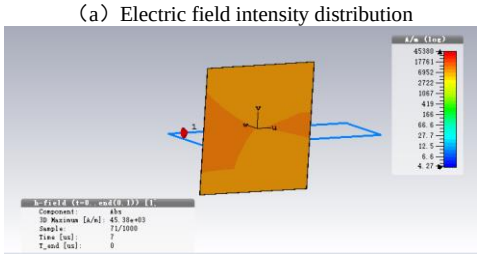

（b）Magnetic field intensity distribution

Fig.2 Surface electromagnetic field distribution of isotropic carbon fiber panel（t=7 μs）

2) Spatial electromagnetic field distribution

The electromagnetic field waveforms are all double exponential, but the peak time lags behind the source current, which is related to the redistribution of the current. In addition, the electric field signal has spikes and oscillations in the initial stage, which may be related to the setting of the dielectric constant. Figure 3 shows the distribution of the electromagnetic field at 9 points with a height of 1 mm. The distribution law is roughly the same as the electromagnetic field distribution of the surface[3]. The peak value of the electromagnetic field is significantly reduced as the height increases, because the surrounding space is free, and the electromagnetic wave only scatters energy continuously without any reflection and refraction. For anisotropic materials, the electromagnetic components in the three directions are very different, the components in the Z direction are the largest, the Y direction are in the middle, and the X direction are the smallest, which is positively related to the conductivity. There is basically no change in the size and distribution of the electromagnetic field after laying the copper mesh. Because only one side of the sheet is coated with copper, and the diameter of the copper mesh is large, so the effect is not obvious.

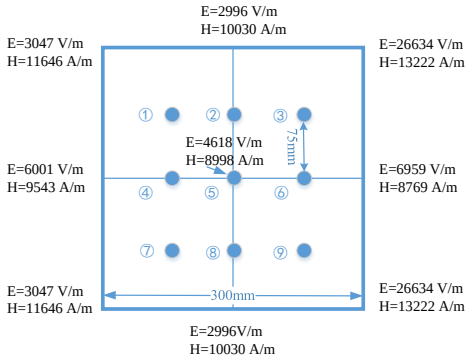

（a）Isotropic material

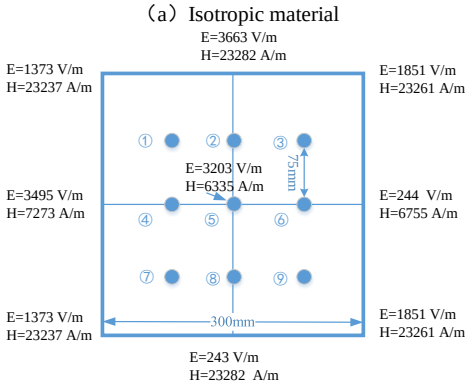

（b）Anisotropic material

Fig.3 Comparison of electromagnetic field distribution at 1mm

3) Shielding effectiveness

The linearly polarized plane wave is irradiated to the fiber panel. Figure 4 shows that the shielding effectiveness of the carbon fiber is significantly lower than that of the aluminum alloy, which is about 25 dB lower.

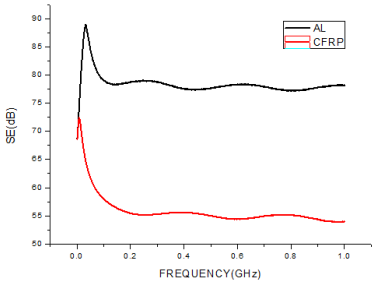

Fig.4 Shielding effectiveness of the CFRP panel and aluminum panel

B. CFRP cube simulation results

1) Surface current distribution

As shown in Figure 5, the current density at the corners of the cube is larger than that of other flat portions, especially the current density around the slot.It is due to the edge effect of the electric field. The current at the lightning attachment point is also relatively large, which is determined by the lightning current itself. It can be inferred that the irregular part of the real aircraft

(especially the part with small radius of curvature) has a large current density and should be protected specially.

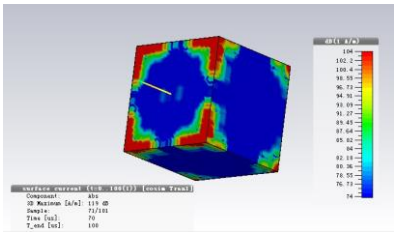

Fig.5 Surface current distribution of CFRP cube(t=70 μs)

2) Internal electromagnetic field distribution

The frequency domain curves of the electromagnetic field are shown in Figures 6. The electromagnetic field energy disappears at 30 MHz, the electric field intensity spectrum is relatively simple, and the magnetic field strength amplitude fluctuates greatly at high frequencies. Because the simulation time is not enough.The peak distribution of the electromagnetic field is shown in Figures 7 and Figures 8. It is obvious that no matter what kind of material or waveform, the closer the observation point is to the slot, the larger the corresponding electric field strength and magnetic field strength[4].

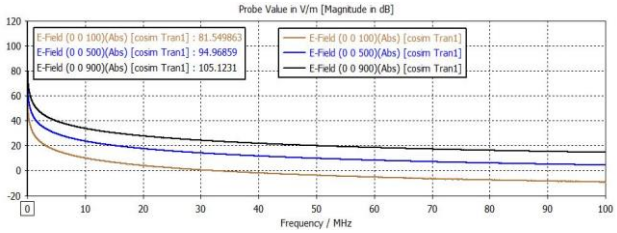

(a) Electric field frequency domain curve

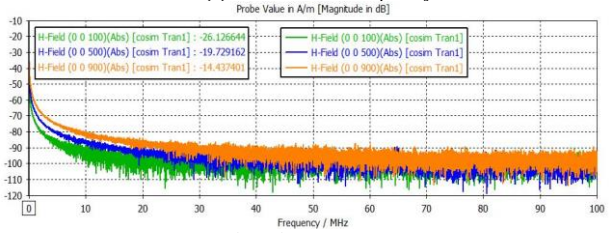

(b) Magnetic field frequency domain curve

Fig.6 Electromagnetic field frequency domain curves in three parts of CFRP model under A wave

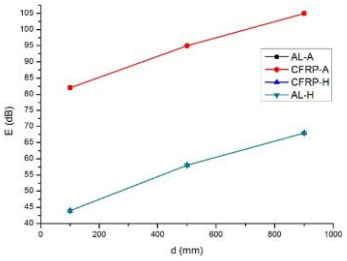

Fig.7 Peak distribution of electric field intensity in three parts of the model

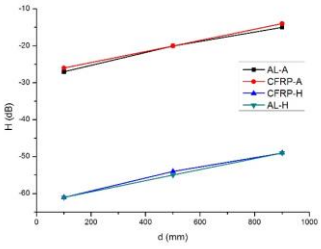

Fig.8 Peak distribution of magnetic field intensity in three parts of the model

3) Internal cable coupling

As shown in Figures 9 to 12, no matter what kind of material or waveform, the induced current on the single line (ampere level) is larger than on the twisted, and the induced current on the twisted is larger than on the coaxial cable (mA level). The current on the shield is the largest (tens of ampere level). The wider the gap, the larger the peak value of the induced current.

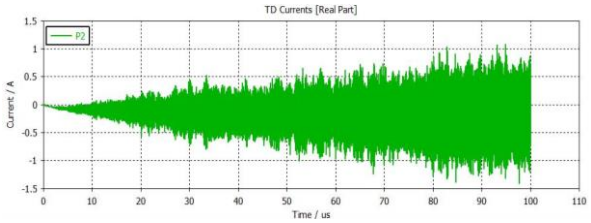

Fig.9 Waveform of cable induced current of CFRP model under A wave

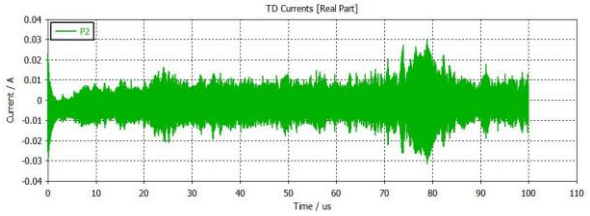

Fig.10 Waveform of cable induced current of CFRP model under H wave

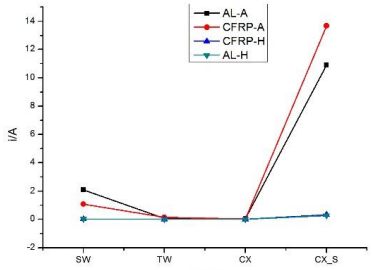

Fig.11 Peak value distribution of cable induced current in four cases

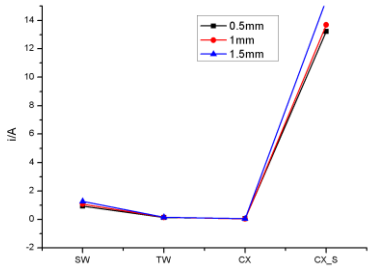

Fig.12 Effect of different slot widths on induced current Peak of Cable

REFERENCES

[1] Aircraft Lightning Environment and Related Test Waveforms, SAE Aerospace Recommended Practice (ARP) 5412B, Jan. 2013.

[2] Meng, Xuesong , et al. "Modeling Curved Carbon Fiber Composite (CFC) Structures in the Transmission-Line Modeling (TLM) Method." IEEE Transactions on Electromagnetic Compatibility 57.3(2015):384-390.

[3] Meyer, M , et al. "Modeling of lightning indirect effects in CFRP Aircraft." International Symposium on Electromagnetic Compatibility-emc Europe IEEE, 2009.

[4] D'Amore, et al. "Lightning Indirect Effects Certification of a Transport Aircraft by Numerical Simulation." IEEE Transactions on Electromagnetic Compatibility 50.3(2008):513-523.

Effect Research on HPEM to Explosives

YAO Hongzhi
Science and Technology on Applied Physical Chemistry Laboratory
Shaanxi Applied Physics-Chemistry Research Institute
Xi'an,China
yao_hong_zhi@126.com

Zhao Tuan
Science and Technology on Applied Physical Chemistry Laboratory
Shaanxi Applied Physics-Chemistry Research Institute
Xi'an,China

Ji Xiangfei
Science and Technology on Applied Physical Chemistry Laboratory
Shaanxi Applied Physics-Chemistry Research Institute
Xi'an,China

Yin Ming
Science and Technology on Applied Physical Chemistry Laboratory
Shaanxi Applied Physics-Chemistry Research Institute
Xi'an,China

Hazards from Electromagnetic Radiation to Ordnance, that is the potential for electromagnetic radiation to affect adversely munitions or electro‐explosive devices is a well known problem identified since the 50's.And experimental observations indicate that electromagnetic (EM) radiation is emitted after the detonation of high explosives charges. On the contrary, when the explosive is placed in an electromagnetic field, the effect of the problem is also worthy of attention.

As a high-density energetic material, explosives require a lot of energy to detonate them. The electromagnetic field generated in free space is difficult to make it work. But in high power electromagnetic fields（HPEM）, the safety and reliability of explosives are very likely to have certain hidden dangers.

When the explosives is placed in HPEM, the explosives will have a microscopic effect under the influence of electromagnetic waves, maybe causing changes in the microstructure or related performance.

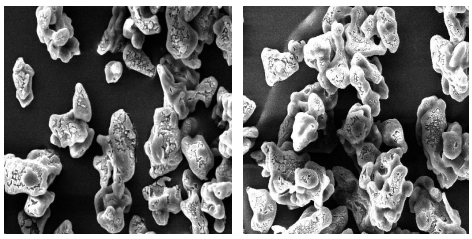

FIG I. MICROSCOPIC CHANGES IN EXPLOSIVE STRUCTURE

From the results of scanning electron microscopy, the microscopic irregular distribution of the particles did not change significantly.

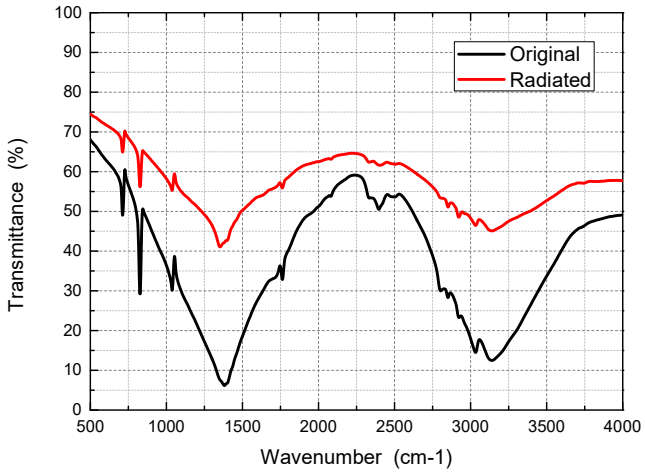

FIG II. INFRARED SPECTROSCOPY

From the results of infrared spectroscopy analysis, the infrared transmission performance did not change significantly before and after the radiation. There was no significant difference in the peak position of the infrared spectrum between the samples, only a difference in intensity, and no shift of the light transmission position occurred.

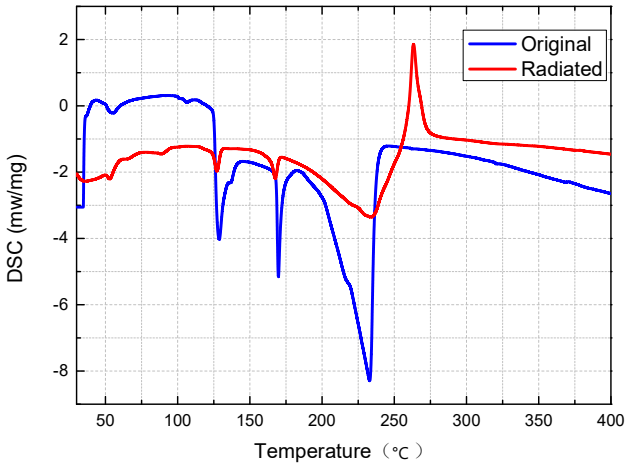

FIG III. DIFFERENTIAL SCANNING CALORIMETRY ANALYSIS RESULTS

The results of differential scanning calorimetry(DSC) analysis show that the explosives are in exothermic state before and after radiation at the front end, and there are three exothermic peaks. However, the explosives after electromagnetic radiation suddenly have heat absorption phenomenon with an increase of temperature.

Analysis of Destruction Characteristic of Bipolar Junction Transistor by Repetitive Pulse Injection

Jeong-Ju Bang
Department of Electrical Engineering
Inha University
Incheon, Korea
camgnm@naver.com

Chang-Su Huh
Department of Electrical Engineering
Inha University
Incheon, Korea
cshuh@inha.ac.kr

***Abstract*— This paper presents the destruction behaviors of a NPN Bipolar Junction Transistor (BJT) by injecting repetitive pulses. The pulse has a rise time of 1.0 ~ 2.1 ns and a maximum peak voltage of 2 kV. As the rate of pulse repetition increases, the threshold voltage for the transistor destruction decreases. The broken transistors show the abnormal current flow of 0.01μA~28mA. The effect of repetition is more clearly observed in the OFF-state transistors. It is also seen that the cumulated transferred energy is more important than the peak voltage of pulses to destruct transistors.**

Keywords— Pulse injection, electromagnetic pulse, bipolar junction transistor

I. INTRODUCTION

As the production technology of semiconductor has developed over decades, the state-of-art electronic devices are designed to consume low power in small scale process. Consequently, the elaborate production technique causes that electronic devices become highly vulnerable to high power electromagnetic pulses.

Electric systems generally consist of wire, via, hole, and housing. When electromagnetic wave passes through a slot of the electric system, the wave is then coupled to the metal components in the circuit board. The coupled wave transfers energy to the system, and hence the abnormal current is generated to cause a malfunction of the electronic system. Therefore, it is important to accurately analyze the characteristics of electric device which is exposed to high power electromagnetic pulses.

In this work, the bipolar junction transistor (BJT) is chosen as the test semiconductor due to its simple structure. If a voltage is reversely applied to PN junctions of the transistor and the voltage exceeds the breakdown threshold, excessive current flows into the PN junction. Consequently, the unexpectedly generated fields or heat lead malfunctions of the semiconductor device.

In the past study [1~4], the main focus of research has been on the effect of single electromagnetic pulse. In recent years, the technique of repetitive radiations has been developed for the electromagnetic pulse generators [5]. Therefore, in this work, we study the effect of repetitive electromagnetic pulses on the electronic device. In Section II, the background theory of the destruction process in NPN-BJT is introduced. We also state the experimental configuration to measure the destruction characteristics of the transistors. In Section III, measured results are shown to be validated. We analyze the data in detail with respect to electric variables such as destruction failure rate, destruction threshold, threshold variation, current distribution, and transferred energy.

II. EXPERIMENT SETUP

Table I lists specifications of the used BC548B transistor. In this BJT, we control the current flow from the collector to the emitter by adjusting the base voltage. Therefore, if there is no current flow into the base of transistor, we cannot switch or amplify the current flow. In other words, this uncontrollable transistor is regarded as a destroyed device.

TABLE I. TRANSISTOR SPECIFICATIONS

Collector-Emitter Voltage	45 V
Collector-Base Voltage	50 V
Emitter-Base Voltage	6 V
Collector Current - Continuous	500 mA

Fig. 1(a) shows the BC548B bipolar junction transistor which is used in this work. We configure the test circuit as Fig. 1(b), After the NPN BJT is connected to the pulse generator by using coaxial cables, pulse injected to the base of BJT. Here both the collector and base are applied by 4.5V voltage source. Attached LED is turned on if a voltage is applied to the base of transistor.

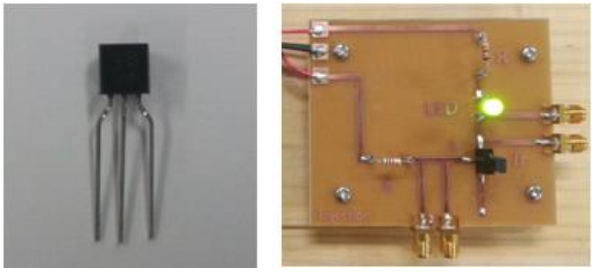

(a) (b)

Fig. 1. (a) BC548B BJT (b) PCB for pulse injection

Fig. 2 shows that the PCB in Fig. 1(b) is connected to the pulse generator. The pulse generator peak voltage of injected pulse can be up to 2 kV. By using the pulse generator, we inject repetitive currents to the circuit.

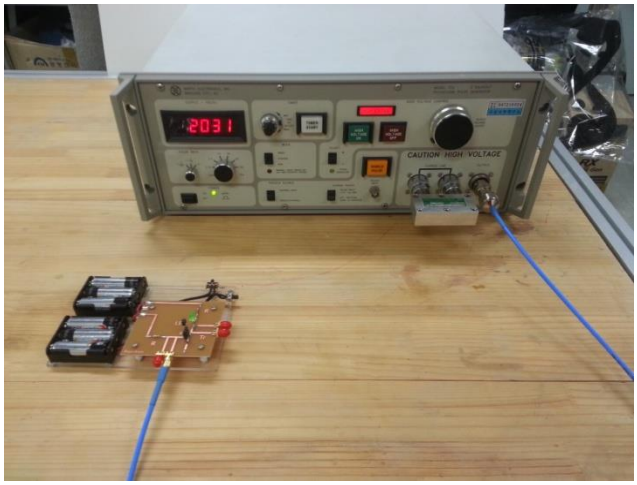

Fig. 2. Experimental setup

In this experiment, we apply three different pulses such as Pulse 1, Pulse 2, and Pulse 3. The waveforms of three kinds of pulses are represented in Fig. 3. Table II indicates the details of three pulses. These differences of pulse shapes influence on the amount of transferred energy. We compute the energy ratio by using the following equation.

$$E = \int P\,dt = \int \frac{V(t)^2}{R}\,dt \cdot \tag{1}$$

Assuming that all pulses have the same peak voltage, the energy ratio of pulses is easily computed. The amount of energy of Pulse 1 is set as a reference 1.0. The energies of Pulse 2 and Pulse 3 are then 1.2 and 2.5 as indicated in Table II.

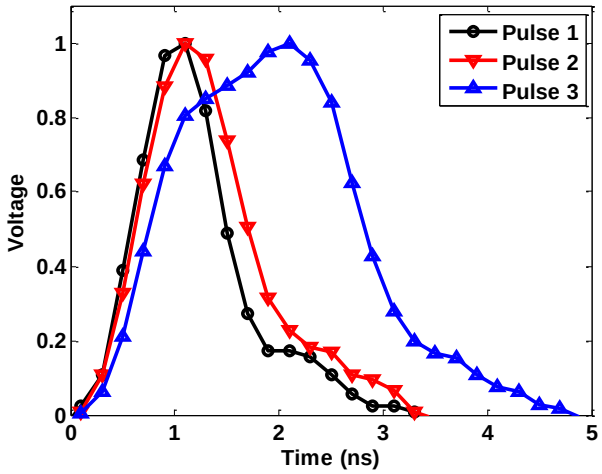

Fig. 3. Waveforms of applied pulses

TABLE II. INJECTED PULSES

	Rise time(ns)	Pulse width(ns)	Energy ratio
Pulse 1	0.75	1.1	1.0
Pulse 2	0.75	1.2	1.2
Pulse 3	1.10	2.1	2.5

In point of transferred energy, the rate of pulse repetition is one of important factors. Therefore, we apply three different repetition rates for each pulse. Firstly, we inject a single pulse. Secondly, the 60Hz repetitive pulse is injected for 2 seconds. Lastly, we inject the 120Hz repetitive pulse for 2 seconds. In addition, to observe the effect of existing current inside BJT, we execute the same experiment in both transistor turned-on and transistor turned-off.

III. ANALYSIS OF MEASURED DATA

A. Abbreviations and Acronyms

We utilize the destruction failure rate (DFR) to quantify the degree of transistor functional failure. It is the ratio of the number of destructed devices to the total number of devices as follows [5, 6]:

$$DFR = \frac{Number\ of\ Destructed\ Devices}{Total\ Number\ of\ Tested\ Devices} \tag{2}$$

Transistors are exposed by three different pulses such as Pulse 1, Pulse 2, and Pulse 3 as listed in Table II. We use the pulse generator to inject the pulses at the base of the target transistor. Fig. 5 shows the DFR as the voltage of Pulse 1 changes. At each voltage, 10 experiments are executed to obtain the probability of transistor failure. In the legend of figure, Tr–OFF represents that there is no current in the base of transistor before the injection. DFR of this OFF-state transistor is drawn by solid lines. Tr–ON denotes that the operating current is flowing through the base of transistor when we inject the experimental pulses. Dotted lines represent the DFR of this OFF-state transistor. Fig. 5 shows that a higher voltage is required to destroy ON-state transistor compared to OFF-state transistor. For both ON and OFF cases, as the repetition rate increases, the voltage at transistor destruction decreases. This is more clearly observed in the case of ON-state transistors. For example, in Tr-ON cases, the voltage at DFR 1.0 is reduced from 1900V to 1600V while the repetition rate increases from 60Hz to 120Hz. In addition, by a single pulse, it does not show DFR 1.0 in this experiment.

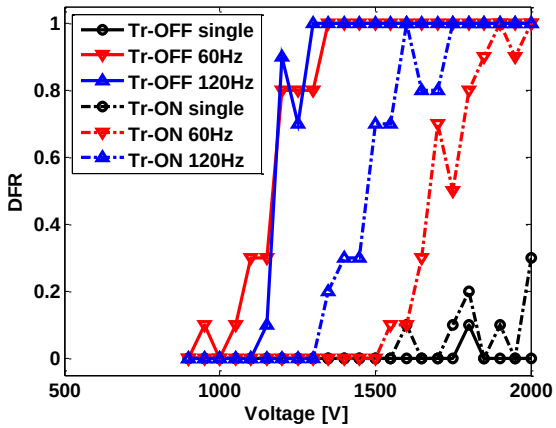

Fig. 5. Destruction failure rate (DFR) by Pulse 1

Fig. 6 shows the DFR as the voltage of Pulse 2 changes. The result is similar to that of Pulse 1 in Fig. 5. As the repetition rate of pulse increases, the voltage of transistor destruction decreases. It needs higher voltage to destruct ON-state transistors compared to OFF-state transistors. For both in Pulse 1 and Pulse 2, it is not reached DFR 1.0 by injecting the single pulse.

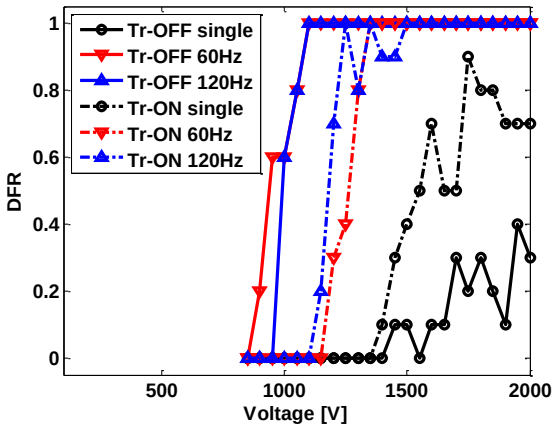

Fig. 6. Destruction failure rate (DFR) by Pulse 2

Fig. 7 shows the DFR for Pulse 3. In contrary to the previous two cases of Pulse 1 and Pulse 2, it reaches DFR 1.0 even in the case of single pulse. Therefore, it is derived that the voltage is not the sole factor to destruct transistor.

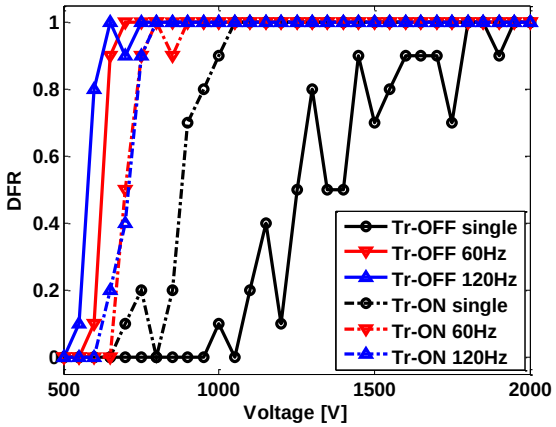

Fig. 7. Destruction failure rate (DFR) by Pulse 3

In Fig. 5, 6, and 7, the probability of transistor destruction becomes higher as the repetition rate increases. In the point of energy view, the repetitive pulses would deliver more energy to transistor. This overflowing energy can generate the thermal damage or abnormal current. Therefore, the total amount of energy is the critical factor for the transistor destruction. This can be explained by that 1.0 DFR by single pulse appears only in the case of Pulse 3. In the cases of Pulse 1 and Pulse 2, it requires the 60Hz pulses to deliver sufficient energy of transistor destruction. Since the pulse of Pulse 3 has more energy than those of Pulse 1 and Pulse 2, even the energy of single pulse is enough to reach 1.0 DFR as shown in Fig. 7.

IV. Conclusions

In this work, the destruction characteristics of NPN BJT are examined with respect to the pulse shape and the pulse repetition rate. Firstly, as the pulse repetition increases, DFR increases. Secondly, in the repetitive pulses, DT dramatically decreases. The effect of pulse repetition is more obviously observed for the case of OFF-state transistor. Thirdly, as the transistor is damaged more, the amount of abnormal emitter current becomes larger. Lastly, we compute the voltage and the energy at which the DFR reaches 1.0. To reach the point, it is clearly seen that the transferred energy is more important than the peak voltage of electric pulses.

References

[1] Hwang, S. M., J. I. Hong, S.-M. Han, C. S. Huh, and J.-S. Choi, "Susceptibility and coupled waveform of microcontroller device by impact of UWB-HPEM," Journal of Electromagnetic Waves and Applications, vol. 24, no.8-9, 1059-1067, 2010

[2] Mats G. Bäckström, "Susceptibility of electronic systems to high power microwaves: Summary of test experience", IEEE Transactions on Electromagnetic Compatibility, vol. 46, no.3, Aug 2004.

[3] Xie, H., J. Wang, D. Sun, R. Fan, and Y. Liu, "Analysis of EMP coupling to a device from a wire penetrating a cavity aperture using transient electromagnetic topology," Journal of Electromagnetic Waves and Applications, vol.23, no.17-18, 2313-2322, 2009.

[4] Golestani-Rad, L. and J. Rashed-Mohassel, "Reconfiguration of personal computers internal equipment for improved protection due against penetrating EM pulses," Journal of Electromagnetic Waves and Applications, vol.20, no.3, 677–88, 2006.

[5] S. Korte and H. Garbe, "Breakdown behavior of electronics at variable pulse repetition rates", Advances in Radio Science, 4, 7-10, 2006.

[6] Hong, J. I., S. M. Hwang, S. M. Han, and C. S. Huh, "Damage Effect and Delay Time of CMOS Integrated Circuits Device with Coupling Caused by High Power Microwave", The Journal of Korea Institute of Electromagnetic Engineering and Science, vol.19, no.6, 2008

Research on the Characteristics of Absorbed Dose in Rats under Radio Frequency

Jiajin Lin
Department of Radiation Biology, Faculty of Preventive Medicine Air Force Medical University
Xi'an, China
linjiajin913@126.com

Jing Li
Department of Radiation Biology, Faculty of Preventive Medicine Air Force Medical University
Xi'an, China
jingli@fmmu.edu.cn

Guirong Ding
Department of Radiation Biology, Faculty of Preventive Medicine Air Force Medical University
Xi'an, China
dingzhao@fmmu.edu.cn

Shenglong Xu
Department of Radiation Biology, Faculty of Preventive Medicine Air Force Medical University
Xi'an, China
shenglxu@126.com

Wei He
Department of Radiation Biology, Faculty of Preventive Medicine Air Force Medical University
Xi'an, China
afmmuhw@163.com

***Abstract*—This paper analyzed the characteristics of absorbed dose in rats and explored the optimized layout of radio frequency experiment between 200 MHz - 8 GHz. The results show that the incident direction and polarization direction of plane wave are extremely sensitive to SAR values. It could keep a high SAR value under the polarization direction along the long axis of the rat body. Besides, the frequency or wavelength of the plane wave is another sensitive parameter to SAR value. Under the condition of long axis polarization, an obvious peak could be formed when the length of long axis is half of the wavelength. Furthermore, the ideal operation and fixed position was discussed. For short-term experiments, the frequency below inflection point should be avoided. For long-term experiments, SAR value should be optimized by adjusting the external power density in order to ensure a relatively stable value. In the fixed position, the polarization can maintain a higher SAR value along the long axis of the rat body. While in the free position, the SAR value of side irradiation was higher at the frequency less than about 2000 MHz, and lower at the frequency more than about 2000 MHz. The results of this paper provide a theoretical reference for the design of radio frequency bio-effect experiment.**

Keywords—absorbed dose, rats, radio frequency, SAR, characteristics

I. INTRODUCTION

In the process of bioelectromagnetics research, dosage is an important parameter to determine the effects and standards. For radio frequency radiation larger than 5 MHz, the absorbed dose is a decisive parameter to decide the thermal effect of organisms. The Institute of Electrical and Electronic Engineers (IEEE) and the International Commission on Nonionizing Radiation Protection (ICNIRP) have strict regulations on basic restrictions (BRs) caused by absorbed dose [1-2]. These regulations are applied to the exposure limitation of public and the professional population. Moreover, in the laboratory experiment, the absorbed dose value is also a parameter related to animal experiment and human effect standard. In other words, based on the absorbed dose and effect of animals, the relevant data are extended to the human standard. Rats are one of the commonly used target animals in radio frequency experiments. The study of rat absorbed dose has also been mentioned in references [3-6] and other literatures. But how to design experiments accurately and effectively, such as how to maximize the use of radiation efficiency and rationally design irradiation conditions, is rarely involved. The main purpose of this paper is to analyze the characteristics of absorbed dose in rats under the action of common radio frequency from 200 MHz - 8 GHz. Besides, combining the effect requirement and the actual limitation of the experimental environment, the optimized layout of rat radio frequency experiment was explored. It provides a theoretical reference for the experimental design in rats about radio frequency effect.

II. MATERIALS

A. Basic Materials

With the help of XFDTD software and rat model provided by Remcom corporation, the research work was carried out. The body weight of rat model was 307.8g. As shown in Fig. 1, the basic size was 98 mm X 42 mm X 243 mm. The model of rat contains 35 kinds of dielectrics such as fat and blood. The dielectrics of these dielectrics are nondispersive and four Cole-Cole models. The electrical parameters of these dielectrics refer to the parameters provided by IFAC-CNR [7].

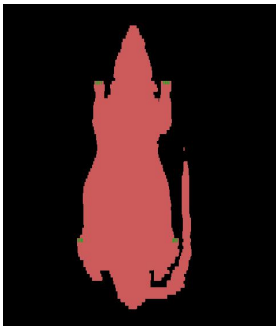

Fig. 1. Rat model

B. Dielectric Data

The dielectric data across the frequency range is a summation of four Cole-Cole expressions as follows.

$$\varepsilon(\omega) = \varepsilon_{\infty} + \sum_{m=1}^{4} \frac{\Delta\varepsilon_m}{1+(j\omega\tau_m)^{(1-\alpha_m)}} + \sigma_j / j\omega\varepsilon_0 \qquad (1)$$

Where, ε_∞ is the infinite permittivity, m is the order number, ω is the angular frequency, $\Delta\varepsilon_m$ is the limits of the dispersion, τ_m is the time constant, α_m is the distribution parameter, σ_j is the static conductivity, ε_0 is the permittivity of free space.

Equation (1) can be explicitly written as follows.

$$\varepsilon(\omega) = \mathrm{ef} + \frac{\mathrm{del1}}{1+(j\omega\mathrm{tau1})^{(1-\mathrm{alf1})}} + \frac{\mathrm{del2}}{1+(j\omega\mathrm{tau2})^{(1-\mathrm{alf2})}} + \frac{\mathrm{del3}}{1+(j\omega\mathrm{tau3})^{(1-\mathrm{alf3})}} + \frac{\mathrm{del4}}{1+(j\omega\mathrm{tau4})^{(1-\mathrm{alf4})}} + \mathrm{sig}/j\omega\varepsilon_0 \quad (2)$$

The parameters above could refer to the data provided by IFAC-CNR.

C. Definition of Absorbed Dose

The metrics of specific absorption rate (SAR) in biologica systems or tissue models have been adopted as the dosimetric quantities, especially at RF frequencies. The metric SAR (in W/kg) is defined as the time derivative of the incremental energy absorbed by (or dissipated in) an incremental mass contained in a volume of a given density. From an induced electric field E (in V/m), the SAR can be derived as

$$\mathrm{SAR} = \frac{\sigma E^2}{\rho_m} \quad (3)$$

Where σ is the bulk electrical conductivity and ρ_m is the mass density of tissue.

D. Simulation Environment

The simulation environment is shown in Fig. 2. The boundary condition is perfectly matched layer (PML) and the absorption layer is 7. The excitation condition is plane wave. The incident direction and polarization direction of plane wave can be adjusted. According to the incident direction and polarization direction, plane wave could be excited in six ways. TABLE 1 gives the definition of various plane waves.

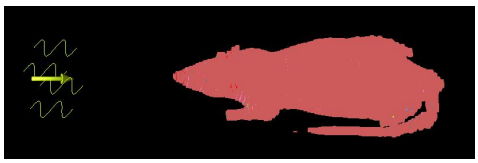

Fig. 2. Simulation environment

TABLE I. DEFINITION OF VARIOUS PLANE WAVES

Item	Incident direction	Polarization direction
F-V	Front	Vertical polarization
F-H	Front	Horizontal polarization
S-V	Side	Vertical polarization
S-H	Side	Horizontal polarization
T-L	Top	Polarization along long axis
T-S	Top	Polarization along short axis

III. RESULTS

A. SAR Value

Absorbed dose in vivo was calculated under six modes at frequencies of 200 MHz - 8 GHz. The amplitude of plane wave is 1 V/m. Fig. 3 shows the results of SAR value. In order to analyze the characteristics in detail, the following characteristics were defined: (1) the maximum value under each irradiation condition, (2) the frequency at the maximum value, (3) and the normalized curve under each irradiation condition.

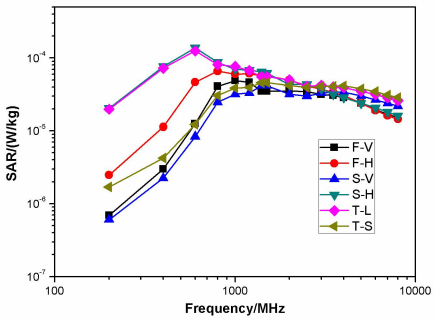

Fig. 3. SAR value

B. Maximum SAR Value

Fig. 4 shows the maximum values in each mode. The results show that the maximum values in S-H mode and T-L mode are obviously larger, which are one order of magnitude higher than the maximum values in other modes.

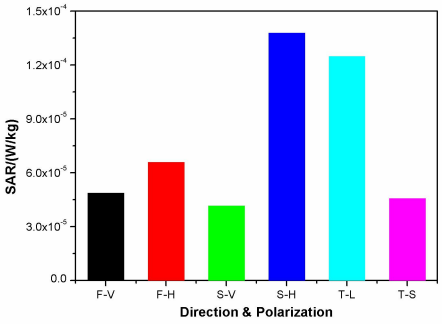

Fig. 4. Maximum SAR value

C. Frequency at Maximum SAR Value

The frequency at Maximum SAR value in modes S-H and T-L reached about 600 MHz, which is the lowest. The frequency at Maximum SAR value in modes S-V and T-S reached about 1500 MHz, which is the highest.

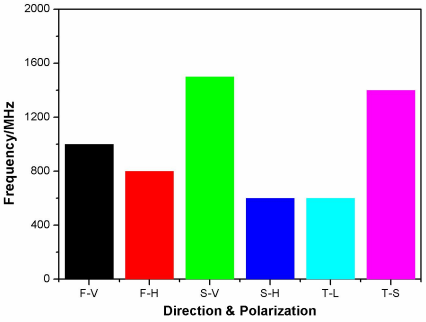

Fig. 5. Frequency at maximum SAR value

D. Normalized Curve

The values of each mode are normalized and presented in Fig. 6. The results show that the modes S-H and T-L have obvious inflection points. In these two modes, SAR values are lower at low frequencies, highest at about 600 MHz, and then gradually decrease with the increase of frequency. The SAR values of modes T-S and S-V are lower at low frequencies, but higher after 1500 MHz, and the decreasing trend is not obvious. Modes F-V and F-H are moderate among the 6 modes.

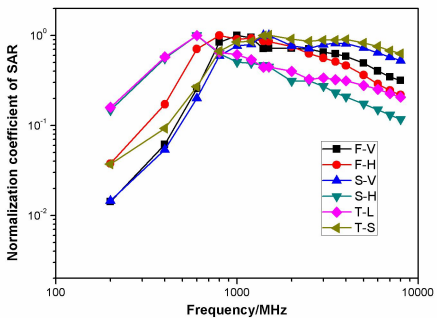

Fig. 6. Normalized curve

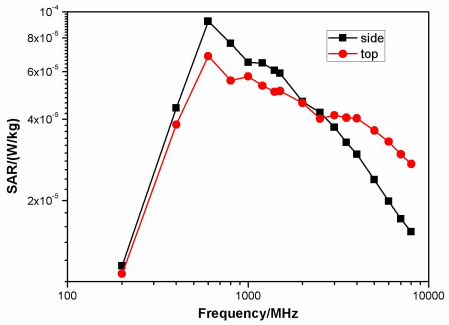

Fig. 7. The average SAR value

IV. DISCUSSION

A. Incident and Polarization Directions

The simulation results show that the incident direction and polarization direction of plane wave are extremely sensitive to SAR values. Generally, the SAR value is higher in modes S-H and T-L. By comparing the relative positions of the rats, the polarization direction of electric field in modes S-H and T-L is along the long axis or head-tail direction of the rat body, while the other modes are along the short axis direction. Therefore, it could keep a high SAR value under the polarization direction along the long axis of the rat body.

B. Short-term and Long-term Experiments

The simulation results show that the frequency of plane wave is another sensitive parameter to SAR value. Generally speaking, the SAR value under the low frequency is relatively low and that under the high frequency is relatively high, which may be related to the frequency characteristics of the medium and the transmission and reflection characteristics of electromagnetic wave. In addition, it is obvious that the modes S-H and T-L have obvious maximum values near 600 MHz. The wavelength at this frequency is 0.5 m, while the body length is 0.243 m. That is to say, under the condition of long axis polarization, when the length of long axis is half of the wavelength, an obvious peak could be formed. This phenomenon may be caused by half-wave resonance. Therefore, in order to maximize the efficiency of rat experiments, the relative relationship between body length and frequency (or wavelength) must be considered.

For short-term experiments, the length and weight are relatively fixed, and the frequency below inflection point should be avoided.

For long-term experiments, body length and weight are gradually increasing and becoming saturated. Therefore, the SAR value changes with time under the condition of fixed radiation. In order to ensure a relatively stable SAR value, it can be optimized by adjusting the external power density. Before adjusting, it is necessary to calculate the ratio of power density and SAR of rats at different stages in advance.

C. Fixed Position and Free Position

Generally speaking, there are two ways to fix the body position of rats: free position and fixed position.

Under the fixed position, the rats were immobile, and the direction of incidence and polarization of the plane wave and the rat were fixed. According to the foregoing, the higher SAR values could be obtained in modes S-H and T-L.

In the free position, rats move freely in the plane. We generally consider two radiation modes, vertical polarization and top irradiation. The average SAR values under these two modes are calculated, as shown in Fig. 7. The results showed that the SAR value of side irradiation was higher at the frequency less than 2000 MHz, while lower at the frequency more than 2000 MHz.

V. CONCLUSION

Based on the numerical simulation, this paper analyzed the characteristics of absorbed dose in rats and explored the optimized layout of radio frequency experiment between 200 MHz - 8 GHz. The results show that the incident direction and polarization direction of plane wave are extremely sensitive to SAR values. It could keep a high SAR value under the polarization direction along the long axis of the rat body. Besides, the frequency or wavelength of the plane wave is another sensitive parameter to SAR value. Under the condition of long axis polarization, an obvious peak could be formed when the length of long axis is half of the wavelength. Furthermore, the ideal operation and fixed position was discussed. For short-term experiments, the frequency below inflection point should be avoided. For long-term experiments, SAR value can be optimized by adjusting the external power density in order to ensure a relatively stable value. In the fixed position, the polarization can maintain a higher SAR value along the long axis of the rat body. While in the free position, the SAR value of side irradiation was higher at the frequency less than about 2000 MHz, and lower at the frequency more than about 2000 MHz.

REFERENCES

[1] Ahlbom A, Bergqvist U. Guidelines for limiting exposure to time-varying electric, magnetic, and electromagnetic fields (up to 300 GHz). Health Phys. 1998, 4, 494-522.

[2] The Institute of Electrical and Electronics Engineers. IEEE standard for safety levels with respect to human exposure to radio frequency electromagnetic fields, 3 kHz to 300 GHz. IEEE Std C95.1. 2005 edition, New York, 2006.

[3] Lovely, Richard H , D. E. Myers , and A. W. Guy . "Irradiation of rats by 918-MHz microwaves at 2.5 mW/cm2: Delineating the dose-response relationship." Radio Science 12.6S(1977):139-146.

[4] Lary, Joseph M. , et al. "Dose-response relationship between body temperature and birth defects in radiofrequency-irradiated rats." Bioelectromagnetics 7.2(1986):141-149.

[5] Gajsek, P. , et al. "Empirical validation of SAR values predicted by FDTD modeling." Bioelectromagnetics 23.1(2002):37-48.

[6] D'Andrea, John A. , et al. "Behavioral and physiological effects of chronic 2,450 ㎝ Hz microwave irradiation of the rat at 0.5 mW/cm2." Bioelectromagnetics 7.1(1986):45-56.

[7] http://niremf.ifac.cnr.it/tissprop/

Advances of X-band Relativistic Triaxial Klystron Amplifier Research at the National University of Defense Technology*

Jinchuan Ju
College of Advanced Interdisciplinary Studies
National University of Defense Technology
Changsha, China
jujinchuan@126.com

Wei Zhang
College of Advanced Interdisciplinary Studies
National University of Defense Technology
Changsha, China
weizhang09@126.com

Yunxiao Zhou
College of Advanced Interdisciplinary Studies
National University of Defense Technology
Changsha, China
xinghuazongyu@163.com

Jun Zhang
College of Advanced Interdisciplinary Studies
National University of Defense Technology
Changsha, China
zhangjun@nudt.edu.cn

Huihuang Zhong
College of Advanced Interdisciplinary Studies
National University of Defense Technology
Changsha, China
zhonghuihuang@hotmail.com

***Abstract*—We present the research of an improved X-band triaxial klystron amplifier (TKA) to generate phase-locked long pulse high power microwave (HPM) radiations carried out at the National University of Defense Technology in China. By optimizing the electromagnetic structure, the proposed TKA can generate efficiently HPMs and more importantly without parasitic mode oscillation. The improved TKA is fully investigated in particle-in-cell simulation and experiment. The associated results demonstrate that the TKA is capable of producing X-band radiations typically a power of 1.1 GW and a pulse duration of about 105 ns in experiments. Furthermore, the phase of the radiated HPM is stably locked by the input seed microwave over more than 90 ns, and the shot-to-shot phase fluctuation is controlled to be less than 10.8 degree in operation of 20 Hz repetitive mode. The reported advances open up prospect to fulfill spatial coherent power combining of X-bands HPMs in the near future.**

Keywords—triaxial klystron amplifier, coherent power combining, high power microwave, X-band, long pulse

I. INTRODUCTION

High power microwave (HPM), owing to its broad potential applications in scientific and civil fields, has become a hotspot of research in the domain of relativistic vacuum electronics [1]. The existing HPM generators are capable of producing gigawatt-class radiations in the frequencies ranging from P-band to Ku-band, whereas further increase of the output power of a single HPM generator is essentially restricted by the issues of space charge effects and radio-frequency breakdown. Coherent power combining of multi-HPM generators thus provides an alternative scheme to overcome the above-mentioned limits [1], which would lead to the realization of equivalent output peak powers in the level of hundreds of GWs in the future, and provide opportunities to explore microwave related fundamental physics at extremes.

The relativistic triaxial klystron amplifier (TKA) using coaxial interaction cavities has attractive merit of high power capacity in high-frequency bands [2,3], which is a promising candidate for spatial coherent power combining of HPMs. Nevertheless, the progress of TKA was hindered by the issue of parasitic modes excitation [3], which would interrupt beam wave interaction, and result in output power drop, pulse shortening and microwave phase unlocking. This issue casts somewhat shadow on the feasibility of coherent power combining of high frequency band microwaves by using TKAs. In this paper, we present our investigations into an X-band TKA performed at the National University of Defense Technology in China, which achieved a breakthrough of producing phase-locked long pulse GW-class X-band HPM radiations in experiments.

*This work was supported by the National Natural Science Foundation under the grant NO. 61771481.

II. DESIGN OF THE STRUCTURE

The configuration of the proposed X-band TKA is shown in Fig. 1. It is basically a coaxial structure, which mainly consists of a reentrant input cavity, a three-gap buncher cavity, and a double-gap output cavity. The seed microwave is provided by a small klystron amplifier with stable phase and output power up to 90 kW at the frequency of 9.375 GHz. In order to simplify the seed microwave input system, we develop a transverse injection scheme, which first divides the seed microwave signal by half/half into two branches and then injects into the input cavity through two rectangular waveguides. In this design, a highly uniform longitudinal electric field can be obtained in the input cavity gap. The external quality factor Q_e of the input cavity is designed to be about 340. The beam loaded quality factor Q_b can be estimated by $Q_b=1/(G_eR/Q)$, where G_e and R/Q are electron beam loaded conductance and shunt impedance, respectively. For an electron beam of 590 kV and 6.4 kA, the calculated

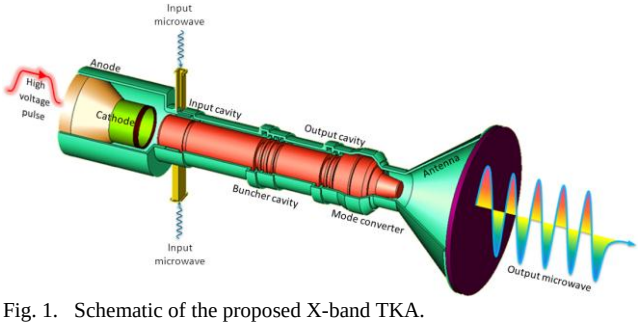

Fig. 1. Schematic of the proposed X-band TKA.

Q_b is about 370, which roughly satisfies the matching condition of seed microwave absorption, so a high ratio (>90%) of seed microwave absorption can be achieved, and the electron beam acquires a modulation depth of about 6%.

The operation principle of the TKA can be described as follows. The electrons are first modulated in velocity by the coaxial TM_{011} mode excited in the input cavity gap. The velocity modulation then slowly induces modulation in electron beam density during propagating in the coaxial drift tube. The modulation is then strengthened dramatically to a depth of about 100% by the three-gap buncher cavity operating at the coaxial TM_{013} mode. The resonant frequency of the buncher cavity (9.425 GHz) is designed deliberately to be higher than the operation frequency of 9.375 GHz, which can lead to a stronger electron beam modulation. The Q_e of the buncher cavity is about 560. Particularly, the structure of the buncher cavity was carefully optimized to achieve a low degree of TEM mode leakage [4], which favors suppressing parasitic TEM mode oscillation in the tube. In the output cavity, the well-bunched electron beam transfers partially its kinetic energy to the electromagnetic field, giving rise to an HPM radiation. In order to generate GW-class long pulse radiation in X-band, the output cavity is designed with two gaps to reduce the maximum electric field strength on the cavity surface, so the power capacity can be enhanced accordingly. After optimization, the output cavity is designed to have an external quality factor Q_e of about 20, and the maximum electric field strength is less than 700 kV/cm for an output power of 1 GW.

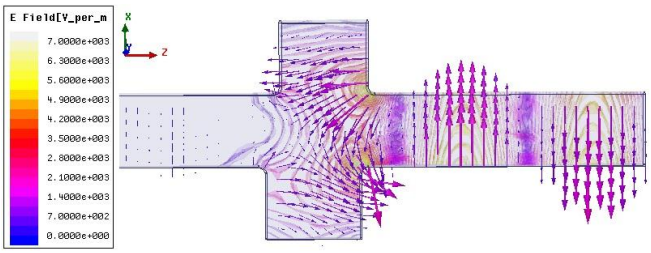

Fig. 2. Electric field distribution of TEM mode microwave at 9.375 GHz.

One critical issue that should be carefully addressed is parasitic TEM mode oscillation. As coaxial structure can not cut off TEM mode, it can couple between the cavities, which leads to parasitic mode self-oscillation and break normal beam wave interaction [3]. As the microwave powers in the input, the buncher, and the output cavities are in the levels of kWs, hundreds of MWs, and GW, respectively, slight TEM mode leakage from a downstream cavity to an upstream one would disrupt the latter's normal performance. In order to address this issue, specially designed coaxial reflectors are placed respectively in front of the buncher and the output caivities. Fig. 2 is the associated numerical result calculated for the reflector in front of the buncher cavity. The electric field shown in Fig. 2 suggests that no appreciable microwave can pass the reflector when a 9.375 GHz signal is injected in TEM mode. The power reflection coefficient is about 99% at 9.375 GHz. Meanwhile, there is no longitudinal electric field in the cavity along the electron beam propagation path, so the reflector would not lead to additional undesired electron beam modulation. Last but not least, the reflector cavity has a coaxial TM_{011} eigenmode with frequency of 5.83 GHz. Its corresponding electron beam loading conductance is positive, which means electrons would take energy from this mode. In other words, the eigenmode can not acquire energy from the electron beam to amplify itself, which avoids parasitic mode oscillation from the reflectors.

III. Simulation And Experimental Results

The proposed TKA structure was studied and optimized by 3D full electromagnetic particle-in-cell (PIC) method. The guiding magnetic field was 0.8 T, and the electron beam voltage and current were 570 kV, and 6.4 kA, respectively. Using the TEM mode reflectors, parasitic TEM mode oscillation was successfully suppressed, whereas serious asymmetric parasitic mode oscillation was observed, which leads to pulse shortening. Once parasitic mode oscillation starts, normal beam wave interaction is disrupted, and as a consequence the output power quickly drops nearly to zero.

Diagnostic in PIC simulation finds that when the parasitic mode oscillation starts, the buncher cavity voltage increases quickly. Fourier analysis shows that the buncher cavity voltage signal has an additional frequency of 11.46 GHz, corresponding to the coaxial TM_{612} mode of the buncher cavity. The spectral intensity of the parasitic mode is even higher than that of the operation frequency, implying this parasitic mode oscillation is fairly serious. The mechanism of the parasitic asymmetric mode oscillation can be understood as follows. (*i*) The longitudinal $2\pi/3$ modes of the buncher cavity are likely to be excited by electron beam. The beam loading conductance of the TM_{612} mode is negative, which means electron beam would transfer its energy and amplify this mode. (*ii*) Comparing with other $2\pi/3$ modes, such as TM_{512} or TM_{712} modes, the shunt impedance of the TM_{612} mode is relatively higher, so TM_{612} mode has a higher probability to be excited firstly. (*iii*) The external quality factor of the TM_{612} mode is relatively small, which means it can easily leaks from the buncher cavity. At the structural discontinuities of the TKA, the leaked TM_{612} mode can convert to coaxial TE_{61} mode, which is not cut-off by the coaxial drift tube. The TE_{61} mode can further stimulate the TM_{611} mode in the input cavity to modulate the electron beam. In this case, a feedback loop is established, and parasitic mode oscillation happens.

Instead of changing the buncher cavity, we adopt a passive approach to suppress parasitic asymmetric mode oscillation. Considering the parasitic mode excitation relies on coupling between the input and the buncher cavities, we intend to block the feedback loop. In principle, we can further optimize the coaxial reflector cavity in front of the buncher cavity to suppress leakage of asymmetric TE modes, but in this case the leakage of TEM mode would increase. We thus insert microwave absorbing materials in the inner and the outer walls of the coaxial drift tube between the input and the buncher cavities.

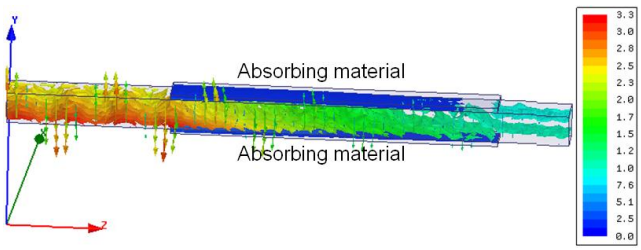

Fig. 3. Attenuation of TE_{61} mode microwave.

By controlling conductivity of the absorbing material, one can obtain different attenuation effects of the microwave. Numerical simulation shows that the attenuation effect for

TE_{61} mode at 11.46 GHz reaches -11.8 dB when the material conductivity is around 25 S/m, as shown in Fig. 3. Furthermore, the absorbing material have broad operation frequency band, which can also suppress the leakages of other high order asymmetric TE modes. When the absorbing material is 100 mm long and 1 mm in thickness, the associated attenuations for the TE_{71} and TE_{81} modes keep below -11 dB over the frequency range of 11 GHz to 14 GHz. In such levels of attenuation, high order parasitic asymmetric mode oscillations could be suppressed successfully inside the TKA device.

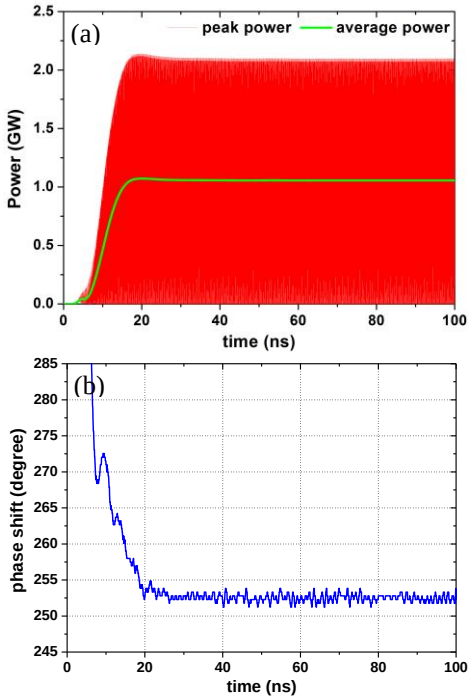

Fig. 4. (a) HPM power and (b) phase obtained in PIC simulation.

Fig. 4 demonstrates typical PIC simulation results when the microwave absorbing materials are included in the drift tube between the input and the buncher cavities. As seen, the output microwave power becomes saturated at t=20 ns and stable till t=100 ns, and no pulse shortening is observed. The output microwave frequency is pure at 9.375 GHz without other parasitic component. Since parasitic mode oscillation is well eliminated by the proposed scheme, the TKA operates stably in amplification mode, so the phase of the output microwave is locked by the input microwave. As seen in Fig. 4, the phase shift between the input and the output microwaves is stable after t=20 ns when the output microwave power becomes saturated. The phase shift fluctuation is about 3 degrees during the phase-locking stage from t=20 ns to t=100 ns.

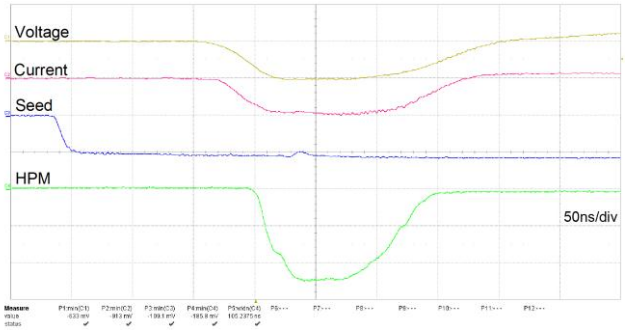

Fig. 5. Typical waveforms measured in experiment.

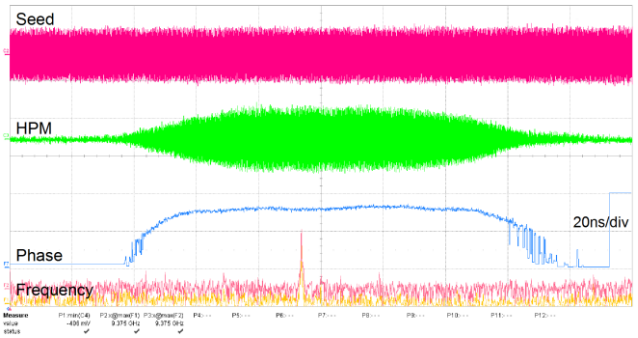

Fig. 6. Frequency and phase shift recorded in experiment.

After optimization by particle-in-cell (PIC) simulation, the proposed TKA was examined in experiment based on a spiral long pulse accelerator, which could provide an electrical pulse with 150 ns in width and with a power about 5 GW. The electron beam was produced by a knife-edge graphite cathode with a radius of 4 cm, and the tube was evacuated by turbo pump to a background pressure of the order of 10^{-3} Pa. The generated HPM was radiated by a horn antenna and measured by detectors at a distance of 6 m away from the radiation horn antenna. More details of the experimental setup can be found in [5]. Typical experimental results are shown in Figs. 5-6. When the diode voltage and current are respectively 580 kV and 6.9 kA, HPMs with power of 1.1 GW and pulse duration of 105 ns was measured. The corresponding efficiency is about 27%. The seed microwave power was 60 kW, which yields a gain of 42.6 dB. Real-time measurement with a high resolution digital oscilloscope shows that both the input and output have pure spectra peaking at 9.375 GHz. Particularly, the output microwave phase is locked over more than 90 ns. The shot-to-shot phase shift fluctuation deviation between the input and the output microwaves is around 10 degree, which shows good reproducibility of the designed TKA.

IV. Conclusions and Prospects

We present the investigations into an improved TKA for phase-locked X-band HPM generations. The experimental results successfully demonstrate productions of HPMs with peak power of 1.1 GW and duration of 105 ns. Particularly, the output microwave phase is locked by the input seed microwave signal, which paves the way to accomplish spatial coherent power combining of X-band HPMs. As a forward step, an improved high-gain and high-efficiency TKA is being studied, and the associated results will be reported in the future.

References

[1] J. Benford, J. Swegle, and E. Schamiloglu, High power microwaves, 2nd ed., New York: Taylor & Francis, 2007.

[2] J. Pasour, D. Smithe, and M. Friedman, “The triaxial klystron,” AIP Conf. Proc., vol. 474, pp. 373-385, 1999.

[3] J. Pasour, D. Smithe, and L. Ludeking, “X-band triaxial klystron,” AIP Conf. Proc., vol. 691, pp. 141-150, 2003.

[4] Z. M. Qi, J. Zhang, H. H. Zhong, D. N. Zhu, and Q. F. Qiu, “A non-uniform three-gap buncher cavity with suppression of TEM mode leakage in the triaxial klystron amplifier,” Phys. Plasmas, vol. 21, pp. 013107, 2014.

[5] J. C. Ju, J. Zhang, Z. M. Qi, J. H. Yang, T. Shu, J. D. Zhang, and H. H. Zhong, “Towards coherent combining of X-band high power microwaves: phase-locked long pulse radiations by a relativistic triaxial klystron amplifier,” Sci. Rep., vol. 6, pp. 30657, 2016.

Effect of Ground on Wide-band High Power Microwave Testing

Cai Jinliang
Key Laboratory of Science and Technology on Complex Electromagnetic Environment , CAEP
Institute of Applied Electronics, CAEP
Mianyang, China
caijl@caep.cn

Qin Feng
Key Laboratory of Science and Technology on Complex Electromagnetic Environment , CAEP
Institute of Applied Electronics, CAEP
Mianyang, China
qinfeng@caep.cn

Fan Jun
Key Laboratory of Science and Technology on Complex Electromagnetic Environment , CAEP
Institute of Applied Electronics, CAEP
Mianyang, China
wilsonfj@163.com

Yan Zhiyang
Key Laboratory of Science and Technology on Complex Electromagnetic Environment , CAEP
Institute of Applied Electronics, CAEP
Mianyang, China
ms_hit_yay@163.com

***Abstract*—In order to investigate effect of ground on electromagnetic environment in wide-band high power microwave (HPM) testing, the antenna pattern and electric field distribution are computed. Electric fields in front of wide-band HPM antenna are compared at different positions with and without a metallic ground plane. Results from simulations show that metallic ground can impact electromagnetic environment generated by wide-band HPM source obviously.**

Keywords—ground, wide-band HPM, antenna pattern

I. INTRODUCTION

With the development of high power microwave (HPM) and the application of electronic technology, it is important to evaluate the adaption to electromagnetic environment of a system with electronic equipment [1]. Testing is an effective method. However, whether a ground should be considered, it is worthy to pay attention. Effect of ground on coupling issues of metallic cylinder has been investigated with excitation of log period dipole antenna [2]. HPM testing is always carried out in anechoic chamber or open space, ground is less considered [3, 4, 5]. To investigate effect of metallic ground, simulation comparison performed on a wide-band antenna is provided in this paper. Antenna pattern, electric field waveform, and electric field distribution are analyzed.

II. ELECTROMAGNETIC MODEL AND SIMULATION

A. Electromagnetic Model

Electromagnetic model of a wide-band HPM antenna is shown in fig.1. The boundary conditions are absorbs, and the antenna is over a plane. Comparison is performed by changing material of the plane, PEC for metallic ground, and vacuum for no ground. Electric fields are observed in front of antenna at the height of 30 cm, 80 cm, and 130 cm. And the distances between observations and antenna are 1 m, 2 m, 4 m, and 8 m respectively. There are 12 observations in simulation. Point A with the distance 8 m and height 130 cm, as shown in fig.1, is a typical observation.

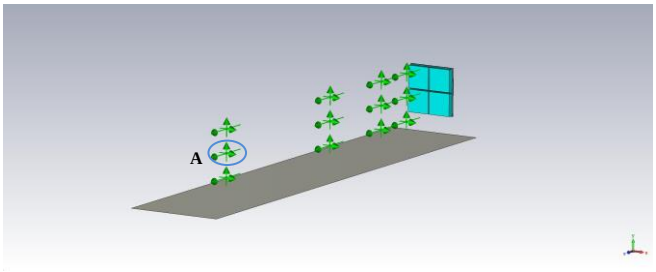

Fig. 1. Electromagnetic model of generator and ground.

B. Antenna Pattern

When ground is not considered, the antenna pattern of wide-band HPM generator is nearly centrosymmetric of z-axis, as shown in fig.2. However, when ground is taken into computation, symmetry of pattern varies significantly (fig.3). And, the output becomes larger near ground caused by metal reflection.

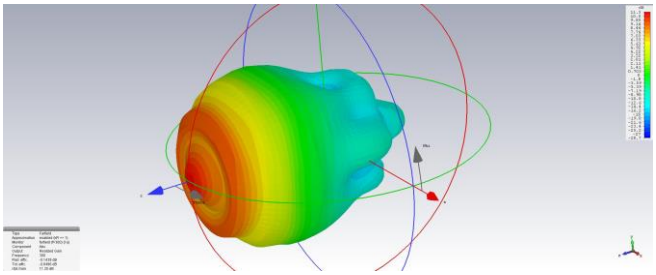

Fig. 2. Antenna pattern of generator without metallic ground.

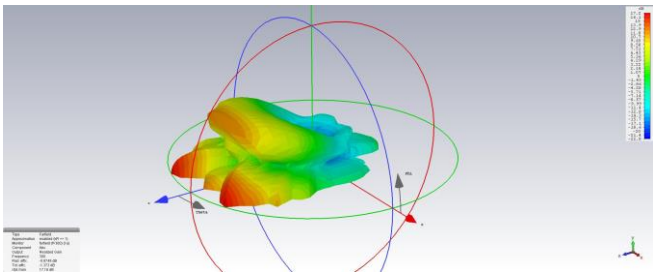

Fig. 3. Antenna pattern of generator with metallic ground.

C. *Electric Field Waveform at the Typical Observation*

Electric filed waveforms at point A with and without consideration of ground are shown in fig.4. When ground is considered, the waveform is wider than the waveform without ground, and peak value of electric field increases from 18.7 kV/m to 24.8 kV/m.

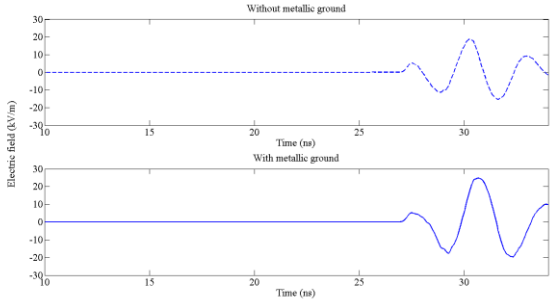

Fig. 4. Electric field waveforms at the typical observation (height 80cm, distance 8m) with and without metallic ground.

D. *Electric Field Distribution*

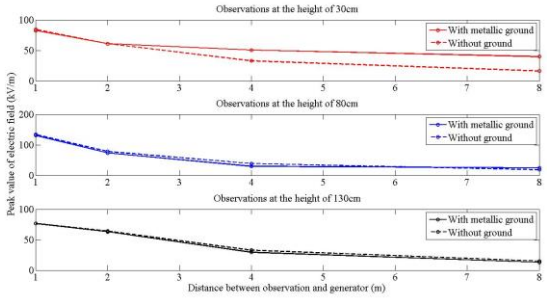

Fig. 5. Comparison of electric field distribution at different heights with and without metallic ground.

The peak values of electric fields of 12 observations are compared at different heights, as shown in fig.5. At higher observations, such as the heights of 80 cm and 130 cm, peak values, with and without ground, are similar at the same distance. However, at the height of 30 cm, there is an obvious difference of peak values between the computation with and without a metallic ground. With the accretion of distance between observation and antenna, the difference is more and more obvious. When observations are near to the antenna, peak values under the two conditions are nearly same. But at farer observation, such as the distance of 8m, the peak value with the consideration of metallic ground is almost the twice of the one without the consideration of ground. So it is better to lay a metallic ground in the wide-band HPM testing of a system operating inherently close to ground.

III. CONCLUSION

A wide-band HPM antenna is computed with and without a metallic ground, to discuss the ground effect to HPM testing. Results show that symmetry of pattern varies significantly caused by the reflection of ground. Because of the same reason, electric field near ground becomes larger. When a system operating inherently close to ground needs to test its adaption to wide-band HPM environment, it is better to consider effect of ground.

REFERENCES

[1] Electromagnetic Environment Effects Requirements for Systems. Department of Defense Interface Standard, MIL-STD-464C, 2010.

[2] T. H. Shumpert, M. L. Waller, and S. H. Wong, “Coupling issues associated with electromagnetic vulnerability (EMV) testing of vehicles over ground,” Progress in Electromagnetic Research, Vol. 124, pp. 457–471, 2012.

[3] J. G. Wang, Y. S. Chen, and R. Y. Fan, “Numerical studies on nonlinear coupling of high-power microwave pulses into a cylindrical cavity,” IEEE Transactions on Plasma Science, vol. 24, pp. 193–197, 1996.

[4] J. H. Zhang, X. Q. Chen, and P. Jiang, “Coupling Effects of High Power Microwave,” 3rd International Conference on Computational Electromagnetics and Its Applications, China, p. 280, 2004.

[5] X. Q. Chen, J. H. Zhang, and Y. R. Huang. “The Simulation of Electromagnetic Pulse Coupling with Computer Box,” 3rd International Conference on Computational Electromagnetics and Its Applications, China, p. 260, 2004.

Study on the coupling effect of Aircraft nuclear electromagnetic pulse

Jinrong Zhu
Shenyang Aircraft Design and Research
Aviation Key Laboratory of Science and Technology on Electromagnetic Environment Effects
Shen Yang, Liao Ning,China
zhu_jr@126.com

Wenjie Zhang
Shenyang Aircraft Design and Research
Aviation Key Laboratory of Science and Technology on Electromagnetic Environment Effect
Shen Yang, Liao Ning,China
wjzhang0118@163.com

Abstract: This paper discusses the high-altitude electromagnetic pulse environment that military aircraft may encounter. It combines cavity and cable electromagnetic pulse(EMP) coupling test to analyze the EMP coupling effect of aircraft and the protective measures that should be taken for aircraft and airborne equipment.

Keywords: electromagnetic pulse, coupling, protection technology.

I. INTRODUCTION

Previous hydrogen bomb tests have shown that not only does a nuclear explosion destroy everything near the core, but also caused an impact on the electronic system within thousands of kilometers, causing the air defense radar to burn out and thousands of kilometers of communication to be interrupted. The troops were out of command for some time. Modern military aircraft are equipped with a large number of excellent electronic systems and equipment, and the adoption of a large number of digital integrated circuits and computers has gradually increased the sensitivity of airborne electronic devices to electromagnetic interference. When these systems and equipment are in an electromagnetic pulse environment, they may be disturbed or damaged, weakening or destroying the combat effectiveness of the aircraft. Therefore, it is necessary to conduct in-depth research on the electromagnetic pulse environment that the aircraft is subjected to.

II. NUCLEAR ELECTROMAGNETIC PULSE OVERVIEW

Nuclear electromagnetic pulses are electromagnetic radiation caused by Compton's recoil electrons and photoelectrons generated by gamma rays during nuclear explosions. The electromagnetic fields can be coupled to electronic and electrical systems to generate destructive voltage and current surges. The nuclear electromagnetic pulse has a high peak field strength, the electric field strength can reach 104V/m~105V/m, and the magnetic induction intensity can reach 10mT. In particular, electromagnetic pulse (HEMP) generated by high-altitude nuclear explosion has the characteristics of coverage frequency bandwidth, high peak field strength, short rise time and wide range of effects, which poses a serious threat to electronic information systems and electrical systems.

The high-altitude electromagnetic pulse environment is described by the expression (1). Figure 1, Figure 2 and Figure 3 are the time domain waveforms of HEMP (IEC 61000—2—9 "HEMP Environment Description Radiation Disturbance", 1996), spectrum and Energy distribution map in the frequency domain.

$$E(t) = kE_p(e^{-\alpha t} - e^{-\beta t}) \qquad (1)$$

Where k=1.3 (normalized constant), EP=50kV/m (peak field strength), α=4×107 s-1 (determines the pulse width), β=6×108 s-1 (determines the pulse rise time)).

The pulse waveform parameters are: peak field strength 50kV/m, rise time 2.5ns, peak time 4.8 ns, pulse width 23 ± 5ns (half-peak width), energy flow 0.114 J/m2.

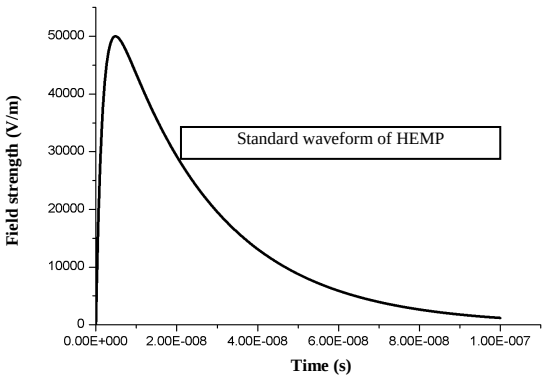

Fig.1 HEMP time domain waveform

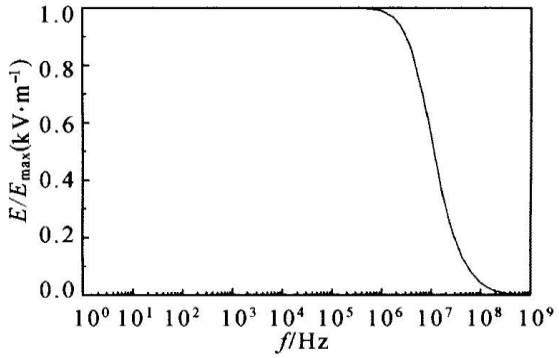

Fig. 2 HEMP normalized spectrum diagrma

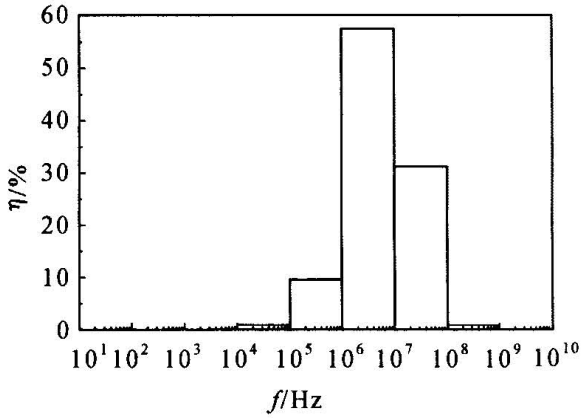

Fig. 3 HEMP Energy distribution diagram

It can be seen from the figure that the peak electric field intensity is as high as 50kV/m, the spectrum covers the entire frequency band from ultra-long wave to the low end of the microwave, and more than 99% of the energy is concentrated in 10 kHz to 1 GHz, which may be for radio communication, navigation, etc. The system constitutes interference and damage.

III. AIRCRAFT EMP COUPING EFFECT

A. Aircraft coupling to electromagnetic pulses

The aircraft is a large metal structure, and its frame and skin are basically metal components. In general, large metal structures are capable of coupling a large amount of electromagnetic pulse energy. When an electromagnetic pulse hits an aircraft, an induced electromagnetic field is generated on the surface and inside of the aircraft fuselage. Figure 4 and Figure 5 show the induced electric field of the aircraft as a function of time.

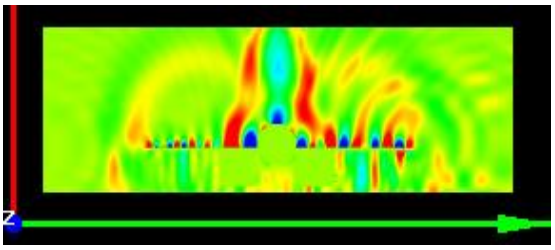

Fig. 4 Two-dimensional electric field distribution at six time points of the cross section at x=7.93m

(The interval between each time point is about 2.9ns in sequence)

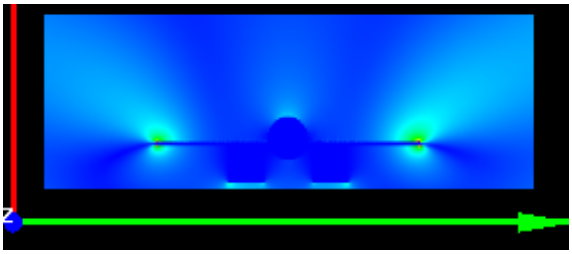

Fig. 5 Two-dimensional electric field distribution of five frequency points at the section of x=7.93m
(starting frequency 20Mhz, span 40Mhz)

In addition, a large number of antennas on the fuselage, various hatch covers, maintenance covers, cables, etc. can also couple electromagnetic pulse energy. A part of the energy is coupled into the interior of the aircraft and the equipment compartment through the hatch cover, the flap and the gap, and the other part of the energy is passed through the connected transmission line and waveguides, cables, pipes, etc. through the antenna into the internal electronic and electrical systems, and coupled to the wires, cables, On the equipment accessories, the sensitive electronic circuit suddenly withstands a large inrush current, thereby interfering with or even damaging the electronic system and electrical equipment, resulting in degradation of the aircraft's operational performance and even endangering the safety of the aircraft.

In order to understand the coupling effect of nuclear electromagnetic pulse on the aircraft, a large number of vertical cavity-polarized EMP bounded wave simulators were used to carry out a large number of metal cavity joint coupling tests and electric coupling tests.

B. Electromagnetic pulse hole test

Since the test area of the EMP system is 2m × 1m × 1m (width × length × height), it is impossible to place the aircraft or equipment cabin in the field for testing. We use a metal cavity of 0.5m × 0.4m × 0.4m (iron sheet) The thickness of 2mm) is used to simulate the equipment compartment of the aircraft and the outer casing of the military electronic equipment. The protective effect of the metal body on the electromagnetic pulse and the coupling effect of the opening and the hole on the shield on the electromagnetic pulse are studied. During the test, the electric field probe is placed on the bottom surface of the metal casing and grounded through the metal body. The connecting cable is led out along the cavity wall and connected to the console oscilloscope, so as to minimize the influence of the cable. The test is divided into several groups of different situations. Figures 6 and 7 are photographs and schematic diagrams of the electromagnetic pulse cavity coupling test.

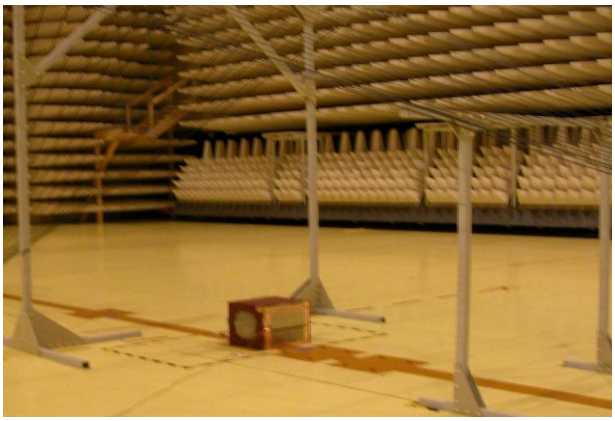

Fig. 6 Cavity hole joint coupling test

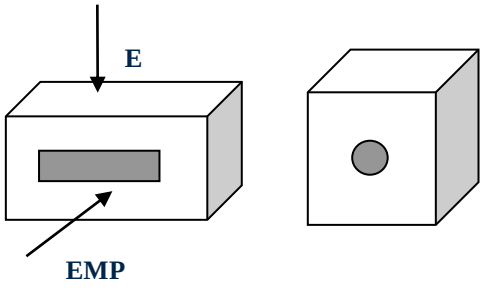

Fig. 7 Cavity hole joint coupling test diagram

The tests are mainly divided into the following groups:

- 34cm × 24cm opening coupling test: the opening orientation is four kinds of upward, rightward, forward and backward directions, each direction has two sides of the open long side parallel and perpendicular to the electric field direction;
- the coupling test of the slit gradually narrowing : The hole is facing forward, the transverse hole is slit, the short side is gradually reduced and gradually narrowed;
- The coupling test is gradually shortened: the hole is facing forward, the transverse hole is slit, the narrow side is unchanged, and the long side is gradually reduced;
- Coupling test of different shapes of the same area: the hole is facing forward, and the shape of the hole is rectangular, square and round.

Tables 1 to 4 are test results in various test cases, and Figures 8 to 11 are field strength test curves in the metal cavity in several cases.

Table 1 Coupling electric field values in a 34 cm × 24 cm open metal cavity

No.	Opening orientation	Opening and electric field relationship	Max reading (mV)	Max field strength value (kV/m)
1	upward	opening perpendicular to the direction of the electric field	6.3	2.835
2	right	opening long side perpendicular to the electric field	3.6	1.62
		The long side of the opening is parallel to the electric field	2.18	0.981
3	forward	long side perpendicular to the electric field	5.5	2.475
		The long side of the opening is parallel to the electric field	6.08	2.736
4	Backward	Open long side perpendicular to the electric field	6.3	2.835
		The long side of the opening is parallel to the electric field	2.9	1.305

Table 2 results of the silt narrowing coupling test

No.	Slit size	Max reading (mV)	Max field strength (kV/m)	Resonant frequency (MHz)
1	34cm×10cm	7.6	3.42	488
2	34cm×5cm	7.9	3.555	500
3	34cm×2.5cm	16.9	7.605	500
4	34cm×1.5cm	12.3	5.537	503
5	34cm×0.5cm	10.1	4.545	498

Table 3 Results of the coupling test with the silt becoming shorter

No.	Slit size	Max reading (mV)	Max field strength (kV/m)	Resonant frequency (MHz)
1	34cm×1.5cm	12.3	5.537	503
2	24cm×1.5cm	6.2	2.79	455
3	14cm×1.5cm	1.3	0.585	473
4	24cm×1.5cm (vertical slit)	1.03	0.464	444

Table 4 Results of coupling test of different shapes of holes in the same area

No.	Slit size	Max reading (mV)	Max field strength (kV/m)	Resonant frequency (MHz)
1	34cm×1.5cm	12.3	5.537	503
2	20.4cm×2.5cm	2.26	1.008	473
3	7.14cm×7.14cm	1.57	0.767	420
4	8.04cm round	1.33	0.599	105

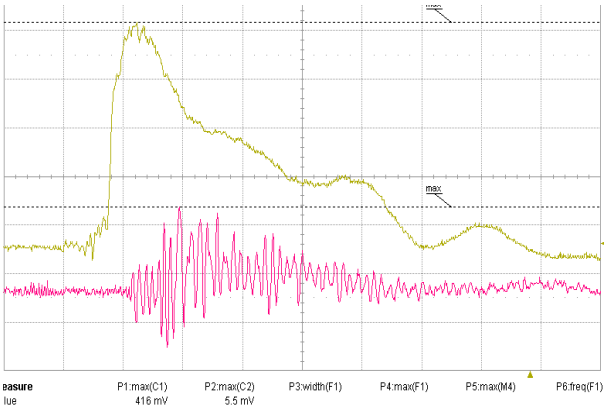

Fig. 8 Field strength of 34cm × 24cm opening coupling

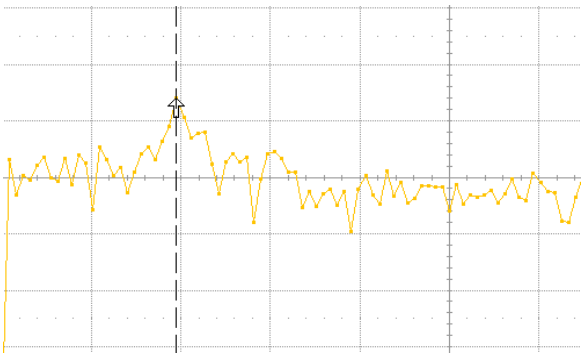

Fig. 9 34cm × 24cm open field strength FFT transform

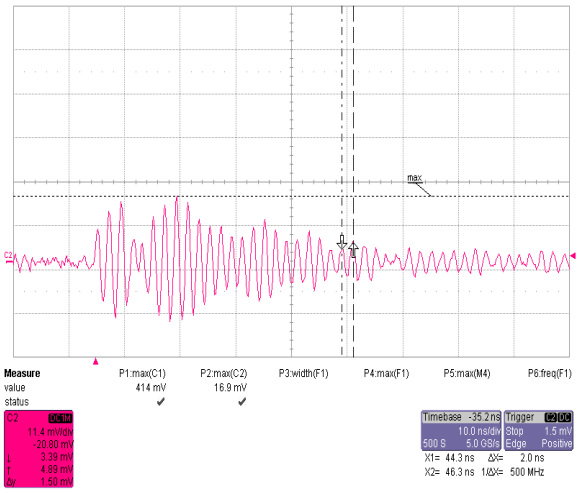

Fig.10 Field strength coupling of 34cm×2.5cm hole joint

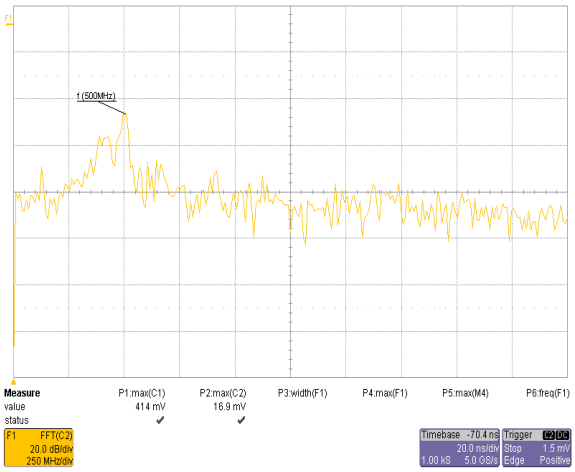

Fig.11 Field strength FFT transformation of 34cm×2.5cm hole joint coupling

From the test results and test curves, it can be seen that the coupling effect of the metal cavity in the high-altitude nuclear electromagnetic pulse field is consistent with the electromagnetic wave shielding theory. The main laws are as follows:

- Shielding is a more effective measure for electromagnetic pulse protection, but HEMP is coupled to the inside of the metal cavity through the hole on the shield and resonates. The field strength at the resonant frequency is large, so that the shielding effectiveness of the shield is at resonance. The area is greatly reduced;
- the resonance of the electromagnetic energy coupled into the interior through the slot on the shield, the resonant frequency of which is not only related to the structural size of the shield cavity, but also related to the size of the slot on the shield;
- the coupling field strength is small when the opening on the metal cavity is parallel to the direction of the electric field, large when perpendicular to the direction of the electric field, and the coupling field is strong for the lateral opening of the vertically polarized wave, and the vertical opening is small;
- When the incident conditions of the electromagnetic pulse are the same, it can be seen from Table 2 and Table 3 that when the slot is sufficiently narrow, a significant coupling effect of the slot will occur. The narrower the slot, the smaller the coupled field strength and the resonant frequency is basically unchanged. The shorter the hole is, the smaller the coupled field strength is, but the resonant frequency will change;
- If the device chassis needs to be opened, it should be rounded as much as possible. Because the circular hole has less energy than the rectangular hole, in addition, the resonant frequency of different shapes is different. It can be said that the frequency of the device is considered comprehensively, and the hole is reasonably selected. shape.

C. Electromagnetic pulse cable test

The cable coupling test is to make the 20m long shielded cable transversely pass through the HEMP field. The midpoint of the cable is at the center of the electromagnetic pulse field test area. The electric field is about 50kV/m. The induced current on the shield layer is measured by the Rogowski coil. 8m from the center of the cable. Figure 14 is a measured induced current waveform.

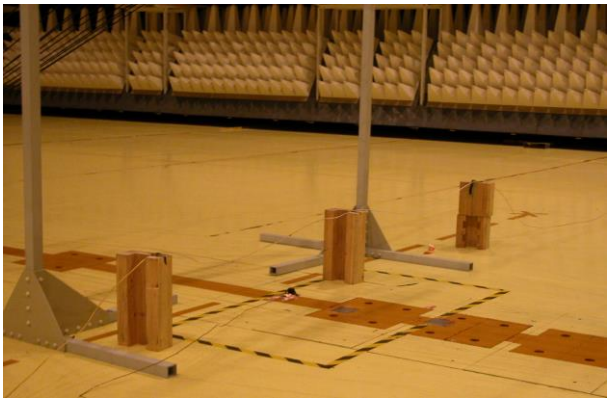

Fig.12 Cable coupling test

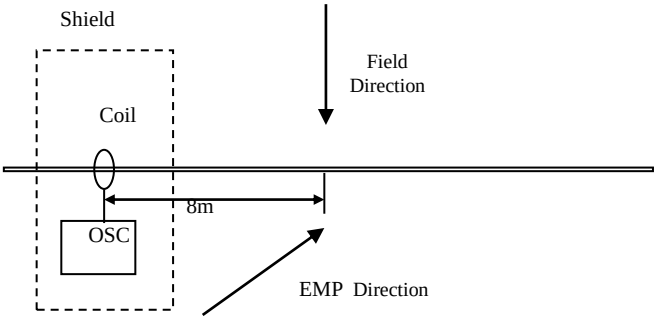

Fig. 13 Cable joint coupling test diagram

Table 5 Results of 20m shielded cable coupling test

No.	Cable connection status	Shield induced current(kA)	Current oscillation frequency (MHz)
1	not connected to the load at both ends, and both ends are suspended.	13.1	45.5
2	not connected to the load at both ends, single-ended floating	10.6	10.68
3	connected to the load at both ends and the two ends are suspended	8.9	10.82

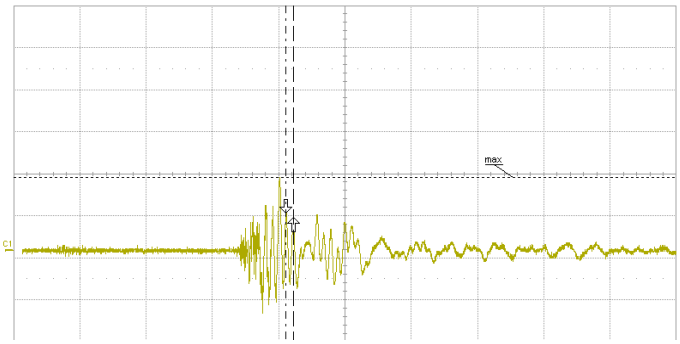

Fig. 14 The cable is not connected to the load at both ends, the two ends are suspended, and the skin induces current

Conclusion: In the high-altitude electromagnetic pulse field of 50kV/m, the shield of the long cable can generate 10kA induced current, and the current is a damped oscillation waveform with an oscillation frequency of several tens of megahertz.

IV. ELECTROMAGNETIC PULSE DAMAGE TO ELECTRONIC EQUIPMENT

The main energy of the electromagnetic pulse is concentrated in the normal radio frequency range. When the electromagnetic pulse enters the electronic and electrical equipment on the aircraft, it will adversely affect the equipment. This effect can be temporary or permanent.

A. Work failure

The temporary malfunction of the equipment caused by the impact of electromagnetic pulses is called work failure. There are two situations in which work fails. One is a circuit that causes an interference signal to enter an airborne device caused by an electromagnetic pulse, and is amplified by an amplifying circuit and used as a control signal to cause the system to malfunction. For transient interference, the input line of the digital circuit is the most sensitive part, followed by the DC power line and ground. Low-power or high-speed digital processing systems, flight navigation control systems, digital transmission systems, etc. in aircraft electronic warfare equipment are all systems that are susceptible to transient interference and malfunction.

Another situation in which the work fails is that after the electromagnetic pulse is hit, the semiconductor device in the device circuit is blocked, causing the device to crash. At this time, the power of the circuit must be removed before the circuit can be restored to the working state.

B. Functional damage

Functional damage means that the electromagnetic pulse coupling energy may cause permanent failure of the electronic components. The damage mechanism is: metallization system burning, oxide layer dielectric breakdown, junction surface breakdown, and junction heat breakdown. For most components of a typical electronic system, the damage threshold is energy dependent. The amount of energy can be obtained by (2):

$$E = \frac{U^2 \tau}{R} \qquad (2)$$

Where E— the energy on the transistor, J;

U—the electromagnetic pulse induced voltage in the loop, V;

R—transistor junction avalanche resistance, Ω;

T—electromagnetic pulse width, s.

Table 6 Noise level limits for some semiconductor devices

Semiconductor equipment	malfunction limit (J)	Damage limit (J)
CMOS integrated circuit	10^{-7}	10^{-6}
Small power transistor	10^{-6}	10^{-5}
Switching diode, low power transistor	10^{-5}	10^{-4}
Ordinary Diode	10^{-4}	10^{-3}
Zener Diode	10^{-3}	10^{-2}
Ordinary triode	10^{-2}	10^{-1}
Power transistor	1	10
Power DC, SCR	10	100

V. AIRCRAFT ELECTROMAGNETIC PULSE PROTECTION TECHNOLOGY

The purpose of aircraft electromagnetic pulse protection is to prevent the energy of electromagnetic pulses from entering sensitive equipment and sensitive system areas. This requires effective shielding and isolation from the external electromagnetic environment while using insensitive electronic and electrical systems. The thick aluminum plate and metal structure and riveting process used in the aircraft will provide near-ideal electromagnetic pulse shielding. However, the aircraft's equipment hatch cover and numerous maintenance flaps use insulating glue, which makes the aircraft shell have many gaps, which damages the continuity of the shield and greatly reduces the shielding effectiveness of the body. In addition, the internal equipment compartment of the aircraft should provide good shielding and less open apertures, but there must be multiple penetrations between the various compartments inside the aircraft for cable laying, so the integrity of the shielding cannot be maintained.

The electromagnetic pulse reinforcement of the aircraft should use a three-stage reinforcement method to jointly block and attenuate the electromagnetic pulse energy and combine it with aircraft design and equipment installation. The first level is platform reinforcement, which uses the aircraft skin as the primary shielding layer and strengthens the shielding of equipment bays equipped with sensitive electronic equipment. Non-metallic components other than the radome on the skin shall be sprayed with aluminum, adhered to a conductive coating, etc. Shielded between the mouthpiece and the mouthpiece shall be made of conductive adhesive. Cables under non-metallic skins should be shielded to control the cable and avoid introducing electromagnetic pulses into the interior. The second stage is system reinforcement, which is to shield the grounding of sensitive signal cables in the metal skin of the aircraft and replace the electrical transmission with the optical fiber transmission system to form a protective barrier for the electronic equipment to prevent electromagnetic pulses from entering the equipment through the cable. When the effects of the first and second stages are insufficient or cannot be achieved for functional reasons, the third level of reinforcement measures are used. The third level of reinforcement is for the reinforcement of electronic equipment and should be considered at the beginning of the design. There are many reinforcement methods, including good shielding of the device casing, installation of filters, common mode suppression circuit, etc. It is also possible to provide transient interference protection devices on the circuit board and chip to ensure that the device can withstand the impact of residual electromagnetic pulse energy.

VI. ELECTROMAGNETIC PULSE TEST

A. aircraft System electromagnetic pulse test

The system electromagnetic pulse test refers to the whole-machine electromagnetic pulse test conducted on the aircraft, and investigates the influence of the electromagnetic pulse aircraft on the aircraft and the airborne projectile. Figure 15 shows the whole-machine electromagnetic pulse test conducted abroad, but there is currently no simulator for large-scale systems that can perform whole-machine testing.

Figure 15 Aircraft electromagnetic pulse test

B. Electromagnetic pulse test of airborne equipment

In order to evaluate the ability of the equipment to resist electromagnetic pulse interference, the CS115, CS116 and RS105 tests can be carried out in accordance with GJB151B Military Equipment and Subsystem Electromagnetic Emissions and Sensitivity Requirements/Measurements. CS115—Cable beam injection pulse excitation conduction sensitivity test is to investigate the influence of transient current generated by external transient environment such as lightning, electromagnetic pulse and switching operation on equipment; CS116-10kHz～100MHz cable and power line damping sinusoidal transient conduction In the sensitivity test, the test waveform is a damped sinusoidal signal because when the platform is exposed to an external environment such as lightning or electromagnetic pulses, the induced current and voltage waveforms inside the platform are often damped sinusoidal waves due to the inherent resonance. RS105—Transient electromagnetic field radiation sensitivity test, the HEMP field shown in Figure 1 is generated by the electromagnetic pulse generation system to investigate whether the equipment can withstand the impact of nuclear electromagnetic pulse.

VII. CONCLUSION

The electromagnetic pulse generated by the nuclear explosion poses a serious threat to the electronic and electrical systems on the aircraft, and the system is subject to interference, which in turn causes permanent damage to the equipment. At present, with the development of nuclear weapons technology, the third generation of nuclear weapons, electromagnetic pulse bombs, has been produced. The reduction of other effects enhances the electromagnetic pulse effect, further enhancing the energy and power of nuclear electromagnetic pulses, and the rising front is faster and the spectrum is wider. The damage to electronic and electrical systems is even more serious. In addition, electromagnetic pulse weapons such as electromagnetic bombs and high-power microwave weapons have emerged and will be put into use in modern warfare. Therefore, in order to improve the survivability of aircraft electronic and electrical systems in a strong electromagnetic pulse environment, a more in-depth study of the aircraft's magnetic pulse effect and its protection should be carried out.

REFERENCES

[1] GJB 1389A-2005 Electromagnetic compatibility requirements for systems.

[2] GJB 151B-2013 Electromagnetic emission and susceptibility requirements and measurements fo military equipment and subsystems.

[3] ZHOU Bi-hua，CHEN Bin，SHI Li-hua，EMP and EMP protection[M].Beijing，China：National Dfence Industry Press，2003.

[4] SHI Shou-xun， Research on Protection of Electronic Systems from Electromagnetic Pulse Damage[D].Hefei，China：Hefei University，2006.

HPEM regulatory standard (KINAC/RS-020) for IEMI Protection of Nuclear Facilities in ROK

Jinho Ryu
Cyber Security Division
Korea Institute of Nuclear Nonproliferation and Control
Daejeon, Republic of Korea
halloyu@kinac.re.kr

Donghoon Song
Daejeon, Republic of Korea
igiveitashot@kinac.re.kr

Hojong Hwang
Daejeon, Republic of Korea
fredhwang@kinac.re.kr

Sujin Park
Daejeon, Republic of Korea
sjpark@kinac.re.kr

***Abstract*—Nuclear facilities are of utmost importance among various type of national infrastructure. Based on related law, nuclear facilities are under cyber security regulation and control to protect electronic infringement which includes HPEM threat. In this paper, HPEM regulatory standard KINAC/RS-020 is introduced which serves as an acceptable reference for the application of HPEM protective measures. According to the design basis threat (DBT) of nuclear facilities revised in 2018, IEMI threat become under the scope of nuclear licensee's responsibility to protect. Following the revision of DBT, KINAC/RS-020 describes the identification procedure of facility and device, vulnerability assessment procedure to protect nuclear facility against IEMI threat.**

Keywords—HPEM standard, Protection standard, IEMI threat, KINAC/RS-020, Design Basis Threat, Nuclear facility

I. INTRODUCTION

As of the revision of ACT ON PHYSICAL PROTECTION AND RADIOLOGICAL EMERGENCY [1] (APPRE) in 2015, electronic infringement against nuclear facilities became a threat that nuclear licensee shall protect. As the legal term "electronic infringement" contains HPEM (High-Power Electromagnetic) threat in its definition, which is adopted from ACT ON THE PROTECTION OF INFORMATION AND COMMUNICATIONS INFRASTRUCTURE [2], nuclear licensees in Republic of Korea (ROK) are now required to evaluate vulnerability to HPEM threat.

Based on the protocols of the APPRE, nuclear facilities shall prepare protective measures against threat defined in the Design Basis Threat (DBT), which designate the licensee's responsibility to cover. Recent revision of DBT in 2018 reflects HPEM threats, therefore the licensee's action is becoming more imminent.

In advance of the licensee's action, KINAC (Korea Institute of Nonproliferation and Control) which is technical support organization of regulatory body (NSSC, Nuclear Safety and Security Commission) of ROK has prepared and provided the standard (KINAC/RS-020) for HPEM protection of nuclear facility in 2018 [3]. KINAC/RS-020 considers specific characteristic of nuclear facilities, so as to achieve the protection goal "Unauthorized removal of nuclear material and Sabotage on nuclear facility" of APPRE. In this paper, the methodology of application of HPEM protective measure to nuclear facilities is introduced based on KINAC/RS-020.

This work was supported by the Nuclear Safety Research Program through the Korea Foundation Of Nuclear Safety(KoFONS), granted financial resource from the Nuclear Safety and Security Commission(NSSC), Republic of Korea (No. 1804023).

II. HPEM THREAT IN DBT AND PROTECTION STANDARD

In 2018, DBT for nuclear facilities in ROK is revised. Among HPEM threats, only specific IEMI (Intentional Electromagnetic Interference) threat is included (confidential). Regarding the path of infringement for the IEMI threat, both radiative and conductive path are considered. KINAC/RS-020 recommends the reference value for the protection of IEMI threat as below graphs in Fig. 1. Based on the protection standard in DBT, IEMI protective measures are required along the frequency band of 10 MHz ~ 18 GHz.

III. IDENTIFICATION OF PROTECTION TARGET

To prepare the protective measures defined in DBT, the nuclear facility that has to be protected against the IEMI threat should be firstly identified. Note that not all the nuclear facilities are subject to the IEMI threat according to the DBT. 'Nuclear facility' is legal term in APPRE which contains following types of facilities: nuclear power plant, research reactor, fuel-cycle facility, nuclear waste management facility and facility where a radioactive isotope

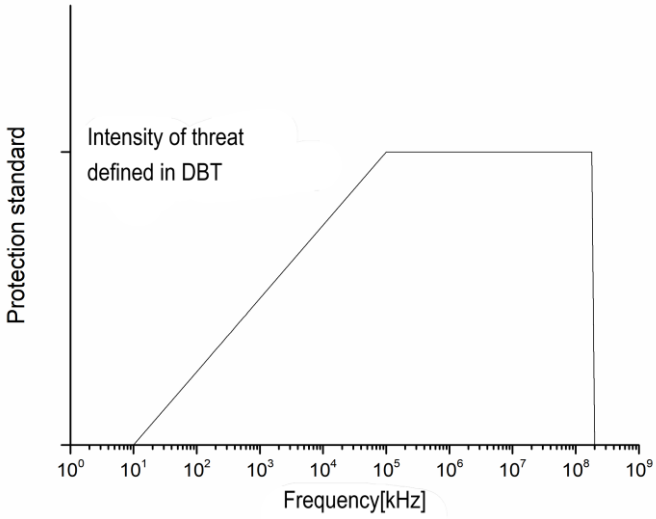

Fig. 1. Protection standard of nuclear facility for the specific IEMI threat

of at least 18.5 petabecquerels is produced. Among these nuclear facilities, the protection target is closely related with the protection of goal of APPRE explained previously.

A. Identification of Nuclear Facility

Among nuclear facilities, KINAC/RS-020 recommends that the sabotage should be prevented for the facility where the nuclear materials are used and stored. Here, the term 'nuclear material' is also a legal term defined in APPRE, which covers Pu, U^{235}, U^{233} and radiated nuclear fuel with their weight and enrichment. Therefore, mid-low level nuclear waste management facility and radioactive isotope producing facility are exempted from the view point of sabotage.

For the facilities where the prevention of unauthorized removal of nuclear material is required, as these facilities are already defined in terms of the legal term 'nuclear material', the same category of facilities with sabotage are required to prepare protective measures. Therefore, for both sabotage and unauthorized removal of nuclear material, only those facilities where the 'nuclear material' is being used and stored shall identify the target devices to be protected against the IEMI threat.

B. Identification of Devices

Different from the general target devices of cyber security, the objects of HPEM protection are not only digital, but also include analogue devices, thus being the electronic equipment. If the electronic equipment is comprised of several digital/analogue instruments, it can be identified as one single target device, so that protective measures apply as a whole.

KINAC/RS-020 recommends that following devices in TABLE I. should be protected from the IEMI threat defined in DBT.

Along with the identification of devices, KINAC/RS-020 requires the documentation of followings: identification procedure, basis for the identification, list of devices, function and composition of devices, infringement impact assessment of target devices and result of review for new device installation. After the identification of nuclear facility, the device-level identification should be followed.

TABLE I. DEVICES OF NUCLEAR FACILITY TO BE PROTECTED AGAINST HPEM THREAT DEFINED IN DBT

Major Category	Sub Category (Function based)
Devices for Reactor Shutdown and maintaining safety shutdown status	Reactor Shutdown
	Maintaining safety shutdown status
	Supporting devices for above functions
Devices for Protecting Radiological Material Release and Radiation protection	Prevention of radiological material release
	Radiation Protection
	Miscellaneous devices for above functions
Security Devices related to Unauthorized Removal of Nuclear Materials	Maintaining physical barrier
	Access Control
	Searching
	Detection and Judgement
	Communication
	Response

IV. VULNERABILITY ASSESSMENT

Based on the result of the identification of protection target, vulnerability assessment of nuclear facility for the IEMI threat can be proceeded. The vulnerability assessment is comprised of regional protection status identification and evaluation of regional protection efficiency. The unit of protection region is a closed compartment of building.

A. Identification of Regional Protection Status

The regional protection status of nuclear facility should be documented including these information : the shortest path from outer physical barrier to the target device, identification of vulnerable point(openings, gaps etc) along with the shortest path, status of compartment arrangement from outer surface of building to the target device, diameter of compartments and status of construction material, and electronic/communication/control line connected to the target device and preexisting HPEM protective measures.

B. Evaluation of Regional Protection Efficiency

After identifying the regional protection status of nuclear facility, regional protection efficiency can be evaluated by summation of all protection efficiency from the outer surface of building to the target device including efficiency of preexisting protective measures. For the conductive path, protection efficiency of all kinds of lines will be added.

Evaluation of protection efficiency can be conducted either survey experiment or using simulation program. Protection efficiency of preexisting protective measures can be accepted if related documents prove its performance. The application of additional protective measures to the nuclear facility can be decided based on the result of this evaluation procedure.

V. CONCLUSION

In this paper, the regulatory standard KINAC/RS-020 is introduced which serves as an acceptable reference for preparing protective measures to HPEM.

As the recent revision of DBT confines HPEM threat as the IEMI threat, regulatory standard KINAC/RS-020 recommends the methodology of protecting nuclear facilities against DBT based on the IEMI threat. This methodology includes guideline for the identification of both nuclear facility and device to be protected. Moreover, the vulnerability assessment procedure is described to review the necessity of additional protective measures. This vulnerability assessment procedure covers identification of regional protection status and evaluation of protection efficiency of each region of facility.

Since 2019, regulatory actions will be practiced on nuclear licensees in ROK for the evaluation of threat/response scenario, which reflects the latest DBT including the IEMI threat. Especially for the IEMI threat, licensee's threat/response scenario will be evaluated based on KINAC/RS-020, so that regulatory authority will assess the need of additional protective measures of facilities against the IEMI threat.

REFERENCES

[1] ACT ON PHYSICAL PROTECTION AND RADIOLOGICAL EMERGENCY, 2017

[2] ACT ON THE PROTECTION OF INFORMATION AND COMMUNICATIONS INFRASTRUCTURE, 2018

[3] Protection of Electro-Magnetic Pulse for Nuclear facility (KINAC/RS-020), 2018.

A Compact, Low Jitter, High Voltage Pulse Generator Based on Fractional-turn Ratio Saturable Pulse Transformer

Jiuyuan Geng
College of Opto-electronic Science and Engineering
National University of Defense Technology
Changsha, China
gengjiuyuan@foxmail.com

Jianhua Yang
College of Opto-electronic Science and Engineering
National University of Defense Technology
Changsha, China
jianhua.yang@nudt.edu.cn

Ting Shu
College of Opto-electronic Science and Engineering
National University of Defense Technology
Changsha, China
1827647942@qq.com

***Abstract*—In this paper, the design and the operation characteristics of a solid-state high voltage pulse generator are investigated. Its utilization is aimed at triggering a three-electrode spark gap with pulse power up to several gigawatts. The trigger generator has been developed based on a fractional-turn ratio saturable pulse transformer and a compact 6-stage Marx generator. The main components of the system are comprised of a DC power supply for charging the primary storage capacitors, a thyristor, two pieces of magnetic core as the basis of transformer, and six pairs of diodes and ceramics capacitors. A pulse with risetime of 141ns and magnitude of 79.6kV is achieved when operated on the 50Ω load. And the frequency is up to hundreds of Hz, but it is tens of Hz when applied in an existing switch, since it is limited by the operating frequency of a power system and the available magnetic cores. The jitter from initial control signal to the rising edge of the pulse is 0.6ns. At present, the trigger generator successfully applies to the IEBA and operates stably.**

Keywords—high voltage, trigger generator, fractional-turn ratio saturable pulse transformer, low jitter

I. INTRODUCTION

With the trend of pulse power technology to be miniaturization and modularization. The trigger generator of a main gaseous spark gap, which is irreplaceable for present intense electron beam accelerator(IEBA), is tend to be more compact and stabilized. A Marx generator is always used to boost a pulse voltage up to about one hundred kilovolts in the traditional trigger generator [1,2]. The design of the Marx circuitry uses gas/vacuum switches frequently due to their high-power capacity, high di/dt rates and easy to operate [3]. In addition, some semiconductor switches such as MOSFETs and IGBTs [4,5] play an important part of the pulse generator designs. They have characteristics of low jitter but low power capacity relatively. Weidong Ding et al. introduce A sub-nanosecond jitter trigger generator combining semiconductor switch and gas switch in a Marx generator circuit. It generates a 37kV pulse with a risetime 2.2ns [6]. Except designs mentioned above, tesla pulse transformers still have a wide application in pulse generator designs. In addition, magnetic pulse compressor and transmission line transformer have been developed these years. And more recently the saturable pulse transformer (SPT) utilizing of magnetic core and Tesla transformer windings is present [7]. It achieves a risetime of 52ns and peak voltage of 71kV and its charging voltage is 2.5kV.

In this paper, a novel design of triggering device based on fractional-turn ratio saturable pulse transformer (FRSPT) is devised, and its characteristics are investigated. The whole design consists of a photoelectric control system, a charging system and a step-up system. A SPT based on fractional-turn ratio principle is the key component of the step-up system since it acts as a step-up transformer and synchronous magnetic switches of a Marx circuit. The saturate characteristic of magnetic core is exploited, which is the impedance changes with the varying voltages. Therefore, the secondary windings of SPT are able to switch transformer mode into magnetic switch mode. The miniaturization of SPT achieves because magnetic switches replace traditional spark gaps in a Marx circuit and integrate with the transformer precisely. However, there is dilemma that the step-up ratio of transformer increases while saturable inductance rises. The fractional-turn ratio achieves the desire of high step-up ratio and low secondary saturable inductance. The method is enwinding primary windings on each magnetic core separately. Furthermore, the step-up ratio is up to 140, so that the system requires a pretty low charging voltage of 500V, which is supplied by two DC power in parallel. With all the components solid-state and sealed in the electric insulating oil, the compact trigger generator shows strong capacity of stability and high step-up ratio in practical application. Details about the design and experimental results are present in Section II and Section III.

II. DESIGN OF THE PULSE GENERATOR

A. Overview of The Triggerator

In this section, the whole system design is shown with schematic diagram, and the operational principle of every component is present in details. As shown in FIG.1, this design consists of a photoelectric control system, a primary capacitor and a thyristor in charging system, a step-up system concluding a FRSPT and a 6-stage Marx generator. In a high frequency application, an energy recycle circuit is usually added in the charging system.

B. Charging System

The main part is sealed in an electric insulation box which is full of the electric insulating oil. The air in the box is pumped down for a greater insulation. In order to reduce the interference and unanticipated trigger in a complex electromagnetic environment, the entire process is controlled by the photoelectric signals. The DC power supply is out of

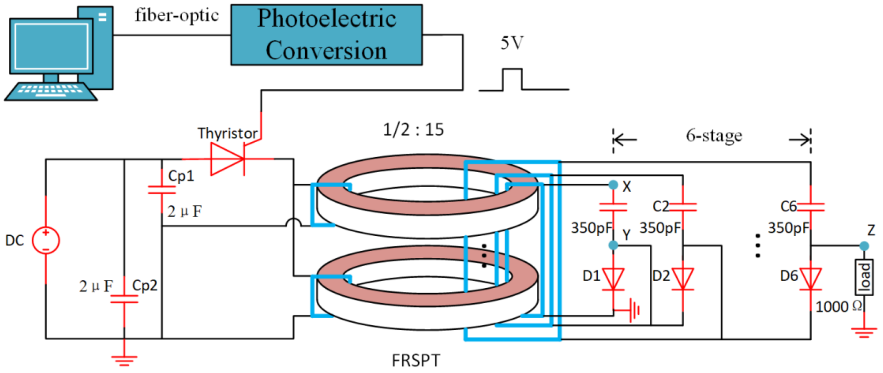

FIG.1 Schematic diagram of the trigger generator design with measurement points

the box and output 500V constant voltage with 220V AC input. The thin-film capacitor is used as the primary capacitor for its wide frequency response which is necessary for a slow charging and fast discharging system. There are four capacitors of 1μF in parallel actually for a higher charging power, and each two are separately connected to two sets of primary windings which are wounded on one magnetic core. The thyristor in main circuit was controlled by a 5V photoelectric signal, part number KP6000A 3000V. With a photoelectric signal from a computer the thyristor switches and allows the capacitors C_p discharging to primary windings.

Since the trigger generator operated in high frequency depends heavily on the charging time and charging power of the capacitor, an energy recovery circuit is required but only exist in the design, the reason is given in Section Ⅲ Part A. As shown in FIG.2, two inductances, two diodes and a resistance are added in the circuit on the basis of the charging system in FIG.1 and L_p is inductance of primary windings. Voltage on C_p is reversed after discharging the windings, the added circuit is able to recycle the residual energy via D_{p2}, L_d and L_0. Since there is fractional voltage on C_p, it accelerates the next charging process.

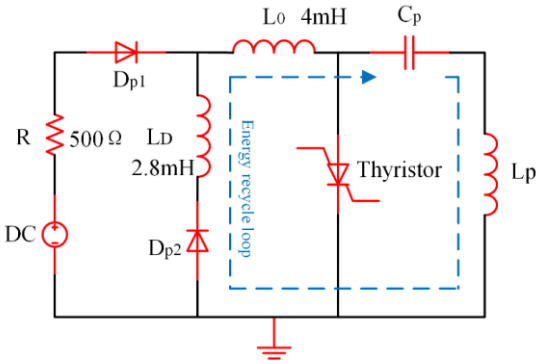

FIG.2 Energy recycle circuit schematic

C. Pulse Transformer

FRSPT is a pulse transformer with high step-up ratio and high couple efficiency. The structure layout is shown in FIG.3. The main part is two pieces of Fe-based amorphous toroidal magnetic cores which is wounded with primary windings and secondary windings. The secondary windings are able to be regard as a short solenoid with a magnetic core. And the B-H curve of a magnetic core is square, which means an abrupt change occurs in relative permeability μ_r at a specific voltage-second product. That is to say, μ_r is large with magnetic core non-saturated while μ_r drops sharply with the magnetic core saturated. For the magnetic core used in this paper, the rang of μ_r is from 15 up to 4100 approximately.

According to the compactly calculated formula of inductance for solenoid:

$$L = \frac{K_\alpha \mu_0 \mu_r N^2 S}{l}$$

where K_α is Nagaoka coefficient, L is inductance of solenoid, μ_0 is space permeability, N is winding turns, S and L are the cross-sectional area and length of the solenoid. It shows that L is proportional to μ_r. It is precisely the change in inductance that achieves the combination of pulse transformer and magnetic switch in the FRSPT.

In order to make the magnetic core saturated adequately and obtain a large current capability, the primary windings are in parallel and each gets one turn. They are divided into four groups and each two are encircled on one magnetic core. The secondary windings are double layered and fifteen turns in total, encircling all two magnetic cores. They are divided into six groups and connect the 6-stage Marx generator separately. According to REF. 8 the voltage step-up ratio of a fractional-turn ratio pulse transformer is:

$$U_1 / U_2 = 1 : Nn$$

where n is the number of the magnetic cores. So, the step-up ratio of this FRSPT is up to 30. As it is shown in the equation, the step-up ratio is proportional to n. But for a trigger generator design, n has an optimal value instead of being largest. Because the secondary inductance which is employed in the Marx circuit relates with n, and the impedance of the circuit extends rise time of output pulse. A concise proof is present in the following. Firstly, supposing the secondary windings are short solenoids with square cross-section and the width of the square is k times the length of solenoids, namely $a = c/n = kb$. Secondly, the inductance of the secondary windings can be approximated and it becomes

$$L_n = \mu_0 \mu_r N^2 \frac{ac}{b} F' \qquad (1)$$

For a short solenoid

$$F' = \beta_1 \gamma + \beta_1' \gamma \ln \frac{1}{\gamma} + \beta_2 \gamma^2 + \beta_3 \gamma^3 - \beta_5 \gamma^5 + \cdots \qquad (2)$$

in which

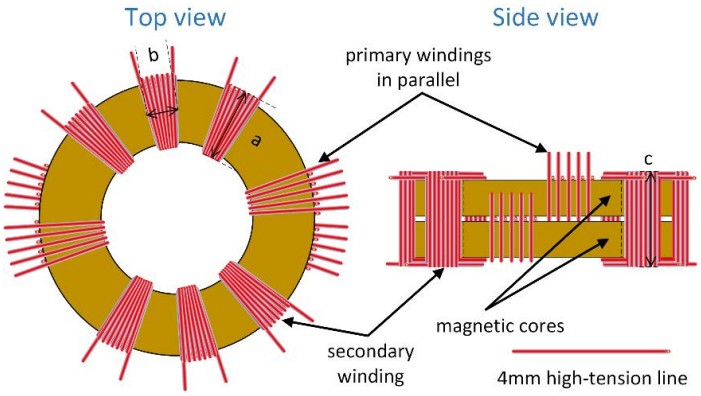

FIG.3 The structure layout of FRSPT in two main views and parameters of secondary windings

$$\gamma = \frac{b}{c} \qquad (3)$$

and the coefficients β are functions of the ratio

$$\xi(n) = \frac{a}{c} = \frac{1}{n} \qquad (4)$$

Supposing k=2 and combining equation (1) to (4). So, the inductance L_n about n is expressed in the following form:

$$L(n) = \mu_0\mu_r N^2 a(\beta_1 + \beta_1' \ln 2n + \beta_2 \frac{1}{2n} + \beta_3\left(\frac{1}{2n}\right)^2 - \beta_5\left(\frac{1}{2n}\right)^4 + \cdots) \qquad (5)$$

Finally, sets values of $\beta(\xi)$ can be found from Chapter 10 of REF. 9, and then $L(n)$ varies with n is given in the forms of scatter and fitted curve. As shown in FIG.4 the relationship between $L(n)/\mu_0\mu_r N^2 a$ and n is linear. And for a specific solenoid the value of $\mu_0\mu_r N^2 a$ is constant. Hence, $L(n)$ and n are linearly related. In conclusion, the number of cores is related to the step-up ratio and secondary inductance. Further it increases the rise time of output pulse. Based on the comprehensive consideration of the both two and several experiments, two pieces of magnetic cores are selected in the design.

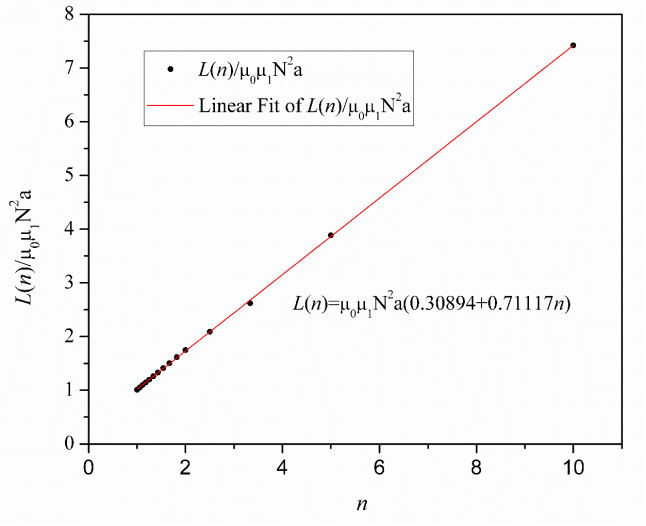

FIG.4 Secondary inductance varies with the number of magnetic cores

D. Marx Generator

Since the usage of FRSPT, there is a positive pre-pulse at the beginning of the output pulse. In order to improve this situation, two 60kV 500mA rated diodes in parallel are used instead of a traditional inductor in the Marx circuit. And the circuit consists of diodes and a 350pF ceramic capacitor together with a group of secondary windings. For the secondary windings are on the same cores, the 6-stage Marx operates synchronously and promotes the step-up ratio further. However, compared with a spark gap the closing time of the magnetic switch is approximately 150ns.Since the energy stored in capacitors is losing during the switching time, the step-up ratio of this Marx generator is lower than that of a circuit with great synchronous spark gaps [10]. Some output pulses of different stages in Marx are shown in FIG.5 and they are all recorded on a LeCroy 44MXs-B Digitizing Oscilloscope. The charging voltage of 1st-stage Marx measured at point X in FIG.1 is 14.91kV with the magnetic switch closing time of about 170ns, and the 1-stage Marx voltage measured at point Y in FIG.1 is 13.6kV. Hence, the final output pulse is only 5.24 times of charging voltage as analysis above, in the meanwhile the FRSPT step-up ratio is 29.82. The rise time (10%-90%) is 141ns which is mainly influenced by closing time and secondary saturated inductance. So, the mothed to decrease the saturated inductance and improve the performance of the magnetic core remains to be found.

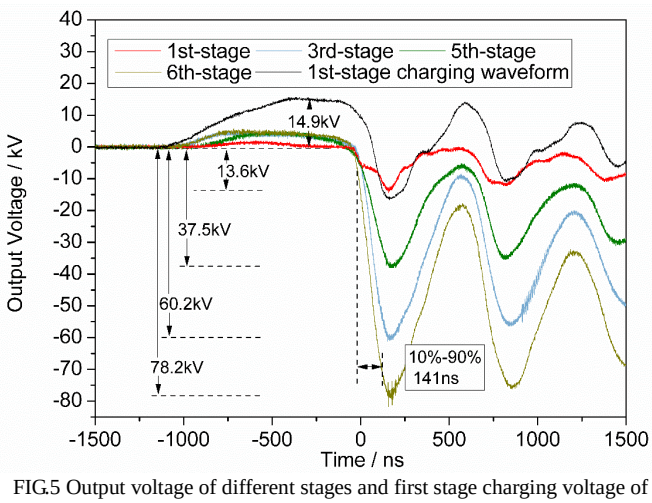

FIG.5 Output voltage of different stages and first stage charging voltage of Marx

E. Compact Design

An experimental device is fabricated with compact spatial structure and its photograph is shown in FIG.6. The whole is divided into three parts as described above. Because the distance between different components is very close, to prevent undesired sparks, the whole device is placed in an insulated box filled with insulating oil. Thin plastic films are used wrapping capacitors for a larger dielectric strength [11]. And the measured secondary inductance of FRSPT is 1.09mH. The boundary dimension is length of 36cm, width of 24cm and height of 23cm.

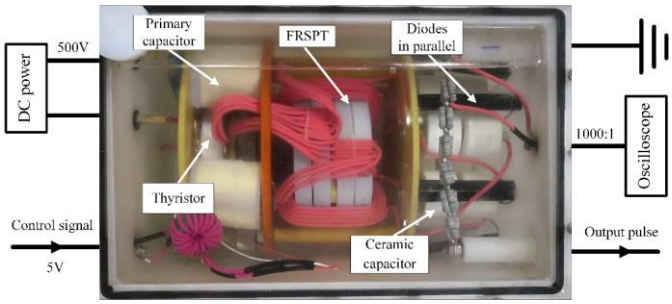

FIG.6 Photograph of the trigger generator

III. EXPERIMENTAL RESULTS

The following results were obtained by the testing device in FIG.6. The initial repetition signals were generated by computer and controlled the thyristor operating repetitiously. In this process it was important to keep the voltage of the primary constant at 500V. The magnetic cores might be unsaturated with a lower voltage and it resulted a waveform distortion and instability of the output pulse. For a high repetition frequency(>100Hz), the energy recovery circuit is essential. However, since there is a main problem on available magnetic cores. Their mode conversion speed restricts the device operating at low repetition frequency, for higher stability and longer lifetime, the energy recovery circuit is rather excess for a practical compact device operating at 10Hz-50Hz. The device introduced above achieved to operate at 10Hz which was needed by the main spark gap of IEBA. As shown in FIG.7, it was 50 output pulses and control signal superposed at 10Hz. The maximum output voltage measured at point Z was 79.6kV while the minimum was 74.9kV with rise time of 141ns. In this paper, time delay (t_d) was counted from rising edge of the control signal to 10% of the peak of output voltage and its measured value was 36.88μs. To evaluate the stability of a repetition frequency process, jitter (σ_j) of t_d is an important parameter, it writes

$$\sigma_j = \sqrt{\frac{1}{N}\sum_{i=1}^{N}(t_{di} - \overline{t_d})^2}$$

$$\overline{t_d} = \frac{1}{N}\sum_{i=1}^{N} t_{di}$$

in witch, N is 50 which meant 50 pulses composed a series of data and t_{di} was each part of t_d measured from each oscillogram of output pulse. And then the calculated jitter in FIG.7 was 0.67ns. The time range of 50 output pulses was 2.9ns and it was smaller of control signals since the oscilloscope was triggered by the control signals. In actual experiments, the spark gap[12] had a low requirements for trigger signal and triggered at 50kV approximately. Therefore, the main factor affected the switch stability is the jitter of the trigger, the oscillation behavior and the dropping edge had little influence on the stability

A three-minute continuous repetitive experiment was operated on the device at 10Hz. The relationship between jitter and operation time was shown in FIG.8. The jitter varied from 0.64ns to 3.03ns for each 50 pulses. A longer

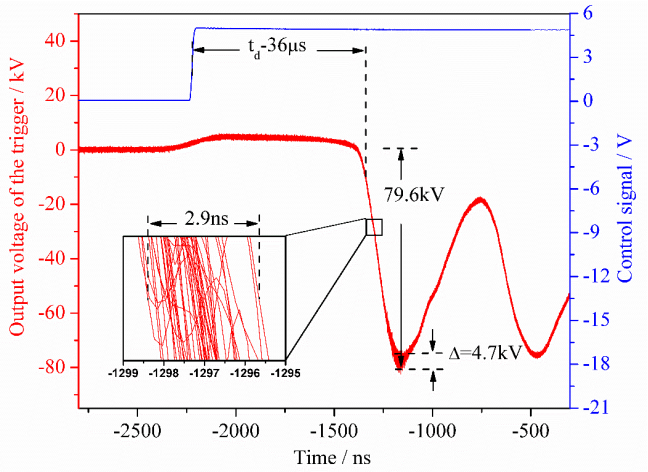

FIG.7 Superposed oscillogram of 50 output pulses and control signals at 10Hz

time operation was attempted and the stability of the device dropped a little as the operation time increased, and there was a little distortion at the wave tail on several pulses when operated for a longer time. Besides, the magnetic cores needed several minutes to resume between two long-time operations. As it is shown above, the trigger generation was reliable for a rising edge triggered spark gap which is always employed in IEBA.

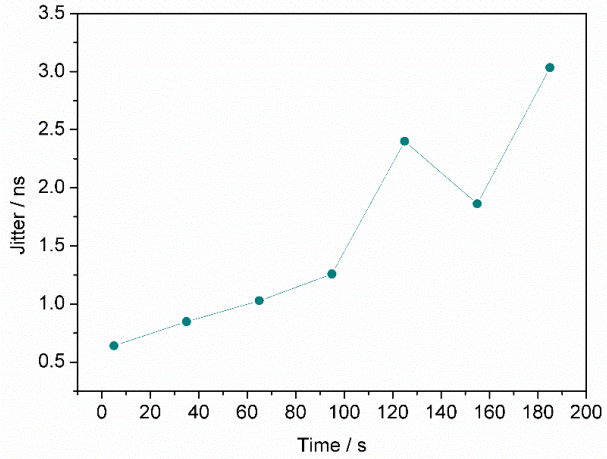

FIG.8 Effect of operation time on jitter (every point calculated by 50 repetitive pulses)

IV. CONCLUSION

The design of a high step-up ratio, compact and low jitter trigger generator is introduced in this paper. And the effect on step-up ratio and secondary inductor of magnetic core number has been demonstrated. Based on the consideration of rise time and step-up ratio of the trigger pulse, two pieces of magnetic cores were selected There is a high couple efficiency in FRSPT, and with the employment of compact

Marx circuit the trigger generator is able to operate in low charging voltage. A testing device was fabricated for a further experiment, as the results showed, a 79.6kV pulse with rise time of 141ns is generated. And it has been demonstrated that the trigger operated reliably at 10Hz for three minutes or even more. At present, it has been successfully applied to an IEBA for long time operation due to its eminently stability, compact structure and long lifetime. Future goals include increasing the step-up voltage ratio and the operation frequency. Besides, higher performance magnetic cores are desired for a longer lifetime and faster switching time.

ACKNOWLEDGMENT

This work was supported by National Natural Science Foundations of China under Grant No. 51707198 and No. 51641707. The authors wish to thank Xiang Zhou, Jianchun Wen and Min Zhu for their assistance to the experiment.

REFERENCES

[1] Kekez M M. Simple sub‐50‐ps rise‐time high voltage generator[J]. Review of Scientific Instruments, 1991, 62(12):2923-2930.

[2] Ding W, Wang Y, Fan C, et al. A Subnanosecond Jitter Trigger Generator Utilizing Trigatron Switch and Avalanche Transistor Circuit[J]. IEEE Transactions on Plasma Science, 2015, 43(4):1054-1062.

[3] Barnett D H, Parson J M, Lynn C F, et al. Optically isolated, 2 kHz repetition rate, 4 kV solid-state pulse trigger generator. [J]. Review of Scientific Instruments, 2015, 86(3):034702.

[4] Chaney A, Sundararajan R. Simple MOSFET-based high-voltage nanosecond pulse circuit[J]. IEEE Transactions on Plasma Science, 2004, 32(5):1919-1924.

[5] Kim J H, Ryu M H, Min B D, et al. High voltage pulse power supply using Marx generator & solid-state switches[C]// Industrial Electronics Society, 2005. IECON 2005. Conference of IEEE. IEEE, 2005:4 pp.

[6] Ding W, Wang Y, Fan C, et al. A Subnanosecond Jitter Trigger Generator Utilizing Trigatron Switch and Avalanche Transistor Circuit[J]. IEEE Transactions on Plasma Science, 2015, 43(4):1054-1062.

[7] Zhang Y, Liu J. Physical suppression effects of the reversed magnetic coupling on the saturation inductance of saturable pulse transformer[J]. Applied Physics Letters, 2013, 102(25):335.

[8] Chen R, Yang J, Cheng X, et al. Research of a fractional-turn ratio saturable pulse transformer and its application in a microsecond-range pulse modulator[J]. Plasma Science and Technology, 2017, 19(6):95-101.

[9] Grover F W. Inductance Calculations[J]. Nature, 2012, 586:59-73.

[10] Sharma A, Kumar S, Mitra S, et al. Development and Characterization of Repetitive 1-kJ Marx-Generator-Driven Reflex Triode System for High-Power Microwave Generation[J]. IEEE Transactions on Plasma Science, 2011, 39(5):1262-1267.

[11] Gaudet J A, Barker R J, Buchenauer C J, et al. Research issues in developing compact pulsed power for high peak power applications on mobile platforms[J]. Proceedings of the IEEE, 2004, 92(7):1144-1165. G. Eason, B. Noble, and I. N. Sneddon, “On certain integrals of Lipschitz-Hankel type involving products of Bessel functions,” Phil. Trans. Roy. Soc. London, vol. A247, pp. 529–551, April 1955.

[12] Geng J , Yang J , Cheng X , et al. The development of high-voltage repetitive low-jitter corona stabilized triggered switch[J]. Review of Scientific Instruments, 2018, 89(4):044705.

Using Modelling Software to Predict HEMP Filter Circuits that Meet PCI Requirements

John Lindsay
Design Engineer
MPE Limited
Liverpool, UK
JLindsay@mpe.co.uk

David Rimmer
Design Engineer
MPE Limited
Liverpool, UK
DRimmer@mpe.co.uk

***Abstract*— This paper describes the design process of filters for use in high-altitude electromagnetic pulse (HEMP) protection of power line points of entry (POE) on a shielded facility. This process was applied to different EMP standards, each with their own levels of facility hardening, to develop the most compact and cost-effective filter for that application. New results from pulse current injection (PCI) tests on a filter with a short circuit load are presented.**

Keywords—HEMP, filter, pulse current injection

I. DESIGN PROCESS

Early EMP filter designs were generally adapted EMI filters fitted with input delay lines and high-energy transient suppressors at the front end to provide pulse protection in accordance with NATO specifications [1]. The introduction of MIL-STD-188-125 [2] established a more dedicated PCI test requirement for HEMP protection of C^4I facilities conducting critical, time-urgent missions. The standard defines Acceptance testing of a HEMP power filter as a measure to demonstrate the performance of the protective device. It must reduce a well-defined early-time (E1) double exponential waveform pulse to less than a 10 A residual current and also be capable of tolerating the higher energy intermediate-time (E2) pulse, both without any degradation of the filter.

New filter circuits in the style of Figure 1 were designed from first principles to meet the PCI requirements rather than EMI attenuation. Core to this design process was the use of PSpice circuit modelling software, this simulated the pulse generator and filter components in order to achieve the necessary residual performance. The type of transient suppressor along with the inductive and capacitive filter component values were all varied in numerous permutations to find the best integrated solution. Circuits rated for a range of currents from 6 A up to 1200 A were built and then tested at an independent test laboratory. The peak let-through current was measured along with the rise time and root integral (energy content) of the residual pulse. The insertion loss of the filters and varistor parameters were measured before and after to check the circuits had not suffered degradation. Analysis of the measured results gave good correlation with computer simulation. This design approach produced superior residual currents compared to earlier modified EMI filters.

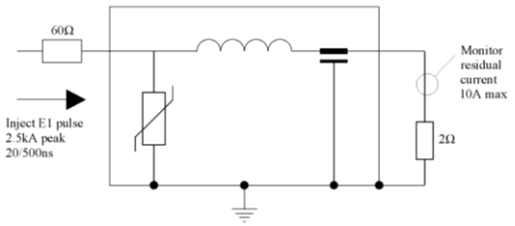

Fig. 1. Example of a simplified HEMP filter circuit.

II. LOWER REQUIREMENTS

Another international standard, IEC 61000-4-24 [3] describes test criteria for HEMP protection filters used in hardening important commercial sites, such as data centers and utility infrastructure. This is also particularly useful for applications were full protection is not warranted. The established design process was used to develop a range of power filters to meet the requirements of this standard. It uses the same E1 and E2 pulse defined in MIL-STD-188-125 meaning the same pulser could be used to evaluate the filter circuits. With a higher residual current limit of 50 A for Severity Level 2, the filter designs are much smaller, lighter and cheaper than standard HEMP filters.

III. A SHORT-CIRCUIT LOAD

MIL-STD-188-125 also defines Verification testing in order to determine the operational performance of the facility hardening. The protected circuit is now powered with the filter in situ. The load impedance will be dependent on the equipment being protected and characteristics of the specific installation. The difference between the Verification load impedance and the Acceptance 2 Ω resistive load can have a large effect on the residual current. A potential problem is introduced where a filter could pass Acceptance test, yet fail Verification test upon installation. In an attempt to understand the filter performance under worst-case conditions the circuit was modelled with a short-circuit to ground on the load. The simulated result predicted that the residual current of an existing filter was now failing at 85 A. Failure was confirmed during independent laboratory tests. This filter had previously been tested and provided a residual current of 4 A with a 2 Ω load.

It was clear that the existing filter circuit was not suitable. Now the same PSpice design process was needed to develop a new circuit, in order to meet the residual current limit with a short-circuit on the load. An extra inductive component was inserted on the load side after the capacitive element and facing the short-circuit. A prototype filter was built and then tested by an independent laboratory and found to successfully meet the residual current limit.

REFERENCES

[1] NATO 2202.2.5/SHORC/C-83:1985

[2] MIL-STD-188-125-1 7 April 2005 “High-Altitude Electromagnetic Pulse (HEMP) Protection for Ground Based C4I Facilities Performing Critical, Time-Urgent Missions, Part 1 Fixed Facilities”.

[3] IEC 61000-4-24:2015 “Testing and Measurement Techniques – Test Methods for Protected Devices for HEMP Conductive Disturbance”.

Covert Information Embedding in Remote Targets with HPEM

José Lopes Esteves
Wireless Security Lab
National Security Agency of France
(ANSSI)
Paris, France
jose.lopes-esteves@ssi.gouv.fr

Emmanuel Cottais
Wireless Security Lab
National Security Agency of France
(ANSSI)
Paris, France
emmanuel.cottais@ssi.gouv.fr

***Abstract*—In this paper we explore the idea of using some specific effects of HPEM on electronic systems in order to store information remotely and covertly into a non cooperating target. As pointed out by previous studies, some effects have an impact which spreads to the software (logical) layer. Such impact can be further cascading towards a modification of a logical state of the target, resulting in a storage channel. An example of application of such technique has been implemented on a civilian UAV, which has shown to fit particularly well for such so-called electromagnetic watermarking. Indeed, it provides an interesting alternative to complete neutralization as a defense against intruding UAVs.**

Keywords—HPEM, IEMI, electromagnetic watermarking, security, UAV

I. Introduction

For several decades, the effects of high power electromagnetic (HPEM) [1] on electronic devices and complex electronic systems have been studied [2-8], mostly for the characterization of mission critical effects for both designing offensive and defensive strategies. The exploitability of the effects and their consideration in risk analysis has also been investigated, both from a functional safety [9] and an information security [10-13] perspective. In this study, a novel HPEM effect exploitation technique is investigated. It is proposed to focus on effects which have a logical impact on the target system and which impact is somehow stored by the target. The exploitation of this kind of effects opens the way to embedding information into the target. As a proof of concept, this technique is applied to an unmanned aerial vehicle (UAV) as a way to insert a mark allowing an a posteriori proof of its presence during an incident, in the case neutralization techniques failed or could not be used.

II. HPEM Effects and Logical Storage

A classification of the HPEM effects on electronic devices based on their duration has been proposed and improved in [4-5] as summarized in Table 1. Moreover, several studies have pointed out the fact that some effects have an impact at the software level which can be caused by bit-flips [5, 12], which can be detected by software agents that monitor impacted logical observables [13, 14]. When effects from categories (E) and (T) lead to logical impacts that can be observed by a piece of software, it becomes possible to take advantage of IEMI effects to create a unidirectional physical covert communication channel [15].

TABLE I. Classification of EM Effects by Duration [5]

Category	Duration
U	Unknown
E	Exposure only
T	Some follow up time after exposure
H	Until human intervention
P	Permanent until replacement of HW/SW

This makes effects from those categories more adapted to a covert channel establishment. Effects from category (H) allow sending one piece of information per human intervention and effects from category (P) allow sending one piece of information only once. Thus, communication channels exploiting effects from those categories will have a very restrained channel capacity.

If the logical repercussion of an effect directly or indirectly alters the state of the target, then it can be exploited as a storage channel. Effects from category (P) can lead to a permanent write once storage. As for effects from the other categories, sometimes the effect occurrence is logically stored in the target electronic systems (e.g. in the operating system logs) [14].

III. Electromagnetic Watermarking

Electromagnetic watermarking (EMW) can be defined as the process of exploiting both HPEM based covert communication channel and storage channel in order to introduce (to store) a piece of information (the watermark) into a non cooperating electronic target. This piece of information can then be detected and extracted in order to at least determine that the target has been in contact with the EMW environment. The watermark capacity defines the data storage rate and depends on the effect category, the effect appearance time and the storage process.

IV. First Results on an UAV

Hereafter the application of electromagnetic watermarking to an unmanned aerial vehicle is proposed. To this aim, the target was put in specific EM environments during the tests and the flight logs were analyzed afterwards in order to identify stored logical impacts.

The EM immunity of UAVs has been investigated in the context of emergency operations [16] focusing on close proximity of radio transmitters and radars [17, 18]. The effects observation was focused on the behavior of the RF links of the UAVs during parasitic illumination. HPEM effects on UAVs have also been reported, affecting the motors and the RF links [19, 20], embedded communication links and sensors from the inertial measurement unit [21, 22].

Civilian UAVs are usually designed for relatively short flight durations (around 25 minutes) [23, 24] and can enclose a high frequency logging system. The logging rates range from 600~Hz to tens of MHz depending on the model [25] and it is common to find raw sensor readings and information about the drone's attitude and position [26].

An effect impacting the value called “accel:z” in the flight logs has been identified. This value seems to be sampled in the logs at a frequency of nearly 250 Hz (according to the timestamps in the log file).

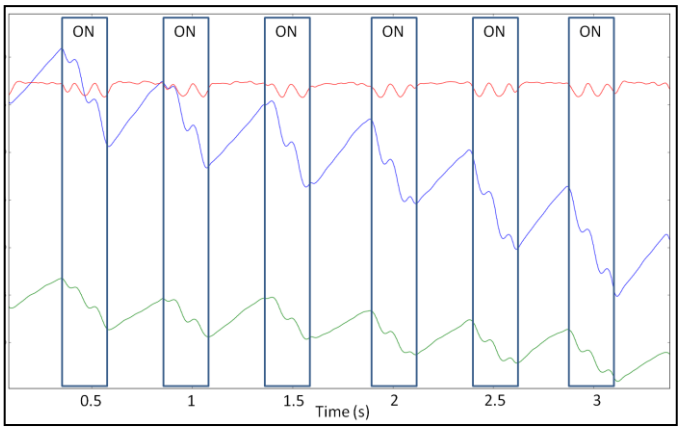

Fig. 1. Effects on the vertical acceleration measurement (red), the pitch (blue) and the roll (green), when the EM source is on and off, as extracted from the flight logs.

The effect results in the appearance of a 15 Hz sinusoidal offset on the actual vertical acceleration value, as shown in Fig. 1. Simultaneously, the roll and pitch angle values are also affected and the 15 Hz component is also present. Those category (E) effects appear as soon as the signal source is switched on. Thus, an on-off keying NRZ encoding can be considered as a storage format. A pulse duration based modulation can also be envisioned. The presence of the carrier signal in several observable values allows for a robust detection and extraction of the embedded information.

V. Conclusion

In this study, it was demonstrated the possibility of embedding information remotely into non cooperative electronic devices by using HPEM. More precisely, the exploitation of category (E) and (T) effects impacting the logical layer in such a way that a non volatile logical state change occurs can be exploited as a covert remote storage channel, resulting in what we call an electromagnetic watermarking system. The applicability of such technique has been demonstrated on a civilian UAV. It is a promising application context as UAVs enclose a lot of sensors and log a lot of information at high frequency. An electromagnetic watermarking system could then be an interesting alternative or complement to existing electromagnetic based UAV neutralization techniques, allowing for the insertion of a watermark proving the exposure of the target to the specific electromagnetic environment generated during the incident response.

References

[1] W. A. Radasky, C. E. Baum and M. W. Wik, “Introduction to the special issue on high-power electromagnetics and intentional electromagnetic interference,” Electromagnetic Compatibility, IEEE Transactions on, vol.46, no. 3, pp. 314-321, Aug. 2004.

[2] [2] J. Mirschberger, F. Sonnemann, J. Urban and R. H. Stark, “High-Power Electromagnetic effects on Distributed and Automotive CAN-bus systems”, In Proc. of EUROEM 2012, pp. 85, July, 2012

[3] M. G. Bäckström and K. G. Lövstrand, “Susceptibility of electronic systems to high-power microwaves: Summary of test experience,” IEEE Transactions on Electromagnetic Compatibility, vol. 46, no. 3, 2004.

[4] F. Sabath and D. Nietsch, “Electromagnetic Effects on Systems and Components,” in *American Electromagnetics International Symposium AMEREM 2006*, Santa Barbara, CA, USA, 2006.

[5] F. Sabath, “Classification of electromagnetic effects at system level,” in *2008 International Symposium on Electromagnetic Compatibility - EMC Europe*, 2008, pp. 1–5.

[6] Y. V. Parfenov, W. A. Radasky, B. A. Titov, L. N. Zdoukov, “Some Features of the Pulse Electrical Disturbances Influence on Digital Devices Functioning,” *URSI General Assembly*, August 2014, doi: 10.1109/URSIGASS.2014.6929514.

[7] M. Kreitlow, F. Sabath, and H. Garbe, “A test method for analysing disturbed ethernet data streams,” *Advances in Radio Science 13 (2015)*, vol. 13, pp. 149–153, 2015.

[8] M. Kreitlow, F. Sabath, and H. Garbe, “Analysis of IEMI effects on a computer network in a realistic environment,” in *2015 IEEE International Symposium on Electromagnetic Compatibility (EMC)*, 2015, pp. 1063–1067.

[9] K. Armstrong, “How to Do EM Functional Safety – the Latest Guidance From the IET”, Special Session on EM Functional Safety, APEMC 2016, Shenzhen, China, May 18-21 2016.

[10] A. Kreth, O. Doering. E. Genender and H. Garbe, “Predetection for the identification of electromagnetic attacks against airports”, In Proc. of EUROEM 2012, pp. 81, July, 2012.

[11] R. Hoad, L. Sutherland, “The Forensic Utility of Detecting Disruptive Electromagnetic Interference”, In Proc. of the 6th European Conference on I-Warfare and Security, pp. 77-87, July, 2007.

[12] C. Kasmi and J. Lopes Esteves, “IEMI threats for information security: Remote command injection on modern smartphones,” *IEEE Transactions on Electromagnetic Compatibility*, vol. 57, no. 6, pp. 1752–1755, 2015.

[13] J. Lopes Esteves, C. Kasmi, A. Degraeve, D. Pissoort, and K. Armstrong, “Analysis of Effects induced by EM disturbances on COTS Devices, from an EM Security and Functional Safety perspective,” in Developments in System Safety Engineering - Proceedings of the Twenty-fifth Safety-Critical Systems Symposium, Bristol, UK, 2017, pp. 313–324.

[14] C. Kasmi et al., “Event logs generated by an operating system running on a COTS computer during IEMI exposure,” IEEE Transactions on Electromagnetic Compatibility, vol. 56, no. 6, pp. 1723–1726, 2014.

[15] C. Kasmi, J. Lopes Esteves, and P. Valembois, “Air-gap Limitations and Bypass Techniques:‘Command and Control’ using Smart Electromagnetic Interferences,” *The Journal on Cybercrime & Digital Investigations*, vol. 1, no. 1, pp. 13–19, Jan. 2016.

[16] C. Adami, S. Chmel, M. Jöster, T. Pusch., and M. Suhrke, “Definition and Test of the Electromagnetic Immunity of UAS for First Responders,” *Adv. Radio Science*, **13**, 3, November 2015, pp. 141-147, doi: 10.5194/ars-13-141-2015.

[17] L. Torrero, P. Mollo, A. Molino, and A. Perotti, “RF immunity testing of an Unmanned Aerial Vehicle platform under strong EM field conditions,” in Antennas and Propagation (EuCAP), 2013 7th European Conference on, pp. 263–267, 2013.

[18] Z. Tao, C. Yazhou, and C. Erwei, “Continuous wave radiation effects on UAV data link system in 2013 Cross Strait Quad-Regional Radio Science and Wireless Technology Conference , pp. 321–324, 2013.

[19] Q. Zhijun, P. Xuchao, H. Yong, C. Hong, S. Jie, Y. Cheng, "Damage of high power electromagnetic pulse to unmanned aerial vehicles," High Power Laser and Particle Beams, vol. 29, no. 11, November 2017, doi: 10.11884/HPLPB201729.170216.

[20] K. Sakharov, A. Sukhov, V. Ugolev, and Y. Gurevich, "Study of UWB Electromagnetic Pulse Impact on Commercial Unmanned Aerial Vehicle," in *2018 International Symposium on Electromagnetic Compatibility (EMC Europe 2018)*, Amsterdam, Netherland, 2018.

[21] J. Lopes Esteves, E. Cottais, and C. Kasmi, "Analysis of HPEM perturbations induced on the navigation system of a UAV," in *American Electromagnetics International Symposium AMEREM 2018*, Santa Barbara, CA, USA, 2018.

[22] J. Lopes Esteves, E. Cottais, and C. Kasmi, "Software Instrumentation of an Unmanned Aerial Vehicle for HPEM Effects Detection," in *Radio Science Conference (URSI AT-RASC), 2018 2nd URSI Atlantic*, Las Palmas, Spain, 2018.

[23] DJI, "Mavic Air Specifications." Online: https://www.dji.com/fr/mavic-air/info#specs, Accessed on 01/03/2019.

[24] Parrot, "Parrot ANAFI Specifications." Online : https://www.parrot.com/fr/drones/anafi, Accessed on 01/03/2019. .

[25] DatCon, DJI DAT File parsing Tool, Online: https://datfile.net, Accessed on 01/03/2019.

[26] D. R. Clark, C. Meffert, I. Baggili, and F. Breitinger, "DROP (DRone Open source Parser) your drone: Forensic analysis of the DJI Phantom III," Digital Investigation, vol. 22, pp. S3–S14, 2017

Singularity Expansion Method for Thin Wires with the Full-Wave Transmission Line Theory

Juergen B. Nitsch
Chair of Electromagnetic Compatibility
Otto von Guericke University
Magdeburg, Germany
juegen.nitsch@ovgu.de

Sergey V. Tkachenko
Chair of Electromagnetic Compatibility
Otto von Guericke University
Magdeburg, Germany
sergey.tkachenko@ovgu.de

Felix Middelstaedt
Chair of Electromagnetic Compatibility
Otto von Guericke University
Magdeburg, Germany
felix.middelstaedt@ovgu.de

Ralf Vick
Chair of Electromagnetic Compatibility
Otto von Guericke University
Magdeburg, Germany
ralf.vick@ovgu.de

***Abstract*—The Full-Wave Transmission Line Theory developed earlier as a generalization of Classical Transmission Line Approximation for arbitrary frequencies and geometry of the transmission line is applied for the Singularity Expansion Method (SEM) analysis of loaded thin-wire structures. A general equation for the SEM poles is derived. The comparison with earlier obtained results for canonical structures shows an excellent agreement.**

Keywords—Thin wire, Singularity Expansion Method, Full-Wave Transmission Line Theory

I. Introduction

The investigation of the coupling of high-frequency electromagnetic fields with different wiring structures is one of the main problems in electromagnetic compatibility. Different direct numerical methods, as MoM, Method of Finite Elements, etc. allow to consider specific cases but do not give a full physical picture of such interaction and require timely computer calculations. The analytical Singularity Expansion Method (SEM) allows to obtain the analytical results much faster and in practical form.

The Singularity Expansion Method (SEM) was first introduced by Baum in 1971 in an US Air Force note series [1]. It was later thoroughly documented in a book chapter by Baum and has been discussed in a large number of other publications. The method was developed further by Tesche, Giri [2,3] and other researches. The modern description of the method is given in [4]. The essential point of the SEM analysis for antennas or scatterers is that the behavior of the induced current on the structure in the frequency domain can be represented by a sum of terms involving the natural resonances of the structure and the corresponding current modes. This is similar to the representation of the response of a conventional circuit using a pole-residue analysis. When the SEM poles are known it is easy to transform the response from frequency into the time domain.

There are several different methods to calculate the complex natural frequencies of a straight wire or scatterer. Up to now, the most exact method for a wire of arbitrary geometric form is the numerical solution of the integral equation for the current along the conductor [5] and subsequent extraction of roots from a response function [6,7]. Since this solution procedure is quite complicated many other approximations have been developed and applied in the past. They deal with geometrically simple structures, as a straight wire in free space (see review in [8], [23] and [9]) and a circular loop [10]. The more complex structures: long transmission lines above a ground, which can have terminal parts with arbitrary geometry and arbitrary loads were considered in [13-15] by using hybrid asymptotical approach [11-12].

In this paper we present an analytic approximation for the SEM poles of the loaded wire of arbitrary geometrical form, using the Full-Wave Transmission line Theory (FWTL). The presented investigations in this paper are new and quite different from known results.

II. Methods and Results

The Full Wave Transmission Line Theory [16-21] is a generalization of the classical Transmission Line approximation [5,12] for the loaded line of arbitrary geometrical form, which can be excited by lumped terminal sources with arbitrary frequencies (see Fig. 1).

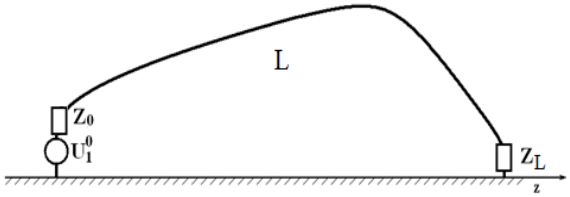

Fig. 1 Sketch of the loaded thin-wire system of arbitrary geometric form excited by a lumped source.

The equations of FWTL (1) describe the current and scalar potential along the wire in dependence of its length. They are derived from the Mixed Potential Integral Equations for such wire system, which, in turn is derived directly from Maxwell equations.

$$\frac{d}{dl}\begin{pmatrix}\varphi(l)\\ I(l)\end{pmatrix}+ j\omega\mathbf{P}(j\omega,l)\cdot\begin{pmatrix}\varphi(l)\\ I(l)\end{pmatrix}=0 \qquad (1)$$

The parameter matrix $\mathbf{P}(j\omega,l)$, in contrast to the case of Classical Transmission Line Approximation (CTLA), is complex-valued, length dependent and contains diagonal elements. It is a functional of the geometry of the system. For low frequencies, when the wavelength is greater than the transverse size of the line, it coincides with the CTLA parameters matrix with zero-valued diagonal elements and the per-unit-length inductance and capacitance, as off-diagonal elements. For higher frequencies the non-classical

elements of the parameter matrix (diagonal elements and imaginary pars of off-diagonal elements) define the radiation of the system. The parameter matrix can be found by using different kinds of perturbation theory ([16-18] or [19-21]), which yield good results even in the lowest orders.

The solution of the system (1) with given boundary conditions $\varphi(0)=\varphi_0$, $I(0)=I_0$ (a Cauchy problem) can be obtained by using the matrizant $\mathbf{M}(l,l_0)$ [22], which is a fundamental matrix of a system of homogeneous linear ordinary differential equations normalized in the initial point l_0 : $\mathbf{M}(l_0,l_0)=\mathbf{E}$. To obtain the matrizant, which is a functional of the geometry of the line one can use , e.g., the technique of product integral [22,16,17,21].

$$\begin{pmatrix}\varphi(l)\\ I(l)\end{pmatrix}=\mathbf{M}(l,0)\cdot\begin{pmatrix}\varphi(0)\\ I(0)\end{pmatrix} \qquad (2)$$

Then, one can obtain the solution of the boundary value problem for the system (1) for the loaded line, with lumped excitation U_0 , e.g., at the left terminal, which correspond to the boundary conditions:

$$\varphi(0)=U_0-Z_0I(0) \quad \text{and} \quad \varphi(L)=Z_LI(L) \qquad (3)$$

Taking into account (2) and (3) after some re-arrangement it is possible to obtain equations for the terminal currents $I(0)$, $I(L)$ (4), which, together with (2) and (3a) yield the current and potential in any point of the line.

$$\begin{pmatrix}M_{11}(L,0)Z_0-M_{12}(L,0) & Z_L\\ M_{21}(L,0)Z_0-M_{22}(L,0) & 1\end{pmatrix}\cdot\begin{pmatrix}I(0)\\ I(L)\end{pmatrix}=\begin{pmatrix}M_{11}(L,0)\\ M_{21}(L,0)\end{pmatrix}\cdot U_0 \qquad (4)$$

The condition of nontrivial solution of (4), if $U_0=0$, is

$$\det\begin{pmatrix}M_{11}(L,0)Z_0-M_{12}(L,0) & Z_L\\ M_{21}(L,0)Z_0-M_{22}(L,0) & 1\end{pmatrix}=0 \qquad (5)$$

which gives the basic equation for the determination of the SEM poles, where the matrizant depends on the frequency and geometry of the wire.

$$\begin{aligned}&-M_{12}(L,0)+M_{11}(L,0)Z_0+\\ &M_{22}(L,0)Z_L-M_{21}(L,0)Z_0Z_L=0\end{aligned} \qquad (6)$$

Note that since the SEM poles are an internal property of the wire and are determined only by its geometry and loads, they do not depend on the excitation method: a lumped source, a plane wave, etc. Thus, equation (6) is of a general nature.

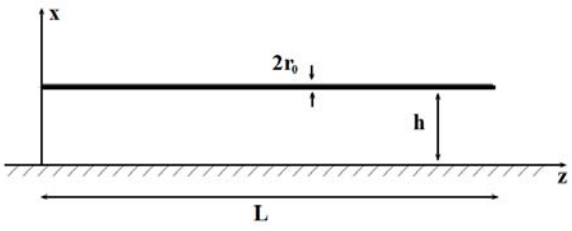

Fig. 2 Sketch of the open-circuit horizontal line.

The comparison of the SEM poles of the first layer for two simple examples of the horizontal open-circuited line [13]

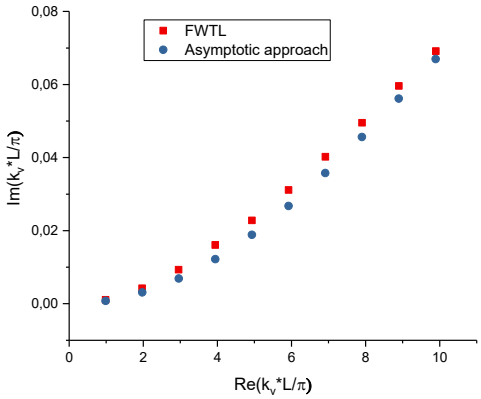

Fig. 3 SEM poles for the horizontal open-circuited wire calculated by the asymptotic approach and FWTL. Parameters of the wire: r_0=1mm, h=0.5m, L=10 m.

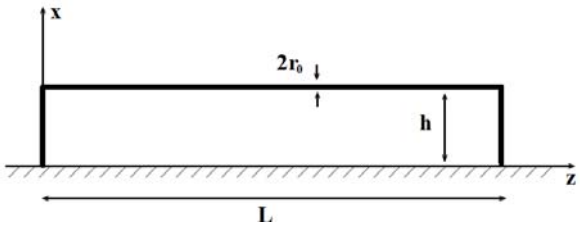

Fig. 4 Sketch of the short-circuit horizontal line with vertical risers.

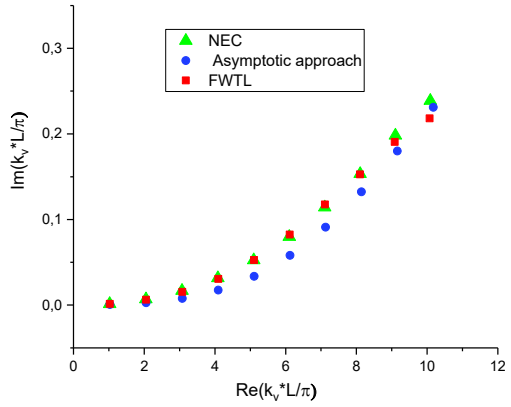

Fig. 5 SEM poles for the horizontal short-circuited wire with vertical risers calculated by NEC, the asymptotic approach and FWTL. Parameters of the wire: r_0=1cm, h=0.5m, L=10 m.

TABLE 1 SEM POLES FOR THE HORIZONTAL OPEN-CIRCUIT WIRE

Method	**FWTL**		**Asymptotic approach [13]**	
N	$\mathrm{Re}(k_v\cdot L/\pi)$	$\mathrm{Im}(k_v\cdot L/\pi)$	$\mathrm{Re}(k_v\cdot L/\pi)$	$\mathrm{Im}(k_v\cdot L/\pi)$
1	0,9847	0.00107	0,985	$7.75\cdot10^{-4}$
2	1,9700	0,00421	1,971	0,00309
3	2,9558	0,00932	2,95	0,0069
4	3,9429	0,0161	3,94	0,0122
5	4,9323	0,0228	4,938	0,0188
6	5,9224	0,0311	5,92	0,0267
7	6,9137	0,0402	6,91	0,0357

8	7,9066	0,0495	7,90	0,0456
9	8,9006	0,0596	8,89	0,0561
10	9,8964	0,0691	9,89	0,0669

TABLE 2 SEM POLES FOR THE HORIZONTAL SHORT-CIRCUIT WIRE WITH VERTICAL RISERS

	FWTL		**Asymptotic approach [15,24]**		**NEC [15,24]**	
N	$Re(k_vL/\pi)$	$Im(k_vL/\pi)$	$Re(k_vL/\pi)$	$Im(k_vL/\pi)$	$Re(k_vL/\pi)$	$Im(k_vL/\pi)$
1	1.0261	0.0015	1.027	$7.0\cdot10^{-4}$	1.0238	0.0014
2	2.0516	0,0064	2.053	0.0028	2.0462	0.007
3	3,.0747	0.01542	3.074	0.0077	3.0665	0.0168
4	4.0947	0.03065	4.093	0.0175	4.0833	0.0315
5	5.1051	0.05267	5.107	0.0336	5.0959	0.0525
6	6.1136	0.08251	6.1204	0.0581	6.1036	0.0798
7	7.1105	0.1176	7.1316	0.0910	7.1071	0.1141
8	8.1033	0.1526	8.1435	0.1323	8.1057	0.1533
9	9.0835	0.1906	9.1582	0.1799	9.1043	0.1981
10	10.071	0.2182	10.176	0.2310	10.090	0.2388

and horizontal short-circuited line with vertical risers [15, 24], obtained by the NEC, solution of (6 a,b) and by the asymptotic approach [12] is shown in Fig. 3 and Fig. 5 and in Tables 1 and 2. One can observe a good agreement.

III. CONCLUSION

The general equation for the SEM poles of thin-wire line of arbitrary geometric form was obtained by the using of earlier developed Full-Wave Transmission Line Theory. The numerical examples have shown a good agreement with earlier obtained results. The method can be easily generalized for the case of multiconductor transmission lines [21].

REFERENCES

[1] C. E. Baum, "On the singularity expansion method for the solution of electromagnetic interaction problems," Air Force Weapons Laboratory, Kirtland Air Force Base, Albuquerque, NM, USA, *Interaction Note* Note **88**, Dec. 1971. [Online]. Available: http://eceresearch.unm.edu/summa/notes/In/0088.pdf.

[2] F.M. Tesche, "On the Analysis of Scattering and Antenna Problems Using the Singularity Expansion Technique", IEEE Transactions on Antennas and Propagation, vol. **AP-21**,No.1, January 1973.

[2] D.V.Giri, F.M.Tesche, "On the Use of Singularity Expansion Method for Analysis of Antennas in Conducting Media", *Electromagnetics* vol. **1**, Nr. 4, pp.455-471, 1981.

[4] C.E.Baum, *The Singularity Expansion Method in Electromagnetics*, Edited by D.V.Giri and F.M. Tesche, Lulu Enterprices, 2012.

[5] F.M. Tesche, M.V. Ianoz, T. Karlsson, *EMC Analytical Methods and Computational Model*s, Willey&Son, 1997, Chapter 4.5.

[6] B.K.Singaraju, D.V.Giri and C.E. Baum, "Further Development in the Application of Contour Integration to the Evaluation of the Zeros of Analytic Functions and Relevant Computer Programs", *Mathematical Note*s, Note 42, March 1976. Available at http://ece-research.unm.edu/summa/notes/Mathematics/0042.pdf.

[7] T.B.A. Senior and J.M. Pond, "Pole Extraction in the Frequency Domain", *Interaction Note*, **411**, December 1981. Available at http://ece-research.unm.edu/summa/notes/In/0411.pdf.

[8] F.M. Tesche and D.V. Giri, "On the natural oscillation frequencies of a straight wire", *Interaction Note*, **621**, June 2011.

[9] J.M.Myer, S.S.Sandler and T.T.Wu, "Electro-magnetic resonances of a straight wire", *IEEE Transactions on Antennas and Propagation*, **vol. 59**, Jan.2011, pp.129-134.

[10] K.R. Umashankar and D.R. Wilton, "Transient Characterization of Circular Loop Using Singularity Expansion Method", *Interaction Note,* **259**, Aug. 1974. Available at http://ece-research.unm.edu/summa/notes/In/IN259.pdf

[11] S.Tkatchenko, F.Rachidi, M.Ianoz, "High-frequency electromagnetic field coupling to long terminated lines", *IEEE Transactions on Electromagnetic Compatibility*, vol. **43**, Nr. 2, 2001, pp. 117-129.

[12] F. Rachidi and S. Tkachenko, ed., *Electromagnetic Field Interaction with Transmission Lines: From Classical Theory to HF Radiation Effects*", Ch. 1, 4 and 5, WIT Press 2008, ISBN: 978-1-84564-063-7.

[13] S.V.Tkachenko, J.Nitsch, R.Vick, F.Rachidi, D.Poljak, "Singularity expansion method (SEM) for long terminated transmission lines", *2013 International Conference on Electromagnetics in Advanced Applications (ICEAA)*, Torino, 9-13 Sept. 2013, DOI: 10.1109/ICEAA.2013.6632411

[14] S.Tkachenko, F.Middelstaedt, J.Nitsch, R.Vick, G.Lugrin, F.Rachidi, "High–Frequency Electromagnetic Field Coupling to a Long Finite Line with Vertical Risers", *GA URSI 2014* Beijing. DOI: 10.1109/URSIGASS.2014.6929526

[15] F.Middelstaedt, S.V.Tkachenko, R.Rambousky and R.Vick, "High-Frequency Electromagnetic Field Coupling to a Long, Finite Wire With Vertical Risers above Ground" *IEEE Transactions on Electromagnetic Compatibility ,* vol.58, Nr. 4, 2016, pp. 1169 - 1175

[16] H. Haase and J. Nitsch, "Full-wave transmission line theory (FWTLT) for the analysis of three-dimensional wire-like structures," in *14th Int. Zurich Symposium and Technical Exhibition on Electromagnetic Compatibility*, pp. 235–240, Feb. 2001.

[17] H. Haase, J. Nitsch, T. Steimetz, "Transmission-line super theory: A new approach to an effective calculation of electromagnetic interactions", *Radio Science Bulletin* **307** , Dec. 2003, pp. 33-60.

[18] J. Nitsch, F. Gronwald, G. Wollenberg, *Radiating Nonuniform Transmission-Line Systems and the Partial Element Equivalent Circuit Method*, Willey, NY, 2009.

[19] J.B.Nitsch, S.V.Tkachenko, "Global and Modal Parameters in the Generalized Transmission Line Theory and Their Physical Meaning", *Radio Science Bulletin*, **312**, March 2005, pp.21-31.

[20] J.B.Nitsch, S.V.Tkachenko „Propagation of Current Waves along Quasi-Periodical Thin-Wire Structures: Taking Radiation Losses into Account", *Radio Science Bulletin*, No **322**, September 2007,pp.19-40.

[21] J.Nitsch, S.Tkachenko, „High-frequency Multiconductor Transmission line Theory", *Foundations of Physics* (2010) **40**: 1231-1252.

[22] F.R.Gantmacher, *The Theory of Matrices*, vol. 2. Chelsea, NY (1984)

[23] D.V. Giri, F.M. Tesche, " An Overview of the Natural Frequencies of a Straight Wire by Various Methods", IEEE Transactions on Antennas and Propagation, vol. **60**,No.12, Dec. 2012, pp.5859-5866.

[24] S.V.Tkachenko, J.B.Nitsch, F Middelstaedt, M.Magdowski, D.Helge-Theune, F.Rachidi, R.Rambousky, M.Schaarschmidt, R.Vick, "Application of the Singularity Expansion Method (SEM) to Non-Uniform Transmission Lines", The European Electromagnetics Symposium (EUROEM), London, UK, 2016. http://ece-research.unm.edu/summa/notes/AMEREM-EUROEM/EUROEM%202016%20Book%20of%20Abstracts.pdf

Effect of Non-Vertical Risers in the Electromagnetic Field Coupling with Overhead Lines

Jun Guo
School of Electrical Engineering
Xi'an Jiaotong University
Xi'an, China
junguo@mail.xjtu.edu.cn

Marcos Rubinstein
University of Applied Sciences
Western Switzerland
Yverdon-les-Bains, Switzerland
marcos.rubinstein@heig-vd.ch

Vernon Cooray
Department of Engineering Sciences
Uppsala University
Uppsala, Sweden
vernon.cooray@angstrom.uu.se

Farhad Rachidi
Electromagnetic Compatibility group
Swiss Federal Institute of Technology
(EPFL), Lausanne
Lausanne, Switzerland
farhad.rachidi@epfl.ch

Yan-zhao Xie
School of Electrical Engineering
Xi'an Jiaotong University
Xi'an, China
yzxie@mail.xjtu.edu.cn

***Abstract*—Recently, a simple and efficient method was proposed to take into account non-vertical risers at the end of transmission lines through an equivalent partial inductance. This paper evaluates the frequency above which the inductance needs to be taken into account. In addition, the proposed method is validated in the time domain.**

Keywords—Transmission line model, transient electromagnetic field, non-vertical riser, induced current, total voltage

I. Introduction

Transient electromagnetic fields may couple to transmission lines inducing currents and voltages which may cause interferences in the connected equipment. Therefore, it is important to perform numerical simulations to assess the susceptibility of the equipment and the relevant protection systems.

Several models have been used in the literature to estimate the voltages and currents induced on transmission lines due to an impinging transient electromagnetic field [1-5]. These studies are mainly based on the classical transmission line theory and they only consider the case of a transmission line terminated by vertical risers at both ends. However, in some cases, the risers at the end of the transmission lines are not vertical and may have an arbitrary shape. Such a problem can be handled by full-wave methods, which entail high computational cost.

A simple and efficient method taking into account non-vertical risers at the ends of the transmission lines has been proposed recently to solve this problem [6]. In the method, the classical transmission line theory is adopted and the non-vertical risers are taken into account through an equivalent partial inductance. Since the classical transmission line model is applied, the transmission line response can be solved efficiently. The aim of this paper is to study the effect of the equivalent inductance and, in particular, the frequencies above which the inductance needs to be taken into account. Moreover, the performance of the proposed method in the time domain will be assessed.

The remainder of this paper is organized as follows. Section II describes the basic concept of the proposed approach. Section III presents the results associated with several case studies to investigate the effect of the equivalent inductance and the conditions under which it is required. Finally, Section IV presents the conclusions of the work.

II. Basic Concept of The Proposed Approach

In the case where the transmission line is terminated with vertical risers, the field-induced response of the line can be evaluated using the classical transmission line theory [1-3]. In this method, the Agrawal *et al*. [1] model in the frequency domain is adopted:

$$\begin{aligned} &\frac{dV^s(x,\omega)}{dx} + (R' + j\omega L')I(x,\omega) = E_x^e(x,0,h,\omega) \\ &\frac{dI(x,\omega)}{dx} + j\omega C' V^s(x,\omega) = 0 \end{aligned} \tag{1}$$

in which R', L' and C' are, respectively, the per-unit-length resistance, inductance and capacitance of the line, $I(x,\omega)$ is the induced current, $V^s(x,\omega)$ is the scattered voltage, and h is the height of the conductor above the ground. The boundary conditions at the two line ends terminated in impedances Z_A and Z_B are given by:

$$\begin{aligned} V^s(0,\omega) &= -Z_A I(0,\omega) + \int_0^h E_z^e(0,0,z,\omega)dz \\ V^s(L,t) &= Z_B I(L,\omega) + \int_0^h E_z^e(L,0,z,\omega)dz \end{aligned} \tag{2}$$

Consider a transmission line is terminated by a non-vertical riser that has an arbitrary shape at the left end, as shown in Fig. 1.

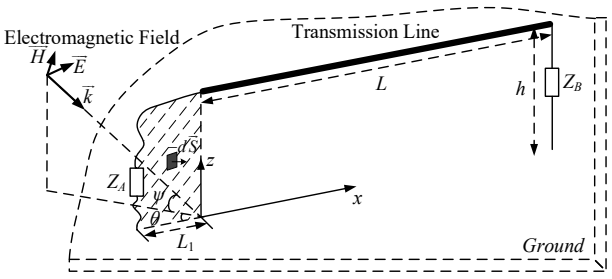

Fig. 1. Transmission line with a non-vertical riser excited by an incident plane wave.

Since the riser is not vertical, the source at the termination is the line integral of the exciting electric field along the riser's non-vertical geometry. Moreover, the termination impedance, represented by Z_A in Fig. 2, is the series combination of the actual termination and an

additional inductive impedance stemming from the more general geometry for the risers. The boundary condition at the left end can be rewritten as

$$V^s(0,\omega) = -(Z_A + j\omega L_A)I(0,\omega) + \int_{Riser} \vec{E}^e \cdot d\vec{l} \qquad (3)$$

in which [6]

$$L_A = \frac{\iint \vec{B}^s \cdot d\vec{S}}{I(0)} \qquad (4)$$

The surface over which the scattered magnetic field is integrated in shown in Fig. 1.

The value of the inductance L_A depends only on the geometry of the riser. Fig. 2 illustrates the equivalent circuit for the left hand side of the line based on (3).

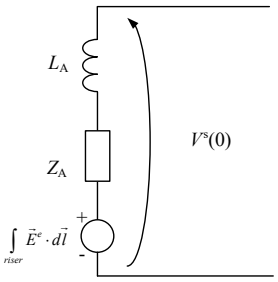

Fig. 2. Equivalent circuit for the left termination when the riser is not vertical.

Thus, the integrals of the exciting electric field at the two line ends are evaluated along a path defined by the geometry of the risers.

III. Case Studies to Investigate the Effect of the Equivalent Inductance

In this section, three validation examples are considered to further investigate the capability and the applicability of the proposed method. The configuration of the transmission line is shown in Fig. 1. The terminal riser at the right end is assumed to be vertical, while two different shapes, namely rectangular and triangular, will be considered for the riser at the left-end, as illustrated in Figs. 3a and 3b). The equivalent (partial) inductance L_A can be evaluated using the Biot-Savart law. The field-to-transmission-line coupling equations including the treatment of non-vertical risers are solved using the BLT equations [7]. In order to validate the calculation results, the Numerical Electromagnetics Code NEC-4, a full-wave solver based on the Method of Moments, is adopted. In what follows, we will consider a 20-m long wire located at a height of 0.1 m above a perfectly-conducting ground. The conductor radius is 1 mm. The azimuth angle, elevation angle and the polarization angle of the exciting plane wave are 0°, 45° and 0°, respectively.

A. Validation in the Frequency Domain

In the first example, we considered the two cases for the geometry of the left-end riser shown in Fig. 3. In both cases, the value of L_1 (see Fig. 3) was set to 0.5 m. The calculated equivalent inductances L_A for the rectangular (Fig. 3a) and for the triangular (Fig. 3b) terminations are, respectively, 0.66 μH and 0.49 μH. The line is terminated at both ends in 100 Ω resistive loads. The frequency range of the wave is 10 kHz-50 MHz, and the amplitude of the E-field is 1 V/m across the complete frequency spectrum. The calculated results for the induced currents at the left-end are shown in Fig. 4. It can be seen that the results calculated using the classical transmission line theory deviate from the full-wave results obtained using NEC-4. Taking into account the non-vertical riser using the equivalent (partial) inductance leads to significantly more accurate results.

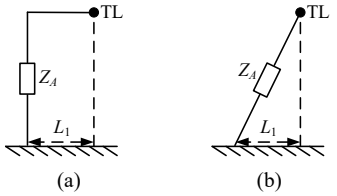

Fig. 3. Cross-section of the two considered geometries for the left-end riser. (a) rectangular, and (b) triangular.

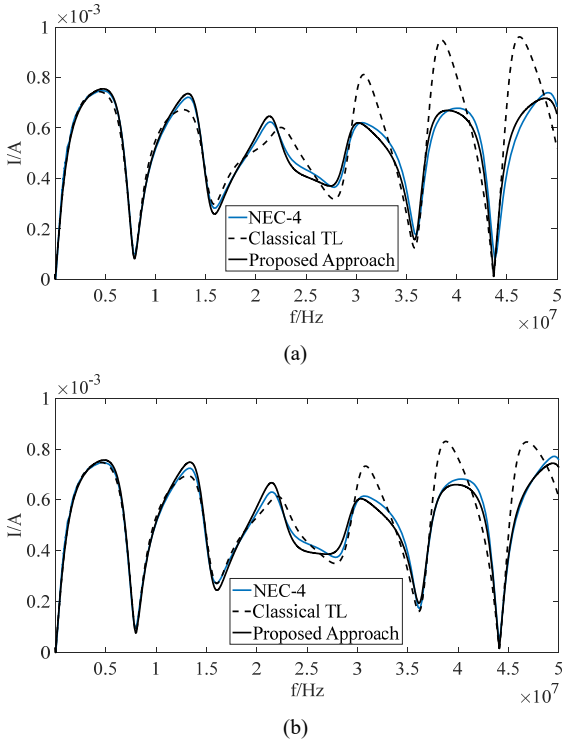

Fig. 4. Left-end induced currents as a function of frequency when the left end geometry is considered to be: (a) rectangular, and (b) triangular. Calculations obtained using the classical transmission line theory, the transmission line theory including the partial inductance, and NEC-4.

B. Investigation of the Frequency Beyond which the Inductance Needs to be Considered

To evaluate the frequency above which the equivalent inductance L_A needs to be taken into account, a parameter $A(f)$ is defined as the logarithm of the ratio of the results obtained using the classical transmission line method and those obtained using NEC-4:

$$A(f) = 20\left|\log_{10}\left(\frac{|I_{CTL}(f)|}{|I_{NEC}(f)|}\right)\right| \qquad (5)$$

where A is a measure of the accuracy at a given frequency f, I_{CTL} is the current obtained from the classical TL method, and I_{NEC} is the current obtained using NEC-4.

The threshold value of the calculation accuracy to indicate that the obtained solution is acceptable is defined to be 3 dB. If A is larger than 3 dB, the result obtained from the

classical TL method is no longer considered acceptable, and the equivalent inductance L_A needs to be taken into account. The threshold frequency, defined as the smallest frequency at which A is larger than 3 dB, is denoted by f_a. For the case in which the geometry of left riser is considered as rectangular, the value of f_a in Fig. 4(a) is 37.6 MHz.

It is reasonable to consider that the value of f_a may be related to the ratio of $j\omega L_A$ to the total impedance. To test this hypothesis, 7 cases with the rectangular-shape left riser but different values of Z_A and L_1 are considered; the parameters are listed in Table 1. All other parameters are the same as in the first example. The classical transmission line method and NEC-4 were used to calculate the current response at the left-end in these 7 cases. Then, the values for f_a were calculated and listed in the second to the last column in Table 1.

Table 1. Parameters for the Validation Examples

	Z_A (Ω)	Z_B (Ω)	L_1 (m)	L_A (μH)	f_a (MHz)	$f_{a\text{-}e}$ (MHz)
Case1	100	100	0.5	0.66	37.6	40.8
Case2	100	100	1	1.25	27.6	21.6
Case3	100	100	1.5	1.83	16.2	14.7
Case4	100	100	2	2.43	9.3	11.0
Case5	20	20	0.5	0.66	7.4	8.1
Case6	50	50	0.5	0.66	22.8	20.4
Case7	80	80	0.5	0.66	35.1	32.6

Let us now define a parameter K as follows:

$$K = \frac{2\pi f_a L_A}{\left|2\pi f_a j L_A + Z_A\right|} \tag{6}$$

The parameter K was calculated for the 7 cases and presented in Fig. 5. It can be seen that the value of K remains relatively constant for the seven cases regardless of the differences in the transmission line parameters. This suggests that the ratio K of ωL_A to the magnitude of the total impedance can be used to roughly estimate the value of f_a beyond which the equivalent inductance L_A needs to be taken into account. Indeed, by setting K in (6) to its average value of 0.86 (obtained from Fig 5) and solving for f_a, we obtained estimates of the threshold frequency for each of the 7 cases. The estimates, which we call $f_{a\text{-}e}$, are listed in the last column of Table 1. It can be seen that f_a can indeed be estimated roughly by the calculated $f_{a\text{-}e}$.

It is to be noted that the inferred mean of the parameter K cannot be generalized to any arbitrary riser. There are still many other factors (*e.g.*, the height or the radius of the line, the shape of the riser.) that may influence the results.

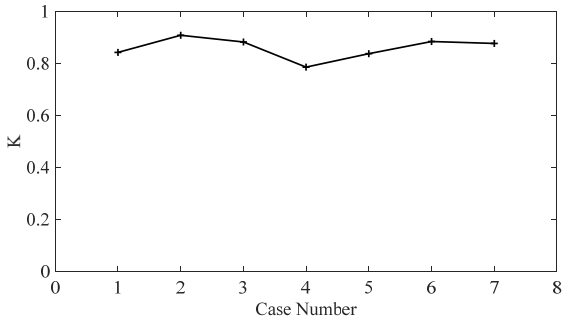

Fig. 5. The value of parameter K for the considered 7 cases.

C. Validation in the Time Domain

In order to investigate the capability of the proposed method to predict induced signals over a wide frequency band, time domain simulations were also carried out. We considered a value for length L_1 equal to 1 m. The terminal loads at both ends were assumed to be 100 Ω. The EMP standard waveform defined in IEC 61000-2-5 was adopted for the electric field. The calculated results for the induced current at the left-end terminal are shown in Fig. 6. It can be seen that the time domain results calculated using the classical transmission line theory deviate from the results obtained using NEC-4, whereas the results obtained from the proposed approach agree well with those obtained using NEC-4.

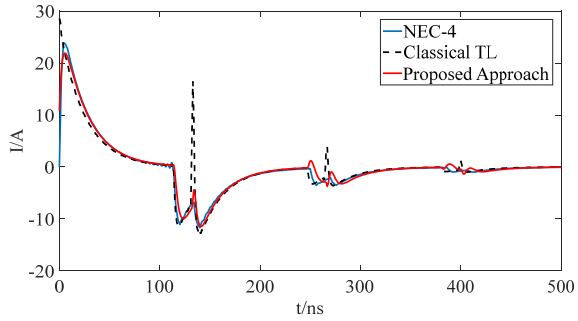

Fig. 6. Time-domain waveform for the left-end current induced by a standard EMP. Calculations were carried out using the classical transmission line theory, the transmission line theory including the partial inductance, and NEC-4.

IV. Conclusions

In this paper, a simple and efficient method to take into account non-vertical risers through an equivalent partial inductance is discussed and validated.

In particular, the frequency f_a beyond which the equivalent inductance L_A needs to be taken into account is evaluated. It was shown that the value of f_a is related to the magnitude of the ratio of $j\omega L_A$ to the total impedance of the riser.

Finally, the efficiency of the proposed method is also illustrated when applied to wideband signals.

References

[1] Agrawal A.K., H.J. Price, S.H. Gurbaxani, "Transient response of a multi-conductor transmission line excited by a nonuniform electromagnetic field", IEEE Trans. on Electromagnetic Compatibility, Vol. EMC-22, No. 2, pp. 119-129, May 1980.

[2] Taylor, C. D., R. S. Satterwhite, C.W. Harrison, "The response of a terminated two-wire transmission line excited by a non-uniform electromagnetic field", IEEE Transactions on Antenna and Propagation, Vol. AP-13, 1965.

[3] Rachidi, F., "Formulation of the field-to-transmission line coupling equations in terms of magnetic excitation fields", IEEE Trans. on Electromagnetic Compatibility, Vol. 35, No. 3, Aug. 1993.

[4] Chowdhuri, P., Analysis of lightning induced voltages on overhead lines, IEEE Trans. On Power Delivery, Vol. 6, No. 1, January, 1989.

[5] Cooray, V., F. Rachidi and M. Rubinstein, Formulation of the Field-to-Transmission Line Coupling Equations in Terms of Scalar and Vector Potentials, IEEE Transactions on Electromagnetic Compatibility Volume: 59, Issue: 5, pp 1586 – 1591, 2017.

[6] J. Guo, M. Rubinstein, V. Cooray, F. Rachidi, On the Modeling of Non-Vertical Risers in the Interaction of Electromagnetic Fields with Overhead Lines, IEEE Transactions on Electromagnetic Compatibility, in press, 2019.

[7] C. E. Baum, T. K. Liu, and F. M. Tesche, "On the analysis of general multiconductor transmission line networks," Interaction Note, vol. 350, no. 6, pp. 467–547, 1978.

Technical Paper for Lightning Test Standard of Automobiles from Japanese Automotive Standards Organization

Kazuo Yamamoto
Chubu University
Kasugai, Japan
kyamamoto@isc.chubu.ac.jp

Noriaki Hiraga
ROHM Co., Ltd.
Yokohama, Kanagawa
noriaki.hiraga@adm.rohm.co.jp

Hiromasa Uchida
SUZUKI MOTOR CORPORATION
Hamamatsu, Shizuoka
uhiro@hhq.suzuki.co.jp

Takuya Kaneda
Subaru Corporation
Mitaka, Tokyo
kaneda.takuya@subaru.co.jp

Hitoshi Tsukahara
Nissan Motor Co., Ltd.
Atsugi, Kanagawa
h-tsukahara@mail.nissan.co.jp

Shigetada Tanigawa
Daihatsu Motor Co., Ltd.
Ikeda, Osaka
Shigenori_Tanigawa@dk.daihatsu.co.jp

Shinichiro Ito
National Traffic Safety and Environment Laboratory
Chofu, Tokyo
itoh@ntsel.go.jp

Akihiko Nojima
Toyota Motor Corporation
Toyota, Aichi
akihiko_nojima@mail.toyota.co.jp

Yoshihiro Teshima
Mazda Motor Corporation
Aki, Hiroshima
teshima.y@mazda.co.jp

Takeshi Ishida
NOISE LABORATORY CO., LTD.
Sagamihara, Kanagawa
t-ishida@noiseken.com

***Abstract*— The popularity of automobiles that have less impact on the environment such as electric (EV) and hybrid vehicles has grown rapidly in recent years. In addition, from the viewpoint of environmental conservation, vehicles are aiming to reduce weight, new materials are applied. Furthermore, for the purpose of improving safety and amenity, installation and progress of electronic control equipment and electric power system are proceeding.**

Such cars are more susceptible to electromagnetic disturbances such as lightning surges than conventional automobiles. When the vehicle is struck by lightning, the lightning current runs through its body and its internal parts, and is discharged into the ground from the tires. The excessive electromagnetic field produced at that moment may damage the control and power supply systems, or cause it to malfunction. Therefore, investigation of the state of the vehicle at the time of lightning strike is important from the viewpoint of securing the safety of the vehicle.

In the future, when developing new vehicles, vehicle manufacturers are working on standardization of vehicle test method for lightning strike in order to investigate the effect of lightning appropriately. In Japan, the technical paper (TP) relating to vehicle test method for lightning has been published from JASO (Japanese Automotive Standards Organization). In this paper, we introduce the main contents of the TP.

Keywords— Vehicles, Lightning strike, Securing the safety of the vehicle, Standardization of vehicle test method, Lightning test methods

I. INTRODUCTION

In the case of passenger cars and light trucks, these car bodies are generally composed of metal panels. Therefore, when a vehicle receives lightning strikes, it is considered that the lightning strike current flows out from the vehicle body to the ground via the internal gear section, the axle, the wheel, and the like.

From the viewpoint of environmental protection, new materials are applied to vehicles in order to reduce weight, and many electronic control systems and electric power systems are installed and advanced for the purpose of improving safety. There is concern that such vehicles may be weakened by electromagnetic interference such as lightning surge [1]–[3]. Under such circumstances, it is important to investigate the influence of the vehicle structure and electronic parts at the time of lightning strike from the viewpoint of securing the safety of the vehicle. When developing new vehicles in the future, some vehicle manufacturers are proceeding with commonization of vehicle direct hit lightning test methods to appropriately investigate the strike on lightning. In Japan, the technical paper (TP) relating to vehicle test method for lightning has been published from JASO (Japanese Automotive Standards Organization). This paper introduces the outline of the vehicle test method in the TP.

II. SCOPE OF APPLICATION

This TP is to standardize the test method for direct strike lightning of four-wheeled passenger cars and light trucks (hereinafter, test vehicles). The test vehicle is not limited to the type of propulsion system (spark ignition engine, diesel engine, electric motor, etc.).

III. USING THE TEMPLATE

When the vehicle is struck by lightning, the lightning current flows out from the body to the ground via the internal gear parts, axles, wheels, and the like. Transient electromagnetic fields generated by such currents also carry a risk of causing malfunctioning and breakdowns in electric and electronic equipment inside the car [4]-[6]. In addition, when the lightning current through discharge the inside of the tire, there is a possibility that the tire busts. When verifying the effect of lightning striking on a vehicle, there is a high possibility that a vehicle will break if a large current is

applied to the vehicle from the first time. Therefore, there is a high possibility that it is not possible to verify the influence of the current flowing place and current on the equipment. Therefore, we think that it is desirable to conduct a test using a small current level that does not destroy the vehicle. A test for injecting such a small lightning current waveform is referred to as a small current test here.

The small current test is a test aiming to estimate the overcurrent and overvoltage generated in the current path, in-vehicle equipment and its wiring by applying a current of a level at which the equipment of the vehicle and the inside of the vehicle does not break.

IV. SMALL CURRENT TEST METHOD

Fig. 1 shows an example of the vehicle arrangement. The vehicle is located at the center of the conductor plate which is at least 0.6 m greater than the distance between the axes (distance between front wheel shaft and rear wheel shaft) and the distance between the wheels (distance between right and left wheels). The material and thickness of the conductive plate are not specified.

The place where current is injected to vehicle is the center of the roof. The current injection point is fixed to the roof with screws or bolts. It is preferable to use a braided wire for the injection line, and this braided wire was connected to a current injection point at which the coating on the surface was scraped away in order to make it easy to apply current thereto.

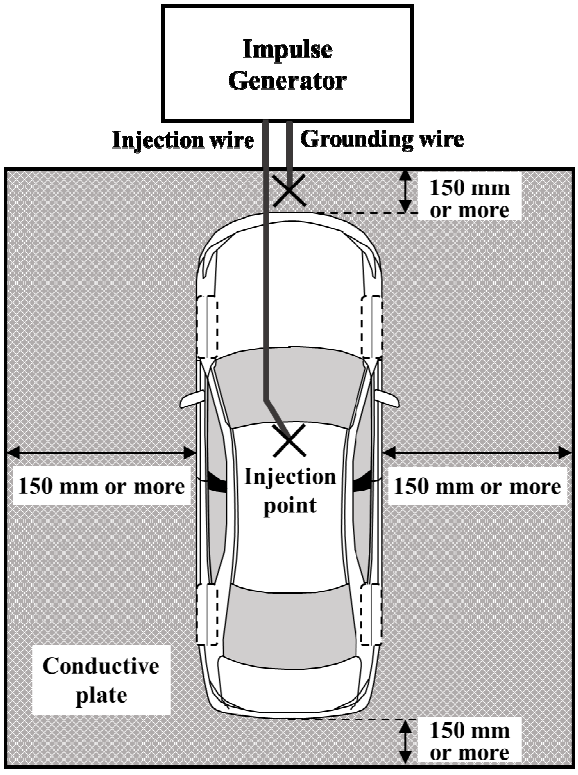

Fig. 1 Example of arrangement of test vehicle

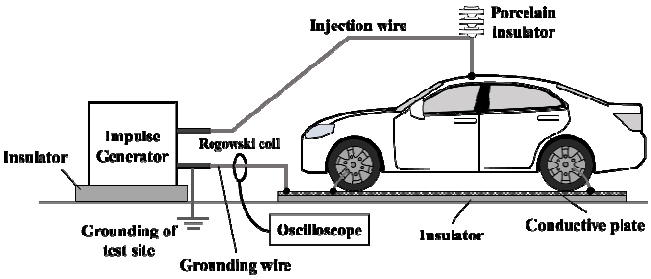

Fig. 2 Test circuit example

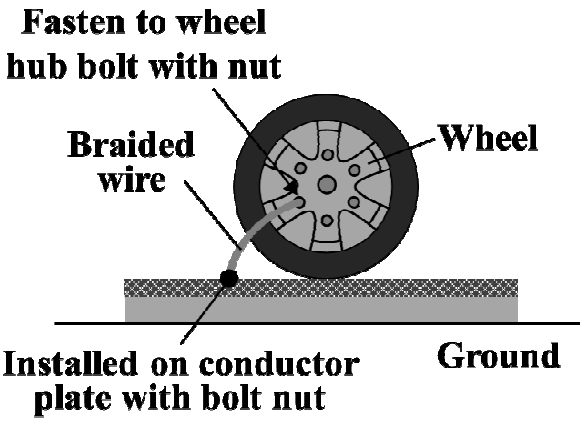

Fig. 3 Braided wire connection example

The vehicle-side outflow point of the lightning current shall be the wheel nut.

Grounding (coupling with test equipment GND) is realized by bypassing the tire rubber part which is an insulator with a braided wire. When the vehicle is rubber portion of the tire from the tire wheel and flows to the ground. If a large current is passed without bypass, the tire may burst. It is to avoid it.

In the case of a four-wheel vehicle, the bypass positions by the braided wires are four wheels. With the combination of these four wheels' grounds, ①: 4 wheels simultaneous grounding, ②: independent grounding of each wheel (4 places) are totally 5 conditions.

An example of a test circuit is shown in Fig.2. The conductive plate and the wheel nut are connected by a conductor having a large current tolerance such as a braided wire, and the tire rubber is bypassed. An example of the connection of an eccentric wire to a tire is shown in Fig.3. The connections of the eccentric wire and the wheel are conducted by bolt nuts, and the connection is fixed so that the braided wire does not come off.

Current is applied by impulse generator, injection current is measured with current probe and each measurement site is measured with Rogowski coil. The current value used in the small current test is several amperes to several hundred amperes. The measurement current of each part of the vehicle is performed within the range of the signal level distinguishable from the noise level and within the range where the vehicle is not destroyed, and the distribution path of the lightning current is clarified. An example of the test results performed so far is shown in Fig. 4 (injection current, current flowing out from all wheels) [7].

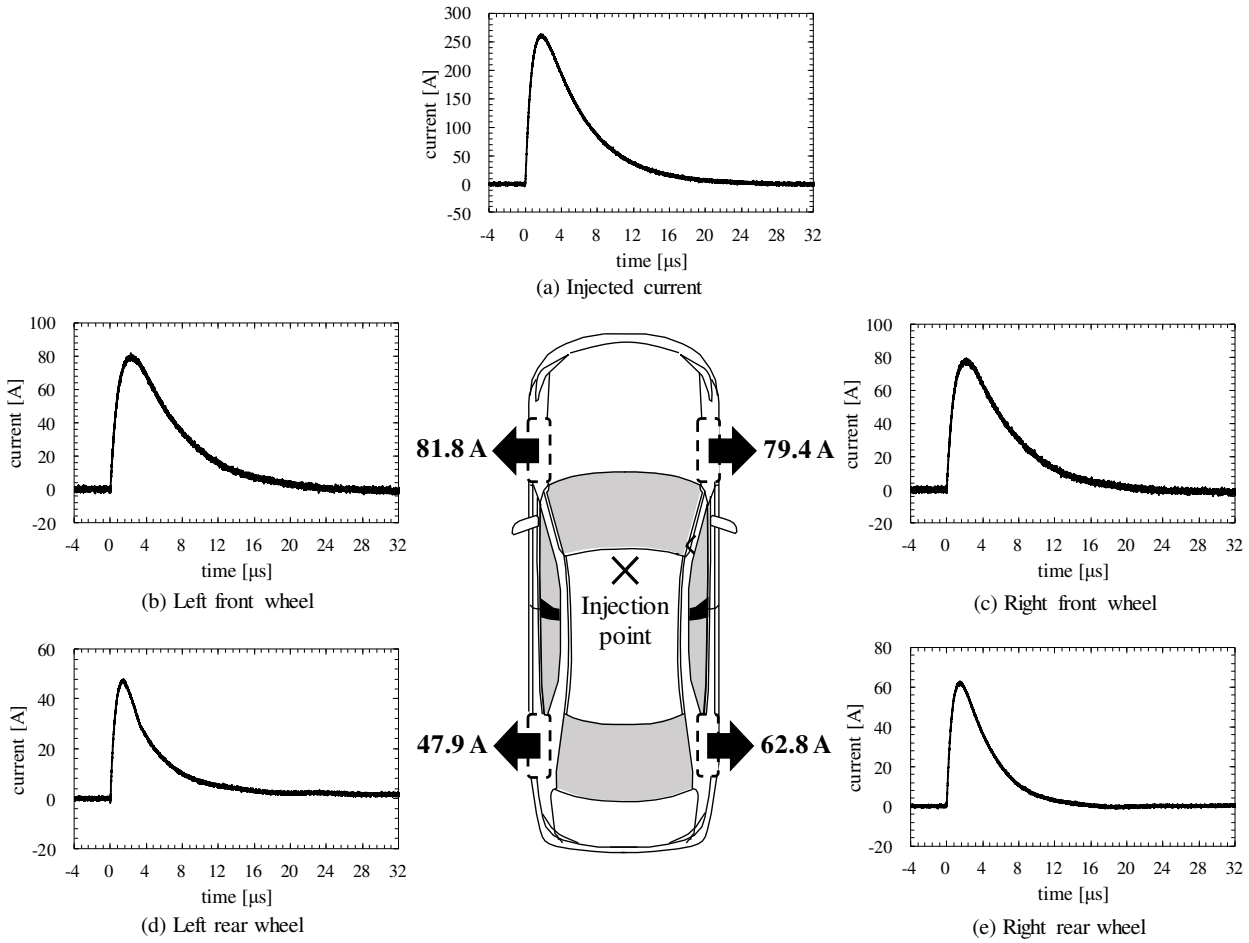

Fig. 4 Examples of test results

V. HIGH CURRENT TEST

The high current test is a test aimed at injecting electric current equivalent to lightning strike from the lightning striking point to the equipment inside the vehicle and the vehicle and grasping the lightning current performance of the vehicle.

In the large current test, an impulse large current generator using a crowbar switch or the like is used (a crowbar circuit type) in order to generate a current waveform simulating direct hit lightning and a long current duration.

A. Calibration test using pseudo load

In order to prevent the discharge failure of the crowbar circuit of a current impulse generator to the vehicle, it is necessary to perform calibration using a pseudo load before applying a large current into an actual automobile. Fig. 5 shows an example of a test circuit. Although the vehicle is arranged, the braided wire is wired along the wooden post without connecting to the vehicle. The direction of the vehicle was the same as in the small current test, and the simulated load was simulated with the braided wire. The braided wire simulates from the injection point to each wheel by branching four from the injection wire. Impedance between the injection point and the conductor plate can be made approximately equal by making the shape of the vehicle and the shape of the simulated load almost equal.

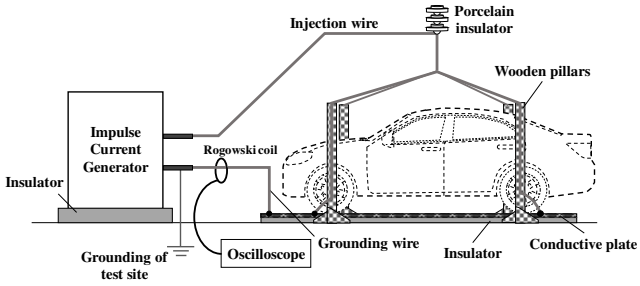

Fig. 5 Test circuit example

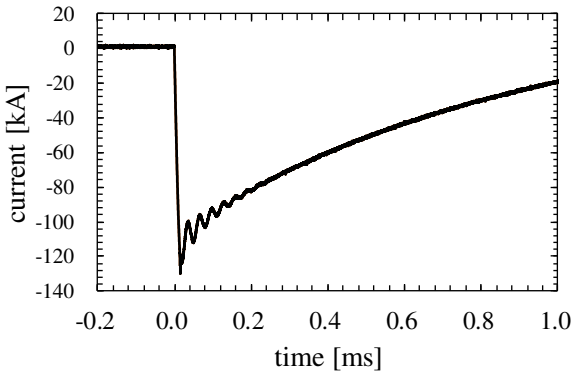

Fig. 6 Injection current waveform

B. *High current test to the vehicle*

Test placement etc. are the same as in the case of the small current test in Chapter 2. In the high current test, only the case of simultaneous grounding of four wheels is carried out. Discharge is visually confirmed when current is caused to flow by the impulse high current generator, and each part in the vehicle is photographed with a single lens reflex camera or the like.

Also, the injection current is measured using CT, Rogowski coil or the like. After injection, check the vehicle situation (appearance change, physical damage, control / power communication system state) and photographs taken.

In principle, the number of times of injection is 1 time. However, when it can be confirmed that there is no breakdown of the vehicle, it may be injected multiple times using the vehicle. Fig. 6 shows an example of the injection current waveform when a large current is injected to the vehicle using the impulse large current generator.

VI. CONCLUSION

In this paper, we introduced the vehicle structure at the time of lightning stroke and the vehicle test method for investigating the influence of electronic parts. The test method here is a method currently under consideration. In the future, we will continue to standardize test methods to appropriately investigate the effect of the lightning strike on the vehicle, we will aim for establishment of future "vehicle lightning strike test method" by repeated investigation.

REFERENCES

[1] K. Yamamoto, Kanata and A. Ametani, “Transient magnetic Fields and Current Distributions in an Electric Vehicle Caused by a Lightning Stroke”, IEEJ Transactions on Power and Energy, Vol.132, No.7, pp.667-675, Jul. 2012

[2] Y. Naito, S. Yanagawa, K. Yamamoto and N. Takahashi, “High Voltage Impulse Experiment on Electric Automobiles and its Verification part2”, IEEJ Technical Meeting on High Voltage Engineering, HV-16-25, pp.27-32, Jan. 2016

[3] K. Yamamoto, “Lightning damage and countermeasures against moving objects such as aircraft, automobiles, railways” OHM, pp.15-19, Jun. 2014

[4] K. Yamamoto, H. Okajima, J. Kanata and A. Ametani, “Transient magnetic Fields in an Electric Vehicle”, IEEJ Proceedings of the Twenty-Second Annual Conference of Power & Energy Society, No.252, pp.27-1 - 27-2, Aug. 2011(in Japanese)

[5] Hyok J. Song, et al., “Modeling Effect of Lightning Induced EMP on Wire Hamess in Automobiles”, IEEE Antennas and Propagation Society International Symposium, Vol.2B, pp.383-386, Jul. 2005

[6] S Ficheux, et al., “Testing of Automotive Electronic Components Regarding Influence of Electromagnetic Field Strength Levels Radiated by Lightning Discharges-application to a Multiplexing Communication System”, 8th International Conference on Automotive Electronics, pp.68-73, Oct. 1991

[7] S. Niwa, K. Yamamoto, Y. Naito, H. Itozakura, Y. Morita, and A. Nojima, “Current Distribution on a Monocoque Construction Vehicle and Lightning Protection Methodologies”, 2017 International Conference on Lightning and Static Electricity

Frequency-domain calibration method for D-dot sensor

Ke Wang
National Key Laboratory on Electromagnetic Environment Effects and Electro-Optical Engineering
1363611280@qq.com

Yantao Duan
National Key Laboratory on Electromagnetic Environment Effects and Electro-Optical Engineering
dcmchdyt@126.com(Corresponding author)

Lihua Shi
National Key Laboratory on Electromagnetic Environment Effects and Electro-Optical Engineering
shilih@tom.com

***Abstract*—D-dot sensors are widely used for electromagnetic pulse (EMP) measurements. In order to improve the calibration accuracy of D-dot sensors in the laboratory environment, this paper proposes a frequency-domain calibration method. On the basis of FFT, linear fit of system transfer function can be used to characterize the sensor's sensitivity. Compared with the traditional time-domain calibration method, the proposed method has stronger stability faced with colored noise due to application of statistical thought in calibration.**

Keywords—D-dot, calibration method, frequency domain.

I. INTRODUCTION

D-dot sensors can realize the measurement of the transient electric field in a non-contact way based on the principle of coupling; they are widely used for EMP measurements with characteristics of the wide frequency band, high linearity, and good stability [1-3].

Sensitivity estimation of D-dot sensor is critical to the accuracy of the field measurement, but its calculation in theory is difficult to implement due to stray capacitance [4-7]. Therefore, it is necessary to recalibrate the D-dot sensor in the laboratory environment. From the existing laboratory conditions, the observed data is highly susceptible to contamination by colored noise. When the noise causes distortion at the peak of the waveform, the traditional peak calibration method has large errors. This paper proposes a frequency-domain calibration method in order to reduce the errors caused by colored noise.

II. THE PRINCIPLE OF FREQUENCY-DOMAIN CALIBRITION METHOD

D-dot sensors are generally analyzed using the Norton equivalent circuit shown in Fig. 1 [8]. The sensor probe can be regarded as a current source in the equivalent circuit, and the current magnitude can be determined by

$$I_S = \dot{D}A_e \tag{1}$$

According to Norton's theorem, the current in the time domain can be represented as

$$i_s = C\frac{\mathrm{d}u_0(t)}{\mathrm{d}t} + \frac{u_0}{R} \tag{2}$$

Converting to the frequency domain, the output voltage of the D-dot sensor can be expressed as [8]

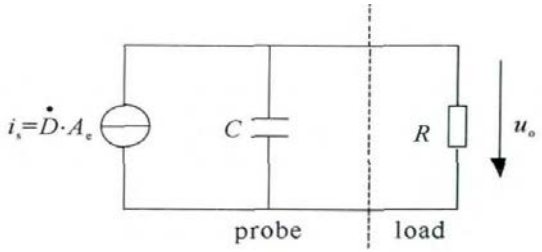

Fig. 1. Equivalent circuit of D-dot sensor. where D refers to the electric flux density of incident electric field; A_e refers to probe equivalent area. C refers to the equivalent capacitance of the D-dot sensor; R refers to the characteristic impedance of the transmission line; u_o refers to the output voltage of the D-dot sensor induced by the EMP signal.

$$U_0(\mathrm{j}\omega) = \frac{\mathrm{j}\omega\varepsilon_0 EA_e R}{\mathrm{j}\omega RC + 1} \tag{3}$$

When the capacitance C and resistance R in the circuit are determined, the frequency response curve, illustrated in Fig. 2 [8], can be obtained. It can be concluded that the D-dot sensor has three working modes—the first-order differential mode ($f < f_{3d}$), the transition mode ($f_{3d} < f < f_{3i}$), and the self-integration mode ($f > f_{3i}$). The first-order differential mode, namely the D-dot mode, is the main working mode in which the difference between the actual output voltage and the calculated output is not more than 0.3dB.

Since the output voltage of the sensor is proportional to the actual electric field change rate in D-dot mode, the system frequency response can be approximated as a straight line with a slope of constant k and passing the origin.

When $\omega << \omega_0 = 1/RC$ or $RC << t_r$ (t_r is the rise time of the pulse to be measured), system transfer function can be approximated to

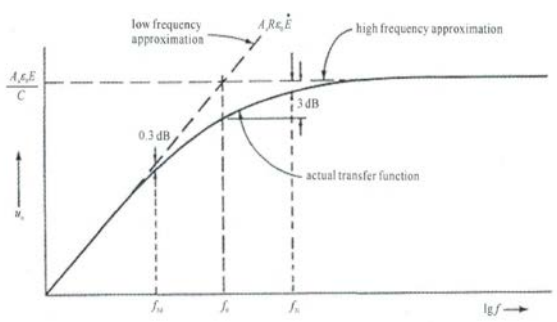

Fig.2. Frequency response curve of D-dot sensor

$$\left|H(\mathrm{j}\omega)\right| = \frac{\mathrm{k}}{2\pi}\omega \tag{4}$$

After eliminating stochastic white noise, the approximate relation of the system can be represented as

$$y(\mathrm{t}) = \frac{\mathrm{k}}{2\pi} \cdot \frac{\mathrm{d}x(t)}{\mathrm{d}t} \tag{5}$$

At the same time, the actual electric field change rate can be determined by

$$\dot{E}(t) = \frac{1}{\varepsilon_0 h} \cdot \frac{\mathrm{d}x(t)}{\mathrm{d}t} \tag{6}$$

where ε_0 refers to dielectric constant in vacuum, ε_0=8.86×10^{-12} S/m; h refers to height difference between core plate and the D-dot sensor. Therefore, the sensitivity coefficient k_s of D-dot sensor is given as

$$k_s = \frac{\dot{E}(t)}{y(t)} = \frac{2\pi}{\varepsilon_0 h \cdot \mathrm{k}} \tag{7}$$

III. Experimental Verification

A. Experimental Design

A calibration platform for D-dot sensor was built in our laboratory and its experimental setup is illustrated in Fig. 3. EMP waveforms in the vicinity of the D-dot sensor can be calculated from the excitation source voltage of the TEM cell, so the voltage on the inner conductor of the TEM cell output port was regarded as the input of the D-dot sensor, then the input and output of the D-dot sensor can be measured by the oscilloscope.

The double-exponential impulse voltage generated by the Prima EFT61004B pulse group generator, which could output a double exponential wave impulse voltage with 5 ns

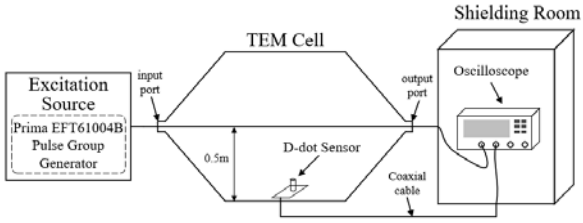

Fig. 3. Schematic of calibration platform for D-dot sensor. where TEM cell has an input port and an output port, which both match to the coaxial connectors of 50 ohms. Eventually, a uniform EMP environment caused by the excitation source is formed in the middle transition section.

of the rise time and 50 ns of halfwidth. At the same time, it can achieve a continuous change of output voltage peak from 0.4kV to 2kV.

B. Frequency-Domain Calibration Method

a) Pretreatment process: Firstly, in order to improve data accuracy, this paper preprocessed the observed data. Since the observed data contain DC component, the static gain removal processing of the data is done in this paper. There were bad values in the directly observed data, which affected the description of the system by the slope *k*. Savitzky-golay filter was selected to smooth observed data and improve data accuracy, as shown in Fig. 4(a). This kind of filter can keep the waveform of the signal unchanged while filtering out noise. Due to the different transmission

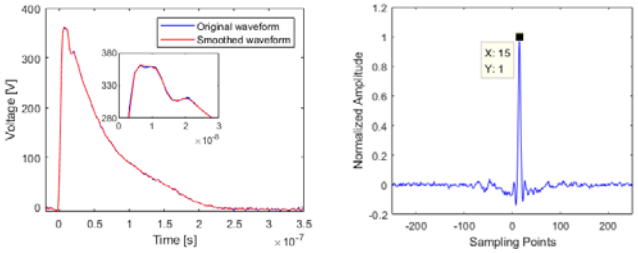

(a) (b)

Fig. 4. Pretreatment process of frequency-domain calibration method. where (a) refers to the treatment of smoothing data, (b) refers to the treatment of removing the relatively time delay.

distances of the input and output signals, there was a relative time delay between them. The estimation method of the time delay by cross-correlation is illustrated in Fig. 4(b)

b) Linear Fit: Secondly, the actual electric field waveform is considerd as the input signal, and the measured waveform by the D-dot sensor is regarded to the output signal. Then according to Fast Fourier Transform, the frequency response of the D-dot sensor can be determined. Fig. 5 illustrates the linear fit of the frequency response of D-dot sensor. It can be seen that there is an intercept for fitting straight lines, while the ideal amplitude-frequency response should go through the origin. Through analysis, we believe that the possible reason is that the energy of colored noise is mainly concentrated above 80MHz, which causes

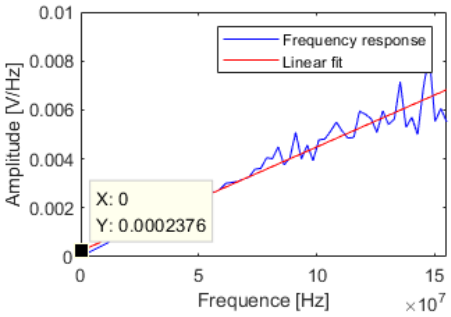

Fig. 5. Linear fit of frequency response

the fitting curve to rotate a certain angle. This leads to a decrease in the slope of the fitting line, which affects the calibration accuracy.

IV. Comparison Results

The peak calibration method is a common calibration method in the laboratory environment. Since the signal-to-noise ratio at the peak is the highest for a specific background noise, the peak ratio of the input and output can largely represent the linear response characteristics of the D-dot sensor [9-10].

However, in laboratory environment, observed data is inevitably interfered by noise, and due to impedance mismatch and inherent structure, the reflection wave causes waveform distortion of oscilloscope acquisition, which may also occur at the peak position. When this waveform distortion occurs at the peak position, it is often accompanied by overshoot and ringing, which may reduce the accuracy of

peak calibration. Eventually, the calibration coefficient fluctuates near the real value, resulting in a large increase in the number of experimental samples.

TABLE I shows the sensitivity coefficient k_s of D-dot

TABLE I. COMPARISON OF TWO CALIBRATION METHODS

U(kV)	k_s (Frequency)	k_s (Peak)
0.4	2.71E+11	2.57E+11
0.6	2.76E+11	2.47E+11
0.8	2.64E+11	2.37E+11
1	2.74E+11	2.42E+11
1.2	2.71E+11	2.48E+11
1.4	2.77E+11	2.64E+11
1.6	2.77E+11	2.61E+11
1.8	2.64E+11	2.77E+11
2	2.73E+11	2.60E+11

Where U refers to the input pulse voltage amplitude, k_s refers to the sensitivity coefficient.

sensor for two calibration methods with input pulse voltage amplitude ranging from 400 V to 2 kV, it can be seen that the results are comparable.

In addition, 25 sets of calibration data are randomly

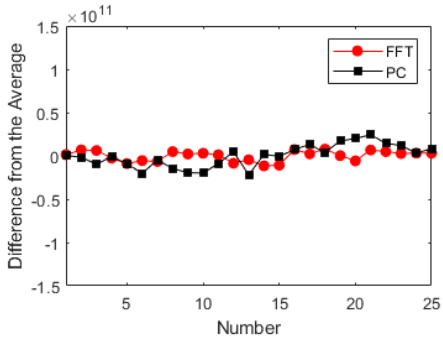

Fig. 6. Comparison of calibration method stability. where the red line refers to the frequency-domain calibration method, the black line refers to the peak calibration method.

selected to verify the universality of two methods. From Fig. 6, frequency-domain calibration method exhibits stronger stability for linear systems calibration than peak calibration method.

V. CONCLUSION

This paper proposes a frequency-domain calibration method of D-dot sensors, which has been carried out on the basis of a TEM cell and high-voltage impulse excitation source. According to error analysis, it is considered that the results of the frequency-domain and peak calibration method are comparable, which verifies that the frequency domain calibration method is feasible. Since frequency-domain calibration is a calibration method based on statistical models, it exhibits stronger stability for linear systems calibration.

However, the reflected wave superimposed on the time domain waveform is not processed, thus the system error of frequency-domain calibration results in a larger sensitivity coefficient. Subsequent work focuses on the processing of non-negligible noise in frequency domain components.

References

[1] C. Baum, E. Breen, J. Giles, et al. Sensors for electromagnetic pulse measurements both inside and away from nuclear source regions[J]. IEEE Transactions on Antennas and Propagation, 1978,26(1):22-35.

[2] Carl E. Baum, Edward L. Breen, Felix L. Pitts, et al. The measurement of lightning environmental parameters related to interaction with electronic systems[J]. IEEE Transactions on Electromagnetic Compatibility, 1982, 24(2):123 – 137.

[3] Metwally I A. D-dot probe for fast-front high-voltage measurement[J]. IEEE Transactions on Instrumentation and Measurement, 2010,59; 59(8; 8):2211-2219.

[4] Wang J, Gao C, Yang J. Design, experiments and simulation of voltage transformers on the basis of a differential input D-dot sensor[J]. Sensors (Basel, Switzerland), 2014,14(7):12771-12783.

[5] Al Agry A, Schill R A. Calibration of Electromagnetic Dot Sensor-Part 2: D-Dot Mode[J]. IEEE Sensors Journal, 2014,14(9):3111-3118.

[6] Yao L, Huang J, Kang N, et al. Implementation of a measurement system on field uniformity of transient electromagnetic field[J]. IEEE Electromagnetic Compatibility Magazine, 2016,5(1):43-49.

[7] Huiskamp T, Beckers F, Heesch B V, et al. B-Dot and D-Dot Sensors for (Sub)Nanosecond High-Voltage and High-Current Pulse Measurements[J]. IEEE Sensors Journal, 2016,16(10):3792-3801.

[8] Wang Q, Li Y, Shi L. Design and experimental research of D-dot probe for nuclear electromagnetic pulse measurement[J]. High Power Laser and Particle Beams, 2015(11):239-245.

[9] Jiang Z, Zhou B, Qiu S, et al. Time-Domain Calibration of the LEMP Sensor and Compensation for Measured Lightning Electric Field Waveforms[J]. IEEE Transactions on Electromagnetic Compatibility, 2014,56(5):1172-1177.

[10] Ma R, Shi L, Huang Z, et al. EMP Signal Reconstruction Using Associated-Hermite Orthogonal Functions[J]. IEEE Transactions on Electromagnetic Compatibility, 2014,56(5):1242-1245.

Investigation of gene expression alterations in human peripheral blood cells after continuous wave exposure at 900 MHz

Lars Ole Fichte

Theory of Electrical Engineering, Helmut Schmidt University

Interactions between electromagnetic fields and biological tissue have been investigated multiple times in the past in epidemiological studies (e.g. [1]) or exposure tests (e.g. [2] for *in vitro*, or [3] for *in vivo* tests), yet until now the only harmful effect that has been identified by reproducible, well designed experiments is the thermal damage by overheating. Hence, statutory thresholds for radio frequency electromagnetic fields (RF-EMF) have been established in order to limit relevant heat supply in human tissue, measured via the specific absorption rate (SAR). Although non-thermal biological effects are believed to be much weaker, new versions of microarrays (8x60k v2) allow for a more detailed detection of even non-coding RNAs and are hoped to display different adaptive processes in cells after irradiation.

In an *ex vivo* study, peripheral blood cells from 5 donors were exposed to a RF-EMF continuous wave of 900 MHz for 0, 30, 60 and 90 min [4]. Additional samples were either SHAM exposed or treated with a temperature of 2°C over room temperature (RT+2°C). Significant gene expression changes which show in addition at least a 2-fold change with respect to the SHAM exposed samples were identified by microarray analysis. The data were finally compared with data from the RT+2°C samples. While an open TEM waveguide was used for the experiments, other exposure environments (e.g. electromagnetic reverberation chambers and micro TEM cells) were considered, and their advantages and restrictions will be discussed.

To be able to relate biological observations to the radiation dose, a rigorous SAR dosimetry has been performed based on the measured temperature rise of the samples during the irradiation. To this end, temperature values captured by a thermography camera have been related to the corresponding SAR via a physical model of the transient power balance inside the samples.

In total 521 significantly deregulated transcripts were detected in all RF-EMF exposed groups relative to the SHAM exposed samples. Moreover, these transcripts were not expressed in their corresponding RT+2°C controls. An attempt to verify these indications by microarray data-based bioinformatics approaches, including enrichment and network analyses administered to expressed gene subset profiles, failed to identify the targeted biological response. Correspondingly, 14 candidate transcripts examined by qRT-PCR revealed an absence of correlation with respect to the microarray results.

As an intermediate conclusion, we find that 900 MHz EMF exposure to whole blood cells at a SAR between 7.2 and 13.3 W/kg induces no detectable alterations in gene expression during short-time exposure until 90 min [4]. Future investigations will include more donors and an optimized exposure setup for additional results.

[1] Chapman, S., Azizi, L., Luo, Q., Sitas, F.: Has the incidence of brain cancer risen in Australia since the introduction of mobile phones 29 years ago? Cancer Epidemiology, Vol. 42, pp. 199-205, 2016.

[2] Herrala, M., Mustafa, E., Naarala, J., Juutilainen, J.: Assessment of genotoxicity and genomic instability in rat primary astrocytes exposed to 872 MHz radiofrequency radiation and chemicals, International Journal of Radiation Biology, Vol. 94, No. 10, pp. 883-889, 2018.

[3] Akdag, M., Dasdag, D., Canturk, F., Akdag M. Z.: Exposure to non-ionizing electromagnetic fields emitted from mobile phones induced DNA damage in human ear canal hair follicle cells, Electromagnetic Biology and Medicine, Vol. 37, No. 2, pp. 66-75, 2018.

[4] Lamkowski, A., Kreitlow, M., Radunz, J., Willenbockel, M., Sabath, F., Schuhn, W., Stiemer, M., Fichte, L. O., Dudzinski, M., Böhmelt, S., Ullmann, R., Majewski, M., Franchini, V., Eder, S., Rump, A., Port, M., Abend, M.: Gene Expression Analysis in Human Peripheral Blood Cells after 900 MHz RF-EMF Short-Term Exposure. Radiation Research 189(5), pp. 529-540, 2018.

Uncertainties Evaluation of Numerical Simulations with a FD-TD Solver – GORF3D

Laurent Labarbe
CEA, DAM
CEA-Gramat
F-46500 Gramat, France
laurent.labarbe@cea.fr

Jean-Pierre Adam
CEA, DAM
CEA-Gramat
F-46500 Gramat, France
jean-pierre.adam@cea.fr

Jean-Marc Lopez
CEA, DAM
CEA-Gramat
F-46500 Gramat, France
jean-marc.lopez@cea.fr

***Abstract*—This article deals with the uncertainties evaluation linked to the employment of numerical simulations in the case of electromagnetic coupling constraints determination induced by a plane wave on a system. The knowledge of this information is very important in order to control the results provided by the solver. The solver object of this study is GORF3D, property of CEA and based on the Finite-Difference Time-Domain (FD-TD) method. The first source of uncertainties presented in this work is the GORF3D propagation error due to the numerical dispersion of the FD-TD algorithm. The dispersion has a direct impact on the total field / scattered field separation surfaces (Huygens surfaces). The other sources of errors studied are the staircase mesh of perfectly conductive material and the Perfect Matched Layers (PML) / Convolution PML (CPML) boundary conditions.**

Keywords—uncertainties, time domain, numerical simulation, FD-TD solver, GORF3D

I. INTRODUCTION

In order to achieve a high level of confidence in the results of electromagnetic coupling numerical simulation cases, it is necessary to have a good idea of the uncertainties induced by the use of a solver. Moreover, CEA started adopting a reasoning which consists in proving the complete control of numerical results. The different steps of this approach are: a detailed user guide available to the beginners, the numerical models carefully validated by experiments, the control of the developments in the code, the non-regression tool, the validation domain of the solver, and of course the uncertainties evaluation, which is the topic of this article. This work is performed on GORF3D FD-TD solver, developed at CEA, and used to calculate electromagnetic constraints on systems or equipments.

II. ESTIMATION OF NUMERICAL DISPERSION OF THE FD-TD METHOD – THEORETICAL APPROACH

A. Dispersive character of FD-TD algorithm

The numerical algorithm defined by FD-TD solution causes dispersion of the simulated wave [1]: more precisely, for a given mesh, the phase velocity of numerical wave depends on the wavelength, the direction of propagation in the grid, and the grid discretization [2] [3]. In Fig.1, we can observe that the propagation velocity decreases when the frequency increases, compared to the vacuum speed of light.

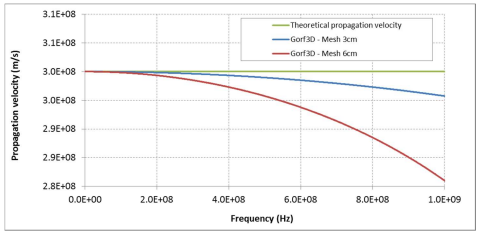

Fig.1. Propagation velocity variation according to the size mesh

For a wide band pulse signal, a distortion appears the further the shifting of waves in the numerical solution.

B. Analytical expression of FD-TD numerical dispersion

The numerical dispersion can be calculated as described in [4]. It is explicitly determined below to the full three-dimensional case involving all six coupled electric and magnetic field vector components.

We can consider 3 cases for the analytical expression of FD-TD numerical dispersion that links the wave number k to the pulsation ω:

- In the propagation direction, Eq. (1):

$$k = arcsin\left(\sin\left(\frac{\omega.dt}{2}\right).\frac{dx}{(c.dt)}\right).\frac{2}{dx} \quad (1)$$

- Onto the diagonal in 2D dimension, Eq. (2):

$$k = arcsin\left(\sin\left(\frac{\omega.dt}{2}\right).\frac{dx}{(c.dt.\sqrt{2})}\right).\frac{2.\sqrt{2}}{dx} \quad (2)$$

- Onto the diagonal in 3D dimension, Eq. (3):

$$k = arcsin\left(\sin\left(\frac{\omega.dt}{2}\right).\frac{dx}{(c.dt.\sqrt{3})}\right).\frac{2.\sqrt{3}}{dx} \quad (3)$$

Where dx=dy=dz and dx is the cell mesh size; the time step dt is derived from dx with the current criterion.

C. Dispersion impact on time domain signals

A Gaussian waveform is used for this study: the maximum amplitude of the electrical field (E) is 1kV/m before numerical dispersion occurs.

We can see in Fig.2. that the maximum E field level is decreasing during the propagation in the calculation volume: in order to compare simulation results, different points are referenced by their distance to the incident wave front and this distance is given in number of wavelengths. For a given time domain signal, the wavelength is set for the highest frequency in the power spectrum of the signal.

We can also see the deformation of the signal during the propagation in Fig.2.

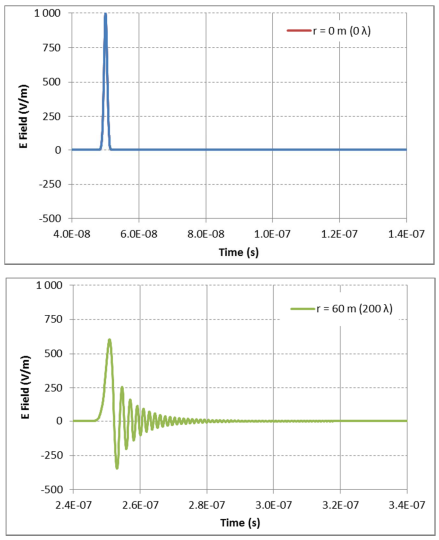

Fig.2. Gaussian signal distortion due to dispersion of the FD-TD method

For example, with an exponential quotient signal and a sensor placed at 100λ, the Table I represents the maximum errors on the maximum amplitude and rise time (time from 10% to 90% of peak level).

TABLE I. DISPERSION WITH EXPONENTIAL QUOTIENT SIGNAL

MESH	MAX AMPLITUDE ERROR (%)	RISE TIME ERROR (%)
λ/5	17.6	95
λ/10	10.7	36.5

The maximum amplitude error is always below 20%. It is not the case of the rise time error which reaches 95% for λ/5 mesh. This result confirms the necessity to use a mesh of at least λ/10 cells in order to take care of the dispersion effect [5] [6].

III. UNCERTAINTIES EVALUATION OF HUYGENS SURFACES

Huygens surfaces are used in order to generate an incident plane wave in the case of non-localized source. This chapter deals with the propagation error associated to the use of Huygens surfaces. The aggression considered is exponential quotient with a 1kV/m amplitude.

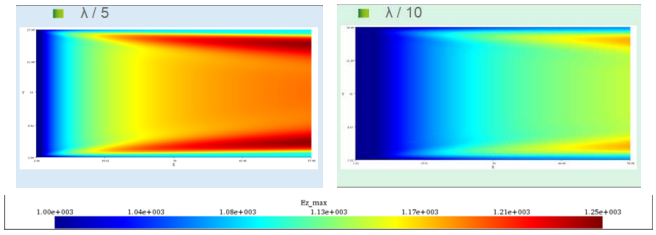

Fig.3. Huygens surfaces influence on the propagation of exponential quotient E Field

The observed error in Fig.3 comes from the calculation of incident field on these surfaces without taking into account the FD-TD solution dispersion. As the incident wave propagates, this error increases. In order to delete this error, the incident field deformation due to the propagation must be integrated in the solver, but this solution has a significant influence on the calculation time.

We can conclude that Huygens surfaces have an important impact on the propagation error and this effect is very dependent on the transversal plane dimension.

IV. UNCERTAINTIES EVALUATION OF PERFECTLY CONDUCTIVE MATERIAL MODEL WITH A STAIRS DISCRETIZATION

A generic box is chosen here for this study; an antenna (A) and a wire (B) are placed on the top of it. The staircases approximation is exact when the faces of the box are parallel to the grid planes. This case (named "Straight") can be considered as the reference (Fig.4).

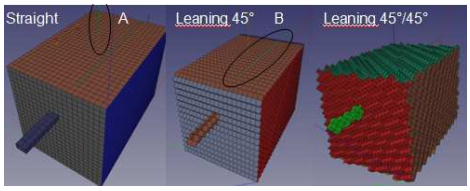

Fig.4. Mesh orientation on a generic box

The observed elements are: the E field in general, the E field maximum amplitude signal in time domain, the rise time and the antenna current.

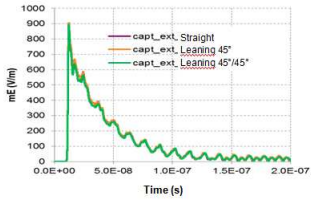

Fig.5. Comparison of a sensor outside the box which measures E Field

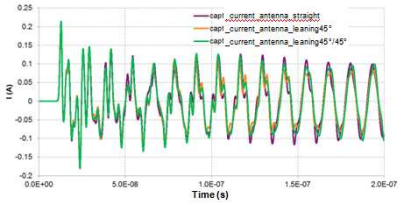

Fig.6. Comparison of a current sensor on the antenna

We can observe the same results even for the E field module and the antenna current: there are few differences (Fig.5 and Fig.6). For the E field, most of the discrepancies are related to the sensors position near the antenna, while good agreement is achieved for the sensors position far from the structure. For the currents, the results are identical for the first time steps.

The 3D results visualization shows that the influence of the mesh orientation is only observed near the object edges (Fig.7). In order to minimize the difference, the solution is to resort to a better mesh refining.

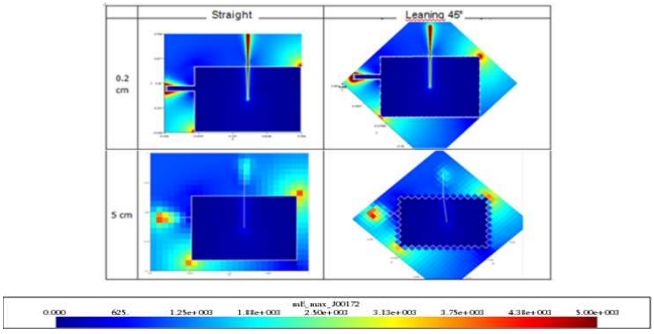

Fig.7. Maximum 2D results with a straight mesh and a 45° leaning mesh

Finally, the errors due to the perfectly conductive material model remain low:

- The maximal error observed on E is lower 10% if mesh size is lower λ/10 (> 30% if mesh size > λ/10),
- The error decreases far from the structure or the wire,
- The difference observed on the currents has a value between 10% and 30%.

The wire orientation has an effect and the discretization influence for a perfectly conductive surface could be even stronger in the reverberating environment involving multiple reflections.

V. UNCERTAINTIES DUE TO THE USE OF PML/CPML BOUNDARY CONDITIONS

The absorbing boundary conditions allow simulating an infinite domain modelling the free space surrounding the studied structure. GORF3D proposes two methods to take into account such boundaries: PML [7] or CPML. The goal of this chapter is to analyze the reflection produced by boundary conditions (ideally zero).

The parameters of this study are: λ=0.3m, absorbent layers number: 6, 10 or 20, mesh step: λ/5, λ/10 and λ/20, the distance to the calculation volume border: 6λ, 8λ, 10λ, 12λ, 16λ and 18λ, and calculation volume: 40λ x 200λ x 200λ.

The radiated point is located in the middle of the calculation volume and delivers a Gaussian signal (λ=30cm). Only the Ex component is analyzed (Ex is component along x axis).

The calculation points are located on the (Ox) axis as represented in Fig.8. These points are situated at the middle calculation volume in the two other directions (at 100λ far from the borders).

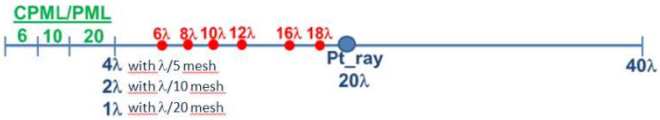

Fig.8. PML and CPML: calculation points localization

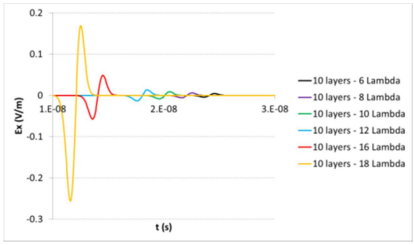

Fig.9. CPML model, with λ/10 mesh, incident signal according to the distance to the border point.

For the CPML (Fig.9), the maximum level of the reflected signal is much lower than the maximum level of the incident signal: in the worst case, the ratio is equal to 65dB (for 6 layers, λ/5 and the point which is the nearest to the border). Moreover, the ratio decreases when we move away from the border, whatever the mesh step and the number of absorbing layers.

For the PML, the results are the same with 6, 10 or 20 absorbent layers and also whatever the mesh step. The dispersion is less important than CPML, so the reflected signal level is globally much stronger than the CPML one (cf. Table II).

TABLE II. PML AND CPML MODELS COMPORTMENT

PML	CPML
-50dB	-65dB

VI. CONCLUSION

In this study, numerical uncertainties were determined for several GORF3D models:

- regarding the dispersion, FD-TD solver, , deforms time domain signals by slowing down the high frequencies,
- Huygens surfaces, which interact with the dispersion, can amplify the errors,
- The perfectly conductive material model which is discretized has a slight influence on simulation results,
- The boundary conditions induce a negligible parasitic reflection.

For an exponential quotient signal and a mesh criterion of λ/10, the uncertainties are about:

- For the maximum amplitudes : 10% to 20%,
- For the rise time: 30% to 60%,
- These errors principally come from numerical dispersion.

ACKNOWLEDGMENT

This study has been carried out for Direction Générale de l'Armement (DGA).

REFERENCES

[1] M. Mrozowski, « Stability condition for the explicit algorithm of the time domain analysis of Maxwell's equations » IEEE Microwave and Guided Wave Letters, vol. 4, n°8, August 1994.

[2] P. Thoma and T. Weiland, « Numerical Stability of Finite Difference Time Domain Methods », IEEE transactions on Magnetics, vol.34, n°5, pp. 2740-2743, September 1998.

[3] J. A. Pereda, A. Vegas and A. Prieto, « FDTD Modeling of Wave Propagation in Dispersive Media by Using the Mobius Transformation Technique », IEEE Transactions on Microwave Theory and Techniques, vol. 50, n°7, pp. 1689-1695, 2002.

[4] A. Taflove and S. C. Hagness, « Computational Electrodynamics – The Finite-Difference Time-Domain Method, 3e éd., Norwood, MA: Artech House Inc., 2005.

[5] S. Liu, N. Yuan and J. Mo, « A Nobel FDTD Formulation Dipersive Media », IEEE Microwave and Wireless Components Letters, vol. 13, n°5, pp. 187-189, 2003.

[6] A. Vial, A. –S. Grimault, M. Demetrio, D. Barchiesi and M. Lamy de la Chapelle, « Improved analytical fit of gold dispersion: Application to the modeling of extension spectra with finite-difference time-domain method », Physical Review B, vol. 71, p. 085416, 2005.

[7] J-P. Bérenger, « A perfecty matched layer for the FDTD solution of wave-structure interaction problems », IEEE Transaction on Antennas and Propagation, vol. 44, n°1, pp. 1-8, January 1996.

Optimizing the Positioning of the Coil for Deeper Transcranial Magnetic Stimulation

1st Lei Yang
China Academy of Information and Communications Technology
Beijing, China
yanglei@caict.ac.cn

2nd Chang Liu
China Academy of Information and Communications Technology
Beijing, China
420503134@qq.com

3rd Tongning Wu
China Academy of Information and Communications Technology
Beijing, China
wutongning@caict.ac.cn

Abstract—The distribution of the induced electric field (E-field) during transcranial magnetic stimulation (TMS) depends on the individual anatomical structure of the head/brain as well as the coil positioning. Inappropriate or insufficient stimulation may degrade the efficacy or even induce adverse effects. Therefore, optimization of the induced E-field according to the clinical needs became the research focus. In this paper, multi-objective particle swarm optimization (PSO) is, for the first time, applied in the positioning of the TMS coils with an anatomical head model. The optimization can achieve a deeper cortical stimulation and ensuring a steeper E-field strength gradient (superficial E-field strength was reduced), whilst using a popularly used eight-shaped coil. The technique has the potential application for the deeper TMS. This study benefits not only to the clinics but also to the research on brain modulation.

Keywords—transcranial magnetic stimulation, scalar potential finite-difference, bi-objective optimization, particle swarm optimization, electric field

I. INTRODUCTION

Transcranial magnetic stimulation (TMS) [1] is a widely used non-invasive tool for modulating human brain activities. Short pulses of magnetic fields are delivered to the brain cortex through current-carrying coils. The rapidly changing magnetic field induces electrical currents within the cortex and stimulates activity over a predefined cortex region [2]. In most cases of coil design, we need to make trade-off for stimulation depth and focus.

Numerical simulation became an effective and non-invasive tool to characterize the E-field distribution in the brains. The induced E-field is described in terms of electric scalar potential satisfying an elliptic partial-differential (finite-difference) equation (SPFD), which is to be discretized by various numerical methods, e.g., finite-element method [3,4], boundary element method (BEM) [5], finite-difference time-domain (FDTD) [6] and impedance method (IM) [7].

By aids of the numerical tools, researchers found that the distribution of the induced E-field in the brain was determined by the coil geometry, placement [8] and by the individual anatomy as quantity of the CSF [9], local gyral orientation and anisotropy of the brain tissue [3] and sulcus width [10]. Researchers thus recognized the importance for designing the stimulation configuration per subject and conducted a number of studies to derive the optimal stimulating regions [11].

Evolutionary algorithms, e.g., Genetic Algorithm (GA) or improved GA [12] have been applied to facilitate the device design and the treatment optimization during TMS. In comparison, particle swarm optimization (PSO) is less complicated and easy to be implemented in comparison to GA because neither mutation nor crossover operator is involved [13]. Recently, the application of PSO to coil design has been mentioned [14] but its clinical feasibility and efficiency for positioning optimization has not been demonstrated.

In this work, we would optimize the positioning of the eight-shape coil, a popular commercial coil in clinical uses, by using bi-objective particle swarm optimization (BOPSO). The optimization could enhance the E-field strength in a deeper region whilst reduce the E-field strength on the cortical surface.

II. PSO AND BOPSO

A. Basic PSO and parameterization

The optimization is initialized with a number of particles to search for optima. The current solution of the particle at ith iteration is:

$$x_i=\left(pos_i(x,y,z),rot_i(x,y,z)\right) \tag{1}$$

Where, $pos(x,y,z)$ represents the position of the coil center in the Cartesian coordination; $rot(x,y,z)$ represents the tilt angles rotating along the three axes. The best solution that a particle has ever achieved is:

$$p_i=\left(pos_{pi}(x,y,z),rot_{pi}(x,y,z)\right) \tag{2}$$

The best solution of the particle swarm is:

$$p_g=\left(pos_{pg}(x,y,z),rot_{pg}(x,y,z)\right) \tag{3}$$

And the velocity of the particle is:

$$v_i=\left(vpos_i(x,y,z),vrot_i(x,y,z)\right) \tag{4}$$

After finding the two best values, the particle updates its velocity and position by:

$$\begin{aligned} v_i &= \omega v_i + c_1 \cdot rand()\left(p_i - x_i\right) + c_2 \cdot rand() \cdot \left(p_g - x_i\right) \\ x_i &= x_i + v_i \end{aligned} \tag{5}$$

where, *rand()* is a random number between (0, 1), c_1 and c_2 are learning factors (exploration and exploitation abilities), usually $c_1=c_2=2$ to balance the cognitive and social

influences [15]; ω is the inertial weight factor between (0.9, 1.2) [16] with the self-adaptive method as $\omega = \omega_{max} - t / t_{max} (\omega_{max} - \omega_{min})$ [16], ω_{min} and ω_{max} being the minimum and the maximum weight, respectively; t and t_{max} are the current iterative number and the maximum iterative number.

Particles' velocities on each dimension are limited to a maximum velocity V_{max}. To prevent a particle from flying out of the searching space, the value of V_{max} is usually imposed to 10-20% of the dynamic range of that dimension [17]. Invisible boundary condition is used to reduce the computational cost [18].

B. BOPSO

PSO for multiple objectives based on conventional weighted aggregation (CWA) is applied [19]. The focality of the induced E-field is an important consideration for TMS [20]. That is, the activation site has high E-field strength whilst the value decreases rapidly outside the stimulation locus [21]. As an example, mean E-field strength and E-field gradient in a 10 mm×10 mm surface on the primary motor cortex is selected as the region of interest (ROI, Fig 1). To ensure an effective stimulation, the E-field strength and the gradient in the region is preferred to be maximized. We hence define the weighted fitness function in CWA format as:

$$Fitness = \omega_1 \cdot E_{avg} + \omega_2 \cdot Grad_{avg} / 100 \quad (7)$$

where, E_{avg} is the E-field strength averaging over ROI; $Grad_{avg}$ is the mean E-field spatial gradient at ROI, being divided by 100 to ensure the same magnitude as E_{avg} ω_1=ω_2=0.5 are weighted factors.

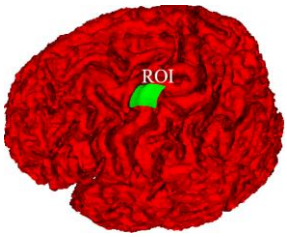

Fig.1. Target region for the experiment

For the abovementioned case, the distance between the coil and the scalp is kept as 1 cm according to the clinical treatment protocol. The parameters of the searching space are subjected to:

pos(x, y, z)∈{(center of the stimulated locus ±3 cm along three axis)}, and rot(x, y, z) ∈{(± 20º, ± 20º, ± 20º)}The abovementioned searching space is recommended by the published literature [22] and the clinical condition (with a distance of 1 cm, the maximal rotational angle of the coil is about ± 20º).

III. Numerical Models

The numerical head models of Chinese female adult and an 8-shape coil are used in the simulations. The head model (Fig 2A) contains 49 identified tissues with a spatial resolution of 1mm×1mm×1mm [23]. The operating frequency of the 8-shape one-turn coil is 2.5 kHz Hz and the current is 1000 A (Fig 2B).

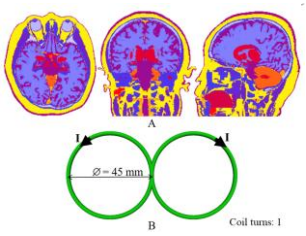

Fig.2. Numerical model and the TMS coil (Coil turns :1)

IV. Results

A. Comparison of the induced E-fields in human head model

The in-house SPFD solver was used to calculate the induced E-field distribution in the brains [24]. The solver used the incomplete lower- and upper- matrix preconditioner to speed up the solution of the derived septa-diagonal matrix, where block Forward-Elimination and Backward-Substitution algorithm was developed to facilitate the multi-thread parallelization of GPUs. This solver has been validated with the commercialized software which is free to download at (https://github.com/licongsheng/OpenSPFD).

B. Positioning optimization of the TMS coil

Using the aforementioned hardware, the optimization with CWA objectives converges at 10th iteration (100 min) and 13th iteration (130 min), respectively. The convergence process for CWA objectives is shown in Fig 3. We found that the local E-field strength and its gradient have been improved by 200%. The conformal transformation [25] was used to map the E-field on RIO(s) to a plane. The induced E-field distribution at the respective iteration is shown in Fig 4.

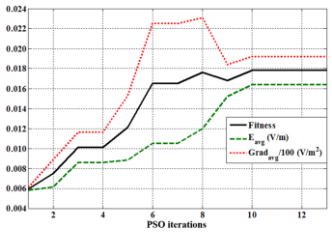

Fig. 3. Convergence of BOPSO

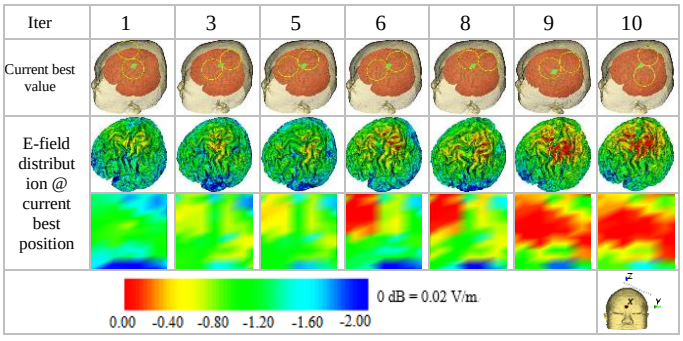

Fig.4. E-field distribution for different iterations. The coil position at Iter 10 was translation (-2.91mm, 44.55mm, 73.05mm) and rotation (-26.15°, -12.49°, 93.97°) (The conformal transformation was used to map the e-field distribution on ROI to a plane)

V. Discussion

To note, although PSO has been widely applied in many engineering problems, the theory itself is under development

with many issues to be solved and its dynamics and potential limits have not yet been extensively addressed [26,27]. By the same reason, the applicability of the technique to more stimulating cases (including large anatomical variability and various stimulating sites) can be fully comprehended only after a thorough mathematic validation of the PSO. The study has not concentrated on the robustness of the optimization algorithm although a preliminary discussion has been made to determine the parameters of the algorithm. Theoretically, a trial-and-error analysis may further optimize the objective function as well as the parameters in the PSO iteration. However, the problem is highly case-dependent and the improvement with one case is not always applicable to other cases. So, we adopted the general parameter optimization strategy from the previous literatures. BOPSO optimizations by CWA are presented. We can adopt the prior knowledge from the physicians to decide the relative importance of the objectives. The format of CWA is easy and straightforward to apply. Therefore, CWA based PSO has practical advantage for the study.

VI. CONCLUSION

This study proposes the numerical methods to optimize the positioning of the coils according to clinical needs. The application of the PSO-based optimization in the TMS coil positioning is firstly studied in the work. The method could raise the E-field strength in the stimulation site for 200% while ensuring a high E-field gradient. As such, the E-field decreased rapidly at the surface, which was benefit for a much deeper stimulation. The present methods enable the application of a precise stimulating plan per patient.

REFERENCES

[1] M. Hallett, "Transcranial magnetic stimulation and the human brain," Nature, vol. 406(6792), pp. 147-150, July 2000.

[2] M. T. Wilson, D. P. Goodwin, P. W. Brownjohn, J. B. Shemmell, and J. N. Reynolds, "Numerical modelling of plasticity induced by transcranial magnetic stimulation," J. Comput. Neurosci, vol. 36(3), pp. 499-514, June 2014.

[3] A. Opitz, M. Windhoff, R. M. Heidemann, R. Turner, A. Thielscher, " How the brain tissue shapes the electric field induced by transcranial magnetic stimulation," Neuroimage, vol. 58(3), pp. 849-859, October 2011.

[4] I. Laakso, and A. Hirata, "Fast multigrid-based computation of the induced electric field for transcranial magnetic stimulation," Phys. Med. Biol, vol. 57(23), pp. 7753-7765. November 2012.

[5] F. S. Salinas, J. L. Lancaster, and P. T. Fox, "3D modeling of the total electric field induced by transcranial magnetic stimulation using the boundary element method," Phys. Med. Biol, vol. 54(12), pp. 3631-3647. May 2009.

[6] F. Fanjul-Vélez, I. Salas-García, N. Ortega-Quijano, and J. L. ArceDiego, "FDTD-based Transcranial Magnetic Stimulation model applied to specific neurodegenerative disorders," Comput. Meth. Prog. Bio, vol. 118(1), pp. 34-43, January 2015;

[7] A. Paffi, F. Camera, F. Carducci, G. Rubino, P. Tampieri, M. Liberti, and F. Apollonio, "A computational model for real-time calculation of electric field due to transcranial magnetic stimulation in clinics," Int. J. Antennas. Propag, vol. 2015, pp. 1-11, October 2015.

[8] J. P. Brasil-Neto, L. G. Cohen, M. Panizza, J. Nilsson, B. J. Roth, and M. Hallett, "Optimal focal transcranial magnetic activation of the human motor cortex: effects of coil orientation, shape of the induced current pulse, and stimulus intensity," J. Clin. Neurophysiol, vol. 9(1), pp. 132-136, February 1992.

[9] X. L. Chen, S. Benkler, N. Chavannes, V. De Santis, J. Bakker, G. van Rhoon, J. Mosig, and N. Kuster, "Analysis of human brain exposure to low‐frequency magnetic fields: A numerical assessment of spatially averaged electric fields and exposure limits, " Bioelectromagnetics. vol. 34(5), pp. 375-384, February 2013.

[10] A. M. Janssen, S. M. Rampersad, F. Lucka, B. Lanfer, S. Lew, U. Aydin, C. H. Wolters, D. F. Stegeman, and T. F. Oostendorp, "The influence of sulcus width on simulated electric fields induced by transcranial magnetic stimulation," Phys. Med. Biol, vol. 58(14), pp. 4881-4896, June 2013.

[11] M. C. Ridding, B. Brouwer, T. S. Miles, J. B. Pitcher, and P. D. Thompson, "Changes in muscle responses to stimulation of the motor cortex induced by peripheral nerve stimulation in human subjects," Exp. Brain. Res, vol. 131(1), pp. 135-143, March 2000.

[12] J. Liu, J. Lu, C. Liu, and Y. Hu, "Coil arrays modeling and optimization for Transcranial Magnetic Stimulation," 2009 2nd International Conference on Biomedical Engineering and Informatics, 2009 Oct 17-19; Tianjin, China. IEEE, pp. 1-5, October 2009.

[13] R. C. Eberhart, and Y. Shi, "Comparison between genetic algorithms and particle swarm optimization," International Conference on Evolutionary Programming, Heidelberg. Berlin. Springer, pp. 611-616, 1998.

[14] H. Xiong, J. H. Shi, X. W. Hu, and J. Z. Li, "The focusing optimization of Transcranial Magnetic Stimulation system," Prog. Electromagn. Res. M, vol. 48, pp. 145-154, June 2016;

[15] N. Jin, and Y. Rahmatsamii, "Particle swarm optimization for antenna designs in engineering electromagnetics," J. Artif. Evol. Appl, vol. 2008(9), pp. 1-10, January 2008;

[16] Y. Shi, and R. C. Eberhart, "A modified particle swarm optimizer," Evolutionary Computation Proceedings, 1998, IEEE World Congress on Computational Intelligence., The 1998 IEEE International Conference on; 1998 May 4-9; Alaska, USA, IEEE, pp. 69-73, May 1998.

[17] R. C. Eberhart, and Y. Shi, "Comparing inertia weights and constriction factors in particle swarm optimization," Evolutionary Computation, 2000, In: Proceedings of the 2000 Congress on; 2000 July 16-19; California, USA, IEEE, pp. 84-88, July 2000.

[18] J. T. Robinson, and Y. Rahmatsamii, "Particle swarm optimization in electromagnetics" IEEE. Trans. Antennas. Propag, vol. 52(2), pp. 397-407, April 2004.

[19] M. Reyes-Sierra, and C. A. C. Coello, "Multi-objective particle swarm optimizers: A survey of the state-of-the-art," Int. J. Comput. Intell. Res, vol. 2(3), pp. 287-308, April 2006;

[20] L. Pu, T. Yin, H. An, S. Li, and Z. P. Liu. "Optimization of the coil to focalize the electrical field induced by magnetic stimulation in the human brain," J. Biomed. Eng. Res, vol. 19, pp. 366-372, February 2008;

[21] Z. D. Deng, S. H. Lisanby, and A. V. Peterchev, "Electric field depth–focality tradeoff in transcranial magnetic stimulation: simulation comparison of 50 coil designs," Brain. Stimul, vol. 6(1), pp. 1-13, January 2013.

[22] M. V. De Ruit, M. J. Perenboom, and M. J. Grey, "TMS brain mapping in less than two minutes," Brain. Stimul, vol. 8(2), pp. 231-239, April 2015.

[23] T. N. Wu, L. W. Tan, C. Zhao, S. X. Zhang, and B. S. Lu, "Chinese human voxel models for evaluation of EMF exposure purpose: in development." 2010 Asia-Pacific International Symposium on Electromagnetic Compatibility, 2010 April 12-16, Beijing, China, IEEE, pp. 25-28, April 2010.

[24] C. S. Li, Z. F. Ye, Y. W. Wei, and T. N. Wu, "An optimized block forward‐elimination and backward‐substitution algorithm for GPU accelerated ILU preconditioner in evaluating the induced electric field during transcranial magnetic stimulation," Bioelectromagnetics, March, 2019.in press.

[25] P. K. Kythe, Computational Conformal Mapping, Boston, MA: Birkhäuser, 1998.

[26] X. Hu, Y. Shi, and R. C. Eberhart, "Recent advances in particle swarm," Proceedings of the 2004 Congress on Evolutionary Computation (IEEE Cat. No. 04TH8753), 2004 June 19-23, Portland, OR, USA, vol. 1, pp. 90-97, June 2004.

[27] J. Kennedy, and W. M. Spears, "Matching algorithms to problems: an experimental test of the particle swarm and some genetic algorithms on the multimodal problem generator," Proceedings of the IEEE international conference on evolutionary computation, 1998 May 4-9, Alaska, USA, pp. 78-83, May 1998.

Modeling Subject-Specific Head Model:Application to Calculation of Induced Electric fields by TMS

Lin LIN
School of Electrical Automation and Information Engineering
Tianjin University
Tianjin, China
linlinlook@163.com

Jiang Wang
School of Electrical Automation and Information Engineering
Tianjin University
Tianjin, China
jiangwang@tju.edu.cn

XiLe Wei
School of Electrical Automation and Information Engineering
Tianjin University
Tianjin, China
xilewei@tju.edu.cn

Bin Deng
School of Electrical Automation and Information Engineering
Tianjin University
Tianjin, China
dengbin@tju.edu.cn

***Abstract*—Transcranial magnetic stimulation (TMS) is a tool to achieve non-invasive brain stimulation. It holds significant promise as a tool for cognitive neuroscience and the treatment of neurological disorders. High-precision model is the key and foundation of establishing TMS stimulation dosage, mechanism and other theoretical research. We put forward a "voxel mapping method" and established a high precision finite element model called "subject-specific model". Recognition accuracy of subject-specific model is in the order of millimeters. In order to illustrate the importance of model precision, we constructed a layered and uniform head model according to the existing literature method (namely simplified model).In the case of deep TMS, the induced electric field and induced eddy current distribution pattern in the deep brain region were analyzed. The results shows that the more explicit conclusion of TMS should be based on the high precision model, and the simplified model can underestimate the TMS effect. Our conclusion accurately response actual electric field distribution in the brain, and have important value for the mechanisms of TMS and clinical research.**

Keywords—Noninvasive brain stimulation, stimulation depth, sparse focus , transcranial magnetic stimulation (TMS)

I. INTRODUCTION

Transcranial magnetic stimulation is a non-invasive technique that can be used as a tool for cognitive neuroscience and neurological disorders [1]-[2]. Recent studies used numerical simulations based on the whole head model to achieve a more realistic estimation of the induced field. Five tissue types were considered, namely skin, skull, cerebrospinal fluid(CSF), grey matter(GM) and white matter(WM) [3]-[4]. They simplified subsequent surfaces were fully contained within each other. Each kind of brain tissue was simplified to a single conductivity value.

However, tissue geometry and heterogeneity both must be taken into account to predict accurately distribution of induced electric field in TMS. Here, we propose a new method called "volex mapping method" and using its build a high precision model which accurately reflect three-dimensional heterogeneous conductivity of the WM and GM. We set 9 parameters (adjustable) to characterize the non-uniformity of total brain conductivity. We named our model "subject-specific model". The subject-specific model is a more accurate reconstruction of the heterogeneity of brain tissue, which is the base of the study of the TMS system performance and brain stimulation response mechanism. For the convenience of comparison, we constructed a simplified model, using the same MR image T1 data. The parameters of the two models are shown in table 1.

Table 1

Tissue	Gray value of MRI	Conductivity (simplified model)	Conductivity (subject-specific model)
CSF	0~100	1.654	1.654(Deep blue)
GM	101~200	0.276	0.376(Light blue)
	201~300	0.276	0.276(Light green)
	301~400	0.276	0.176(Dark green)
WM	401~500	0.126	0.146(Light yellow)
	501~600	0.126	0.136(Deep yellow)
	601~700	0.126	0.126(Orange)
	701~800	0.126	0.116(Light red)
	801~1322	0.126	0.106(Dark red)
Skull		0.010	0.010
Skin		0.465	0.465

Some treatment and research on the target area is located in the deep brain area. Depression, schizophrenia, autism spectrum disorders associated with the deep structure of the brain. Deep TMS is one of research hotspots. We designed and realized a deep brain magnetic stimulation setup ,namely as " TMS Multicoil Arrays Setup". The device can realizes the shallow local stimulation and deep global stimulation.

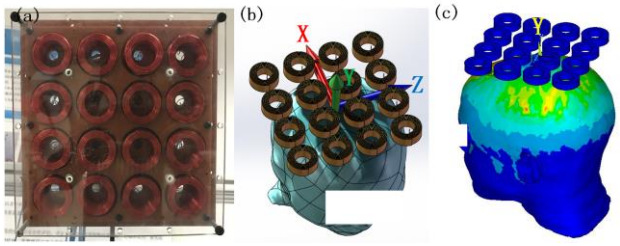

Fig.1. Multicoil array and head model.

We used coil selection and current direction to adjust the stimulus intensity, acting on two types of models. The results show that the deep global stimulation caused within the brain tissue of subject-specific model and simplified model there are different forms of distribution. Heterogeneous conductivity of the WM and GM affect the local field in a systematic way and result in localized increases of up to 30% in the deep global stimulus. The pattern of high field intensity distribution within the WM is consistent with

Thielscher's conclusion [3]. Considering the heterogeneity of GM and WM at the same time, our model has higher precision than Thielscher's model.

Through the study of whole-brain simulation, we found that heterogeneity in GM also has an important effect on the distribution of electric fields, confirming goodwin's prediction[5]. The increase of the local field strength is significant for the stimulation of some therapeutic target areas (such as the medial frontal lobe and orbitofrontal cortex) in the brain region of 3-5 cm depth[6].

II. METHODS

A. Construction of the two types of head models

The data of the head model we constructed came from the standard MR image head T1 data module (healthy male). Imaging parameters: slice thickness=1mm, transversal slices=255,voxel size=1.098mm*1.098mm*1.0mm. We segmented scalp,skull,CSF,WM,GM based on Mimics 17 and 3matic9.0 (Materialise Inc., Leuven, Belgium), and used 3matic9.0 to reconstruct the shape of the five tissue types. We generated optimized volumetric mesh using Hypermesh 11. The number of total tetrahedra was 2.95 million. Subject-Specific model is constructed using the voxel mapping method and reflects the characteristics of heterogeneity. The simplified model adopts the construction method of literature [3-4].

The build of the subject-specific model is based on the following considerations: Under the same measurement conditions, the typical values of electrical conductivity of the brain tissue measured by different documents are not consistent and the difference is larger. This difference objectively reflects that the conductivity value of each brain tissue is not constant. Using MR image, we can accurately locate the heterogeneity of brain tissue through the corresponding relationship between the gray value and the coordinate. We propose novel modeling idea "voxel mapping method", based on the general assumption is that specific electrical conductivity values of brain tissue can be reflected by theirs grey value of MR images. The basic idea of assignment of conductivity value is to establish a mapping relationship between the voxel element of MR image and the tetrahedral volume mesh of the brain tissue. Therefore, the voxel and tetrahedron satisfy the following mapping relationship.

$$Voxel(x, y, z, gray\,value) \rightarrow Tetrahedron(x, y, z, \sigma_i) \quad (i = 1, 2, ..., 9) \tag{1}$$

Once the mapping relationship is established, each tetrahedron will obtain the properties of the certain voxel according to its coordinate position, such as conductivity value , permittivity, magnetic permeability. This allows us to use the transition of gray value of images to manage the properties of volume mesh so that the finite element model can have more complex properties to simulate the real brain. This is a big innovation of our model compared to the conventional approach.

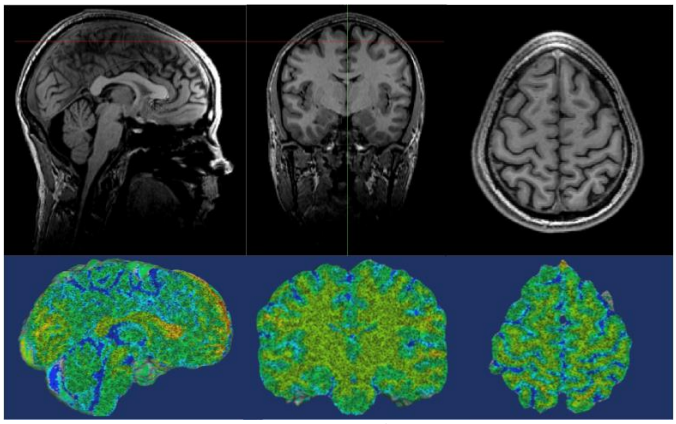

Fig 2 T1-Weighted MRI and cross section of tetrahedral volume mesh.

The relationship between the number of voxel and the gray value of the whole brain(GM and WM) is shown in Fig.2. There is a large amount of liquid material(low gray values and high conductivity value) scattered in the brain, which are small and discrete, but they can be accurately positioned in the model using voxel mapping method. Based on the determination of the subinterval of gray value and the voxel mapping, we can divide the 1.41 million tetrahedron into 9 parts, and the conductivity of each part has the same value(Table 1). Through the classification of tetrahedral attributes, we can divide the structure of the brain with high resolution and high accuracy. In addition, it successfully avoids the disadvantage of introducing larger errors in the segmentation process of the tissue boundary. Through such operations, even a few tetrahedron, which is far apart, can be classified into the same subinterval due to the same gray value and electrical conductivity value. Fig.2 shows that after the completion of the voxel mapping operation, the MR image is compared with the tetrahedral mesh. We use several colors to indicate that the tetrahedron is divided into different subintervals. Although the tetrahedra are discrete, which with the same color have the same electrical conductivity value.

B. Method of calculation

The stimulator output (peak excitation current's time derivative) is originally set to $1A/\mu s$ .Simulation was performed using the electromagnetic module of the finite-element package *ANSYS*15 with element type solid236(twenty-node). The heterogeneous conductivity value has no influence on magnetic vector potential($\mathbf{A}$) and has a great influence on the electric scalar potential (ϕ)[7].Finally, we determined induced field by Eq. (2).

$$\mathbf{E} = -\frac{\partial \mathbf{A}}{\partial t} - \nabla\phi \tag{2}$$

The rate of current change of $1A/\mu s$ is used to compare with existing literatures[3-4,7], so as to explain the rationality of our model.

III. SIMULATION

A. Inducted electric field and current distribution

Fig.3 shows field strength and current distribution of the subject-specific model and simplified model under the stimulus of deep global.

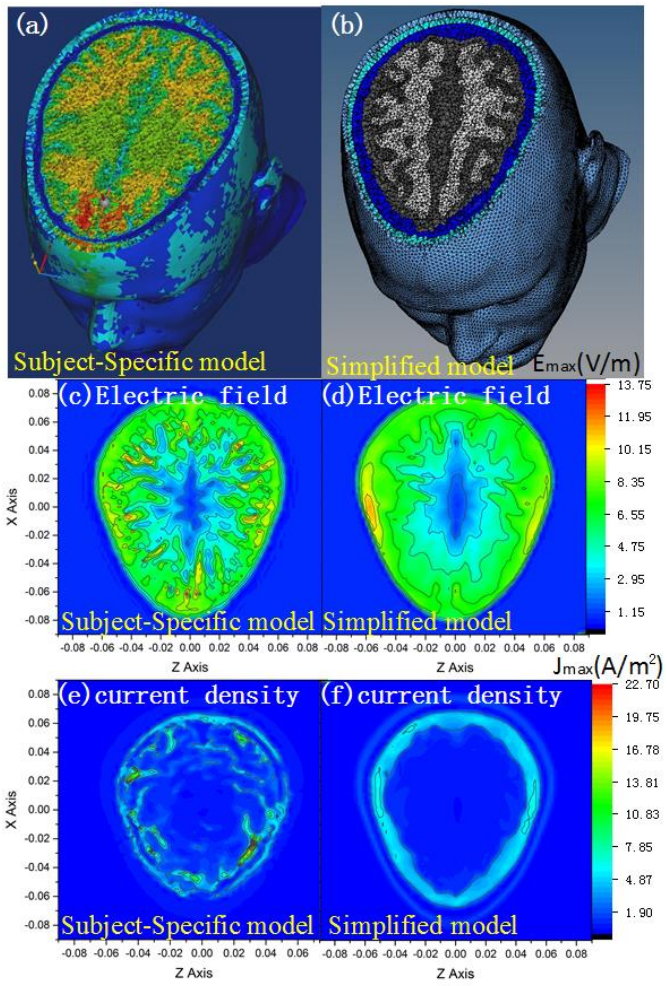

Fig. 3. Volume mesh and field induced and induced current in brain.

In the WM and GM of the subject-specific model, we observed that there are multiple discrete distributions of high field strengths showing the state of "sparse focus"[5]. In the simplified model, The region of high field strengths is more close to the scalp and skull along the border with air. The high magnitude current in the simplified model is distributed in the CSF, which is related to the structure of the simplified model. The simplified model has constant conductivity and a layered structure, which results in a large error compared with the actual situation.

IV. Conclusion

In this paper, the electric field distribution characteristics of two models are compared. In the global deep TMS, multiple isolated regions of high field strengths exist in the GM and WM of subject-specific model. High field strengths showing the characteristics of sparse distribution (sparse focus). The pattern of the field's distribution is consistent with Goodwin's prediction. In the simplified model, the distribution of high field strength has no such complex characteristics, but only shows the characteristics of rapid attenuation along the radial direction. These results indicate that the heterogeneity of the brain can produce very huge effect to the induced electric field distribution within the brain, which directly lead to the existence of discrete distribution of high field strength in the deep brain area. The method of voxel mapping proposed in this paper is applicable to the establishment of a complete brain heterogeneity model. Our conclusion is also consistent with Goodwin's prediction that considering the non-uniformity of the entire brain, which can cause TMS to have more focal (and perhaps sparse) effects. Comprehensive the above conclusion, we believe that only build model which can accurately reflect three-dimensional heterogeneous conductivity of the WM and GM is prerequisite to gain actual distribution of induced field. The data calculated by using the simplified model will underestimate the TMS stimulation effect on the brain. At the same time, we should further discuss how to correctly evaluate the sparse focus, which requires us to define a series of performance indicators to quantify the complex distribution characteristics, and use them to guide TMS coil design and related mechanism research.

References

[1] Peterchev A V, Wagner T A, Miranda P C, et al. Fundamentals of transcranial electric and magnetic stimulation dose: definition, selection, and reporting practices.[J]. Brain Stimulation, 2012, 5(4):435-453.

[2] Bersani F S, Minichino A, Enticott P G, et al. Deep transcranial magnetic stimulation as a treatment for psychiatric disorders: a comprehensive review[J]. European Psychiatry the Journal of the Association of European Psychiatrists, 2013, 28(1):30-39.

[3] Thielscher A , Opitz A , Windhoff M . Impact of the gyral geometry on the electric field induced by transcranial magnetic stimulation[J]. NeuroImage, 2011, 54(1):234-243.

[4] De G N, Crevecoeur G, Leemans A, et al. Effective electric fields along realistic DTI-based neural trajectories for modelling the stimulation mechanisms of TMS[J]. Physics in Medicine & Biology, 2015, 60(2):453-471.

[5] Goodwin B D, Butson C R. Subject-specific multiscale modeling to investigate effects of transcranial magnetic stimulation[J]. Neuromodulation, 2016, 18(8):694-704.

[6] Bersani F S, Minichino A, Enticott P G, et al. Deep transcranial magnetic stimulation as a treatment for psychiatric disorders: a comprehensive review.[J]. European Psychiatry the Journal of the Association of European Psychiatrists, 2013, 28(1):30-39.

[7] Chen M, Mogul D J. Using increased structural detail of the cortex to improve the accuracy of modeling the effects of transcranial magnetic stimulation on neocortical activation.[J]. IEEE Transactions on Biomedical Engineering, 2010, 57(5):1216-1226.

A 400 kV gas-insulated low-jitter compact Marx generator

Xie Linshen
State Key Laboratory of Intense Pulse Radiation Simulation and Effect, Northwest Institute of Nuclear Technology
Xi'an, China
710024

Chen Zhiqiang
State Key Laboratory of Intense Pulse Radiation Simulation and Effect, Northwest Institute of Nuclear Technology
Xi'an, China
710024
State Key Laboratory of Electrical Insulation and Power Equipment, Xi'an Jiaotong University
Xi'an, China
710049

Jia Wei
State Key Laboratory of Intense Pulse Radiation Simulation and Effect, Northwest Institute of Nuclear Technology
Xi'an, China
710024
State Key Laboratory of Electrical Insulation and Power Equipment, Xi'an Jiaotong University
Xi'an, China
710049

***Abstract*—With the request of synchronization of optical measurement devices in the discharge study under nanosecond pulses, a 400 kV gas-insulated low-jitter compact Marx generator is designed and developed in this paper. Firstly the main factor affecting the erection time jitter is analyzed, and the key to reduce the time jitter is to improve the overvoltage coefficient of the self-breakdown gas switches. Then based on the analysis, a 10-stage bipolar-charged coaxial Marx generator was designed. 3 forestage switches of the whole 10 work in the trigger mode to enhance the overvoltage coefficients of the latter switches. The Marx module is linearly arranged in the middle of a metal cylinder, which is inflated with 0.4MPa SF6 to avoid insulation failure. A PMMA cylinder is inserted between the Marx module and the metal cylinder to make the structure more compact, thus the distribution capacitance between the gas switch and the metal cylinder is increased and the overvoltage coefficients are enhanced accordingly. The experimental results show that when the gas switches are inflated with 0.1-0.3MPa N2, the Marx generator could erected with an operating ratio 0.4-0.9, and the amplitude of the output nanosecond pulse is from 64 kV to 442 kV. When the N2 pressure is between 0.2MPa and 0.3MPa, and the operating ratio is between 0.7 and 0.8, the erection time jitter of the Marx generator is lower than 2 ns.**

Keywords—nanosecond pulse; Marx generator; low-jitter; operating ratio; overvoltage coefficient; erection time delay

I. INTRODUCTION

With the development of pulse power technology, the study of nanosecond pulse discharge has attracted much attention [1-5]. In the observation process of nanosecond pulse discharge, the form and discovery speed of discharge channel can be directly observed by using high-speed framing camera to obtain images of discharge process, which is a common diagnostic method in the field of gas discharge. Nanosecond pulse discharge has a short duration and a fast development speed. In order to obtain images that can reflect the discharge process, it is required not only that the framing camera has a shutter time as low as some nanoseconds, but also that the synchronization between the pulse generator and the camera is good, that is the pulse generator is required to have a low erection time jitter. As a classic high-power pulse generator, Marx generator has been widely used. Compared with tesla transformer and other pulse generators, Marx generator has higher energy transmission efficiency, simple structure, low cost and other advantages [6-12]. In this paper, a 400kV low-jitter compact Marx generator is designed and developed by analyzing the factors affecting the time jitter of the generator and optimizing the structure of the generator..

II. DESIGN OF LOW-JITTER MARX GENERATOR

The erection time jitter of the Marx generator is mainly determined by the breakdown delay and jitter of each switch, while the breakdown delay of the switch is affected by the triggering mode and overvoltage coefficient. It has been pointed out in the literature that the dithering of Marx generator erection time mainly comes from previous switches, and its contribution to the dithering of generator erection time can reach more than 60% [7].During the erection of the Marx generator, after the conduction of the front switch, the load voltage on the later switches U is affected by the stray capacitance C_i and gap capacitance C_g. [8].

$$U=nU_0\left\{1-\frac{C_g}{C_i+C_g}\exp\left[-\frac{t}{R\left(C_i+C_g\right)}\right]\right\} \quad (1)$$

Where n is the series of switches，U_0 is capacitor charging voltage C_i is stray capacitance of switch，C_g is distributed capacitance between two electrodes in spark gap，R is charge resistance。

From equation 1, it can be seen that if only the first stage switch is triggered, and the subsequent switch is conducted in the way of voltage doubling self-breakdown, the actual load voltage of the second stage switch will be lower than twice the voltage of the first stage. The breakdown delay of the switch is affected by the over-voltage coefficient of the load voltage. When the over-voltage coefficient is low, the breakdown delay and the corresponding jitter are both large. In order to reduce the erection time and jitter of the Marx generator, the overvoltage coefficient of the self-breakdown switch should be increased as for as possible. Therefore, in this project, the first three switches are externally triggered.

At the same time, equation 1 shows that increasing the stray capacitance of the switching electrode to the ground is

conducive to improving the partial voltage at both ends of the switch. Therefore, the metal outer tube is lined with an insulating tube to minimize the size of the outer tube of the Marx generator and change the dielectric constant distribution in the Marx generator cavity, so as to increase the stray capacitance of the switching electrode to the ground. On the other hand, the size of the outer barrel is reduced, and the components on the Marx generator movement are arranged in a compact manner. Sufficient insulation distance should be ensured between the components in the design process。

In addition, multiple spark switches are arranged in the same insulating cavity structure, and the ultraviolet light generated by gap conduction of the former stage spark switches will irradiate to the later stage switches, which is beneficial to the gap conduction of the later stage switches, thus reducing the time delay and jitter of Marx generator erection.

To sum up, in the design process of low-jitter compact Marx generator, three methods are mainly adopted to reduce the erection time delay and jitter: (1) The external triggering mode is adopted in the first three switches to improve the voltage multiplication factor of the load voltage of the rear self-breakdown switch;(2) The diameter of outer tube of generator is decreased. The stray capacitance of switch is increased, and the load voltage of self-breakdown switch is increased;(3)All switches are installed in the same cavity, and the ultraviolet irradiation generated after the conduction of the first few switches will promote the conduction of other switches, further reducing the statistical time delay of switch conduction.

III. STRUCTURE DESIGN OF MARX GENERATOR

The schematic diagram of the designed Marx generator circuit, the actual Marx module and the Marx generator are shown in Fig. 1.The Marx generator adopts bipolar charging scheme, witch 10 stages in total. The Marx module is located in the center of the metal cylinder, among which 10 gas switches and 20 can withstand 50kV, and the capacitance is 3.3nF. To ensure inter-stage insulation, ceramic capacitors of all levels are installed on nylon separator, and the insulation distance along the surface between all levels is not less than 70mm. The outer metal cylinder is designed to withstand pressure of 0.4Mpa, filled with SF6, and lined with a PMMA insulated inner cylinder to achieve high-voltage insulation under compact design conditions. The charging resistance and grounding resistance are both 800 k Ω 。

Ten gas spark switches share one switch chamber. The first three switches are three-electrode trigger switches, and the last seven are self-breakdown switches. The gap of spark switch is 7mm.。

The total length of the Marx generator is 830mm, the maximum external diameter is 350mm, and the weight is about 45kg.

The trigger is a 5-stage Marx generator. When charging 18.5kV, the peak output voltage of the open circuit can reach 80kV. The trigger and the Marx generator are connected by a 4m long high voltage coaxial cable.

IV. EXPERIMENTAL RESULTS

The schematic diagram of the electrical connection among the Marx generator, trigger, test chamber and time association device is shown in fig.2.

After the Marx generator is charged to the preset voltage, the trigger outputs a high-voltage pulse with a amplitude of about 80kV, and a high-voltage pulse with a rise time of about 15ns to the Marx generator. The Marx generator is established, and the high-voltage pulse is output to the test chamber. The trigger output is connected to a resistance voltage divider, and the measured signal is connected to the time association device and an oscilloscope by a power divider, respectively. The Marx generator output end is also connected with a resistance voltage divider, and the measured signal is connected to the same oscilloscope. The output voltage waveform of the trigger and the Marx generator can be measured by an oscilloscope at the same time. The time difference between the two is the erection time delay of the Marx generator. The jitter of the erection time delay can be obtained by repeating it several times

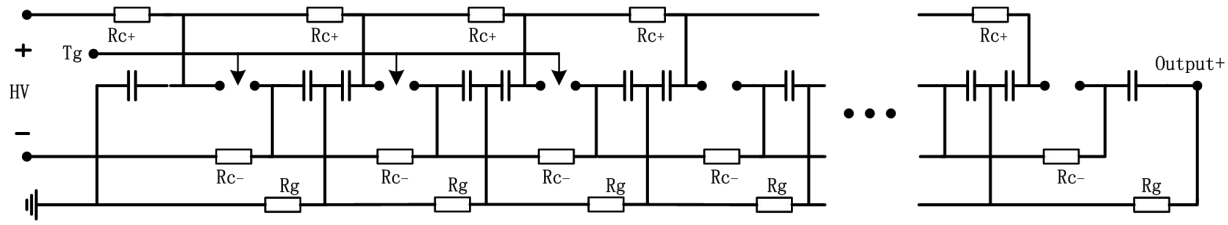

(a) circuit diagram of the Marx generator

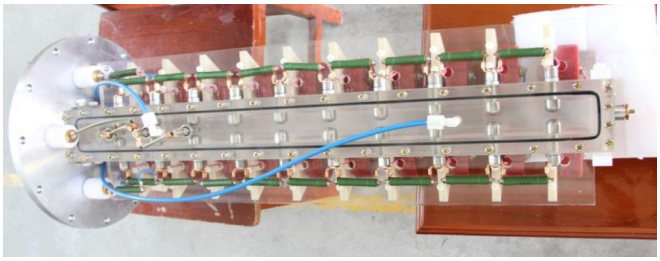

(b) image of the Marx module

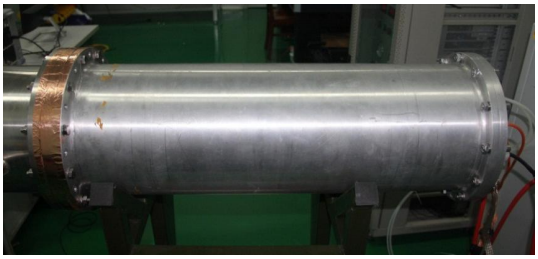

(c) image of the Marx generator

Fig.1 The circuit diagram and images of the Marx generator

under the same condition。

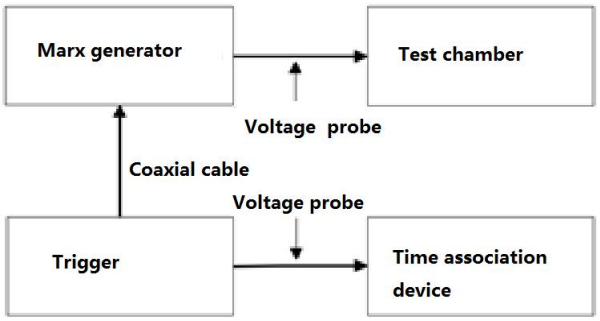

Fig.2 schematic diagram of the electrical connection

The Marx generator cavity adopts 0.3Mpa SF6 as the insulating medium, the switches are filled with N2, and under the conditions of 0.1MPa, 0.2MPa and 0.3MPa, the Marx generator self-breakdown mode and external trigger mode tests are carried out. Typical output waveform of the Marx generator is shown in Fig.3, the rise time is about 30ns, treads oscillation caused by distributed capacitance for generator output port, due to the Marx generator output cables and shell, and the test chamber between the input cable and chamber distributed capacitance, and resistor voltage divider as the Marx generator output load. The capacity of distributed capacitance value is less than the Marx generator equivalent capacitance. The existence of the output waveform is no longer a double exponential wave.

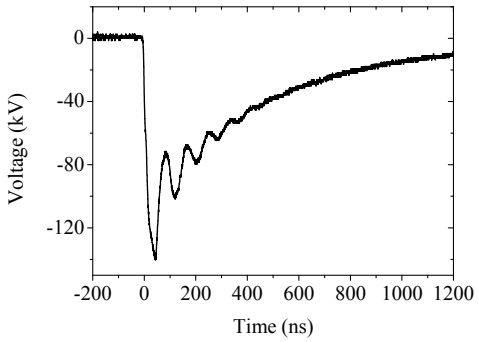

Fig.3 typical output waveform of the Marx generator

Repeated tests were carried out in each state to obtain the relationship between self-breakdown voltage, peak output voltage and air pressure, as well as the relationship between different operating ratios and peak output voltage in the external trigger mode, as shown in Fig.4.

In the self-breakdown mode, the output voltage of the Marx generator has a linear relationship with the gas pressure. When the gas pressure is 0.1MPa, 0.2MPa and 0.3MPa, the corresponding average charging voltage is respectively 10.25kV, 17.9kv and 25.3kV, and the corresponding peak output voltage is respectively 189.71kV, 316.81kV and 472.69kV.

When the generator works in the external trigger mode, it can work stably in the range of 0.4 to 0.9 operating ratio, and the output voltage basically increases linearly with the increase of operating ratio. When the switching gas pressure is 0.1Mpa and the operating ratio is 0.4, the lowest stable output voltage of the Marx generator is about 64kV. When the switching gas pressure is 0.3MPa and the operating ratio is 0.9, the highest stable output voltage of the Marx generator is 442kV.

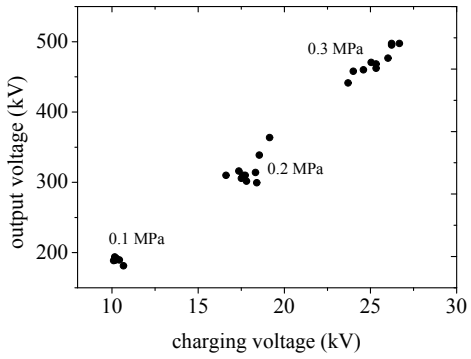

(a) self-breakdown mode

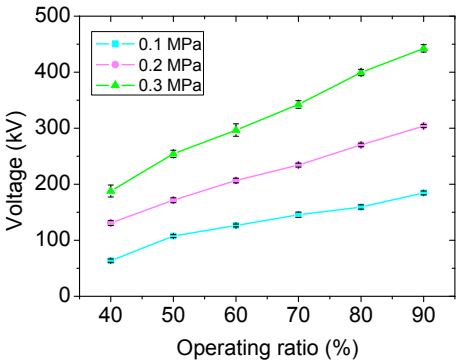

(b) trigger mode

Fig.4 the peak amplitude of the output voltage in different erection modes

The Marx generator erection time delay is defined as the time between the trigger output pulse starting point and the Marx generator output pulse starting point. Under the conditions of different gas pressure and operating ratio, the measured erection time delay and jitter of the Marx generator working in the external trigger mode are shown in Fig.5. As can be seen from Fig.5, the time delay and jitter for the erection of the Marx generator are both very large when the operating ratio is 0.4. As the operating ratio increases, the erection time delay and jitter both decrease gradually. But the jitter of erecting time delay reaches the minimum when the operating ratio is 0.7 and0.8.When the operating ratio is 0.9, it will rise slightly. When the switching pressure is 0.2MPa and 0.3MPa and the operating ratio is 0.7 or 0.8, the jitter of Marx generator erection time delay is less than 2 ns.

V. CONCLUSIONSS

This paper introduces a 400kV gas-insulated low-jitter compact generator, whose stable output voltage ranges from 64-442kV, the switches use nitrogen as the insulating gas, the gas pressure range is 0.1-0.3MPa and the normally operating ratio range is 0.4-0.9. When the gas pressure of the

switches is 0.2MPa and 0.3MPa and the operating ratio is 0.7 or 0.8, the jitter of its erection time delay is less than 2ns.The low-jitter Marx generator meets the requirements of time synchronization for high-speed frame splitter cameras and spectral diagnostic equipment. It can be used for the diagnosis and measurement of optical signals in nanosecond pulse discharge research.

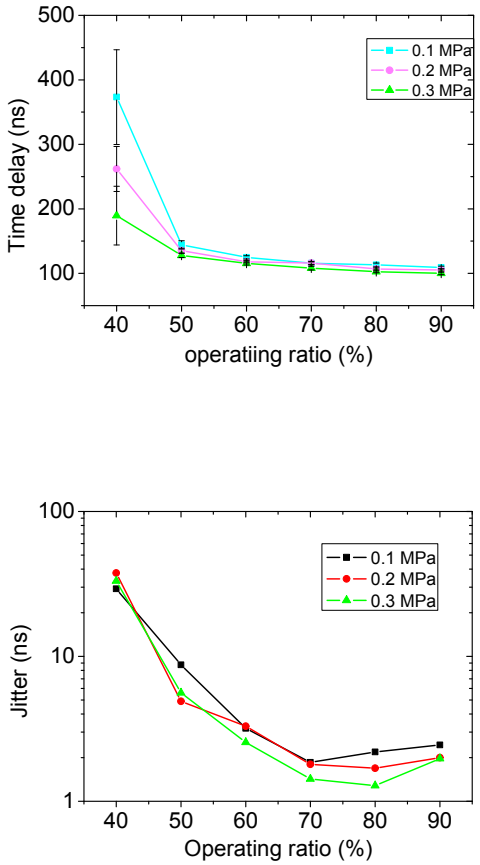

(a) erection time delay (b) jitter of the erection delay time

Fig.5 erection time delay and jitter of the Marx generator in the trigger mode

The Marx generator has been operated for thousands of times under the switching pressure of 0.1-0.3Mpa, with reliable operation and stable output waveform. The Marx generator switches are designed to withstand the gas pressure of 0.4MPa. In the actual debugging process, it was found that under the working condition of 0.4MPa switching pressure, the charging voltage of the self-breakdown mode has a large dispersion and the output voltage is unstable. In the follow-up work, corresponding measures will be taken to solve this problem and the stable output voltage range will be increased to 500kV.

ACKNOWLEDGMENT

The author wishes to thank He Xiaoping, Lei Tianshi, and Zhao Xin of NINT for their support and encouragement.

REFERENCES

[1] T. Kamagahara, N. Ashizuka, T. Furusato, et al. Investigation of pulsed breakdown characteristics in high-pressure CO2 including supercritical phase under non-uniform electric field[C]. The 19th IEEE International Conference on Dielectric Liquids, Manchester, United Kingdom, June, 2017.

[2] Wang Tao, Wang Jue, Yan Ping. Research of electrical treeing characteristics in PMMA under nanosecond pulses [J]. Advanced Technology of Electrical Engineering and Energy, 2017, 36(6):62-67

[3] Xu Shuangyan, Cai Jinsheng, Lian Yongsheng. Investigation of nanosecond-pulsed dielectric barrier discharge actuators with powered electrodes of different exposures[J]. Plasma Science and Technology, 2017, 19: 095504.

[4] Tian Xuemin, Tian Xihui, Che Xueke, et al. Nanosecond pulse discharge characteristics under different pressure[J]. High Voltage Technology, 2016, 42(3): 813-820

[5] Wang Yang, Zhang Cheng, Xie Qing, et al. Experimental and optical characteristics of nanosecond-pulse surface sliding discharge[J]. Transactions of China Electrotechnical Society, 2017, 32(8): 63-73

[6] Qiu Aici. Application of the pulse power technology. Xi`an: Shaanxi Science and Technology Press, 2016

[7] Yao Weibo, Qiu Aici, Zhang Yongmin, et al. Building time and jitter of hundreds of kJ Marx generator[J]. High Power and Particle Beams, 2010, 22(4): 761-764

[8] Feng Shuping, Li Hongtao, Cao Wenbin, et al. High voltage low jitter Marx generator of prototype module of primary test stand[J]. High Power and Particle Beams, 2009, 21(1): 152-156

[9] Li Yuan, Li Jin, Liu Xiaoping, et al. Design and experiment of 450kV low jitter Marx generator[J]. High Power Laser and Particle Beams, 2010, 22(4): 743-747

[10] Wu Zhaoyang, Zhang Xianfu, Zhang Jinqi, et al. Development of 14-staged compact and repetitive Marx generator[J], High Power Laser and Particle Beams, 2013, 25(S0): 169-172

[11] Yao Weibo, Guo Jianming, Zhang Yongmin, et al. System of ns time-resolved spectroscopy diagnosis and radioprotection[J]. Spectroscopy and spectral analysis, 2014, 34(6):1446-1449.

[12] Jia Wei, Chen Zhiqiang, Guo Fan, et al. Drivers of small and medium scale electromagnetic pulse simulator based on Marx generator. High Power Laser and Particle Beams, 2018, 30: 073203

Design and test verification of a test fixture for field-to-line coupling*

Longquan Zhong
Complicated Electromagnetic Environment Laboratory of CAEP
Science and Technology on High Power Microwave Laboratory
(of Institute of Applied Electronics)
Mianyang, China
lorne216@163.com

***Abstract*—In this paper we design a flexible plate-cable test fixture which is to be used as a test method and effectiveness verification device in the study about field-to-line coupling. This test fixture is suitable for coaxial port cables and takes into account several variable parameters. Then the repetitive test of coupling effect of single-core cable under broadband high power microwave pulse is carried out. Statistical analysis of test data shows that the dispersion of coupling signal is consistent with the dispersion of incident field and both conform to the characteristics of normal distribution.**

Keywords—field-to-line coupling, plate-cable test fixture, broadband high power microwave, statistical analysis

I. Introduction and Motive

Field-to-line coupling is one of the important concerns of electromagnetic environmental effects research. There are many factors affecting the test results of cable coupling in actual objects, which cannot be determined one by one, resulting in poor test repeatability. Therefore, this is very unfavorable for the effectiveness verification of test method or test system, so it is necessary to design test fixture to reduce uncontrollable factors.

II. Desigh of Plate-cable Test Fixture

In order to simulate the actual deployment scenario of the tested cable, a plate-cable test fixture is designed for the cable of the coaxial port, as shown in Fig.1.

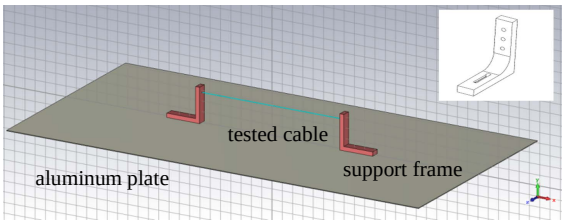

Fig. 1. Schematic of the plate-cable test fixture

A. Consititution

The plate-cable test fixture is made up of a plate and two support frames. Both are fixed with screws. The bottom is an aluminum plate with a thickness of 3mm and a length of 2m and a width of 1m. The support frames are made of plexiglass, whose vertical surface has three coaxial connectors with different heights, and the horizontal plane is designed with grooves, which can be flexibly adjusted to facilitate the tension of the tested cables.

B. Adaptability and advantages

- Cable for N-type coaxial port is available.
- Adjustable parameter range: plate-cable spacing 8cm/12cm/16cm optional, cable length 50-130cm, discretionary termination impedance.
- Simple structure, it is easy to arrange coupling test in different polarization and incident direction.

III. Statistical Analysis of Coupling Signal Parameters

With this test fixture, the test of field-to-line coupling of single-core cable under broadband high power microwave pulse is carried out. The tested single-core cable, which is obtained by stripping the shielding layer from a 50-ohm coaxial cable, is a copper cylinder with a length of 1m and a diameter of 1.2mm. The coupling signal is attenuated and then acquired by an oscilloscope. The width of broadband high power microwave pulse is about 5 ns, and the frequency range is 100MHz to 600MHz.

100 samples were collected by repetitive test, and the peak-to-peak values of the coupling signals of the tested cable were statistically analyzed, a scatter plot, a stem plot, a frequency histogram, and a normal probability plot were drawn, as shown in Fig.2.

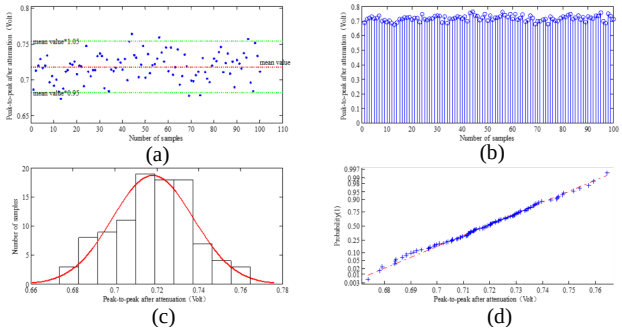

Fig. 2. Statistical plot of peak-to-peak values of coupling signals. (a) scatter plot. (b) stem plot. (3) frequency histogram. (4) normal probability plot.

From (2a) and (2b), the dispersion of peak-to-peak of the coupling signal is small, and the fluctuation range is almost within $\pm$ 5% of the mean value. This characteristic is equivalent to the fluctuation range of the field signal.

From (2c) and (2d), the coupling signal exhibits a normal distribution characteristic. After the data are normalized, it is very close to a normal distribution with a mean of 1 and a standard deviation of 0.5.

To summary, this plate-cable test fixture can carry out research on the influence of various parameters on the field-to-line coupling law, which meets the test needs, especially in terms of verifying the test method and the effectiveness of the test system.

Deep Transcranial Magnetic Stimulation Using Different Coil Configurations

Mai Lu
Key Lab. of Opt-Electronic Technology and Intelligent Control (Lanzhou Jiaotong University), Ministry of Education
Lanzhou, 730070, China.
mai.lu@hotmail.com

Shoogo Ueno
Department of Applied Quantum Physics
Graduate School of Engineering
Kyushu University
Fukuoka, 812-8581, Japan.
ueno@athena.ap.kyushu-u.ac.jp

***Abstract*—Direct stimulation of deeper brain tissues by transcranial magnetic stimulation (TMS) plays an important role in the study of reward and motivation mechanisms, which may be beneficial in the treatment of several neurological and psychiatric disorders. This work presents numerical simulation of deep TMS (dTMS) by considering different coils. Three dimensional distributions of the induced magnetic field and electric field in realistic head model were obtained by impedance method, and the results were compared with the normal figure-of-eight coil. Results show that double cone and H-coils have significantly deep field penetration at the expense of induced higher and wider spread electrical fields in superficial cortical regions. The combination of Halo-coil with a conventional circular coil produce deeply penetrating electric field the same as double cone and H-coils, but the stimulation in superficial brain tissues are much lower. The coaxial circular coils provide a flexible way to stimulate deep brain regions with improved focality.**

Keywords—deep transcranial magnetic stimulation, dTMS coil, induced fields, impedance method

I. INTRODUCTION

Transcranial magnetic stimulation (TMS) is a technique for brain stimulation that is able to probe the brain circuitry and network in a non-invasive manner. In the past two decades, there has been a dramatic increase in the usage of TMS for studying the functional organization of the human brain as well as a therapeutic tool to improve psychiatric disease [1].

Many studies indicate that reward circuit is the focus in the study of depression. Medial prefrontal and orbitofrontal cortices and their connections to deeper brain sites are associated with reward processes and motivation [2]. The subgenual anterior cingulate cortex (SACC) is central to this network. Other emerging targets include the mesolimbic dopaminergic pathway consisting of the nucleus accumbens and the ventral tegmentum area, both interconnected with the dorsal and ventral lateral prefrontal cortices [3]. The SACC, the nucleus accumbens, and the inferior thalamic peduncle lie at depths of approximately 6 and 8 cm, respectively. The orbitofrontal, medial frontal cortices, and the frontal pole which have strong connectivity to anterior cingulate cortex lie at depths of 3 to 5 cm. There is a reason to assume that activation of these deeper prefrontal and limbic regions may increase the antidepressant effect.

To stimulate deeper neuronal regions such as reward-related pathways directly, much higher stimulation intensities are needed, as the electric field decreases rapidly as a function of tissue depth. However, even if stimulation intensities could be highly increased at the source, the use of standard TMS coils at such high stimulation intensities does not allow safe stimulation and can lead to undesirable side effects. These limitations have led to the development of novel coil designs suitable for dTMS. In the last years, a method to stimulate deep brain regions was obtained by a specifically designed coils i.e double cone, H-, Halo-circular assembly coil (HCA coil), coaxial circular coils (CC coil). The present study explores the effect of coil configurations on the stimulation depth and focality in deep brain regions.

II. 3D REALISTIC HEAD MODEL WITH COILS

The realistic human head model employed in this work was obtained from Virtual Family Project (VFP) [4]. This realistic model, as shown in Fig. 1, was generated from MRI data of a 34-year-old male adult, comprising 36 separated tissues. The head model is composed of 10 million cubic voxels with resolution of 1 mm. Some important brain subregions such as hippocampus, midbrain, pons, pineal body, thalamus, etc., have been included in the model.

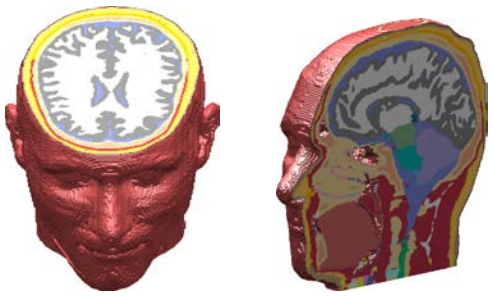

(a) (b)

Fig. 1. Realistic head model. (a) cut at cross-sectional plane, and (b) cut at sagittal plane.

Four coil designs for dTMS have been numerically designed as shown in Fig 2, where Figs 2(a)-(d) show the double cone, H-, HCA and CC coils which are placed on the surface of the head model. For comparison, Fig 2(e) shows the modelled figure-of-eight (Fo8) coil.

The double cone coil was composed with two large circular coils with a fixed angle (95 deg) between them. The H-coil was composed of base and return portions. The HCA coil was composed one Halo coil operated simultaneously with a typical circular coil. The CC coil was composed with three circular coils with different radius. For comparison, we have also modeled the Fo8 coil. The same pulse currents with amplitude of I=5.0 kA and working frequency 2381 Hz was fed into each of the four coils.

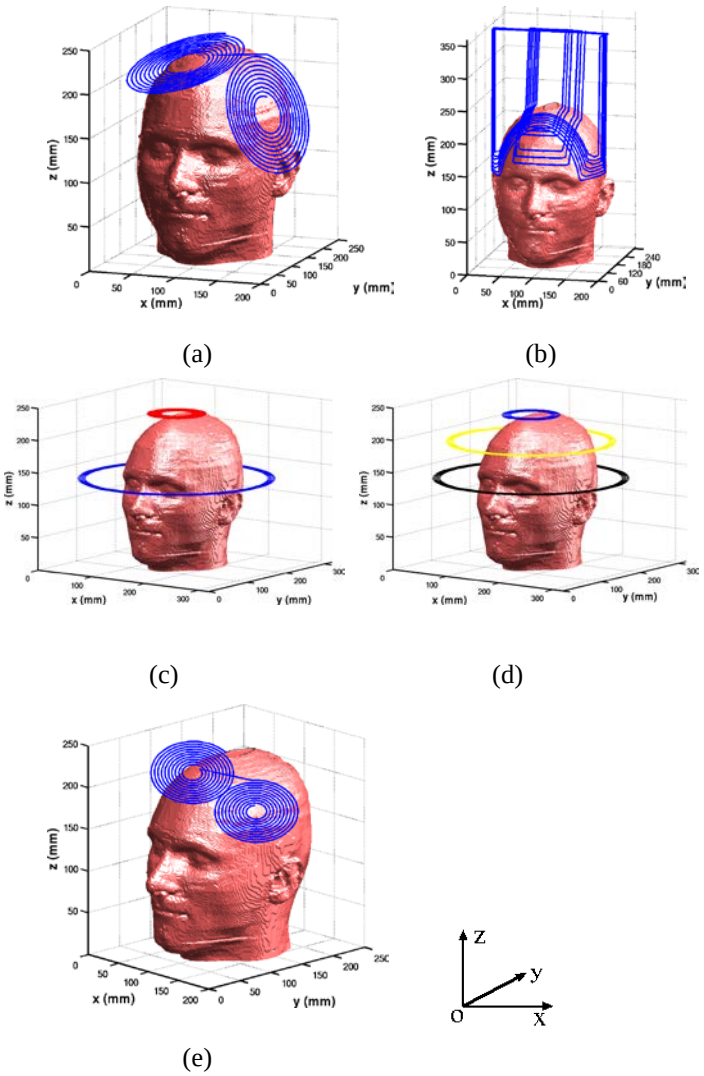

Fig. 2. Realistic head model with dTMS coils. (a) Double cone coil, (b) H-coil, (c) HCA coil, (d) CC coil, and (e) Fo8 coil.

III. NUMERICAL METHOD AND TISSUE PROPERTIES

The time variation of the applied magnetic field causes induced currents in the head through Faraday's induction mechanism. These currents can be calculated using the impedance method [5]. The impedance method has been found to be highly efficient as a numerical procedure for calculations of induced current densities and/or electric field in tissue-classified anatomically based models during exposure to low-frequency electromagnetic field [6][7].

TABLE I. TISSUE PROPERTIES AT 2381 Hz

Tissue	Conductivity (S/m)	Tissue	Conductivity (S/m)
Artery	7.00e-01	Hypothalamus	5.26e-01
Blood vessel	3.10e-01	Marrow bone	2.44e-03
Cartilage	1.75e-01	Midbrain	4.65e-01
Cerebellum	1.24e-01	Muscle	3.31e-01
CSF	2.00e+00	Nerve	3.04e-02
Eye-cornea	4.25e-01	Pineal body	5.26e-01
Eye-lens	3.31e-01	Pons	4.65e-01
Fat	2.32e-02	Skin	2.00e-04
Gray matter	1.04e-01	Skull	2.03e-02
Hippocampus	1.04e-01	Spinal cord	3.04e-02
Hypophysis	5.26e-01	White Matter	6.44e-02

The electrical properties of head tissues were calculated using the 4-Cole-Cole model [8]. In which the biological tissues subject to an electric field with angular frequency is modelled by relaxation theory and tissue properties can be obtained by fitting to experimental measurement [9]. Since the number of tissue type in Virtual Family models is more than that in original Gabrial list, various tissues in Virtual Family models have been simulated with conductivities and permittivities of similar tissues (i.e. hippocampus and thalamus have the dielectric properties of brain grey matter from the Gabriel list). The tissue conductivities are shown in Table I.

IV. RESULTS AND DISCUSSIONS

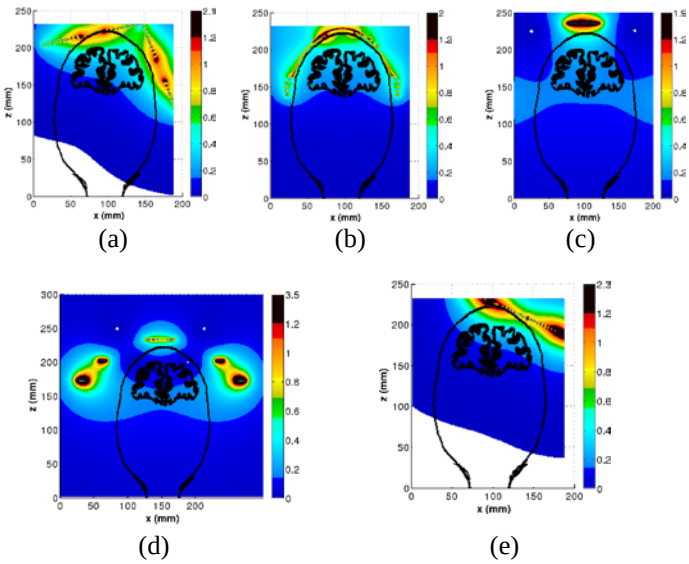

Fig. 3. Distribution of B-field (Tesla) with the contour outline of scalp and GM in the coronal slice of y = 80 mm. (a) Double cone coil, (b) H-coil, (c) HCA coil, (d) CC coil, and (d) Fo8 coil.

Fig. 3(a)-(e) show the comparison of the calculated B-field

for different dTMS coils at coronal slice of y=80 mm. The contour outlines of scalp and gray matter were also included in each of the figures. As expected, higher magnetic field is presented on the coil surface. However, the B-field decays quickly. It was found the stimulation depth in the brain were significantly increased by double cone, H-, HCA and CC coils (Fig 3(a)–3(d)) compared to that by Fo8 coil (Fig 3(e)).

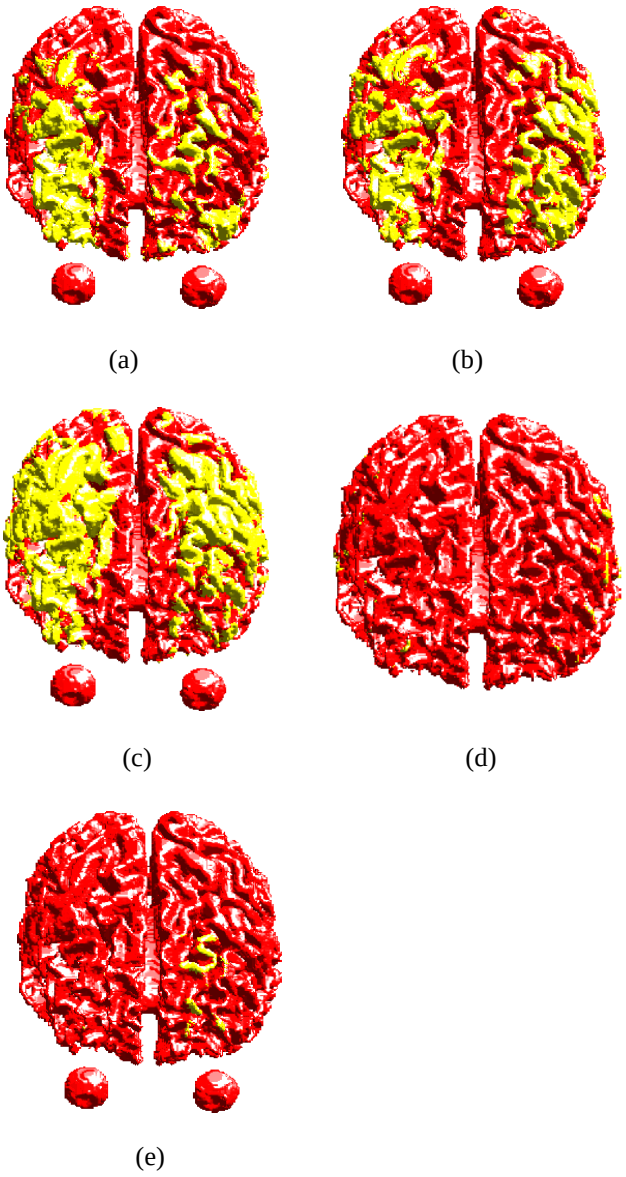

Fig. 4. Electric field distributions on the surface of white matter. (a) Double cone coil, (b) H-coil, (c) HCA coil, (d) CC coil, and (e) Fo8 coil.

Fig. 4 shows the 3-D distribution of E-field on the surface of white matter (WM) for different coil configures. The yellow colors indicate field magnitude above the threshold for neuronal activation, which was set to 100 V/m. The WM surface were represented by red color. It can be found the double cone, H- and HCA coils induce electric fields in wide area on the surfaces of WM. Especially for the HCA coil, it produces wide electric field at the periphery of the WM surface. However, the CC and Fo8 coils induce much more focal electric fields.

V. Conclusions

In this paper, typical coil designs such as double cone, H- , HCA, and CC coils which were employed for dTMS have been numerically designed. 3D distributions of magnetic flux density, induced electric field in realistic head model using dTMS these coils were obtained by the impedance method. Results were compared with that of Fo8 coil. It was found that deeper electric field penetration can be obtained by double cone, H-, and HCA coils through reducing the rate of decay of the field as a function of distance, which inevitable induce higher and wider spread electrical fields in superficial cortical regions. The CC coil produces the over-threshold electric fields in deep brain regions, while the sub-threshold fields were produced in superficial cortical areas. Results show that since there exit no coil configuration that is capable of achieving both deep stimulation with improved focality, the selection of the most suitable coil setting in dTMS should be based on a balance between the stimulation depth and focality.

ACKNOWLEDGMENT

This work is supported in part by the National Nature Science Foundation of China (No. 51567015，No. 51867014).

REFERENCES

[1] C. M. Epstein, E. M. Wassermann, and U. Ziemann, Oxford Handbook of Transcranial Stimulation,1st ed. New York, NY, USA: Oxford Univ. Press, 2008.

[2] H.C. Breiter, and N.R. Rosen, “Functional Magnetic Resonance Imaging of Brain Reward Circuitry in the Human,” Annals of the New York Academy of Sciences, 877, 1999, pp. 523-547.

[3] 6. A.A. Gershon, P.N. Dannon, and L. Grunhaus, “Transcranial Magnetic Stimulation in the Treatment of Depression,” The American Journal of Psychiatry, 160, pp.835-845.

[4] A. Christ, W. Kainz, E.G. Hahn, K. Honegger, M. Zefferer, E. Neufeld et al., “The virtual family-development of anatomical CAD models of two adults and two children for dosimetric simulations,” Phys. Med. Biol., vol. 55, pp. N23-N38, 2010.

[5] N. Orcutt and O. P. Gandhi, “A 3-D impedance method to calculate power deposition in biological bodies subjected to time-varying magnetic fields,” IEEE Trans. Biomed. Eng., vol. 35, no. 8, pp. 577–583, Aug. 1988.

[6] M. Lu, S. Ueno, T. Thorlin, and M. Persson “Calculating the current density and electric field in human head by multichannel transcranial magnetic stimulation,” IEEE Trans. Mag., vol. 45, no. 3, pp. 1662–1665, Mar. 2009.

[7] M. Lu and S. Ueno, “Dosimetry of exposure of patients to pulsed gradient magnetic fields in MRI,” IEEE Trans. Mag., vol. 47, no. 10, pp. 3841-3844, Oct. 2011.

[8] K.S. Cole and R.H. Cole, “Dispersion and absorption in dielectrics I. Alternating current characteristics,” J. Chem Phys., vol. 9, pp. 341-351, 1941.

[9] S. Gabriel, R.W. Lau, and C. Gabriel, “The dielectric properties of biological tissues: II. Measurements in the frequency range 10 Hz to 20 GHz,” Phys. Med. Biol., vol.41, pp. 2251-2269, 1996.

ASIAEM 2019−Some Optimization Techniques of Lightning Field Calculations

Marcos Rubinstein
IICT
University of Applied Sciences Western Switzerland
Yverdon-les-Bains, Switzerland
marcos.rubinstein@heig-vd.ch

Antonio Sunjerga
EMC Labortory
Swiss Federal Institute of Technology
Lausanne, Switzerland
farhad.rachidi@epfl.ch

Farhad Rachidi
EMC Labortory
Swiss Federal Institute of Technology
Lausanne, Switzerland
farhad.rachidi@epfl.ch

***Abstract*—The calculation of the fields from lightning is of importance in studies of lightning effects on equipment, towers, wind turbines, transmission lines and other infrastructure. In the case of the study of overvoltages induced by lightning on transmission and distribution lines, it is necessary to calculate different components of the lightning-generated fields at a large number of positions along the line. In this paper, we propose techniques to reduce the computational burden involved in those calculations.**

Keywords—Lightning, Simulation, LEMP, Overvoltages

I. INTRODUCTION

The calculation of lightning electromagnetic radiation for research and for lightning protection studies can be time-consuming since it often involves the use of lightning return stroke models that require numerical integration of the lightning current along channels with lengths that can extend to several kilometers, and different components of the fields have to be calculated at a large number of positions. Sensitivity analyses also require the calculations to be carried out with different lightning channel-base currents having varying risetimes and widths. In this paper, we propose methods that can be used to ease the computational burden involved in applications such as the calculation of voltages induced on long lines.

II. METHODS BASED ON THE LINEARITY OF THE FIELD CALCULATIONS

A. Upstream Optimization for Current Waveshape

The calculation of some components of the electric and the magnetic fields from lightning using engineering models starts with a channel-base current following several steps. Let us consider as an example the calculation of the magnetic field from the lightning return stroke for the case of a flat, perfectly conducting ground.

Engineering return stroke models represent the lightning channel as a straight and vertical line extending up from the ground. Regardless of the specific return stroke model used, the computation of the azimuthal magnetic flux density under the assumed conditions is generally carried out starting with the expression for the field from an infinitesimal dipole and integrating it over the length of the channel as expressed in Equation (1) [1],

$$B_\phi(t,z=0)=\frac{\mu_0}{2\pi}\left[\int_{z'=0}^{h(t)}\frac{r}{R^3}i\left(z',t-\frac{R}{c}\right)dz'+\int_{z'=0}^{h(t)}\frac{r}{cR^2}\frac{\partial i\left(z',t-\frac{R}{c}\right)}{\partial t}dz'\right] \quad (1)$$

where R is the distance from the current element at height z' along the channel to the field point, r is the horizontal distance from the channel base to the field point, and $h(t)$ is the height of the channel at time t as seen at the observation point.

The calculation is carried out numerically and, as mentioned, it is resource-intensive, especially if it has to be carried out at different distances from the channel and if it is repeated for different channel-base currents $i(0,t)$. We will now show that, if the fields are required for different channel-base currents, the numerical integration needs only be carried out once. To see this, let us write the current $i(0,t)$ as the convolution of a current $i_c(0,t)$ and a function $f(t)$:

$$i(0,t)=i_c(0,t)*f(t) \quad (2)$$

Plugging (2) into (1), we get

$$B_\phi(t,z=0)=\frac{\mu_0}{2\pi}\left[\int_{z'=0}^{h(t)}\frac{r}{R^3}[i_c\left(z',t-\frac{R}{c}\right)*f(t-\frac{R}{c})]dz' + \int_{z'=0}^{h(t)}\frac{r}{cR^2}\frac{\partial[i_c\left(z',t-\frac{R}{c}\right)*f(t-\frac{R}{c})]}{\partial t}dz'\right] \quad (3)$$

Applying the convolution's translation equivalence along with convolution's integration and the derivation properties, (3) can be written as

$$B_\phi(t,z=0)=f(t)*\left\{\frac{\mu_0}{2\pi}\left[\int_{z'=0}^{h(t)}\frac{r}{R^3}i_c\left(z',t-\frac{R}{c}\right)dz'+\int_{z'=0}^{h(t)}\frac{r}{cR^2}\frac{\partial i_c\left(z',t-\frac{R}{c}\right)}{\partial t}dz'\right]\right\} \quad (4)$$

The right-hand side of (4) is recognized as the convolution of the function $f(t)$ and the magnetic flux density from current $i_c(0,t)$. If we use $B_{\varphi c}(t,z=0)$ to denote the magnetic flux density from $i_c(0,t)$, we can write

$$B_\phi(t,z=0)=f(t)*B_{\phi c}(t,z=0) \quad (5)$$

According to (5), once the magnetic flux density $B_{\varphi c}(t,z=0)$ from a current $i_c(0,t)$ has been found by numerical integration along the lightning channel, the magnetic flux density for any other current $i(t)$ can be found by carrying out the convolution in (5). The function $f(t)$ can be obtained by dividing, in the Fourier transforms of the currents $i(0,t)$ and $i_c(0,t)$ and inverse Fourier transforming the result.

B. Upstream Optimization by Pre-processing the Source

Any linear operation that is performed on a field component after the numerical integration can be performed only once at the source instead of each time a field

calculation is performed. We will exemplify this technique by way of the so-called Cooray-Rubinstein formula [2], [3], used to estimate the horizontal component of the electric field taking into account the finite ground conductivity,

$$E_r(r,\omega,h) = -H_{\varphi_p}(r,\omega,0)\frac{\sqrt{\mu_g}}{\sqrt{\varepsilon_g + \frac{\sigma_g}{j\omega}}} + E_{r_p}(r,\omega,h) \quad (6)$$

where the subindex p is used to identify field components calculated using a perfectly conducting ground, r is the distance to the channel, h is the height of the observation point, and the other variables are the electric parameters of the ground. Equation (6) produces estimates of the horizontal component of the electric field at a height h and distance r from the lightning channel. The application of (6) involves first the calculation by numerical integration of the azimuthal component of the magnetic field using (1) (divided by the permeability of free space to obtain H), in a process similar to that described in the previous section[1]. The resulting field is then converted to the frequency domain, typically by application of the FFT, and multiplied by the frequency-dependent factor in the first term of the right-hand side of (6) that depends on the electrical properties of the ground. The radial electric field (which is the second term on the right-hand side of (6)) also needs to be calculated by numerical integration using an expression similar to (1) but for that particular field component. The two terms just calculated are then added together to obtain the radial component of the electric field at a height h for a finitely conducting ground and, since the result is often required in the time domain, an inverse transformation is also often carried out.

The process described in the previous paragraph is repeated at each one of the required field point positions, the number of which can be in the tens or even hundreds in the case of the calculation of voltages induced on overhead lines.

Let us now identify operations that take place at every calculation location and that can actually be performed only once at the source.

If the channel-base current is $I(\omega,z=0)$, then, for a given return stroke model, the relation between the current and the azimuthal magnetic field is, as determined in Section II.A, linear. We can therefore write

$$H_{\phi_p}(t,z=0) = P_H(r,\omega,RSM)I(\omega,z=0) \quad (7)$$

in which RSM stands for Return Stroke Model.

Plugging (7) into (6), we get

$$E_r(r,\omega,h) = -P_H(r,\omega,RSM)I(\omega,z=0)\frac{\sqrt{\mu_g}}{\sqrt{\varepsilon_g + \frac{\sigma_g}{j\omega}}} + E_{r_p}(r,\omega,h) \quad (8)$$

Noting that the transfer function P_H represents the calculation of the field by way of numerical integration along the channel, we recognize the first term on the right-hand side of (8) as the magnetic field from a modified channel-base current I_m equal to

$$I_m(\omega,z=0) = I(\omega,z=0)\frac{\sqrt{\mu_g}}{\sqrt{\varepsilon_g + \frac{\sigma_g}{j\omega}}} \quad (9)$$

[1] Note that time-domain formulations of the Cooray-Rubinstein formula are also available (e.g.,[4])

For the calculation of the first term in (6), it is considerably more efficient to use the modified channel-base current obtain using (9) for the integration along the channel rather than the actual channel-base current that requires, at each field point location, to Fourier transform the field, multiply it by the frequency dependent factor that depends on the ground parameters, and inverse Fourier transform the result.

C. Pre-Calculation of Canonical Field Components

As in Section II.A, it is possible to take advantage of the linearity of the field calculations to create a database of fields at different distances and for different ground parameter combinations using, as an input, a canonical current waveform. It is of course not possible to pre-calculate the fields for all possible conditions but a finite number of calculations for commonly encountered cases can be used to obtain electromagnetic field waveforms at any point and for specific electrical parameters by way of techniques such as interpolation or by recovering the fields from the finite set of waveforms using Nyquist's sampling theorem.

To particularize the results for a given current waveform, the technique presented in II.A can be used by performing the convolution of the pre-calculated fields with the time-domain transfer function between the actual current and the current that was used for the canonical calculations.

III. Conclusions

In this paper, we discussed several techniques that can be used to diminish the computation time in calculating fields from lightning return strokes, although they are also applicable to other lightning processes such as M components or to cloud lightning discharges.

One of the techniques is based on the calculation of fields from a canonical current and the use of a convolution to obtain the fields from an arbitrary current waveform. A second technique uses a pre-processed channel-base current that is then used in a return stroke model to avoid having to perform multiple passages between the frequency and time domains at each field point. A third technique, which could be loosely described as a "waveform look-up table" technique, is based on the pre-calculation of fields at different distances that can be used at run-time together with interpolation and the first technique described here to quickly obtain fields from an arbitrary channel-base current.

Acknowledgement

This work was supported in part by the Swiss National Science Foundation (Project No. 200020_175594), the European Union's Horizon 2020 research and innovation program under grant agreement No 737033-LLR, the Spanish Ministry of Economy and the European Regional Development Fund (FEDER) ESP2015-69909-C5-5-R and ESP2017-86263-C4-2-R, and European Union's Horizon 2020 research and innovation programme under the Marie Skłodowska-Curie grant agreement SAINT 722337.

References

[1] M. A. Uman, D. K. McLain, and E. P. Krider, "The electromagnetic radiation from a finite antenna," *Am. J. Phys.*, vol. 43, no. 1, pp. 33–38, Jan. 1975.

[2] M. Rubinstein, “An approximate formula for the calculation of the horizontal electric field from lightning at close, intermediate, and long range,” *IEEE Trans. Electromagn. Compat.*, vol. 38, no. 3, pp. 531–535, Aug. 1996.

[3] V. Cooray, “Horizontal fields generated by return strokes,” *Radio Sci.*, vol. 27, no. 04, pp. 529–537, Jul. 1992.

[4] A. Andreotti, F. Rachidi, L. Verolino, "A New Formulation of the Cooray-Rubinstein Expression in Time-Domain", *IEEE Transactions on Electromagnetic Compatibility*, Vol. 57, No 3, pp. 391-396, 2015.

Observations of Lightning Discharges to the 356 m High Shenzhen Meteorological Tower

Mingli Chen
Dept. of Building Services Eng.
Hong Kong Polytechnic Univ.
Hong Kong, China
mingli.chen@polyu.edu.hk

Zongxu Qiu
Meteorological Service Center
Shenzhen Meteorological Bureau
Shenzhen, China
qiuzongxu@szmb.gov.cn

Zilong Qin
Dept. of Building Services Eng.
Hong Kong Polytechnic Univ.
Hong Kong, China
zilong.qin@connect.polyu.hk

Yuexing Yang
Meteorological Service Center
Shenzhen Meteorological Bureau
Shenzhen, China
yangyuexin@szmb.gov.cn

Yan Gao
Dept. of Building Services Eng.
Hong Kong Polytechnic Univ.
Hong Kong, China
15902133R@connect.polyu.hk

Hongbo Guo
Meteorological Service Center
Shenzhen Meteorological Bureau
Shenzhen, China
guohongbo@szmb.gov.cn

***Abstract* — To obtain firsthand lightning stroke current waveforms, a comprehensive lightning observation platform around the 356-m-high Shenzhen Meteorological Gradient Tower (SZMGT) was established in 2016. The platform includes: a lightning current measuring system on top of the tower, atmospheric electric field mills mounted at different heights along the tower, and a main observation site located at 440 m away from the tower. Since then, a number of lightning discharges to the tower have been observed and analyzed. As the preliminary results, we present here: 1) two upward positive stepped-leaders initiated from the top of SZMGT, which the step lengths, time intervals and overall speeds are in the ranges of 0.5 – 4.4 m, 13.3 - 46.7 μs and 0.24 – 2.21 ×10^5 m/s, respectively; 2) two current waveforms of return strokes recorded on the top of SZMGT, which the peak currents are -110.4 kA and -87.7 kA respectively; and 3) a comparison of the electric field mill records at different heights during a thunderstorm, which shows the enhancement effect of the electric field at higher part of the tower and the shielding effect of the electric field at lower part of the tower.**

Keywords—lightning to tall tower, lightning current waveform, electric and magnetic fields, optical image.

I. INTRODUCTION

Lightning can affect human activities in a very serious manner, causing death and damage [1]. According to the statistics from Shenzhen Meteorological Service Center, the number of failure of electric and electronic equipment due to lightning has been increasing during last decade. In natural, the lightning occurs randomly, making the measurement of the lightning current difficult. On the other hand, the lightning current measurement plays an important role for both the lightning research and the lightning hazard mitigation. There are two basic approaches to measure the lightning current: one is at the channel base of a rocket-triggered lightning discharge [2-7], the other is at the top or ground base of a tall structure struck by a lightning discharge [8-13].

To make further contributions on the study of lightning discharges to tall structures, we have launched a comprehensive observation campaign around the Shenzhen Meteorological Gradient Tower (SZMGT) since 2016. Since then, several lightning discharges to the SZMGT have been documented. In following sections, we would like to have firstly an introduction of the experiment setup around the SZMGT and then a briefing of some observed lightning discharges to the tower.

II. EXPERIMENT SETUP AROUND SZMGT

The SZMGT was built in May of 2016 in suburban area of Shenzhen, China (Figure 1). The height from the tower tip to ground is 356 m. The main purpose of the tower is for the gradient observation of conventional meteorological parameters in earth surface boundary layer and for monitoring the atmospheric environment.

To take the advantage of SZMGT, a current measurement system was installed around a lightning rod at the top of the tower to record the lightning current. In addition, there are 6 sets of electric field mills installed at different heights of the tower to monitor the electric field during a thunderstorm. Besides, there are the high-speed cameras, fast and slow electric change antennas, magnetic field change antennas, and VHF antenna arrays installed on the roof of a short building located 440 m away from the tower.

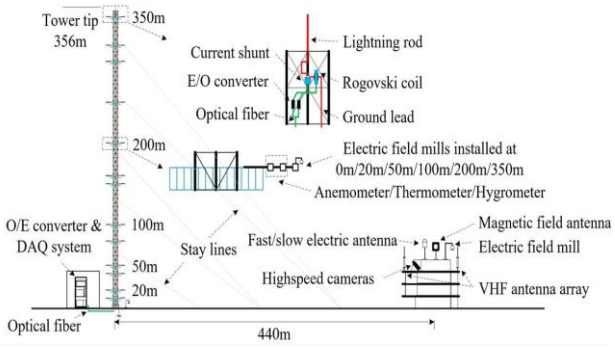

Figure 1. Setup of lightning observation on and round SZMGT

III. PRELIMINARY RESULTS

A. *Two upward positive stepped leaders*

On 30 July 2016, two upward positive leader (UPL) processes were captured with the high-speed camera at the main observation site: No. 20160730-1 and No.20160730-2. According to the electric field change records, both were classified as upward discharge processes trigged by nearby intra-cloud discharges. Based on the high-speed camera images and the magnetic field records, these two leaders are found to behave step-wisely when they propagated from the tip of tower upward.

Shown in Figure 2 are the high-speed camera images and magnetic field records for one of the two upward positive stepped leaders from the SZMGT.

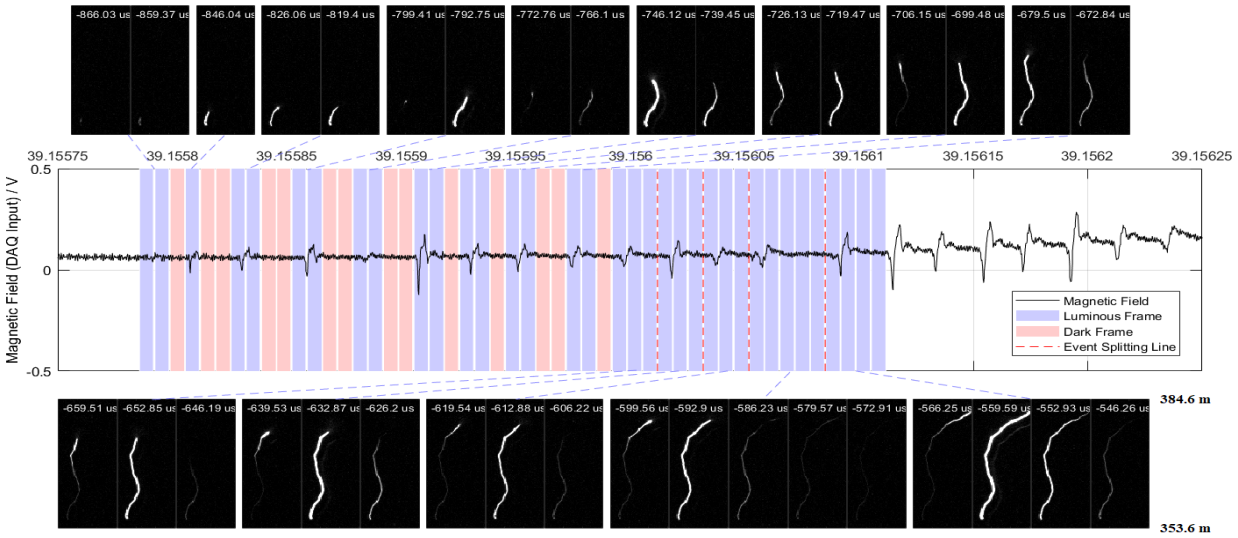

Figure 2. High-speed camera images and magnetic fields of one upward positive stepped leaders (No. 20160730-2) from SZMGT on 30 July 2016.

Leader No. 20160730-1 occurred at 15:23:22 on 30 July of 2016. There are 14 steps within the field view of the high-speed camera. The step length ranges from 0.5 m to 2.7 m with a mean of 1.7 m, and the step interval ranges from 13.34μs to 26.68 μs with a mean of 21.04 μs, resulting in an overall 2-D leader speed ranging from 0.24×10^5 m/s to 1.37×10^5 m/s with a mean of 0.82×10^5 m/s.

Leader No. 20160730-2 occurred at 15:35:38 on 30 July of 2016. There are 12 steps within the field view of the high-speed camera. The step length ranges from 1.6 m to 4.4 m with a mean of 2.7 m, and the step interval ranges from 20.01μs to 46.69 μs with a mean of 25.47 μs, resulting in an overall 2-D leader speed ranging from 0.48×10^5 m/s to 2.21×10^5 m/s with a mean of 1.12×10^5 m/s.

B. Two return stroke current waveforms

On 4 May of 2017, we have got the first ever current waveforms of a lightning discharge struck to the SZMGT. Shown in Figure 3 are the current waveforms recorded for the flash struck to the SZMGT on May 4, 2017. It is a negative cloud-to-ground flash with two return strokes. The time interval between the two strokes is about 289 ms. The first stroke is with a peak current of -110.4 kA, a 10%~90% front rise-time of 1.81 μs, a maximum rising rate of 80.74 kA/μs, and a 50%~50% half peak width of 12.74 μs, resulting in a charge transfer of about 2.12 C. The subsequent stroke is with a peak current of -87.72 kA, a 10%~90% rise-time of 1.25 μs, a 50%~50% half peak width of 20.2 μs, and a maximum rising rate of 129.1 kA/μs, resulting in a charge transfer of 2.42 C.

The peak currents of these two strokes are over 95% of the stroke current in Berger's statistics [13]. However, the charge transfers of these two strokes are relatively small (2.1C and 2.4 C, respectively), while that there were 50% of strokes having a charge transfer of over 4.5 C in Berger's statistics. The time interval between the 2 strokes in this flash is 289 ms, while that there were only 5% of inter-stroke time intervals exceeding 150 ms in Berger's statistics. The maximum current rising rate of the first stroke in this flash is as high as 80.72 kA/μs, while that there were only 5% of the first return stroke with a maximum current rising rate exceeding 32 kA/μs in Berger's statistics.

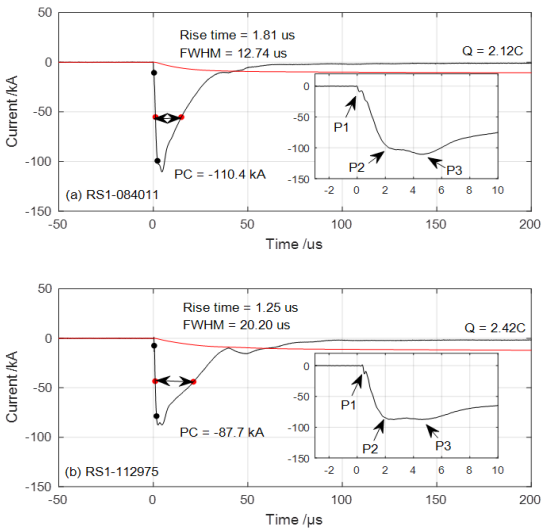

Figure 3. Current waveforms and charge transfers recorded for two return strokes in a lightning discharge to SZMGT on May 4, 2017.

Besides, according to Berger's statistics, the peak current of the first stroke was usually 2~3 times that of the subsequent stroke, while the charge transfer of the first stroke was usually only one-fourth more than that of the subsequent stroke. But in this flash, the peak current of the first stroke is just 1.26 times that of the subsequent stroke and the charge transfer of the first stroke is less than that of the subsequent stroke.

C. Atmospheric electric field enhancement on top of SZMGT

In general, due to the corona discharge effect of ground plants, the atmospheric electric field on ground under a thunderstorm is usually less than 10 kV/m [14]. However, the atmospheric electric field over sea water surface under a thunderstorm may reach 30 kV/m [15]. With balloon-electric-filed-mill technique, Soula & Chauzy [16] measured the electric field at 5 different heights from 0 m – 900 m above ground under a thundercloud. They found that while the electric field on ground was 5 kV/m， the value at 603 m

high was 65 kV/m. Other studies show that a tall structure usually makes the electric field on its top stronger and that at its lower parts weaker.

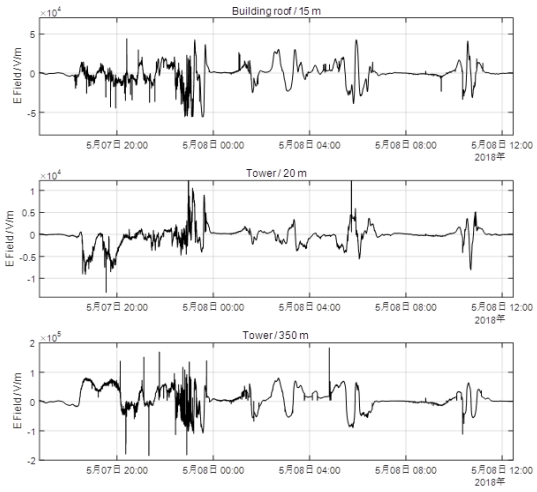

Figure 4. Electric field mill records at the main site (building roof/15m high above ground), lower part of SZMGT (tower/20m high above ground) and top of SZMGT (tower/350m high above ground) during a thunderstorm.

Shown in Figure 4 are the electric field mill records at different height above ground in the period from 17:00 of 07 May of 2018 to 13:00 of 08 May of 2018 during a thunderstorm. From top to bottom of the figure are the records at the main site building roof (15 m high), at low part of the tower (20 m high) and at the top of the tower (350 m high), respectively. In general, the trends and fluctuations of the three are similar, but their amplitudes are quite different from each other. With the values around the time 23:00 of 07 May as an example: the value at the main site building roof is -50.5 kV/m，while that at the tower 20 m high is +10 kV/m and that at the tower 350 m high is -190 kV/m. This is just a reflection of the fact that there is a strong electric field enhancement effect near the tower top but a significant electric field shielding effect near tower lower part.

IV. SUMMARY

a) Most of observations of lighting discharges to tall towers are in the high-latitude regions in the world. The SZMGT is located in a low-latitude and subtropical region in southern China. The lightning observation campaign around the SZMGT provides us a unique opportunity to get lightning current parameters for the protection of high-rise building against the lightning in low-latitude regions.

b) With the Rogowski coil and current shunt as the current sensors, an adequate E/O and optical fibber unit as the data acquisition and transfer device and a well-designed power supply unit, we have succeeded in measuring the lightning current on the SZMGT. As the example, two of the return stroke current waveforms recorded were analyzed and discussed. More lightning current data are expected in next few years.

c) With the high-speed camera and electric and magnetic field antennas at the main observation site, two upward positive stepped leaders initiated from the top of the SZMGT were captured and analyzed. The results show that their step lengths ranged from 0.5 m to 4.4 m, and the step interval ranged from 13.3 μs to 46.69 μs, while their overall 2-D leader speed ranged from 0.24×10^5 m/s to 2.21×10^5 m/s.

d) With the electric field mills mounted along the tower body, the electric fields under a thunderstorm at different heights above ground have been measured. The results show that there is strong electric field enhancement effect around the top of the tower and an obvious electric field shield effect at low part of the tower. We hope that we can get simultaneous measurements of the lightning current, high-speed camera images and electric fields at the top of the tower in near future, which can help us get insight of the mechanism of lightning initiation from the tower.

ACKNOWLEDGMENTS

Works leading to this paper are supported by The Hong Kong Polytechnic University and Research Grant Council of Hong Kong Government (Grant No.: PolyU 152652/16E).

REFERENCES

[1] B. Abchirm and P. Basabe, "United Nations International Strategy for Disaster Reduction." Living with risk: 1-412, 2003.

[2] R. Fisher et al.,"Parameters of triggered-lightning flashes in Florida and Alabama," *J. Geophy. Res.: Atmos.*, 98(D12), 22887-22902, 1993.

[3] X. Liu *et al.*, "Experiment of artificially triggering lightning in China," *J. Geophy. Res.: Atmos.*, 99(D5), 10727-10731, 1994.

[4] X. Qie *et al.*, "Characteristics of triggered lightning during Shandong artificial triggering lightning experiment (SHATLE)," *Atmos. Res.*, 91, no. 2-4, 310-315, 2009.

[5] V. A. Rakov, M. Uman, and K. Rambo, "A review of ten years of triggered-lightning experiments at Camp Blanding, Florida," *Atmos. Res.*, 76, no. 1-4, 503-517, 2005.

[6] Y. Zhang *et al.*, "Experiments of artificially triggered lightning and its application in Conghua, Guangdong, China," *Atmos. Res.*, 135, 330-343, 2014.

[7] D. Wang et al., "Observed leader and return-stroke propagation characteristics in the bottom 400 m of a rocket-triggered lightning channel," *J. Geophy. Res.: Atmos.*, 104(D12), 14369-14376, 1999.

[8] J. Takami and S. Okabe, "Observational results of lightning current on transmission towers," *IEEE Trans. on Power Delivery*, 22, no. 1, 547-556, 2007.

[9] F. Heidler, W. Zischank, and J. Wiesinger, "Statistics of lightning current parameters and related nearby magnetic fields measured at the Peissenberg tower," *Proc. 25th Int. Conf. on Lightning Protection, Rhodes, Greece*, 2000, pp. 78-83.

[10] C. Romero *et al.*, "A system for the measurements of lightning currents at the Säntis Tower," *Electric Power Systems Research*, 82, no. 1, 34-43, 2012.

[11] S. Visacro et al., "Statistical analysis of lightning current parameters: Measurements at Morro do Cachimbo Station," *J. Geophy. Res.: Atmos.*, 109(D1), 2004.

[12] G. Diendorfer, H. Pichler, and M. Mair, "Some parameters of negative upward-initiated lightning to the Gaisberg tower (2000–2007)," *IEEE Trans. on EMC.*, 51, no. 3, 443-452, 2009.

[13] K. Berger, "Parameters of lightning flashes," *Electra*, 41, 23-37, 1975.

[14] R.B. Standler and W.P. Winn, "Effects of coronae on electric fields beneath thunderstorms." *Q.J.R. Meteorol. Soc.*, 105, 285-302, 1979.

[15] R.B. Toland and B. Vonnegut, "Measurement of maximum electric field intensities over water during thunderstorms." *J. Geophys. Res.*, 82(No.3): 438-440, 1977.

[16] S. Soula and S. Chauzy, "Multilevel measurement of the electric field underneath a thundercloud 2. Dynamical evolution of a ground space charge layer." *J. Geophys. Res.*, 96(D12), 22327-22336, 1991.

Simulation Analysis on Return Conductor Settings for Lightning Indirect Effect of Metal Cabin

Mingxin DU
Lightning and Electromagnetic Environmental Laboratory
Xi'an Airborne Electromagnetic Technology Co., Ltd.
Xi'an, China
du.mingxin@airborne-em.com

Yanchao DUAN
Lightning and Electromagnetic Environmental Laboratory
Xi'an Airborne Electromagnetic Technology Co., Ltd.
Xi'an, China
duan.yanchao@airborne-em.com

Xiu XIONG
Lightning and Electromagnetic Environmental Laboratory
Xi'an Airborne Electromagnetic Technology Co., Ltd.
Xi'an, China
xiong.xiu@airborne-em.com

***Abstract*—In this paper lightning indirect effect of metal cabin is simulated by COMSOL Multiphysics. The effects of different numbers of return conductors and different distances between conductors and specimen on surface current distributions are analyzed. Then selecting the appropriate return conductor configuration, the effects of non-metallic materials and holes on the electromagnetic environment in the cabin are simulated. Results show that when the number of return conductors is 12 and conductors are 1m from the cabin surface, the surface current distribution is uniform, and return conductors have less influence on the cabin current distribution. Existences of non-metallic materials and holes in the cabin increase the coupled electromagnetic field. Results of this paper can provide the foundation for the further experiment method of lightning indirect effect.**

Keywords—lightning indirect effect, return conductors, simulation, current distribution, electromagnetic field

I. INTRODUCTION

Lightning is a strong natural discharge process. With the direct effects of high pressure shock wave, electromagnetic force and heat, as well as the indirect effect of high intensity electromagnetic field, it will cause ablation, explosion and structural distortion damages to the aircraft system, and also cause the electronic system to be invalidated or destroyed[1]. Both direct[2-4] and indirect effects[5-7] of lightning have been studied by scholars both at home and abroad, from simulation methods to test methods.

SAE-ARP 5416 gives the method of lightning indirect effect test for small aircraft using return conductors[8]. GJB 8848-2016 gives the method of lightning indirect effect test for rocket ordnance using return conductors[9].

The main function of building the return conductor is to form a current circuit, simulating current distribution on the surface of the aircraft system of real lightning as far as possible. From this we can judge the electromagnetic environment in the cabin in which the equipment is located. Because the above standards do not clearly specify how to configure the return conductor system, the return conductor system is complex to configure and cost is high in the test. Therefore, it is necessary to use numerical simulation method to analyze and optimize the return conductor settings before experiment.

Firstly, considering aircraft fuselage, rocket, missile and other aircraft are mostly cylindrical, a capsule-type metal cabin is established in this paper. Secondly, current distributions on the cabin are simulated under 5 kinds of conductor numbers and 6 kinds of distances between conductors and specimen using COMSOL Multiphysics finite element software. Finally, selecting the appropriate return conductor configuration, the effects of non-metallic materials and holes on the electromagnetic environment in the cabin are simulated.

II. SIMULATION SETTINGS

SAE ARP 5412A defines the ideal current waveforms for describing the direct effect of lightning current as A, B, C, D [10]. Current A component is called the first backstroke. And its peak value is up to 200kA. It is an important component that affects the physical damage of structures. The current A is expressed as follows:

$$I(t)=I_0(e^{-\alpha t}-e^{-\beta t})$$

Where I_0 = 218810A, β=11354s^{-1}, α=647265s^{-1}. The waveform is shown in Fig. 1.

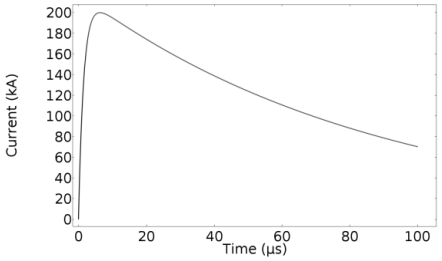

Fig. 1. Waveform of current A

According to the method of lightning indirect effect test based on return conductor in GJB 8848-2016, considering aircraft fuselage, rocket, missile and other aircraft are mostly cylindrical, a capsule-type metal cabin model is established in this paper, shown in Fig. 2. The lightning current A is injected into one end of the SUT and then flows out from the other end to form a current circuit through return conductors. Current distributions under 5 kinds of conductor numbers and 6 kinds of distances between conductors and specimen are simulated. The settings are shown in TABLE Ⅰ and Ⅱ. H in TABLE Ⅱ is the distance between conductors and the outermost plane of the specimen, shown in Fig. 2. Then selecting the appropriate return conductor configuration, a model of capsule-type cabin with partial non-metallic materials is established, shown in Fig. 3. In the head of the cabin, about 40% on one end of the cylinder is non-metallic material. And it is isolated by a metal plate with a diameter of 0.1m hole. Lightning current injection mode is the same as above.

Free tetrahedral structure is used to mesh the model. Fine structures such as the current injection point should be meshed carefully and its structure is characterized well. Then meshing the rest of the structure at a certain rate of growth. The total mesh number is about 210000, and the minimum

mesh size is about 0.1m. Mesh design results are shown in Fig. 4.

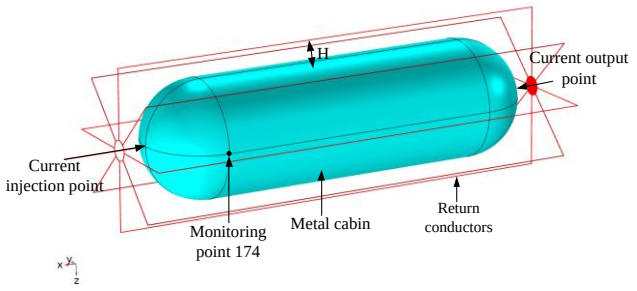

Fig. 2. A capsule-type metal cabin model

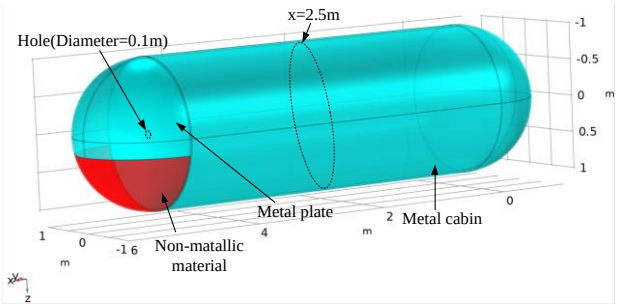

Fig. 3. A model of capsule-type cabin with partial non-metallic materials

TABLE I. Return conductors settings of N

Item	Value				
Numbers of return conductors N	6	8	10	12	14

TABLE II. Return conductors settings of H

Item	Value					
Distances between conductors and specimen H(m)	0.375	0.5	0.75	1.0	1.25	1.5

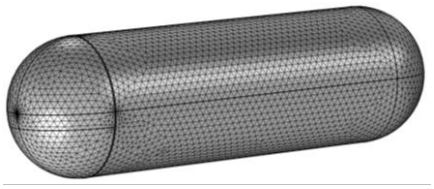

Fig. 4. Mesh design results

III. ANALYSIS OF SIMULATION RESULTS

A. *Influence of return conductors number on current distributions*

The determination of current distribution on the cabin is one of the most important contents of lightning indirect effect analysis. Because the current in the return conductors close to the cabin will affect its surface current distribution, it is necessary to design the structure of return conductors. It is expected that the current distributed on the cabin in the test can simulate the real state of the lightning strike as much as possible. It can be seen from Fig. 2 that return conductors are evenly distributed around the cabin. In order to research the effect of the return conductor number on the surface current distribution of the metal cabin, current distributions on the metal cabin is simulated according to TABLE Ⅰ and Ⅱ are shown in Fig. 5, when the N=6, 8, 10, 12 and 14.

At the same time, the current density on the cross section at x=2.5m are drawn by the height expression in COMSOL post-processing, as shown in Fig. 6. It can be seen that the current density on the metal cabin surface directly below conductors is obviously higher than that of the rest, and the peak current density appears at the same times as the number of conductors. The bigger N is, the less the current density is affected by conductors. Thus the current distribution is more uniform. There is little difference in the uniformity of surface current distribution between N=12 and N=14.

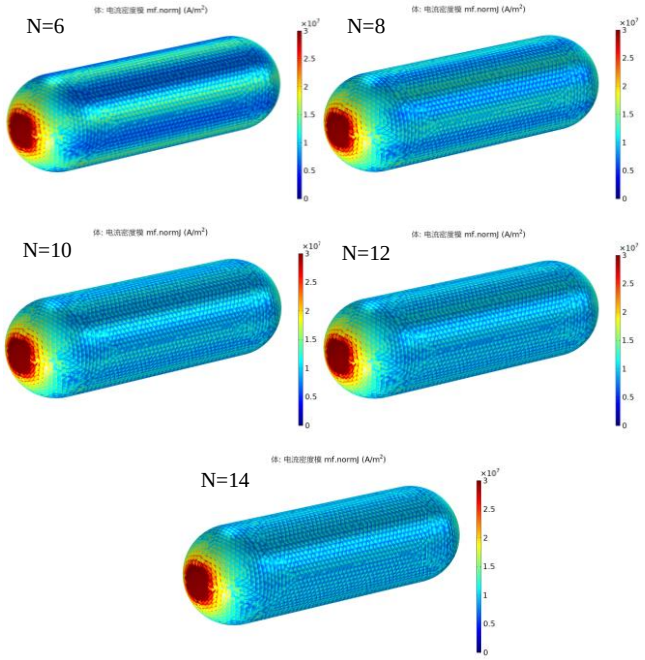

Fig. 5 Current distribution of metal cabin with different N

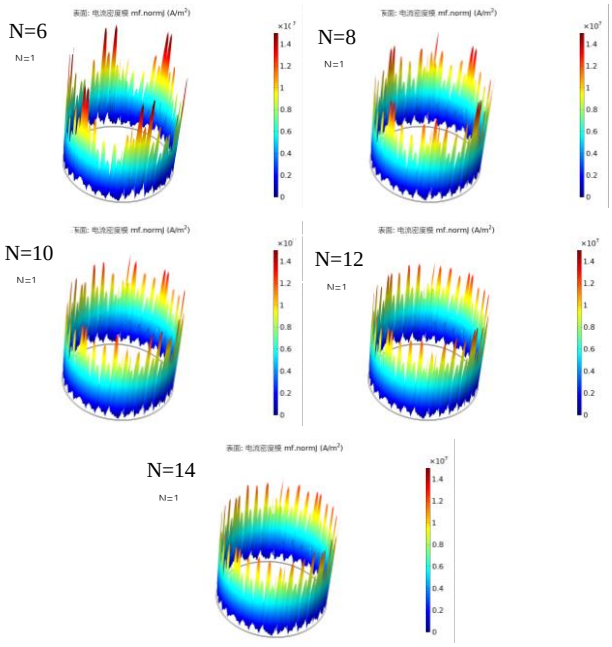

Fig. 6 Current distribution on the cross section at x=2.5m with different N

B. *Influence of distances between conductors and specimen on current distributions*

The distance between the conductors and the specimen will also affect the current distribution on the surface of the metal cabin. According to the simulation results of section *A*, and considering the difficulty of the experiment, the current distribution on the metal cabin is simulated according to TABLE Ⅱ, when H=0.375, 0.5, 0.75, 1.0, 1.25, 1.5. Selecting a monitoring point on the metal cabin, as shown in Fig. 2, current density with different H at 6 μs are shown in Fig. 7. It can be seen that the bigger H is, the more stable current density is. Considering the cost savings in experiment, it is recommended that H=1. 0(m) is suitable.

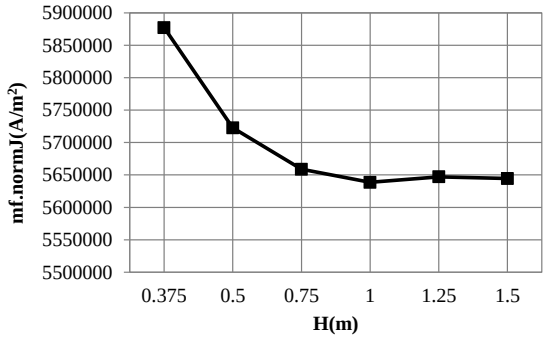

Fig. 7 Current density curve of monitoring point with different H

C. *Internal electromagnetic environment of cabin which has non-metallic materials and holes*

According to the simulation results in Sections *A* and *B*, finally choosing N=12 and H=1.0. Fig. 8 shows the current distribution in the cabin. The current density on metallic materials is much bigger than that on non-metallic materials. Current density at the place of material mutations is much bigger.

The internal electromagnetic field intensity is shown in Fig. 9 where Fig. 9 (a) is a section of electric field, and Fig. 9(b) is a section of magnetic field. It can be seen that most of the electromagnetic fields are coupled to the head of cabin from the non-metallic material, and small part of the electromagnetic fields are coupled into the interior compartment through the hole in the metal partition. The electromagnetic shielding effect of non-metallic materials is much less than that of metallic materials. The electromagnetic field intensity at the monitoring points in Fig. 9(a) are drawn in Fig. 10. It can be seen that the closer to the current injection point, the closer to the non-metallic material, the higher the electromagnetic field intensity coupled into the cabin.

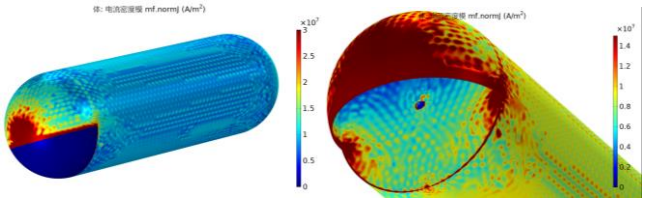

Fig. 8 Current density curve of monitoring point with different H

(a) electric field

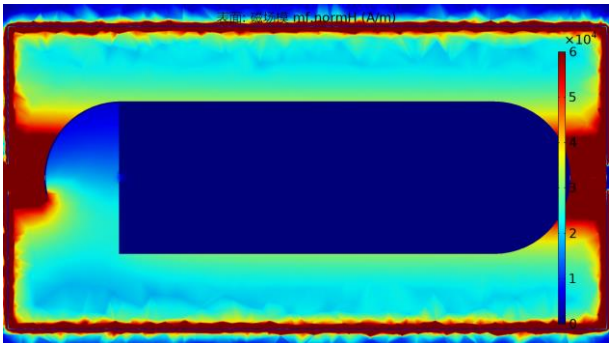

(b) magnetic field

Fig. 9 Cross-sectional view of electromagnetic field intensity inside cabin

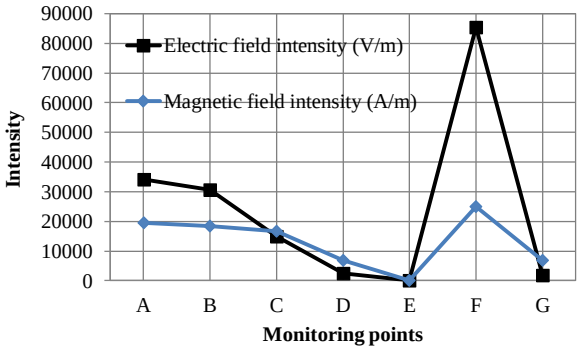

Fig. 10 The electromagnetic field intensity at the monitoring points

IV. CONCLUSION

Different settings of return conductor in lightning indirect effect are simulated in this paper. With a certain configuration, electromagnetic environment in cabin with non-metallic materials are carried out. The following conclusions can be obtained.

Surface current distributions of cabin are affected by numbers of return conductors and distances between conductors and specimen. N=12 and H=1.0 is the recommended setting.

The lightning current is mainly conducted on the metal material. Most of the electromagnetic fields are coupled to the head of cabin from the non-metallic material, small part of the electromagnetic fields are coupled into the interior compartment through the hole. The closer to the current injection point, the closer to the non-metallic material, the higher the electromagnetic field intensity coupled into the cabin. So protection design needs to be carried out according to the actual situation.

REFERENCES

[1] ZHOU B H, CHEN B, SHI L H. EMP and EMP protection[M]. Beijing: National Defense Industry Press, 2003.

[2] FERABOLI P, MILLER M. Damage resistance and tolerance of carbon/epoxy composite coupons subjected to simulated lightning strike[J]. Composites Part A: Applied Science and Manufacturing, 2009, 40(6): 954-967.

[3] CHEMARTIN L, LALANDE P, PEYROU B, et al. Direct effects of lightning on aircraft structure: analysis of the thermal, electrical and mechanical constraints[J]. Journal Aerospace Lab 2012, 5(AL05-09): 1-15.

[4] FU S C, ZHOU Y H, SHI L H, et al. Experimental and electrical-thermal coupled simulation for lightning current damage of carbon fiber resinforced plastic[J]. Acta Materiae Compositae Sinica, 2015, 32(1): 250-259.

[5] MEYER M, FLOURENS F, ROUQUETTE J A, et al. Modeling of lightning indirect effects in CFRP aircraft[C]//2008 International Symposium on Electromagnetic Compatibility-EMC Europe. Hamburg, Germany : IEEE, 2008 : 1-5.

[6] HUANG R T, DUAN Y T, SHI L H, et al. Simulation analysis on return conductor configuration for lightning indirect effect test of metal cylinder[J]. Chinese Journal of Ship Research, 2018, 13 (Supp 1) : 66-70, 91.

[7] GUO Fei, ZHOU Bi-hua, GAO Cheng. Analysis for lightning indirect effects of the aircraft by numerical simulation[J]. CHINESE JOURNAL OF RADIO SCIENCE, 2012, 27(6): 1129-1134.

[8] SAE. ARP 5416 Aircraft lightning test methods[S]. Warrendale, PA: SAE, 2013.

[9] GJB 8848-2016 Electromagnetic environment effects test methods for systems[S]. Beijing: Equipment Development Department of People's Republic of China Central Military Commission, 2016.

[10] SAE. ARP 5412A Aircraft lightning environment and related test waveforms[S]. Warrendale, PA: SAE, 2013.

Analysis on Eddy Current Loss and Temperature Distribution for Ultra High Voltage Transformer in No-Load

Mingyang Li
Key Laboratory of High Voltage & EMC
NORTH CHINA ELECTRIC POWER UNIVERSITY
Beijing, China
762504044@qq.com

Zezhong Wang
Key Laboratory of High Voltage & EMC
NORTH CHINA ELECTRIC POWER UNIVERSITY
Beijing, China
wzzh@ncepu.edu.cn

Bing Li
Key Laboratory of High Voltage & EMC
NORTH CHINA ELECTRIC POWER UNIVERSITY
Beijing, China
ncepu_lb@163.com

Ke Liu
Key Laboratory of High Voltage & EMC
NORTH CHINA ELECTRIC POWER UNIVERSITY
Beijing, China
2827859117@qq.com

Mengzhen Xuan
Key Laboratory of High Voltage & EMC
NORTH CHINA ELECTRIC POWER UNIVERSITY
Beijing, China
dreamtxuan@163.com

Suxin Guo
Key Laboratory of High Voltage & EMC
NORTH CHINA ELECTRIC POWER UNIVERSITY
Beijing, China
2814966154@qq.com

***Abstract*—The presence of core joint increases the magnetizing current of the transformer, it is equivalent to an thin air gap in the FEM(finite element) model of this paper. Based on circuit-field coupling and magnetic-thermal coupling FEM model，the magnetic flux leakage, loss and temperature distribution characteristics of Ultra High Voltage main transformer under no-load operation are calculated and analyzed.**

Keywords—geomagnetically induced current,UHV transformer, air gap, magnetic losses, temperature

I. INTRODUCTION

The single-phase four-column UHV main transformer has a single-column capacity of up to 500 MVA, and the volume of the transformer limited by transportation, space, etc. cannot be increased synchronously, which may cause stray loss and local overheating of the UHV transformer. The key to the calculation of the hot spot problem of the transformer is the calculation of the loss and heat transfer coefficient[1].

II. MAGNETIC CIRCUIT AND AIR GAP MODEL

Fig. 1 shows the magnetic circuit model of the single-phase four-column UHV main body transformer, there exist core joint at the intersection of the column and the yoke. l_0、l_1、l_2、$l_{\delta1}$ and $l_{\delta2}$ are the lengths of the magnetic circuits of each segment respectively, and δ_1、δ_2 are core joint air gaps, and the magnetic field strengths corresponding to each segment are respectively recorded as H_0、H_1、H_2、$H_{\delta1}$ and $H_{\delta2}$, corresponding to each segment. The core areas are denoted as S_0、S_1、S_2、$S_{\delta1}$ and $S_{\delta2}$, respectively, and the magnetic fluxes corresponding to the segments l_0、l_1 and l_2 are denoted as Φ_0、Φ_1、Φ_2, respectively.

This work is supported in part by the National Key R&D Program of China under Grant (No. 2016YFC0800100) and Fundamental Research Business Expenses of Central Universities(2018QN005)

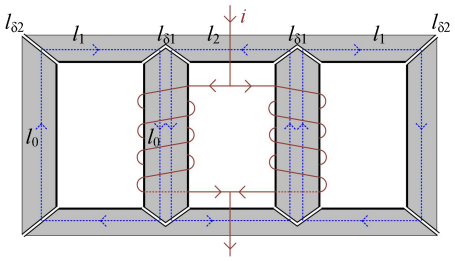

Fig. 1 the magnetic circuit model of the single-phase four-column UHV main body transformer

From magnetic flux continuity law:

$$H_1\mu_1 S_1 = H_{\delta2}\mu_0 S_{\delta2} = H_{\delta1}\mu_0 S_{\delta1} \quad (1)$$

According to the Ampere loop law,

$$H_0 l_0 + H_1(2l_1 + l_0) + 2H_{\delta1}l_{\delta1} + 2H_{\delta2}l_{\delta2} = N\frac{i}{2} \quad (2)$$

$$2H_0 l_0 + 4H_{\delta1}l_{\delta1} + 2H_2 l_2 = 2N\frac{i}{2} \quad (3)$$

and

$$\phi_1 + \phi_2 = \phi_0 \quad (4)$$

$$E = 4.44 f N \phi_0 \quad (5)$$

Where N is the number of turns of the coil, i is the exciting current, and E is the effective value of the induced electromotive force. Given the E of voltage source, the solutions of H_0、H_1、H_2、$H_{\delta1}$ and $H_{\delta2}$ can be obtained by simultaneous (1) to (5). The relationship between H and μ is determined by the BH curve.

When the core joint is neglected, excitation current Im obtained by the magnetic circuit method has a large error

(76%) with the value measured by the manufacturer on the low voltage side. It can be known that the presence of an air gap at the core joint increases the magnetizing current of the transformer.

The air gap lengths $l_{\delta 1}$ and $l_{\delta 2}$ determined by the magnetic circuit model are 0.22 mm and 0.22 mm respectively. In order to verify the effectiveness of this air gap model, the no-load current when different voltages are applied on the low-voltage side is obtained based on finite element software simulation and compared with the test data provided by the manufacturer.

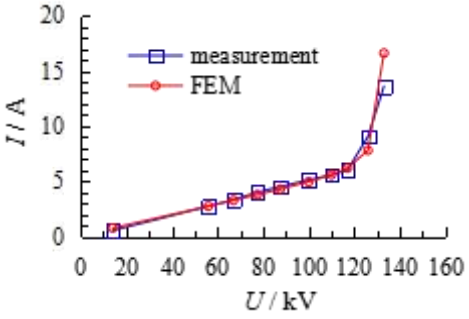

Fig. 2 Comparison of no-load current between FEM model and measurement on low-voltage side

When different voltages are applied to the low voltage side, the comparison of the no-load current calculated by the FEM model with the test current is shown in Fig. 2. It can be seen from the comparison results that after considering the air gap in the finite element simulation, the simulation results are in good agreement with the measured results, and the validity of the air gap parameters is verified.

III. MAGNETIC FLUX LEAKAGE AND LOSS IN NO-LOAD

The no-load loss is mainly the core loss because the magnetic flux leakage and coil current are small at no load. Only the coil, core, and fuel tank are considered in the FEM model, and the loss and temperature distribution are calculated. Fig. 3 shows the meshing of the FEM model.

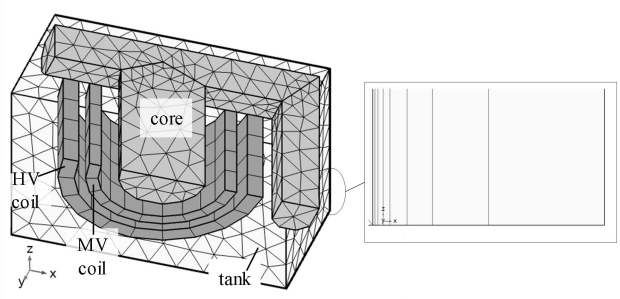

Fig. 3 Meshing of FEM model for loss calculation

Fig. 4 shows the loss distribution of the core and the fuel tank. The eddy current loss of the fuel tank is averaged in one cycle, and is used as a heat source for temperature field simulation. The core loss is obtained from the core Bm and the core loss curve.The total core loss of the complete model is 137 kW calculated by multiplied of the symmetry coefficient of 8.

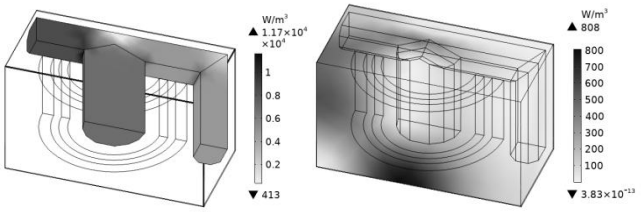

a) core loss b) tank loss

Fig. 4 Loss distribution

IV. TEMPERATURE CHARACTERISTICS

The cooling mode of the UHV main transformer is OFAF. The empirical formula for the convective heat dissipation coefficient of the outer surface of the fuel tank is[2]

$$h_1 = \frac{\Delta\theta^{0.25}}{0.262^{1.25}}\ ,(\mathrm{W/(m^2\cdot K)}) \qquad (6)$$

The empirical formula for the heat dissipation coefficient of the inner surface of the fuel tank and the outer surface of the structural member is[2]

$$h_2 = 38\Delta\theta^{0.25}\left(\frac{\theta}{50}\right)^{0.5}\ ,(\mathrm{W/(m^2\cdot K)}) \qquad (7)$$

Where, Δθ is the temperature difference between the heating element and the medium outside the convection zone, K; θ is the average surface temperature of the heating element, °C;

Assume that the ambient temperature, the bottom oil temperature and the top oil temperature of the transformer are set to 30 °C, 50 °C and 60 °C respectively. The temperature of the transformer oil increases linearly with height[3]-[5]. Fig. 5 shows the temperature distribution of the core and the fuel tank. The hot spot temperature rise meets the limits specified by the relevant standards.

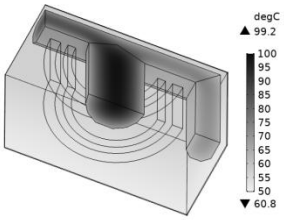

Fig. 5 Steady state temperature distribution

Fig. 6 shows the heat dissipation coefficient distribution. It can be seen that the heat dissipation coefficient of the outer surface of the oil tank is about 12 W/(m^2·K), and the minimum heat dissipation coefficient of the outer surface of the core is 91.8 W/(m^2·K), and the maximum is 197 W/(m^2·K). The larger the temperature difference between the heating element and the cooling medium, the larger the heat dissipation coefficient.

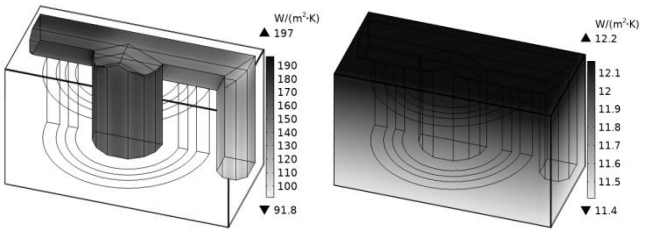

a) core b) tank

Fig. 6 Convective heat dissipation coefficient distribution

V. CONCLUSION

The core joint is equivalent to the air gap in the FEM model, and the effectiveness of the air gap model is verified by comparison with test data. The loss and temperature distribution of the transformer in no-load are calculated based on the simplified FEM model simulation. The calculation results can provide reference for the optimal design and protection of the UHV transformer.

REFERENCES

[1] K. Preis, O. Biro, G. Buchgraber, et al. “Thermal-electromagnetic coupling in the finite-element simulation of power transformer,” *IEEE Trans. Magn.*, vol. 42, no. 4, pp. 999-1002, 2006.

[2] X. Yucheng. Power Transformer Manual[M]. Beijing： China Machine Press，2003.pp. 297

[3] M. E. Rosillo, C. A. Herrera, G. Jaramillo. “Advanced thermal modeling and experimental performance of oil distribution transformers,” *IEEE Trans. Power Del.*, vol. 27, no. 4, pp. 1710-1717, 2012.

[4] X. M. Lopez-Fernandez, P. Penabad-Duran, J. Turowski. “Three-dimensional methodology for the overheating hazard assessment on transformer covers,” *IEEE Trans. Ind. Appl.,* vol, 48, no. 5, pp. 1549-1555, 2012.

[5] F. Farahmand, F. P. Dawson, J. D. Lavers. “Temperature rise and free-convection heat-transfer coefficient for two-dimensional pot-core inductors and transformers,” *IEEE Trans. Ind., Appl.,* vol. 45, no. 6, pp. 2080-2089, 2009.

Modeling the Triggering Requirements of Synchronized Marx Generators

N. Mora, B. Daout

montena technology, Switzerland, {nicolas.mora;bertrand.daout}@montena.com

Abstract

We discuss numerical and experimental modeling of the simultaneous erection of two or more Marx generators, and the switching jitter requirements to achieve optimal performance.

Keywords: Marx generators

1 Introduction

The possibility of synchronizing two or more Marx generators has been studied in the past for different Pulsed Power applications [1], [2]. There are also several HPEM generators that make use of synchronized Marx generators for e.g. beam steering [3], target interrogation [4],or bipolar feeding of bounded wave or hybrid EMP simulators [5].

In this work, we present the results of numerical simulations and experiments for modeling the simultaneous erection of two Marx generators. Based on the results, the admissible delay between the erection of the generators is obtained after fixing the so-called required generator unbalance.

Marx generators for typical HPEM applications can be usually modeled with circuit theory. We discuss the obtention of accurate circuit models and the synchronization requirements through numerical simulation or experiments. We also discuss observed runtime differences between Marx generators depending on the trigger circuit and possible solutions to achieve a synchronized system.

2 Circuit modeling of Marx Generators

The erection of a Marx generator can be simply modeled by the discharge of a series RLC circuit [1], [2]. Depending on the complexity of the Marx generator, the determination of its RLC parameters can be done by using circuit simulators. However, when the size of the generator becomes comparable to the expected wavelength, the determination of the parameters is better performed through experiments, or if possible, full-wave numerical simulations.

The RLC model of the Marx generator can be experimentally determined by analyzing its short-circuit current. The erected capacitance of the generator is usually a known parameter, and therefore, the inductance and internal resistance of the generator can be calculated from the resonance frequency and the damping factor (see e.g. chapter 2.3 of [2]). Fig. 1 presents an example of the RLC parameter extraction based on a short circuit measurement performed on a 4-stages Marx generator. Alternatively, the generator inductance can also be extracted from a full wave electromagnetic simulation if a good 3D model of the generator geometry is available. Further insight about the numerical and experimental determination of RLC models of complex Marx generator will be shown in the final presentation.

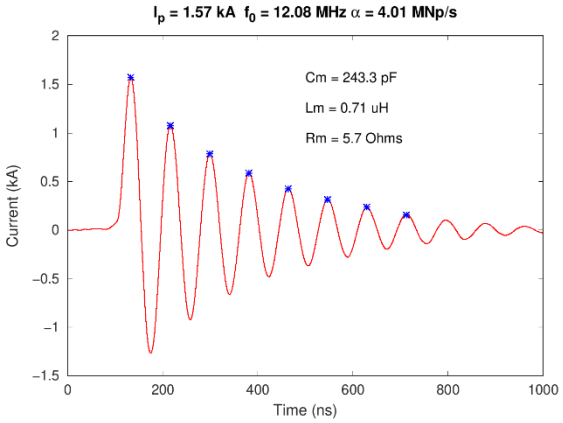

Fig. 1 Experimental extraction of the RLC parameters of a 4 stage Marx generator

3 Synchronization requirements of Marx generators

Once the generator model has been obtained, the relative delay between the generators needs to be experimentally determined. The correct synchronization will depend on the runtime and jitter of each separate generator.

Consider the differential voltage obtained by the simultaneous erection of positive and negative Marx generators. In a perfectly synchronized system, each generator contributes 50% of the differential voltage; any delay in the generator will produce an undesired unbalance that could be critical if the relative delay becomes comparable to the risetime of the generators. Fig. 2 illustrates the expected unbalance vs. runtime delay of two identical 8-stage Marx generators.

Depending on the maximum allowed source unbalance, the acceptable runtime delay is determined, as well as the jitter requirements for each individual Marx generator. Examples of the runtime measurement of two identical generators and the jitter requirements for good synchronization will be shown in the final presentation.

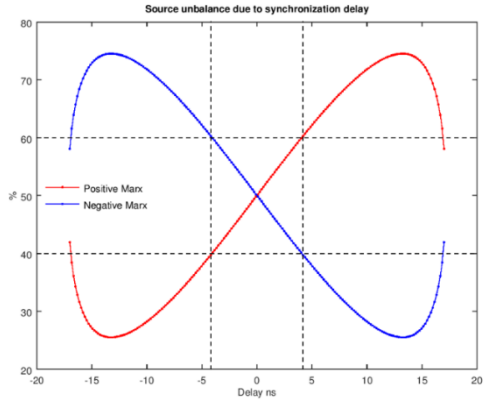

Fig. 2 Marx generators unbalance vs erection delay

2 References

[1] J. Lehr and P. Ron, *Foundations of Pulsed Power Technology*. John Wiley & Sons, 2017.

[2] S. T. Pai and Q. Zhang, *Introduction to high power pulse technology*. Singapore [u.a.]: World Scientific, 1995.

[3] D. V. Giri, H. Lackner, G. Franceschetti, J. Tatoian, V. Carboni, and J. M. Lehr, "Design, fabrication and testing of a timed-array of TEM horns for beam steering," *Sens. Simul. Notes*, vol. 469, 2002.

[4] D. V. Giri and T. T. Wu, "Double-Pulse Technique for Defending from Hostile SystemsSwiss Impulse Radiating Antenna (SWIRA) Characterization in the Presence of a Local Ground Plane (Earth)," *Interact. Notes*, vol. 602, 2006.

[5] C. E. Baum, "EMP Simulators for Various Types of Nuclear EMP Environments: An Interim Categorization," *Sens. Simul. 0240*, Jan. 1978.

Study of the electromagnetic protection of infrastructures with alternative shielding strategies

N. Mora, Z. Wang*, C. Romero§, M. Nyffeler§, F. Rachidi**

**EMC Laboratory, Swiss Federal Institute of Technology (EPFL), Switzerland, nicolas.mora@epfl.ch*
§ HPE Laboratory, Armasuisse Science and Technology, Switzerland

Abstract

We assess the suitability of alternative shielding schemes composed of conductive fabrics and/or wire meshes by performing direct measurements on an experimental mockup. The shielding configurations are implemented on a reduced scale model of a protected enclosure that is tested against radiated and conducted HEMP environments.

Keywords: HEMP Environment, Shielding

1 Introduction

This work studies the adequacy of alternative electromagnetic (EM) shielding requirements of typical underground facilities for reducing the installation and maintenance costs. Given that the shielded enclosures are usually made of very thick metallic walls (required attenuation levels in the range of 80-100 dB), the HPEM transmitted fields inside the protected volumes are usually considered as negligible. We address the question of whether it would possible to reach non-negligible but adequate protection levels with alternative shielding strategies using less complex and lighter EM shields.

To address this problem, numerical EM analyses and experiments are performed to evaluate the effectiveness of different alternative protection schemes including conductive mesh and conducted fabrics. The considered EM disturbance is a HEMP coupled through penetrating conductors or diffusing through the concrete and the enclosure materials.

A reduced scale model (RSM) of a protected enclosure was designed and excited with conducted and radiated interferences, and common-mode (CM) induced voltage and currents along a coupling wire are used to assess the effectiveness of the shield under test. The effectiveness of the shield is estimated by comparing the results obtained with and without the shields.

2 General overview of the RSM

A schematic diagram of the RSM is presented in Fig. 1. It consists of a concrete room that lies above a metallic ground plane. The room walls can be alternatively covered from the inside with an additional shielding material, i.e. wire mesh or a conductive fabric. To study the CM coupling, a coupling wire is placed at a certain height from the ground plane.

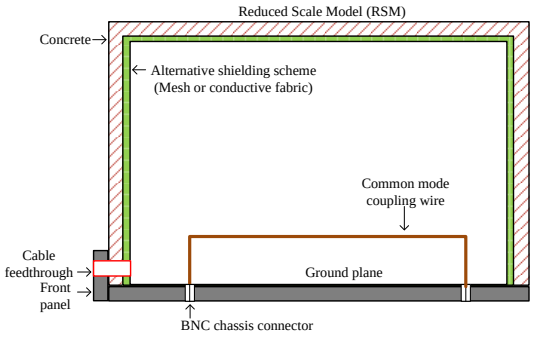

Fig. 1 Schematic diagram of the RSM

3 Numerical electromagnetic simulations

Numerical EM simulations in CST microwave studio were performed to predict the results of the RSM tests. The geometry is excited with a plane wave and the induced CM current and voltage along the wire are compared for different shielding schemes. A plot of the ratio between the induced current without any shield and by using different shielding materials is presented in Fig. 2.

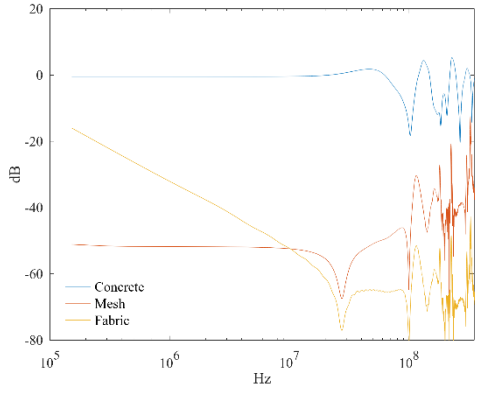

Fig. 2 Induced-current/E-field transfer functions for different shielding scheme.

According to the results, the presence of the concrete structure provides a slight attenuation with respect to the reference case. On the other hand, the presence of the mesh or the conductive fabric attenuates the induced current to acceptable levels. Further discussions about the results of the experimental campaigns and the EM modeling will be presented in the final presentation.

Measurement and Analysis of the Breakdown Strength of Different Liquid Dielectric Materials

N. Mora†, A. Mostajabi*, B. Daout†, F. Rachidi*

† Montena technology, Switzerland, nicolas.mora@montena.com
**EMC Laboratory, Swiss Federal Institute of Technology (EPFL), Switzerland*

Abstract

This study focuses on the breakdown performances of four liquid dielectrics including rapeseed oil, silicon oil, ethylene glycol, and an engineered product, under short pulse, lightning impulse, and DC voltage, by considering the effect of gap distance and moisture content.

Keywords: Breakdown Voltage, Liquid Dielectrics

1. Introduction

In high voltage pulse generators, the components are working in a fast risetime regime and at the same time at a very high voltage. Hence the insulating materials have to be overstressed in order to reduce the current path length (i.e. the inductance reduction) as much as possible. This is the case for solid dielectric (e.g. capacitor sheets or different mechanical holders and containers) and for gas and liquids used to surround and insulate the high voltage components.

Although comprehensive literature exists concerning the specifications of insulating material at AC, low frequencies or at lightning pulse [1]–[4], only few information could be found concerning the short pulse regime (nanosecond regime). Furthermore, studies on the breakdown strength of some liquids such as silicon oil and ethylene glycol are very limited. To bridge the gap, this study has as its primary goal to investigate the breakdown strength of four types of dielectric liquids under three test regimes considering different gap distances and relative humidity values. The liquids under test are rapeseed oil, silicone oil, ethylene glycol, and an engineered product.

2. Breakdown strength measurement

Adopting one of the recommendations in ASTM D 3300 [5] standard entitled "Dielectric breakdown voltage of insulating oils of petroleum origin under impulse conditions", in this study, sphere-sphere electrode configuration is used to provide the quasi-uniform field. Lightning impulse (LI) and short impulse (SI) tests are considered to investigate the influence of the waveform on the breakdown strength of the samples and various testing methods including rising-voltage and up-and-down method are examined. Besides LI and SI electrical strengths, it is also essential to know the DC electrical strength of insulation materials. These data are not only important in designing the insulation systems, but also allow to compare the effect of waveform shapes on the breakdown strength of different materials. In this study, we used the rising voltage method (1 shot/step) to perform the DC tests.

3. Moisture content variation

In addition to the breakdown strength of the dry samples, it is important to see how the insulation strength of liquid dielectric materials changes in the case that the moisture content increases inside the liquid. Several previous studies have already addressed this issue and have shown that the humid samples could follow different trends compared to the dry samples. This implies that liquid dielectric rankings due to their breakdown strength could be different among dry and humid samples. For example, Dan et al. [6] showed that although the lightning impulse dielectric strengths of esters are lower than mineral oil when dry, they are comparable when the moisture content of the mineral oil is greater than around 10 ppm. In [1], the breakdown voltages of synthetic ester, natural ester, silicone and mineral oil at ambient temperature are compared under different moisture contents. The results showed that even a small amount of moisture in mineral oil caused a rapid deterioration in breakdown voltages whereas both types of ester oils indicated high breakdown strength at high dissolved moisture level. In this study, both dry and humid samples are tested to investigate the impact of moisture on the breakdown strength of the four considered liquid insulation materials.

4. Conclusions

Various test procedures including the so-called rising-voltage method and up-and-down method were used to obtain the breakdown strength of the liquid samples. In all three test regimes, rapeseed oil has shown to outperform the other three liquids. In general, it is concluded that breakdown strengths of rapeseed oil are higher than those of silicon oil, ethylene glycol and the engineered product at various gap distances ranging from 1 mm to 4.5 mm in a quasi-uniform field. Looking at results from sequential tests at the same gap and relative humidities, rapeseed oil shows less scattering range for breakdown voltages compared to the other three materials. Ethylene glycol and silicon oil are seen to have higher sensitivity to the moisture content compared to rapeseed oil and the engineered product. The results under different voltage waveforms showed that changing the duration of the waveform affects the difference between the breakdown voltages of the liquids.

5. References

[1] M. Rafiq *et al.*, "Use of vegetable oils as transformer oils – a review," *Renew. Sustain. Energy Rev.*, vol. 52, pp. 308–324, Dec. 2015.

[2] D. Vukovic, S. Tenbohlen, J. Harthun, C. Perrier, and H. Fink, "Breakdown strength of vegetable-based oils under AC and lightning impulse voltages," in *2011 IEEE International Conference on Dielectric Liquids*, 2011, pp. 1–4.

[3] K. J. Rapp, J. Corkran, C. P. Mcshane, and T. A. Prevost, "Lightning Impulse Testing of Natural Ester Fluid Gaps and Insulation Interfaces," *IEEE Trans. Dielectr. Electr. Insul.*, vol. 16, no. 6, pp. 1595–1603, Dec. 2009.

[4] Q. Liu and Z. D. Wang, "Breakdown and withstand strengths of ester transformer liquids in a quasi-uniform field under impulse voltages," *IEEE Trans. Dielectr. Electr. Insul.*, vol. 20, no. 2, pp. 571–579, Apr. 2013.

[5] A. D. 3300, "Dielectric breakdown voltage of insulating oils of petroleum origin under impulse conditions," in *ASTM International*, 1994.

[6] M. Dan, I. Khan, and W. Zhongdong, "An overview of the suitability of ester oil dielectrics for use in large power transformers," in *Euro TechCon*, 2006.

Assessment of Varistor withstand capacity against CG generated transient voltages

Nilantha Sapumanage
Department of Physics
University of Colombo
Colombo, Sri Lanka
nilanthasapu@yahoo.com

Sankha Nanayakkara
Department of Physics
University of Colombo
Colombo, Sri Lanka
sankha84@live.com

Sidath Abegunawardana
Department of Physics
University of Colombo
Colombo, Sri Lanka
sidathjayalal@yahoo.com

Mahendra Fernando
Department of Physics
University of Colombo
Colombo, Sri Lanka
mahendra.fernando@gmail.com

Vernon Cooray
Department of Engineering Science
Uppsala University
Uppsala, Sweden
vernon.cooray@angstrom.uu.se

***Abstract*—The present study was devised to investigate the types of varistor categories that could effectively be employed to provide satisfactory protection for class 2 electronics as per IEC 60601-1-2: 2014. The actual varistor unit and the MATLAB-based module were tested against the IEC standard impulses to ascertain the behavior of the model. After verifying the performance of the MATLAB-based varistor module, same was simulated against real transient voltages to determine varistor currents, clamping voltages, and absorbed energies to compare with manufacture's specifications. Study disclosed that some varistors were not capable to withstand against selected real transient voltages, although their basic specifications met certain stipulated minimum requirements such as maximum energy capacity, clamping voltage, RMS ratings, maximum current etc.**

Keywords—CG, energy, IEC, impulse, pulse-rating, transient, voltage, varistor, electronics

I. INTRODUCTION

Modern electronic equipment and microprocessor-based systems exhibit a deficiency in immunity against the transient fluctuations in voltage supply [1], [2], [3], and [4].

Few different types of power quality issues identified owing to multiple nonlinearities that could induced on 230 V, 50 Hz utility supply due to intrinsic and extrinsic disturbances [5] and [6]. Lightning induced transient voltage is one of the prominent and frequent power quality related concerns to affect sensitive electronics-based systems [7] and [8]. Lightning generated transient voltages could induced frequently on nominal power frequency signal in random magnitudes from few volts to many kilovolts [9], [8], and [4]. The magnitude and the frequency of transient voltages induced by lightning are unpredictable as lightning discharges have a high randomness.[10] and [8]. Thus, during a thunderstorm, the presence of lightning generated transients is frequent and hence, may create catastrophic failures in sensitive systems if not designed with built in resilience or protected by other purpose-built external devices. [10] and [11].

Although lightning induced transient voltages inherently possess minute pulse spans in the order of several microseconds, they may bear sufficient energies to drive sensitive systems into impairment or failure [12] and [9]. Moreover, time-varying magnetic fields associated with lightning discharges have the potential to induce three to four or even more transient voltages in a raw on utility signal within a few hundreds of microseconds [12]. Thus, such induced voltages may become detrimental not only to sensitive systems but also to different energy absorbing devices installed in low voltage power installations (LVPI) [8] and [13].

Therefore, in regulated environment integrate self-surge immunity for all class 2 electronics is mandatory. The built-in surge immunity of consumer electronics and microprocessor-based systems should be in accordance with IEC 61000-4-5 and IEC 60335-1. Hence, all class 2 electronics must contain a sufficiently rated built -in surge protector to withstand and cushion the transient impulses up to a peak voltage of 1000 V [14].

Such protective devices shall characterize a fast response time, sufficient capacity to absorb excessive energy, and dissipate the same immediately to recover to default setting to address subsequent impulses [15] and [2]. A varistor is one such electronic component inherited with nonlinear electrical resistance [16]. Varistors can absorb much higher transient energies and can be arranged in many configurations to address increased voltage ratings and high current capabilities [16]. The maximum peak current allowable through a varistor is depends on a few factors such as pulse shape, duty cycle, and certain consecutive pulses. Therefore, in general, each varistor model has its own "withstand pulse current" or maximum non-repetitive surge current [16]. A surge more than the designated withstanding current may cause a short circuit or package rupture with the expulsion of material. On the other hand, if more than one impulse is applied or varistor is exposed to a transient impulse of longer pulse duration, its lifespan could be determined through respective pulse rating curves [16]. Therefore, in general, the amount of energy dissipated by a varistor when encountered with transient impulses would depend on the amplitude of the current, corresponding voltage, rise and decay time of impulse, and non-linearity of the varistor [16] and [17].

The original default parameter of any varistor would degrade from the day one of commissioning if repeatedly exposed to the influence of elevated transient voltages.

Therefore, with time, varistor's thermal capabilities would reduce in directly proportionate manner to the degree of strenuous operations it would undergo.

Lightning discharges could generate a sequence of impulses in quick successions, and this phenomenon may happen regularly throughout the year. Hence, the said basic minimum self-immunity specified by the standards might not retain forever, and electronics would be subjected to aging due to the influence of transient voltages. Therefore, electronics would undergo spurious degradation to fail before the guaranteed or expected service life, if not protected with sufficiently large surge suppression device [13], [18], and [19].

II. Materials And Methods

As per IEEE standard (C62.33-1982, subsection 2.3 and 2.4), varistors are tested against IEEE standard impulse to test their withstand capabilities before commercial use.

Following are some of the critical parameters investigated in this work. The rated peak single pulse transient current , maximum peak current applicable for a single impulse without causing device failure, Rated single pulse transient energy, the energy which may be dissipated for a single impulse of maximum rated current at a specified wave shape with rated RMS voltage or rated DC voltage applied without causing device failure. Further, pulse rating curves are defined for different product series to better understand upper threshold limiting the performances of diverse varistors. However, devising a study to test those devices against transient voltages generated by real lightning is an extremely rigorous exercise due to many practical constraints [9].

Therefore, simulating a reliable model would be one of the best options to consider. MATLAB is a proven software platform frequently employed to model real-world systems and processes to understand and predict outcomes of such phenomenon through simulations. Therefore, this study was devised with a MATLAB-based model.

A nonlinear resistor or a varistor can be mathematically modeled by equation 1 [20],

$$i = I_0 * \left(\frac{v}{V_0}\right)^{\alpha} \quad (1)$$

Where, v and i are instantaneous voltage and current, V_0 is protection voltage, I_0 is reference current used to specify the protection voltage, and α is the exponent defining the nonlinearity characteristics (typically between 10 and 50). Figure 1 illustrates the typical characteristic curve of a varistor [20].

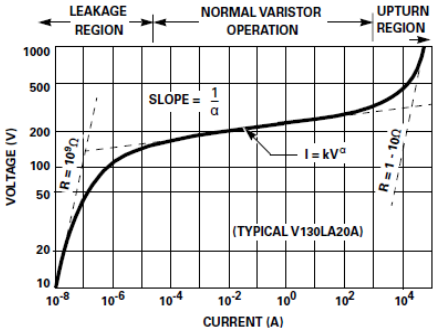

Fig. 1. Current vs. Voltage characteristics of the typical varistor (Source: Littelfuse product catalogue and a design guide on MOV, 2017)

To model the above nonlinear varistor in MATLAB-based model, first the actual varistors are selected and tested against IEC impulses for a range of voltages starting from 1000 V to 3000 V with the step increment of 250 V.

Figure 2 demonstrates the laboratory test arrangement employed to test varistor. Current through the device was measured by a Rogowski coil with conversion ratios of 10.0 A: 0.5 V.

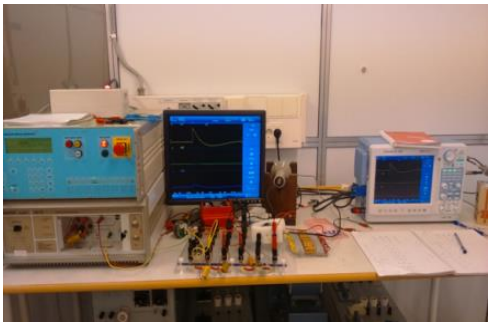

Fig. 2. Experiment setup used to test varistors against IEC impulses

The 10:1 attenuator was used for equipment safety to measure the respective current on the scope. The voltage across the varistor was measured through a high voltage probe of 1000:1, and all three inputs were connected to a Tektronix P6015 digitizer. Current through the varistor and voltage across the device were measured after superimposing IEC impulse at π/2 phaser angle on 230 V, 50 Hz utility signal.

Later, MATLAB-based model illustrates in Fig. 3 was simulated against the same range of IEC impulses, and calibrated the varistor model until it delivers similar performances to the actual varistors.

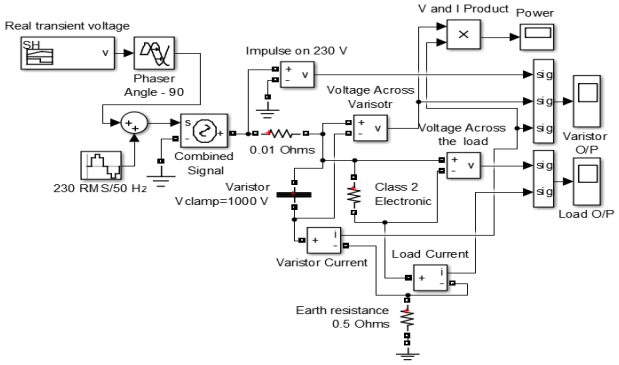

Fig. 3. MATLAB-based circuit model and the varistor module

Table I illustrates the laboratory experiment outcome and the result of the simulation.

TABLE I. ENERGY ABSORBED AND CURRENT CHANNELLED THROUGH THE VARISTOR UNIT

IEC IMPULSE (V)	Energy Absorbed (J)			Current Passed through (A)		
	Actual	*Model*	*% Diff*	*Actual*	*Model*	*% Diff*
1000	0.15	0.04	115.79	40.12	17.34	79.29
1250	0.27	1.73	51.16	213.56	263.13	-20.80
1500	8.30	6.40	25.85	568.62	580.74	-2.11
1750	15.42	13.31	14.69	893.09	916.36	-2.57
2000	23.84	21.91	8.44	1202	1246.78	-3.66
2250	32.92	31.77	3.56	1557	1603.54	-2.95
2500	44.25	42.68	3.61	1959	2017.37	-2.94
2750	55.59	54.34	2.27	2330.89	2382.21	-2.18
3000	66.63	66.68	-0.08	2695	2746.69	-1.90

Table I allows to conclude that both actual varistor and MATLAB-based varistor model performances are close to each other. Hence, it is reasonable to conclude that, the MATLAB-based varistor module as a potential candidate to simulate against real transient voltages to predict the actual varistor behavior under the influence of real transient voltages.

The CG discharges used for this study were captured during the first inter-monsoon period (April to May) of the year 2014. Measurements were taken at the interface between low voltage power installation and the utility service wire of an isolated dwelling unit selected in the Western Province of Sri Lanka [12] and [21]. The captured data were further differentiated into basic signature types as per the previous study of Nanayakkara *et al*. to facilitate analysis [21] and [22].

Figure 4, Fig.5 and Fig.6 demonstrate 1950 V IEC impulse and two real transient voltages generated by CG discharges selected for the analysis. The IEC impulses and real transient voltages were selected in such a way that their pairwise peak-to-peak voltages are similar, and analysis restricted up to 50% impulse decay time to ease comparisons.

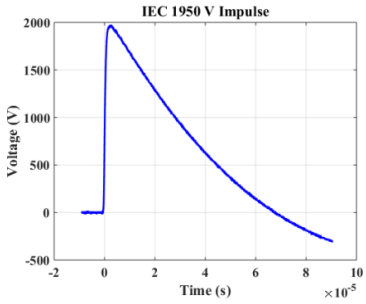

Fig. 4. 1950 V IEC impulse at zero phase angle

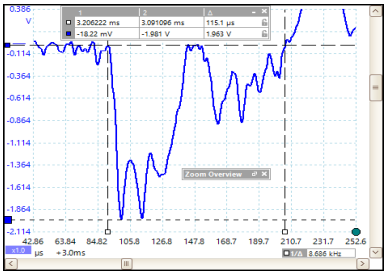

Fig. 5. 1963 V real transient voltage generated by CG discharge at zero phaser angle

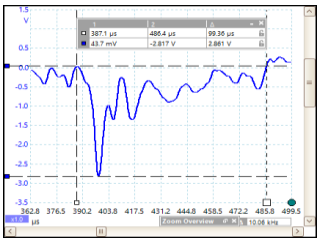

Fig. 6. 2861 V real transient voltage generated by CG discharge at zero phaser angle

Table II illustrates peak-to-peak voltage and respective pulse spans up to 50% decay.

TABLE II. SELECTED IMPULSES

Attribute	IEC 2800 V	IEC 1950 V	CG 2861 V	CG 1963 V
Pulse Span (µs) up to 50% decay	29.67	28.39	17.62	50.01
Total Pulse Duration (µs)	68.87	68.05	70.59	110.11
Peak-Peak Voltage (V)	2827	1971	2861	1963

The selected voltage signatures were exported into the MATLAB software package to perform simulations. The varistor module was simulated against the above IEC impulses and real transient voltages to predict the behavior of commercially available varistor under transient conditions. The energy absorbed by the varistor unit is calculated by integrating the product of current through the varistor unit and clamping voltage over the time span of current impulse (see Fig.8, Fig.10 and Fig.12). If the current impulse period is longer than 50% decay time, then integration was restricted up to 50% decay time.

In order to simulate the worst-case scenario, IEC impulses were placed at + π/2 phaser angle as they have positive polarity, conversely real transient voltages were positioned at -π/2 phaser angle, owing to have prominent negative polarities.

III. RESULTS AND DISCUSSION

A. Analysis of 1950 V and 2800 V IEC impulse voltages

Once superimposed on +π/2 phase angle, IEC impulses were artificially elevated by +325 V. Figure 7 illustrates the applied 1950 V IEC impulse (in red), the voltage across the Varistor (i.e., the clamping voltage in black) and varistor current (in blue). Figure 8 demonstrates the product of varistor current and clamping voltage against the time. In this analysis, the amount of energy absorbed by the varistor was considered for two situations; First, the entire impulse was deemed to be followed by recalculated energy absorbed by the varistor up to 50% decay time of the impulse.

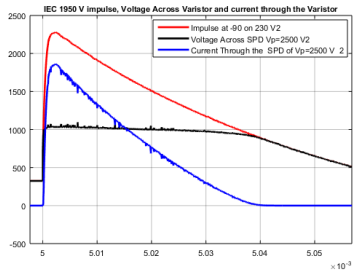

Fig. 7. 1950 V impulse at +π/2 (Red), clamping voltage (Black), and current through the Varistor (Blue)

It was noted that when IEC impulse decays up to 50% of the amplitude, it can incident almost 90% of the total energy embedded in the impulse.

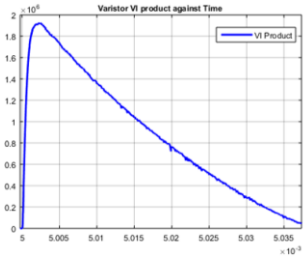

Fig. 8. The product of Varistor current and clamping voltage vs. Time graph of IEC 1950 V impulse

Similar procedure helped to obtain the varistor performance against the 2800 V IEC impulse, and Table III depicts the summary of the analysis.

TABLE III. SUMMARY OF IEC IMPULSE ANALYSIS

Impulse Pk-Pk (V)	Pk-Pk at π/2 Phaser Angle	Energy of total impulse (J)	Energy of 50 % impulse decay (J)	% Energy up to 50%
1950	2290	32.89	30.12	91.58
2800	3150	66.11	59.42	89.88

B. *Analysis of 1963 V real transient voltage*

Since selected real transient voltages have perfect negative attributes, their negative attributes would further increase if they incident on a negative half cycle of the 230 V, 50 Hz utility signal.

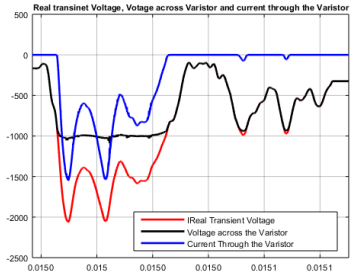

Fig. 9. 1963 V impulse at -π/2 (Red), clamping voltage (Black), and current through the Varistor (Blue)

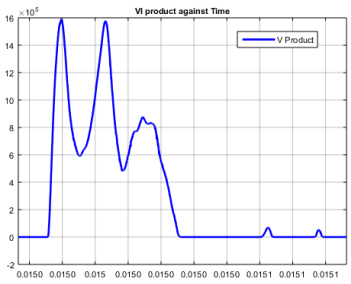

Fig. 10. The product of varistor current and clamping voltage vs. Time graph of 1963 V real transient voltage

Further, it may reach its highest potential if it superimposes on –π/2 phaser angle. Thus, in this analysis, both real transient voltages were pitched at - π/2 phaser angle to estimate their worst influence on the varistor. Table IV summarizes outcome of 1963 V real transient voltage.

TABLE IV. SUMMARY OF 1963 V REAL TRANSIENT VOLTAGE ANALYSIS

Impulse Pk-Pk (V)	Pk-Pk at π/2 Phaser Angle (V)	Energy of total impulse (J)	Energy of 50 % impulse decay (J)	% Energy up to 50%	Varistor Current (A)
1963	2063	32.18	32.13	99.84	1549
					1535
					874
					73.41
					57.10

C. *Analysis of 2861 V (peak-to-peak) real transient voltage*

A similar procedure was adopted to analyze the second transient voltage and outcome summarized in Table V.

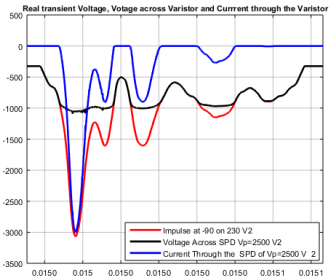

Fig. 11. 2861 V impulse at -π/2 (Red), clamping voltage (Black), and current through the Varistor (Blue)

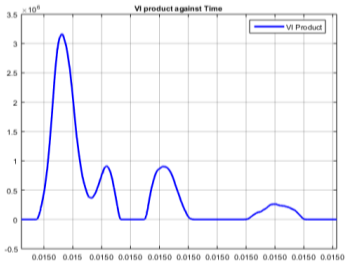

Fig. 12. The product of varistor current and clamping voltage vs. Time graph of 2861 V real transient voltage

TABLE V. SUMMARY OF 2861 V REAL TRANSIENT VOLTAGE ANALYSIS

Impulse Pk-Pk (V)	Pk-Pk at π/2 Phaser Angle (V)	The energy of total impulse (J)	Energy of 50 % impulse decay (J)	% Energy up to 50%	Varistor Current (A)
2861	3070	17.45	16.77	96.10	3002
					906
					889
					270.20
					6.16

Table VI comprises salient parameters of both IEC and real transient voltages

TABLE VI. SUMMARY OF BOTH IEC AND REAL TRANSIENT VOLTAGE ANALYSIS

Pk-Pk (V)	Pk-Pk at π/2 Phaser Angle (V)	Energy of total impulse (J)	Energy of 50 % impulse decay (J)	% Energy up to 50%	Varistor Current (A)	Pulse duration (µs)
1950	2290	32.89	30.12	91.58	1861	35.51
2800	3150	66.11	59.42	89.88	3120	45.33
1963	2063	32.18	32.13	99.84	1549	10.41
					1535	12.76
					874	20.24
					73.41	7.91
					57.10	4.30
2861	3070	17.45	16.77	96.10	3002	10.82
					906	5.34
					889	10.40
					270.20	16.51
					6.16	9.40

Various manufacturers produce range of varistors for diverse applications. In this study, the authors considered a varistor family having clamping voltages more than 1000 V as the focal point of this study with class 2 type electronics and their inbuilt surge immunity. The authors used the name 'type A" to denote the selected varistor family instead of their real product series, and referred to Littelfuse Inc, 2017 product catalog for this study.

As per the product catalogue, type A series of varistors have a range of clamping voltages starting from 340 V to 1650 V. Table VII illustrates salient parameters of varistors, which have a clamping voltage of 1025 V, as the first varistor in the series that could be employed to impart inbuilt surge immunity for class 2 electronic devices.

TABLE VII. PARAMETERS OF THE SELECTED VARISTORS

Varistor series: Type A					
Nominal Dia (mm)	RMS Voltage (V)	Max Energy, W_{TM}, (J)	Peak current, I_{TM}, (A)		Clamping voltage, V_C, (V)
			I_{TM} x 1	I_{TM} 2	
7	385	36	1750	1200	1025
10	385	75	3500	2500	1025
14	385	150	6000	4500	1025
20	385	300	10000	6500	1025

D. Varistor capability analysis against 1950 V IEC impulse and 1963 V real transient voltage

According to the outcome of Table VI, when a varistor suppresses 1950 V IEC and 1963 V real transient voltage at 1000 V, it is compelled to absorb nearly 30.12 J and 32.13 J of energy respectively (up to 50% decay). Further, varistor had to channel significantly large inrush currents through it under each case. However, time domain current profiles of IEC impulse and real transient voltages vastly differ from each other. Current through the varistor due to IEC impulse follows its voltage profile; hence, it only has a single peak.

Nevertheless, as per Fig 9, varistor current due to real transient voltage consists of few comparable peaks. The first current impulse had a magnitude of 1549 A and a pulse duration of 10.41 µs. Further, the second inrush current impulse immediately began where the first one stopped. It possessed the magnitude of 1535 A and sustained for the period of 12.76 µs. In addition to the first and second current impulses, the third impulse continued where the second impulse diminished. The third impulse had a magnitude of 874 A and continued over 20.24 µs. In addition to the above composite current impulse, another two lower magnitude isolated current impulses with 73 A and 57 A passed through the varistor.

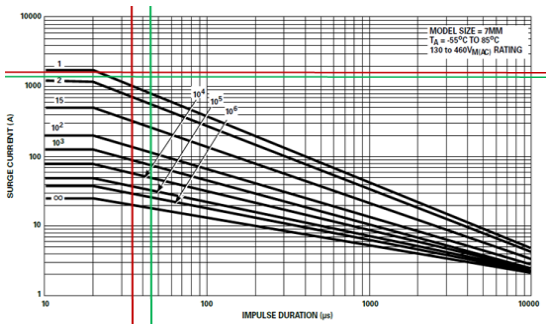

Fig. 13. Impulse duration plot of Varistor 7 mm Varistors

According to the manufacturer's data sheet, 7 mm diameter varistor has a maximum energy rating of 36 W. Table VI revealed that at both IEC 1950 V and 1963 V transient voltages, the incident energy on varistor was almost equal to its maximum energy handling capacity. According to Fig.13, 7 mm varistor's peak current capacity was limited to 1750 A, but against repetitive impulses, it tended to reduce until 1200 A. Further, if, assumed that the above three current impulses (see Fig. 9) formed a composite current impulse, then they acted as a single impulse with a much larger pulse duration of 43.41 µs.

According to characteristic curves in the impulse duration plot, when it increased, same magnitude of varistor deterioration could happen against a small current impulse. For example, the above impulse (composite one) has an impulse duration of 43.41 µs and peak varistor current of 1549 A. According to the characteristic curves of 7 mm varistor, if exposed to 800 A peak impulse current over 43.41 µs duration, it could produce the same damage that would impose by the 1750 A peak current with impulse duration around 10 - 20 µs. Hence, if a 7 mm varistor is used from type A series to contain the voltage across class 2 electronic device at 1000 V, 1950 IEC impulse and 1963 V real transient voltage would trigger nearly 1860 A and 1550 A inrush currents through the varistor respectively. However, as per Fig.13, both Brown (IEC impulse) and Green (real transient voltage of 1950 V) lines intersect beyond the characteristic curves of 7 mm varistors. Therefore, 7 mm varistors cannot be employed to contain 1950 V IEC impulse and 1963 V real transient voltage.

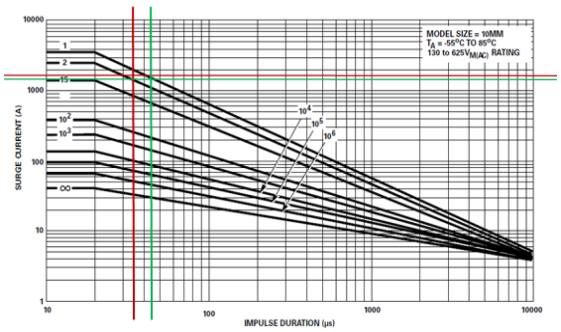

Fig. 14. Impulse duration plot of Varistor 10 mm Varistors

If the characteristic curves of type A series of 10 mm varistors are considered, then 1950 V IEC impulse intersection point falls between 1st hit and 2nd hit characteristic curves (compare impulse rating plot and Table V).

However, 1963 V real transient's intersection point almost falls on the 1st hit characteristic curve to indicate that if 10 mm varistor is exposed to 1963 V, that varistor will perish by the first hit. consequently, a real induced voltage almost falls on the 3500 A characteristic curve to indicate that 1550 A impulse with 43.41 µs pulse span has the same effect of 3500 A impulse with 20 µs or less impulse span. Hence, this selection does not have safer margins (see Brown lines on Fig.14). Therefore, if it is required to provide 1000 V self-surge immunity for class 2 electronics, it is necessary to consider varistors with higher ratings. The next commercially available option is 14 mm varistor and Fig.15 illustrates characteristics curves of the same.

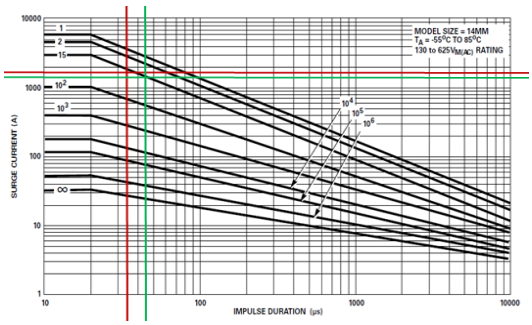

Fig. 15. Impulse duration plot of Varistor 14 mm Varistors

The Brown lines intersect each other just below the 15 hits curve, and Green lines intersect almost on the 15 hit curve. This observation indicates that if 14 mm varistor is employed to suppress 1950 IEC impulse, it may last more than 15 similar hits and may survive for about 15 hits if exposed to 1963 V transient voltage. Therefore, 14 mm varistors could be employed to provide 1000 V self-surge immunity for class 2 electronics. However, it shall be noticed that their service life would be limited to 15 hits if exposed to similar transient voltages.

Under real lightning conditions, multiple transient voltages are frequent, and in most of the time there could be five to six transient voltages with considerably large magnitudes [8], [21] and [9]. Therefore, 14 mm varistors may not have a sufficient buffer or safer margin over transient voltage in the order of 2000 V. Moreover, if impulse duration found to be even marginally larger than present values, the safer margin would further reduce until two hits

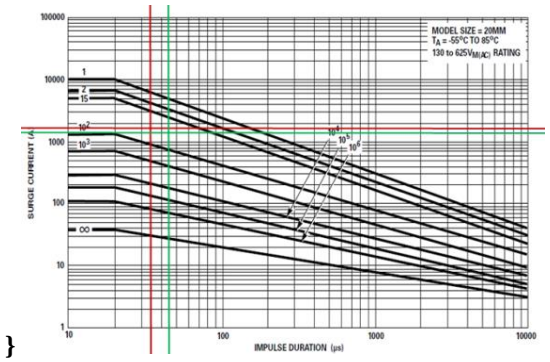

}

Fig. 16. Impulse duration plot of Varistor 20 mm Varistors

Considering the 20mm varistors, Both IEC and real transient impulse fall in between 15 hits and 100 hits. Thus, 20 mm varistor is having much safer buffer than 14 mm varistors.

E. Varistor capability analysis against 2800 V IEC impulse and 2861 V real transient voltages

According to Table VI, if a varistor employed to clamp the voltage across class 2 electronic device at 1000 V against the 2800 V IEC impulse and 2861 V real transient voltage, the varistor would have to absorb nearly 59.42 J and 16.77 J of energy respectively. Moreover, under the said circumstances, varistor had diverted considerably large inrush currents in the order of 3000 A in 45.33 µs and 10.82 µs respectively. Furthermore, as far as real transient voltage is concerned, it may generate a second inrush current immediately after the first one with a magnitude of 906 A for the duration of 5.34 µs (see Fig.11). Moreover, after the said composite current impulse, another two isolated current impulses passed through the varistor respectively. The first one has peak current of 890 A for the duration of 10.40 µs and second one has peak current of 270 A for 16.51 µs.

Since both IEC and real transient current impulses have more than 10 µs impulse durations and high current in the order of 3000 A, a 7 mm varistor is not an option to consider as its maximum peak impulse current confined to 1750 A (see Fig.17).

Next commercially available disk size is 10mm. Fig.18 illustrates 10 mm varistor characteristics curves. Even though real transient voltage falls between a single hit and double hit range, IEC impulse falls beyond the 10 mm varistor maximum limit. When comparison is made between the composite current impulse with the magnitude of 3002 A and 16.16 µs pulse span, it may further approximate to a single hit curve.

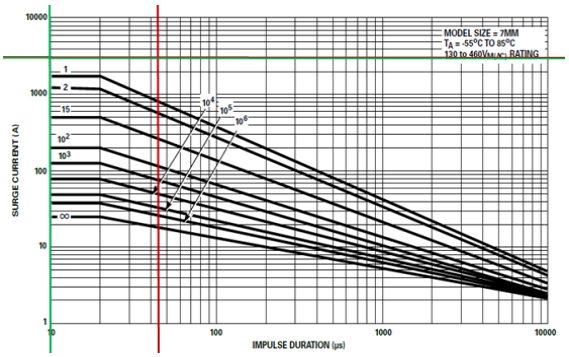

Fig. 17. Impulse duration plot of Varistor 7 mm Varistors

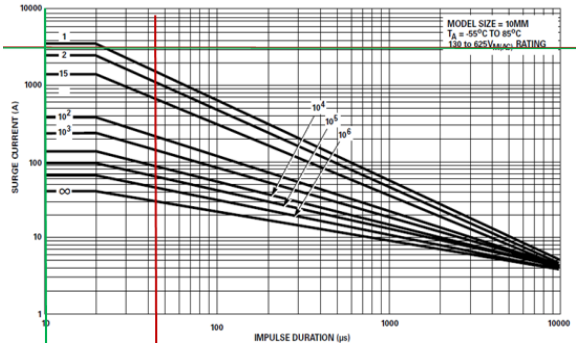

Fig. 18. Impulse duration plot of Varistor 10 mm Varistors

Therefore, type A series of varistors with diameter 10 mm would not have the capacity to address the transient voltages with the magnitude of 2800 V or above. Even a marginal change in impulse duration or varistor current

towards the high side, 10 mm varistor would not be able to sustain its safer margin. Hence, if required to provide 1000 V self-surge immunity for class 2 electronics, a 10 mm disk size varistors would not be an option for the above said transient voltages or transient voltages in the same order or above.

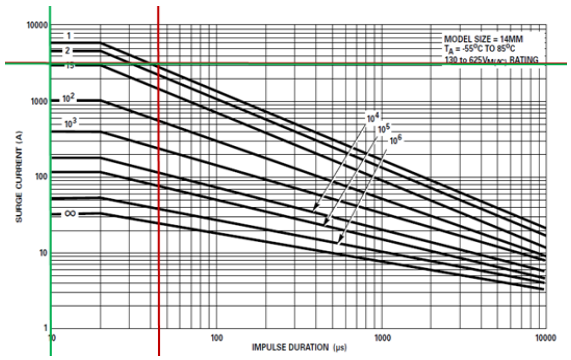

Fig. 19. Impulse duration plot of Varistor 14 mm Varistors

Next available option is 14 mm varistors. As per Fig.19, still, the IEC impulse falls beyond the maximum limits of the varistor. However, the real transient voltage falls on 15 hits characteristic curve to indicate that varistor can accommodate within very thin corridor of safer limits. Furthermore, if impulse duration is found to be marginaly larger to the current value, the safer margin would further decline and may pivot closer to double hit curve.

A 20 mm varistor is the last available option to consider in type A family. According to Fig.20, real transient voltage fall in-between 15 hits curve and 100 hits curves. Thus, 20 mm varistor has a much safer buffer for real transient voltages in the order of 2800 V than 14 mm varistors. However, still, IEC impulse literaly falls on the double hit curve. As per equation (1), varistor current is directly proportional to the power of α (typically 10-50), and hence, if the value of $I_0 * \left(\frac{v}{V_0}\right)$ is < 1 (i.e., $v < V_0$), then the varistor current could be minimal. On the other hand, if $v > V_0$, then the varistor current can become substantially high. Thus, selecting a varistor with lower clamping voltage may be negatively impact on exposure to a comparably higher peak-to-peak voltage. Hence, it is advantages to select a varistor with a higher clamping voltage.

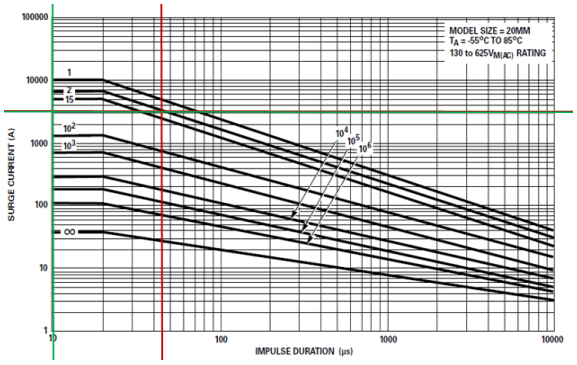

Fig. 20. Impulse duration plot of Varistor 20 mm Varistors

IV. Conclusion

The study disclosed that the MATLAB-based varistor model performs almost identical manner to commercially available varistors. Hence, the MATLAB-based varistor model could be simulated to predict the behavior of actual varistors under the influence of real transient over-voltages. The real transient voltages were noted to produce multiple inrush currents from a single voltage impulse if it possesses awkward time domain voltage profiles (e.g., 1963 V voltage impulse).

The investigation further unveiled that the peak-to-peak voltage and other physical attributes such as impulse width and the time domain voltage profile would decide the fate of varistor.

The inrush current generated by real transient voltages may also act as a composite current impulse with considerably large impulse span to degenerate varistors. According to the impulse rating characteristics curves of different varistor families, varistor withstanding capacities dramatically vary with the magnitude of the surge current and impulse span, hence all varistors cannot be employed or would qualify for some specific design even though their basic parameters seems beyond the stipulated specifications. Accordingly, when selecting varistors to provide self-surge immunity for class 2 electronics, particular attention must be paid to choose varistor with a marginally larger size. Further, regional lightning statistics would assist in selection of varistors to provide optimum protection and assuring minimal cost.

Acknowledgment

Authors acknowledge the use of services and facilities of the Department of Physics, University of Colombo. The contribution of Hiran De Silva and D. Prematilake in manuscript correction is highly appreciated.

References

[1] Panicali, A.R., Folho, J.P., Barbosa, F.C., Silva, J.C.O., Alves, N.V.B., "Protection of Electronic Equipment Inside Buildings." in *33rd International conference in Lightning proetction.*, Portugal, 2016.

[2] OVR Practical guide for the protection against surges, March 2014, ABB France-Low Voltage Products Division, www.abb.com/lowvoltage.

[3] McGranaghan, M. (2001) https://www.scribd.com/document/345119248/Power-Quality-Standards.

[4] Clark, O.M., Gavender, R.E., "Lightning protection for microprocessor-based electronic systems," *IEEE Trans.Ind.Appl.*, vol. 26, no. 5, pp. 947-953, 1990.

[5] Seymour, J., Horsley, T., "The seven types of power problems," Schneider Electric., White paper June 2005.

[6] Rojin, R.K., "A review of power quality problems and solutions in electrical power systems," *International Journal of advanced research in electrical, electronics, and instrumentation engineering*, Vol. 2, Issue 11, November 2013.

[7] Brian, M., Daniel, U., Laurel, P., Kelsey, S., "Flash Back: a Review of Lightning-Related Damage and Disruption Literature," *Environment Canada*, no. 604, pp. 1-28, 2009.

[8] Silfverskiöld, S., Thottappillil, R., Ye, M., Cooray, V., Scuka, V., "Induced voltages in a low voltage power installation network due to lightning electromagnetic fields," *EEE Trans.Electromagn.Compat.*, vol. 41, no. 3, pp. 265-271, August 1999.

[9] Sapumanage, N., Nanayakkara, N., Abegunawardana, S., Fernando, M., Hettiarachchi, P., Cooray,V., "Simulation of the surge performance of the external lightning protection system," in *2018 34th International Conference on Lightning Protection (ICLP)*, Rzeszow, Poland, Poland, 2018, p. 8.

[10] Kern, A., Dikta, G., Flisowski, Z., Marzinotto, M., Mazzetti, C., "Probability and frequency of damage of electrical and

electronic systems due to indirect lightning flashes.," in *Power Tech.*, Lausanne Switzerland., 2007.

[11] Gururaj, P., Kandasamy, C., "Indirect effects of lightning discharges," *Serbian Journal of Electrical Engineering*, vol. 8, no. 3, pp. 245-262, 2011.

[12] Sapumanage, N., Nanayakkara, N., Abegunawardana, S, Fernando, M., Cooray, V., "Time-Frequency and Energy Correlations of the Transient Voltages Triggered by Cloud to Cloud Discharges," *IEEE Transactions on Electromagnetic Compatibility (Early Access)*, p. 11, September 2018.

[13] Brashear, K., "Lightning and surge protection of Modern Electronic systems," ILD Technologies, LLC., San Antonio, TX, Online 2007.

[14] Andy, E. (2017, April) 2017 Europe EMC guide review of IEC 60601-1-2: 2014. [Onlinehttps://interferencetechnology.com/wp-content/uploads/2017/04/EEG_2017_Digital_Final_Low-Res.pdf

[15] Transients and lightning protection system., 2015, TBS Catalogue 2015, www.obo-bettermann.com.

[16] "Product catalog and design guide," Littlelfuse.Inc, 2017.

[17] "The 8 kA MOV characteristic curves for different let-through currents," Eaton Corporation, March 16, 2009.

[18] Kern, A., Dikta, G., "Probability of damage of electrical and electronic systems due to indirect lightning flashes-Investigation data from German insurance companies," in *ICLP*, Uppsala Sweden., 2008, p. 14.

[19] Kulkarni, K., Shetty, V. J., "Power quality issues in healthcare centre," *International Journal of current engineering and technology*, vol.4, no.3, June 2014.

[20] (2015) Simulink User's Guide. [Online]. https://fenix.tecnico.ulisboa.pt/downloadFile/845043405443232/sl_using_r2015a.pdf

[21] Nanayakkara, S., Mendis, U., Fernando, M., Abegunawardana, S., Liyanage. P., Cooray, V., "Lightning-induced voltages in overhead power lines due to Cloud to Ground Flashes in Sri Lanka," in *APL*, Nayoga, 2015.

[22] Nanayakkara, S., Mendis, U., Fernando, M., Abegunawardana, S., Liyanage, P., Cooray, V., "Voltages induced by Cloud flashes on rural utility electrical power lines in Sri Lanka," in *APL*, Nayoga, 2015.

Probabilistic assessment on efficiency of a selected SPD array

Nilantha Sapumanage
Department of Physics
University of Colombo
Colombo, Sri Lanka
nilanthasapu@yahoo.com

Sankha Nanayakkara
Department of Physics
University of Colombo
Colombo, Sri Lanka
sankha84@live.com

Sidath Abegunawardana
Department of Physics
University of Colombo
Colombo, Sri Lanka
sidathjayalal@yahoo.com

Mahendra Fernando
Department of Physics
University of Colombo
Colombo, Sri Lanka
mahendra.fernando@gmail.com

Vernon Cooray
Department of Engineering Science
Uppsala University
Uppsala, Sweden
vernon.cooray@angstrom.uu.se

***Abstract*—This study is intended to investigate how the pitching phaser angle and the time domain voltage profile affect the efficiency of surge protective devices (SPDs). In order to analyze above, 403 transient voltages were selected with different physical features with peak-to-peak voltages, ranging from 175 V up to 2861 V. The sample is comprised with induced voltages from 218 cloud-to-cloud, and 185 clouds-to-ground with mean and median peak voltages of 676.80 V and 551.00 V respectively. Impulses have segregated into three subclasses based on their physical attributes and assessed the tendency of drifting through the protection array once they are placed at the +π/2, zero, and - π/2 phaser angles. The study outcome revealed that 100% of positive impulses in the sample that could drift through the selected array once it is pitched at any phaser angle on 230 V, 50 Hz utility signal. It was observed during the analysis that out of the negative pulses, 90.35% at + π/2, 74.39% at zero, and 42.21% at - π/2 phaser angles that could freely move through the array.**

Keywords—CC, CG, bipolar, SPD, protection array, phaser angle, transient voltage, impulse, energy, probability

I. INTRODUCTION

In the light of modern-day technology, the ICT systems are inherited with some susceptibilities towards power quality issues [1], [2], and [3]. Nevertheless, modern electronic and microprocessor-based systems are predominantly presumed that they would be served with quality power [4], [5] and [6]. However, in reality, many intrinsic and extrinsic sources, initiate power quality issues [7], [8], and [2]. Momentary voltage fluctuations are in the order of several kilovolts on the supply voltage which could easily incident substantially large energies to initiate thermal agitations at the component level to perish them immediately or in the next few subsequent similar events [9], and [10].

Lightning is identified as one of the most recurrent extrinsic events which has inherent potential to generate power quality issues. Mitigation of harmful effects of lightning become difficult due to its random presence, magnitudes, frequency, and locations etc., that are beyond human control [5], [11], [12], [13], and [7].

According to Kern *et al*., and Brain *et al*., several millions worth of equipment damages and hours-long system downtimes are reported annually due to lightning-induced transient voltages [14], and [15]. Protective devices such as surge protective devices (SPDs), which are employed to seek the intended protection from the transient voltages [6] and [2]. SPDs are manufactured under contemporary technologies that have good reputations to work under the said cumbersome circumstances to absorb and dissipate harmful energy [17], and [18]. Henceforth, it is very remote to conclude that inferior quality and loopholes associated with SPD technology as root causes for sensitive system failure.

However, some investigations that are carried out to determine root causes of system failures, have been established that penetration of surges through the protection schemes caused component level damages to trigger sensitive system failure, although the protection schemes are healthy or undamaged at time of investigation[19]. Thus, it is vital to understand why sometimes the SPD's fall short in providing the intended protection [5].

According to Brashear, microprocessors are subjected to weaken and may lead to permanent damage from electrical energy, that as little as one microjoule, and the integrated circuits can run into partial or total failure from energy as small as 10 μJ [9]. Therefore, it is crucial to suppress small but frequent transient impulses. Conversely, if an SPD array designed with more focus to suppress small transient voltages under the presence of a sizable transient voltage, the protection array may, subject to heavy stress and drive to premature failure [20], and [21].

II. MATERIAL AND METHODS

Lightning generated transient voltages are highly random and one impulse cannot be compared with another in terms of pulse time, time domain voltage profile, polarity, and energy content [7], [22], and [23]. The intention of the study is to analyze the transient voltages to identify how their physical attributes that influence the efficiency of protection array, upon such impulses are superimposed on different phaser angles on 230 V, 50 Hz utility systems. Four-hundred-and-three transient voltages are selected for the analysis that starts from the lowest peak-to-peak voltage of

175 V. Primarily the recorded impulses were segregated under the lightning discharge types CC and CG. Consequently, 218 CC generated impulses, and 185 CG generated impulses have identified. Furthermore, transient voltages were differentiated into three subclasses to ease the analysis by considering their physical attributes, and named them as Positive, Negative, and Bipolar. However, it shall be noticed that, above mentioned signature types differ from the polarity of discharge. Classification was done to emphasis the significance of physical attributes, when such impulses are superimposing on different phaser angles from zero to 2π on the 230 V, power frequency signal.

The following rule was employed to segregate impulses into different signature types. For illustration purposes, a transient impulse with a peak-to-peak voltage of 100 V was assumed [13].

TABLE I. RULE USED TO CLASSIFY IMPULSES

Peak to peak Voltage (V)	Positive portion	Negative portion	Pulse type
100	90 < V Positive	V Negative <10	Positive
100	V Positive <90	V Negative >10	Bipolar
100	V Positive > 10	V Negative< 90	Bipolar
100	V Positive <10	V Negative >90	Negative

Furthermore, it was presumed that considered low voltage power installation (LVPI) equipped with a coordinated protection array comprising three SPDs at the primary, secondary, and equipment level with following configurations.

1. The first SPD with protection voltage 2500 V was placed at the main distribution board (MDB).

2. The second SPD with protection voltage 1300 V was placed on the sub-distribution board (SDB).

3. The third SPD was placed just before the sensitive system with a protection voltage of 900 V.

Induced voltages, which are used for this analysis generated by the CC and CG discharges during the first inter-monsoon period (April to May) of the year 2014. The measurements were made at the interface between LVPI, and the utility service wire of an isolated dwelling unit. The dwelling unit internal wiring has configured to the terra-terra (TT) topology and energized by a 230 V, 50 Hz single phase utility supply. Throughout the data acquisition period, all the electrically driven accessories and appliances were isolated from the LVPI. Surge protection devices (SPDs) are not connected to the LVPI and the internal wiring of the dwelling unit that was fed through an overhead bare utility service wire. The utility owned step down transformer (33 kV: 400 V) was located approximately 800 m away from the selected LVPI [16], and [17].

The wave shape of the induced voltage signatures at the interface of LVPI may have different shapes owing to various factors [7]. Following three different transient voltages were selected to discuss different attributes. Two of them were used for further analysis to demonstrate their salient differentiations and to indicate the way how such characteristics regarding their relative positions and time domain voltage profile could contribute different degrees of influences on the sensitive systems.

The methodology illustrated in Table I differentiates the surges into three different classes, and Table II presents the details.

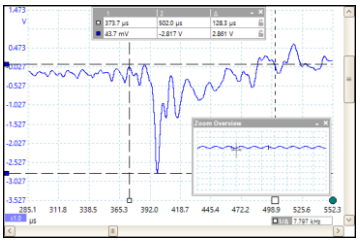

Fig. 1. CG induced voltage with a peak to peak voltage 2861 V

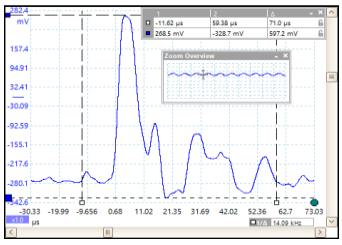

Fig. 2. CC induced voltage with a peak to peak voltage 597.2 V

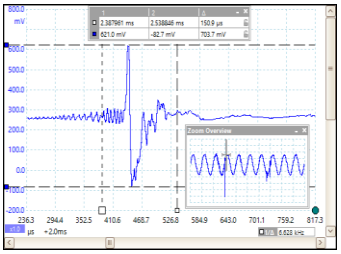

Fig. 3. CG induced voltage with a peak to peak voltage 703.7 V

TABLE II. DISCHARGE TYPE AND POLARITY TYPE OF THE SELECTED IMPULSES

Type	Pk-Pk Voltage (V)	Positive Portion (V)	Negative Portion (V)	Signature type
CG	2861	222.6(7.78%)	2638.4(92.22%)	Negative
CG	703.7	349.9(49.73%)	353.8(50.27%)	Bipolar
CC	597.2	544.5 (91.18 %)	52.7 (8.82 %)	Positive

III. RESULTS AND DISCUSSION

The statistical analysis revealed that the sample minimum and maximum as 175.00 V and 2861.00 V respectively. Furthermore, it was also found that sample mean pivoted at 676.80 V.

A. Analysis of positive impulses

There were 20 impulses with positive polarity, and two of them were generated by CG discharges while the CC discharges induced the balance 18. The sample mean, maximum, and minimum were 345.10 V, 598.00 V, and 176.00 V respectively.

1) Positive pulse incident at + π/2 phaser angle

Once superimposed on the + π/2 phaser angle on the 230 V, 50 Hz system, all impulses artificially elevated their relative positions by +325 V reference to the ground voltage.

This is the highest possible gain for any positive impulse. Hence, chances to reach cutoff voltage of the SPD array would increase when positive impulses are superimpose between - π/2 to + π/2 through zero phaser angle and conversely, same would decline if superimpose between + π/2 to - π/2 through zero phaser angle.

According to the statistical analysis, neither positive portions nor negative portions of positive impulses would elevate beyond at least a single protection level of the selected SPD array. Therefore, to suppress positive type surges in the sample, it needs to employ SPDs with lower protection voltages. According to the literature, not only highly elevated impulses, but also many small impulses can impart detrimental consequences to sensitive systems [19], and [24]. Brusher, discusses that swarms of small impulses can produce incident harmful energy to initiate component level deformations in sensitive systems [9]. Thus, the study outcome validates the observation that the selected SPD array is not capable of encountering transient voltages with positive polarities up to about 575 V, 900 V, and 1225 V, if the incident at + π/2, zero, and - π/2 phaser angles respectively. However, nature has no pure positive polarity surges as they are always accompanied by very small (usually <10 % of peak-to peak-value) negative portion under practical conditions. Thus, practically surges with 640 V, 1000 V, and 1361 V may drift into the LVPI, bypassing the protection array if superimpose on above said phaser angles .

B. Analysis of negative impulses

The sample with negative attributes had 175 impulses, and 56 of them were generated by the CC flashers, and the balance 119 was induced due to CG discharges. The negative impulse minimum, mean, and maximum equated as 190.00 V, 805.00 V, and 2861.00 V.

1) Negative pulse analysis at + π/2 phaser angle

According to the Statistical analysis, none of the positive portion peaks would elevate beyond at least 900 V protection level. However, 22 negative impulses can breach at least one protection level of the SPD array. The minimum and maximum peak-to-peak voltages that would breach at least one or more protection voltages were found as 1461 V and 2861 V respectively. Thus, all other impulses with slightly lesser peak-to-peak voltages may infiltrate through the protection array. Accordingly, 153 negative transient voltages in the sample could freely drift into the LVPI through the SPD array.

Even though the theoretical value of the negative portion that could penetrate through the selected SPD array was close to -1225 V, in actual conditions an impulse always accompanied with a small positive portion (> 10% of Peak-Peak value). Therefore, under the present SPD array, an impulse with peak-to-peak voltage 1361.11 V can drift through the SPD array. However, according to the considered negative pulses, the impulse with 1361 V peak-to-peak voltage is the highest in the sample that can escape through the selected SPD array.

The outcome of the analysis indicated that although some impulses in the sample can elevate beyond the 900 V and 1300 V protection stages, none could reach the level of 2500 V if pitched at + π/2 phaser angle. Moreover, according to statistics, only 9 surges are elevated beyond the 1300 V, and another 13 surges will be clamped only at the equipment level SPD. Hence, if negative impulses fall at the + π/2 phaser angle, 153 non-clipped impulses and the balance portion of the energy accompanied in 22 impulses which were clamped by the protection array can propagate into sensitive loads.

Fig. 4 demonstrates the outcome of the analysis in a more elaborated statistical viewpoint. Minitab statistical software application was used to identify the individual distribution pattern and derived statistical inference of the sample dataset which is belonged to the negative portion of the impulses. According to the goodness-of-fit test, the smallest extreme value distribution was determined as the closest distribution to represent the data set.

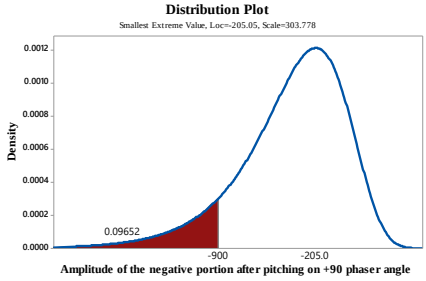

Fig. 4. Distribution plot of the data set to predict the probability of exceeding the 900 V protection by the negative type impulses

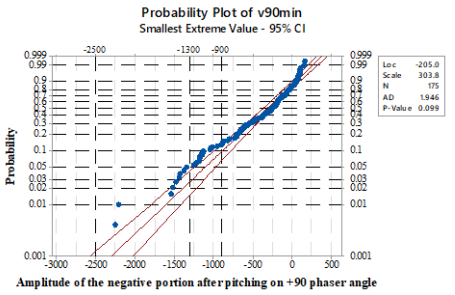

Fig. 5. Probability plot of the data set to predict the probability of exceeding the protection voltages of the SPD array

Fig.4 and Fig.5 reveal nearly 9.65% probability where negative impulses can exceed at least the minimum protection voltage of 900 V. Moreover, the outcome provides the evidence to show a 2.68% probability of negative impulses to exceed secondary SPD's protection voltage of 1300V. Conversely, the statistical findings imply that all negative impulses can reach up to secondary protection stage, 97.32% of them can reach up to equipment level, and 90.35% negative pulses can penetrate up to sensitive systems through the SPD array if superimposed on the + π/2 phaser angle.

2) Negative pulse analysis at a zero-phaser angle

As illustrated in Fig. 6, when negative impulses fall at a zero-phaser angle, the number of surges that can penetrate through the SPD array becomes larger in comparison with + π/2 phaser angle owing to the shift negatively by a 325 V. The selected sample has 49 impulses that could elevate beyond at least one protection stage of the SPD array. According to the statistical calculations, minimum, peak-to-peak voltages that would elevate beyond at least one or more protection voltages are reduced to 1028 V from 1461 V due to negative shift by 325 V with reference to the ground.

However, the balance 126 impulses can still penetrate through the selected protection array. Further, the said 126 impulses now have more energy compared to the + π/2 phaser angle due to the relative displacement with reference to the ground. Statistics revealed that the minimum peak-to-peak voltage that needs to elevate above the minimum protection level had reduced to 1028 V from 1416 V when the phaser angle changed from + π/2 to zero; this denotes an enhancement of protection level over the margin of 388 V. It can be observed that two impulses are clamped by the SPD at the MDB level, another 19 impulses at the SDB level and 28 more impulses are at the equipment level. Even though superimposing at the zero phaser angle compels more significant number of surges to undergo the surveillance of the SPD array; still, a majority would pass to LVPI through the protection array.

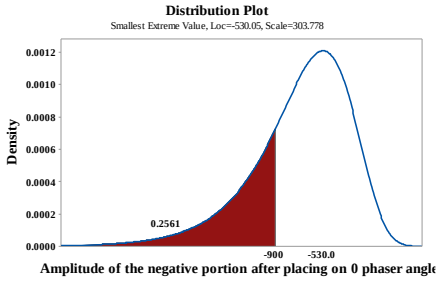

Fig. 6. Distribution plot of the data set to predict the probability of exceeding the 900 V protection by the negative type impulses

Smallest extreme value distribution identified as the perfectly fitting distribution to govern the characteristics of the negative impulses at a zero-phaser angle.

Fig.6 and Fig.7 provide evidences, if negative impulses superimposed on the zero-phaser angle of 230 V, 50 Hz system, it has nearly 25.61% probability to exceed at least the minimum protection stage (900 V) at 95% confidence level. Moreover, it reveals 7.62% and 0.15% probability that negative impulses could exceed secondary protection voltage of 1300V and primary protection voltage of 2500 V respectively. However, 99.85% of negative impulses still could reach up to the secondary protection stage, 92.38% of them which can reach up to the equipment level, and 74.39% negative pulses could infiltrate into sensitive systems through the assumed SPD array of an incident on a zero-phaser angle.

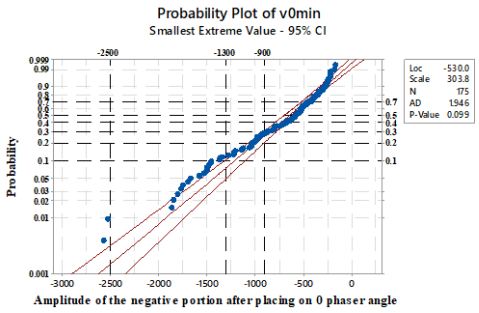

Fig. 7. Probability plot of the data set to predict the probability of exceeding the protection voltages of the SPD array

3) Negative pulse analysis at - π/2 phaser angle

This placement enables the negative impulses to further elevate their relative positions by another -325 V reference to the ground. The SPD array will clamp 88 impulses under the present scenario, and the minimum peak-to-peak voltage to clip by the array further reduced till 644 V. The statistics indicate two impulses at the MDB level, 40 at the SDB and a further 46 at the equipment level, would be clipped if they were placed at the - π/2 phaser angle. Accordingly, 87 impulses can drift through the protection array to reach the loads.

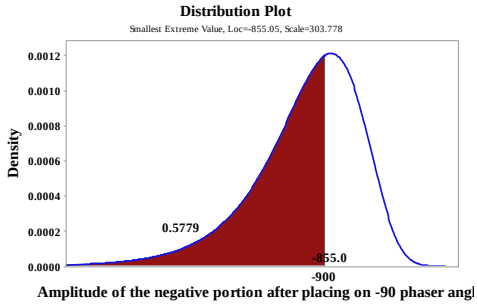

Fig. 8. Distribution plot of the data set to predict the probability of exceeding the 900 V protection by the negative type impulses

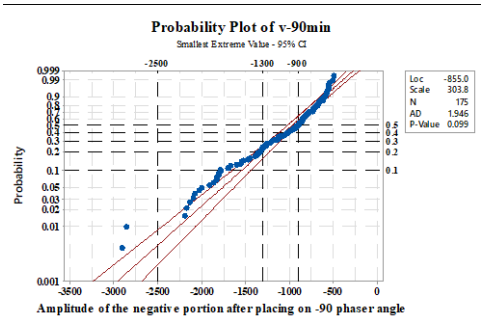

Fig. 9. Probability plot of the data set to predict the probability of exceeding the protection voltages of the SPD array

Therefore, an incident on the most negative extreme could reduce the number of negative impulses that can freely move into the LVPI. However, small negative impulses still have a fair chance to drift into the system through the protection array and at – π/2 phaser angle such small impulses may possess extra harmful energy as their energy capabilities elevate with positional change reference to the ground than zero and +. π/2 phaser angles.

Fig.8 and Fig.9 illustrate that when negative impulses superimpose on - π/2 phaser angle, it maximizes the chances of clamping negative impulses by the protection array.

There is a 57.79% probability for negative impulses to exceed at least the minimum protection voltage. Statistical inferences also elaborate the chances of surpassing the secondary protection voltage and the primary protection level by nearly 20.64% and 0.44% respectively. This observation qualifies previous evidences, to consolidate that impulses with negative attributes which will elevate the chances of subjecting to the surveillance of protection array when they superimpose on negative phaser angles and probabilities become maximum if the incident is on - π/2 phaser angle.

Hence, nearly 99.56% of negative impulses still could reach up to the secondary protection stage, 79.36% of them which can reach up to equipment level, and 42.21% negative pulses could infiltrate into sensitive systems through the selected SPD array if the incident on - π/2 phaser angle. Table III summarizes salient outcomes of the analysis.

TABLE III. SUMMARY OF THE NEGATIVE PULSES

Pulse Type	**Negative**					
Phaser angle	+ π/2		*0*		- π/2	
Polarity	+Ve	-Ve	+Ve	-Ve	+Ve	-Ve
Probability of Exceeding 900 V (%)	0	9.65	0	25,61	0	57.79
Probability of Exceeding 1300 V (%)	0	2.68	0	7.62	0	20.64
Probability of Exceeding 2500 V (%)	0	0	0	0.15	0	0.44

C. *Analysis of bipolar impulse*

There are 208 impulses with bipolar attributes, and 144 of them were generated by the CC flashers, and the balance 64 was induced due to CG discharges. The bipolar sample minimum value was 175.00 V, and minimum and maximum were 609.90 V and 2498.00 V respectively.

1) Bipolar pulse analysis at + π/2 phaser angle

Due to symmetric or near symmetric physical attributes, bipolar pulses may clip from its both peaks by the protection array. However, when the bipolar impulses in the sample incident on the + π/2 phaser angle, none of the impulses clips from both positive and negative portions simultaneously. Moreover, analysis of positive parts of the bipolar impulses revealed that only three impulses could elevate beyond the lowest protection voltage of the SPD array, and none of the positive portions reached the secondary level protection voltage. Statistical evidences indicate the smallest bipolar to penetrate SPD array from its positive portion particular impulse should have a minimum peak-to-peak voltage of 926 V.

TABLE IV. POSITIVE PORTIONS OF THE BIPOLAR IMPULSES CLIPPED BY THE SPD ARRAY ONCE SUPERIMPOSED AT + Π/2 PHASER ANGLE

At + π/2 positive polarity			
No.	**900 V**	**1300 V**	**2500 V**
1	926	**	**
2	1261	**	**
3	1463	**	**

Further, outcome of the study revealed that, the first bipolar impulse which clipped from its negative portion once incident on + π/2 phaser angle has peak- to-peak voltage of 1592 V. Three bipolar impulses in the sample can elevate beyond the secondary protection stage. Hence altogether 10 impulses would go under the surveillance of the protection array.

TABLE V. NEGATIVE PORTIONS OF THE BIPOLAR IMPULSES CLIPPED BY THE SPD ARRAY ONCE SUPERIMPOSED AT + Π/2 PHASER ANGLE

At + π/2 negative polarity			
No.	**900 V**	**1300 V**	**2500 V**
1	1592	2125	**
2	1852	2269	**
3	1886	2498	**
4	1889	**	**

Therefore, if 208 bipolar impulses superimposed on + π/2 phaser angle, 198 impulses can freely propagate along with utility signal up to the sensitive loads. The study further, discovered that none of the impulses had been subjected to the clipping at both polarities, and hence, a considerable amount of the energy contained in the non-clipped portions of the said 10 impulses would drift into the LPVI.

Fig. 10 depicts the graphical illustration of the probabilities that the positive portions would exceed the protection level of the SPD array. According to the plot, 2.65% probability exceeds the 900 V level by the positive portions. Contrary wise the energy in all the other 97.35% of positive portions can freely propagate into the LVPI.

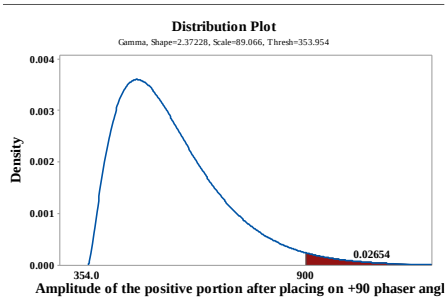

Fig. 10. Distribution plot of the data set to predict the probability of exceeding the 900 V protection by the positive portions of bipolar impulses

The outcome of the goodness-of-fit test (Fig. 11) revealed that negative portions of the bipolar impulses do not significantly follow any of the distribution patterns embedded in the Minitab software tool. Therefore, the EasyFit Software package was employed to analyze negative portions of the bipolar pulses. The outcome of the analysis reveals the dataset follows the Johnson SB Distribution.

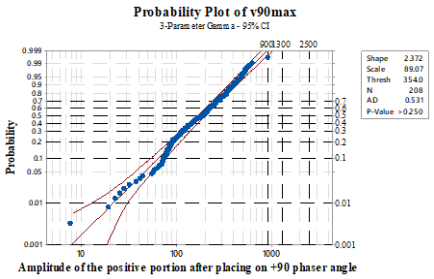

Fig. 11. Probability plot of the data set to predict the probability of exceeding the protection voltages of the SPD array by negative portions

According to the EasyFit Software tool, there is a 3.99% probability for negative portions to exceed 900 V protection voltage and 1.45% probability to elevate beyond the 1300 V protection voltage (Fig. 12). Hence, all negative portions would reach the secondary level SPDs, and nearly 98.55% of negative impulses would reach up to equipment level protection, and more than 96.01% of the negative portion would infiltrate into the sensitive systems connected to the LVPI.

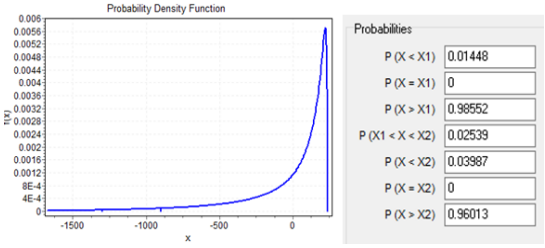

Fig. 12. Probability plot of the data set to predict the probability of exceeding the protection voltages of the SPD array

2) Bipolar pulse analysis at the zero-phaser angle

The bipolar impulses in the sample have prominent negative portions. Hence, once incident on the zero phaser angle, the relative positions of the impulses could further negatively increase analogous to the + π/2 phase angle and increase the chances of clipping by the SPD array. Conversely, this phenomenon would elevate the chances of positive portions to passage through the SPD array. The outcome of the statistical analysis evidences that only one impulse with a peak-to-peak voltage of 1463 V would clip from its positive portion at the equipment level and 16 impulses would clip from their negative portions. Further, out of these 16 impulses, ten would clip from the 900 V protection voltage at the equipment level, while another six impulses from 1300 V protection at the SDB level.

According to the statistical inferences generated by the EasyFit software package, which indicates that 0.14% of positive portion, would elevate beyond the 900 V protection voltage. Hence, if bipolar pulses superimposed on the zero-phaser angle harmful energy contained in 99.86% of positive portions would drift into the sensitive systems.

TABLE VI. NEGATIVE PORTIONS OF THE BIPOLAR IMPULSES CLIPPED BY THE SPD ARRAY ONCE SUPERIMPOSED AT ZERO PHASER ANGLE

At zero- negative polarity			
No.	**900 V**	**1300 V**	**2500 V**
1	1163	1852	**
2	1370	1886	**
3	1218	1889	**
4	1218	2125	**
5	1250	2269	**
6	1296	2498	**
7	1426	**	**
8	1476	**	**
9	1417	**	**
10	1592	**	**

With regard to the negative portions, the EasyFit outcome equates that the probabilities of clamping by equipment level SPD and SDB level SPD as 8.27% and 3.35% respectively. Further, nearly 96.65% of negative impulses would reach up to equipment level protection, and more than 91.73% of the negative portion would use incident harmful energy on loads connected into LVPI if bipolar impulses superimpose at the zero-phaser angle.

3) Bipolar pulse analysis at the –π/2 phaser angles

As per the statistical analysis, there are no positive portions would elevate beyond any of the protection levels, but 40 impulses have surpassed at least the minimum protection voltage of 900 V from their negative portions. The minimum peak-to-peak voltage to undergo the surveillance of the SPD array has reduced to 663 V. The statistical outcome further evidence that the SPD array would clip 27 impulses at the equipment level and 13 other impulses at the SDB level.

Table VII summarizes the number of impulses subjecting to clamping at different protection voltages.

TABLE VII. NEGATIVE PORTIONS OF THE BIPOLAR IMPULSES CLIPPED BY THE SPD ARRAY ONCE SUPERIMPOSED AT - Π/2 PHASER ANGLE

- π/2 **negative polarity**				
No.	**900 V**	**900 V**	**1300 V**	**2500 V**
1	663	944	1218	**
2	681	974	1250	**
3	682	1001	1296	**
4	718	1048	1417	**
5	722	1052	1426	**
6	750	1052	1476	**
7	756	1104	1592	**
8	801	1104	1852	**
9	811	1163	1886	**
10	811	1189	1889	**
11	879	1218	2125	**
12	898	1370	2269	**
13	931	1463	2498	**
14	935	**	**	**

These observations denote harmful energy contained in 168 bipolar impulses are still free to propagate into the LVPI. In addition, the energy contained in the positive portions of the 40 number of clamped impulses and whatever the remaining energy in the clipped negative polarity can be drifted into sensitive loads.

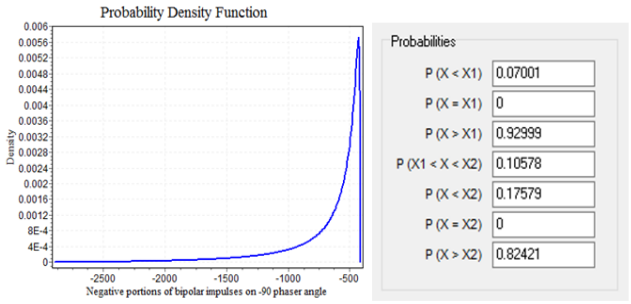

Fig. 13. Probability plot of the data set to predict the probability of exceeding the protection voltages of the SPD array

The probabilistic outcome generated by the EasyFit Analytical tool on negative portions of the bipolar impulses revealed that nearly 7.00% impulses would clamp by the SPD placed at the secondary stage and 17.58% of negative portions would suppress at the equipment level. Conversely the, above observations implies that harmful energy contained in all positive portions of bipolar impulses and nearly 82.42% of negative portions that would drift into the sensitive loads if bipolar impulses superimpose at - π/2 phaser angle.

Table VIII indicates that positive to negative ratios of 15:85, 20:80, and 40:60 are dominating the bipolar impulses with more negative attributes. Furthermore the, Table VIII also evidences that the impulse with a comparatively larger peak to peak voltages which also belong to this category. Alternatively, impulses with more positive attributes belong to the positive to negative ratios of 60:40 and 70:30.

TABLE VIII. DETAILED SEGREGATION OF BIPOLAR PULSES AND THEIR BASIC STATISTICS

Positive portion (%)	**Negative portion (%)**	**No. of pulses**	**Min (V)**	**Mean (V)**	**Max (V)**
10	90	1	663	**	663
15	85	24	224	968	2125
20	80	19	241	1013	2498

25	75	1	944	**	944
30	70	8	372	763	1370
35	65	2	208	**	1048
40	60	18	175	512.2	1189
45	55	10	468	811	1463
Total		**83**			
50	50	62	189	424.5	1139
Total		**62**			
55	45	11	252	570.2	1004
60	40	21	211	436.6	920
65	35	10	271	520.5	926
70	30	16	289	432.8	664
75	25	3	300	**	1261
80	20	1	644	**	644
85	15	1	535	**	535
Total		**63**			

Table IX presents the summary of probabilities that bipolar impulses in the sample would exceed the protection levels of the SPD array.

TABLE IX. SUMMARY OF THE BIPOLAR (NEGATIVE PORTION ONLY)

Pulse Type	**Bipolar**					
Phaser angle	$+\pi/2$		***0***		$-\pi/2$	
Polarity	+Ve	-Ve	+Ve	-Ve	+Ve	-Ve
Probability of Exceeding 900 V (%)	2.65	3.99	0.14	8.27	0/0	17.58
Probability of Exceeding 1300 V (%)	0	1.45	0	3.35	0/0	7.00
Probability of Exceeding 2500 V (%)	0	0	0	0	0/0	0

The energy incident capacity of a transient voltage is inherited by its time domain voltage profile and the pulse duration. However, the study proved that impulse's pitching phaser angle on the 230 V, 50 Hz utility signal could artificially further elevate or demote the relative position of the impulse reference to the ground voltage. Thus, both physical attributes and the phaser angle at which it superimposes on the utility signal will decide the ultimate energy capability of the transient voltage. For example, a 638.89 V negative or positive impulse may or may not be clamped by the selected SPD array, depending on the phaser angle at which it falls on the 230 V, 50 Hz system, but a virtually symmetric impulse with a peak-to-peak voltage of 1800 V can infiltrate through the same array if incident on zero phaser angle. If the impulses attributed with prominent positive polarities, their energy capabilities would maximize at $+\pi/2$ phaser angle and vice versa.

Contrarily, if a positive impulse is pitched at a more negative phaser angle, the entire impulse or the majority of the impulse may escape through the protection array to reach sensitive systems connected to the LVPI. Moreover, the study also emphasized that when an impulse artificially shifts its relative position (e.g., sizable negative impulse on $-\pi/2$ phaser angle), the chances of subjecting to the surveillance under SPD array also proportionally increase, but even after clamping at the protection array, impulse may infiltrate more energy than at any other lower phase angle. Although positive and negative impulses have shown tendency to go under the surveillance of protection array subjecting to the incident phaser angle, an impulse with virtually symmetric physical attributes can escape through the array if it falls closer to zero phaser angle. Since both phaser angles, and the physical attributes, are highly random, predictions are rather difficult, and mitigation options would work within some tolerances. Thus, both wave shape and the pitching phaser angle have considerable significance as both can impart different degrees of havocs to sensitive systems.

The considered protection array configured to have a three-level cascaded system, placing SPDs at MDB, SDB, and the equipment level. The individual protection voltages were selected as 2500 V, 1300 V, and 900 V respectively. However, the study indicates that SPD array does not have any control or autonomy to decide to clamp incoming impulses as the same impulse clipped differently depending on its point of the incident on the utility power signal. Thus, placing a single SPD may allow some impulses to escape through it, and some may be clipped by the SPD, subjecting to the pitching phaser angle and its physical attributes. Therefore, it is always highly advantageous to have an SPD array than a single SPD.

The study outcome proved that random SPD array would not address the intended protection to the satisfactory level. Therefore, the rationale shall be involved in designing the protection array. A mismatched or poorly coordinated array may bring adverse consequences to both protection system and the systems to be protected. The study further revealed that even though the selected sample has few impulse voltages with large amplitudes, the sample mean peak-to-peak voltage is pivoted at 676.80 V. Moreover, the selected SPD array allowed many impulses to infiltrate into the LVPI. Thus, it needs to re-design the SPD array if containing the swarm of small and moderate impulses are necessary.

Therefore, if possible, it would be ideal to design the array to address large impulses, moderate, and small impulses by adding a few more intermediate stages to the SPD array. However, the most realistic and cost-effective protection array would be the one designed to address the true hazardous level about the region, or more preciously, to the particular location as per the historical data.

In general, most small-scale LVPIs are fed through overhead power lines, and only have a single consumer unit or a panel board. Thus, most LVPI have one single control point to fix the SPD. Since there are no physical provisions to install secondary level protection SPDs or SPD at SDB level, class 3 SPDs placed at equipment level would directly expose to the impulses which are passing through the MDB level. This investigation emphasizes, the need to accommodate more intermediate SPDs before the equipment level protection to achieve high reliability. However, most practical installations do not support the required physical infrastructure to implement multistage protection arrays. Thus, constraints in the scale of LVPI may hinder the ability to devise optimum protection. Hence, in general, an ordinary LVPI can only be accommodated two SPDs, and this inherent deficiency to a placed array of SPDs can be detrimental to sensitive systems that connected to the ordinary LVPI.

IV. CONCLUSION

The phaser angle at which the transient voltage is pitching on the 230 V, 50 Hz utility system and the physical attributes of the impulse have a close correlation to the

amount of energy incident by a particular impulse and the percentage that would bypass the protection array.

The nature of the time domain voltage profile plays a significant role in deciding the efficiency of the protection array and the degree of stress that protection array would undergo confronting with incoming surges. The study proves that as both incident phaser angle and impulse nature are highly random, it is challenging to design a universal protection scheme to contain the full range of impulses. Moreover, it also emphasized that to reduce the contingencies associated with lighting, it can consider a few more intermediate levels in the SPD array. Further, the study also highlighted that customization of the protection array to local and regional conditions would be advantageous than oversizing or under sizing array. Additionally, the constraints in the small-scale LVPI have elevated the vulnerabilities, as there is no physical infrastructure to accommodate intermediate SPDs.

Therefore, all the above-elaborated observations concluded that, in general, SPDs cannot provide guaranteed protection against the transient voltages under all circumstances, and such deficiencies in providing adequate protection are mainly driven by the random nature of lightning but not the quality or reliability issue on modern SPDs.

ACKNOWLEDGMENT

This project is funded by NRC 15-32. Measurements were conducted with the support of the University of Colombo research grant AP/3/2012/CG/24. Participation of S. Nanayakkara was funded by HETC/CMB/SCI/QIGW3. Contribution by H. Wickramaratne in Statistical data analysis and the support of Public Utility Commission, Sri Lanka, for N. Sapumanage is highly acknowledged.

REFERENCES

[1] Kulkarni, K., Shetty, V.J., "Power quality issues in healthcare center," International Journal of current engineering and technology, Vol.4, No.3, June 2014.

[2] Seymour, J., Horsley, T., "The seven types of power problems," Schneider Electric., White paper June 2005.

[3] Almeida, A. de, Moreira, L., Delgado, J., "Power quality problems and new solutions," RE&PQJ, Vol. 1, No.1, April 2003.

[4] Andy, E. (2017, April) 2017 Europe EMC guide review of IEC 60601-1-2: 2014. [Online]. https://interferencetechnology.com/wp-content/uploads/2017/04/EEG_2017_Digital_Final_Low-Res.pdf.

[5] Martzloff, F. D., "Transient Overvoltage Protection Seminar," Corporate research and development, General Electric Company, White paper 2004.

[6] McGranaghan, M. (2001) https://www.scribd.com/document/345119248/Power-Quality-Standards.

[7] Silfverskiöld, S., Thottappillil, R., Ye, M., Cooray, V., Scuka, V., "Induced voltages in a low voltage power installation network due to lightning electromagnetic fields," EEE Trans.Electromagn.Compat., Vol. 41, No. 3, pp. 265-271, August 1999.

[8] Sapumanage, N., Nanayakkara, S., Jayalal, S., Fernando, M., Cooray, V., "Energy incident from lightning-induced voltages on low voltage power installation due to cloud-to-cloud flashes in Sri Lanka," in International Conference on Lightning Protection (ICLP), Estoril, Portugal, 2016, p. 6.

[9] Brashear, K., "Lightning and surge protection of Modern Electronic systems," ILD Technologies, LLC, San Antonio, TX, Online 2007.

[10] Punekar, G. S., Chandrasekaran, K., "Indirect effects of lightning discharges," Serbian Journal of Electrical Engineering., Vol. 8, No. 3, pp. 245-262, November 2011.

[11] Sapumanage, N., Nanayakkara, S., Chandimal, L., Hettiarachchi, P., Fernando, M., Cooray,V., "Simulation of SPD performances against the CG induced voltages under the different grounding conditions," in International Conference on Computational Modeling & Simulation, Colombo, Sri Lanka, 2017, p. 5.

[12] Sapumanage, N., Nanayakkara, N., Abegunawardana, S., Fernando, M., Cooray,V., "Insight of SPD Limitations Caused by Incident Phaser Angle and Physical Attributes of Transient Voltages," in 34th International Conference on Lightning Protection (ICLP), Rzeszow, Poland, 2018, p. 8.

[13] Sapumanage, N., Nanayakkara, N., Abegunawardana, S., Fernando, M., Cooray, V., "How physical attributes of transient voltages limit the efficiency of SPD array," in 34th International Conference on Lightning Protection (ICLP), Rzeszow, Poland, Poland, 2018, p. 8.

[14] Kern, A., Dikta, G., Flisowski, Z., Marzinotto, M., Mazzetti, C., "Probability and frequency of damage of electrical and electronic systems due to indirect lightning flashes," in Power Tech., Lausanne Switzerland., 2007.

[15] Brian, M., Daniel, U., Laurel, P., Kelsey, S., "Flash Back: a Review of Lightning-Related Damage and Disruption Literature," Environment Canada, No. 604, pp. 1-28, 2009.

[16] Dalibor, C., Alan, K., "Electronic systems protection via advanced surge protective devices," in NTELEC, International Telecommunications Energy Conference, 2002, pp. 22–26.

[17] (2012) www.abb.com. [Online]. https://library.e.abb.com/public/./1TXH000083C0202_OVR_proM.pdf.

[18] Bettermann, A., “Lightning protection guide.” Menden, Germany: OBO Bettermann, 2017.

[19] Samaras, K., Sandberg, C., Salmas, C. J., Koulaxouzidis, A., "Electrical surge-protection devices for industrial facilities," IEEE Trans.Ind.Appl., Vol. 43, No. 1, pp. 150-161, 2007.

[20] Sapumanage, N., Nanayakkara, N., Abegunawardana, S., Fernando, M., Hettiarachchi, P., Cooray,V., "Study on Responses of SPDs Against the Transient Voltages Generated by CG Flashes," in 34th International Conference on Lightning Protection (ICLP), Rzeszow, Poland, Poland, 2018, p. 7.

[21] "The 8 kA MOV characteristic curves for different let-through currents," Eaton Corporation, March 16, 2009.

[22] Nanayakkara, S., Mendis, U., Fernando, M., Abegunawardana, S., Liyanage, P., Cooray, V., "Lightning-induced voltages in overhead power lines due to Cloud to Ground Flashes in Sri Lanka," in APL, Nagoya, 2015.

[23] Nanayakkara, S., Mendis, U., Fernando, M., Abegunawardana, S., Liyanage, P., Cooray, V., "Voltages induced by Cloud flashes on rural utility electrical power lines in Sri Lanka," in APL, Nagoya, 2015.

[24] Panicali, A. R., Folho, J. P., Barbosa, F. C., Silva, J. C. O., Alves, N. V. B., "Protection of Electronic Equipment Inside Buildings," in 33rd International Conference in Lightning protection., Portugal, 2016.

HEMP environment distribution simulation and statistical analysis

Ning Dong, Yanzhao Xie
State Key Laboratory of Electrical Insulation and Power Equipment
National Center for International Research on Transient Electromagnetic Enviroments and Applications
School of Electrical Engineering, Xi'an Jiaotong University, Xi'an, Shaanxi, China
dongning96@163.com; yzxie@mail.xjtu.edu.cn

***Abstract*—The spatiotemporal distribution of HEMP on the Earth's surface is most concerned for large-scale infrastructure reliability analysis and protection design, including the time domain waveform and other key parameters all around the burst. An improved HEMP E1 simulation method based on space current parallel computing is proposed to realize fast simulation of HEMP waveform in large area. The correctness is verified by comparison with IEC standard. The probability distribution of HEMP generated can be approximated as bimodal Gauss distribution. The statistical result of HEMP amplitude with uncertainty parameters such as burst height is studied and quantified.**

Keywords—HEMP environment; numerical simulation; statistical analysis

I. INTRODUCTION

The early-time component (E1) of the high-altitude electromagnetic pulse (HEMP) with high amplitude, wide spectrum and wide distribution range is a kind of extreme threaten for large-scale infrastructure. The spatiotemporal distribution of HEMP on the Earth's surface, including time domain waveform, amplitude, pulse wide, energy, start time and other key parameters all around the burst, is what we concerned during reliability analysis and protection design. The key parameters of HEMP are different everywhere surrounding one burst. Meanwhile, different burst cause different HEMP spatiotemporal distribution as well. Due to the economical consideration, 100% failure free under the worst-case HEMP is not necessary for the large-scale infrastructure. One waveform recommend in IEC standard and other reference is not enough. Statistical analysis and uncertainty quantification method need to be obtained statistical result of potential HEMP.

II. SIMULATION METHOD AND NUMERICAL RESULT

Classical HEMP simulation method EXEMP developed by K.D. Leuthäuser is utilized to simulate the generator of HEMP [1]. The current in spherical coordinate system with retarded time $\tau = t - z/c$ can be calculated by a convolution integral of motion electron:

$$\mathbf{J}=\mathbf{J}_p+\mathbf{J}_s$$

$$\mathbf{J}_p = -eS(r)\int_0^{\infty}\mathbf{v}_p(\tau')\,f(\tau-\tau'+\frac{1}{c}(r-r'))d\tau'$$

$$\mathbf{J}_s = -ekS(r)\mathbf{v}_s(\tau)\int_0^{\tau}(\int_0^{\infty}v_p(\tau')\,f(\tau'-\tau''+\frac{1}{c}(r'-r''))d\tau'')d\tau' \quad (1)$$

Where $f(\tau)$ is gamma source function. $S(r)$ is proportional unscattered gamma flux. The speed of electrons $\mathbf{v}_p, \mathbf{v}_s$ can be calculated by relativistic electron motion equation.

$$\frac{d\mathbf{v}}{dt} = -\frac{e}{m\gamma}(\mathbf{E}) - \frac{e}{m\gamma}\mathbf{v}\times(\mathbf{B}_0+\mathbf{B}_1) - \frac{v_C}{\gamma}\mathbf{v} \quad (2)$$

EXEMP using Maxwell under high frequency approximation to simulate the electromagnetic field.

$$\begin{aligned}\frac{\partial(r\mathbf{E}_\theta)}{\partial r} &= -\frac{2\pi r}{c}\mathbf{J}\\ \frac{\partial(r\mathbf{E}_\phi)}{\partial r} &= -\frac{2\pi r}{c}\mathbf{J}\\ \frac{\partial\mathbf{E}_r}{\partial\tau} &= -4\pi\mathbf{J}\end{aligned} \quad (3)$$

The best way to solve function (3) is finite-difference time-domain method. The field is calculated alternately in time and space. For large scale electromagnetic field simulation, the main factor of restricting computing efficiency is that the current along the propagation way need to be calculated while current at each place is a consequence of convolution integral. To improve the time consulting, the space current can be calculation parallelly and renew at each time step instead of re-integral. Because the gamma source function is an exponential function, the convolution integral can be rewrite as:

$$\begin{aligned}&\int_0^{\infty}\mathbf{v}_p(\tau')\,f[\tau-\tau'+\frac{1}{c}(r-r')]d\tau'\\ &=f(\tau)\int_0^{\infty}\mathbf{v}_p(\tau')\,f[-\tau'+\frac{1}{c}(r-r')]d\tau'\end{aligned} \quad (4)$$

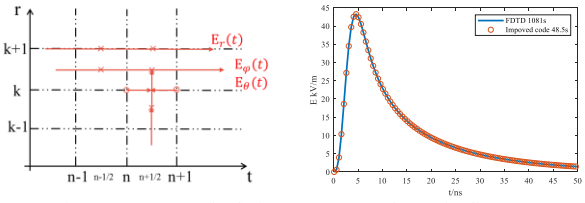

Fig. 1 a) FDTD calculation sequence schematic diagram
b) HEMP waveform simulated by FDTD and improved method

This improvement can speed up the computing by 95% without changing the result.

According to IEC 61000-2-9 standard, the HEMP amplitude distribution on Earth's surface of 100km-500km burst between 30°-60°N latitude, the time-domain waveform of A,B,C points with 100km burst height at 40°N is shown in Fig. 2, the relative relationship of HEMP amplitude at each place is consistent with IEC standard[2].

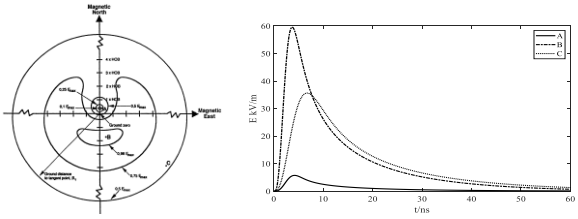

Fig. 2 a) IEC 61000-2-9 standard HEMP distribution on Earth's surface
b) Time-domain HEMP waveform at A, B, C

III. STATISTICAL RESULT OF HEMP

HEMP on Earth's surface is affected by the position, height, energy, and gamma source function of the burst as well as the air density and geomagnetic field around the burst. Some of the parameters vary in a certain range, some are uncertainty and can't be obtained exactly.

The HEMP environment distribution with variable parameters can be simulated by Monte Carlo method and described by statistical method, which shows more realistic situation than considering the radiation as 50kV/m standard waveform all around.

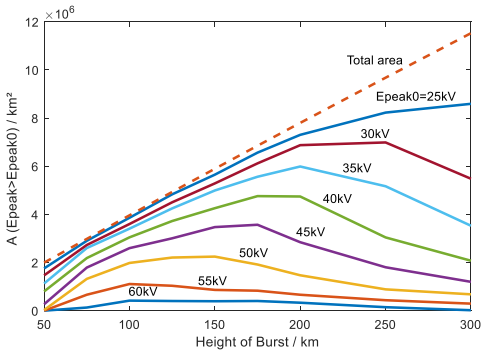

Fig. 3 Area distribution of HEMP amplitude for different burst height

Fig. 3 shows the area distribution of HEMP amplitude for different height of burst. It can be easily telling that the percent of low amplitude area is growing when the height of burst become larger.

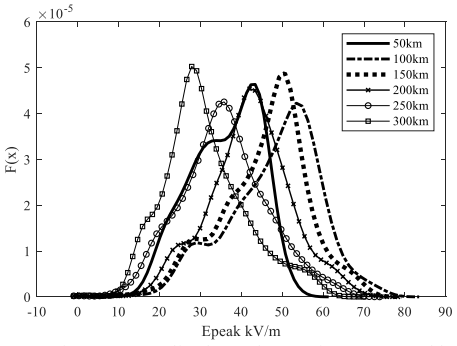

Fig. 4 PDF of HEMP amplitude at observation generated by bursts of different height

The probability density curves for HEMP generated by bursts of different height are shown in Fig.4. the PDFs can be approximated as bimodal Gauss distribution. The lower peak with smaller probability refers to the low amplitude area at the magnetic north of the burst.

Consider a set observation point, the bursts might happen around the observation flowing uniform probability the cumulative probability density of HEMP generated at the observation are shown in Fig.5 As the range of burst height increasing, both the average and 90% confidence interval amplitude become lower.

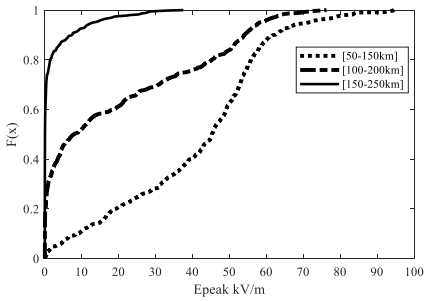

Fig. 5 CDF of HEMP amplitude at observation generated by bursts of different height within 200km radius

IV. CONSLUSION

The HEMP is different everywhere surrounding one burst, and its amplitude probability distribution follow a bimodal Gauss distribution. The statistical result of rise time, energy and other key parameter of HEMP will be studied in the future.

All computing in this paper are run on MATLAB R2018a under win10 operating system, 16GB memory,1.8GHz main frequency Intel (R) Core (TM) i7-8550U CPU PC Computer.

REFERENCES:

[1] K. Leuthäuser, A complete EMP environment generated by high-altitude nuclear bursts[R]. EMP Theor. Notes TN-363, 1992

[2] Electromagnetic Compatibility (EMC) - Part 2: Environment - Section 9: Description of HEMP Environment - Radiated disturbance, IEC 61000-2-9 Ed. 1.0, Feb. 1996.

Characterization of CG Flashes with Multiple Terminations Using a 3D Lightning Mapping System FALMA

Panliang Gao
Department of Electrical, Electronic and Computer Engineering
Gifu University
Gifu, Japan
x3914003@edu.gifu-u.ac.jp

Daohong Wang
Department of Electrical, Electronic and Computer Engineering
Gifu University
Gifu, Japan
wang@gifu-u.ac.jp

Dongdong Shi
Department of Electrical, Electronic and Computer Engineering
Gifu University
Gifu, Japan
w3914102@edu.gifu-u.ac.jp

Ting Wu
Department of Electrical, Electronic and Computer Engineering
Gifu University
Gifu, Japan
tingwu@gifu-u.ac.jp

Nobuyuki Takagi
Department of Electrical, Electronic and Computer Engineering
Gifu University
Gifu, Japan
takagi-n@gifu-u.ac.jp

***Abstract* — We have characterized 205 multiple-termination negative cloud-to-ground (CG) lightning flashes that were imaged well by Fast Antenna Lightning Mapping Array (FALMA) during the summer of 2017. The parameters we used include return stroke (RS) number, termination number, termination distance, interval between the first RS of each termination and fork height. The most frequent RS number is 4, accounting for 20% (41/205) and the largest RS number in one flash is 18. Termination number ranges from 2 to 5 and the majority of multiple-termination flashes (148/205) have two terminations. The termination distance, with high possibility, is between 2 km and 4 km. The minimum interval between the first RS of each termination in one flash is 0.5 ms and the most frequent interval is less than 100 ms. The most (146/205) flashes have forked between the height of 4 km and 6 km, indicating that the channel branching process mostly occurred inside the cloud.**

Keywords—multiple termination, negative CG lightning, FALMA

I. INTRODUCTION

Negative cloud-to-ground (CG) flashes with multiple ground terminations have been studied previously by a number of authors [e.g., 1-3]. In those studies, most authors used videos for identifying multiple terminations. However, as pointed out in [3], video has several limitations for doing such kind of identification: (1) only the lightning channel below the cloud base can be recorded; (2) it is impossible to estimate the distance between multiple terminations; (3) the time resolution is usually not good. Recently, using an array of fast antenna, we have developed a 3D lightning mapping system, called FALMA [4], that allowed us to locate lightning ground termination points with an accuracy of about 30 m. From FALMA data, we are able to not only estimate the distance between multiple ground terminations, but also study how the leader for a different ground termination is formed even inside the cloud. By taking these advantages, we have performed a study on the negative CG lightning flashes with multiple ground terminations. This paper is to report our results.

II. EXAMPLE CG FLASES WITH MULTIPLE TERMINATIONS

Fig.1 shows an example negative CG lightning flash that had two ground terminations marked with triangle and square, respectively. Fig. 1a is its electric field change (E-change) waveform recorded at one of 12 sites of FALMA. As can be identified from this E-change waveform, this flash contains 7 return strokes (RSs). Fig. 1b is the height with time. The lightning flash started at a height of about 9 km above sea level and lasted about 2.3 seconds. From its locations shown in Fig. 1c, 1d, 1e and 1f, the first stroke terminated in one place and the remaining 6 strokes terminated in another place with a distance separated about 6 km.

III. STATISTICS AND CHRACTERISTICS

We identified 205 negative CG flashes that exhibited multiple terminations from the data recorded by FALMA during the summer of 2017. Their statistics and characteristics are shown in the following.

A. Return stroke numbers

Fig.2 shows the histogram of return stroke numbers for the CG flashes with multiple terminations. The maximum return stroke number is 18, while the most frequent return stroke number is 4.

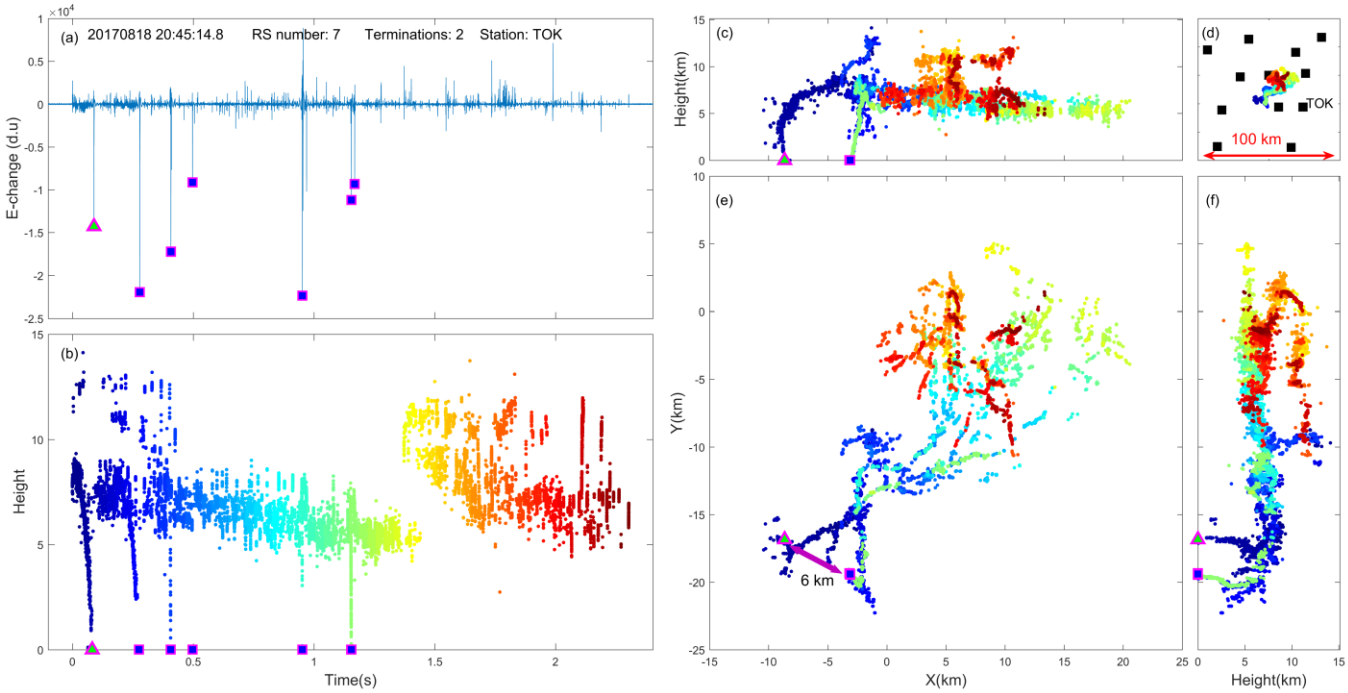

Fig.1. An example of negative CG lightning with multiple terminations. (a) E-change waveform recorded at station TOK. Triangles and squares indicate the identified RSs. (b) Locating height versus time. (c) x-z vertical view. (d) Geographical positions of FALMA station. (e) x-y view. (f) y-z vertical view.

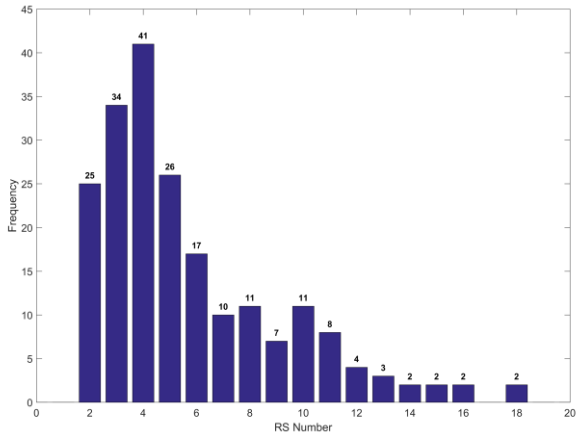

Fig.2. Histogram of RS number in each multiple-termination CG lightning flash.

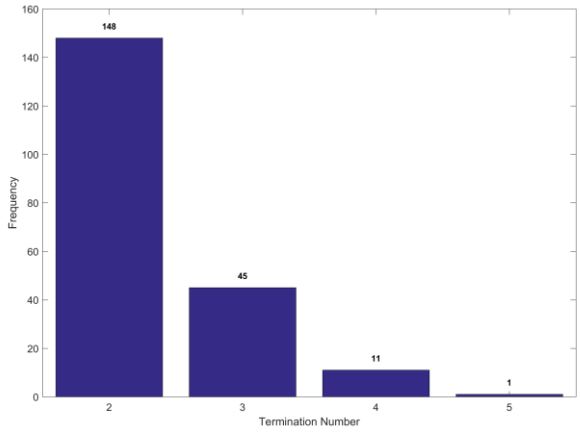

Fig.3. Histogram of termination numbers in each multiple-termination CG lightning flash.

B. Termination number

Fig.3 presents the histogram of termination numbers. Most CG flashes with multiple terminations contain only two return strokes. In such cases, each termination has only one return stroke. This histogram is surprisingly similar to that obtained in [2] for Arizona lightning flashes with the video recordings.

C. Termination distance

Fig.4 shows the histogram of the distances between two terminations in each individual CG flashes. As seen in this figure, the different terminations of a few lightning flashes have a distance longer than 10 km. The most frequent termination distance is around 3 or 4 km.

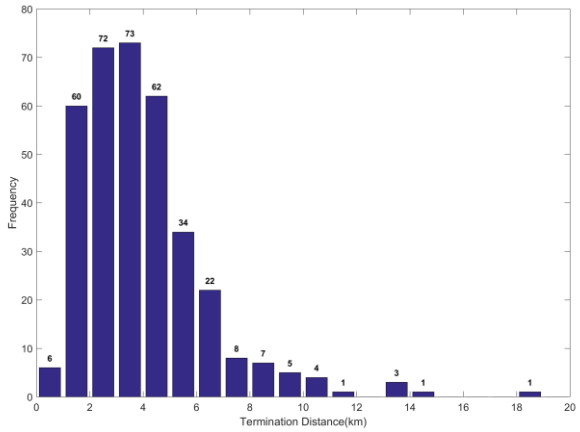

Fig.4. Histogram of distance between any two terminations in each multiple-termination CG lightning flash.

D. *Time difference between the first strokes of each termination*

Fig.5 shows the histogram of the time difference between the first strokes of each termination. The time difference could be as much as roughly 1 second. For most CG flashes with multiple terminations, the time difference is less than 300 ms. The shortest time difference is 0.5 ms.

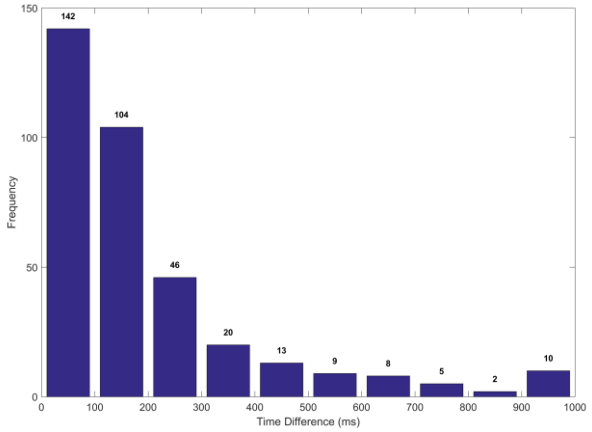

Fig.5. Histogram of time difference between the first RSs of each termination in the same CG lightning.

E. *Fork height*

Fig.6 shows the histogram of the height where the fork of the leaders leads to different terminations. It appears that most of the forks occur at a height of more than 4 km well inside thundercloud.

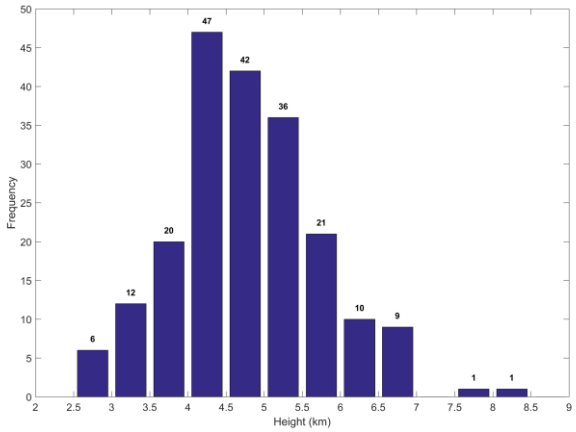

Fig.6. Histogram of fork height.

IV. Concluding Remarks

In this paper, by using 205 multiple-termination CG lightning flashes recorded by FALMA, we have analyzed their characteristics, such as RS number, termination number and termination distance. In the future, we are going to subdivide those 205 flashes in order to discuss their properties in more detail.

Acknowledgment

This work was supported by Ministry of Education, Culture, Sports, Science, and Technology of Japan (Grant number: 15H02597).

References

[1] Rakov, V. A., M.A. Uman, and R. Thottappillil, "Review of Lightning Properties from Electric Field and TV Observations", J. Geophys. Res., 99, 10,745-10,750, 1994.

[2] William C. Valine and E. Philip Krider, “Statistics and characteristics of cloud-to-ground lightning with multiple ground contacts,” J. Geophys. Res., vol.107 (D20), pp. 4441-4452, October 2002.

[3] Saba, M. M. F., M. G. Ballarotti, and O. Pinto Jr. (2006), “Negative cloud-to-ground lightning properties from high-speed video observations,” J. Geophys. Res., vol.111, pp.0148-0227, February 2006.

[4] Ting Wu, Daohong Wang, Nobuyuki Takagi, “Lightning Mapping with an Array of Fast Antennas,” Geophysical Research Letters, vol. 45, pp.3698-3705, April 2008.

Short-pulse HPM measurements using a resistive sensor

Paulius Ragulis
Department of Physical Technologies
Center for Physical Sciences and Technology
Vilnius, Lithuania
paulius.ragulis@ftmc.lt

Rimantas Simniškis
Department of Physical Technologies
Center for Physical Sciences and Technology
Vilnius, Lithuania
rimantas.simniskis@ftmc.lt

Mindaugas Dagys
Department of Physical Technologies
Center for Physical Sciences and Technology
Vilnius, Lithuania
mindaugas.dagys@ftmc.lt

Žilvinas Kancleris
Department of Physical Technologies
Center for Physical Sciences and Technology
Vilnius, Lithuania
zilvinas.kancleris@ftmc.lt

Dmitrii Andreev
Department of Electrical and Computer Engineering
University of New Mexico
Albuquerque, NM, USA
dandreev@unm.edu

Antonio Breno De Alleluia
Department of Electrical and Computer Engineering
University of New Mexico
Albuquerque, NM, USA
antonioalleluia@unm.edu

Edl Schamiloglu
Department of Electrical and Computer Engineering
University of New Mexico
Albuquerque, NM, USA
edls@unm.edu

***Abstract*— Resistive sensors for WRD250 and WRD750 double ridged waveguides were developed. A flat frequency response of the sensors was sacrificed in order to measure short high power microwave pulses but still maintaining a wide operating frequency band. Using the developed sensors HPM pulses covering frequency ranges 2.6 – 7.8 GHz and 7.5 – 18 GHz can be directly measured.**

Keywords— resistive sensor, high power microwaves, short pulses.

I. Introduction

A resistive sensor (RS), the performance of which is based on electron heating effect in a semiconductor, consists of a sensing element (SE) made from n-type Si [1]. The SE is actually a bulk resistor, with two Ohmic contacts, placed in a waveguide. Electric field of microwave pulse heats electrons in the SE, its resistance increases and by measuring this resistance change pulse power in the waveguide can be determined. Since strong electric field is necessary to heat electrons in a semiconductor sample the RS founds its applications for high power microwave (HPM) pulse measurement. Some advantages can be mentioned when comparing the RS with a semiconductor diode which is also sometimes used for HPM pulse measurement. The RS measures HPM pulses directly, is overload resistant and demonstrates perfect long-term stability [1]. The frequency band these sensors can be used in is limited only by the waveguide in which they are mounted. In order to measure HPM pulses over a wide frequency range, a few RSs mounted in rectangular waveguide should be used.

In this study, a RS mounted in double ridged WRD250 and WRD750 waveguides was investigated. By mounting the RS into the double ridged waveguide it is possible to expand the frequency band of the sensors. By using only the two sensors in a double-ridged waveguide a frequency range from 2.6 GHz to 18 GHz can be covered.

This research has received a funding from the European Social Fund (project No 09.3.3-LMT-K-712-02-139) under grant agreement with the Research Council of Lithuania (LMTLT)

II. Resistive sensor

In our previous paper [2] we presented resistive sensors implemented in WRD840 and WRD250 waveguides. Parameters of the sensing elements of these sensors were chosen in such a way that the frequency response of the sensor shall be as flat as possible. The RS of these sensors is made of two sensing elements that are separated from each other. On the top of them there is a dielectric concentrator [2]. This configuration was chosen since it allowed us to use smaller sensing elements, significantly reducing in this way the reflection from the sensor as a whole.

A sensitivity of the RSs is written down as its relative resistance change in a microwave electric field $\Delta R/R$ divided by a pulse power P of the HPM pulse:

$$\zeta = \frac{\frac{\Delta R}{R}}{P}$$

Unfortunately, in order to have a flat frequency response the resistance of the sensing elements should be as high as 1000 Ω and this is a reason why such sensors are of little use for the measurement of short (a few tens of ns) duration HPM pulses.

III. Frequency response measurements

In order to measure short HPM pulses the total resistance of the sensing elements should match the impedance of the measurement circuit. There is no other solution to fulfill this condition than to sacrifice the flatness of the frequency response of the sensor.

The dependences of the sensitivity on frequency for the manufactured RS are shown in Fig. 1 for the sensor mounted in WRD750 waveguide and in Fig. 2 for the sensor mounted

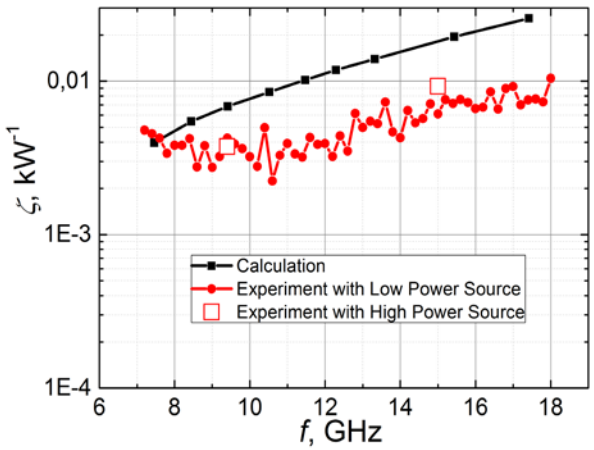

Fig. 1. Dependences of WRD750 RS sensitivity on frequency. Black Line: simulation results. Red line: Measurement results using low power source. Red squares: Measurement results using high power magnetron generators.

in WRD250 waveguide. The sensitivities determined from experiments with magnetron generators are also shown in the figures by red squares. It is seen that they fairly well correspond to the results obtained using low power meander modulated technique [2]. Together with measurement results, the calculated data using a FDTD method are presented. The calculated results for WRD750 resistive sensor (Fig. 1) predict more significant increase of the sensitivity, in comparison with the measurement results. They agree well in a low frequency region but split at a higher frequency. The agreement between measured and calculated results for WRD250 sensor is much better. The main reason for the disagreement between calculated and measured sensitivity for WRD750 sensor is the size of the sensing elements. The cross sectional dimensions of the sensing element are less than 0.5 mm and thickness ~100 μm. Therefore, even a small change in them due to, for example, by uncontrolled thickness of solder can lead to the noticeable alteration of the sensitivity of the sensor. The measured sensitivity variation of recently designed WRD250 and WRD750 sensors, is as large as 1.8 times within a frequency pass band of the RS for WRD750 sensor and 2.2 for WRD250 sensor.

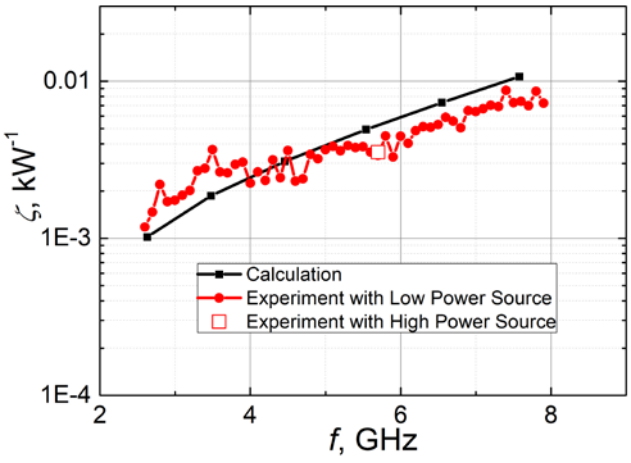

Fig. 2. Dependences of WRD250 RS sensitivity on frequency. Black Line: simulation results. Red line: Measurement results using low power source. Red squares: Measurement results using high power magnetron generators.

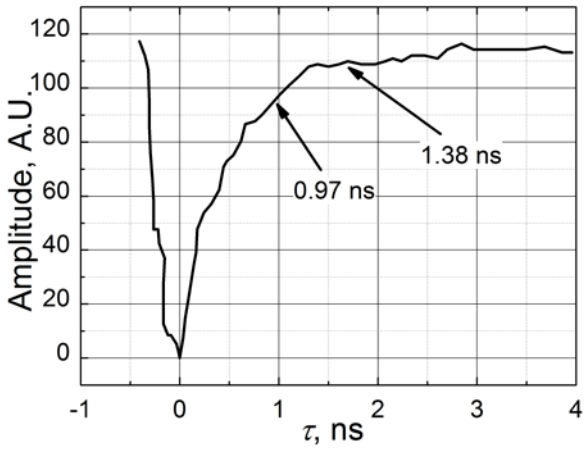

Fig. 2. Measurements of the rise time of a resistive sensor mounted into WRD750 waveguide

IV. Response Time

In order to measure the nanosecond duration HPM, the resistance of the sensor was decreased to match the measurement circuit – 50 Ω. The response time of the manufactured resistive sensor for WRD750 waveguide was measured using the time domain reflectometry method. Pulse generator, impedance of which is 50 Ω, produces 100 ns duration pulses with the rise time of 0.05 ns. The output of the generator is linked to the tee-joint. One of the arms of the tee-joint is connected to the RS under test whereas the other one is joined to the oscilloscope. The measured transient being a result of two signal superposition is shown in Fig. 3. As can be seen from the figure the duration of the transition process is approximately 1.38 ns while the rise time is on the order of 1 ns. The achieved response time of the sensor should allow us to measure HPM pulses which duration is on the order of 5 ns.

Wishing to decrease the response time one has to decrease the additional capacitance *C* which is connected in parallel to the sensing element ant serves as low pass filter preventing microwaves from getting to DC pulse measuring circuit. The value of this capacitance can be easily estimated by using the formula:

$$C = \frac{1}{2\pi f_c R}$$

where R is resistance of the RS and f_c is a cut off frequency of the waveguide. This value should be chosen carefully, because too large C could also increase the response time of the RS.

The measured response time lets one assume that manufactured sensor has a high potential for short pulse high power microwave signal measurements in a wide frequency range.

References

[1] M. Dagys, Z. Kancleris, R. Simniskis, E. Schamiloglu, and F. J. Agee, "The resistive sensor: a device for high-power microwave pulsed measurements," *Antennas and Propagation Magazine, IEEE*, vol. 43, pp. 64-79, 2001.

[2] P. Ragulis, R. Simniškis, M. Dagys, and Ž. Kancleris, "Wideband Resistive Sensors for Double-Ridged Waveguides," *IEEE Transactions on Plasma Science*, vol. 45, pp. 2748-2754, 2017.

Prediction of Trichel pulse amplitude for smooth conductors and stranded conductors based on improved effective ionization integral

Pengfei Xu
Dept. Electrical Engineering
Tsinghua University
Beijing, China
xpftsh@126.com

Bo Zhang
Dept. Electrical Engineering
Tsinghua University
Beijing, China
shizbcn@tsinghua.edu.cn

Jinliang He
Dept. Electrical Engineering
Tsinghua University
Beijing, China
hejl@tsinghua.edu.cn

Jianben Liu
State Key Laboratory of Power Grid Environmental Protection
China Electric Power Research Institute
liujianben@epri.sgcc.com.cn

***Abstract*—Trichel discharge is a typical kind of electrostatic discharge, which can generate harmful electromagnetic filed to microelectronic devices. In this paper, an improved effective ionization integral is proposed to predict the amplitudes of Trichel pulses from both the smooth and stranded conductors. The proposed integral is based on the calculation of ion-flow field, and can be regarded as the integral of effective ionization integral along the ionization boundary. The present method makes good explanation to the characteristics of Trichel pulse amplitude for both smooth and stranded conductors, having an apparent advantage in the prediction of Trichel pulse amplitude.**

Keywords—trichel pulse, ESD, amplitude, effective ionization integral, stranded conductor.

I. INTRODUCTION (*HEADING 1*)

Trichel pulse is a typical kind of negative corona current firstly observed by Trichel, and can produce harmful electromagnetic field to microelectronic devices [1]-[2]. The characteristics of the Trichel pulses, including repetition rate, peak value of each pulse, and mean current, have been studied by many scholars [3]-[4]. However, few of them are related to the electrode of stranded conductor, which is the general shape for the sub-conductors of transmission lines. Moreover, although there are some formulas to predict the characteristics of Trichel pulses under certain electrode structures [3], there is no common benchmark for the comparison of different characteristics of corona currents under distinct electrodes. In this paper, an improved effective ionization integral is proposed, which can be used as a benchmark for the comparison of Trichel pulse amplitude between smooth conductors and stranded conductors. Besides, a well behaved formula for the prediction of Trichel pulse amplitude from both smooth and stranded conductors is presented. The results will be helpful for the effective predictions of electromagnetic environment near transmission lines, too.

II. IMPROVED EFFECTIVE IONIZATION INTEGRAL

The measured amplitude of Trichel pulses is shown in Fig. 1. Three smooth conductors with different diameters were used in the experiment. It is found that at the beginning of onset, the amplitude of Trichel pulses is slightly low. And then, if the applied electric field is higher than the onset electric filed, the amplitude becomes almost unchanged with the increase of applied electric field. Besides, the amplitude of Trichel pulses is higher for the conductor with larger diameter.

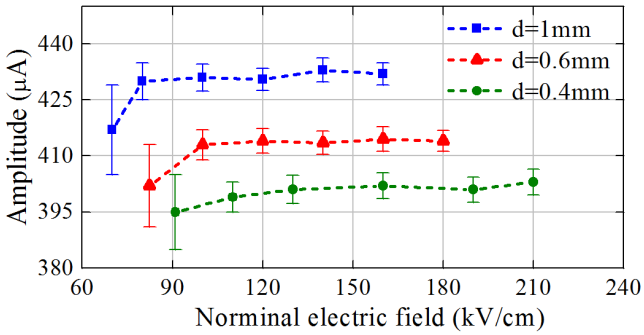

Fig. 1. Trichel pulse amplitude under different smooth conductors.

Usually, the amplitude of Trichel pulses is considered to have a close relationship with the effective ionization integral ξ, which can be expressed as [5]

$$\xi = \int_l (\alpha - \eta) dl \tag{1}$$

where α, η, and l are ionization coefficient, attachment coefficient, and path of integration respectively.

The negative ions generated by negative DC corona full fill the entire space, resulting in the distortion of electric field especially at the surrounding of conductors. Thus, it is more suitable to use the composite electrical field instead of the nominal electric field for the calculation of effective ionization integral. The calculation of composite electrical field is referred to [6]. The calculated effective ionization integral is presented in Table I. For the conductor with certain diameter d, the calculated ξ remains unchanged, which can be an explanation of the phenomenon that the unchanged amplitude of Trichel pulses. However, the value of ξ decreases when the diameter of the conductor increases, which contradicts with the fact that the amplitude increases with the increase of diameter, as shown in Fig. 1.

TABLE I. CALCULATION OF EFFECTIVE IONIZATION INTEGRAL ξ

Electric filed (kV/cm)	ξ (d = 0.4 mm)	ξ (d = 0.6 mm)	ξ (d = 1 mm)
100	8.01	7.70	7.13
120	8.03	7.71	7.14
140	8.04	7.73	7.14
160	8.05	7.74	7.15

The reason for this contradiction is the neglect of the electric field distribution near the electrode. Therefore, an improved effective ionization integral ξ_L is proposed as shown in (2). The integral ξ_L can be regarded as the integral of ξ along the ionization boundary L. The meaning of ξ_L is the times of ionization that an electron which is randomly distributed on ionization boundary can excite from the ionization boundary to conductor surface. The calculation of ξ_L is shown in Table II. It is apparent that the value of ξ_L almost remains the same with the variation of applied electric field, and moreover, ξ_L increases as the diameter increases, due to the longer ionization boundary in larger conductors.

$$\xi_L = \int_L \int_l (\alpha - \eta) dl dL \tag{2}$$

TABLE II. CALCULATION OF IMPROVED EFFECTIVE IONIZATION INTEGRAL ξ_L

Electric filed (kV/cm)	ξ_L (mm) (d = 0.4 mm)	ξ_L (mm) (d = 0.6 mm)	ξ_L (mm) (d = 1 mm)
100	20.78	31.08	43.33
120	21.09	31.21	43.60
140	21.13	31.27	43.63
160	21.18	31.33	43.67

III. APPLICATIONS OF THE IMPROVED EFFECTIVE IONIZATION INTEGRAL

Traditionally, it is difficult to compare the amplitude of Trichel pulses among stranded conductors and smooth conductors. This is due to the extremely uneven electric field distribution of stranded conductor as illustrated in Fig. 2 and Fig. 3.

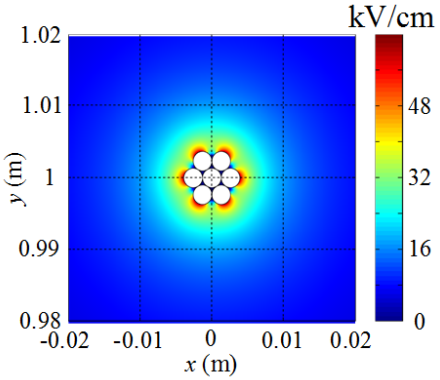

Fig. 2. Electric field distribution for a stranded conductor (d = 3 mm).

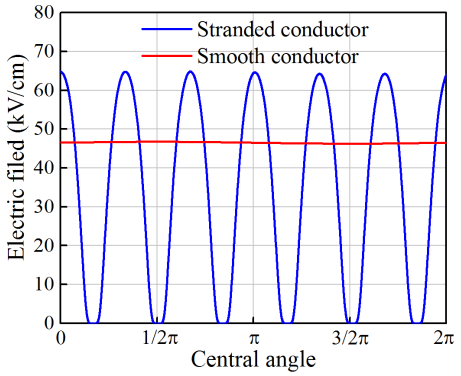

Fig. 3. Comparison of electric field distribution for a stranded conductor and smooth conductor (d = 3 mm).

However, the proposed integral ξ_L can be used to compare the amplitude of Trichel pulses among both smooth conductors and stranded conductors, as it takes the distribution of electric field into consideration. The measured amplitude of Trichel pulses for stranded conductors is also kept unchanged with the variation of applied electric field, as shown in Fig. 4, which is similar with the pattern of smooth conductors. But the amplitudes are much higher than that of smooth conductors.

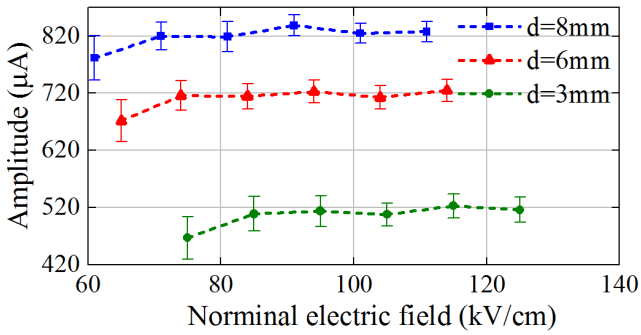

Fig. 4. Electric field distribution for a stranded conductor (d = 3 mm).

There is a quite good linear relationship between the amplitude and corresponding improved effective ionization integral ξ_L for both the smooth and stranded conductors, as demonstrated in Fig. 5, The linear relationship can be characterized as

$$A = K_A \xi_L + K_0 \tag{3}$$

where A, K_A, and K_0 are the amplitude of Trichel pulses, proportional constant of the amplitude formula, and constant of the amplitude formula respectively. Based on the experimental results, the values of K_A and K_0 are about 1.37 μA/mm and 372.27 μA.

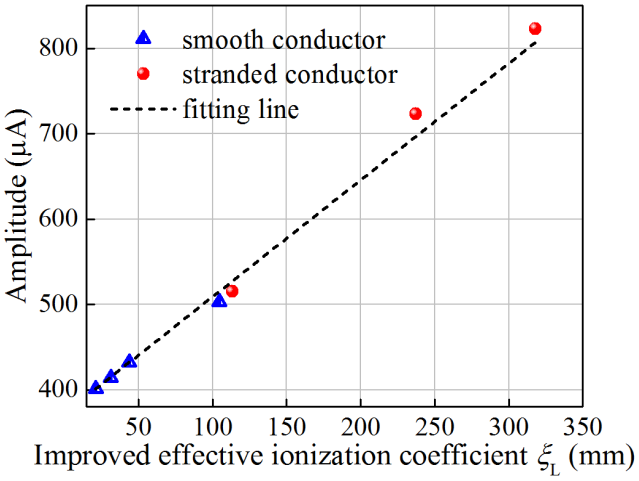

Fig. 5. Relationship between amplitude and ξ_L.

The proposed method works quite well for the prediction of Trichel pulse amplitude for both smooth and stranded conductors. For the positive polarity, more research will be conducted in the near future.

ACKNOWLEDGMENT

Supported by Open Fund of State Key Laboratory of Power Grid Environmental Protection

REFERENCES

[1] X. Hu, S. Liu, M. Wei, and L. Wang, "Measurement and analysis of Electromagnetic Fields Radiated by Corona Discharge," *2007 International Symposium on Electromagnetic Compatibility*, IEEE, 2007.

[2] Y. Shen, S. Chen, Y. Wu, and Q. Yang, "EMD from Negative Corona Discharge," *2002 International Symposium on Electromagnetic Compatibility*, IEEE, 2002.

[3] Z. Li, B. Zhang, and J. He, "Specific characteristics of negative corona currents generated in short point-plane gap," *Phys. Plasmas*., vol 20, no. 9, pp. 093507, 2013.

[4] H. Yin, B. Zhang, J. He, and C. Zhuang, "Modeling of Trichel pulses in the negative corona on a line-to-plane geometry," *IEEE Trans. Magn.,* vol 50, no. 2, pp. 473-476, Feb. 2014.

[5] Y. Liu, X. Cui, T. Lu, Z. Wang, X. Li, Y. Xiang, and X, Wang, "Detailed characteristics of intermittent current pulses due to positive corona," *Phys. Plasmas*., vol 21, no. 8, pp. 082108, 2014.

[6] B. Zhang, H. Yin, J. He, and R. Zeng, "Computation of ion-flow field near the metal board house under the HVDC bipolar transmission line," *IEEE Trans. Magn.,* vol 28, no. 2, pp. 1233-1234, Apr. 2013.

Preliminary test of high power RF generation from 6H-SiC photoconductive switch

Qilin Wu*, Yuxin Zhao*, Tao Xun*, Hanwu Yang*, Wei Huang†
*College of Advanced Interdisciplinary Studies, National University of Defense Technology, Changsha, 410073, China †Shanghai Institute of Ceramics, Chinese Academy of Sciences, 1295 Dingxi, Shanghai, 200050, China

***Abstract*—High-power photoconductive semiconductor switch (PCSS) working in linear mode can be used for RF generation by modulating the illuminating light. This paper presents a design and preliminary test of optoelectronic class B push-pull microwave power amplifier (MPA) using a 6H-SiC photoconductive switch. The initial tests have been conducted with bias voltage of ±2.5 kV, at 80 kW peak laser pulse power, demonstrating that the SiC PCSS working in linear mode can produce microwave. Then circuit simulation is conducted to study the factors affecting the electric efficiency, such as the quantum efficiency, the peak laser pulse power, the bias voltage. It is speculated that the MPA could output 1 MW microwave power and achieve electric efficiency of more than 60% with the bias voltage of 15 kV, quantum efficiency of 0.2 and peak laser pulse power of 100 kW.**

***Index Terms*—6H Silicon Carbide (6H-SiC), class B microwave power amplifier (MPA), photoconductive semiconductor switches (PCSS), microwave photonics (MWP)**

I. Introduction

Traditional high power microwave (HPM) generation is realized with various vacuum tubes with electron beams and high-frequency electromagnetic structures or cavities. The output parameters of the microwave generated this way, such as the frequency, is usually fixed or difficult to adjust [1]. Furthermore, the size of the vacuum tube is usually bulky, as the electromagnetic structure is on a scale up to several microwave wavelengths, which is on the order of 1 meter.

Solid state microwave generation utilizing the photoconductive semiconductors is becoming more attractive, as the interests in the study of beam-less HPM generation are increasing in recent years [2], and the technology of microwave photonics (MWP)is emerging [3], where photonic devices are used for microwave generation.

Researchers have studied the photoconductive semiconductors, such as gallium arsenide (GaAs) and silicon carbide (SiC), and their photoelectric characteristics during the last few decades [4] [5], having verified their high power, low jitter, fast response, high frequency and high repetition rate capabilities and applications.

PCSSs have linear and non-linear working mode. In linear mode the conductance of the PCSS is proportional to the illuminating light, and in nonlinear mode the PCSS behaves like a switch, i.e., it locks into conduction with a trigger light. Both modes can be utilized to generate microwaves. In addition, PCSSs have the advantage of low jitter, which allows power combination of multiple branches to enhance power. Karabegovic and O'Connell [6] employed a GaAs PCSS to generate single frequency microwaves at 10 GHz, with output power about several watts, as the thickness of the GaAs substrate is very thin and the allowed bias voltage is limited to several volts.

Corresponding author: H. Yang (email: yanghw@nudt.edu.cn).

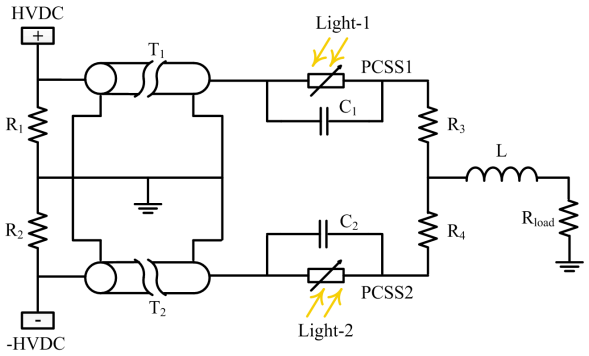

Fig. 1: Scheme of an optoelectronic class AB push-pull microwave power amplifier, where T_1, T_2 are pulse forming lines.

Superior to GaAs, SiC has a higher breakdown field strength (3-4 MV/cm). For example, March [7] reported the power capacity of a single thickness of 300 μm and side width of 12.7-mm square 4H-SiC wafer was as high as 11.7 MW; and Wu [8] achieved 10.65 MW with a thickness of 800 μm and side width of 11-mm square 6H-SiC. These studies indicate that the SiC PCSS is a potential compact device for HPM generation.

This paper presents an optoelectronic (OE) Class B push-pull microwave power amplifier (MPA), as shown in Fig. 1, achieving 46 W output power. Megawatt operation will be possible if the quantum efficiency of the photoconductor is improved and the bias voltage is increased.

II. The scheme of the OE class B push-pull microwave power amplifier

The scheme of the OE class B push-pull MPA is shown in Fig. 1. The optical signals driving PCSS1 and PCSS2 in Fig. 1 are assumed to be a pair of sinusoidal optical pulse trains, which are 180 degrees out of phase with each other, so each of the PCSSs is illuminated in half the cycle. Here the

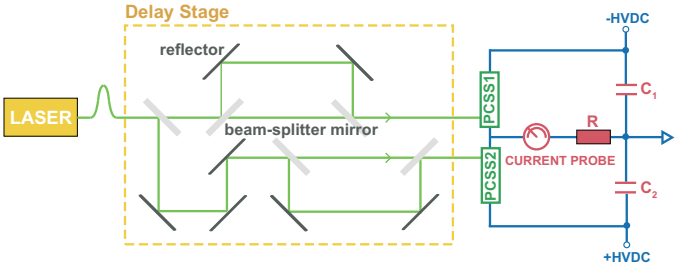

Fig. 2: The experiment setting.

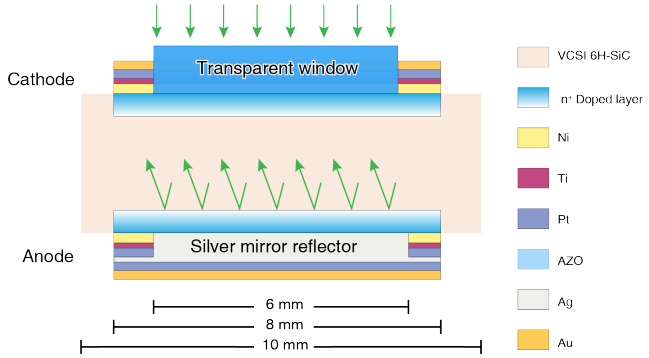

Fig. 3: Sketch of the SiC PCSS wafer structure [8]: the upper surface of SiC is coated with AZO and the opposite with silver mirror reflector to enhance the reflection.

light intensity modulation is imitated by Gaussian pulse trains, obtained by splitting and delaying a very short laser pulse.

Compared to traditional class A amplifier [8], the OE class B push-pull MPA in Fig. 1 not only has the high efficiency, but also can reduce the adverse effect of the inherent capacitance of the PCSS.

III. Experiment

The experiment is conducted as the setting in Fig. 2, with high voltages of 2.46 kV and -2.37 kV, mainly including the optical part, the electric circuit part and two high voltage power supply. In the circuit, the capacitors C_1 and C_2 are of 4 nF, and the load resistor is 25 Ω. The output current of the OE class B APM is monitored by a current viewing resistor (CVR).

A. Extrinsic SiC photoconductive semiconductor switch

The PCSS devices are fabricated from samples of hundreds of micrometers thick, 1 cm per side, square substrate of "a" plane sliced, vanadium compensated, semi-insulating 6H-SiC, as shown in Fig. 3. Vanadium-compensated, semi-insulating 6H-SiC is selected in this research as it has high dark resistivity and can be triggered by a laser with a sub-bandgap wavelength. Also, the sub-bandgap light's penetration depth is higher, on the order of 1 cm, which makes the photocurrent more uniformly distributed in the bulk, and the current density is lower to ensure a longer lifetime.

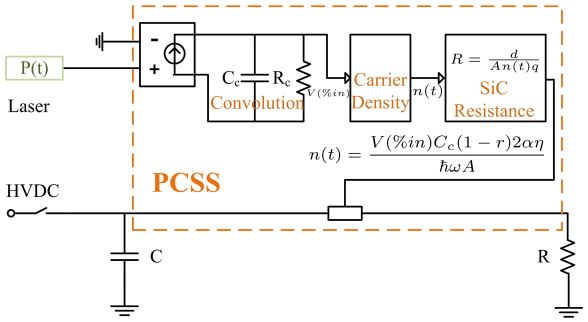

Fig. 4: The resistance model of the PCSS

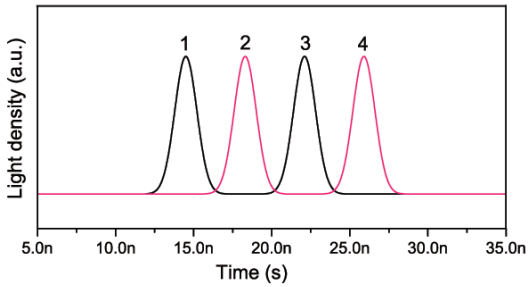

Fig. 5: The light sequence of the experiment

B. The construction of the time complementary light path

Photoconductivity tests are performed using 532 nm wavelength light from a Q-switch Nd:YAG laser with 1.7 ns of full width at half magnitude (FWHM). Reflectors and beam-splitter are used to produce two complementary optical pulse trains, as the delay stage shown in 2, and each of them contains two optical pulses. The peak optical power is 80 kW.

IV. Simulation Results and Analysis

To predict and analyze the experiment results, a circuit model of the PCSS is built in PSpice based on the equivalent photo resistance formula of the PCSS [8], shown in Fig. 4. In the model, $n(t)$ is the carrier concentration, $\tau_r = 0.13$ ns is the recombination time, $P(t)$ is the real-time input optical power, $\eta = 0.002$ is the quantum efficiency of the semiconductor material, $r = 0.2$ is the surface reflectance of SiC wafer, $A = 1$ cm^2 is the cross-section of the light path, $d = 200$ μm is the thickness of the wafer, and $\hbar\omega$ is energy of one incident photon.

The illuminating optical pulses to surface of the PCSS is assumed to be a Gaussian function,

$$P_i = P_0 \exp\left[-\left(\frac{t - t_0 - t_i}{t_r}\right)^2\right], i = 1, 2, 3, 4 \qquad (1)$$

where $P_0 = 80$ kW is the peak optical power, $t_r = 1$ ns is the rise time, $t_i + t_0$ is the delay time of each optical pulse P_i. According to the setting of the experiment in Section III, $t_1 = 0$ ns, $t_2 = 3.8$ ns, $t_3 = 7.6$ ns, $t_4 = 11.4$ ns. The light sequences are shown in Fig. 5, where t_1, t_3 are for the upper branch in Fig. 2 while t_2, t_4 are for the lower branch.

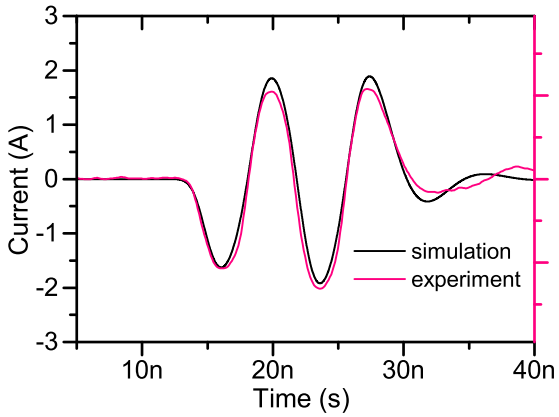

Fig. 6: The waveforms of load current in experiment and simulation

TABLE I: Performance of the MPA at various operating conditions

P_0 (kW)	η	V_{HV} (kV)	P_{HV} (kW)	P_{out} (kW)	Eff. (%)
80	0.002	2.4	1.84	0.047	2.5
100	0.02	15	584	135	23
100	0.2	15	1670	1100	65.9

The output current of the OE push-pull MPA in both experiment and simulation are shown in Fig. 6, where the waveform of the simulation agrees well with the experiment. The experiment is summarized below. (1)the peak incident light power to the PCSS $P_0 = 80$ kW; (2)the consumed high voltage power $P_{\text{HV}} = I(t)V_{\text{bias}} = 1.84$ kW; (3)the load RF power $P_{\text{out}} = I(t)^2 R_{\text{load}} = 46.6$ W; (4)the efficiency $\eta = P_{\text{out}}/P_{\text{HV}} = 2.5\%$.

It is obvious that the output power of the load resistor and electric efficiency are both low. We attribute this to the poor quantum efficiency. Wu [8] speculates that with higher quantum efficiency, the resistance of the PCSS will reduce to below 10 Ω, which greatly increases the photocurrent and voltage of the load resistor, and improves the output electric power and efficiency.

To predict the potential performance of the MPA and improve the electric efficiency, simulations are run with variable quantum efficiency, peak light power, and pulse shape. The results are shown in Fig. 7. It can be seen from the figure that by increasing optical power, the maximum efficiency can reach 78.5%, the theoretical limit of class B amplifier. This means that PCSSs' resistance is the main cause of the loss. Also we can reduce the photo resistance by improving the quantum efficiency. The efficiency increase slower after 50%, so it gives a hint to optimize the laser power.

Some simulation results of interest are listed in Table I. In the table, the second row is the actual result of the experiment, while the third and forth rows are speculated parameters to guide the future design, where the quantum efficiency and bias voltage should improve greatly.

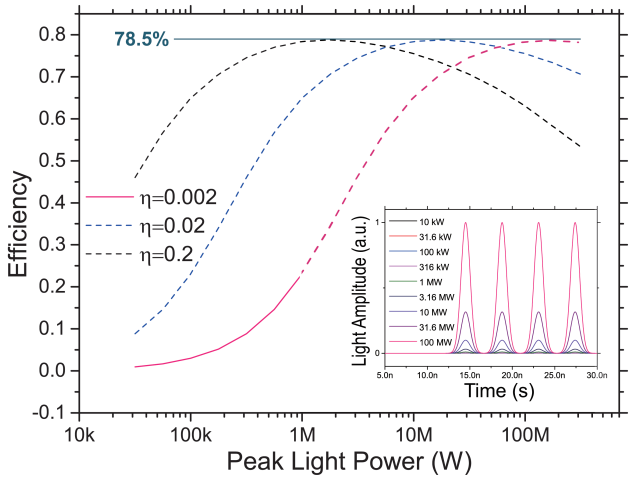

Fig. 7: Simulation effect of quantum efficiency and peak light power on the efficiency of the MPA.

V. Conclusion

This paper puts forward an optoelectronic class B high power microwave amplifier with 6H-SiC, which can operate at kilovolts level and microwave frequency. Initial experiment with bias voltage of $\sim \pm 2.5$ kV and laser of $\sim$100 kW confirms the feasibility of the design. Currently the electric efficiency of the optoelectronic amplifier is limited because of the high photo resistance of the PCSS, where most of the energy is consumed. It is speculated that by improving the quantum efficiency of the 6H-SiC, thus reducing the conducting resistance, much higher efficiency will be achieved. For example, with higher applied bias voltage of 15 kV and quantum efficiency of 0.2, simulations predict that the system could achieve 1 MW microwave power, at the incident laser of 100 kW, and the electric efficiency reach more than 60%.

References

[1] J. Zhang, X. Ge, J. Zhang, J. He, Y. Fan, Z. Li, Z. Jin, L. Gao, J. Ling, and Z. Qi, "Research progresses on cherenkov and transit-time high-power microwave sources at nudt," *Matter & Radiation at Extremes*, vol. 1, no. 3, pp. 163–178, 2016.

[2] J. Benford, J. A. Swegle, and E. Schamiloglu, *High Power Microwaves, Third Edition*. Apple Academic Press Inc., 2015.

[3] J. Capmany and D. Novak, "Microwave photonics combines two worlds," *Nature Photonics*, vol. 1, no. 6, pp. 319–330, jun 2007.

[4] K. S. Kelkar, "Silicon carbide as a photoconductive switch material for high power applications," Ph.D. dissertation, Missouri-Columbia, 2006.

[5] J. S. Sullivan, "Wide bandgap extrinsic photoconductive switches," Ph.D. dissertation, Lawrence Livemore National Laboratory, jul 2013. [Online]. Available: http://www.osti.gov/scitech/servlets/purl/1088462

[6] A. Karabegovic, R. M. O'Connell, and W. C. Nunnally, "Photoconductive switch design for microwave applications," *IEEE Transactions on Dielectrics and Electrical Insulation*, vol. 16, no. 4, pp. 1011–1019, aug 2009.

[7] D. Mauch, W. Sullivan, A. Bullick, A. Neuber, and J. Dickens, "High power lateral silicon carbide photoconductive semiconductor switches and investigation of degradation mechanisms," *IEEE Transactions on Plasma Science*, vol. 43, no. 6, pp. 2021–2031, jun 2015.

[8] Q. Wu, T. Xun, Y. Zhao, H. Yang, and W. Huang, "The test of a high-power, semi-insulating, linear-mode, vertical 6h-SiC PCSS," *IEEE Transactions on Electron Devices*, vol. 66, no. 4, pp. 1837–1842, apr 2019.

Simulation of an X-band Dual-mode Relativistic Backward Wave Oscillator Operating at Low Magnetic Field

Renzhen Xiao
Science and Technology on High Power Microwave Laboratory
Northwest Institute of Nuclear Technology
Xi'an, China
xiaorenzhen@nint.ac.cn

Yanchao Shi
Science and Technology on High Power Microwave Laboratory
Northwest Institute of Nuclear Technology
Xi'an, China
shiyanchao@nint.ac.cn

Huida Wang
Science and Technology on High Power Microwave Laboratory
Northwest Institute of Nuclear Technology
Xi'an, China
wanghuida@nint.ac.cn

***Abstract*—This paper describes the design and simulation results of an X-band dual-mode relativistic backward wave oscillator operating at low magnetic field. In the device, the electron beam interacts with TM_{01} mode and TM_{02} mode in the two-sectioned nonuniform slow-wave structure simultaneously, and the output mode is the mixture of the two modes. In the particle-in-cell simulation, when the diode voltage is 850 kV, diode current is 12 kA, and the guiding magnetic field is 0.64 T, the output microwave power is 3.9 GW, corresponding to a power conversion efficiency of 38%, and the frequency is 9.96 GHz. The maximum axial electric field contributed to electron emission on the electrodynamic structure surface is about -540 kV/cm, and above 85% of the electrons are collected by the collector, which are tolerable in experiment. The experiment is now in preparation.**

Keywords—Cherenkov radiation, high power microwave, relativistic backward wave oscillator, slow-wave structure.

I. Introduction

Since an overmoded relativistic backward wave oscillator (RBWO) with efficient dual-mode operation was presented in 2014 [1], many related studies have been carried out [2-6]. Especially, V. V. Rostov et al. conducted a series of simulative and experimental work on the X-band, Ka-band, and 4 mm wavelength two-wave relativistic Cherenkov oscillators and achieved great results [4-6]. Among them, for the X-band device, power conversion efficiencies in simulation up to 47% and in experiment up to 45% for a high (~4 T) guiding magnetic field were obtained. However, for a low (~1 T) guiding magnetic field, the efficiencies in simulation and in experiment were only 30% and 25%, respectively [4], and the output power was less than 2 GW. In this paper, the simulation of an X-band dual-mode RBWO operating at low guiding magnetic field will be given, aiming at increasing the conversion efficiency and output power.

II. Model Description

The overmoded X-band RBWO is shown in Fig. 1. The electron beam emitted from the annular cathode is modulated during propagating through the AK gap and the two pre-modulation cavities, and the microwave is generated in the two-sectioned nonuniform slow-wave structure (SWS). It should be noted that the cathode holder plays an important role in the reflection of the backward wave, which is similar to the case in an overmoded Ku-band RBWO presented in 2012 [7].

The dispersion curves for a trapezoid SWS with a period of 1.3 cm, a smaller radius of 3.5 cm, and a larger radius of 3.9 cm are shown in Fig. 2. It is obvious that the electron beam interacts with the TM_{01} surface wave synchronously. As for the TM_{02} mode, since the synchronous beam energy is very low (186 keV) and the corresponding coupling impedance (point A) is small [4], the nonsynchronous interaction (point B) will be dominant, especially in the case that the SWS in each section is very short.

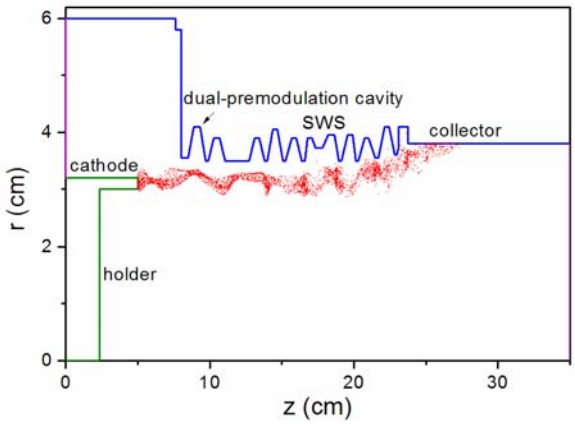

Fig. 1 Schematic model of the overmoded X-band RBWO.

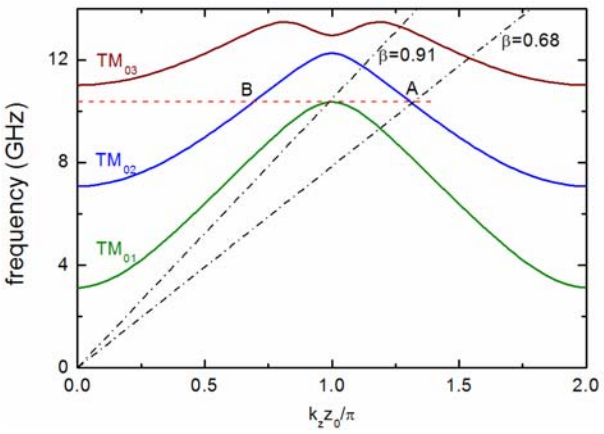

Fig. 2 Dispersion curves of the SWS

III. Simulation Results

After careful optimization of the structure dimensions, when the diode voltage is 850 kV, diode current is 12 kA, and the guiding magnetic field is 0.64 T, the output microwave power is 3.9 GW (Fig. 3), corresponding to a power conversion efficiency of 38%, and the frequency is 9.96 GHz. The maximum axial electric field contributed to electron emission on the electrodynamic structure surface is about -540 kV/cm (Fig. 4), and above 85% of the electrons are collected by the collector (Fig. 5). The operation mode is hybrid TM_{01} and TM_{02} modes. In the output waveguide, the power percentage of TM_{01} mode is 0.34, and that of TM_{02} mode is 0.66. In our opinion, since mode conversion from any mixed TM modes to TM_{01} mode is feasible [8, 9], it is not necessary to restrict the output mode to either pure fundamental mode or pure high order mode while optimizing the structure. Therefore, instead of uniform and symmetrical two-sectioned SWS used in [4], nonuniform and asymmetrical SWS is used. As a result, the efficiency is increased from 30% to 38%.

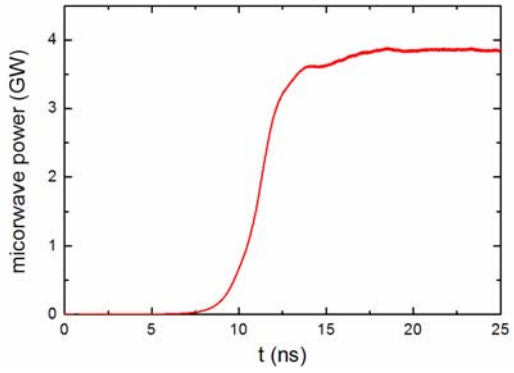

Fig. 3 Output microwave power.

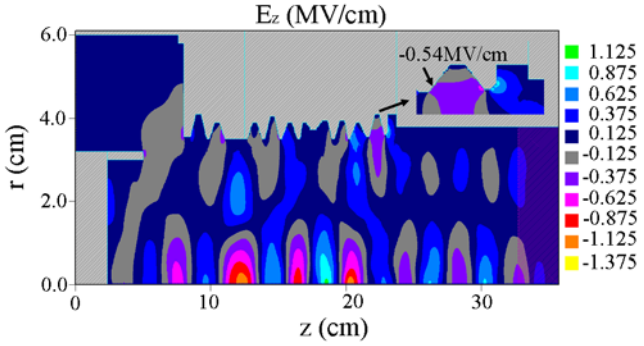

Fig. 4 Axial electric field distribution.

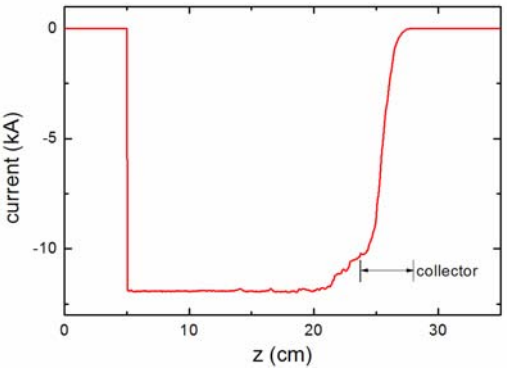

Fig. 5 Electron beam current distribution.

IV. Future Work

Now we are preparing the experiment. Because the output modes are mixed and might vary with the beam parameters and structure dimensions, a radiation field measurement array will be utilized to obtain the output power in one shot, rather than moving one detector shot by shot [10]. Also, an on-line measurement array (Fig. 6) is planned to determine the amplitudes and phases of different modes. According to this result, the mode converter will be designed, and pure TM_{01} mode can be obtained.

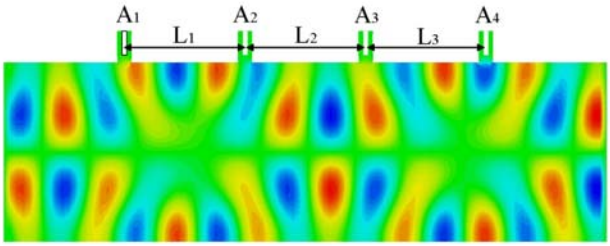

Fig. 6 On-line measurement array. As the mixed TM_{01} mode and TM_{02} mode are propagating in the circular waveguide, the signals obtained from the four probes inserted at different locations are varied, and then the amplitudes and phases of the TM_{01} mode and TM_{02} mode can be solved.

References

[1] R. Z. Xiao, et al., "An overmoded relativistic backward wave oscillator with efficient dual-mode operation, " Appl. Phys. Lett., vol. 104, 093505, March, 2014.

[2] Z. Bai, J. Zhang, and H. H. Zhong, "A dual-mode operation overmoded coaxial millimeter-wave generator with high power capacity and pure transverse electric and magnetic mode output," Phys. Plasmas, vol. 23, 043109, April, 2016.

[3] S. Y. Chen, J. Zhang, and Z. Bai, "A 57 GHz overmoded coaxial relativistic backward wave oscillator with high conversion efficiency and pure TM_{01} mode output," AIP Advances, vol. 7, 105113, October, 2017.

[4] V. V. Rostov, A. V. Gunin, R. V. Tsygankov, I. V. Romanchenko, and M. I. Yalandin, "Two-wave Cherenkov oscillator with moderately oversized slow-wave structure," IEEE Trans. Plasma Sci., vol. 46, pp. 33-42, January 2018.

[5] V. V. Rostov, et al., "Two-wave Ka-band nanosecond relativistic Cherenkov oscillator," IEEE Trans. Electron. Dev., vol. 65, pp. 3019-3025, July 2018.

[6] V. V. Rostov, et al., "Numerical and experimental investigation of 4 mm wavelength microwave oscillator based on high-current compact accelerator, Phys. Plasmas, vol. 25, 073110, July 2018.

[7] R. Z. Xiao, W. B. Tan, X. Z. Li, Z. M. Song, J. Sun, and C. H. Chen, "A high-efficiency overmoded klystron-like relativistic backward wave oscillator with low guiding magnetic field," vol. 19, 093102, September 2012.

[8] D. Zhang, J. Zhang, H. H. Zhong, Z. X. Jin, and Y. Z. Yuan, "Purification of the output modes of overmoded relativistic backward wave oscillators," vol. 21, 023115, February 2014.

[9] J. W. Li, et al., "Dual-cavity mode converter for a fundamental mode output in an over-moded relativistic backward- wave oscillator, " Appl. Phys. Lett. vol. 106, 113505, March, 2015.

[10] Z. Q. Zhang, H. J. Wang, L. J. Zhang, and Y. C. Zhang, "Development of array device for power measurement of high power microwave radiation field," High Power Laser and Particle Beams, vol. 22, pp. 883-886, April, 2010 (in Chinese).

Realization of a wide-band rotationally symmetric antenna for use in reverberation chambers

Ronny Gunnarsson
Saab Aeronautics
Linköping, Sweden
ronny.gunnarsson@saabgroup.com

Carl Samuelsson
Saab Aeronautics
Linköping, Sweden
carl.samuelsson@saabgroup.com

Mats Bäckström
Saab Aeronautics
Linköping, Sweden
mats.backstrom@saabgroup.com

***Abstract*— A realization of a wide-band rotationally symmetric antenna for use in reverberation chambers is presented. The design goal was to obtain a compact antenna and a reflection coefficient lower than -10 dB over at least 0.4 – 18 GHz. Numerical simulations reveal that in order to fulfill the bandwidth requirements it is critical to have a carefully designed transition from the feeding coaxial cable to the antenna element. Additive manufacturing was used to fabricate a demonstrator antenna using PLA-plastic, which was subsequently metallized using electrically conducting paint. Results from both free-space and reverberation chamber measurements verify that the design goals were fulfilled.**

Keywords—antenna, wide-band, numerical simulation, measurement, reverberation chamber, finite integration technique (FIT), additive manufacturing.

I. Introduction

Most antennas used in reverberation chamber (RC) measurements are intended for other test environments and therefore often constructed to meet a specific requirement on the radiation pattern. In a reverberation chamber, the radiation pattern is usually of little importance as long as it does not lead to a direct coupling between the transmitting antenna and the EUT, i.e. to an unstirred component. As pointed out in [1], the ideal antenna for reverberation chamber measurements have low reflection coefficient and losses over the frequency band of interest, and preferably also a compact size. To our knowledge, the hybrid antenna reported in [1] is the only antenna specifically designed for reverberation chambers which has a comparable bandwidth to the antenna proposed in this paper. Basic principles for the type of antenna presented in this paper were published in [2]-[3].

The work reported in this paper was initiated by the EMC-laboratory at Saab Aeronautics. When performing reverberation chamber measurements we currently use a log-periodic antenna (EMCO 3148) in the frequency range 0.4 – 1 GHz and a double-ridged horn (EMCO 3115) in the frequency range 1 – 18 GHz. With a single antenna covering 0.4 – 18 GHz it would no longer be necessary to switch antennas during the measurement campaign and the time for testing would therefore be reduced.

The antenna proposed in this paper was designed using parametric variation and the Finite Integration Technique (FIT) solver in CST Microwave Studio. A demonstrator antenna was fabricated using additive manufacturing and subsequent metallization using electrically conducting paint. Numerical results as well as results from measurements in free-space and reverberation chamber are presented.

II. Geometry

The geometry of the rotationally symmetric antenna is illustrated in Fig. 1. The antenna element, which is mounted above a circular ground plane, consist of three main parts. Closest to the ground plane is a conical section, to which the center pin of the coaxial cable is attached. Next there is an exponentially tapered section, the taper of which is defined by

$$y(z) = C_1 e^{-Rz} + C_2 \tag{1}$$

The constants C_1 and C_2 determines the coordinates of the starting and end point of the taper while R determines the curvature of the taper. The upper most part of the antenna element is an ellipsoid intersected in such a way that the derivative is constant in the intersection between the tapered section and the ellipsoid. (Numerical results, however, reveals that the continuity of the derivative only have minor effects on the impedance matching. The upper section could therefore just as well be replaced by an ellipsoid cut in half.)

A coaxial cable protruding the circular ground plane is used to feed the antenna, see Fig. 2. The coaxial cable has a center pin with diameter d_{coax} and a dielectric with diameter D_{coax} and relative permittivity $\varepsilon_{r,coax}$. The center pin of the coaxial cable is connected to a cylindrical extension with height h_{ext} and diameter d_{ext}, which potentially could be different than d_{coax}.

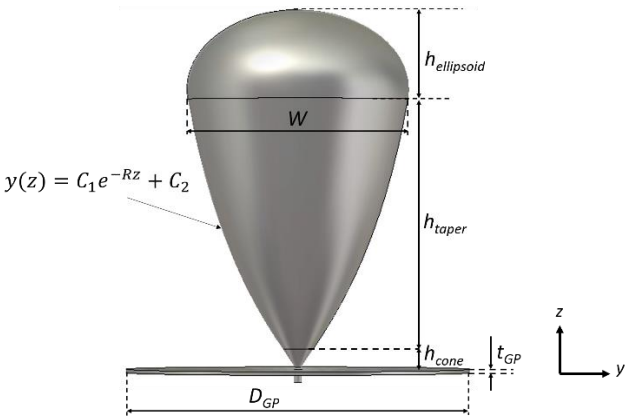

Fig. 1. Geometry of the rotationally symmetric and exponentially tapered antenna.

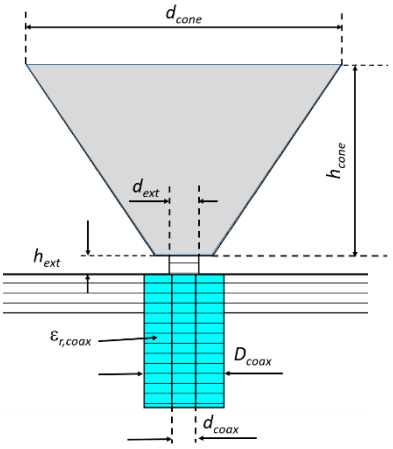

Fig. 2. Cross-section illustrating lower part of the antenna in Fig.1, which constitutes a monocone. Coaxial cable (inner diameter d_{coax}, outer diameter D_{coax} and relative permittivity $\varepsilon_{r,coax}$) protruding the circular ground plane and attaching to the cone with upper diameter d_{cone} and height h_{cone}. The height and diameter of the cylindrical extension between the center pin and the cone is h_{ext} and d_{ext}, respectively.

III. Numerical Simulations

To find a good starting point for the design, parametric variations were performed using the FIT solver in CST Microwave Studio 2018. Apart from the dielectric in the coaxial cable, the entire antenna was modelled as a perfect electrical conductor (PEC). The resulting values of the geometrical parameters of the final antenna design are shown in Table 1. Including the ground plane, the total height of the antenna is 198 mm while the maximum extension in the two orthogonal directions is 187.5 mm. The electrical size of the antenna at the lowest usable frequency is thus approximately $(\lambda/4)^3$, where λ denotes the wavelength at 400 MHz.

The results from the parametric variations revealed that the transition from the coaxial cable to the antenna element is the single most sensitive part in the antenna design. This is illustrated in Fig. 3 where we present the reflection coefficient as a function of the height of the antenna element above the ground plane, i.e. h_{ext} in Fig. 2.

TABLE I. Geometrical Parameters

Parameters	*Value*	*Unit*
h_{taper}	136.25	mm
$h_{ellipsoid}$	48.75	mm
R	0.01	mm^{-1}
D_{GP}	187.5	mm
t_{GP}	2	mm
d_{cone}	16.5	mm
d_{coax}	1.25	mm
h_{cone}	10	mm
D_{coax}	4.18	mm
$\varepsilon_{r,coax}$	2.1	mm
h_{ext}	1	mm
d_{ext} [a]	1.55	mm

[a] "optimal" value. In the manufactured antenna $d_{ext} = d_{coax}$

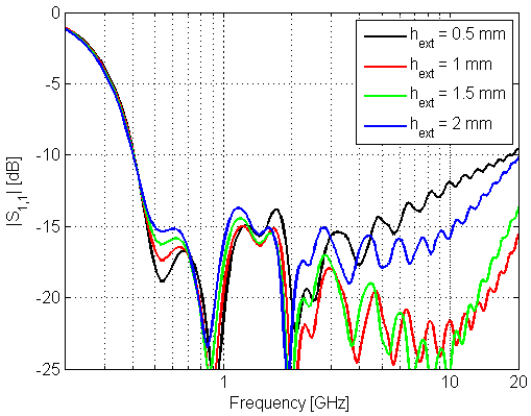

Fig. 3. Magnitude of reflection coefficient as a function of frequency for different values of h_{ext}, see Fig.2. Geometrical parameters according to TABLE I. except that d_{ext} = 1 mm. Frequency range 0.2 – 20 GHz.

For our design, the range of acceptable values in order to obtain low reflection at high frequencies is approximately h_{ext} = 0.75 – 1.5 mm. In order not to compromise the impedance match at high frequencies, the diameter of the cylindrical extension, d_{ext}, should be equal to or slightly larger than the diameter of the center pin of the coaxial cable, d_{coax}. Choosing a slightly larger diameter will result in a stepped impedance transformer and therefore a slightly lower reflection than if $d_{ext} = d_{coax}$.

The results presented in Fig. 3 illustrate that care has to be taken when designing the feed region of the antenna. It should, however, be pointed out that with a careful design the antenna is very well impedance matched over at least 0.4 – 18 GHz.

Since powerful amplifiers are often used in reverberation chamber measurements, and since the separation between the antenna element and the ground plane is small, the risk of electrical flashover needs to be investigated. Assuming that the antenna is perfectly impedance matched, the peak electric field strength can be approximated by $E_{peak} = \sqrt{PZ}/h_{ext}$, where P denotes the peak power of the amplifier and Z denote the impedance of the coaxial cable. For an amplifier with peak power P = 200 W and a coaxial cable with impedance Z = 50 Ω the resulting estimate becomes E_{peak} = 1 kV/cm. This is considerably lower than the often-quoted value for the field strength required for flashover in air, which is 30 kV/cm.

To verify the validity of the estimated value above, a numerical simulation was performed where the electrical field strength in the feed region was calculated. Since the simulations were performed with a peak input power P = 1 W it follows from the equation above that E_{peak} should be approximately equal to 7 kV/m (= 77 dBV/m). This corresponds well with the numerically calculated values, which ranged from 6.9 – 7.8 kV/m over the frequency range 0.5 – 18 GHz. The numerically calculated electrical field strength at 4 GHz is illustrated in Fig. 4.

IV. Manufacturing

Additive manufacturing was used to fabricate a demonstrator antenna consisting of PLA (polyactic acid) plastic. The ground plane was, however, manufactured from aluminum. To simplify the 3D-printing, the antenna was divided into its three constituent parts, i.e. the conical section, the exponentially tapered section and the intersected ellipsoid.

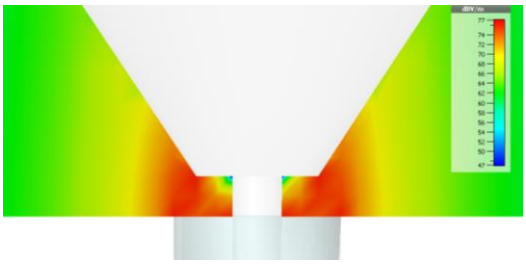

Fig. 4. Magnitude of numerically calculated electrical field strength (dBV/m) at 4 GHz when the peak input power P = 1 W. The colorbar extends from 77 dBV/m (red) to 47 dBV/m (blue). Close-up of the feed region of the antenna in Fig.1.

The printed parts were subsequently metallized using electrically conducting paint and the two larger sections of the antenna element were glued together. Next, the conical section was connected to the center pin of the coaxial cable mounted into the ground plane. A test measurement of the reflection coefficient for this so called monocone antenna, see Fig.2, was performed in order to verify that the sensitive transition from coaxial feed to antenna element had been properly installed. Since excellent agreement was obtained between the measured and simulated results we could proceed with the final assembly of the antenna.

V. Measurements

The reflection coefficient, $S_{1,1}$, of the antenna was first measured outside the reverberation chamber at a location far from any reflecting metallic objects. These "free space" measurements were conducted partly since all numerical simulations were performed on an antenna in free space.

Next, the antenna was placed in a reverberation chamber at Saab Aeronautics which has a volume of 5×3×2.5 m^3 and a lowest usable frequency of 200 MHz. Two sets of 3-port measurements where performed. In the first case we used our antenna and two EMCO 3148 antennas and in the second case we used our antenna and two EMCO 3115 antennas. Prior to the reverberation chamber measurements, a full 3-port calibration was performed. Reflection, $S_{1,1}$, and transmission, $S_{2,1}$, was measured at 1601 logarithmically spaced frequencies over the frequency range 0.2 – 18 GHz and with a total of 143 independent positions for the two mode stirrers. The vector-averaged reflection coefficient from the reverberation chamber measurement is presented in Fig. 5 along with the measured and simulated free-space reflection coefficient. Excellent agreement is obtained between the free-space results, except in the frequency range 10 – 16 GHz, where the measured free-space reflection is very low. The reverberation chamber results agrees well with the free-space results especially at frequencies between 3 and 10 GHz. As of yet we cannot explain the deviations at lower frequencies. It should, however, be emphasized that the vector-averaged reflection coefficient is still lower than -10 dB over 0.4 – 18 GHz.

Over the frequency range 0.4 – 1 GHz, the vector-averaged transmission, $<|S_{2,1}|^2>$, between our antenna and the EMCO 3148 antennas is within ± 0.5 dB of that between the two EMCO 3148 antennas. The same holds true when comparing the results over 1 – 18 GHz for the measurement set including the EMCO 3115 antennas. This indicates that the losses in our antenna are comparable to those of the two commercial antennas currently used for RC-testing.

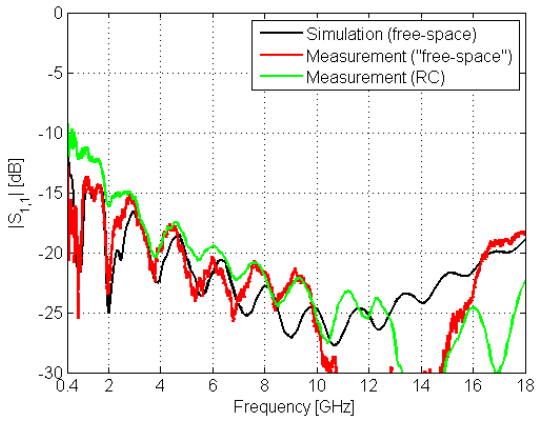

Fig. 5. Magnitude of reflection coefficient simulated (black) and measured in "free space" (red) and in RC (green). Numerical simulation performed with a finer mesh than the one used when producing the results in Fig. 3.

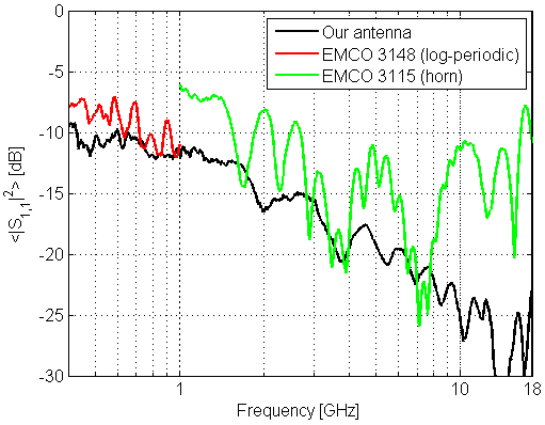

Fig. 6. Vector-averaged reflection, $<|S_{1,1}|^2>$, calculated from reflection, $S_{1,1}$, measured in the RC. Results for our rotationally symmetric antenna (black), EMCO 3148 log-periodic antenna (red) and EMCO 3115 horn antenna (green). Frequency range 0.4 – 18 GHz.

VI. Conclusions

A compact and wide-band rotationally symmetric antenna for reverberation chamber measurements has been described. Numerically calculated as well as measured reflection coefficient is lower than -10 dB over at least 0.4 – 18 GHz. Excellent agreement is obtained between simulated and measured results for an antenna in free-space. The vector-averaged reflection measured for our antenna is on average lower than that of the two commercial antennas we currently use for RC-testing, see Fig.6. At the conference additional numerical results will be presented which demonstrate that, if required, the upper bandwidth limit can be extended to at least 40 GHz by using coaxial cables with smaller dimensions, i.e. cables with higher cutoff frequencies.

References

[1] I. D. Flintoft et al., "Analysis of a hybrid broadband reverberation chamber antenna", IEEE/EMC Europe 2015, Dresden ,Germany, 16-22 August,, 2015.

[2] C. E. Baum, "A circular conical antenna simulator", Sensor and Simulation Notes 36, March 1967.

[3] G. D. Sower, "Optimization of the asymptotic conical dipole EMP sensors", Sensor and Simulation Notes 295, 30 October 1986.

Study on the δ-Domain Model of Electromagnetic Pulse Test

Rupo MA
Department of Computer Information and Cyber Security
Jiangsu Police Institute
Jiangsu，China
mrpjet@163.com

Jun Zhang
Department of Computer Information and Cyber Securit
Jiangsu Police Institute
Jiangsu，China
Zhang-jun@jspi.cn

Zhenli Wang
Department of Computer Information and Cyber Securit
Jiangsu Police Institute
Jiangsu，China
dongwen3619@sina.com

***Abstract*—In the time-domain test of electromagnetic pulse, the z-domain discrete system transfer function is usually used to describe the response characteristics of the test system. However, with the change of sampling frequency, the parameters of the z-domain model should change accordingly, which leads to inconvenience in modeling the test system. In this paper, a δ-domain transfer function model of the test system is constructed by the transformation from z-domain. And the δ-domain model has better stability at high sampling rate and can be approximately equivalent to the system transfer function in the continuous-time domain.**

Keywords—electromagnetic pulse, time-domain test, z-domain model, δ-domain model, system transfer function

I. INTRODUCTION

Due to the influence of parasitic circuit parameters, impedance matching and bandwidth, the electromagnetic pulse test results are often distorted. The time-domain dynamic calibration model based on system identification can better solve this problem [1-2]. Through the time-domain calibration model, the pulse response index, sensitivity, dynamic range, response bandwidth and nonlinear distortion of the system can be obtained, and then the waveform of the test field can be reconstructed and restored.

Since the time-domain test results of electromagnetic pulse are generally discretized data, the z-domain discretized transfer function model H(z) is usually adopted to represent the system transfer function. This model is simple in structure, convenient for calculation, and can be used to analyze the response characteristics in time-domain and frequency-domain. However, the z-domain transfer function model is closely related to the sampling interval of the measured waveform. With different sampling intervals, the parameters of the z-domain model will change. When sampling at a high speed, the z-transform may appear that the poles are located on the stable boundary, and its quantization error may lead to the deterioration of the system stability [3]. To solve this problem, a δ-domain transfer function model is proposed in this paper. By applying δ transformation from the z-domain model H(z), a stable system transfer function model with approximate continuous-time domain (s-domain) is constructed.

II. δ OPERATOR AND TRANSFORMATION

The δ transform was first proposed as Euler approximation and was used in digital filtering [4-5], but it was not noticed at that time. The δ transformation was carried out as a pioneering research until 1986 by Goodwin et al. and began to attract wide attention [6]. The δ transform is a new discretization method, which can solve the instability of the system model caused by the small sampling interval of the z model [7-8]. In the case of fast sampling, the discrete model of the δ operator approaches the continuous-time domain model. Therefore, the δ operator is used as a unified description method for continuous-time domain model and discrete-time domain model [9].

δ operator is defined as [10]

$$\delta = \frac{q-1}{T} \tag{1}$$

where, q is the forward shift operator, and T is the sampling interval. In the δ-domain, the corresponding variable of the δ operator is γ . When mapping from z-domain to δ-domain, the above formula can be written as

$$\gamma = \frac{z-1}{T} \tag{2}$$

For the z-domain system model

$$H(z)=\frac{b_0+b_1z^{-1}+b_2z^{-2}+\cdots+b_nz^{-n}}{a_0+a_1z^{-1}+a_2z^{-2}+\cdots+a_mz^{-m}} \tag{3}$$

substitute $z=T\gamma+1$ into the above equation,

$$H(\gamma)=\frac{b_0+b_1(T\gamma+1)^{-1}+b_2(T\gamma+1)^{-2}+\cdots+b_n(T\gamma+1)^{-n}}{a_0+a_1(T\gamma+1)^{-1}+a_2(T\gamma+1)^{-2}+\cdots+a_m(T\gamma+1)^{-m}} \tag{4}$$

the δ-domain system model can be obtained by expanding the above formula

$$H(\gamma)=\frac{b_0'+b_1'\gamma^{-1}+b_2'\gamma^{-2}+\cdots+b_n'\gamma^{-n}}{a_0'+a_1'\gamma^{-1}+a_2'\gamma^{-2}+\cdots+a_m'\gamma^{-m}} \tag{5}$$

The coefficients of b_i' and a_i' are [11]

$$a_i'=T^i\sum_{j=i}^{m}a_jC_j^i \tag{6}$$

$$b_i'=T^i\sum_{j=i}^{n}b_jC_j^i \tag{7}$$

where， $C_j^i=\frac{j!}{i!(j-i)!}$.

Fund project: scientific research project of introducing high-level talents into Jiangsu Police Institute (project no. 2911118010)

When the zero-pole method is used to represent the system model, the transformation of the zero-pole from the z-domain to the δ-domain is linear. Supposing the zero-poles of the z-domain are z_k and p_k, the zero-poles o_k and ρ_k of the δ-domain are

$$o_k = \frac{z_k - 1}{T} \tag{8}$$

$$\rho_k = \frac{p_k - 1}{T} \tag{9}$$

III. INTERPRETATION OF RESULT

A. Inconsistency of H(z)

A group of time-domain waveforms measured by the magnetic field (B) sensor are shown in figure 1, and the system transfer function H(z) curve obtained by system identification tool is shown in figure 2. It is found by comparison that when the sampling interval is changed, the transfer function curves of the system are obviously different, which means the sampling frequency has significant influence to z-model. In figure 2, the system transfer function curves at sampling intervals of 1ns, 0.5ns and 0.2ns are significantly different, while the system transfer function curves at sampling intervals of 0.1ns tend to be consistent with that at 0.2ns.Therefore, the sampling interval of 0.2ns is a limit value of the transfer function of the system, and the corresponding sampling frequency is about 10 times the highest frequency of the input signal.

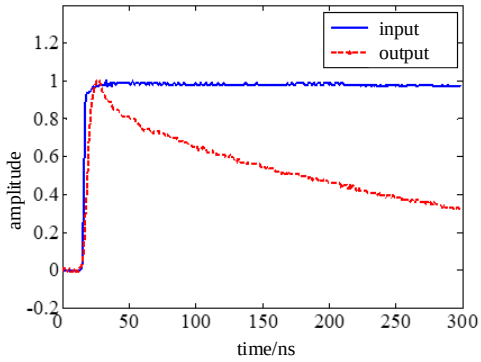

Figure 1 Measured input and out put in B sensor calibration

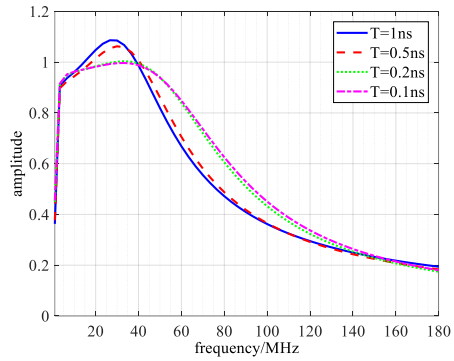

Figure 2 Amplitude-frequency curve of the discrete transfer functions in z-domain

B. Validity of the δ Transform

Taking a given continuous-time domain system function model as an example, the validity of the transformation from z-domain to δ-domain is verified. Let the continuous-time domain system model be

$$H(s)=\frac{0.2s^2+0.3s+1}{s^3+0.5s^2+0.4s+1} \tag{10}$$

For the above formula H(s), the transformation from s-domain to z-domain is realized through the Matlab function c2dm (custom sampling interval T), and the transfer function H(z) in discrete-time domain is obtained. The zero-poles of H(z) are substituted into the formulas (8) and (9) to obtain the zero-poles of the δ-domain, and then the δ-domain model coefficients are obtained through the function zp2tf. Because the δ-domain model could approximate to the continuous-domain model at high sampling rate, the amplitude-frequency curve and step response curve of the transfer function can be obtained by functions freqs and step respectively.

When the sampling interval T of H(s) is different, the numerator and denominator coefficients of the system model mapped to the δ-domain are shown in table 1. The amplitude-frequency curve of the system transfer function is shown in figure 3, and the system step response curve is shown in figure 4.

TABLE 1 NUMERATOR AND DENOMINATOR COEFFICIENTS OF δ-DOMAIN MODEL

T (s)	numerator coefficients			denominator coefficients			
	b_0'	b_1'	b_2'	a_0'	a_1'	a_2'	a_3'
0.1	0.2113	0.3903	0.9751	1	0.5316	0.5367	0.9751
0.01	0.2010	0.3092	0.9975	1	0.5028	0.4140	0.9975
0.001	0.2001	0.3009	0.9998	1	0.5003	0.4014	0.9998
0.0001	0.2	0.3001	1	1	0.5	0.4001	1

As can be seen from table 1, with the decrease of the sampling interval, the differences between the coefficients of the δ-domain system transfer function obtained at different sampling intervals become smaller. In the table, when the sampling interval is 0.001s and 0.0001s, the numerator and denominator coefficients of the system transfer function is very close to the continuous-time domain(s-domain) function. It can also be seen from the figure 3 and figure 4 that the amplitude-frequency curves and the step response curves of the system are in good agreement with these of the continuous-time domain when the sampling interval is 0.001s and 0.0001s. It means the frequency response and the step response remain consistent in small sampling intervals, and the δ-domain model can approximate the s-domain model.

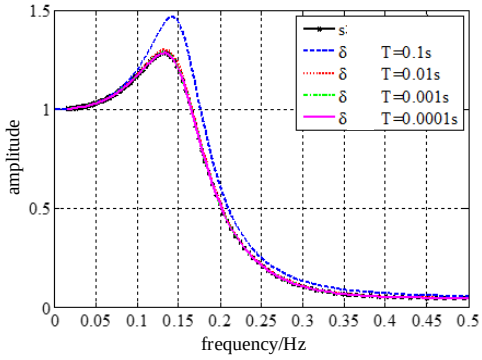

Figure 3 Amplitude-frequency curve of the system transfer function

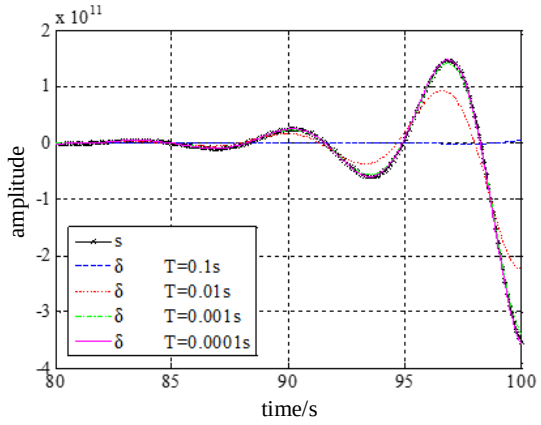

Figure 4 Step response the system obtained at different sampling interval

C. δ-Domain System Model of the B sensor

As for the z-domain transfer function model of the B sensor shown in figure 2, δ transformation can be carried out to obtain the δ-domain system model. The B sensor δ-domain model with sampling intervals of 1ns, 0.2ns, 0.1ns and 0.05ns can be obtained by linear interpolation method, and the numerator and denominator parameters are shown in table 2, the amplitude-frequency curve of the transfer function is shown in figure 5, and the step response is shown in figure 6.

TABLE 2 NUMERATOR AND DENOMINATOR COEFFICIENTS OF δ-DOMAIN MODEL OF B SENSOR

T (ns)	numerator coefficients			denominator coefficients			
	b_0' ($\times 10^8$)	b_1' ($\times 10^{17}$)	b_2' ($\times 10^{23}$)	a_0'	a_1' ($\times 10^8$)	a_2' ($\times 10^{17}$)	a_3' ($\times 10^{24}$)
1	1.9613	0.4731	0.3299	1	3.1551	0.5251	0.2419
0.2	1.5476	1.3206	2.4322	1	4.8443	1.4093	0.9502
0.1	1.5142	1.4667	2.8492	1	5.0894	1.5584	1.0809
0.05	1.5179	1.5330	3.0087	1	5.1992	1.6264	1.1351

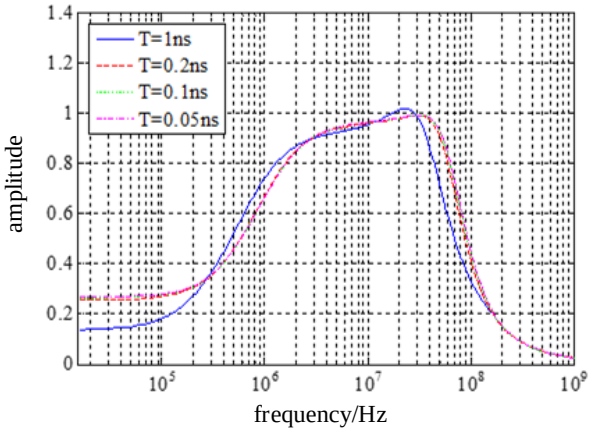

Figure 5 Amplitude-frequency response of B sensor

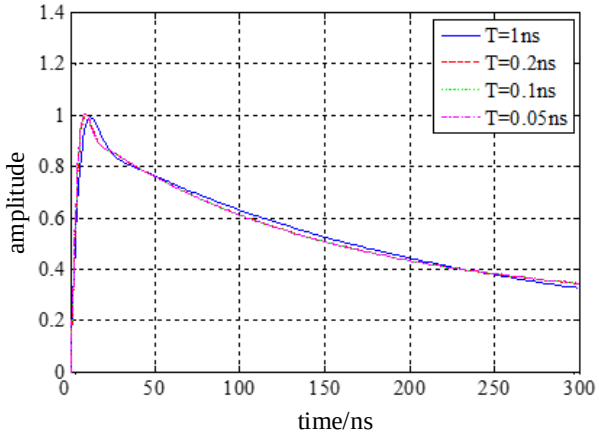

Figure 6 Step response of B sensor

It can be seen from the table 2, when the sampling interval is 0.1 ns and 0.05 ns, The difference of the numerator and denominator coefficients of the system transfer function is not much. The amplitude-frequency response and the step response as also remain almost the same in figure 5 and figure 6. Therefore, the δ-domain model could approximate s-domain model when the sampling interval is less than 0.1 ns.

IV. CONCLUSION

In time-domain test of electromagnetic pulse, discrete transfer function model in z-domain is usually adopted. This model can conveniently describe the response characteristics of the measurement system with limited parameters, but with the change of sampling interval, the parameters of the z-model should change accordingly. This paper proposes a δ transformation method to construct a δ-domain transfer function model. It is verified that the δ-domain model is more stable and approximates the s-domain system transfer function at higher sampling frequencies, and which provides a convenient tool for transforming z-domain models between different sampling frequencies.

REFERENCES

[1] Shi L H, Tan J W, Zhou B H. Time domain calibration of pulsed current probe [J]. Electromagnetic Compatibility. 17th International Zurich Symposium on, 2006: 296-299.

[2] Shi L H, Zhou B H, Tao B Q. A discrete transfer function model for the time-domain calibration data of EMP sensors [J]. Electromagnetic Compatibility, 13th International Zurich Symposium on, 1999: 149-152.

[3] Yang H J, Xia Y Q, Li H G. An Overview of Delta Operator Systems[J]. Control Theory & Applications, 2015, 32(3): 569-578.

[4] Agarwal R C, Burrows C S. New recursive digital filter structures having low sensitivity and roundoff noise [J]. Circuits System, IEEE Transactions on, 1975, 22(12): 921-927.

[5] Orlandi G, Martinelli G. Low-sensitivity recursive digital filters obtained via the delay replacement [J]. Circuits System, IEEE Transactions on, 1984, 31(7): 654-657.

[6] Goodwin G C, Sin K S. Adaptive Filtering, Prediction and Control [M]. Englewood Cliffs, NJ: Prentice-Hall, 1984.

[7] Zhang D J. Modeling and Control of Delta Operator Systems[D]. Nanjing: Degree thesis of Nanjing University of Technology, 2007.

[8] Astrom K L, Hagander P, Sternby J. Zeros of sampled systems [J]. Automatica, 1984, 20(1): 31-38.

[9] Middleton R H, Goodwin G C. Improved finite word length characteristic in digital control using delta operators [J]. Automatica control, IEEE Transactions on, 1986, 31(11): 1015-1021.

[10] Middleton R H, Goodwin G C. Digital Control and Estimation: A Unified Approach [M]. Englewood Cliffs, NJ: Prentice-Hall, 1990.

[11] Zhang W Y, Zhang D J. Coefficient Vectors Between Transformation of δ and Z Domain Transfer Functions[J]. Journal of Zhengzhou University, 2003, 35(1): 23-26.

Simulation Study on Lightning Indirect Effect of Metal Cylinder

1st Ruitao Huang
No. 1 Xiaolingwei, Xuanwu District
Nanjing, China
190485346@qq.com

2nd Yantao Duan
National Key Laboratory on Electromagnetic Environmental Effects and Electro-optical Engineering, Nanjing, China
dcmchdyt@126.com
(Corresponding author)

3rd Lihua Shi
National Key Laboratory on Electromagnetic Environmental Effects and Electro-optical Engineering, Nanjing, China
lihuashi@aliyun.com

4th Wei He
No. 1 Xiaolingwei, Xuanwu District
Nanjing, China
hovijfj@163.com

5th Lili Shan
No. 1 Xiaolingwei, Xuanwu District
Nanjing, China
18020106855@qq.com

6th Zhenhai Zheng
No. 1 Xiaolingwei, Xuanwu District
Nanjing, China
451140811@qq.com

***Abstract*—In order to study the lighting indirect effects on the metal cylinder, this paper studies and analyzes the electromagnetic field coupled inside the metal cylinder model and the transient current on the internal cable based on the CST simulation software. By simulating the internal magnetic field intensity distribution and the internal cable coupling current, the response law is summarized. The result is helpful for the further research on the lightning indirect test of metal cylinder.**

Keywords—metal cylinder, lightning indirect effect, magnetic field intensity, coupling current

I. INTRODUCTION

Lightning is a natural discharging process with intense intensity [1]. The lightning effect on the flying objects is divided into direct effect and indirect effect. The direct effect cause the physical damage, such as the holes in flying metal skin around the hit point. Indirect effect is that when lighting hit the flying object, a large current pulse produces during the discharging process of lightning and it is a pulse with a fast rise time and a short duration. At the same time it produces a strong transient electromagnetic field [2-3]. The strong transient electromagnetic field and the current pulse can interfere or damage the avionics system of the flying object. In the last few years, more and more researchers pay attention to the indirect effects on the flying objects [4-5].

Recently, we presented a method to constructing the experimental device for lightning indirect effect on the metal cylinder flying object [6]. It is showed in Fig.1. A cage-like frame was designed as the coupling device to carrying the impulse current injection tests. This paper studies the coupling law inside metal cylinders based on the CST simulation software.

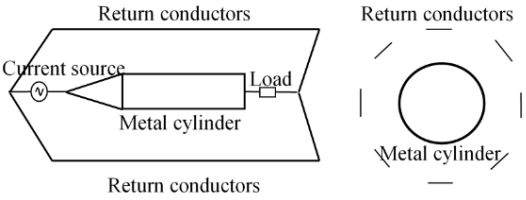

(a)Test system connection (b) The cross section

Fig. 1. The metal cylinder test configuration with coaxial return path

II. MODEL

Figure 2 is the simulation model. The length of metal cylinder is 2m, the thickness of metal cylinder is 3mm, and the end of the cylinder is open. Lightning current flows from the head to tail of the metal cylinder.

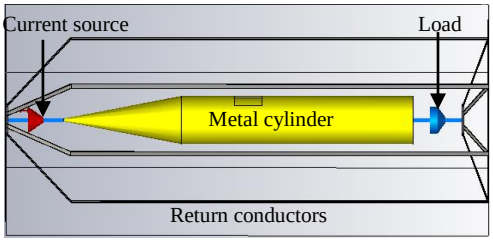

Fig. 2. The CST model

There are 16 magnetic field probes inside the model. The probe distribution is shown in the figure 3. The magnetic field probe is placed on the axis of the model every 10 cm. So the distance *L* between the probe and the point (0, 0, 0) is 0, 10, 20, ... , 150 cm.

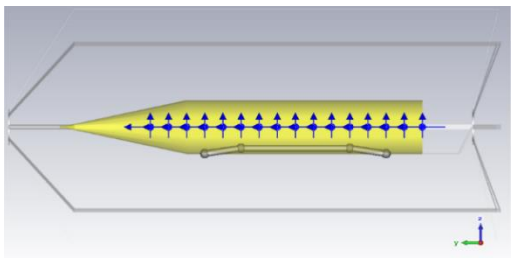

Fig. 3. Distribution of internal electromagnetic field probe and distribution of internal cable

The internal cable settings are shown in the figure 3. The cable includes two types, which are single wire and RG58 coaxial wire. The length is 1 m. The two ends of the single wire are connected to metal cylinder. The outer shield of the coaxial wire is connected to the casing at both ends. Both ends of the core are connected to the ground with 50Ω resistance.

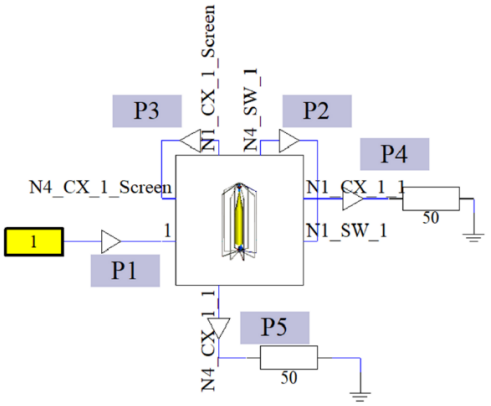

Fig. 4. Schematic diagram

Figure 4 is the schematic diagram of the system simulation circuit. The injected current is lightning current component A with levels of 1, 2, 5, 10, 20 and 50 kA, respectively. The electromagnetic field and cable coupling current are calculated by the method of field path coordination.

III. Simulation Results and Analysis

A. *Internal coupling magnetic field*

Figure 5 shows the magnetic field waveforms at monitoring point (0, 20 cm, 0) and monitoring point (0, 30 cm, 0). It can be seen that the waveform of magnetic field intensity at the two coordinate points is basically same as the waveform of injection current. In addition, it can be seen that the magnetic field strength at L = 30 cm is attenuated by about 13.5 dB compared to the magnetic field strength at L = 20 cm.

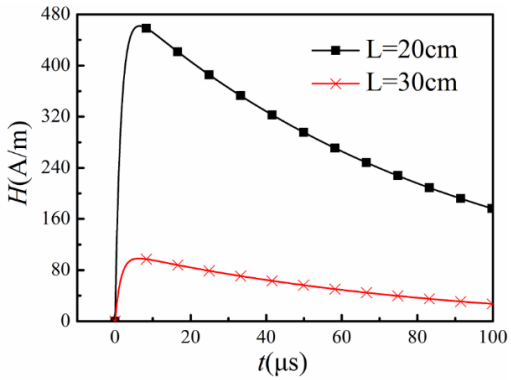

Fig. 5. Magnetic field waveform at two monitoring points when injection current I=2kA

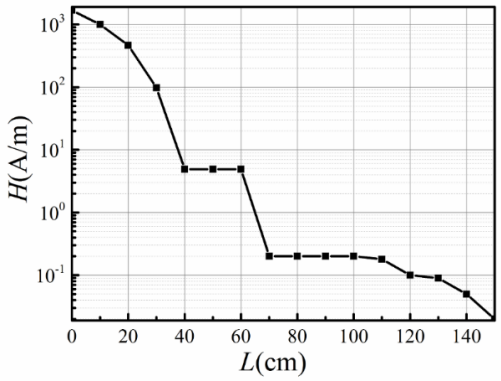

Fig. 6. Magnetic field intensity curve with L when injection current I=2kA

Figure 6 shows the peak value of the magnetic field intensity at different monitoring points with L when the injection current is I=2kA. With the increasing of L, the peak value of the magnetic field intensity generally

decreases. That is, the larger the rear end opening of the rocket model, the weaker the magnetic field strength. The magnetic field intensity at the point (0, 0, 0) is about 1700 A/m, and the magnetic field intensity has rapidly decayed to 5 A/m when L = 40 cm.

B. Internal Coupling Current in Cable

Figure 7 shows the waveform of coupling current on a single wire when injection current is 2kA. It can be seen that the peak value is about 0.28A. And the waveform of the coupled current is narrower than the waveform of injected current. The half-peak width is reduced.

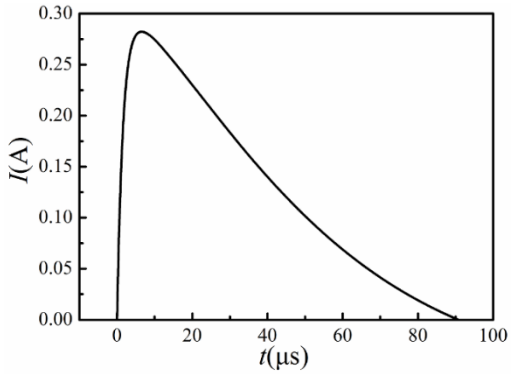

Fig. 7. Coupled current waveform on single wire

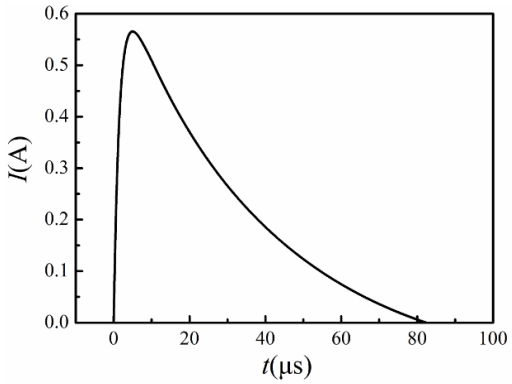

Fig. 8. Coupled current on outer shield

Figure 8 shows the coupling current waveform of the outer shield when the injection current is 2kA.Figure 9 shows the coupling current waveform on the core when the injection current is 2kA. It can be seen that the peak value on the outer shield is about 0.56A, the peak value of the induced current on the core is about 0.0004A. The current value of the core is attenuated by about 63dB from the peak value of the outer shield. Therefore, the outer shield of coaxial wire provides a good shielding effect. In addition, the outer shield current waveform is narrower than the injected current A wave waveform, that is, the full-width at half-maximum is reduced. The induced current waveform in core wire starts from a large oscillation and follows by a double exponential waveform.

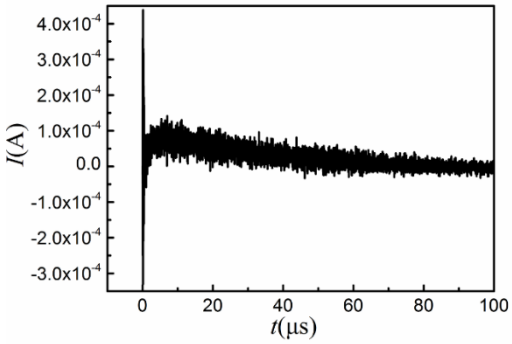

Fig. 9. Coupled current waveform on coaxial wire

CONCLUSION

This paper simulates and analyzes the response law of internal magnetic field and the current on cable. There are some conclusions obtained:

The waveform of magnetic field intensity in the metal cylinder is basically same as the waveform of injection current. With the increasing of L, the peak value of the magnetic field intensity generally decreases.

The coupling current waveform on the internal cable is different from the waveform of the injection current. The waveform of the coupled current is narrower than the waveform of injected current. The half-peak width is reduced. The current value of the core is attenuated by about 63dB from the peak value of the outer shield. Therefore, the outer shield of coaxial wire provides a good shielding effect.

REFERENCES

[1] B. Zhou, L. Shi and C. Gao, “Electromagnetic Protection of National Defense Engineering”, National Defense Industry Press, Beijing, 2005.

[2] S. Qi, X. Li, S. Han, et al. “Discrimination of nuclear explosion and lighting electromagnetic pulse using frequency image analysis”. High Power Laser and Particle Beams, 2013, 25(2), pp: 522-526.

[3] P. Li, L. Song, C. Han, et al. “Rocognition of NEMP and LEMP signals based on auto regression model and neutral network”. High Power Laser and Particle Beams, 2010, 22(12), pp. 3052-3056.

[4] M. Meyer, F. Flourens, J.A. Rouquette and A. Delnevov, “Modeling of lightning indirect effects in CFRP Aircraft”, International Symposium on Electromagnetic Compatibility – EMC Europe, 2008, pp. 1–5.

[5] X Li, Z Zhou, Z Chen, et al. “Propagation and suppression method of lightning wave in coaxial line”. International Journal of Applied Electromagnetics & Mechanics, 2015, 49(3), pp. 315-325.

[6] R. Huang, Y. Duan, K. Luo and L. Shi, “Simulation research on the return conductor configuration for lightning indirect effect test of metal cylinder”. *The 5th* International *Symposium on Electromagnetic Compatibility*, Beijing, 2017, 494-497.

A TEM Horn Array fed by UWB Power Divider

Sen Yan*, Yan Zheng, Anxue Zhang
School of Electronic & Information Engineering Xi'an Jiaotong University, Xi'an, China
Corresponding Email: sen.yan@xjtu.edu.cn

***Abstract*—An ultrawideband (UWB) horn array is proposed in this paper. The element antenna is an exponentially tapered transverse electromagnetic (TEM) horn antenna, and end loop loaded technology is used to enhance the impedance matching at low frequencies. A UWB Wilkinson power divider is used to feed the 4 element array. Two modifications are applied to extend the bandwidth of the power divider with low insert losses. The numerical results show that an impedance bandwidth from 1 GHz to 10 GHz is obtained, and the gain of the array is noticeably improved compared to the single horn antenna, especially at lower frequencies.**

Keywords—TEM horn, horn array, ultrawideband (UWB) power divider

I. INTRODUCTION

Monopulse radar technology has been widely used in through-wall radar (TWR) systems and ground penetrating radar (GPR) systems. Since a monopulse contains much wider frequency spectrums than a narrow band signal, monopulse radar can provide more information than other radar systems. Besides, modulators and demodulators can be replaced by pulse sources and high speed analog-to-digital converters in such a radar system, which will significantly simplify the design and implementation procedures.

Ultrawideband (UWB) antennas are a key component in monopulse radar systems. The normal requirements for the UWB antennas include wide bandwidth, high gain, linear phase delay, compact size, and etc. Several types of UWB antennas have been designed for radar applications, e.g. helical antennas, bowtie antennas, log-periodic antennas, Vivaldi antennas and transverse electromagnetic (TEM) horn antennas. Usually, TEM horn antennas have the highest gain and thus been a perfect candidate in deep ground detection [1-7].

However, the lowest operating frequency of a TEM horn antenna is mainly determined by its length. In this paper, an exponential TEM horn is designed and loaded with an end loop structure, which can help to reduce the length and enhance the matching at low frequencies. The final dimension of the proposed horn is 10 x 9 x 5 cm^3, and the bandwidth covers from 1 GHz to 10 GHz. Besides, a UWB Wilkinson power divider is designed and used to feed a 4-element horn array. By using multi-section transmission lines (TL) and open circuited (OC) stub impedance transformers, the bandwidth of the Wilkinson power divider is extended to 1:10 with reasonable performance [8-13]. The numerical results show that the array can significantly improve the gain at lower frequencies, which can remarkably improve the detecting depth in GPR systems. However, due to the higher insert losses, the gain of the array drops back to the similar value compared to a single element horn antenna at the higher frequencies.

II. TEM HORN ANTENNA

A TEM horn can be recognized as an impedance transformer, whose characteristic impedance gradually changes from 50 Ω of the feeding line to 120π Ω of the free space. To realize such an impedance transformer, a parallel plate TL is usually chosen as the basic topology of the TEM antennas. The characteristic impedance Z of a parallel plate TL can be expressed by

$$Z=\begin{cases}\dfrac{\eta}{2\pi}\ln\left(8\dfrac{d}{w}+4\dfrac{w}{d}\right) & \dfrac{w}{d}\le 1\\ \dfrac{\eta}{1.393+\dfrac{w}{d}+\dfrac{2}{3}\ln\left(\dfrac{w}{d}+1.444\right)} & \dfrac{w}{d}>1\end{cases} \tag{1}$$

where w and d are the width and height of the parallel plate, respectively. η is the characteristic impedance of the free space (120π Ω). Eq. (1) reveals that Z is totally determined by w/d. Adjusting the shape of the parallel plate TL can tune the characteristic impedance at each point of the antenna. Thus, the total reflection coefficient at the input port can be calculated by the theory of small reflections.

$$\Gamma(\theta)=\frac{1}{2}\int_{z=0}^{L}e^{-2j\beta z}\frac{d}{dz}\ln\left(\frac{Z}{Z_0}\right)dz \tag{2}$$

where $\theta = 2\beta l$, and L is the length of the TEM horn.

In theory, a TEM horn with infinite length can provide infinite bandwidth, but that is impossible in practice. A problem is that there is an open circuit point at the end of the horn. Though its impedance can be tuned to match the impedance of the free space, it brings a strong reflection at lower frequencies. Some scholars pointed out that lower aperture impedance at the end of horn can reduce the reflection [4-5]. To get the best matching performance, the aperture impedance of the horn should be set within the range from 200 Ω to 300 Ω. Usually, a relatively large aperture can provide better bandwidth and gain for the antenna, but the length of the horn should also be increased to obtain a gradual change of impedance and the uniform phase of the aperture field. To reduce the length of the horn, end-load technology will be introduced in this design [6,7]. The parallel plates are curved back after the maximum aperture, and form two low frequency loops, which can extend the path of the current flowing, and improve the matching at low frequencies. Besides, the current loop can help to enhance the radiation as a magnetic dipole, which will also increase the gain of the TEM horn antenna. The loaded section should satisfy the impedance matching, i.e.

$$\frac{1}{R_{aperture}}=\frac{1}{R_{loaded}}+\frac{1}{\eta} \tag{3}$$

where $R_{aperture}$ is the impedance of the aperture of the horn, R_{loaded} is the impedance of the loaded section, and η is the characteristic impedance of the free space.

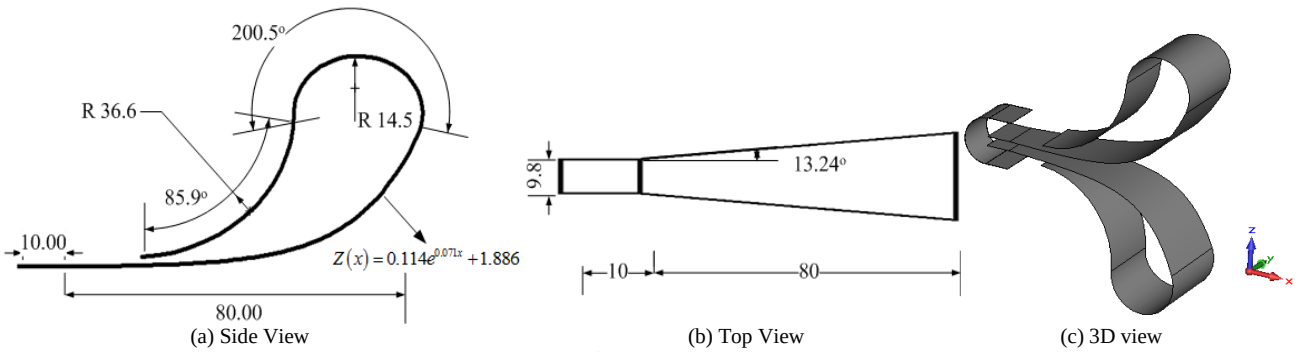

(a) Side View (b) Top View (c) 3D view

Fig. 1 The model of TEM horn antenna (unit: mm.)

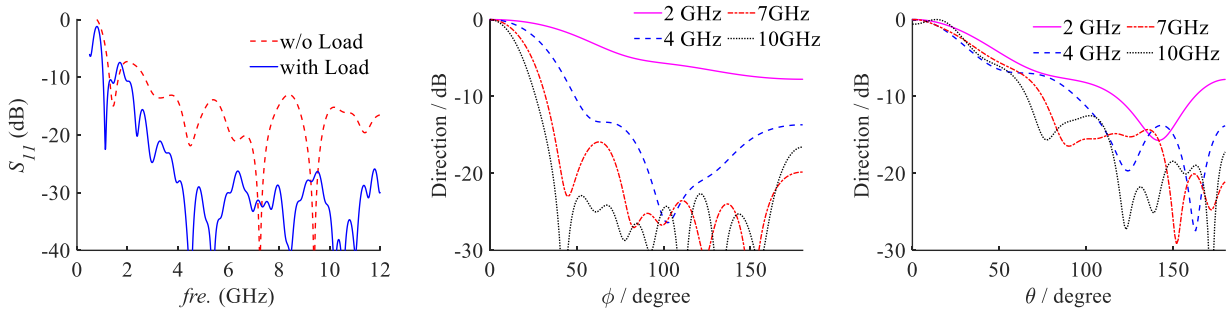

(a) S11 (b) Pattern in H-plane (c) Pattern in E-plane

Fig. 2 Performances of the element horn antenna.

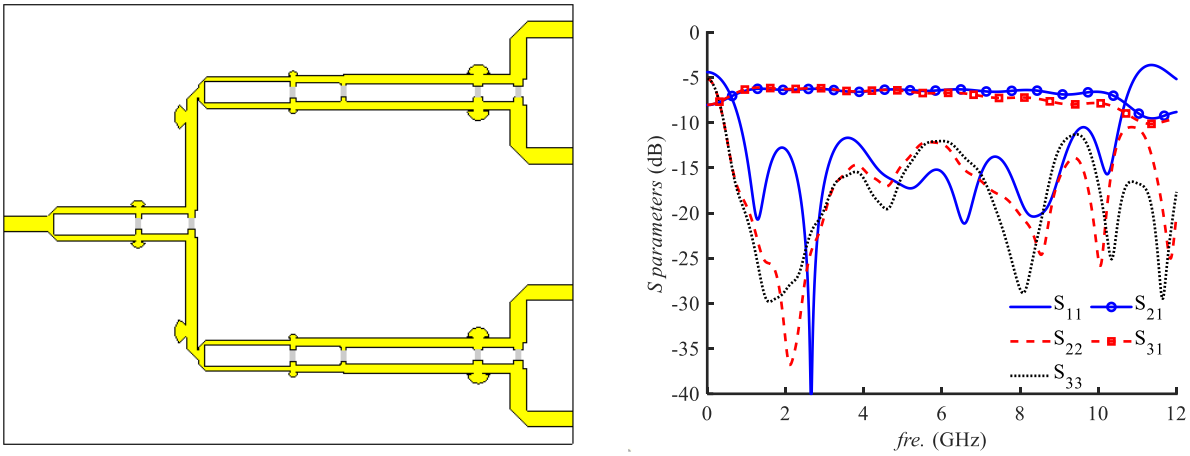

(a) Prototype of the proposed power divider (b) S parameters of the power divider

Fig. 3 The proposed power divider.

The shape of the proposed horn is shown in Fig. 1. In x-z plane, the equation of the exponential curve is

$$Z(x)=0.114e^{0.071x}+1.886 \tag{4}$$

and in x-y plane, the plates have a flare angle about 13.24°, which will help to enlarge the aperture of the horn. The loaded section is composed of two circular arcs. The radius of the first one is 14.5 mm and the length is 200.5°, while the second one is 36.6 mm and 85.9°. The exponential curve and two arcs is tangent with each other to keep the joint smooth and minimize the reflection.

The antenna is calculated by CST MWS, and Fig. 2 shows its performances. It is obvious that the end loading structure can help to improve the matching at lower frequencies. The gain of the proposed antenna drops down as reducing of the operating frequency, since the electrical size of the aperture is becoming smaller, see Fig. 4.

III. UWB WILKINSON POWER DIVIDER

To extend the operating bandwidth of a Wilkinson power divider, two methods are usually adopted. The first one is using multi-section TL impedance transformer to replace a λ/4 TL impedance transformer [8,9]. However, to obtain 1:10 bandwidth, a 7 section TL is needed, which will bring non-negligible insert losses. An alternative method is to insert an open circuited (OC) stub in the λ/4 TL, which has a zero reflection response at the first stop band of the original transformer, and thus the bandwidth would be improved significantly, but the maximum bandwidth of this method is about 1:3 [10-13]. In our proposed design, these two methods are combined, and finally a 1:10 bandwidth power divider is realized by two section TL.

Next, three 2-way power dividers are integrated to realize a 4-way divider. The reason why we do not design a power

divider with four output ports directly is that the microstrip topology can hardly get symmetrical and the layout of the isolation resistors is troublesome. The first divider is a little different from the other two, due to the layout of the printed circuit board (PCB). The prototype and the results of the proposed UWB power divider are shown in Fig. 3 (a) and (b), respectively. The reflection coefficients are always below -10 dB in the targeted bandwidth, and the difference of the transmission coefficients between the different ports is less than 1 dB. The insert loss is a little higher above 7 GHz, which is due to the ohm losses of the substrate. The isolations between different ports are better than 10 dB.

Next, the modified power divider is used to feed a 4-element horn array. The element horns are arranged in a linear array with distance 6 cm along y axis. The power divider and the antennas are connected by 4 coaxial cables with same lengths. Fig. 4 shows the gain of the element antenna and array. A reference value named "ideal array" is also compared in the figure, which means all the four antennas are fed by the equal amplitudes with zero degree phase delay. With this ideal feeding, the gain of the array can be increased 3 dB to 6 dB in the operating band. The lower improvement at the lower frequencies is due to the coupling of the element antenna. In the real implementation, the losses of the power divider and the cables reduce the gain, especially at higher frequencies. Above 9.5 GHz, the gain of the array is approximately equal to the gain of the element antenna. However, the improvement of the gain at lower frequencies is more important to increase the detecting depth for GPR systems, which is the main target of the proposed design. The lower loss substrate and cables could further improve the gain of the UWB array.

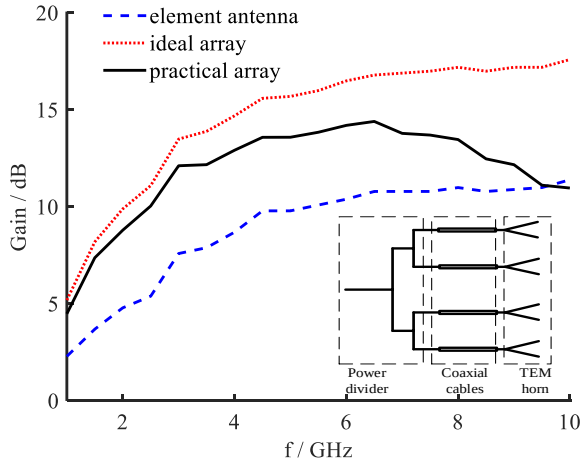

Fig. 4 Realized gain of the proposed antenna and array.

IV. Conclusion

An exponentially tapered TEM horn antenna is designed for UWB monopulse radar systems. By loading external circular loop at the end of the aperture of the horn, the bandwidth of the horn antenna can cover from 1 GHz to 10 GHz. To improve the gain at the lower frequencies, a UWB Wilkinson power divider is designed by using multi section TL and open circuited stubs technologies. A 4-element array is fed by this UWB Wilkinson power divider, achieving significant improvement of the gain at lower frequencies.

References

[1] J.-C. Diot, P. Delmote, J. Andrieu, etal., A Novel Antenna for Transient Applications in the Frequency Band 300 MHz – 3 GHz: The Valentine Antenna. IEEE Transactions on Antennas and Propagation, Vol. 55, No. 3, March 2007

[2] K. Chung, S. Pyun and J.Choi. Design of an Ultrawide-Band TEM Horn Antenna With a Microstrip-Type Balun. IEEE Transactions on Antennas and Propagation, Vol. 53, No. 10, October 2005

[3] L. L. Chen, C. Liao, L. Chang, etal. A Novel Ultra-Wideband Knife-shape TEM Horn Antenna Design for Transient Application. Microwave and Millimeter Wave Technology (ICMMT), 2010

[4] C. Kao, J Li, R Liu, etal. Design and Analysis of UWB TEM Horn Antenna for Ground Penetrating Radar Applications. Geoscience and Remote Sensing Symposium, 2008. IGARSS 2008. IEEE International, 7-11 July 2008

[5] D.A. Kolokotronis, Y. Huang and J.T. Zhang. Design of TEM Horn Antennas for Impulse Rader. 1999 High Frequency Postgraduate Student Colloquium. 17 Sep. 1999.

[6] M. Kanda. Transients in a Resistively Loaded Linear Antenna Compared with Those in a Conical Antenna and a TEM Horn. IEEE Transactions on Antennas and Propagation, Vol. AP-28, No. 1, Jan. 1980

[7] M. Kanda. The Effects of Resistive Loading of "TEM" Horns. IEEE Transactions on Electromagnetic Compatibility, Vol. EMC-24, No 2, May. 1982

[8] E. Wilkinson. An N-way hybrid power divider, IRE Transactions Microwave Theory Technology, Vol. MTT-8, No. 1, pp. 116-118, Jan. 1960.

[9] S. B. Cohn, A Class of Broadband Three Port TEM-mode Hybrids, IEEE Transactions Microwave Theory Technology, Vol. MTT-16, No. 2, pp. 110-116, Feb. 1968.

[10] R. Pazoki, M. R. Ghafouri Fard and H. Ghafouri Fard, A Modification in the Single-Stage Wilkinson Power Divider to Obtain Wider Bandwidth. Proc. Asia-Pacific Microw, Conf., pp. 2325-2328, Dec. 2007.

[11] Ahmed, O. and A. R. Sebak, A modified Wilkinson power divider/combiner for ultrawideband communications, IEEE Antennas and Propagation Society International Symposium, 1-4, 2009.

[12] B. Zhou, H. Wang, and W.-X. Sheng, A modified UWB Wilkinson power divider using delta stub. Progress In Electromagnetics Research Letters, Vol. 19, 49-55, 2010

[13] Xing-Ping Ou and Qing-Xin Chu, A Modified Two-section UWB Wilkinson Power Divider. ICMMT 2008, pp1258 - 1260

High Frequency Electromagnetic Field Coupling with Transmission Lines of Finite Length in a Rectangular Resonator.

Sergey V. Tkachenko
Chair of Electromagnetic CompatibilityOtto von Guericke University
Magdeburg, Germany
sergey.tkachenko@ovgu.de

Juergen B. Nitsch
Chair of Electromagnetic Compatibility
Otto von Guericke University
Magdeburg, Germany
juergen.nitsch@ovgu.de

MoustafaRaya
Chair of Electromagnetic Compatibility
Otto von Guericke University
Magdeburg, Germany
moustafa.raya@ovgu.de

Ralf Vick
Chair of Electromagnetic Compatibility
Otto von Guericke University
Magdeburg, Germany
ralf.vick@ovgu.de

***Abstract*—The coupling of high-frequency electromagnetic fields with thin wire loaded transmission lines with vertical risers inside a resonator is considered. For the analytical solution of the Mixed Potential Integral equation, we used the method of analytical regularization, hybrid representation of the resonator Green's function, and transmission-line approximation.**

Keywords—Transmission Line, Rectangular Resonator, Method of Analytical Regularization

I. Introduction

One of the main challenges in electromagnetic compatibility (EMC) is the penetration of HPEM electromagnetic fields through slots and openings of various resonator-type objects such as aircraft fuselage, satellites, computer casings, etc. This coupling results in further interaction with transmission lines, interconnecting wires, and scatterers located in the cavity [1]. Thus, studying the interaction of high-frequency electromagnetic fields with transmission lines in resonators is an important problem in EMC. A good application of the solution to this problem is the maintenance of internal EMC in airplanes, computers, electric cars, etc. Often, the parameters of the interference field (amplitude, angle of incidence, frequency and time characteristics, etc.) along with the transmission line parameters (geometry, position, characteristic impedances, loads, etc.) are only statistically known, which leads to high calculation costs for qualitative and quantitative analysis. Direct numerical methods, such as theMethod of Moments, the Finite Elements Method, etc. allow only the investigation of specific problems and require large computation time. This necessitates the development of fast approximate analytical and numerical-analytical methods.

Considering the prior art, an exact solution for symmetrical cases can be obtained if the symmetry of the wire coincides with the symmetry of the resonator. This approach was applied to the calculation of a loaded line in a rectangle [2, 3], in which the wire connects two opposing walls and runs parallel to the others, also for the line in a cylinder where the loaded line is connected at the top and bottom to the cylinder and is parallel to its axis [4]. Analytical consideration of non-symmetrical cases requires the use of different kinds of small parameters. In [5, 6, 7] electrically small electrical dipole and magnetic dipole antennas (loop antennas) in rectangular and cylindrical resonators were considered. Another parameter considered was the thickness of the wire. It was used to consider the electrically non-small, finite-length thin wire line in a rectangular resonator [8]. This approach uses the Method of Analytical Regularization (MoAR) [9]. In [8] the method was applied for the horizontal straight open-circuit thin wire in rectangular resonator. In the present research, we apply the method [8] for practically important case of loaded thin-wire transmission line in rectangular resonator.

II. Methods and Results

We consider a loaded transmission line with vertical risers, assuming that the condition of application of the transmission line approachin free space is valid (kh<<1) (see Fig.1). The line is under the action of an electromagnetic field that is excited in one way or another. The excitation of the line is described by the Mixed Potential Integral Equation, which is a system of two integral-differential equations for the current and scalar potential along the line. The first equation is obtained from the zero-boundary condition for the perfect conducting wire, the second from the definition of the scalar potential. The kernels of the corresponding integrals can be obtained using the cavity Green's functions for vector and scalar potentials.

The method is based on splitting the Green's functions for

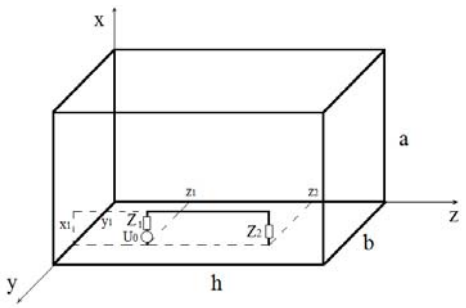

Fig. 1 Sketch of electrically long transmission line of arbitrary length within a rectangular cavity.Parameter of the resonator: a =1.5 m, b = 1.2 m, h = 0.9 m. Parameter of the line: x_1= 2 cm, y_1 = 37 cm, z_1 = 35 cm, z_2=55cm, r_0=1 mm, U_0= 1 V, Z_1 = 0, Z_2 = Z_C = 221.14 Ω

the vector and scalar potentials in the resonator into two parts [10]. The first part is singular for the close spatial arguments

but smooth in the frequency domain. For our configuration, it can be roughly considered as a real part of the Green's function in the half-space with a perfect conducting ground.

The second and regular part of the Green's function is smooth in the space domain but contains all resonances of the cavity in the frequency domain. In our case, it can be represented as a usual modal sum of the double product of eigenfunctions with a resonant denominator, but with a finite number of terms whose eigenfrequencies are close to the current frequency ω (see Fig.2).

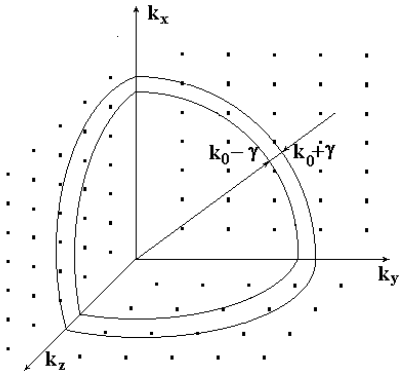

Fig. 2The region of summation in k-space for the calculation of the regular part of the resonator Green's function

As a result, the Mixed Potential Integral MPIE are reduced to a system of Telegrapher's equations with initial excitation plus an additional excitation that forms a set of plane waves with unknown amplitudes. These amplitudes can be calculated from the integrals of the unknown currents with a finite number of eigenfunctions of the resonator. A linear system for these amplitudes is obtained after applying the TL resolution operator (TL Green's function) and calculating these integrals again. The order of this system is equal to the number of eigenfunctions taken into account. The solution of this system yields the current in the finite line. In this way, the solution is reduced to the calculation of matrix elements of the TL resolvent operator with eigenfunctions and the solution of the corresponding linear system.

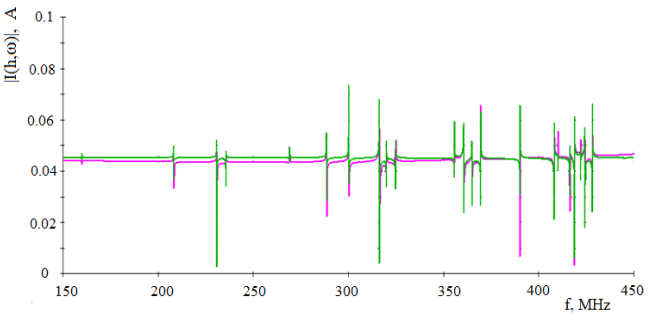

Fig. 3 Electrically long transmission line of arbitrary length within a rectangular cavity. Comparison of numerical calculation MoM (magenta line) and MoAR results (green line) for the current in the second load.

The comparison of the absolute value of the current obtained by the MoAR and results obtained by commercial numerical code is presented in Fig. 3. A good agreement with the result of numerical calculation is observed. It can be seen that the response consists of two parts, the transmission line pure response (horizontal part of the curve) and a part which appears due to the interaction with the modes of the resonator. For relatively low frequencies (up to about 250 MHz) one can use the results of the transmission line approximation, but for higher frequencies, the interaction with the resonator cannot be ignored.

III. Conclusion

The Method of Analytical Regularization developed earlier for the thin wires in rectangular resonator, has been applied to a loaded transmission line with vertical risers. One can observe a good agreement of the analytical results with those of the numerical MoM simulation.

The method can be easily generalized for the case of multiconductor transmission lines in a resonator.

In summary, it can be said that the MoAR yields the Green's function for the pair "current-potential" of a finite transmission line in a resonator, which can be used for the further statistical researches, such as [11-12] by the Method of Symmetrical Line in a rectangular resonator.

References

[1] D.V. Giri, *High-power Electromagnetic Radiators: Nonlethal Weapons and Other Applications*, Harvard University Press, 2004.

[2] S.V.Tkachenko, R.Rambousky, J.B.Nitsch, "Electromagnetic Field Coupling to a Thin Wire Located Symmetrically Inside a Rectangular Enclosure" *IEEE Trans. EMC,* Vol.55, Nr.2, 2013, pp.334-341.

[2] S.Tkachenko, J.Nitsch, and R. Rambousky ,"Electromagnetic Field Coupling to Transmission Lines Inside Rectangular Resonators", *Interaction Notes*, Note 623, June 2011. http://ece-research.unm.edu/summa/notes/In/IN623.pdf

[4] S.Tkachenko, R.Rambousky, J.B.Nitsch, "Analysis of Induced Currents on a Thin Wire Located Symmetrically Inside a Cylinder", *IEEE Trans.EMC*, vol.56, no.6, pp. 1649-1656, 2014.

[5] S. V. Tkachenko, G.V. Vodopianov, L.M. Martynov, "Electromagnetic field coupling to an electrically small antenna in a rectangular cavity", in *Proc. 13th Zürich EMC Symposium 1999*, pp. 379-384.

[6] S.Tkachenko, J.Nitsch, M.Al-Hamid, "High-Frequency Electro-magnetic Field Coupling to Small Antennae in a Rectangular Resonator", *Hindawi Intern. Jour. of Antennas and Propagation* Vol. 2012, Article ID 897074, 6 pages. DOI:10.1155/2012/897074.

[7] S.Tkachenko, J.Nitsch, R.Rambousky, "Electromagnetic field coupling to an electrically small axial dipole antenna in a cylindrical cavity", International Symposium EMC EUROPE 2014, Gothenburg, Sweden. DOI: 10.1109/EMCEurope.2014.6930898

[8]S.V.Tkachenko, J.B. Nitsch, R. Vick, " HF coupling to a transmission line inside a rectangular cavity", URSI Inter. Symp. on EM Theory, 2010, Berlin. DOI: 10.1109/URSI-EMTS.2010.5637177

[9]N.I. Nosich, "The method of analytical regularization in wave scattering and eigen-value problems: foundations and review of solutions", *IEEE Ant. Prop. Magazine*, vol. 41, pp. 34–39, June 1999.

[10] D.I. Wu and D.C.Chang, "A hybrid representation of the Green's function in an overmoded rectangular cavity", *IEEE Trans. MTT*, vol. 36, pp. 1334–1342, Sept. 1988.

[11] S.V. Tkachenko, J.B.Nitsch, M. Raya , R. Rambousky, and R.Vick, "Propagation of current waves along a transmission line with randomly located non-uniformities inside a rectangular resonator", Adv. Radio Sciences, vol. 16, pp. 195–201, 2018. https://doi.org/10.5194/ars-16-195-2018

[12] S.V. Tkachenko, J.B. Nitsch, M.Raya, R.Vick, S.Secnic, D. Poljak, "Propagation of current waves along transmission lines with stochastic geometry in a rectangular resonator", *UMEMA2018, 4th Workshop on Uncertainty Modeling for Engineering Applications*, Split, Croatia, Dec. 10-11, 2018.

Detection and Localization of Lightning Damages in CFRP with Lamb Wave

Shangchen Fu
National Key Laboratory on Electromagnetic Environmental Effects and Electro-optical Engineering
Nanjing, China
fshangchen@hotmail.com

Lihua Shi
National Key Laboratory on Electromagnetic Environmental Effects and Electro-optical Engineering
Nanjing, China
lihuashi@aliyun.com

Yinghui Zhou
National Key Laboratory on Electromagnetic Environmental Effects and Electro-optical Engineering
Nanjing, China
nowaiting@163.com

***Abstract*—Lightning strike pose a serious threat to aircraft composite structures, which makes the requirement of on-line monitoring of lightning damages in composites more and more urgent. In this paper, Lamb wave based structural health monitoring(SHM) method is brought into the lightning damage diagnostic of carbon fiber/epoxy laminates. Artificial lightning strike test is carried out, the reliability of the transducer array is testified, and the internal damages are inspected. After that, the lightning damages are detected with a Lamb wave array scanning system, and then localized with TOA method. Results revealed that the damages can be distinctly identified and located, which demonstrate the rationality of Lamb wave method in lightning damage monitoring of composites.**

Keywords—composites, lightning strike, damage monitoring, Lamb wave

I. INTRODUCTION

Because of their excellent mechanical performances, the application of composites has steadily increased in the manufacture of modern aircrafts. However, the widely use of composite structure also highlights the lightning strike protection issue. Lightning strike has been proven to be a severe threat to flight safety[1]. The relatively lower electrical conductivity makes composites more vulnerable to lightning strike, both of the artificial tests[2] and numerical analysis results[3] reveal that lightning current attached on the surface of composites will conduct into the structure and cause extensive damages inside the material.

Although some protection measures have been proposed[4], it is difficult to completely protect composite structures from lightning strike damage[2]. If the resin under the shielding vaporize due to lightning current, the accumulation of stress will cause explosions and generate more serious damages[5]. Moreover, for an aircraft in flight, lightning strike can hardly be noticed, and these external and internal damages may continue growing to further destroy the structure, so on-line monitoring and assessment of damages in composites caused by lightning strike have become a new requirement.

Structural health monitoring(SHM) method developed in recent years[6] provides a new solution to the above problems, as it can automatically assess the damages in the structure with prior arranged transducer array and advanced signal processing algorithm. In this paper, the feasibility of Lamb wave based SHM method in detecting and localizing lightning damages of CFRP is investigated with a Lamb wave array scanning system we have developed[7]. Artificial lightning strike test on T700/t85 carbon fiber/epoxy laminates is carried out, the reliability of the transducer array is testified, and the damages inside the specimen is inspected with ultrasonic C-scan. After that, a Lamb wave array scanning system is applied to detect the lightning damages. Results reveal that the damages can be distinctly identified in the Lamb wave sensing signals, and the location of the damage region can be localized with ellipse method, which demonstrate the effectiveness of the method.

II. ARTFICIAL LIGHTNING STRIKE TEST ON CFRP

A. Experimental Setup

The T700/t85 specimen used in the study is a 300 mm×300 mm×2 mm plate with the layup of $[45/0/-45/90]_{2s}$. To monitor the lightning damage, 6 PZTs are glued on the surface of the specimen, as is illustrated in Fig. 1. The 'X' spot shows the lightning strike attachment location.

The whole setup for the test is shown in Fig. 2. An impulse current generator is applied to simulate the lightning strike, with which an double-exponential pulse of high peak-value(up to 200 kA) but short duration(rise time/half-peak time=8/20 μs) can be generated. The specimen is fixed on a jig during the test, the surface arranged with PZTs is covered by an aluminum box to shield the electromagnetic interference. P1-P4 are connected to a Tektronix MDO3034 oscilloscope with shield twisted-pairs to testify the reliability of the PZTs during lightning strike.

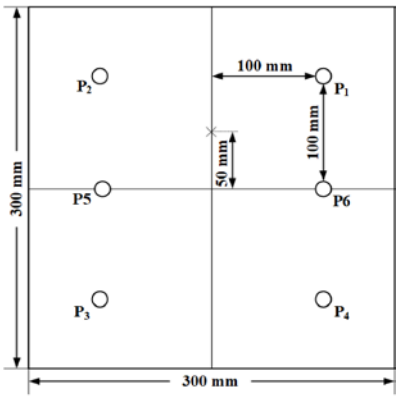

Fig. 1 Illustration of the PZT array.

National Natural Science Foundation of China (Grant No. 51477183).
China Postdoctoral Science Foundation Funded Project (Grant No. 2017M613401)

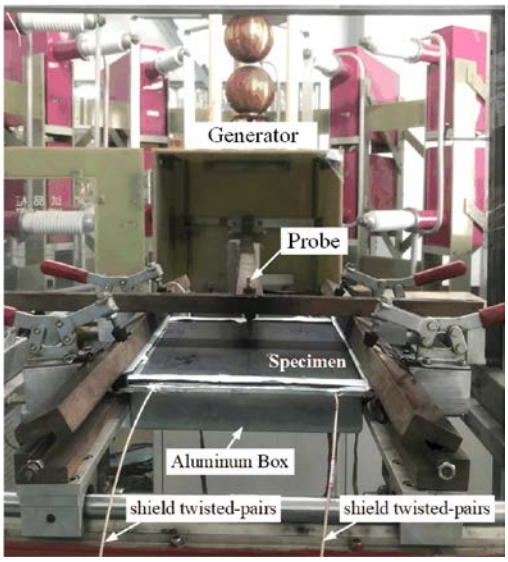

Fig. 2 Experimental setup for lightning strike test.

B. *Results and Disscussion*

The lightning current measured during the test is show in Fig. 3, its actual peak-value is about 75 kA. The lightning damage results are shown in Fig. 4. We can see that the external damages in Fig. 4 (a) appear as a rhombic, ply lift, fiber breakage and resin vaporization are distinctly visible in the vicinity of the lightning attachment location, all the damages expand along the fiber orientation of the surface(45°). Compared to external fiber breakage, internal damages mainly caused by Joule heating effect is more serious, as the C-scan results of depth direction revealed in Fig. 4 (b). Delamination along 45°, 45°/0°, 0°/-45°, -45°/90° and 90°/45°can be observed at the depth of 2 mm, 1.875 mm, 1.75 mm, 1.625 mm and 1.5 mm.

The impact signals collected during the test are shown in Fig. 5. An obvious pulse can be observed at the moment of 4 ms in each waveform, this should be an EM coupling signal caused by lightning strike, which means more measures are needed to improve the shielding effectiveness. Despite this interference, other sensing signals are continuously recorded by all the 4 PZTs in the following time, which demonstrate the reliability of the PZTs during the lightning strike.

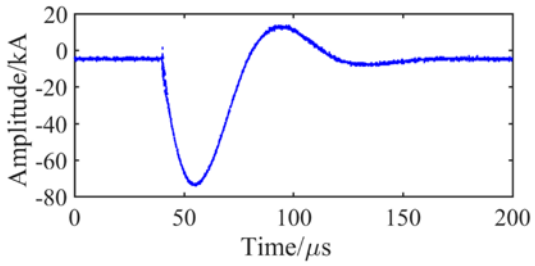

Fig. 3 The impulse current applied in the test.

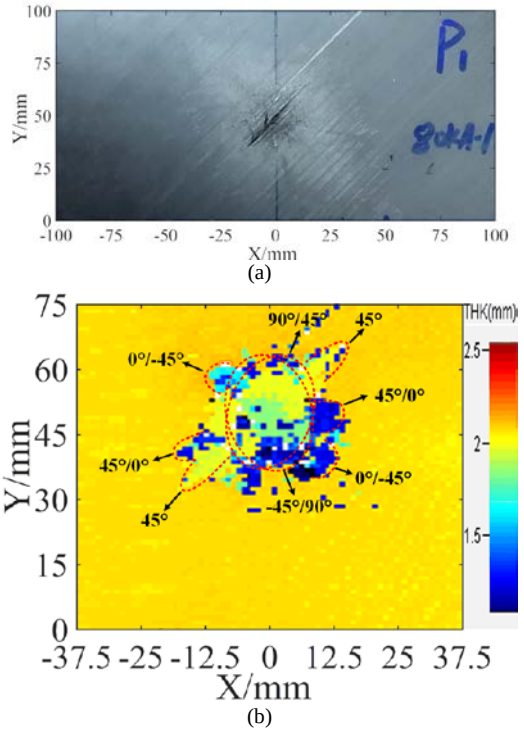

Fig. 4 Lightning damages of the specimen. (a) External damages, (b) C-scan result of internal damages in depth direction.

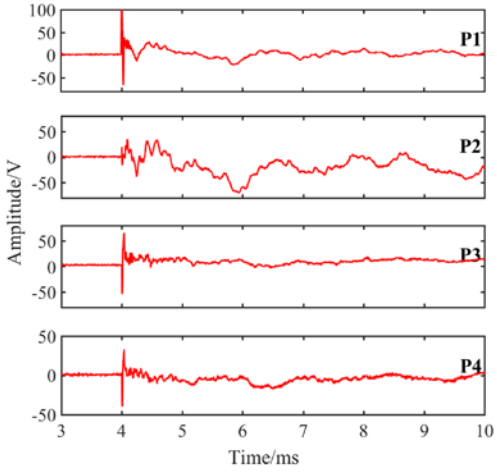

Fig. 5 Impact signals collected during the lightning strike test.

III. Lighting Damage Detection with Lamb Wave

A symmetrical modulated 1-cycle burst wave with the central frequency of 40 kHz is generated with a Lamb wave array system to detect the lightning damages. The group velocity of the burst wave in the specimen is measured in advance at the interval of 15°, and the results are shown in Fig. 6. Due to the fiber orientation of the specimen, the difference of the velocity in different direction is not very obvious, and the mean value is about 1443 m/s.

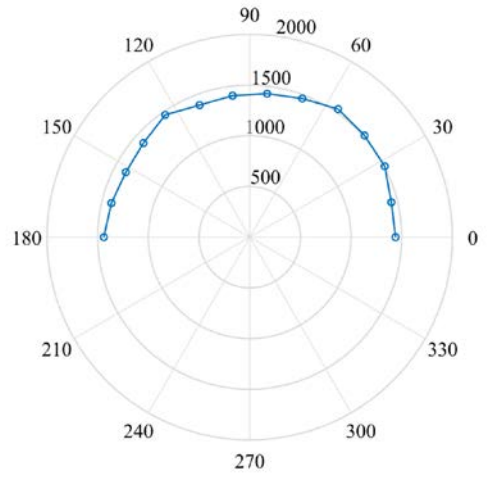

Fig. 6 The measured group velocity.

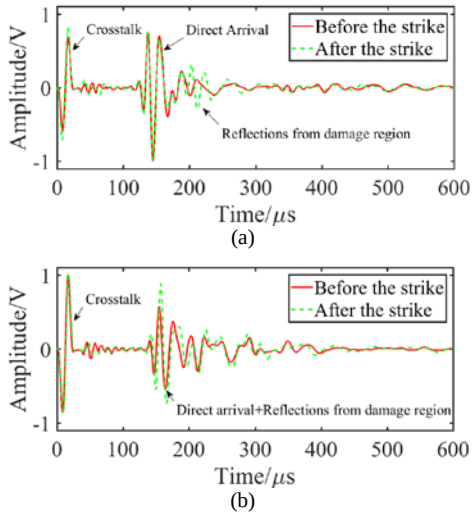

Fig. 7 The sensing signals of transducer pair $P_{2\text{-}3}$ and $P_{2\text{-}8}$ before and after the lightning strike. (a) Sensing signals of $P_{2\text{-}3}$, (b) sensing signals of $P_{2\text{-}8}$.

The sensing signals of transducer pair $P_{2\text{-}3}$ and $P_{2\text{-}8}$ before and after the lightning strike are displayed in Fig. 7, all the results are normalized with its maximum value. The first wave-packets appeared at the beginning of the waveform is crosstalk caused by the system, it can be treated as a reference signal. The damage region is not in the propagation path of the direct arrival of $P_{2\text{-}3}$, so the two direct arrival of signals before and after the strike should match well. According to the measured velocity and the distance between P_2 and P_3, the time of flight(TOF) of the direct arrival is about 164 μs, and two very consistent wave packets can be observed at this moment in Fig. 7 (a). A quite obvious difference can be found near the moment of 200 μs, this should be caused by the damages.

Different from $P_{2\text{-}3}$, the direct arrival of $P_{2\text{-}8}$ directly pass the damage region, so the consistency between the two wave-packets at 180 μs in Fig. 7 (b) is poor, and the amplitude of the direct arrival after the strike is larger as the reflections from the damage region are contained.

By subtracting the healthy signals from the damaged signals, damage scattering signals can be obtained. As the direct arrival and boundary reflections are all eliminated, the remaining signals are all from the damage region. Extracting the damage scattering signals of $P_{1\text{-}2}$, $P_{2\text{-}3}$ and $P_{1\text{-}4}$, and treating these three transducer pairs as focus of three ellipses, respectively, then the location of the lightning damages should be at their intersection, as the imaging results shown in Fig. 8. The 'X' spot in the result shows the exact location of the lighting attachment point. The localization result with ellipse method is very close to the lighting attachment location. Although more one point can be observed in the result, both of them are in the damage region obtained from C-scan in Fig. 4. The localization result can be further improved by bring in other transducer pairs.

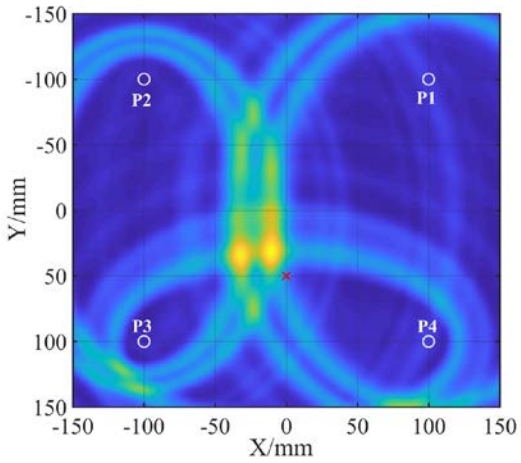

Fig. 8 Lighting damage localization result.

Both the damage detection results in Fig. 7 and the localization result in Fig. 8 demonstrate the effectiveness of Lamb wave in lightning damage detection of CFRP.

IV. Conclusion

The feasibility of Lamb wave SHM method in monitoring lightning damages of carbon fiber/epoxy laminates is investigated. All the experiment results revealed the effectiveness of this method.

References

[1] M. A. Uman, V. A. Rakov, "The interaction of lightning with airborne vehicles," Prog. Aerosp. Sci., vol. 39(1), pp. 61-81, 2003.

[2] Y. Hirano, S. Katsumata, Y. Iwahori and A. Todoroki, "Artificial lightning testing on graphite/epoxy composite laminate," Composites: Part A, vol. 41, pp. 1461-1470, 2010.

[3] T. Ogasawara, Y. Hirano and A. Yoshimura, "Coupled thermal–electrical analysis for carbon fiber/epoxy composites exposed to simulated lightning current," Composites: Part A, vol. 41, pp. 973-981, 2010.

[4] M. Gagné, D. Therriault, "Lightning strike protection of composites," Progress in Aerospace Sciences, vol. 64, pp. 1-16, 2014.

[5] F. A. Fisher, J. A. Plumer, and R. A. Perala, Lightning protection of aircraft, 2nd ed. Pittsfield: Lightning Technologies Inc., 2004.

[6] F. K. Chang, Structural Health Monitoring—the Demands and Challenges. Boca Raton, FL: Chemical Rubber Company Press, 2002.

[7] S. C. Fu, L. H. Shi, Y. H. Zhou, J. Cai. Dispersion Compensation in Lamb Wave Defect Detection with Step Pulse Excitation and Warped Frequency Transform. IEEE Transactions on Ultrasonics, Ferroelectrics, and Frequency Control, 2014, 61(12): 2075-2088.

Compact Design of Novel Combined Antenna Array for the UWB Pulse Radiation

Shao-fei Wang, Yan-zhao Xie
State Key Laboratory of Power Equipment and Electric Insulation
National Centre for International Research on Transient Electromagnetics and Applications
School of Electrical Engineering, Xi'an Jiaotong University
Xi'an, China
wsf2013@stu.xjtu.edu.cn;yzxie@mail.xjtu.edu.cn

***Abstract*—In this report, a kind of compact combined antenna array based on the novel narrow-strip combined antenna is developed to radiate the UWB electromagnetic pulse. The narrow-strip combined antenna is designed based on the research on the dependence of performances of the UWB combined antenna on its 3-D dimensions to minimize the size of the combined antenna. Then, the array of this novel combined antennas is developed to maximize the radiation within finite aperture array. And the radiation fields of the antenna array are measured. Compared with the conventional cubic combined antenna array, the narrow-strip combined antenna array can obtain the same effective potential gain (G_{ep}) while the aperture area is only 50% of that of the former antenna array.**

Keywords—narrow-strip combined antenna; antenna array; UWB; compact

I. INTRODUCTION

Basic combined antenna is usually designed in cubic shape so as to make the half-power beam width in E-plane and H-plane of the antenna the same. However, to improve the effective potential gain within certain aperture area is also very important to make compact UWB antennas. And this report is focused on the compact design of the combined antenna. So, a kind of narrow-strip combined antenna is developed in [1]. In this report, the narrow-strip combined antenna array is developed to furtherly improve the effective potential gain within finite aperture area.

II. DEVELOPMENT OF THE NARROW-STRIP COMBIEND ANTENNA ARRAY

A. The narrow strip combined antnena

In ref. [1], the narrow-strip combined antenna is developed based on the research on the dependence of performances of the UWB combined antenna on its 3-D dimensions to minimize the size of the combined antenna. And the picture of this kind of combined antenna is shown in Fig. 1.

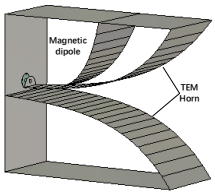

Fig. 1. Picture of the narrow-strip combined antenna.

B. Development of the antenna array

An HP-UWB system based on 4-element combined antenna array was developed and its schematic diagram is shown in Fig. 2. Output impedance of the pulsed source is 50 Ω, and with an impedance transformer, the impedance is converted to 12.5 Ω. Then, the output end of the impedance transformer is connected to 4 cables with impedance of 50 Ω paralleled by a power divider so as to feed the antenna array elements. Finally, the pulsed electromagnetic energy could be transmitted to the free space by the antenna array.

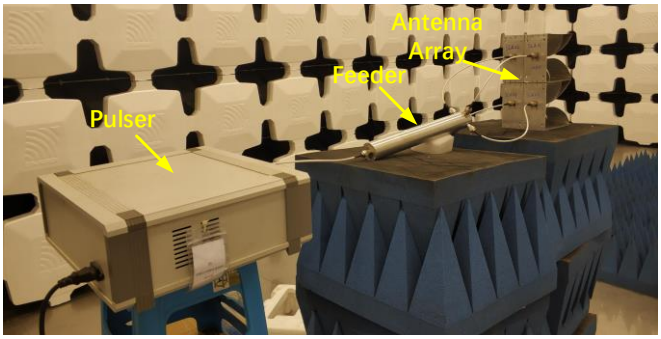

Fig. 2. Picture of the narrow-strip combined antenna.

III. MEASUREMENT OF THE DEVELOPEDANTENNA ARRAY

The dimensions of the conventional cubic combined antenna are 15 cm×15 cm×15 cm, and the corresponding aperture dimensions are 15 cm×15 cm. And the dimensions of the narrow-strip combined antenna are 18 cm×7.5 cm×15 cm, and the corresponding aperture dimensions are 7.5 cm×15 cm. Then the radiation fields of the narrow-strip combined antenna array are measured and compared with those of the conventional cubic combined antenna array with the same pulsed excitation, as shown in Fig. 3.

According to the comparison of the radiation fields, the amplitude of the fields at the same distance is almost the same, while the aperture area of the narrow-strip antenna aray is only half that of the cubic combined antenna array. It means that the novel antenna array can significantly improve the effective potenial gain (G_{ep}), which is defined as the ratio between the effective potential (*rEp*, the product of the distance from the antenna and the peak amplitude of the electric field at the observation point) in the far-field region

and the amplitude of the excitation pulsewithin finit aperture area.

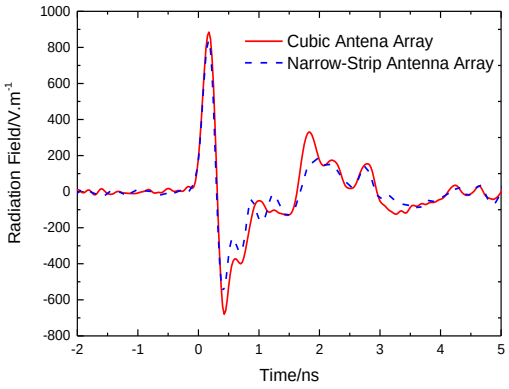

Fig. 3. Comparison of the radiation fields of the two kinds of antenna array.

IV. Conclusions

In this report, a kind of compact combined antenna array based on the novel narrow-strip combined antenna is developed, and its performances are comoared with the conventional cubic combined antenna array, which indicates that the narrow-strip combined antenna array can obtain the same effective potential gain (G_{ep}) while the aperture area is only 50% of that of the former antenna array. It means that the novel antenna array can significantly improve the effective potenial gain within finit aperture area.

References

[1] S. Wang, and Y. Xie. Compact Design of the UWB Combined Antenna. AMEREM 2018, Santa Barbara, the USA, 2018.

[2] Y. A. Andreev, A. P. Gubanov, M. Efremov et al. “High power ultra-wideband radiation source,” Laser and Particle Beams, vol. 21, no. 5, pp. 211-217, 2003.

[3] S. Wang, and Y. Xie, M. Gao, et al. Optimizing High-Power Ultra-Wideband Combined Antennas for Maximum Radiation within Finite Aperture Area. IEEE Transactions on Antennas and Propagation, vol. 67, no. 2, pp. 834-842, 2019..

Analysis of the Primary Current Distribution in Tesla-type Pulse Generators

Shi He
Xi'an Jiaotong University
Xi'an, China
Email Address: heshiyx@163.com

***Abstract*—In Tesla-type pulse generators, small inductance of the primary side is inevitable when a high level voltage gain is required. Consequently, primary series parameters are crucial to ensure the reliability of the generator. In addition, primary current distribution also influences the oscillating condition. A simulation model based on CST Microwave Studio co-simulation is established to calculate the primary current distribution. Thus, a series of verification tests using different primary connecting structure are performed to support the results of simulation. Comparison of the operating condition under different current distribution is also discussed. Both results of the simulation model and the verification test presented that change of the inductance is the main cause to affect the performance of the generator when the primary current distribution varies.**

Keywords—Tesla transformer, current distribution, series parameter, numerical analysis

I. INTRODUCTION

Tesla transformers comprising a wide copper board primary coil and a taper secondary winding built in PFL (pulse forming line) are widely used as pulse generators in many fields[1]~[2]. Generally, the performance of the Tesla-type pulse generators can be significantly affected by the primary stray inductance and ohmic losses[3]. And these parameters are intensively reserached in past few decades. In addition, the resonant condition can be also varied by non-uniform current distribution of the primary winding[4]. Especially in the generator with a high primary dI/dt above 20kA/μs, it is hard to ensure the even current distribution of primary side. According to operation of the practical generator, the current distribution of the primary winding is an important factor when determining the structure of primary external circuit.

In this paper, the current distribution of a practical primary configuration is calculated and discussed by a commercial software CST Microwave Studio[5], using FIT (Finite Integration Technique) method. Hence, a verification test is also presented to support the simulation model. We used a typical wide copper board with multiple connecting points adjusting the current flow of the winding, and we obtained the pulse rising time of the secondary voltage waveform under different primary current distribution. The results of the experiment and the simulation are in agreement.

II. SIMULATION MODEL OF THE PRIMARY SIDE

The simulation model is based on a practical primary copper board which is shown in Fig. 1. Seven connecting points are evenly arranged on the top of the winding[6]. Generally, four points named 1-3-5-7 are grounded, and one of rest points is contacted with the primary capacitor. Aim of the simulation model is to specify the effect caused by the position of the injecting port. The schematic diagram of the co-simulation model is shown as Fig. 2. The excitation source named signal-1 is imported from the simulation results obtained by a circuit analysis of a typical Tesla transformer. The series stray parameters of the transformer are also considered in the simulation model, as shown in the schematic diagram. According to the practical operation of the typical generator, the external resistance of the primary circuit is set to 24 mΩ, and the stray inductance is 50 nH.

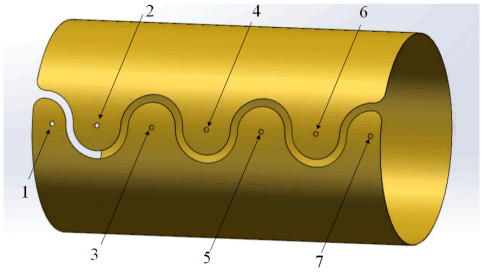

Fig. 1 Configuration of the primary winding.

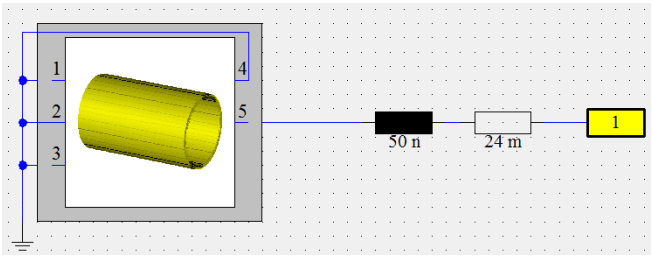

Fig. 2 Schematic diagram of the co-simulation model.

The model was a time-dependent analysis and the total simulation time was set to 8μs. The results of current density distribution and the primary current are illustrated in Fig. 3 and Fig. 4, respectively. We can deduce that the operation condition of the generator will be affected by the primary current distribution due to the change of the primary inductance. It is universally accepted that the ohmic losses caused by windings of both sides can be neglected in most cases[7], because of a very small resistance of the primary winding, which is generally far less than 1mΩ in most Tesla-type generators. Considering the series ohmic parameter in the simulation model, vary of the resistance is not the main cause of the different current waveform in Fig. 4. Hence, we add a 10nH extra inductance in the model and the contacting point is still port 4, the current waveform is similar to the result when using port 2 but without the extra inductance. All the analysis above shows that the inductance varying is the main reason to affect the operation of the generator, when the current distribution of the primary copper board is not uniform.

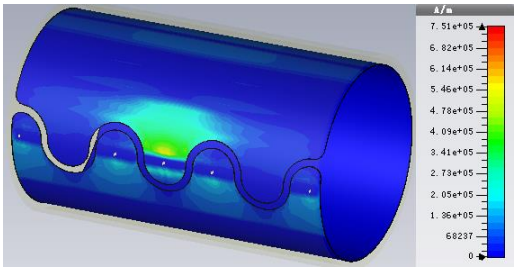

(a)

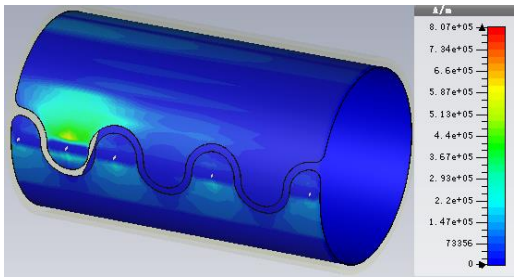

(b)

Fig. 3 Current density distribution simulated by the model under different contacting position when the simulation time t=1.5μs, the primary side is contacted with: (a) port 4; (b) port 2.

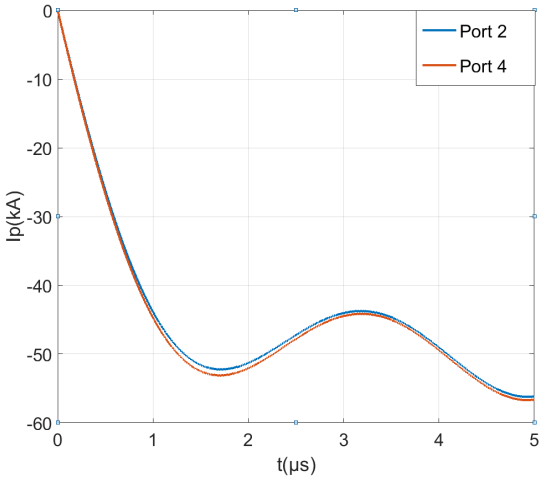

Fig.4 Primary current waveform calculated by the co-simulation model under different contacting points.

III. Verification Tests

To support the co-simulation model, comparison of the generator's operating condition under different primary configuration is discussed. For the typical Tesla transformer, we changed the axially position of the primary components and the contacting port. And we measured the secondary output voltage waveform and the primary current signal in both cases, which are corresponding with the simulation model mentioned above. Result of the secondary output waveform is shown in Fig. 5.

Due to the resonant condition of the transformer, the uncertain primary inductance might cause a more significant effect than the R-L circuit in the simulation model. The tuning ratio of the transformer will change a lot when the primary current distribution varies. From the verification test, the rising time of the secondary waveform has an about 10% delay when the primary capacitor contacts the winding via port 2. The results of the verification experiment and the simulation model are in agreement: the non-uniform current distribution of the primary copper board will lead to a primary inductance change, which might significantly affect the performance of the generator.

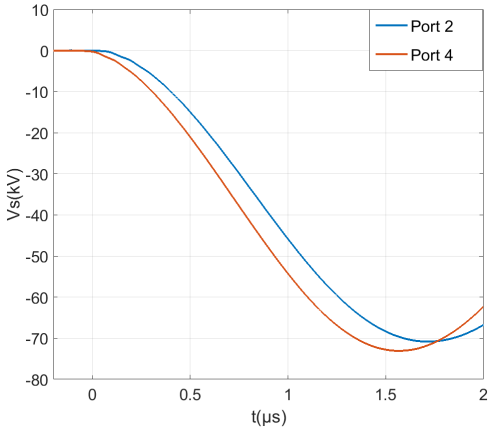

Fig. 5 Secondary voltage waveform under different contacting ports.

IV. Conculsion and Discussion

According to the co-simulation model based on the commercial software CST Microwave Studio, we found a simple method to estimate the effect of the non-uniform primary current distribution. From the verification tests, we can deduce that the performance of the Tesla-type generator can be significantly varied by the primary current distribution, because of the primary inductance change, which might be helpful for reliability and stability of Tesla transformers with a compact primary configuration.

References

[1] Korovin S.D, Rostov V.V. High-current nanosecond pulse-periodic electron accelerators utilizing a Tesla transformer [J]. Russian Physics Journal, 2006, **39**(12): 1177-1185.

[2] Mesyats G.A, Korovin S.D, Gunin A.V, et al. Repetitive pulsed high-current accelerators with transformer charging of forming lines [J]. Laser and Particle Beams. 2003, 21: 197-209.

[3] J. L. Reed. Note: Tesla transformer damping [J]. Review of Scientific Instruments, 2012, 83, 076101.

[4] X. Sun, L. Wang, X. Zhang, et al. Optimization of primary current distribution for Tesla transformer [J]. Modern Applied Physics, 2014, **5**(3), 196-200. (in Chinese)

[5] R. A. Petrella, S. Xiao. An air core pulse transformer with a linearly integrated primary capacitor bank to achieve ultrafast charging [J]. IEEE Transactions on Dielectrics and Electrical Insulation, 2016, **23**(4): 2443-2449.

[6] S. He, J. Li, F. Guo, et al. Analysis of ohmic losses in Tesla transformers utilizing the open magnetic-core [J]. AIP Advances **8**, 0852161(2018).

[7] B. M. Novac, I. R. Smith. A 10 GW Tesla-driven blumlein pulsed power generator [J]. IEEE Transactions on Plasma Science, 2014, **42**(10): 2876-2885.

MARCOS: A VHF Lightning Mapping System and Applications

Shi Qiu
National Key Laboratory on Electromagnetic Environment Effects and Electro-Optical Engineering
zeustone@yeah.net

Tao Wang
National Key Laboratory on Electromagnetic Environment Effects and Electro-Optical Engineering
TaoWang123@tom.com

Lihua Shi
National Key Laboratory on Electromagnetic Environment Effects and Electro-Optical Engineering
shilih@tom.com

***Abstract*—In order to track the weak VHF radiation sources in lightning discharges, a Multiple-Antennas Radiation Continuous Observation System (MARCOS) was developed and applied in lightning detection. The capability of continuously record of 7 VHF antennae, combined with a proposed MUSIC-VHF algorithm, enable the system retrieve weak VHF events and simultaneously occurred branches. An unmanned aerial vehicle (UAV) carried portable VHF radiation source were designed to test the performance of the system. The location error of the system is generally consistent with the electromagnetic time reversal (EMTR) method, but the proposed MUISC-VHF method produces sharp main lobes with lower sidelobes and better spatial resolution. Besides, field observation of artificially triggered flash is conducted. The mapping results show that the temporal and spatial development of two flashes could be well depicted, especially for some weak VHF events, such as the upward positive leaders (UPLs), subsequent return strokes, et al. Moreover, some cases of two VHF sources occurring within the same time window are identified and localized, which prove the system to be a promising tool in investigation of the physical mechanism with lightning discharges.**

Keywords—Lightning; weak VHF radiation source; MUSIC; multi-source localization

I. INTRODUCTION

Lightning mapping techniques using VHF broadband radiation is one of the most effective way to reveal the lightning activities in cloud. In the past decades, various effort have been made to improve the VHF detection capability[1-8], however, the question that how much lightning channel we could "see" by current techniques is still unresolved. A promising way is improving the detection sensitivity to the VHF weak radiation sources.

In this work, a new VHF mapping system - Multiple-Antennas Radiation Continuous Observation System (MARCOS) is developed. Benefited from the continuously record of 7 VHF antennae, combined with the exclusively proposed Multiple Signal Classification (MUSIC) algorithm, the system could depict lightning VHF events with higher spatial resolution and detection efficiency. Field observation proves that detailed lightning activity with weak radiation could be better revealed, compared with EMTR and interferometry methods. Moreover, simultaneously occurred multi-sources during a triggered lightning are first localized and presented.

II. INSTRUMENT AND METHDOLOGY

The proposed MARCOS is based on tradiational VHF broadband interferometer, but has three major improvement: (1) seven VHF antennas arranged with the baseline of 9 m in an "L" shape configuration are used to enhance the array mapping capability (as seen in Fig.1); (2) a LeCroy DSO operated with 12-bit resolution and continuously record for 0.5s to improve the SNR for weak VHF signals; (3) a specialized broadband MUSIC-VHF algorithm is proposed to retrieve weak radiation sources.

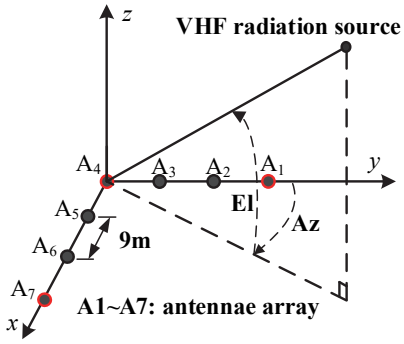

Fig.1. Schematic diagram of MARCOS antennae array

Generally, lightning VHF radiation cover a wide range of bandwidth, therefore, a broadband MUSIC algorithm for direction of arrival (DOA) estimation is proposed as the following procedures:

(1) For a M=7 elements planar VHF antennae array, implement the FFT to each broadband VHF signal at the same time window, and form M frequency domain vector:

$$\mathbf{X}(f_k)=\left[X_1(f_k),X_2(f_k),...,X_M(f_k)\right]^T \tag{1}$$

(2) Construct the $M\times M$ covariance matrix ($\boldsymbol{R}$) with $\boldsymbol{X}(f_k)$:

$$\boldsymbol{R}(f_k)=\boldsymbol{X}(f_k)\boldsymbol{X}^{\mathrm{H}}(f_k) \tag{2}$$

(3) Eigenvalue decomposition of covariance matrix, and deriving the signal eigenvector matrix $\boldsymbol{U}_S$ and noise eigenvector matrix $\boldsymbol{U}_N$:

$$\begin{aligned}\boldsymbol{R}(f_k)&=\boldsymbol{U}(f_k)\boldsymbol{\Sigma}\boldsymbol{U}^{\mathrm{H}}(f_k)\\&=\boldsymbol{U}_S(f_k)\boldsymbol{\Sigma}_S\boldsymbol{U}_S^{\mathrm{H}}(f_k)+\boldsymbol{U}_N(f_k)\boldsymbol{\Sigma}_N\boldsymbol{U}_N^{\mathrm{H}}(f_k)\end{aligned} \tag{3}$$

(4) Searching all the possible direction vectors $\boldsymbol{a}(\varpi_i)$ that satisfies the maximum of the spatial angular spectrum $P(\varpi_i)$ as Equation (4)

$$P(\varpi_i)=\frac{1}{K}\sum_{k=1}^{K}\frac{1}{\boldsymbol{a}^{\mathrm{H}}(f_k,\varpi_i)\boldsymbol{U}_N^{\mathrm{H}}(f_k)\boldsymbol{U}_N(f_k)\boldsymbol{a}(f_k,\varpi_i)}$$
$$\text{where } \varpi_S=\arg\left\{\max\left[P(\varpi_i)\right]\right\} \tag{4}$$

III. EXPERIMENT VALIDATION

An unmanned aerial vehicle (UAV) carried VHF radiation source hovering at fixed azimuth and elevation is

used to evaluate the performance of the proposed algorithm. The experimental setup is illustrated in Fig.2.

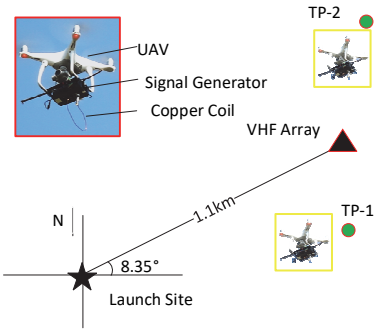

Fig.2. Layout of the VHF radiation source and observation site.

Two test points (TPs) in different directions of the array were selected, with TP-1 and TP-2 about 210 m and 400 away from the array, respectively. At each azimuth, different elevation angles were tested. The true azimuth and elevation were measured by a theodolite with precision less than 0.1º. The test results are listed in Tab. 1, with each point listed location err by MUSIC and EMTR method.

The localization accuracy by the two DOA methods are apparently similar. However, the spatial spectrum distribution of by MUISC method produces sharp main lobes with lower sidelobes and better spatial resolution, as shown in Fig.3.

Table. 1. Statistical results of UAV experiments by MUSIC-VHF and EMTR-VHF methods

True Az, EL (°)	Localization Error (°)	
	MUSIC	EMTR
(241.5, 14.7)	(0.45, 0.50)	(0.96, 0.60)
(241.7, 14.5)	(0.48, 0.17)	(0.75, 0.81)
(242.3, 15.3)	(1.07, 0.40)	(0.92, 0.80)
(241.5, 30.5)	(0.65, 0.26)	(0.68, 0.26)
(241.7, 31.1)	(0.4, 0.53)	(0.41, 0.69)
(244.1, 28.5)	(0.27, 0.33)	(0.56, 0.61)
(77.6, 8.0)	(0.23, 0.10)	(0.19, 0.88)
(77.7, 8.1)	(0.56, 0.64)	(0.53, 1.10)
(77.6, 7.9)	(0.15, 0.50)	(0.30, 0.80)
(78.4, 12.3)	(0.36, 0.63)	(0.28, 0.68)
(78.4, 12.4)	(1.09, 0.66)	(0.34, 0.52)
(78.4, 12.4)	(0.46, 0.38)	(1.04, 0.31)

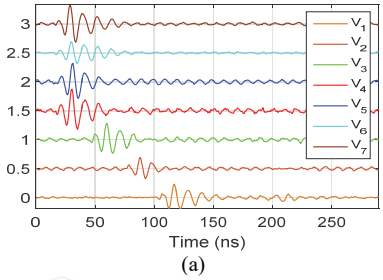

(a)

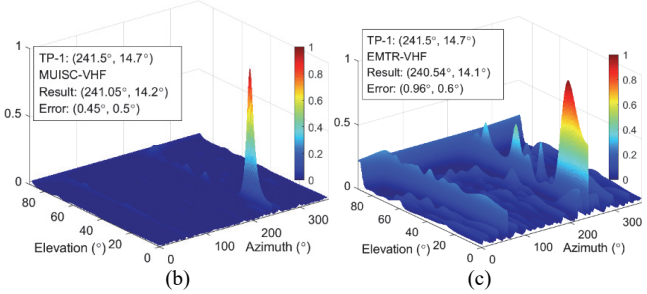

(b) (c)

Fig.3. Received signals (a) and spatial spectrum distribution results (b~c) by the MUSIC and EMTR method

IV. LIGHTNING OBSERVATION

The MARCOS was installed in the North of JiangSu Province for lightning observation from the year 2017. An artificially triggered lightning is used here to illustrate the performance of the system. The discharges were triggered by classical artificial trigger technique. The observation system was 1.1km away from the rocket launcher, as shown in Fig. 2. After the flash being initiated, UPL developed continuously widespread into cloud and then followed by the initial continuous current (ICC) process to the end.

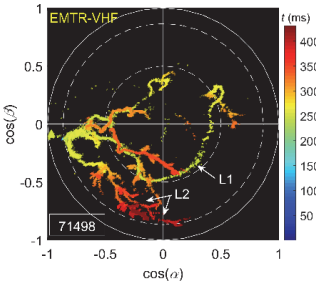

(a) EMTR method

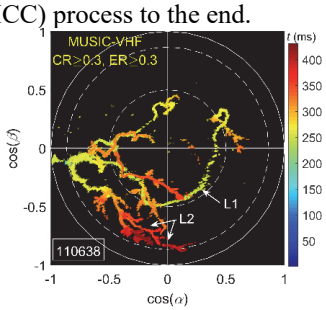

(b) MUSIC method

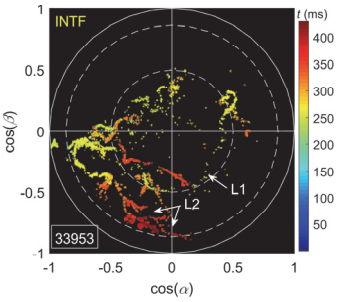

(c) interferometer with 3 antennae

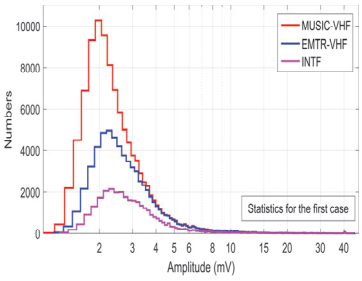

(d) distribution of the signal amplitude

Fig. 4 Mapping results comparing by three method

MUSIC method can provide clearer imaging quality for some branch structures than EMTR method, for instance, branches L1 and L2. Taking further comparisons of performances of the three methods in locating faint sources, Fig. 4(d) show the statistical distribution number of successful located VHF sources along with MUSIC, EMTR and interferometer (INTF) methods, respectively. Note that the other parameter, such as time window number, et al., are all the same for the three methods. The results demonstrate that the number of weak sources located by MSUIC method is significantly more than the other two methods.

Furthermore, the MUSIC VHF algorithm has been proved to locate simultaneously occurred multiple VHF sources.

Fig.5 (a~b) present waveforms from two simultaneous sources which arrive at the VHF array so closely that they could not even be distinguished from waveforms. Benefited from multiple sources localization of the MUSIC algorithm, two sources from different directions could be well recognized, as marked in Fig. 5 (c~e).

To the best of our knowledge, it is the first time that the multi-source radiations in real lightning are located. Although only a few isolated radiation events were found, it suggests that the proposed method hold promise in revealing multiple branches occurring simultaneously, and hence giving more detailed picture of lightning discharges.

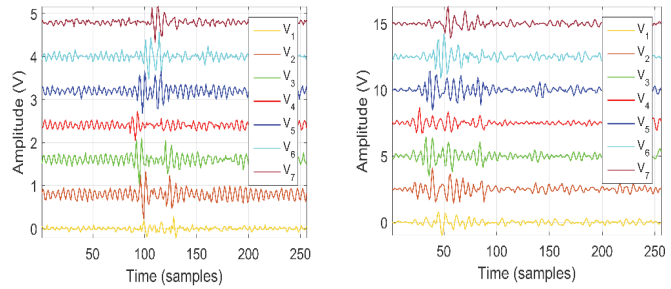

(a) VHF waveforms for case 1

(b) VHF waveforms for case 2

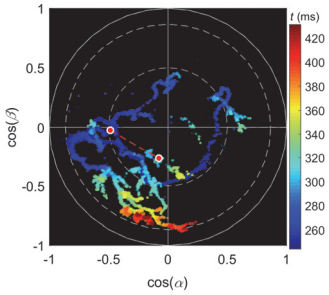

(c) Mapping result for case 1(red dots mark two simultaneous sources)

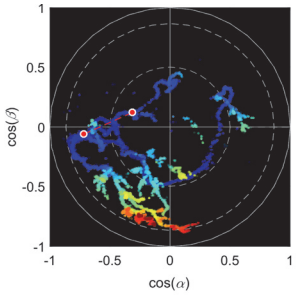

(d) Mapping result for case 2 (red dots mark two simultaneous sources)

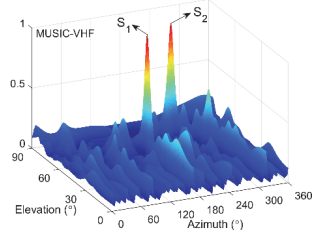

(e) MUSIC spatial spectrum for case 1(S1 and S2 mark two source)

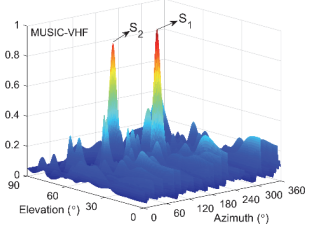

(f) MUSIC spatial spectrum for case 2(S1 and S2 mark two source)

Fig. 5. Cases of multi-source radiations and their localization results:

V. SUMMARY

In this paper, a VHF lightning mapping system - MARCOS with improved capabilities in retrieving weak VHF radiation sources is presented. Both experimental validation and field lightning observation demonstrated its performance.

As we known, VHF track of lightning positive breakdown is a common challenge, since its VHF radiation is considered to be much weaker than its companion – negative breakdown. Therefore, the VHF radiation from positive breakdowns are probably masked by negative breakdown. The proposed system here provide a promising tool to reveal the activities of positive breakdowns, and give a clearer description for the leader development of lightning discharges.

ACKNOWLEDGMENT

The authors would like to thank all the Jiangsu lightning observation team (SLOT) members taking part in the field lightning observation campaign.

This work is funded by National Natural Science Foundation of China (No. 41675002).

References:

[1] Z. Sun, X. Qie, M. Liu, R. Jiang, Z. Wang, and H. Zhang, "Characteristics of a negative lightning with multiple-ground terminations observed by a VHF lightning location system," Journal of Geophysical Research: Atmospheres, pp. 2015JD023702, (2016).

[2] M. G. Stock, M. Akita, P. R. Krehbiel, W. Rison, H. E. Edens, Z. Kawasaki, and M. A. Stanley, "Continuous broadband digital interferometry of lightning using a generalized cross-correlation algorithm," Journal of Geophysical Research: Atmospheres, 119, pp. 3134 – 3165, (2014).

[3] S. Qiu, B. Zhou, L. Shi, W. Dong, Y. Zhang, and T. Gao, "An improved method for broadband interferometric lightning location using wavelet transforms," J. Geophys. Res., 114, (2009).

[4] W. Dong, X. Liu, Y. Yu, and Y. Zhang, "Broadband interferometer observations of a triggered lightning," Chinese Science Bulletin, 46, pp. 1561-1565, (2001).

[5] T. Ushio, Z. I. Kawasaki, Y. Ohta, and K. Matsuura, "Broad Band Interferometric Measurement of Rocket Triggered Lightning in Japan," Geophys. Res. Lett., 24, pp. 2769-2772, (1997).

[6] X. M. Shao, D. Holden and C. Rhodes, "Broad Band Radio Interferometry for Lightning Observations," Geophys. Res. Lett., 23, pp. 1917-1920, (1996).

[7]T. Wang, L. H. Shi, S. Qiu, Z. Sun, Q. Zhang, Y. T. Duan, and B. Liu, "Multiple-Antennae Observation and EMTR Processing of Lightning VHF Radiations," IEEE Access, 6, pp. 26558-26566, (2018).

[8] T. Wang, S. Qiu, L. H. Shi, and Y. Li, "Broadband VHF Localization of Lightning Radiation Sources by EMTR," IEEE T. Electromagn. C., 59, pp. 1949-1957, (2017).

Modeling of Composite Transmission Tower under Direct Lightning Strokes Based on Electromagnetic Field Energy Principle

Shuhong Wang
State Key Laboratory of Electrical Insulation and Power Equipment, School of Electrical Engineering
Xi'an Jiaotong University
Xi'an, China
shwang@mail.xjtu.edu.cn

Youpeng Huangfu
State Key Laboratory of Electrical Insulation and Power Equipment, School of Electrical Engineering
Xi'an Jiaotong University
Xi'an, China
hfyp2027@stu.xjtu.edu.cn

***Abstract*—In this paper, an equivalent model for composite transmission line (TL) tower under direct lightning strokes based on electromagnetic field energy principle is comprehensively presented. There are four parts in the model: double vertical grounding conductor, main legs, cross arms and bracings. The impedances of the vertical grounding conductors and main legs of the composite tower are obtained combining the theory of conical antenna. The influence of composite material and bracings on the wave impedance are considered based on the electromagnetic field energy principle. The metal ground-wire cross arm is equivalent as a two parallel conductors. The composite phase-cross arm is regarded as a lumped capacitance which is determined by using three-dimensional (3D) Finite Element Method (FEM). An accurate model for extended grounding structure (EGS) of the tower base considering the soil ionization is used. The lightning overvoltage characteristic of the equivalent model is compared with the hybrid model in literature which verifies the validity of the model.**

Keywords—Composite Transmission Line Tower, Conical Antenna, Direct Lightning Strokes, Finite Element Method.

I. INTRODUCTION

Several traditional metal tower models have been developed by using theoretical approach [1] or based on experimental works [2]. However, there are few literatures researching the modeling of composite TL tower. In engineering design, the additional vertical grounding conductor is used to propagate the lightning energy into the earth [3]. The composite material in tower head and soil ionization around the EGS are omitted when modeling the tower in [3] and [4]. There is expensive and difficult to obtain the overvoltage characteristics for composite tower using field experimental measurement. Therefore, it is of great significance to model a composite tower model in theory.

The electromagnetic field energy around the composite tower is depends on its structure. In physical, the tower structure reflects the inductance and capacitance of each part or between each other of the tower. Therefore, the electromagnetic field energy principle can be used to determine the influence of composite material and bracings on the impedance for the tower.

In this paper, an equivalent model for composite tower under direct lightning strokes based on electromagnetic field energy principle is presented. The influence of composite material and bracings on the wave impedance are considered by introducing correction coefficients based on electromagnetic field energy principle. The metal ground-wire cross arm is equivalent as a two parallel conductors. The composite phase-arm is regarded as a capacitance determined by FEM. The lightning overvoltage characteristic of the tower is performed considering the soil ionization of EGS. The simulation results are compared with the hybrid model in [4] which verifies the validity of the model.

II. THE UNDER STUDY COMPOSITE TOWER

Fig. 1 (a) presents the composite tower head. Pink and orange, blue colors are representing the metal and composite materials, respectively. What's more, orange and blue colors are on behalf of bracings and main legs. The metal ground wire cross arms and bottom part of the tower body are connected by double vertical grounding conductors.

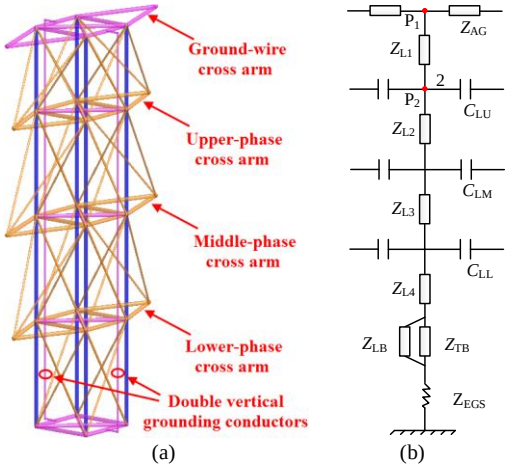

Fig. 1. (a) Schematic diagram of the composite transmission line tower head, and (b) equivalent model of the tower.

III. MODELING OF THE EQUIVALENT TOWER MODEL

The modeling of the impedance for the double grounding conductors, composite main legs and bracings between the grounding-wire and upper-phase arm is presented as follows.

A. Impedance of double vertical grounding conductors

The double vertical grounding conductors can be reduced to a single one by using the electromagnetic field energy method as shown in Fig. 2 (a).

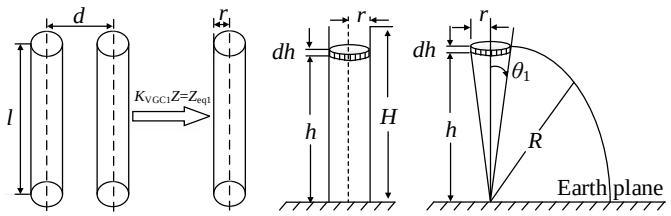

(a) (b) (c)

Fig. 2. (a) Schematic diagram of the double vertical grounding conductors reduction to a single one, (b) a differential element of a vertical cylindrical, and (c) its conical antenna model.

The wave impedance Z_{eq1} of the double vertical grounding conductors can be expressed by multiplying an impedance correction coefficient K_{VGC1} before the impedance Z of single vertical grounding conductor. The correction coefficients for the inductance and capacitance can be obtained further more.

$$Z_{eq1} = K_{VGC1} Z = \sqrt{K_L L} / \sqrt{K_C C} \tag{1}$$

where, K_L and K_C are the correction coefficients for the inductance and capacitance, respectively.

The impedance Z of single vertical grounding conductor is obtained based on the conical antenna theory [1].

A differential element of a vertical cylindrical with radius r at a height h above a perfect earth plane and its conical antenna model are shown in Fig. 2 (b) and (c), respectively.

The wave impedance Z_e of the differential element is

$$Z_e = \frac{1}{2\pi}\sqrt{\frac{\mu}{\varepsilon}} \ln[\frac{\sqrt{h^2+r^2}+h}{r}] \tag{2}$$

where, μ and ε are the permeability and permittivity of the metal.

Based on the electromagnetic field energy method, the inductance correction coefficient K_L is

$$K_L = \frac{1}{2} + \frac{1}{8} \times \frac{2d - 2\sqrt{l^2+d^2} - l\ln(-l+\sqrt{l^2+d^2})}{r - \sqrt{l^2+r^2} + l\ln\dfrac{l+\sqrt{l^2+r^2}}{r}} \tag{3}$$

The determination of correction coefficient of capacitance K_C will be stated in the full paper.

B. Considering composite material and bracings

The influence of the composite material and bracings on the impedance of the double vertical grounding conductors is considered through introducing a correct coefficient K_{G1} based on the electromagnetic field energy method.

$$Z_{G1} = K_{G1} Z_{eq1} \tag{4}$$

where, Z_{G1} and Z_{eq1} are the impedance with and without the composite material and bracings, respectively; and K_{G1} is the correction coefficient given as

$$K_{G1} = \frac{Z_{G1}}{Z_{eq1}} = \frac{\sqrt{L_{G1}/C_{G1}}}{\sqrt{L_{eq1}/C_{eq1}}} = \sqrt{\frac{L_{G1}}{L_{eq1}}} \times \sqrt{\frac{C_{eq1}}{C_{G1}}} = K_{G1L} K_{G1C} \tag{5}$$

where, K_{G1L} and K_{G1C} are correction coefficients of inductance and capacitance, respectively, which given as

$$\begin{cases} K_{G1L} = \sqrt{W_{m2}} / \sqrt{W_{m1}} \\ K_{G1C} = \sqrt{W_{e1}} / \sqrt{W_{e2}} \end{cases} \tag{6}$$

where, W_{m2} and W_{m1} are magnetic field energy with and without the composite material and bracings, respectively; W_{e2} and W_{e1} are the electric field energy with and without the composite material and bracings, respectively.

Those electromagnetic field energy calculated by using 3D FEM are shown in TABLE I when 1 A and 1 V applied on the vertical grounding conductors, respectively.

TABLE I. ELECTROMAGNETIC FIELD ENERGY

Energy (J)	W_{m1}	W_{m2}	W_{e1}	W_{e2}
	1.4027×10^{-4}	1.4021×10^{-4}	1.1071×10^{-31}	5.8638×10^{-31}

The middle cross-section of the magnetic and electric field energy intensity distribution considering composite material and bracings are shown in Fig. 3 (a) and (b), respectively.

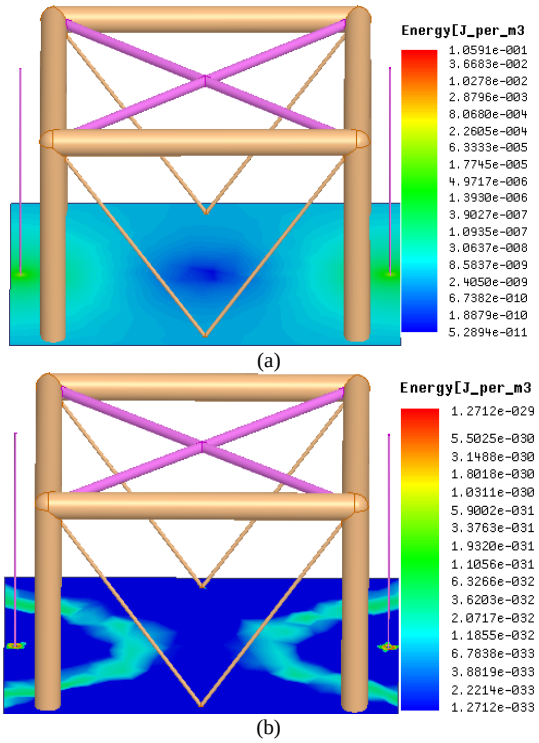

Fig. 3. Energy intensity distribution of (a) Magnetic field, (b) electric field.

The modeling of the metal grounding cross-arm, tower body and composite phase cross-arm will be demonstrated in detail. The influence of the number of the segments of the tower and the soil ionization of the EGS on its overvoltage characteristic will be discussed in the full paper.

IV. Analysis Results

A standard bi-exponential lightning surge with the waveform of 140 kA (2.6/50 μs) is injected into the tower top. The used composite tower model with 5 segments is shown in Fig. 1 (b).

The electric potential of tower top P_1 and the voltage between the vertical grounding conductor and upper-phase wire U_{CU} compared with [4] are shown in Fig. 4 (a) and (b), respectively.

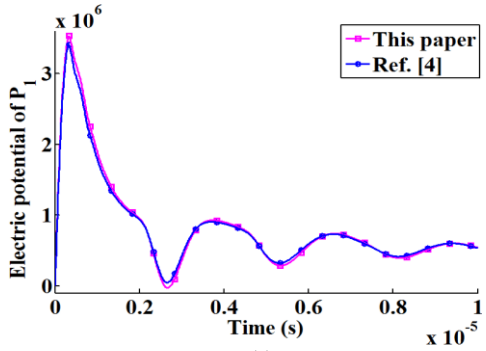

(a)

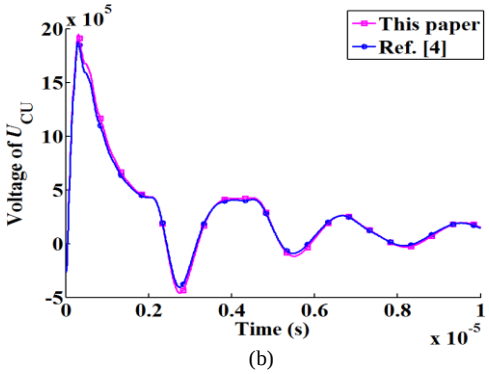

(b)

Fig. 4. (a) Electric potential of P_1, and (b) voltage of U_{CU}.

I. References

[1] J. A. Gutierrez et al., "Nonuniform transmission tower model for lightning transient studies," IEEE Trans. Power. Del., vol. 19, no. 2, pp. 490-496, Apr. 2004.

[2] Motoyama, H., Kinoshita, et al., "Experimental and analytical studies on lightning surge response of 500kV transmission tower," IEEE Trans. Power. Del., vol. 24, no. 4, pp. 2232-2239, Oct. 2009.

[3] Youpeng Huangfu, Shuhong Wang, et al., "Transient lightning impulse performance analysis for composite transmission tower," IEEE Trans. Electromagn. Compat., vol. 57, no. 5, pp. 1103-1111, Oct. 2015.

[4] Youpeng Huangfu, Shuhong Wang, et al., "Surge voltage and environmental electromagnetic field analysis for HV composite transmission tower under lightning strokes," 2014 IEEE International Symposium on Electromagnetic Compatibility, August 3-8, 2014, pp. 445-450, 2014.

[5] Gazzana, D.S., et al., "The transmission line modeling method to represent the soil ionization phenomenon in grounding systems," IEEE Trans. Magn., vol. 50, no. 2, 2014.

Multiple Antennas Radiation Continuous Observation System and its application in lightning mapping

Shulei Li
National Key Laboratory on Electromagnetic Environmental Effects and Electro-Optical Engineering, Nanjing, China
shuleili@hotmail.com

Lihua Shi
National Key Laboratory on Electromagnetic Environmental Effects and Electro-Optical Engineering, Nanjing, China
lihuashi@aliyun.com

Shi Qiu
National Key Laboratory on Electromagnetic Environmental Effects and Electro-Optical Engineering, Nanjing, China
zeustone@yeah.net

***Abstract*—Lightning broadband VHF localization of radiation sources provides an important means for the study of lightning discharge characteristics and its physical mechanisms. In order to improve the capability to locate weak radiation sources, a Multiple Antennas Radiation Continuous Observation System (MARCOS) with seven broadband VHF antennas in an "L" shape is designed, with a LeCroy oscilloscope to acquire signals at sampling rate of 500MHz in continuous recording mode. EMTR method is applied to locate lightning radiation sources in frequency domain for MARCOS system. The method of removing pseudo-points is also described. The application of the system and the method for locating a triggered lightning is presented. The results show that temporal and spatial development of the lightning channels can be well depicted in detail. The mapping results of a dart leader-return stroke process suggest that both the system and the method can provide good performance in locating weak sources, which could be an important tool for lightning research and may reveal new insights into lightning physics.**

Keywords—lightning, VHF, MARCOS, EMTR

I. INTRODUCTION

VHF interferometers can locate sources of lightning discharges in high temporal and spatial resolution, which is of great significance for understanding the physics of lightning [1]. Shao et al. first proposed the broadband VHF interferometer, and since then various VHF lightning locating systems based on short baselines played a significant role in lightning physics research [2-3]. A typical interferometer system, composed of three antennas in orthogonal baseline with length of a few meters to tens of meters, has been widely used and a large number of observation facts have been accumulated [4-6]. However, fewer antennas and sequential recording model would result in missing some sources at very low received power levels.

Stock et al. [7] developed a continuous broadband digital interferometry and designed a four-metric algorithm to filter false solutions. Continuous recording mode had been proved to be more effective than sequentially triggered system in locating weak radiation sources. On the other hand, Stock et al. [8] proposed a multiple baseline lightning interferometry using four VHF antennas, in order to improve the locating accuracy of weak sources. However, the least squares regression technique used by Stock is very prone to locating a side lobe of the cross correlation.

As to the location method, it is mainly divided into interferometric techniques and TOA measurements traditionally. In order to accurately measure the arrival time of TDOA systems, Qiu et al. [9] first applied cross-correlation operation in time domain to map the lightning development process. Stock et al. [7] proposed a more intricate generalized cross-correlation algorithm to process the continuous broadband VHF waveforms, and proved that the cross-correlation and interferometry technique were inherently consistent.

This paper introduced the MARCOS system designed for locating weak sources, which consisted of seven broadband VHF antennas in continuous recording mode. The EMTR method was operated to map the lightning processes for the system, especially the weak radiation regions. Based on this, the localization results of a triggered lighting were presented and analyzed.

II. MARCOS SYSTEM AND EMTR METHOD

A. MARCOS system

During the summer of 2017, comprehensive observation campaigns of lightning physics were conducted by JiangSu Lightning Observation Team (SLOT) in Jiangsu province, China. Observation site was 1.94km away from the rocket launcher. In this site, a MARCOS system was arranged, which was composed of seven broadband (from 50 to 200 MHz) VHF arrays in an "L" shape, as shown in Fig. 1, with distance between two adjacent antennas set to 9m. The VHF radiation was recorded continuously by an 8-channel LeCroy digital oscilloscope, with 12-bit vertical resolution at a sampling rate of 500MHz. The memory depth of the oscilloscope was 250Mpts/Ch; thus, the VHF radiation signals could be recorded for 500ms for each channel. The data acquisition initiated on an amplitude threshold trigger, with a pre-trigger of 250ms to record the preceding weaker processes before the trigger time.

Besides, the electric field signals were measured synchronously by a fast antenna (with time decay constant of 1ms and sampling rate of 30 MHz) and a slow antenna (with time decay constant of 4s and sampling rate of 30 MHz). For a comprehensive analysis, a high-speed video camera (HSV, Photron SAZ) was also installed to acquire the image sequences of lightning progression, at the frame rate of 8000fps with the exposure time of 122μs. In addition, time synchronization information of the system was provided by a high time accuracy GPS, with the timing accuracy better than 100ns. Other detailed site arrangements were presented in [10].

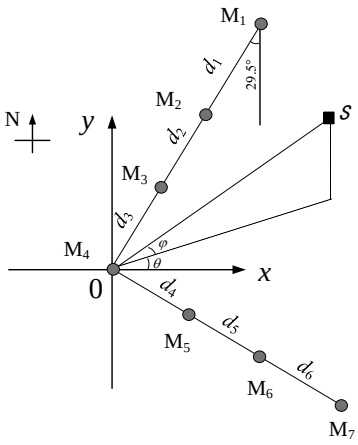

Fig. 1. Schematic diagram of MARCOS system antennas layout

B. EMTR method

The multi-antenna setup of MARCOS enhances the aperture of the mapping array, which means, on the other hand, traditional methods are no longer applicable, such as interferometric techniques and TDOA method. EMTR technique is applied to locate lightning sources, which can automatically converge the energy of the time-reversed signals to the source direction and is applicable to arbitrary array. This method has been successively applied to a three-antenna VHF location system [11]. We further improve it here to our multiple antenna system for clear revealing of the cloud-to-ground lightning channel. The principle of EMTR method is to radiate the receiving signals back from the antennas, and they will interact with each other and focus at the original source position [12]. In the following part, we will introduce the method in frequency domain.

Consider an array of seven antennas exposed a far-field lightning source. The received signal model can be written in frequency domain as:

$$X(f_j)=A(f_j, <\theta, \varphi>)\cdot S(f_j)+N(f_j) \quad (1)$$

where j is the effective frequency points; X is matrix of received signals. S is the Fourier transform of the lightning radiation sources, and A is the steering matrix of MARCOS, and N is the Fourier transform of noise vector.

Then we retransmit the received VHF signals back to space, which can be expressed as:

$$Y(f_j, <\theta, \varphi>)=X(f_j)^H\cdot A(f_j, <\theta, \varphi>) \quad (2)$$

where H denotes complex conjugate transpose. Y represents the time-reversed signals in the $<\theta, \varphi>$ direction. The reversed VHF signals will add in phase, and as a result, will be focalized at the original source position, and noise will be reduced due to its randomness. Therefore, the performance of the algorithm is improved by using multiple antennas.

Then, the energy of the superimposed time-reversed lightning signals can be calculated by:

$$P=\sum|Y(f_j, <\theta, \varphi>)|^2 \quad (3)$$

The best solution of the position of lightning sources can be achieved by searching the peak of P in all directions. However, for lightning broadband VHF signals, according to the principle of ISM (Incoherent Subspace Method) algorithm, the effective frequency points in the frequency band are averaged to obtain the total energy.

In this study, a 1.024μs (512 sample points) signal processing window with a sliding step of 0.256μs (128 sample points) is used. There will be a number of pseudo points not related to lightning sources in located results due to continuous recording mode and a heavy overlapping in window sliding. First, we will define coherence ratio (CR) to remove the pseudo points. Due to overlap analysis procedure, windows are not all independent, and so the sources appear to slowly drift over a small region during a short duration. So, the discontinuous points in a small time period will be removed. Then， the rest points will be additionally processed using the density-based clustering algorithm (DBSCAN) of Ester et al. [13] and the discrete points will be removed..

III. RESULTS OF TRIGGERED LIGHTNING OBSERVATIONS

On August 1st 2017, thunderstorm moved from southeast to northwest in the midnight, when a triggered lightning was triggered at 15:05:53 UTC. The atmospheric electric field was -13.5 kV/m, according to which the triggered lighting was negative polarity. The fast electric field waveform was recorded as shown in Fig. 2. The zero time represented the triggered time of the recording signals. The triggered lightning had five dart leader-return stroke processes, and the duration of the whole discharge process was about 600ms. However, due to the limits of memory depth, only three dart leader-return stroke processes were recorded by MARCOS.

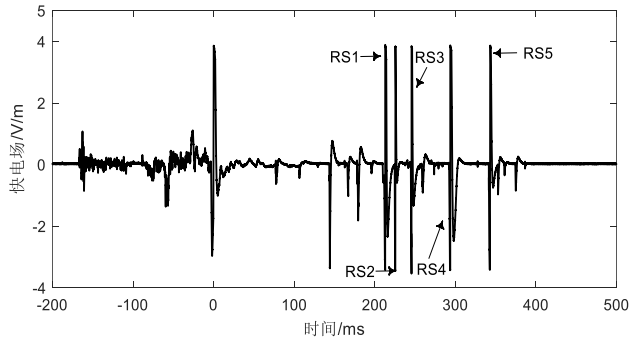

Fig. 2. Fast electric field waveform of triggered lightning.

The mapping results of this triggered lightning for the whole recording period are shown in Fig. 3. Comparison with the result of high-speed video image is also shown in Fig. 3.

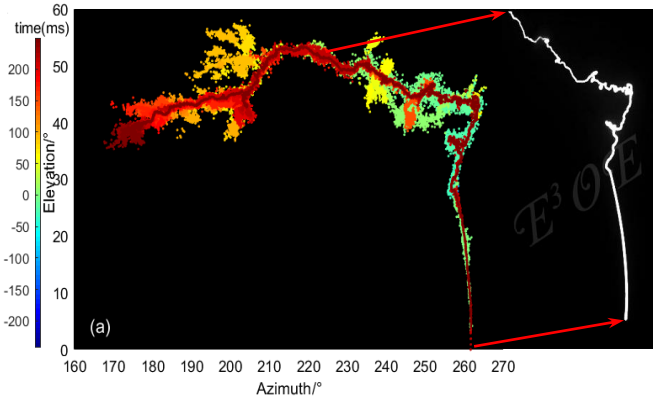

Fig. 3. Locating results of discharge channels of the triggered lightning: (a) Mapping results of VHF arrays; (b) HSV results.

Although the upward positive leader radiates weakly in VHF band, it can still be seen that the located channels are clear, from which the development process of lightning discharges can be distinguished clearly. Comparison with HSV image show that both of them have high consistency in the details of lightning channels, but the HSV image is limited by the field of view, and no other development process of this lightning has been obtained. The mapping based on MARCOS system can better describe the channels beyond the field of view of HSV.

In order to illustrate the capability of MARCOS system and EMTR method for locating weak sources, located sources and VHF waveform for the first dart leader-return stroke process was shown in Fig.4. The return stroke is a process of large amplitude currents flowing in perfect conductivity channels, which radiate extremely weak at VHF. It can be seen in Fig. 4, that the VHF signal related to return stroke is almost equivalent to noise level, which is very different to the strong VHF emissions for dart leader. Statistical results show that the average signal intensity of the return stroke is about 15dB weaker than that for the dart leader. However, the located points are clear and continuous, along the previous dart leader channel. The results show that the MARCOS system and EMTR method described above is in good performance in locating weak sources. It is of great importance for the study of lightning physics.

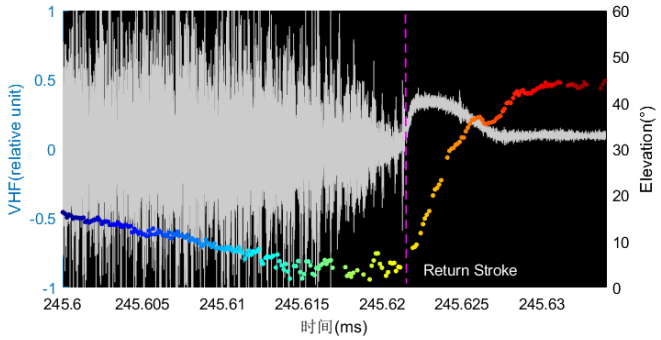

Fig. 4. Located Sources and VHF waveform for the first dart leader-return stroke process. The white curve represents VHF radiation intensity in relative unit. The scattered points represent the located points by MARCOS system, in which the color from blue to red indicating time revolution. The time period of dart-stepped leader and return stroke is separated by the purple dotted line.

IV. Summary

In this paper, a MARCOS system with seven broadband VHF antennas in an "L" shape was introduced, with a LeCroy oscilloscope to acquire signals in seven channels at continuous recording mode. EMTR method was used for this system to locate lightning radiation sources in frequency domain. The method of removing pseudo-points was also described.

The locating results of triggered lightning indicated that the channel shape details and development of lightning discharges could be clearly depicted by applying MARCOS system and EMTR method. The mapping results of return stroke suggested that the system can provide good performance in locating weak sources. It could be an important tool for lightning research and might reveal new insights into lightning physics.

Acknowledgment

The research was supported by National Natural Science Foundation of China (grant 41675002). The authors would like to thank all the Jiangsu lightning observation team (SLOT) members taking part in the field lightning observation campaign.

References

[1] V. A. Rakov, M. A. Uman. Lightning physics and effects[M]. The United Kingdom: Cambridge University Press, 2005.

[2] X. Shao, D. Holden, C. Rhodes. Broad band radio interferometry for lightning observations[J]. Geophys. Res. Lett., 1996, 23(15): 1917-1920.

[3] X. Shao, P. Krehbiel. The spatial and temporal development of intracloud lightning[J]. J. Geophys. Res., 1996, 101(D21): 26628-26641.

[4] W. L. Taylor. A VHF technique for space-time mapping of lightning discharge processes[J]. J. Geophys. Res., 1978, 83(C7): 3575-3583.

[5] Z. Sun, X. Qie, M. Liu, R Jiang, Z Wang, H Zhang. Characteristics of a negative lightning with multiple-ground terminations observed by a VHF lightning location system[J]. J. Geophys. Res. Atmos., 2016, 121: 413-426.

[6] M. Akita, M. Stock, Z. Kawasaki. Data processing procedure using distribution of slopes of phase differences for broadband VHF interferometer[J]. J. Geophys. Res. Atmos., 2014, 119: 6085-6104.

[7] M. G. Stock, M. Akita, P. R. Krehbiel. Continuous broadband digital interferometry of lightning using a generalized cross-correlation algorithm[J]. J. Geophys. Res. Atmos., 2014, 119(6): 3134-3165.

[8] M. G. Stock, and P. R. Krehbiel. Multiple Baseline Lightning interferometry improving the detection of low amplitude VHF Sources[C]. 2014 International Conference on Lightning Protection (ICLP), Shanghai, China, 2014: 2052-2059.

[9] S. Qiu, B Yang, W. Dong, T. Gao. Application of correlation time delay estimation in broadband interferometer for lightning detection [J]. Scientia Meteorological Sinica, 2009, 29(1): 92-96.

[10] Y. Li, S. Qiu, L. Shi, T. Wang. Observed variation of three-dimensional return stroke speeds along the channel in rocket-triggered lightning [J]. Geophys. Res. Lett., 2018, 45: 1-7.

[11] T. Wang, S. Qiu, L. Shi, Y. Li. Broadband VHF localization of lightning radiation sources by EMTR [J]. IEEE Transaction on Electromagnetic Compatibility, 2017, 59(6): 1949-1957.

[12] F. Rachidi, M. Rubinstein, M. Paolone. Electromagnetic Time Reversal: Application to EMC and Power Systems [M]. John Wiley & Sons, Hoboken, USA, 2017, pp: 94-100.

[13] M.Ester, H. P. Kriegel, J.Sander, X. Xu. A density-based algorithm for discovering clusters in large spatial databases with noise [C]. Inproceedings ofthe 2nd International Conference on Knowledge Discovery and Data Mining, 1996, 96(34), 226–231.

Investigation on low impedance high voltage generator based on UV preionization gap switch *

Li Song
National University of Defense Technology
State Key Laboratory of Pulsed Power Laser Technology
Changsha, China
lisong111@nudt.edu.cn

Liu Xiao
National University of Defense Technolog
Changsha, China
City, Country
365790357@qq.com

Gao Jingming
National University of Defense Technology
State Key Laboratory of Pulsed Power Laser Technology
Changsha, China
megod818@163.com

Cai Hao
National University of Defense Technolog
Changsha, China
City, Country
1178818032@qq.com

Shi Chengyu
National University of Defense Technolog
Changsha, China
1098421939@qq.com

Yang Hanwu
National University of Defense Technology
State Key Laboratory of Pulsed Power Laser Technology
Changsha, China
yanghw@nudt.edu.cn

***Abstract* — A low impedance high voltage pulse generator based on UV preionization gap switch was investigated numerically and experimentally. The generator is composed by primary source, pulse forming network, and UV preionization gap switch. Firstly, composition and structure of the generator is introduced with key electrical parameters. Then, Spice software was utilized to analysis influence of stray parameters such as stray inductance. The generator was built in our laboratory, and experiment result shown that pulses with peak voltage over 20kV, repetitive rate of 8Hz were achieved on resistance load. The comparative study shows that UV preionization gap switch can efficiently decrease the jitter of the generator. Experimental results show reasonable agreements with the analyses.**

Keywords—pulsed power technology, UV preionization gap switch, jitter

I. INTRODUCTION

Military and industrial applications have stimulated interests in high voltage pulse generators with high power level, low jitter achievability [1-2]. It is considered that the high power switches are of importance to the performance of the high-voltage pulse generators [3]. As important candidates, gap switches have been used in most of the high voltage generators for their ultra-high power capacity, simple structure, and low cost [4-5]; however, self-break gap switch is limited by high jitter when working at high repetitive rate which is very important for applications including high power microwaves (HPMs), environmental protection, plasma science, food preparation and material surface treatment [6-8]. Thus, we are motivated to study a low impedance high voltage pulse generator based on UV preionization gap switch.

In this paper, a low impedance high voltage pulse generator based on UV preionization gap switch is investigated numerically and experimentally. Firstly, composition and structure of the generator is introduced with key electrical parameters. Then, Spice software was utilized to analysis influence of stray parameters such as stray inductance. The generator was built in our laboratory, and experiment result shown that pulses with peak voltage over 20kV, repetitive rate of 8Hz were achieved on resistance load. The comparative study shows that UV preionization gap switch can efficiently decrease the jitter of the generator. Experimental results show reasonable agreements with the analyses.

II. INTRODUCTION OF LOW IMPEDANCE HIGH VOLTAGE PULSE GENERATOR

Low impedance high voltage pulse generator with peak voltage of tens of kV and pulse duration of hundreds of ns has a lot of applications. Figure 1 shows the diagram of the generator which is composed by primary source, low impedance pulse forming network, high power gap switch , and dummy load.

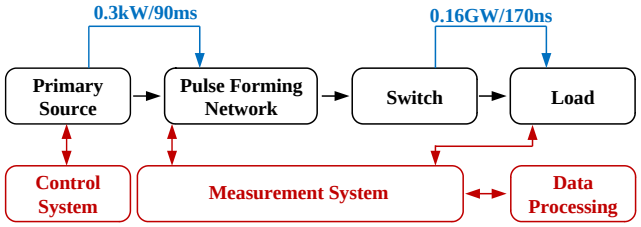

Fig. 1. Diagram of the low impedance high voltage generator

Control system is mainly used for long-range control of output voltage and charging current of the primary source via optical fiber. Voltage divider and Rogowski coil are used to get key singles in the generator. Achieved data from oscilloscope are treated in the processing system.

Table 1 gives key parameters of the generator.

TABLE I. KEY PAREMETERS OF THE GENERATOR

Parameters	*Unit*	*Value*
Charging current	mA	30
Pulse duration	ns	170
Peak voltage	kV	> 20
Impedance	Ω	2.5
Repetitive rate	Hz	10
Energy per pulse	J	> 40

III. Numerical Study Of The Generator

P_Spice software was used to analysis the circuit of the generator (Fig.2). Here, IDC present the primary source; T1 and T2 formed the Blumlein type pulse forming network; GAP is the high power switch, and Z present the dummy load. The working process can be described: initially, mains power from wall is shaped and charged to the low impedance pulse forming network with constant current. When the charging voltage gets to the break voltage of the high power switch, the energy is delivered to the dummy load in a quasi-square voltage pulse.

A. Idea circuit simulation

Circuit model of the circuit was constructed and analyzed in the software.

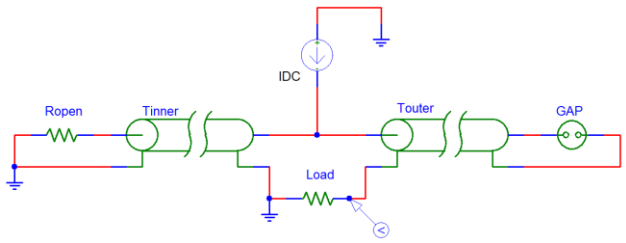

Fig. 2. Circuit of the high voltage generator

The result is shown in Fig.3. It can be seen that the circuit can achieve quasi-square pulse with voltage of 20kV and duration of 170ns when the charging current is 30mA and charging voltage is 20kV.

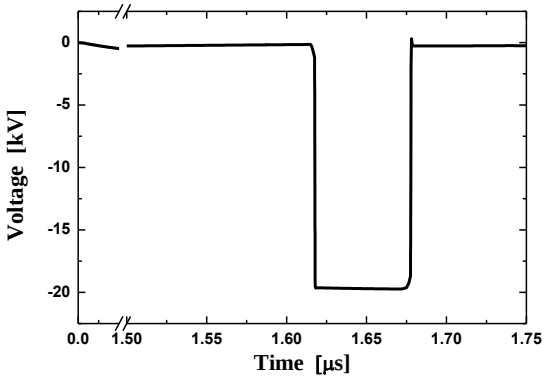

Fig. 3. Numerical result of the high voltage generator

As the impedance of the generator is only 2.5Ω, stray parameters, especially stray inductance of the gap switch, can largely influence the output waveform which directly decide the performance of the generator. Based on the circuit in Spice software, stray parameters were analyzed numerically.

B. Stray inductance of the gap switch

The rise time of the output voltage of the generator is proportional to the ratio of the inductance of the switch to the impedance [9]. In other word, stray inductance in the switch circuit should be well designed in low impedance generator. We added stray inductance series with the GAP in Fig.2.

Setting the stray inductance from 0nH to 50nH, the result shown in Fig.4 illustrated that rise time of output pulse of the generator is rising as the inductance is increasing. The rise time is 30ns when the inductance of the switch circuit is 20nH, which is acceptable for most of the applications. The results also tell us that for this generator, not only the the gap switch, but the structure of the shield should be optimized to decrease the circuit inductance.

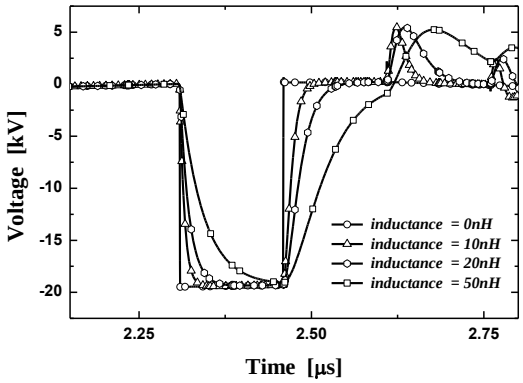

Fig. 4. Numerical result of the high voltage generator with stray inductance of the gap switch

IV. Experimental Study Of The Generator

A. Structure of the gap switch

Figure 5 shows the structure of the gap switch. In this gap switch, 6 UV lights, with wavelength of 254nm, are utilized to decrease the jitter of the gap switch. Intensity and uniformity of the UV light can be adjusted by switched on different number of the light, and when all the light were turned off, the switch was back to a self-break gap switch. Charging voltage is changed by distance of the electrodes and nitrogen pressure inside of the switch.

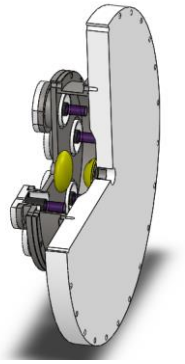

Fig. 5. Structure of the gap switch of the high voltage generator

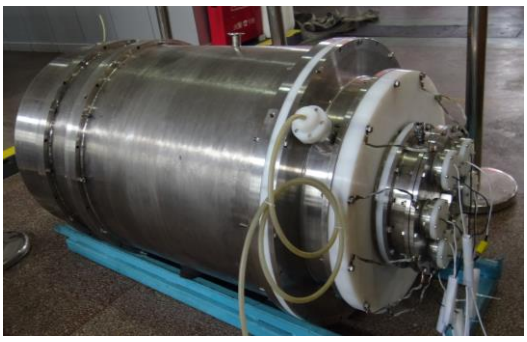

Fig. 6. Picture of the low impedance high voltage pulse generator

The low impedance high voltage pulse generator was built in our laboratory, as shown in Fig.6. The Blumlein type pulse forming network was constructed by inductance and ceramic capacitors.

B. *Experimental study of the generator with self-break gap switch*

When all the UV lights are turned off, the gap switch can be considered as self-break gap switch. The output voltage pulse is shown in Fig.7.

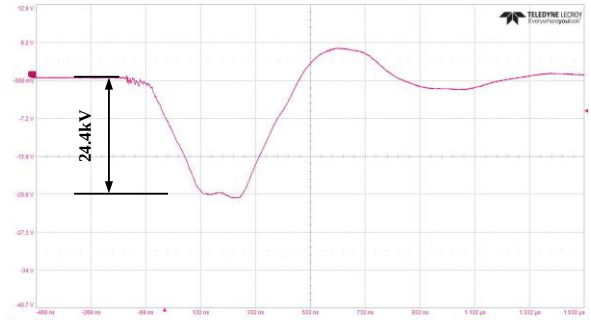

Fig. 7. Output pulse of the generator based on self-break gap switch

(single mode)

It can be seen that when the charging voltage is 25kV, a quasi-square pulse with peak voltage approximately 24.4kV and duration of 180ns was achieved on the dummy load. Experimental result of the generator can meet the requirement of the design parameters; Resonance after the main pulse comes from the mismatching of the resistance.

Setting the charging current to 30mA, the generator can work at repetitive rate of 8Hz. The output waveform is shown in Fig.8.

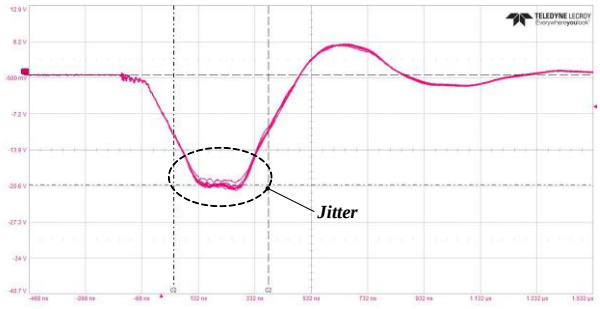

Fig. 8. Output pulse of the generator based on self-break gap switch

(repetitive rate mode)

It is clear that the jitter of the generator is approximately 8%, which should be improved if the generator used in plasma science research and food treatment.

C. *Experimental study of the generator with UV preionization gap switch*

Turning all the UV lights on, preionization scheme is employed in the gap switch. Keeping all the parameters constant, experiment result is shown in Fig.9.

It can be seen that the jitter of the output waveform (approximately 2%) is efficiently decreased, and the peak voltage is a little bit lower, which meet the theoretical analysis.

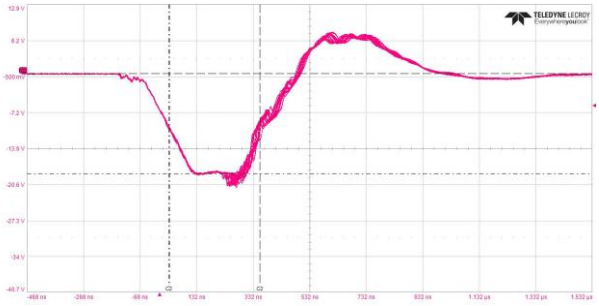

Fig. 9. Output pulse of the generator based on UV preionization gap switch (repetitive rate mode)

It is because that as the UV light can generate initial electrons, the formation of the discharge channel between electrodes of the switch is easier, the randomness of the break-down of the gap is decreased. At the same time, the hold voltage is also decreased. The inconsistent of the latter half of the waveform is reduced by some ceramic capacitors were break when the generator was working at repetitive rate mode, this will be solved by filling SF6 or transformer oil into the pulse forming network in our future study.

V. CONCLUSION

A low impedance high voltage pulse generator based on UV preionization gap switch was investigated numerically and experimentally. Firstly, composition and structure of the generator is introduced with key electrical parameters. Then, Spice software was utilized to analysis influence of stray parameters such as stray inductance. The generator was built in our laboratory, and experiment result shown that pulses with peak voltage over 20kV, repetitive rate of 8Hz were achieved on resistance load. The comparative study shows that UV preionization gap switch can efficiently decrease the jitter of the generator. Experimental results show reasonable agreements with the analyses.

REFERENCES

[1] Bluhm H. Pulsed power systems principles and application. Beijing:Tsinghua University Press,2008:75-149

[2] Liu Xisan. High pulsed power technology. Beijing: National Defense Industry Press, 2005: 380-401.

[3] E Kuffel, W S Zaengl. High Voltage Engineering[M]. Oxford: World Reed Educational and Professinal Publishing Ltd, 2000: 287~308.

[4] Zhang J, Jin Z X. Recent advances in long-pulse HPM sources with repetitive operations in S-, C-, and X-bands [J]. IEEE Transactions on Plasma Science, 2011, 39(6): 1438-1445.

[5] J M Lehr, M D Abdalla. Design and Development of A 1MV, Compact, Selfbreak Switch for High Repetetion Rate Operation [C]. Proc of 12th IEEE International Pulsed Power Conference, 1999:1199-1202.

[6] Schamiloglu E. On the Road to Compact Pulsed Power: Adventures in Materials, Electromagnetic Modeling and Thermal Management [C]. IEEE International Pulsed Power Conference, 2003: 3~8.

[7] S. Li, J. M. Gao, H. W.Yang, et al., Investigation on adjustable magnetic pulse compressor in power supply system, IEEE Trans. On Power Electronics, Vol 34 (2), pp: 1540-1547.

[8] J. M. Gao, H. W. Yng, S. Li. Investigation on a high power, low impedance, and long pulse generator based on magnetic switches. IEEE Trans. on Plasma Science. Vol.42(4), pp: 988-992. (2014).

[9] S. Li, B. L. Qian, H. W. Yang, et al., An improved rolled strip pulse forming line, Review of Scientific Instruments. 84, 064704, 2013.

On the Maximum Voltage Induced by a Wideband HPEM Field in Cascaded Lines with Piecewise-Linear Layout

Tao Liang, Giordano Spadacini, Flavia Grassi, Sergio A. Pignari
Department of Electronic, Information and Bioengineering (DEIB)
Politecnico di Milano
Milan, Italy
{tao.liang, giordano.spadacini, flavia.grassi, sergio.pignari}.polimi.it

***Abstract*—This paper proposes a worst-case analysis for a transmission line (TL) with multiple abrupt bends, illuminated by a wideband, high-power electromagnetic (HPEM) field. The analysis is aimed at predicting the maximum peak of the voltage waveform induced across the terminal loads. It is shown that the input parameters required for HPEM pulse description are only the bandwidth and energy density, whereas no specifications are required for the electric-field waveforms. The proposed analytical expressions build on a previous TL model under additional simplifying assumptions of electrically-long segment length and matched terminal impedances. Numerical simulations corroborate model validity and suggest that the obtained closed-form expressions can be even used with negligible errors in case of mismatched loads. The impact of TL routing on the worst-case voltage peak is also discussed.**

***Keywords*—High Power Electromagnetic (HPEM) environments, Intentional Electromagnetic Interference (IEMI), Radiated Susceptibility, Transmission Lines.**

I. Introduction

With a growing dependency of modern society on miniaturized and integrated information/communication technology (ICT) equipment, it is becoming increasingly vital to protect mission-critical electrical/electronic systems against Intentional Electromagnetic Interference (IEMI) attacks and High-Power Electromagnetic (HPEM) fields [1, 2].

In past years, significant experimental campaigns were carried out to verify the susceptibility level of systems excited by HPEM pulses governed by various time-domain waveforms, e.g. damped sinusoids, double exponential pulses, etc. [3]. However, since the most general definition of wideband HPEM environment relies on bandwidth (i.e., the frequency range containing 90% of signal energy) [4], without specifying details of time-domain waveforms, direction of arrival of the impinging wave, etc., one may assume that testing under specific HPEM condition does not guarantee general representativeness of results. Similarly, simulation models aimed at assessing IEMI effects should account for the variability of the HPEM environment. For instance, the identification of worst-case scenarios is of great interest, as well as the statistical analysis of results.

In this connection, the worst-case HPEM field waveform (with constrained energy and bandwidth) which maximizes the peak of the induced-voltage waveform in an arbitrary port of a generic victim system was addressed in [5] by exploiting the Lorentz reciprocity theorem and a single full-wave simulation. The sensitivity of the worst-case voltage peak to the variation of the electromagnetic environment (i.e., direction of incidence and polarization of the plane-wave field) was modeled by a cumulative distribution function (cdf) [6, 7]. This worst-case model was later reformulated in [6] for a straight wire running parallel above ground, using transmission-line (TL) theory [8]. The interest for such a canonical TL configuration arises from its use as a simplified model for the excitation and propagation of common-mode (CM) interference in an unshielded wiring harness. In addition to improved computational efficiency, the TL formulation of field-to-wire coupling enabled deriving closed-form expressions, unveiling the impacts of parameters like length, height and terminal loads on the worst-case voltage peak [6]. Specifically, it was shown that for sufficiently "long" lines (compared to a sort of wavelength associated to the bandwidth), the worst-case voltage peak reaches a limit value which is independent from line length.

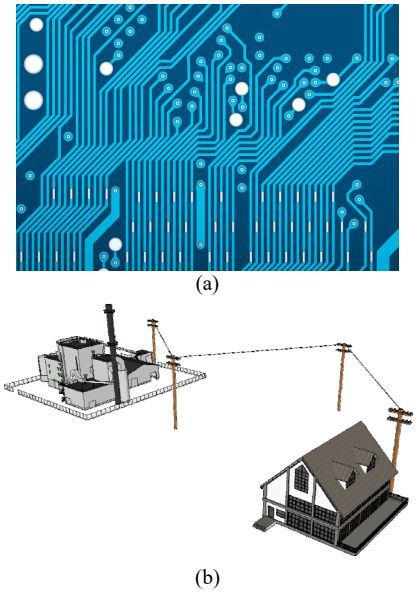

(a) (b)

Fig. 1. Examples of TLs with multiple bends: (a) signal lines with bends in a PCB; (b) power/telecom line with zigzag routing.

In typical applications, wires follow complex path and the presence of bends can be usually observed. For instance, as shown in Fig. 1(a), traces on a printed circuit board (PCB) are bent in order to properly accommodate all of them in the integrated layout design. Similarly, as shown in Fig. 1(b), a power/telecommunication line normally shows zigzag routing.

This paper improves the representativeness of the previous model in [6] with respect to real-world applications, by accounting for the presence of multiple bends in the TL path. The main objective is the derivation of analytical expressions of the worst-case voltage peak highlighting the contributions of different straight segments in the whole TL. To this aim, the TL model [6] will be applied with two simplifying assumptions: a) long straight-line segments (in the aforementioned meaning); b) matched loads, that is, terminal impedances equal to the TL characteristic impedance. Numerical validations will prove the validity of the proposed model and will show that hypothesis b) can be relaxed by accepting low prediction errors.

The paper is organized as follows: Section II summarizes the key steps for evaluating the coupling length of bent TL based on TL model. Section III formulates, simplifies and validates the worst-case voltage peak expression after a brief review of the worst-case concept. Section IV draws conclusions.

II. Field Coupling to TL with Multiple Bends

A. Structure of TL with Multiple Bends

A generalized representation of a bent TL containing n straight segments is shown in Fig. 2(a). For simplicity, all wire segments are assumed to be perfect bare conductor of radius r_w, and running above perfect metallic ground at height h.

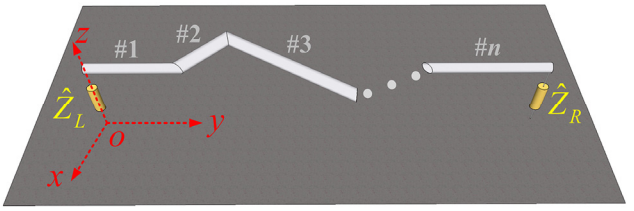

(a)

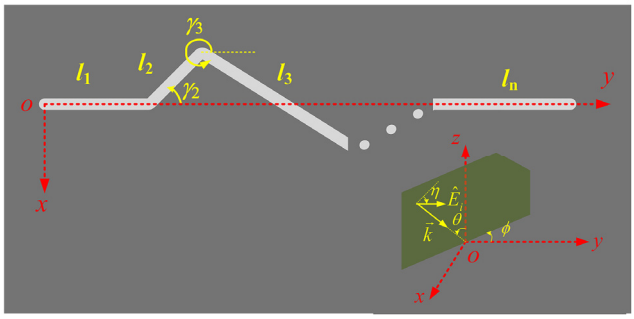

(b)

Fig. 2. TL with multiple bends. (a) 3-dimensional bird view; (b) top view.

Wire segments are enumerated from left to right as wire #1, #2, ⋯, #n, respectively, where the left terminal is placed in the origin (O) of Cartesian coordinates. The corresponding segment lengths are $l_1, l_2, \cdots, l_n$, respectively. This TL network is connected to ground through impedances $\hat{Z}_L$ and $\hat{Z}_R$ at the left and right terminals. The routing geometry is furtherly specified in Fig. 2(b), where each angle γ_i of the i-th segment is defined as an anticlockwise rotation angle with respect to the $+y$ direction.

The impinging HPEM field is modeled as a linearly polarized plane wave with propagation vector $\vec{k}$ and electrical field component $\hat{E}_i$ (in the following, the caret above symbols ^ is used to denote frequency-domain, complex quantities). The incident direction is defined in spherical coordinates by polar angle θ and azimuth angle ϕ, and the polarization is defined by angle η [6, 8].

B. Coupling length solved by TL field-coupling theory

Let us define the *coupling length* as $\hat{L} = \hat{V}_L / \hat{E}_i$, namely, the transfer ratio between the induced voltage across a TL impedance (e.g., the left one, without losing generality) and the electric field.

For a straight TL with length l running along y-axis [like just the first TL segment depicted in Fig.2(b)], connected to matched terminal impedances, the closed-form expression of $\hat{L}$ are solved and reported in [6] as:

$$\hat{L} = 2jhG\sin\left(\frac{\beta l}{2}\left(1+\sin\theta\cos\phi\right)\right)e^{-j\frac{\beta l}{2}(1+\sin\theta\cos\phi)} \quad (1)$$

$$G(\theta,\phi,\eta) = \frac{\cos\eta\left(\cos\phi+\sin\theta\right)+\sin\eta\cos\theta\sin\phi}{1+\sin\theta\cos\phi} \quad (2)$$

where j is the imaginary unit; $\beta = \omega / c_0$ is the phase constant; ω is angular frequency, c_0 is the speed of light in vacuum. These expressions can be readily adapted to model a single segment oriented with rotation angle γ by substituting ϕ with $\phi - \gamma$ in (1) and (2).

Knowing the coupling length of individual segments, it is possible to express the coupling length $\hat{L}_{NW}$ of whole TL network as

$$\hat{L}_{NW} = \sum_{i=1}^{n} \hat{L}_i\left(l_i, \phi_i - \gamma_i\right) e^{-j\beta\sum_{m=1}^{i-1} l_m\left[1+\sin\theta\cos(\phi_m-\gamma_m)\right]} \quad (3)$$

where $\hat{L}_i\left(l_i, \phi_i - \gamma_i\right)$ is the coupling length of segment i, and a suitable phase term accounts for a) the time delay of the wave propagating from segment's terminal to the TL load terminal; b) the phase difference due to reference's origin change in the expressions of the HPEM field.

By defining the auxiliary variables $G_i = G\left(\theta, \phi_i - \gamma_i\right)$ and τ_i as

$$\tau_i = \frac{l_i}{2c_0}\left[1+\sin\theta\cos\left(\phi_i-\gamma_i\right)\right]. \quad (4)$$

one can simplify (3) as

$$\hat{L}_{NW} = 2jh\sum_{i=1}^{n}\sin(\omega\tau_i)\,e^{-j\omega\tau_i}G_i e^{-j\omega\sum_{m=1}^{i-1}\tau_m} \quad (5)$$

III. Analytical Solution to the Worst-Case Voltage Peak for a TL with Multiple Bends

A. Derivation for long TL segments

Let $[\omega_1, \omega_2]$ be the limited band of the radiated HPEM

pulse, and let W_E (expressed in J/m^2) be the finite energy density [9]. Through the solution of a rigorous optimization process, it was demonstrated in [5] that the maximum voltage peak induced under constrained bandwidth and energy (i.e., maximum peak among all the possible waveforms) is given by

$$V_{P,NW} = \sqrt{\frac{Z_0 W_E}{\pi}\int_{\omega_1}^{\omega_2}\left|\hat{L}_{NW}\right|^2 d\omega} = 2h\sqrt{\frac{Z_0 W_E}{\pi}\int_{\omega_1}^{\omega_2}\sum_{i=1}^{n}\sin^2(\omega\tau_i)\left|G_i e^{-j\omega\sum_{m=1}^{i-1}\tau_m}\right|^2 d\omega} \quad (6)$$

where $Z_0 \approx 377\ \Omega$ is the intrinsic impedance of vacuum, and the expression of the coupling length (5) has been substituted in the second term.

Likewise in [6] for a single and straight TL, one can show that each single addend of the summation in (6) becomes independent from length (i.e., from τ_i) if l_i is much greater than a critical electrical length l_s associated to the bandwidth f_2-f_1 :

$$l_i \gg l_s = \frac{c_0}{\pi(f_2 - f_1)\left(1+\sin\theta\cos(\phi_i - \gamma_i)\right)} \quad (7)$$

Provided that all segments of the bent TL satisfy the "long line" criterium (7), an arbitrary, unique value $\tau = \tau_1 = \tau_2 = \cdots = \tau_n$ can be inconsequentially assigned to (6), which can be rewritten as

$$V_{P,NW} = 2h\sqrt{\frac{Z_0 W_E}{\pi}\int_{\omega_1}^{\omega_2}\sin^2(\omega\tau)\sum_{i=1}^{n}\left|G_i e^{-j\omega(i-1)\tau}\right|^2 d\omega} \quad (8)$$

In line with the objective of this paper, it is interesting to clearly recognize and separate in (8) the contributions of each single TL segment. In particular, according to (6) one can define

$$V_{P,i} = \sqrt{\frac{Z_0 W_E}{\pi}\int_{\omega_1}^{\omega_2}\left|\hat{L}_i\right|^2 d\omega} \quad (9)$$

as the worst-case voltage peak when considering the TL segment i alone. After several mathematical manipulations, the worst-case voltage peak (8) for the whole TL can be rewritten as

$$V_{P,NT} = \sqrt{\sum_{i=1}^{n} V_{P,i}^2 - \sum_{i=1}^{n-1}\mathrm{sign}\left(G_i G_{i+1}\right) V_{P,i} V_{P,i+1}} \quad (10)$$

where sign(~) is the signum function.

It is worth noting that, in the absence of the second summation in (10), the worst-case voltage peak of the whole TL would be simply a geometric mean of all worst-case voltage peaks pertaining to individual wire segments. Conversely, the second summation (involving the signum function) introduces effects due to adjacent segments (i.e., i-th and (i+1)-th segments), that is, effects due to the specific routing geometry.

In the special case when all segments are aligned ($\gamma_i = 0$, $\forall i$) forming a straight TL, equation (10) consistently reduces to $V_{P,NT} = V_{P,i}$, that is, to the contribution of just a single segment (anyone), which does not depend on length as said above. In general, wire routing, i.e., the presence of unaligned segments may lead to increase or decrease of the worst-case voltage peak with respect to a straight TL, depending on the results of signum functions in (10).

B. Numerical validations

The closed-form solution (10) can be numerically verified through a case study. Namely, the proposed exemplification refers to a TL composed of 5 straight segments with radius r_w=1 mm; height h = 1 cm, lengths $l_1 = l_2 = l_4 = l_5 = 1$ m , $l_3 = 2$ m , orientations $\gamma_1 = 0°$, $\gamma_2 = 45°$, $\gamma_3 = 315°$, $\gamma_4 = 45°$, $\gamma_5 = 0°$. According to this geometry, the per-unit length parameters of the TL lead to characteristic impedance of about Z_C=180 Ω [8]. The impinging HPEM field is a hyperband pulse with bandwidth 300 MHz – 3 GHz and energy density W_E = 1 mJ/m^2 [5, 9].

An independent TL model exploiting the Baum-Liu-Tesche (BLT) equations [8] was implemented, particularly, without enforcing a priori assumptions related to matched impedances or to the segment lengths. This model was used to directly evaluate the coupling length $\hat{L}_{NW}$, which is used afterwards to compute the worst-case voltage peak (6). The result is compared versus the proposed model in its most simplified form (10), where the coupling length of each segment is given in (1) by substituting ϕ with $\phi - \gamma$.

To account for the variability of incidence and polarization angles, uniform (U) distributions are assigned to the following independent random variables

$$\theta \sim \mathrm{U}[0°, 90°];\ \phi \sim \mathrm{U}[0°, 360°];\ \eta \sim \mathrm{U}[0°, 360°] \quad (11)$$

and Monte Carlo simulations (2000 repeated runs) are performed to evaluate the empirical distribution of the worst-case induced voltage.

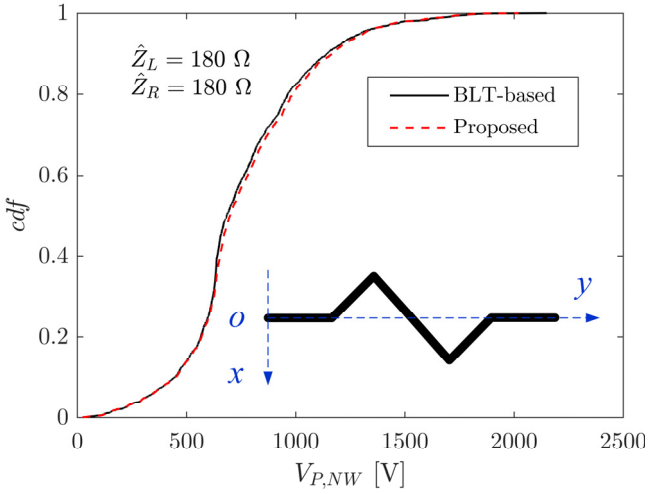

Fig. 3. Comparison of cdfs of the worst-case voltage peak predicted by BLT equations and the proposed simplified analytical expression (10). The inset shows the top view of bent TL under study. The TL is connected to matched terminal impedances.

Hence, the comparison between the proposed model (10) and general BLT equations is presented in statistical form as a comparison of cdfs. Results are shown in Fig. 3 in case of matched terminal impedances, i.e. $\hat{Z}_L = \hat{Z}_R = Z_C = 180\,\Omega$. One can appreciate that the proposed model (10) and the general BLT equations are in almost perfect agreement in Fig. 3.

It is worth investigating whether the assumption of matching can be finally relaxed by applying (10) even in case of unmatched loads, provided that the coupling length in (3) is correctly evaluated. To this aim, Monte Carlo simulations were repeated for two cases: a) $\hat{Z}_L = 50\,\Omega$, $\hat{Z}_R = 100\,\Omega$, and b) $\hat{Z}_L = 250\,\Omega$ and $\hat{Z}_R = 300\,\Omega$. Results presented in Fig. 4 suggest that the prediction error of (10) is largely acceptable in case of unmatching.

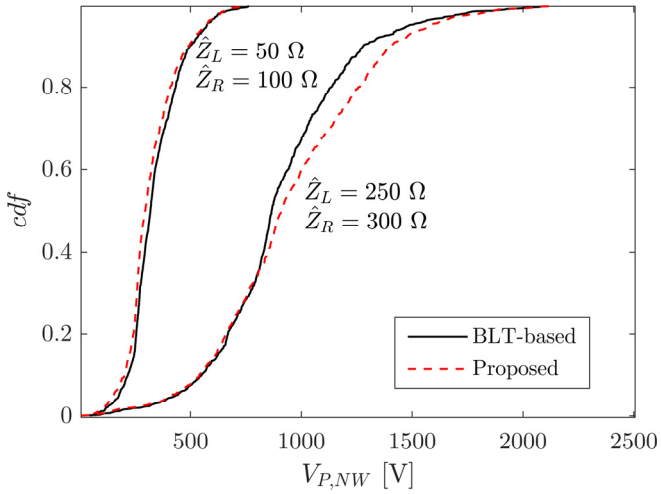

Fig. 4. Comparison of cdfs of the worst-case voltage peak predicted by BLT equations and the proposed simplified analytical expression (10). The TL is connected to unmatched terminal impedances.

IV. Conclusions

This paper investigated the worst-case peak of the voltage waveform that can be induced across terminal loads of a TL with multiple bends by an HPEM field pulse with limited bandwidth and finite energy density. After a general formula (6) derived in line with previous works [5, 6], a simplified expression (10) was obtained and numerically validated. The added value of this expression is that it clearly highlights the contribution of each straight TL segment to the worst-case voltage peak induced at the whole TL terminals.

In particular, physical insight can be gained by the light of (10). First, provided that all segments are sufficiently long so to satisfy inequality (7), it tuns out that the specific segment lengths do not influence the worst-case voltage peak. Hence, the overall line length does not pose a problem about the protection against the induced interference.

Conversely, the routing of the TL network (here modeled by rotation angles γ_i between adjacent wire segments) may exert strong impact on the worst-case scenario. Indeed, as observed in Section III.A, the result of (10) may be either increased or decreased by the second summation term. Consequently, if two TLs (possibly of different lengths) are considered, both starting and ending in the same points, one straight and one with multiple bends, the latter may lead to either a greater or a lower worst-case induced voltage peak depending on the particular routing layout.

Theoretically, if incidence and polarization angles of the HPEM plane wave were deterministically known, it would be possible to exploit (10) so to reduce the worst-case voltage peak by carefully adjusting the number of segments and their relative orientation angles. However, incidence and polarization are practically random in any realistic IEMI scenario, therefore the worst-case voltage peak must be statistically characterized by a cdf.

References

[1] W. A. Radasky, C. E. Baum, and M. W. Wik, "Introduction to the Special Issue on High-Power Electromagnetics (HPEM) and Intentional Electromagnetic Interference (IEMI)," *IEEE Trans. Electromagn. Compat.,* vol. 46, pp. 314-321, Aug 2004.

[2] W. A. Radasky, "Fear of frying electromagnetic weapons threaten our data networks. Here's how to stop them," *IEEE Spectr.,* vol. 51, pp. 46-51, 2014.

[3] F. Brauer, F. Sabath, and J. L. t. Haseborg, "Susceptibility of IT network systems to interferences by HPEM," in *2009 IEEE International Symposium on Electromagnetic Compatibility*, 2009, pp. 237-242.

[4] IEC, "IEC 61000 Electromagnetic compatibility (EMC) – Part 2-13: Environment – High-power electromagnetic (HPEM) environments – Radiated and conducted," ed, 2005.

[5] G. Spadacini, T. Liang, F. Grassi, and S. A. Pignari, "Worst Case and Statistics of Waveforms Involved in Wideband Intentional Electromagnetic Attacks," *IEEE Trans. Electromagn. Compat.,* vol. 60, pp. 1436-1444, Oct 2018.

[6] T. Liang, G. Spadacini, F. Grassi, and S. A. Pignari, "Coupling of Wideband Radiated IEMI to Cables Above Ground," *IEEE Trans. Electromagn. Compat.,* pp. 1-9, 2018.

[7] T. Liang, G. Spadacini, F. Grassi, and S. A. Pignari, "Coupling of Wideband Radiated IEMI to Wiring Harness: A Statistical Analysis of the Main Influencing Parameters," in *2018 IEEE Symposium on Electromagnetic Compatibility, Signal Integrity and Power Integrity (EMC, SI & PI)*, 2018, pp. 357-362.

[8] C. R. Paul, *Analysis of multiconductor transmission lines*. New York: John Wiley & Sons, 2008.

[9] D. Nitsch, M. Camp, F. Sabath, J. L. ter Haseborg, and H. Garbe, "Susceptibility of some electronic equipment to HPEM threats," *IEEE Trans. Electromagn. Compat.,* vol. 46, pp. 380-389, Aug 2004.

Strong electromagnetic pulse harm and protection to the aircraft

Tao Zhang
Aviation Key Laboratory of Science and Technology on Electromagnetic Environmental Effects
Shenyang Aircraft Design and Research Institute, AVIC
ShenYang, China
zhangtaowf86@163.com

Baihan, Liu
Shenyang aerospace university college of electronic and information engineering,
ShenYang, China
liubaihan59@163.com

Zhaohui Lv
Aviation Key Laboratory of Science and Technology on Electromagnetic Environmental Effects
Shenyang Aircraft Design and Research Institute
AVIC
ShenYang, China
syemc@163.com

Yan Wang
Aviation Key Laboratory of Science and Technology on Electromagnetic Environmental Effects
Shenyang Aircraft Design and Research Institute
AVIC
ShenYang, China
sy601wangyan@163.com

Abstract: **This paper starts with the damage mechanism of strong electromagnetic pulse(EMP) to military aircraft, analyzes the front door coupling and the back door coupling of EMP on the aircraft, and gives the technical route and measures of aircraft protection design for EMP.**

Keywords: EMP; Military aircraft; Protective design

EMP weapons as a special kind of powerful weapons, put a serious threat to the survival ability of the equipment battlefield, and changing the traditional operational mode fundamentally, has become an ace in the hole of to win the high-tech information-based war in the future.

I. THE DAMAGE MECHANISM OF EMP ON AIRCRAFT

EMP is caused by a nuclear explosion or lightning discharge, photon scattering is found in the surrounding medium, which produces Compton recoil electronics and optoelectronics leads to a new electromagnetic radiation[1]. Devastating surge voltage and electricity were produced, in where the electric and magnetic fields were generated by EMP and coupled with electric or electronic system[2]. EMP energy is concentrated at 100kHz-10MHz, and the wavelength is 3km-30m.

Strong electromagnetic energy can couple and produce a few volts electrical surge in the cables through antenna, power cord, and the interconnection cables between airborne equipments. High voltage pressure breakdown and thermal effect will damage the electrical and electronic equipment, cause temporary or permanent damage to the equipment or system, and affect the function of the aircraft.

II. THE COUPLING WAYS OF EMP ON AIRCRAFT

There are two coupling ways of EMP effect on the aircraft, the front door effect and the back door effect[3]. The front door coupling is dominated by various types of antennas, and the back door coupling includes hole or slot

coupling and various types of sensors and cable coupling on the aircraft.

1) Antenna coupling

When EMP field is coupled to antenna, a high voltage or current is generated, then the high voltage enters the communication channel, it will interfere with the rear stage. The exposed metal lead and the connector in EMP field have similar receiving effects of a monopole antenna.

2) Hole or slot coupling

There are holes or gaps in any actual weapon platform. The coupling capacity and coupling frequency of EMP field in the shielding body are related to the size of the shielding body and the size of holes. The strong electromagnetic field forms a coupling current and voltage to the equipment inside the machine.

3) Cable coupling

The metal conductors exposed to the electromagnetic field all have the function of a receiving antenna. When EMP wave are coupled to the cable, an interference voltage or current is generated and transmitted to the device. There is a distributed capacitance between the cables installed centrally, and coupling occurs, so that cables that are not directly coupled with EMP also become conductive interference paths.

III. AIRCRAFT PROTECTION TECHNOLOGY APPROACH TO EMP

A. Protective design technology route

The common protection technologies such as shielding, filtering and grounding are effective solutions. The protection of aircraft to EMP should first analyze the interference coupling path. According to different objects and factors, the coupling effect magnitude and hazard degree analysis are carried out, and according to different systems, equipments and different hazard levels,different protective measures are taken. The technical route for aircraft protection to EMP shows in figure 1.

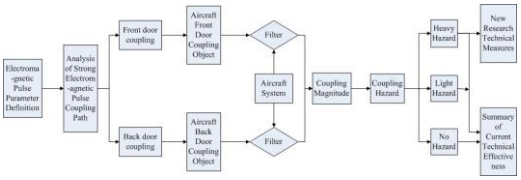

Figure 1 protection design technology roadmap

B. The protection design of aircraft to EMP

For aircraft, the protection design to EMP should follow the technical approach of the platform, system, equipment and devices from simple to difficult, that is, let the platform bear most of the protective measures, and secondly, the system and equipment share a small amount of protective measures, only specific devices are subject to special protective measures. This can reduce the technical implementation difficulty of the protective measures, reduce the design cost, and indeed solve the engineering implementation of the protective technology.

1) Platform structure design

The most important protection measure to EMP is shielding. The aircraft form a metal compartment, which can provide good shielding to protect the aircraft system and equipment. In the design, we should try to ensure good electrical connection between the structural parts, skins, bolts and rivets of the body. The joints of the skin structure should be seamlessly fixed and laminated, so as to effectively ensure the shielding effectiveness of the body.

2) The cover design

The aircraft covers are mainly used for the installation, maintenance, inspection and maintenance of the aircraft system. If the upper cover is not well connected, it will become the leakage window and secondary emitter of the EMP field. Therefore, reduce the gap of the cover is the key to provent the electromagnetic interference. The cover and the structure of the body should be applied with conductive sealant to improve shielding effectiveness.

3) The cockpit shielding design

The cockpit cover consists of a fixed windshield and an openable movable hatch. The

frame material of the windshield and the movable hatch is metal and the rest is plexiglass. The inner layer of plexiglass should be coated with a metal coating, and the metal coating and skeleton of the hatch cover should ensure electrical continuity in the process.

4) Antenna and electromagnetic shielding window protection design

Since the antenna is for the RF receiving, the signal receiving of EMP is unavoidable. To reduce the damage of the high-energy EMP to the receiving channel, the limit or clamp input signal amplitude is the only choice. Adding a low-pass filter or band-pass filter to the antenna terminal or equipment front can reduce the high-frequency part of EMP

The electromagnetic window should use an energy-selective surface or a frequency-selective surface. The energy-selective surface is designed with a controllable material that can be quickly converted to a metal-like low-resistance state when triggered by high power, thus reaching the effect of blocking energy conduction. A targeted frequency-selective surface design for the frequency band in which EMP energy is concentrated can effectively reduce the energy of the corresponding frequency band.

5) The cable layout design

Since the cable crosses the whole machine and the cross-linking length of the device is close to the main energy wavelength of EMP, once the cable is exposed to the EMP field, the coupled interference current will flow along the cable, which will create interference or hazards to the airborne equipment, which is typical of back-door coupling.

In addition to the coaxial cables, other cables will be coupled with EMP field. The method of reducing the coupling amount is only space isolation and shielding measures. The space isolation can be performed on the aircraft are limited, and the shielding measures are the main methods. The key equipment of a airborne system, the cable should be minimized in the composite skin covering area, especially the unshielded bare wire. There are two basic requirements for cable shielding that must be achieved. First, the shielding coverage should be guaranteed. Second, grounding must be guaranteed.

6) Equipment protection design

For the front door coupling protection of RF equipment, transient suppression circuits and devices are generally adopted. The devices with transient suppression capability mainly include gas discharge tubes, solid discharge tubes, and Metals Oxide Varistor (MOV) and Silicon Transient Voltage absorption Diode (TVS).For the back-door coupling protection of RF equipment and general electrical and electronic equipment, there are mainly shielding design, grounding design and filtering.

IV. CONCLUSION

At present, protection of domestic aviation aircraft to EMP is still in its infancy, and relevant industries have carried out EMP simulation, protection measures, equipment electromagnetic reinforcement, etc. China should plan and implement the research and protection to EMP as a whole and enhance the ability of the aircraft adapt to EMP in future wars.

REFERENCES

[1] Debao Zhang, Wenqing Huang, Changan Qiao, Sijun You. Influence and Protection of Electromagnetic on Frequency Equipment [C]. The 4th Special Vehicles Total Electrochemical Technology Development Forum, 2016:507-510.

[2]Junsheng Mao, Fengshou Qiao. Research Status and Trend of Strong Electromsgnetic Pulse Protection[J]. Modern communication technology, 2016(4):29-32.

[3]Zheng Pan, Lihua Shi, Jie Yang, Yuebo Li, Jiuliang Xiong, Zhikai Fu. Discussion on Systematic Protection of Electromagnetic Pulse in Protection Engineering[J]. Protective Engineering, 2017, 39(3):73-77.

Effects of EMP on the osteogenic differentiation in hUC-MSCs*

1st Tian Wang
Department of Radiation Biology
The Air Force Medical University
Xi'an, China
scuwangtian1989@sina.cn

2nd Gang Rui
Department of Radiation Biology
The Air Force Medical University
Xi'an, China
ruirui90@fmmu.edu.cn

3rd Ling Guo
Department of Radiation Biology
The Air Force Medical University
Xi'an, China
guolingclover@163.com

4th Yan Zhou
Department of Radiation Biology
The Air Force Medical University
Xi'an, China
spring18@fmmu.edu.cn

5th Guang-Zhou An
Department of Radiation Biology
The Air Force Medical University
Xi'an, China
ee26310@126.com

6th Gui-Rong Ding
Department of Radiation Biology
The Air Force Medical University
Xi'an, China
dingzhao@fmmu.edu.cn

***Abstract*—In this study, we investigated the effects of consecutive 7 days exposure (once a day) to electromagnetic pulse (EMP) field at 720 kV/m for 100 pulses (40 ns, 1 Hz) on osteogenic differentiation in human umbilical cord mesenchymal stem cell (hUC-MSC). The activity of alkaline phosphatase (ALP) in cells was determined by microplate method. The protein levels of osteogenic specific protein such as COL Ⅰ and OPN were detected by western blotting (WB). The formation of calcified nodules was measured by Alizarin staining. It was found that exposure to EMP did not affect the osteogenic differentiation in hUC-MSCs. However, 7 days EMP exposure could enhance the effect of osteogenic induction medium-induced osteogentic differentiation in hUC-MSCs.**

Keywords—EMP, hUC-MSC, osteogenic differentiation

I. INTRODUCTION

Human umbilical cord mesenchymal stem cell (hUC-MSC) is a kind of stem cell with multidirectional differentiation potential, which is widely used in tissue engineering and disease treatment [1-3]. However, the limited proliferation and orientation differentiation of hUC-MSCs have restricted its further application. In recent years, the effects of electromagnetic radiation on stem cells have been investigated. It is reported that exposure to electromagnetic radiation under some conditions could affect the differentiation of MSCs [4-5]. Till now, no literature is available concerning the biological effects of electromagnetic pulse (EMP) on MSCs. Therefore, in this study, we investigate the effects of EMP on the differentiation in hUC-MSCs.

II. METHODS

The hUC-MSCs were cultured by explant method of Wharton's jelly and the cells of passage [3] were divided into sham group, EMP group, Osteogenic induction medium (OM) group and OM+EMP group. The cells were consecutively sham exposed or exposed to EMP field at 720 kV/m for 100 pulses for 7 days (once a day). The pulse width of EMP was 40 ns. The repetition frequency was 1 Hz. The activity of alkaline phosphatase (ALP) in cells was determined by microplate method. The protein levels of osteogenic specific protein such as COL I and OPN were detected by western blotting (WB), and the formation of calcified nodules was measured by Alizarin staining at different times during osteogenic differentiation.

Funded by Nation Science Foundation Project of China, No. 31770905.

III. RESULTS

Compared with sham group, the ALP activity of hUC-MSCs in EMP group did not change after 7 days EMP exposure. However, the ALP activity and the protein levels of osteogenic specific proteins (COL I and OPN) remarkably increased in OM + EMP group, compared with OM group ($P < 0.05$). In addition, the results of Alizarin staining showed that the area of calcified nodules increased significantly in OM + EMP group compared with OM group ($P < 0.01$).

IV. DISCUSSION

The hypothesis tested in this study was to evaluate whether EMP favor osteogenic differentiation in hUC-MSCs. Early and later osteogenic markers, such as ALP activity, osteogenic specific protein level and matrix mineralization were detected. It was found that the ALP activity did not change in hUC-MSCs after exposure to EMP for 7 days, compared with sham group, which suggest that EMP under this experimental condition could not induce osteogenic differentiation in hUC-MSCs. It was reported that the electromagnetic fields (30/45 Hz, 1 mT) and pulsed electromagnetic fields (75 Hz; magnetic field peak intensity: 1.5 mT) stimulated an early osteogenic induction in MSCs [4,5]. The inconsistence of the effects of the electromagnetic fields on osteogenic differentiation is probably due to the different electromagnetic field conditions. Our further study showed that the ALP activity, the protein levels of osteogenic specific proteins and matrix mineralization remarkably increased in OM + EMP group, compared with OM group, which was consistent with Lu [6] and Ferroni's report [7].

V. CONCLUSIONS

EMP under this experimental condition did not induce osteogenic differentiation in hUC-MSCs, but it could enhance the effect of osteogenic induction medium-induced osteogenic differentiation in hUC-MSCs.

VI. REFERENCES

[1] Wang H, Strange C, Nietert P J, Wang J, Turnbull T L, Cloud C, et al. Autologous Mesenchymal Stem Cell and Islet Cotransplantation: Safety and Efficacy. Stem Cells Transl Med, 2018 Jan;7(1):11-19.

[2] Chelluboina B, Nalamolu K R, Mendez G G, Klopfenstein J D, Pinson D M, Wang D Z, et al. Mesenchymal Stem Cell Treatment Prevents Post-Stroke Dysregulation of Matrix Metalloproteinases and Tissue Inhibitors of Metalloproteinases. Cell Physiol Biochem, 2017, 44(4): 1360-1369.

[3] Saeed H, Ahsan M, Saleem Z, Iqtedar M, Islam M, Danish Z, et al. Mesenchymal stem cells (MSCs) as skeletal therapeutics - an update[J]. J Biomed Sci, 2016, 23: 41.

[4] Kang K S, Hong J M, Kang J A, Rhie J W, Jeong Y H, Cho D W, et al. Regulation of osteogenic differentiation of human adipose-derived stem cells by controlling electromagnetic field conditions. Exp Mol Med, 2013, 45: e6.

[5] Ongaro A, Pellati A, Bagheri L, Fortini C, Setti S, De Mattei M, et al. Pulsed electromagnetic fields stimulate osteogenic differentiation in human bone marrow and adipose tissue derived mesenchymal stem cells. Bioelectromagn, 2014, 35: 426-436.

[6] Lu T, Huang Y X, Zhang C, Chai M X, Zhang J. Effect of pulsed electromagnetic field therapy on the osteogenic and adipogenic differentiation of bone marrow mesenchymal stem cells[J]. Genet Mol Res,2015,14(3):11535-11542.

[7] Ferroni L, Tocco I, De Pieri A, Menarin M, Fermi E, Piattelli A, et al. Pulsed magnetic therapy increases osteogenic differentiation of mesenchymal stem cells only if they are pre-committed[J]. Life Sci,2016,152:44-51.

Study on the Test method of Induced current of EED

ZHAO Tuan, YAO Hongzhi& JI Xiangfei ,ZHANG Rui

(ShaanXi Applied Physic-Chemistry research, State Key Laboratory of Applied Physic-Chemistry research, 710061,Xi ́an, Shaanxi, China, zhaotuan213@sina.com)

Quantitative test technique of induced current of EED is critical technique to evaluate the safety of EED in electromagnetic environment quantificationally. In this paper, through studying the quantitative test technique of induced current of EED, the test principle of three methods was detailedly presented which are infrared optical temperature measurement method and white light interference temperature measurement method and current monitors method，and more, the advantage and disadvantage of these method were analyzed and studied. The typical EED of three categories which are semiconductor and slapper plate and hot bridgewire were chosen to quantificationally measure the induced current in electromagnetic environment, the test result was analyzed and studied, through this, a new test method and technology estimating the safety of EED in electromagnetic environment was provided.

Table 1 the Comparison with test method of induced current of EED

Test method	**Parameter of performance**	**Advantage**	**Disadvantage**
current monitors	maximum current:200A；response time: one nanosecond; frequency : one Gigahertz。	（1）response time is very fast, the rise time is nanosecond level；（2）the result is steady。	The range of frequency is too smaller than one Gigahertz.
white light interference temperature measurement method	The range of temperature：0℃ to 200℃;resolution：0.03℃；response time：less than one microsecond.	It is widely used, this technique properly mature, the test result can repeat well.	The range of temperature is lower, optical sensor and EED is fixed with glue, so the test result is easily effected by the contact of each other, and optical sensor can't use repeatedly and largely.
infrared optical temperature measurement method	The range of temperature：room temperature to 800℃；resolution：1℃；precision：0.1%；response time：1mS。	It is non-contact test, which is suitable to the little thermal capacity and weak signal. The equipment is convenient contact with the EED.	The test result is easy interference by temperature around because the radiated spectrum of EED is very feeble.

Semiconductor detonator、slapper plate detonator and hot bridgewire detonator are chosen to measure the induced current in electromagnetic field, the resistance of hot bridgewire detonator is 4.69 Ω , the resistance of semiconductor detonator is 1.47Ω , the resistance of slapper plate detonator is 54.9mΩ , the length of leg wires of EED are all fifty centimeter, the shape of leg wires is on dipole antenna. When the electric field intensity is equal, the induced current of all EED have been measured with current monitors in electromagnetic field produced in GTEM cell and microwave anechoic chamber, the test result was analyzed and compared; in the same situation, the induced current of hot bridgewire detonator have been measured with current monitors and infrared optical temperature measurement equipment in GTEM cell, the test result was analyzed and compared. The test system is shown as figure1, the fitting curve of test result is shown as table2.

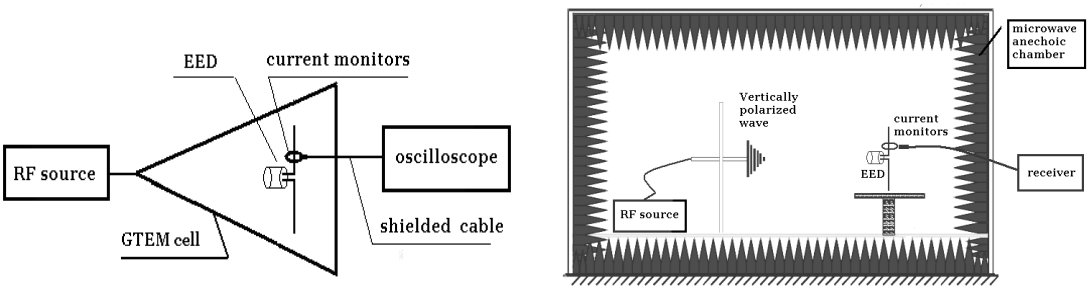

Figure1 The diagram of test system of induced current in GTEM cell and anechoic chamber

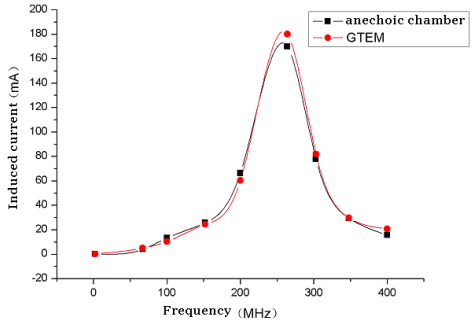

Figure2 The fitting curve of induced current of hot bridgewire detonator

Induced current of EED was measured in in GTEM cell and anechoic chamber, its value is changed with the frequency and the maximum value is on the resonance frequency. Compared with the fitting curve of induced current, the trend of value is synchronous, the difference between them was caused by the change of vertically polarized electric field intensity.

How to Test a Microcontroller for Immunity to HPEMP Influence?

Vladimir M. Chepelev
Joint Institute for High Temperatures
Russian Academy of Sciences
Moscow, Russia
chepelev@ihed.ras.ru

Yury V. Parfenov
Joint Institute for High Temperatures
Russian Academy of Sciences
Moscow, Russia
parfenov@ihed.ras.ru

Yu-hao Chen, Yan-zhao XIE
State Key Laboratory of Electrical
Insulation and Power Equipment
Xi'an Jiaotong University
Xi'an, China
yzxie@xjtu.edu.cn

***Abstract*—The method for a microcontroller test against HPEMP impact is proposed. Main steps of this method are shown. First of all, the critical circuits of a microcontroller device have been identified. Then, key parameters are chosen to characterize the efficiency of electromagnetic action on the most sensitive part of these circuits, namely, on the Reset line. The values of the key parameters are calculated depending on the geometric and electrical characteristics of the Reset circuits, as well as the characteristics of the electromagnetic pulses emitted by the existing test facilities. As a result, the data obtained make it possible to choose the test facility that provide the most strict conditions for microcontrollers testing.**

Keywords—microcontroller, electromagnetic pulse, key parameters

I. INTRODUCTION

Microcontrollers are used in almost all modern electronic devices and provide important functions. In this regard, the problem of microcontrollers immunity assessing is very important. To solve this problem, we propose the algorithm consisting of the following steps:

1. Analyze the device as an object against electromagnetic influence and then choose key parameters characterizing the effectiveness of this influence;
2. Calculate the key parameters to quantify characteristics of electromagnetic influence;
3. Determine the critical (maximum allowable) values of key parameters [1-5].

Performing this procedure allows us to obtain baseline data for comparing the effectiveness of existing testing facilities and choose the one that provides the most strict test conditions. In the case that the effectiveness of the available facilities is insufficient for a reliable assessment of the device under test immunity, the data obtained will make it possible to formulate requirements for a more efficient facility.

The following describes the results of the application of the proposed procedure in order to choose the test facility for typical microcontrollers.

II. OBJECT ANALYSIS

It is known that for the normal functioning of a microcontroller it is necessary to ensure the fulfillment of three conditions: good power, good clock and good reset. It means that the supply voltage must be in the specified range (usually 3V ± 10%); the clock signal must have a predetermined shape (the required edge slope, the absence of significant interference); the "Reset" signal must have the required characteristics (duration, edge slope, absence of significant interference).

Based on these conditions, we can list the critical circuits: the power circuit, the clock circuit and the Reset. The HPEMP influence on these circuits can lead to disruption of the normal operation of the microcontroller.

Impact on the power supply circuits can disrupt the normal operation of the microcontroller and the device as a whole. To prevent this, special methods are used. For example, microcontrollers of PIC family contain an integrated circuit for supply voltage monitoring. When the level of this voltage drops below the minimum level, an internal Reset signal is generated. This prevents incorrect microcontroller operation at a lower supply voltage. However, this feature can lead to the fact that in the presence of periodically repeating disturbance in the power supply circuits, the Reset signal will be periodically generated and for this reason the controller will not be able to proceed to the main program. As a result, the device will be blocked.

The Reset line is a sensitive input circuit subject to electromagnetic influence [6]. This conclusion is confirmed by the experimental data presented in [6, 7]. In this regard, we will consider this particular circuit.

In accordance with the procedure outlined above, it is necessary to select key parameters for characterizing the possibility of the microcontroller malfunction in case of pulse disturbance on the Reset circuit. To this end, simple experiments were carried out, which showed that to initiate the reset process, a voltage pulse with amplitude (U_{in}) and energy (W_{in}) exceeding some critical values is needed to be applied to the Reset input. As a result, these parameters were chosen as the key parameters for the microcontroller.

III. KEY PARAMETERS ESTIMATION

The next step is to solve the problem of estimating the immunity of microcontroller. For this purpose the calculation of the key parameters is needed. To perform such calculations, data source on the characteristics of the electromagnetic pulses emitted by the existing test facilities are required. To obtain such data source we use the information contained in the reference book [8]. Before proceeding with the analysis of this information, we note that from a practical point of view, it makes sense to compare only facilities belonging to the same class. As the classifying attributes, one can choose, for example, the effective radiation potential $E \cdot R$ (E is the amplitude of the emitted pulses, and R is the distance between the source and the point at which the field is measured), the size of installations, the power consumed etc. Let us consider test facilities with the same values of $E \cdot R$ parameter.

Taking into account the last remark, let us estimate the efficiency of three test facilities having the same radiation potential of 2300 kV, namely: a source of narrowband (NB) pulses; a source of mesoband (MB) pulses and a source of ultra wideband (UWB) pulses.

It is necessary to choose a performance indicator and estimate the value of this indicator for each of the installations. As such an indicator, we can take the distance D at which the values of the key parameters U_{in} and W_{in} reach critical (maximum allowable) levels U_{max} and W_{max}, respectively. The values of this indicator for the selected installations can be calculated by the following equations (linear dependence of disturbance amplitude on impact field strength is assumed):

$$D_U = 2300\left(\frac{U_{in}}{U_{max}}\right), \text{ m}; \quad (1)$$

$$D_W = 2300\left(\frac{W_{in}}{W_{max}}\right), \text{ m}. \quad (2)$$

Here U_{in} and W_{in} are the values of the key parameters achieved when the amplitude of the acting pulse is $E = 1$ kV/m . To estimate these values, it is necessary to have the Reset circuit design model, as well as the geometric and electrical characteristics of this circuit. Analysis of a number of electronic devices containing a microcontroller showed that to perform such assessments, one can use the simple strip line model and the Telegrapher's Equations.

Referring to equations (1) and (2), it is easy to see that to estimate the distances at which the critical values of the key parameters U_{in} and W_{in} are reached, the point is to find critical values U_{max} and W_{max}. They can be obtained by direct injection of voltage pulses to the Reset input. Experiments have shown that for typical microcontrollers (for example, ST62T25C, AT90S2313, PIC16C62, etc.), these values are equal, approximately 5V and 10^{-10}J, respectively.

Thus, there are all the initial data necessary for a quantitative estimation of the effectiveness of the considered test facilities, that is, the calculating distances at which critical values of key parameters are reached.

The important conclusion from the results of calculations is that critical levels of key parameters U_{in} and W_{in} are achieved at different distances. For the MB and UWB sources this difference is relatively small (less than 1.7 times), on the other hand, the difference reaches 25 times for the NB source. The noted difference is explained by the high energy of the NB pulses emitted due to their considerable (0.25 μs) duration. Considering that the microcontroller resets occur only in the cases of both key parameters exceeding critical levels. The minimum of two values D_U and D_W should be taken as the distance at which the particular test facility is able to initiate a reboot.

Taking into account the last remark, the plots of the dependence of the blocking distance with respect to the length of the Reset line for the considered test facilities were plotted (Fig.1).

Using the dependencies shown in Fig.1, one can choose a simulator that, with the most confidence, will allow predicting the quality of functioning of the test object under the influence of high power electromagnetic pulses. From the above dependencies, it follows that the most strict test conditions for the microcontroller are provided by using a source of NB pulses with a fundamental frequency of the spectral range of 2-3 GHz or a source of MB pulses with a central frequency of 2 GHz.

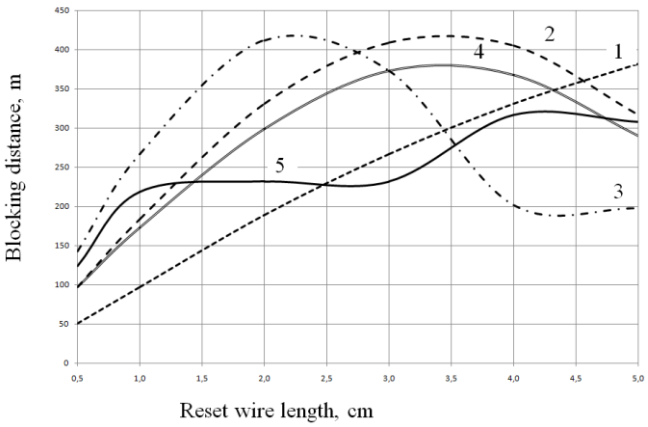

Fig.1. Blocking distance vs. Reset line length for different HPEMP sources: 1-NB source 1 GHz, 2-NB source 2 GHz, 3-NB source 3 GHz, 4-MB source 2 GHz, 5-UWB source.

Of course, , when choosing the simulator that is intended for testing the particular object in practice, in addition to the given considerations on the efficiency, other characteristics will be taken into account. For example, the repetition frequency of the emitted pulses, the setup cost, its mobility, usability, etc. The analysis of these characteristics is beyond the scope of this article.

In conclusion, we would like to list a number of considerations regarding the limits of applicability of the results obtained. Obviously, these results are valid only for the conditions in which the assumptions made during the calculations are satisfied. The main items of these assumptions are recalled as follows.

The Reset line was taken as a critical circuit of the electronic devices, including a microcontroller.

It was assumed that the adopted calculation model, the geometric and electrophysical characteristics of the Reset line, the selected key parameters, as well as the data used at carrying out the calculations of critical levels could adequately reflect the features of the electronic device under consideration.

It was implicitly assumed that if the amplitude and the energy of the pulse disturbance induced on the Reset line were sufficient to initiate the reboot of the microcontroller then the repetition frequency of this interference would also be sufficient to keep it blocked.

It follows from the above that the first and most important stage in the study of the immunity of any electronic device should be the analysis of this device as an object of electromagnetic interference. In the course of this analysis, appropriate design models should be developed and their adequacy to the device under consideration should be confirmed.

Only one critical circuit is considered in detail, but there may be others. In addition to key parameters mentioned above in other situations, other parameters may be selected.

So, the pulse repetition rate may be used. It is known that the pulse repetition rate is an important parameter in some cases. This is true when implementing other mechanisms for blocking the operation of the microcontroller.

IV. Conclusion

This article proposes an approach for solving the problem of choosing a simulator for microcontrollers testing for the action of high power electromagnetic pulses. The essence of this approach is to quantify the effectiveness of the existing test facilities and select the one that provides the most strict test conditions. In the process of solving this problem, the following results were obtained.

The critical circuits of the microcontroller device are identified. The HPEMP impact on these circuits can lead to disruption the normal function of the device. Such circuits are the power supply circuits, the clock generator circuit and the Reset. The most sensitive of these circuits is the Reset.

The key parameters characterizing the effectiveness of electromagnetic effects on the Reset line are selected. These parameters are amplitude (U_{in}) and energy (W_{in}) of the voltage pulses induced in this line by pulsed electromagnetic interference.

The values of key parameters U_{in} and W_{in} were calculated depending on the geometric and electrophysical characteristics of the Reset circuit used in the electronic devices under consideration, as well as the characteristics of electromagnetic pulses emitted by the existing test facilities, namely, the source of narrowband (NB) pulses; the mesoband source (MB) and the source of ultra-wideband (UWB) pulses. In order to ensure the comparability of the calculated results, it was assumed that these facilities have the same effective radiation potential of 2300 kV.

Critical levels of key parameters U_{in} and W_{in} are determined for the microcontroller. In the case of simultaneous exceeding of these two key parameters, the process of microcontroller reboot begins. For typical microcontrollers, these levels are approximately 5V and 10^{-10}J, respectively.

The results obtained allowed us to plot graphs of the dependence of microcontroller blocking distance on the length of the Reset line for the test facilities considered. Based on these graphs, it was concluded that the most strict conditions for the microcontroller testing can be achieved using a NB source of pulses with center frequency of 2-3 GHz or a MB source of pulses with center frequency of 2 GHz.

References

[1] Yury V. Parfenov, Boris A. Titov, Leonid N. Zdoukhov, William A. Radasky, Some standardization problems of high power electromagnetic pulses, formed by test facilities, ASIAEM Conference in Jeju Island, Korea from 3-8 August 2015, Book of Abstracts, 1 p.

[2] Yury V. Parfenov, Boris A. Titov, Leonid N. Zdoukhov, Xie Yanzhao, The detector of dangerous pulse electromagnetic interferences: conception of creation, ASIAEM Conference in Jeju Island, Korea from 3-8 August 2015, 3 p.

[3] Yury V. Parfenov, William A. Radasky, Boris A. Titov, Leonid N. Zdoukhov, About the Assessment of Electronic Device Immunity to High Power Electromagnetic Pulses, In: proc. of the 7th Asia-Pacific Conference on Environmental Electromagnetics (CEEM'2015), Nov. 4-7, 2015 Hangzhou, China, p.503-506.

[4] Yury V. Parfenov, Leonid N. Zdoukhov, Vladimir M. Chepelev, Boris A. Titov, William A. Radasky. Methodical Principles of a Choice of Simulators for Tests of Electronic Devices for Immunity to Ultrashort EMPs, In: proc. of the 7th Asia-Pacific International Symposium on Electromagnetic Compatibility & Signal Integrity and Technical Exhibition (APEMC 2016), Shenzhen, China, May 18 to 21, 2016, 3 p, FR-AM-1-SS-17-1.

[5] Vladimir M. Chepelev, Yury V. Parfenov, William A. Radasky, Boris A. Titov, Leonid N. Zdoukhov, Ke-jie LI, Yu-hao Chen, Xu Kong, Yan-zhao XIE. Methodical Approach for Immunity Assessment of Electronic Devices Excited by High Power EMP // Journal of Electronic Testing, Springer, October 2018, Volume 34, Issue 5, pp. 547–557.

[6] Sven Fisahn, Heyno Garbe, Differences in the Coupling Behavior of Fast Transient Pulses to short PCB Traces, EMC'09/Kyoto, p.361-364.

[7] Fisahn, Sven and Heyno Garbe, Special coupling effects of UWB pulses to short signal traces, 2009 IEEE International Symposium on Electromagnetic Compatibility (2009): 231-236.

[8] IEC standard 61000-4-35: Electromagnetic Compatibility (EMC) – Part 4-35: Testing and measurement techniques – HPEM simulator compendium.

Study on the Influence of Earth Current "Pipeline Effect" on PSP of Pipelines *

WEIFENG ZHAI
College of Information Science and Engineering
China University of Petroleum(Beijing)
Beijing, China
zhaiwf@ncut.edu.xn

ZHISHAN LIANG
College of Information Science and Engineering
China University of Petroleum(Beijing)
Beijing, China
lzs1960@cup.edu.cn

***Abstract*— Based on a recent study by Ingham, this paper analyzes the theoretical model and calculation method of pipeline PSP (Pipe-to-Soil Potentials). It is considered that the DSTL(distributed source transmission line) model is used to calculate PSP of the ideal pipeline. This model is used to evaluate the influence of pipe length, branch and earth conductivity distribution on PSP and GIC under different magnetic storms. The actual pipeline GIC and PSP will be affected by the coating leakage point and the cathodic protection device, so it is inevitable that the calculation result is inconsistent with the actual measurement data. This paper reveals the mechanism of the influence of earth current "pipeline effect" on PSP.**

Keywords—PSP, GIC, Pipeline effect, Cathodic protection device, DSTL

I. INTRODUCTION

Space weather variations induces the geomagnetic induced current (GIC) and pipe-to-soil potential (PSP) in Buried pipelines. When the pipe coating is damaged, the GIC in the pipe will connect the soil through the damage point and form a current loop with the soil, which will aggravate the corrosion at the damage point and reduce the service life of the pipe[1-3]. Compared with GIC, PSP is a more important indicator for evaluating pipeline corrosion risk.

In order to evaluate the impact of geomagnetic storms on pipelines, many research have carried out and different methods for modeling are proposed for PSP and GIC calculations. The distributed source transmission line(DSTL) theory was used for modelling AC induction in pipelines by Taflove and Dabkowski[4]. Boteler and Cookson were the first to use it for GIC in pipelines[5], and Boteler extended the theory to deal with discontinuities of pipelines[6]. Pulkkinen applied DSTL theory to GIC calculations in complex pipeline networks[7]. Boteler then improved the algorithm to compute a more complex pipeline PSP by establishing a node admittance network for the equivalent π circuit[8]. At present, there are two methods for calculating the pipeline PSP most commonly used. The first is based on the three-dimensional earth conductivity structure and DSTL model for pipelines to calculate GIC and PSP[7,8]. The other algorithm is to linearly regress the correlation coefficient between long-term geoelectric field and PSP observation data at a certain location to implement the calculation and prediction of pipeline PSP and GIC[9,10].

A recent study showed that PSP and GIC measurement data at a certain point in the pipeline have a high correlation with the geoelectric field perpendicular to pipeline[11]. The author believes that the DSTL model proposed by Boteler does not consider the contribution of the geoelectric field perpendicular to pipeline to the result, and the method based on the measurement data can make the calculation result more accurate.

Based on the results of Ingham's research, this paper analyzes the theoretical model and calculation method of pipeline PSP and GIC. This paper analyzes the reason why the measurement results contain the geoelectric field perpendicular to pipeline, and reveals the mechanism of the influence of earth current "pipeline effect" on PSP.

II. METHOD FOR PSP AND GIC CALCULATION

The pipeline model based on DSTL is shown in Fig.1[5-7]. *E(n)* is the induced electric field parallel to pipeline in the *n*th section of the pipeline, which is determined by the direction of the pipeline, the northward geoelectric field *Ex* and the eastward geoelectric field *Ey*. It can be expressed as

$$E(n) = E_{x//}(n) + E_{y//}(n) \tag{1}$$

Equation (1) shows the PSP and GIC calculated by the model does not include the influence of the geoelectric field perpendicular to pipeline.

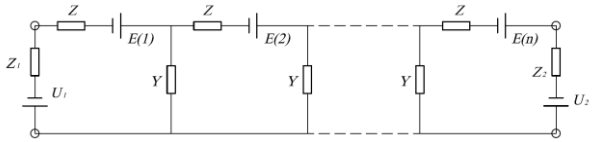

Fig.1. Pipeline model based on DSTL

The parameters of the system are difficult to obtain because of the complex earth conductivity structure. Pulkkinen assume that the geoelectric field in the local area is uniform, and simplified the model of PSP and GIC[9] as

$$\begin{cases} GIC_n = a_n E_x + b_n E_y \\ PSP_n = c_n E_x + d_n E_y \end{cases} \tag{2}$$

The subscript *n* in the formula indicates the position of the pipe, and a_n, b_n, c_n, d_n indicate the correlation coefficient between different components of the electric field and PSP and GIC at each position, which contain information of the topology of the pipe, electrical characteristics, and the three-dimensional earth conductivity structure.

Ingham proposed a simplified model similar to Pulkkinen to calculate GIC on New Zealand power network [10]. Then

This research was supported by the National Key R&D Program of China (No. 2016YFC0800100) .

he compared the PSP and GIC measurement data on a natural gas pipeline in the North Island of New Zealand and found that the trend of the pipeline PSP and GIC is more correlated with the geoelectric field perpendicular to pipeline. The conclusion is more consistent with the result using the simplified model proposed by him than Boteler's DSTL model, so he believes that the latter has a large calculation error due to the fact that the geoelectric field perpendicular to pipelines is not considered[11].

In fact, both methods from Ingham and Pulkkinen based on measurement data are derived from DSTL theory. Since the actual earth conductivity structure is non-uniform, the geoelectric field will not be uniform in a small area (300 km). Meanwhile, since both GIC and PSP are the integral effects of the geoelectric field[9], the results at any point are affected by the various points of the pipeline, so equation (2) should be expressed as

$$\begin{cases} GIC_n = \sum_{i=1}^{N} (a_{in} E_{ix} + b_{in} E_{iy}) \\ PSP_n = \sum_{i=1}^{N} (c_{in} E_{ix} + d_{in} E_{iy}) \end{cases} \quad (3)$$

The pipeline is divided into N segments, and the PSP and GIC of each segment have different correlation coefficients $a_{in}, b_{in}, c_{in}, d_{in}$ with the local *Ex* and *Ey*. Equation (3) can be reduced to equation (2) only if the geoelectric field is uniform. It can be seen that the method used by Ingham is a simplified model algorithm derived from DSTL model, and its accuracy is theoretically lower than that of the DSTL model.

However, this method can obtain the actual calculation results which reflects the geoelectric field perpendicular to the pipeline. It is not due to the fact that the method is more reasonable, but because the measured geoelectric field history data contains a large number of components perpendicular to the pipeline, who affect the value of the correlation coefficient in the process of linear regression.

III. *MECHANISM ANALYSIS OF PSP AND GIC INFLUENCED BY GEOELECTRIC FIELD PERPENDICULAR TO PIPELINE*

Ingham's findings reflect that the time-domain variation of the geoelectric field perpendicular to the pipeline at the location of the measurement point is highly correlated with the PSP and GIC measurements at that point. However, it needs to be clear that the length of oil and gas pipelines is often hundreds of kilometers or even thousands of kilometers, and the path of the pipeline will always be changed by the geological structure and the distribution of surrounding facilities. At the same time, due to the needs of social development, the branching and intersection of pipelines will also increase, and the topology of these pipelines will affect the PSP and GIC of any location. Therefore, the relationship between the entire pipeline and the geoelectric field component cannot be evaluated by analyzing the correlation between the geoelectric field component and the PSP at a certain observation point.

According to Ohm's law, the current in the conductor is proportional to the voltage across the conductor and inversely proportional to the resistance across the conductor. That is to say, the distribution of earth current and induced current inside the pipeline must be related to the conductivity distribution formed by the earth and the pipeline. Current flows through the path of minimum resistance.

During the laying, installation and long-term operation of the pipeline, it is inevitable that the coating will be damaged to form a leak. Once the leak is formed, it forms a highly conductive path with the surrounding earth, where the surrounding earth current collects and forms a loop with the metal of the pipe. Due to the earth conductivity distribution, the earth current entering the pipeline through the leak point is composed of the x, y and even z components of the geoelectric field. The composition is complex and difficult to analyze. The DSTL model is a model based on an ideal pipeline. However, the actual measured PSP and GIC data are interfered by the current components in all directions due to the leakage point. So it is inevitable to differ from the theoretically calculated values.

At the same time, in order to reduce the risk of pipeline corrosion, all pipelines will be installed with cathodic protection devices to automatically adjust the PSP. However, there is currently no uniform standard for the placement and number of cathodic protection devices. This results in different configurations of cathodic protection devices for different pipes. On the one hand, the setting of the cathodic protection device can adjust the PSP to a safe potential to avoid corrosion in the case of a leak point in the pipeline; on the other hand, the anode bed of the cathodic protection device is connected to the earth to form a high-conductivity circuit, and the earth current flows into the pipe through the anode bed and the cathodic protection device. This makes the cathodic protection device an equivalent leak. Therefore, the location where the cathodic protection device is installed introduces complex earth currents into the pipeline, which in turn affects the measurement data of the PSP and GIC.

In this paper, the mechanism that the geoelectric field perpendicular to pipeline affects the PSP and GIC is divided into three cases.

A. Pipe topology and earth conductivity structure

The laying of buried pipelines is affected by the geological structure and the distribution of surrounding facilities, and the direction of pipe in different geographical locations is different. When calculating PSP and GIC, different pipe segments are affected by different electric field components, and the PSP and GIC of any pipe are the result of the joint action of all pipe segments. Therefore, the PSP and GIC measured at any point in the pipeline are affected by any geoelectric component parallel to each section of pipeline.

In practice, the earth conductivity structure is unlikely to be uniform over a wide range, and the induced geoelectric field can produce a boundary effect in the interface of the earth conductivity boundary. As shown in Fig. 3, *AB* is an east-west pipeline in which the point *B* is closer to the coast boundary. Due to the H-polarization effect, a region near the coast boundary produces a large induced electric field on the direction of h perpendicular to the coast. In this case, the PSP and GIC measured at the point *P* farther from the coast are highly correlated with the geoelectric field perpendicular to pipeline.

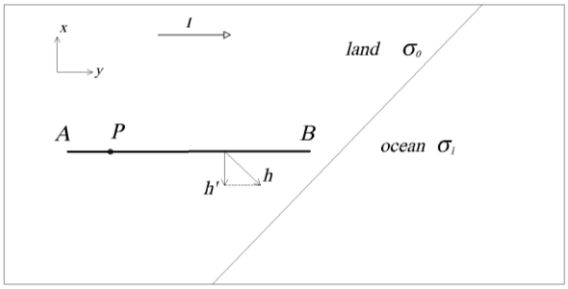

Fig.3. Schematic diagram of the pipeline near the coastal boundary

Assume that the pipeline with multiple corners is as shown in Fig. 4, where the *AB* and *CD* segments are in the east direction, the BC segment is in the northeast direction, and the position *P* is the pipe PSP and GIC measurement points. In the geodetic coordinate system, the *x* direction points to the north, the *y* direction points to the east, the *e* direction in the pipe coordinate system is parallel to the direction of the *BC* segment of pipe, and the *h* direction is perpendicular to the direction of the *BC* segment of pipe. Assuming that the earth conductivity is uniform, the two components of the induced geoelectric field are *Ee* and *Eh*, the components of which in the *x* direction and the *y* direction are E''_e, E''_h and E'_e, E'_h , respectively. When calculating GIC and PSP, the components that have an effect on *AB* are $E'_e = E_e \cos\theta$ and $E'_h = E_h \sin\theta$, and the component that has an effect on *BC* is E_e, when E_h has no effect. When *AB* and *CD* segment are sufficiently long, the E_h component will have sufficient influence on the PSP and GIC of the position *P* under the integral, so that the PSP and GIC data measured at the position *P* are more correlated with E_h. The result is that E_h, which does not affect PSP and GIC at position *P*, affects the final result at other locations in the pipeline. It cannot be used to illustrate the limitations of the DSTL model.

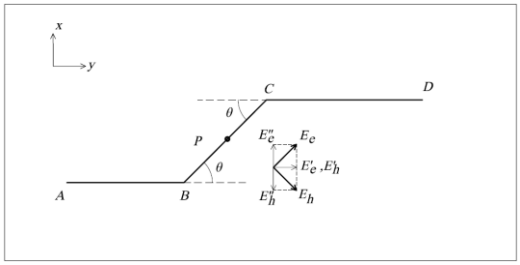

Fig.4. Schematic diagram of a pipe with multiple corners

B. *Influence of pipe coating leakage point*

During the laying, installation and long-term operation of the actual pipeline, it is inevitable that the coating will be damaged, and the metal layer of the pipeline will be in contact with the earth soil to form a current leakage point. Most of the leaked points cannot be located. Once the leak is formed, the surrounding soil current is collected to the leak point to form a current loop with the pipe metal because of the smaller resistance of the pipe metal to the soil. There are many factors affecting the current distribution around the leak point, including not only the *x*, *y*, and *z* components of the geoelectric field, but also the influence of the surrounding earth conductivity structure. As a result, the current cannot be decoupled. This phenomenon is defined as the earth current "pipeline effect".

The DSTL equivalent model of the pipeline considering the leakage point is shown in Fig. 5. The two leakage points of the pipeline are equivalent to the current sources *If1* and *If2*, who form a new loop in the earth. The current source depends on the *x*, *y* of the geoelectric field and surrounding earth conductivity structure.

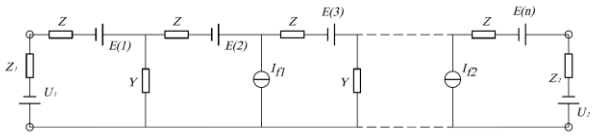

Fig.5. DSTL equivalent model of Pipeline with missing points

C. *Influence of cathodic protection device*

In order to reduce the risk of corrosion of pipelines, all pipelines need to be equipped with cathodic protection devices. The installation method of the insured devices of the general oil and gas pipeline cathodic protection stations is shown in Fig. 5. The cathode of the cathodic protection device is connected to the metal of the pipe, and the anode is connected to the anode bed buried in the ground to maintain the pipe PSP always at a negative potential.

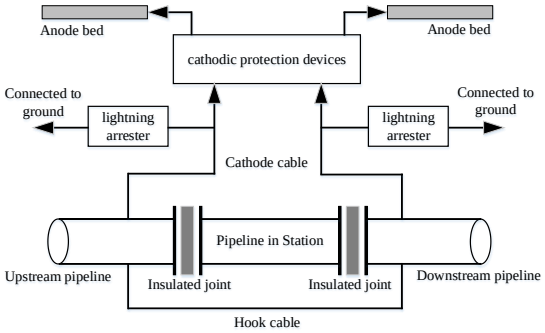

Fig.5. Cathodic protection station

Considering the influence of the cathodic protection device on PSP, the pipeline can be equivalent to the DSTL model shown in Fig. 6. The equivalent circuit is similar to the equivalent circuit of the leakage point. The device can form a loop with leakage or cathodic protection at other locations of the pipeline to introduce other components of the geoelectric field. When a large geomagnetic storm occurs, the earth current flowing through the cathodic protection device is large enough. It may cause damage to the internal circuit of the device.

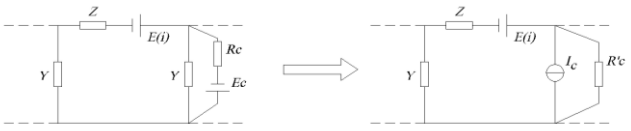

Fig.6. DSTL equivalent model of the pipeline considering the cathodic protection device

When a geomagnetic storm occurs, the geoelectric field around the pipeline changes, and the ground current flowing through the anode bed affects the GIC. When the GIC changes within the adjustment range of the cathodic protection device, the PSP can always be kept constant. When a large geomagnetic storm occurs, the cathodic protection device cannot adjust the PSP to remain constant, and it outputs the maximum current as a constant current source. The measured PSP and GIC data at this time contain both the components output by the cathodic protection device and the earth current of each component. In this case, the insured device becomes an equivalent leak point. When the current flowing through the insured device is large enough, it may cause damage to the internal circuit of the insured device. Similar to the case where the pipeline has a leak point, due to the presence of the cathodic protection device, a new current loop is formed around the pipeline to affect the PSP and GIC, which is also a "pipeline effect" of the earth current.

IV. *CONCLUSION*

Based on the conclusions obtained by Ingham to study the pipeline PSP and GIC in the North Island of New Zealand, this paper analyzes and studies the modeling and algorithm of pipeline PSP and GIC. It is believed that the algorithm proposed by Ingham is a simplified algorithm based on the DSTL model and has the same theoretical basis. The reason why Ingham's conclusion differs from the DSTL theory is not that the DSTL theory itself is flawed, nor that Ingham's algorithm is more accurate, but that the measured geoelectric field history data contains a large number of components perpendicular to the pipeline. These components interfere with the results of the correlation coefficients during linear regression.

This paper considers that the actual pipeline topology, the earth conductivity structure, the leak point of the coating, and the added cathodic protection device introduce the geoelectric field perpendicular to pipeline, resulting in a large difference between measured data and theoretical calculation results. By introducing currents, the leakage point of the coating and the cathodic protection device influence the surrounding earth current. The internal conductor of the pipeline and the earth high-conductivity structure constitute a current loop, which generates the earth current “pipeline effect”. It not only introduces the complex earth current to influence the PSP and GIC, and also affects the cathodic protection device.

ACKNOWLEDGMENT

This work was performed as part of National Key R&D Program of China with support from Ministry of Science and Technology of the People’s Republic of China. Major work was done at China University of Petroleum(Beijing). This work also benefitted from the staff of PetroChina Pipeline R&D Center and member of the research group.

REFERENCES

[1] W. H. Saeger, "Adverse telluric effects on northern pipelines." International Arctic Technology Conference. Society of Petroleum Engineers, 1991.

[2] R. A. Gummow, and P. Eng, “GIC effects on pipeline corrosion and corrosion control systems,” Journal of Atmospheric and Solar-Terrestrial Physics, vol. 64, no. 16, pp. 1755-1764, 2002.

[3] A. Osella, A. Favetto, and E. López, ‘‘Currents induced by geomagnetic storms on buried pipelines as a cause of corrosion,’’ J. Appl. Geophys., vol. 38, no. 3, pp. 219–233, Jun. 1997.

[4] A. Taflove and J. Dabkowski, “Prediction Method for Buried Pipeline Voltages due to 60 Hz AC Inductive Coupling. Part I – Analysis”, IEEE Transactions on Power Apparatus and Systems, Vol. PAS-98, No. 3, 1979, pp. 780-787.

[5] D. H. Boteler and M. J. Cookson, ‘‘Telluric currents and their effects on pipelines in the Cook Strait region of New Zealand,’’ Mater. Perform., vol. 25, no. 3, pp. 27–32, 1986.

[6] D. H. Boteler, "Distributed-source transmission line theory for electromagnetic induction studies" Supplement of Proc. 12th Int. Zurich Symp. Technical Exhibition Electromagnetic Compatibility vol. OE7 pp. 401-408 1997-Feb-18.

[7] A. Pulkkinen, R. Pirjola, D. Boteler, A. Viljanen and I. Yegorov, “Modelling of space weather effects on pipelines,” J. Appl. Geophys., vol. 48, no. 4, pp. 233–256, Dec. 2001.

[8] D. H. Boteler, “A new versatile method for modelling geomagnetic induction in pipelines,” in Geophysical Journal International, vol. 191, no. 2, pp. 98-109, Nov. 2012.

[9] A. Pulkkinen, A. Viljanen, K. Pajunpää and R. Pirjola, “Recordings and occurrence of geomagnetically induced currents in the Finnish natural gas pipeline network,” J. Appl. Geophys., vol.48, no. 4, pp. 219-231, Dec. 2001.

[10] M. Ingham, C. J. Rodger, T. Divett, M. Dalzell and T. Petersen, “Assessment of GIC based on transfer function analysis,” Space Weather, vol. 15, no. 12, pp. 1615-1627, Dec. 2017.

[11] M. Ingham and C. J. Rodger, ‘‘Telluric field variations as drivers of variations in cathodic protection potential on a natural gas pipeline in New Zealand,’’ Space Weather, vol. 16, no. 9, pp. 1396–1409, Sep. 2018.

THE THREAT OF ELECTROMAGNETIC PULSE AND COUNTERMEASURES

Wenjie Zhang
Shenyang Aircraft Design and Research Institute
Aviation Key Laboratory of Science and Technology on Electromagnetic Environmental Effects
Shen Yang, Liao Ning, China
wjzhang0118@163.com

Guodong Song
Shenyang Aircraft Design and Research Institute
Aviation Key Laboratory of Science and Technology on Electromagnetic Environmental Effects
Shen Yang, Liao Ning, China
songguodong16388@163.com

Tao Zhang
Shenyang Aircraft Design and Research Institute
Aviation Key Laboratory of Science and Technology on Electromagnetic Environmental Effects
Shen Yang, Liao Ning, China
zhangtaowf@163.com

Zhuo Liu
Shenyang Aircraft Design and Research Institute
Shen Yang, Liao Ning, China
liuxiaofo@126.com

Jinrong Zhu
Shenyang Aircraft Design and Research Institute
Aviation Key Laboratory of Science and Technology on Electromagnetic Environmental Effects
Shen Yang, Liao Ning, China
1449919975@qq.com

Yan Wang
Shenyang Aircraft Design and Research Institute
Aviation Key Laboratory of Science and Technology on Electromagnetic Environmental Effects
Shen Yang, Liao Ning, China
sy601wangyan@163.com

***Abstract*— With the rapid development of information technology, the integration of electronic devices is getting higher and higher, making the sensitivity and vulnerability of electronic systems increasingly serious. At the same time, it also brought about the comprehensive development of the weapon system. The emergence of new concept weapons such as high-power microwaves (HPM) and electromagnetic pulses (EMP) poses a threat to the safety and reliability of weapons and equipment, electrical and electronic systems, personnel, electric ignition devices and fuel. This paper analyzes the mechanism of EMP, discusses the main threat of EMP, and puts forward specific countermeasures and protective measures.**

Keywords—EMP, Protective measures, Lighting

I. INTRODUCTION

The development of science technology has brought about changes in electronic systems, including weapon systems. Electromagnetic warfare and strong confrontation have become an important trend in future warfare. The complex electromagnetic environment not only jeopardizes the safety of electronic equipment, electric detonating devices and personnel, but also directly affects the performance of information system tactical technology, and relates to the survivability and combat effectiveness of the battlefield [1]. In 1962, Soviet Union conducted a hydrogen bomb test at a distance of 35 kilometers over the Arctic Circle, which caused thousands of kilometers of electronic systems to be impacted, burning out the Soviet defense radar and thousands of kilometers of communication lines. The next year, the United States conducted a nuclear test over the island of Johnston in the Pacific Ocean, causing an impact in Hawaii's Honolulu, 1400 kilometers away from the island. This shows that the power of the EMP is surprisingly high and covers a wide area. As a transient electromagnetic phenomenon, its high-intensity, ultra-wideband characteristics can cause different levels of interference and damage to electronic systems, such as interference, disturbance, degradation and damage. In severe cases, it will cause the local electronic system of the battlefield to be paralyzed.

II. MECHANISM OF EMP

A. Classification and characteristics of EMPs

Electrostatic discharge: The process of electrostatic discharge may generate high potential, strong electric field and instantaneous large current, and generate strong electromagnetic radiation to form EMPs. Fig. 1 shows the waveform of the typical current waveform generated by the electrostatic discharge generator. It can be seen that the electrostatic discharge EMP (ESD EMP) has a steep rising

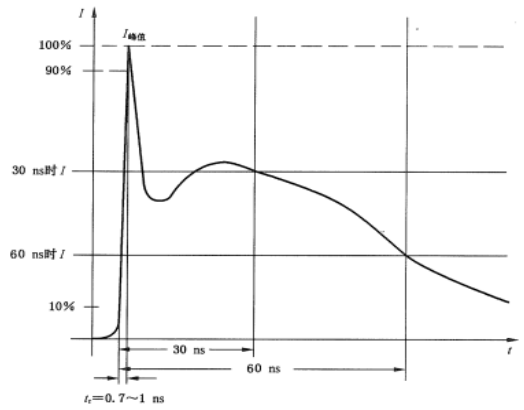

Fig. 1. the typical current waveform generated by the electrostatic discharge generator

edge, a wide frequency band, and a large near-field electric field [2].

Lightning: The length of the discharge path is an instantaneous large current discharge of several kilometers. Fig. 2 shows the current waveform of a lightning strike. It can be seen that a few times of discharge occurs within a short time of a lightning strike. And the energy in the subsequent stages is also very large.

Nuclear electromagnetic pulse (NEMP): It is a transient electromagnetic phenomenon produced by nuclear weapons or non-nuclear EMP weapons. It has the characteristics of large pulse intensity, wide spectrum and

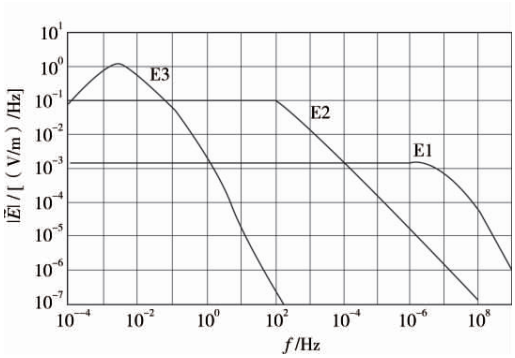

Fig. 2. Spectral characteristics of three stages of EMP radiation field

wide action area. As shown in Figure 2, it can be divided into three stages: E 1, E 2, and E 3 [3].

Power Microwave (HPEM): An RF environment generated by a microwave source that produces high power or high energy density radiated electromagnetic fields. The operating frequency is 100MHz-300GHz and the peak pulse power is above 100MW [4].

B. Effect mechanism

EMP can connect current and voltage transient signals into the electronic system such as weapon equipment through front door coupling and back door coupling, which interferes with or even destroys the normal operation of the equipment [4].

(1) Front door coupling: Refers to the EMP or microwave energy coupled into the electronic system through the antenna on the target, Media linear coupling through transmission lines (including power lines, telephone lines or shielded signal cables, buried cables, and ground loops) can also be referred to as front door coupling.

Using the electromagnetic field theory, the power expression of the EMP entering the receiver through the antenna is:

$$P_{in} = \frac{0.6A}{L} \cdot \frac{P_r cos^2\theta_{0.5}}{8\pi r^2} \cdot G_{rmax} \quad (1)$$

Where A is the aperture area of the antenna, L is the total loss, r is the distance between the high power microwave weapon and the antenna, P_r is the peak power of the high power microwave weapon, the half power angle of the transmitting antenna is $\theta_{0.5}$, and the maximum gain of the antenna is G_{rmax} .

(2) Back door coupling: Mainly refers to the high-energy EMP energy coupled into the casing through the gaps, flaps, holes, windows, etc. on the target, and generates standing waves in which the device is degraded or damaged. Backdoor coupling is very hazardous, Most of the simulation studies of backdoor coupling use time domain difference method, and the incident waveform is a typical pulse waveform.

(3) Penetration: Electromagnetic waves have the ability to penetrate in a conductive medium. It is related to the polarization, power, spectrum, and size of the target, electromagnetic parameters, position, and connection with other components. In a sense, even underground electronic devices can be damaged.

III. COUNTERMEASURES

A. Simulation of EMP environment

Simulating a necessary and complete EMP environment, providing a realistic simulation environment for combat training of communications and weaponry, is the basis for conducting EMP protection research. The construction methods mainly include actual equipment simulation method, semi-physical simulation method, digital simulation, composite simulation. Comparison of several construction methods is shown in Table I [6].

B. EMP protection

Traditional protection methods include shielding, grounding, filtering, lapping, and surge protection. It is attenuated to the extent that the equipment can withstand by reflecting, absorbing, isolating, and venting EMP energy. With the rapid development of EMP weapons, the protection methods are also constantly advancing. The development frontiers and research hotspots of EMP protection technology are:

(1) Electromagnetic bionic technology： It maps to the electronic system working in the electromagnetic environment by determining the target biological system that imitates and understanding the regularity of life phenomena such as structure, control mechanism and information flow. Based on this, the corresponding mathematical model is established and applied to an anti-electromagnetic pulse electronic system with typical characteristics of imitation organisms. It has the characteristics of self-organization, self-adaptation and self-repair [7].

(2) Electromagnetic adaptive protection technology： Using software techniques such as redundancy, fault tolerance, signage and digital filtering, as well as hardware protection measures such as interception, shielding, voltage equalization, shunting, grounding and filtering in weapon equipment systems. It can also reduce electromagnetic interference between systems and enhance the ability to withstand high-power EMP attacks.

(3) Microwave solid state reinforcement technology： It mainly refers to the development of receiving amplifier components with stronger anti-burning capability. It can enhance the anti-burning ability of the antenna. According to the coupling path of EMP, it is divided into front door reinforcement and rear door reinforcement. Front door reinforcement is mainly to limit the coupling of the antenna or sensor. The most effective way to reinforce the back door is shielding and terminal protection.

(4) Frequency selection surface (FSS)： The EMP can be protected by the FSS on the radome, the normal signal in the working frequency band can be transmitted and received, and the energy outside the band can be reflected.

(5) Energy selective surface (ESS): The ESS is a strong electromagnetic protection device with energy low-pass characteristics by utilizing the voltage-controlled conductive characteristics of the semiconductor device, and has an electromagnetic environment adaptive characteristic.

TABLE I. SIMULATION OF SEVERAL CONSTRUCTION METHODS

Simulation Method	Application	Platform or Equipment	Advantage	Disadvantage
Actual equipment simulation method	Combat confrontation exercise, coordinated training	Surface ships, aircraft, shore-based or vehicle equipment, high-power simulators, etc.	Three-dimensional combat space, with the same realism as combat	Expensive, vulnerable, and difficult to build an electromagnetic environment that is too complex
Semi-physical simulation method	Equipment test, training	Microwave darkroom, photoelectric darkroom, RF environment simulator, photoelectric environment simulator and platform motion simulation equipment, etc.	Complex environment and strong dynamics	Difficult to build complex environments in larger areas.
Digital simulation	Equipment training, test results inference, scientific research, operational effectiveness evaluation	Digital simulation system based on computer, software, model and network	Digital simulation of complex electromagnetic environments	Signal level model development is heavy and difficult.
Composite simulation	Equipment training, testing, research, operational effectiveness evaluation	Simulation, semi-physical simulation, digital simulation	Exercising various simulation methods to build an integrated complex electromagnetic environment	Complex system construction

(6) New protective material:

- **Nanomaterial:** Nanomaterial refers to a material whose characteristic size of the material component is on the order of nanometers. The nanomaterial developed by the Massachusetts Institute of Technology in the United States have the same shielding effectiveness against electromagnetic waves in the range of 8 to 18 GHz.
- **Graphene:** Because graphene has excellent electron mobility, by adding different substances to graphene, it can exhibit different shielding properties. In 2012, IBM used several layers of graphene to create a new protective material that effectively protects megahertz radiation and microwave electromagnetic radiation.
- **Optical fiber:** Optical fiber can conduct optical signals without coupling electromagnetic pulses, so optical fibers can be used to transmit signals between various electronic devices while effectively preventing electromagnetic pulse radiation interference [8].
- **Plasma：** The plasma can reflect high-power microwaves under certain conditions, and under certain conditions can absorb high-power microwaves, so that the microwave power transmitted into the electronic device is lower than the interference or destruction threshold. Therefore, plasma has become a new material for strong electromagnetic protection.

(7) Communication design: In the protection of key communication facilities, the frequency hopping spread spectrum communication method can be selected as much as possible, on the other hand, the self-closing system can be added to the system design, that is, the system is quickly turned off before the EMP bomb is predicted to be received. In the design of the communication network, multiple channels should be considered, so that the communication system can be ensured even when a certain node is attacked by the EMP.

REFERENCES

[1] Zhou Bihua, Chen Bin, Gao Cheng. Analysis on high power electromagnetic environment in modern war [J] Journal of Microwaves, 2002, 18 (1): 88－92.

[2] Liu Shanghe, Wu Zhancheng. Perniciousness and protection technology of ESP [M]. Beijing University of Posts and Telecommunications Press, 2004.

[3] IEC 61000-2-9-2017

[4] Ding Wei, Han Fuli. Protection of High Power Microwave Weapons [J]. Digital Technology & Applications, 2011(1):79-79.

[5] Tian Xiaoling, Wangweihua. Research status and development trend of high power microwave pulse and coupling effect［J］Cruise Missile, 2009(4): 39－40.

[6] Liu Liming, Huang Wenliang, Sun Wei. Construction Method of Complex Electromagnetic Environment in Sea Battlefield [J]. Ship Electronic Countermeasure, 2010, 33(4).

[7] Liu Shanghe, Yuan Liang, Chu Jie. Elec Electromagnetic bionics: A new study field of electromagnetic protection［J］. Chinese Journal of Nature, 2009, 31(1): 1－7.

[8] Liu Peiguo, Liu Chenxi, Tan Jianfeng, et al. Research Progress of Strong Electromagnetic Protection Technology [J]. Chinese Ship Research, 2015, 10(2): 2-6.

Development of Antenna Waveforms for Updating IEC 61000-2-10

William A. Radasky
Metatech Corporation
Goleta, California USA
wradasky@aol.com

***Abstract*—This paper describes the process of developing time waveforms for the coupling to simple vertical monopoles and dipoles in order to extend the work already documented in Annex C of IEC 61000-2-10, Description of HEMP environment – Conducted disturbance. These waveforms will be useful to describe conducted immunity tests for communications transmitters and receivers for the E1 HEMP.**

Keywords—Early-time (E1) HEMP, coupling, antennas

I. INTRODUCTION

IEC 61000-2-10, Ed. 1 (the conducted HEMP environment) was published in November 1998 [1]. Conducted cable coupling environments were developed based on technical publications and generally included: Peak current levels as a function of line length for above or below ground cables; Voltage levels also provided through a characteristic impedance; Time waveform information was provided through rise times and pulse widths.

Information for simple antennas (vertical monopoles and horizontal dipoles) was provided for peak values of the induced currents and voltages (using probabilistic analysis). No time waveform information was provided. Information is needed for the time waveforms to test the immunity receivers and transmitters (especially in the HF range). This is the main reason to update Edition 1.

II. APPROACH

The main activity is to determine the waveshapes for different simple antennas. The work in IEC 61000-2-10 mainly dealt with the probabilistic coupling of the incident E1 HEMP field due to the local geomagnetic field. The local geomagnetic field determines the polarization of the incident E1 HEMP fields

Generally if the geomagnetic field dip angle is 90 degrees (location at the magnetic North Pole), then the E1 HEMP field is mainly horizontal which does not couple well to a vertical antenna, for example.

This paper will describe a few simple example antennas and the coupling to them from Annex C of Edition 1 of IEC 61000-2-10. From this information sample time waveforms are developed from coupling calculations.

Given the results, there is a new test publication IEC 61000-4-18 Edition 2, which provides immunity test waveforms for damped sinusoidal waveforms for frequencies up to 30 MHz. This paper will consider the use of this standard for performing immunity tests for the electronics connected to these types of antennas.

III. SAMPLE SIMPLE ANTENNAS

For many applications it is possible to use simple linear antennas, especially in the HF (3-30 MHz) and VHF (30-300 MHz) range of frequencies. IEC 61000-2-10 has considered both vertical monopoles and horizontal dipoles in its Annex C. Statistical E1 HEMP coupling calculations have been performed by Tesche [2] to compute the peak coupling parameters considering random angles of incidence, orientation, and polarization of the incident field (due to the local geomagnetic field). The IEC E1 HEMP waveform [3] was assumed to be the incident field. Figure 1 illustrates the coupling to a 10 m horizontal dipole.

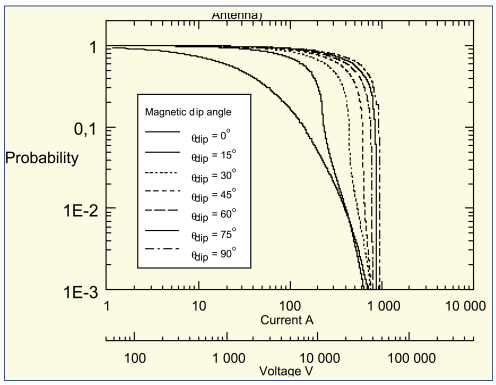

Fig. 1. E1 HEMP Coupling to a 10 meter long horizontal dipole {1}

There are coupling results for vertical monopoles with heights of 1 to 100 meters, and for horizontal dipoles from 1 to 100 meters in IEC 61000-2-10.

IV. TIME WAVEFORM EVALUATIONS

It is well known that the response from these types of linear antennas will oscillate as damped sinusoids. This paper reviews old and new sources of calculations and will provide analytic waveforms (and their formulas) that can be used for different sizes of simple antennas. Further IEC 61000-4-18 will be reviewed as a resource to provide a test method for testing antenna transmitters and receivers to these types of waveforms.

REFERENCES

[1] IEC 61000-2-10 Ed. 1.0 (1998-11-24): Electromagnetic compatibility (EMC) – Part 2-10: Environment – Description of HEMP environment – Conducted disturbance.

[2] F. M. Tesche, "Responses of simple linear antennas to the IEC HEMP environment," August 11, 1995, unpublished.

[3] IEC 61000-2-9 Ed. 1.0 (1996-02-19): Electromagnetic compatibility (EMC) – Part 2: Environment – Section 9: Description of HEMP environment – Radiated disturbance.

Analysis of Fields of Irradiation Cavities with Different Sizes

Xiangqin Zhu[1] Changhua Chen[2] Taijiao Du[1] Long Hu[2] Libing Cai[1]
1. State Key Laboratory of Intense Pulsed Radiation Simulation and Effect (Northwest Institute of Nuclear Technology) Xi'an, China, 710024
2. Science and Technology on High Power Microwave Laboratory (Northwest Institute of Nuclear Technology) Xi'an, China, 710024

***Abstract*-The fields in the working-volume of irradiation cavity, which similar to bounded wave electromagnetic pulse(EMP) simulator with lumped terminator and used for electromagnetic pulse effect experiments, are computed by parallelized finite-difference time-domain(FDTD) method. The electric fields in the working-volume of the irradiation cavity with different sizes are numerical studied and analyzed. The results show that short projection along *x*-axis of the front transitional section and short length along x-axis of parallel plates are needed for getting high peak-values of electric fields. And wide width of working-volume is needed for getting much useful experimental space.**

Index Terms—Irradiation cavity; EMP; FDTD; numerical analysis

I. INTRODUCTION

Electromagnetic pulse effects could be produced if humans or animals exposed in the environment of the strong electromagnetic pulse(EMP) with high electric field intensity[1]-[4]. It is needed to study the fields of irradiation cavities excited by high-voltage pulses, which are similar to bounded wave simulator(BWS) with lumped terminator[5][6] and can afford uniformity strong EMP in their working-volume.

Finite Difference Time Domain (FDTD) method[7] is one of the most popular three-dimensional methods in computational electromagnetics. And bounded wave simulator with lumped terminator for effect experiments of electromagnetic compatibility, interference and damage of complicated electronic systems, is simulated and analyzed by parallelized FDTD in [6]. On the other hand, the electromagnetic interference of dielectric plates and plastic box in the working-volume of a little BWS used for biomedical experiment, is considered in [8].

The fields of irradiation cavities similar to BWS are simulated and analyzed by parallelized FDTD. And the effect of its configuration sizes to the fields in the working-volume is also presented in this paper.

II. STRUCTURE AND SIMULATION METHOD

As shown in Fig.1, the irradiation cavity is made up of a voltage pulser, four inclined plates, two parallel plates and a lumped terminator. The voltage source is afforded by the voltage pulser. The front transitional section and the back transitional section are composed of a group of sloping plates respectively. The space between the two parallel plates belongs to the working-volume. And the lumped terminator is used to absorb the electromagnetic waves from the working-volume.

The configuration parameters of w and h are the maximum of width and height of the irradiation cavity respectively. L_2 is the projection along x-axis of the front/back transitional section. L_3 is the length along x-axis of the two parallel plates. One of testing-points is O point at the center of the working-volume. The location of P point is 15cm away from O point along y-axis.

Parallelized FDTD method[6] is used to simulate the fields in working-volume of the irradiation cavity. The uniaxial perfectly matched layer (UPML)absorbing boundary[9] is used in FDTD computing in this paper.

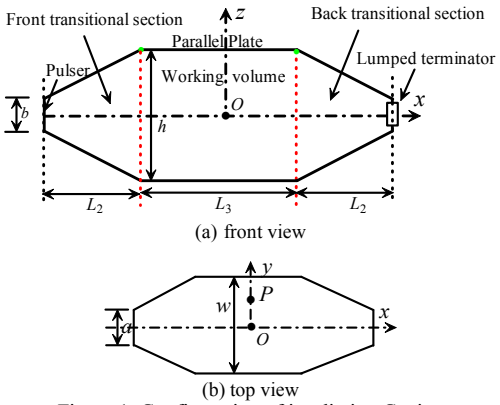

Figure 1. Configuration of irradiation Cavity.

III. NUMERICAL STUDY AND ANALYSIS

The voltage source can afford some source of electric field at the front of the irradiation cavity. And the electric field source is expressed as

$$E(t) = E_0\left[\exp(-\alpha t) - \exp(-\beta t)\right] \quad (1)$$

where $E_0 = 0.1\text{MV/m}$, $\alpha = 2.4\times10^7\,\text{s}^{-1}$ and $\beta = 2.2\times10^8\,\text{s}^{-1}$. The rise-time of the source is about 6.0ns and the FWHM is about 42.7ns. All the FDTD cell sizes in three directions are 0.006m and the time-step is 0.01ns.

A. *The effect of* L_2 to the fields

Let w=L_3=40cm unchanged. The EMPs of Ez at O point with different L_2 are given in Fig.2. We can conclude that the peak-value of E_z at O point reaches the maximum as L_2=40cm.

That is because the leakage energy from the front transitional section decreases as L_2 decreases. The waveform distortion in Fig.2 is produced by the connection of the front/back transitional section and the upper parallel plate.

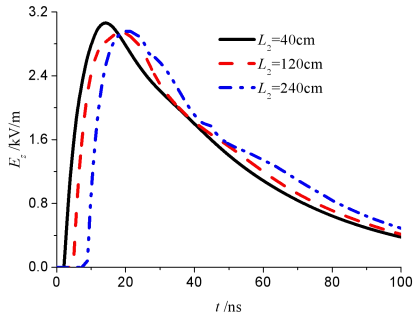

Figure 2. EMPs of E_z with different L_2.

B. *The effect of* L_3 to the fields

Let w=L_2=40cm unchanged. The EMPs of *Ez* at *O* point with different L_3 are given in Fig.3. We can conclude that the peak-value of E_z at *O* point as L_3=40cm is higher than that of E_z at testing-point as L_3=240cm. That is because the leakage energy from the irradiation cavity increases as L_3 increases before the electromagnetic waves from the source reach the testing-point.

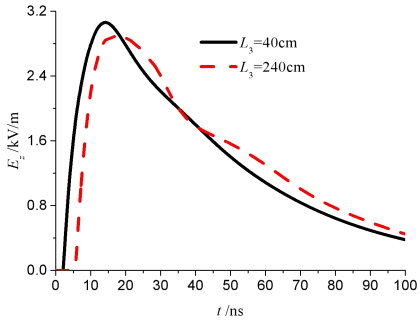

Figure 3. EMP of E_z with different L_3.

C. *The effect of* w to the fields

Let L_2=L_3=40cm unchanged. The location of *Q* point is 20cm away from *O* point along *y*-axis. The EMPs of *Ez* at *O* point, *P* point and *Q* point with different w are given in Fig.4(a), Fig.4(b) and Fig.4(c) respectively. From Fig.4, we can get that the effect of w to the field at *Q* point is most obvious during the three testing-points, because the location of *Q* point is near the edge of the parallel plate than those of other two testing-points. And the peak-values of *Ez* at *P* point and *Q* point increase evidently as w increases, which results in better guiding characteristic of irradiation cavity.

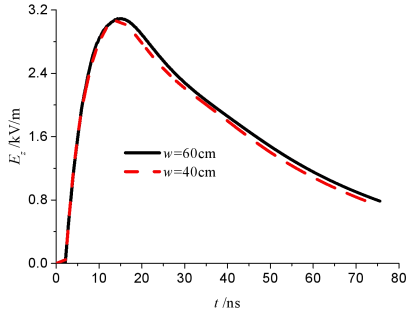

(a) *O* point

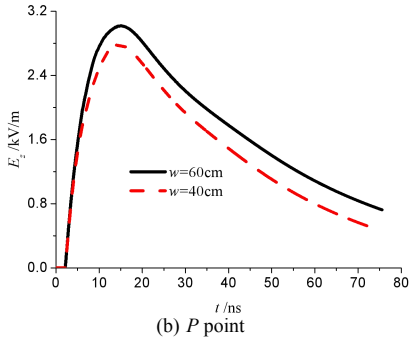

(b) *P* point

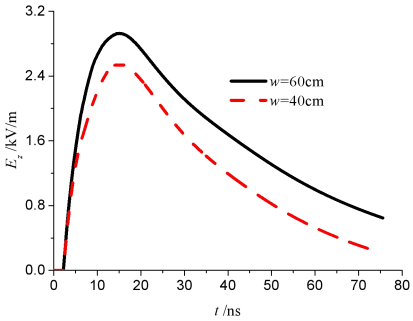

(c) *Q* point

Figure 4. EMP of E_z with different w.

IV. Summary and Conclusions

The electric fields in the working-volume of irradiation cavity for electromagnetic pulse effect experiments are simulated in parallel FDTD method. And the effects of the size parameters on fields are given. The projection along *x*-axis of the front transitional section and the length along *x*-axis of parallel plates should decrease if high peak-value needed. And the maximum of the width should increase if much useful experimental space needed.

Acknowledgment

This work was supported by State Key Laboratory of Intense Pulsed Radiation Simulation and Effect (No. SKLIPR1601Z).

References

[1] Mingjuan Yang, Junye Liu and Yafeng Wang, et al, "Effects of electromagnetic pulse on polydactyly of mouse fetuses," *Theriogenology*, vol. 80, pp. 18-23, July 2013.

[2] Kangchu Li, Shirong Ma, Yurong Li, et al, "Effects of PEMF exposure at different pulses on osteogenesis of MC3T3-E1 cells," *Archives of Oral Biology,* vol. 59, pp. 921-927, September 2014.

[3] Yongbin Chen, Jing Li, Yuhong Qi, et al, "The effects of electromagnetic pulses (EMP) on the bioactivity of insulin and a preliminary study of mechanism," *Int. J. Radiat. Biol.,* vol. 86, pp. 22-26, January 2010.

[4] Jinhui Li, Dapeng Jiang, Yafeng Wang, et al, "Influence of electromagnetic pulse on the offspring sex ratio of male BALB/c mice," *Environmental Toxicology and Pharmacology*, vol. 54, pp. 155-161, September 2017.

[5] Bihua Zhou, Wei He, Jianming Guo, et al, "Standardization of LEMP electric field instrument," *Chinese Journal of Radio Science*, vol. 26, pp. 1034-1039, December 2011.

[6] Xiangqin Zhu, Jianguo Wang, Weiqing Chen, et al, "Parallelized FDTD simulation for flat-plate bounded wave EMP simulator with lumped terminator," *High Power Laser and Particle Beams*, vol. 87, pp.313-330, September 2013.

[7] Debiao Ge, Bing Wei, *Electromagnetic wave*, Beijing: Science Press, 2011.

[8] Xiangqin Zhu, Weiqing Chen, Jianguo Wang, et al, "Simulation and experimental comparison of radiation near-fields of BWS with distributed terminator," *The 2017 International Applied Computational Electromagnetics Society Symposium*, Suzhou, China, August 2017.

[9] S D Gedney, "An anisotrpic PML absorbing media for FDTD simulation of fields in lossy dispersive media," *Electromagnetics*, vol. 16, pp.339-415, July 1996.

Characteristics of Lightning Faults of 220 kV and above Overhead Transmission Lines in Zhejiang Province in last 15 years

1st Xiangxian zhou
State Grid Zhejiang Electric Power Research Institute
Hangzhou, China
zhouxiangxian04@126.com

2nd Hangwei Tong
State Grid Zhejiang Electric Power Research Institute
Hangzhou, China

3rd Jun Tong
State Grid Zhejiang Electric Power Research Institute
Hangzhou, China

4th Wendong Jiang
State Grid Zhejiang Electric Power Company
Hangzhou, China

5th Yang Zou
CEEC Zhejiang Electric Power Design Institute
Hangzhou, China

6th Te Li
State Grid Zhejiang Electric Power Research Institute
Hangzhou, China

***Abstract*—Lightning is the most frequent reason for high voltage overhead transmission lines faults. Due to the stochastic nature of lightning, the theoretic approaches for evaluation of the performance of overhead transmission lines are far from complete. The field experiences from the practitioners are of great value in lightning performance researches. This work collected a large dataset of lightning faults happened during 2004-2018 in the 220 kV and above overhead transmission lines in Zhejiang province. The characteristics, like temporal, spatial and double circuits faults, of the lightning faults are analyzed in this work. The mechanisms behind these characteristics are also explained in this work, which hope will be helpful in the future researches in lightning performance of overhead transmission lines.**

Keywords—Lightning, overhead transmission line, flashover, outage, double circuit fault

I. Introduction

Zhejiang province locates on the west side of Pacific Ocean and has a power grid approximately equal to that of Germany. Lightning caused about 65% of all the faults of 220 kV and above overhead transmission lines and thus one of the major threats to the power grid operation in Zhejiang province[1]. As the research and development branch of State Grid Zhejiang Electric Power Company, State Grid Zhejiang Electric Power Research Institute started tracking the lightning performance of 220 kV and above transmission lines since 2004. This work introduced the characteristics of lightning faults of 220 kV and above transmission lines in the last 15 years.

Lightning performance is influence by factors like lightning density, shielding angle, footing impedance et al[2]. Systematic effort has been made by Both IEEE[4] and CIGRE[4] to evaluate the lightning performance of overhead transmission line. Many theoretic investigations have been done by scholars around the world, which range from the calculation of lightning flashover rate[5], the simulation of lightning leader progression[6] and the simulation of lightning overvoltage propagation[7].

Apart from the theoretic investigation in to the lightning performance of overhead transmission lines, the field experience from the operation of high voltage transmission lines under heavy lightning incidences is an important part in lightning performance researches. Armstrong and Whitehead analyzed the lighting shielding data from 433 miles of high voltage and extra high voltage transmission lines[8]. Shim et al. investigated the lightning characteristics and its influence on the power grid in Korea[9]. Li et al. analyzed the temporal distribution of 425 lightning flashover data collected from 10 power supply companies[10].

This paper is based on the data collected by State Grid Zhejiang Electric Research Institute in the last 15 years. This dataset include 1457 lightning flashovers, including 177 lightning outages. The temporal variations of lightning faults are first analyzed, then the spatial distributions of lightning faults are analyzed, lastly the correlation between the data from the lightning location system and the lightning faults data are analyzed.

II. Temporal Distribution

A. Annual Variation

The annual variation of lightning flashover rate and outage rate from 2004 to 2018 are shown in Fig. 1 (a) and (b) respectively. The ground flash amount of Zhejiang province is also shown in Fig. 1. The flashover rate and outage rate generally decreased over the last 15 years. The flashover rate decreased from 1.37/(100 km·a) to 0.40/(100 km·a) while the lightning outage rate decreased from 0.12/(100 km·a) to 0.07/(100 km·a). The main reason is the decreasing of the ground flash amount from over 0.9 million in 2004 to around 0.4 million in recent 3 years. The correlation coefficient between the flashover rate and the ground flash amount is 0.85 and the correlation coefficient between the outage rate and the ground flash amount is 0.72, which both suggest strong correlation between ground flash amount and lightning faults.

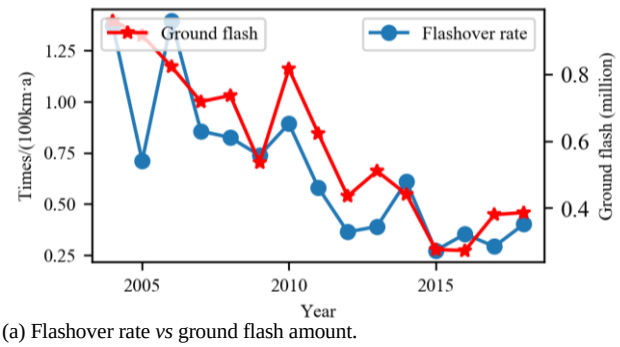

(a) Flashover rate *vs* ground flash amount.

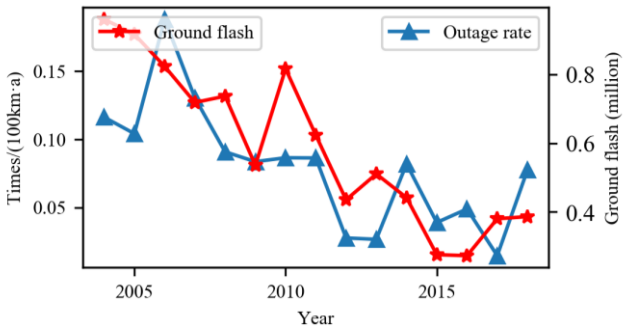

(b) Flashover rate *vs* ground flash amount.

Fig. 1. Annual variation of lightning flashover rate and outage rate.

B. *Monthly Variation*

The monthly distribution of lightning flashovers and outages are shown in Fig. 2. The lightning flashovers and outages are negligible in January, October, November and December, and the lightning flashovers and outages from February to May grow gradually while the lightning flashovers and outages concentrated in the period between June and September. The flashovers and outages happened between June to September accounts up to 85.6% and 81.9% of all the flashovers and outages respectively. The monthly variation of lightning flashovers and outages are drove by East Asian monsoon which transport moisture wind from Pacific Ocean to Zhejiang province, which brings frequent thunder storms. The East Asian monsoon usually peak during July and August[11], which coincident with the 2 months that recorded the highest number of lightning flashovers and outages.

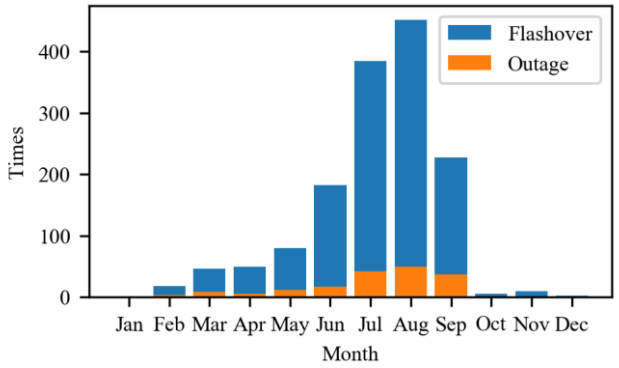

Fig. 2. Monthly variation of lightning flashover and outage.

C. *Hourly Variation*

The hourly variation of lightning flashovers and outages are shown in Fig.3. The lightning flashovers and outages are relatively much fewer during 22:00 to 11:00 next day than during 11:00 to 21:00. The lightning flashovers and outages increase rapidly from 11:00 to 17:00 and then gradually decrease. The hourly variation of lightning flashovers and outages are drove by the sea-land wind circulation of the coastal area of Zhejiang province. The wind generally blows from the land to the sea during 21:00 to 10:00 of the next day, and the wind blow from sea to land prevalent from 10:00 to 21:00 during the day[12]. The wind blow from sea to land is moisture and warm which is warm bed for the formation of thunder storm. The peak hours of lightning flashovers and outages coincident with the prevalent time period of sea to land wind.

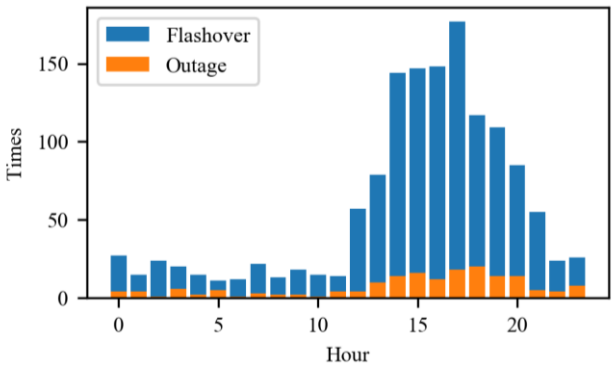

Fig. 3. Hourly variation of lightning flashover and outage.

III. Spatial Distribution

A. *Altitude*

Altitude of transmission line towers is correlated to the terrain of where the tower is locating in. The histogram of the altitude of lightning faults towers and the altitude of all the 220 kV and above transmission line towers in Zhejiang province are both shown in Fig. 4. The average altitude of lightning faults towers is 223m while the average altitude of all the towers is 120m. The proportion of lightning faults towers with altitude between 50m to 400m is much higher than that of all the towers. The reason are twofold, firstly the higher altitude usually means towers are in mountain area where the air is more turbulent than the plain area and thus more convenient for electrification of cloud and then lead to the formation of thunder storms. Secondly, the mountain area in Zhejiang province is usually full of rocks which lead to high footing impedance of towers and thus lead to higher back flashover rate.

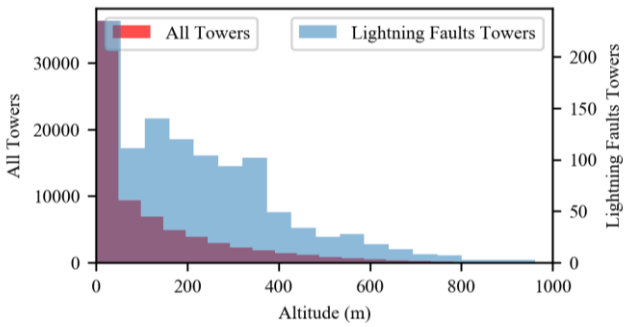

Fig. 4. Altitude of transmission line towers.

B. *Distance to Coast Line*

To verify if the transmission lines in coastal area are more vulnerable to lightning strikes, the distance between the lightning faults towers and the coast line (the shortest distance) of Zhejiang province and that of all towers to the coast line are compared in Fig. 5. The distribution of the distance to coast line of lightning faults towers are quite similar to that of all towers, which peak at 25km and 125km. The average distance between the lightning faults towers and the coast line is 85km, while the average distance between all towers to the coast line is 88km. The data shown in Fig. 5 cannot support the assumption of transmission lines in coastal area are more vulnerable to lightning strikes.

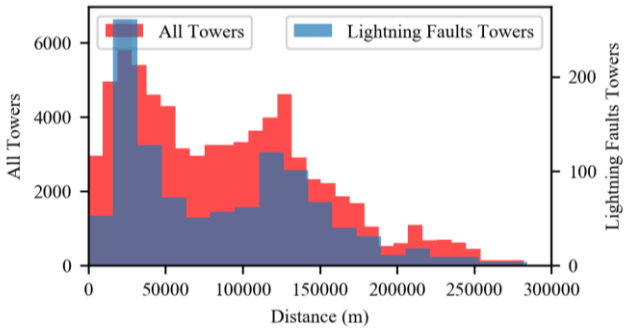

Fig. 5. Distance to coast line of transmission line towers.

C. Span

The histogram of the span of lightning faults towers (average of the two sides span) and that all towers are shown in Fig. 6. The average span of the lightning faults towers is 475 m while the average span of all towers is 372 m. The spans of lightning faults towers are significant higher than that of all the towers. The reason is that the larger span will cause the negative reflection of lightning overvoltage wave from the adjacent towers to travel longer time to come back to the lightning strike point, which will make the lightning overvoltage to be higher and thus cause lightning flashovers.

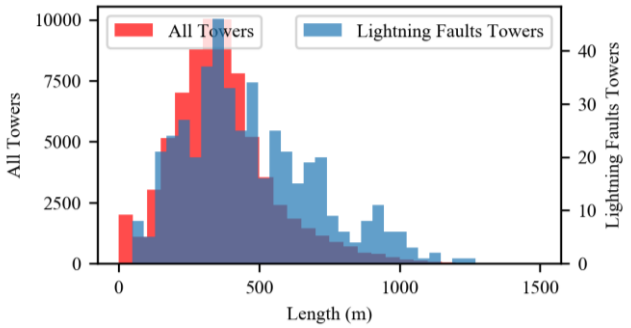

Fig. 6. Span of transmission line towers.

IV. Lightning Fault Classification

A. Faults phase

The lightning flashover fault phase distribution is shown in Fig. 7. The single phase faults accounts for 91.1% of all the lightning flashovers, among which the amount of phase A flashovers and phase C flashover are almost identical while the amount of phase B flashover is 11.3% lower, because phase B conductors in horizontal phase arrangement are usually placed on the center which is almost immune to shielding failure. The successful reclose rate of single phase flashover is 96.1% which will prevent lightning outage. The multiple phase lightning flashovers will lead to outage because the reclose device will only not operate in this condition. The amount of AB, BC and AC are 34, 40 and 37 respectively, while amount of the three phase faults is 16. The multiphase lightning flashovers are usually caused by back flashovers, or in some uncommon but not rare cases are caused by the lightning with multiple terminals, for which a detailed analysis method was developed by the authors of this work[13].

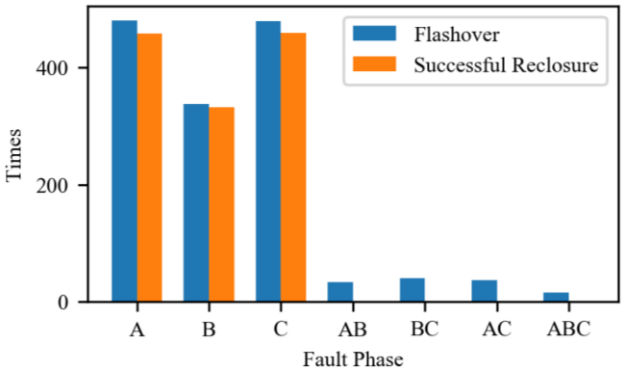

Fig. 7. Phase of the lightning flashovers.

One kind of the most severe lighting faults is the double circuit flashover at the same time, which can lead to the tripping of the transformers in terminal substations[15]. There were 67 double circuits lightning faults happened in the last 15 years in Zhejiang province. The phases of the double circuit faults are shown in Fig. 8, where the same phase faults account for 82% of the total amount. This is because the power frequency voltage on the conductors is not negligible in determine which phase will breakdown during back flashovers. When the power frequency voltage of the conductors is with the opposite polarity to that of the lightning overvoltage, that phase will first breakdown, and vice visa.

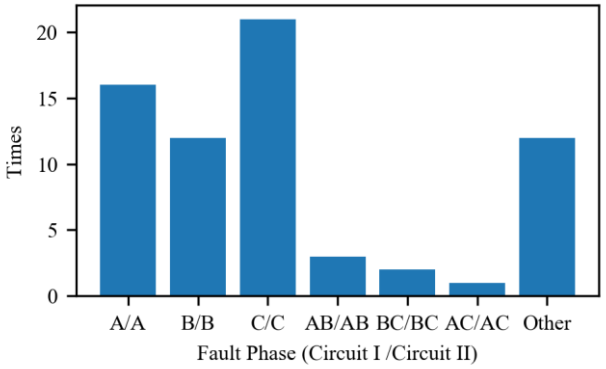

Fig. 8. Phase of the double circuit lightning faults.

B. Lightning Current Magnitude

The parameters of the suspected ground flashes are also recorded, the parameters are from the Lightning Location System installed in Zhejiang province[14]. The lightning current magnitude distribution for both the flashover and outage are shown in Fig. 9. 63.2% of the lightning currents that caused flashovers are smaller than 40 kA which is usually the up limit current of the shielding failure in 220 kV and above overhead transmission lines. The lightning currents that are larger than 40kA will have much higher strike distance which will lead the downward leader jump to the ground wire or the ground. The lightning currents that caused lightning outages are generally higher than that of lightning flashovers, because it takes much higher energy to cause outages. The largest lightning current that caused lightning outage is 382 kA which far exceeded the lightning current withstand level of overhead transmission lines.

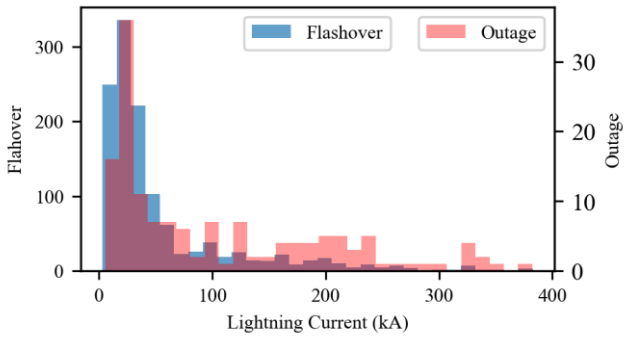

Fig. 9. Lightning current that cause lightning flashovers and outages.

The distribution of current magnitude that caused double circuits flashovers is shown in Fig. 10, where 61.0% of the currents magnitudes are larger than 80 kA, because most of the double circuit lightning flashovers are caused by back flashovers. The Lightning Location System's accuracy on the measurement of lightning current magnitude is subject to the influence of the attenuation effect of the mountains and high buildings. However, the lightning current magnitude measured by the Lightning location system has proved to be very helpful in discerning back flashovers from shielding failures. The location error of the Lighting Location System is about within 3 km, which is accurate enough for the analysis in this work.

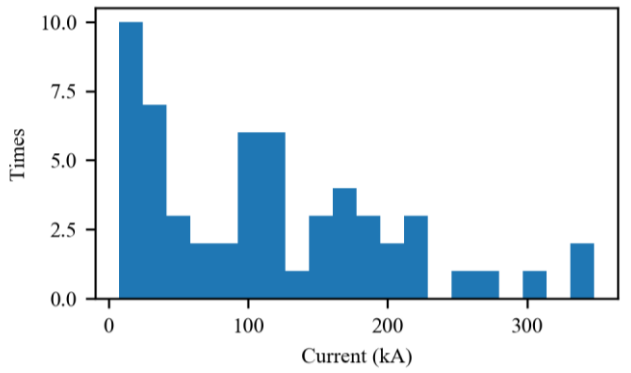

Fig. 10. Lightning current that cause double circuits faults.

C. Distance between Ground Flashes and Towers

The distance between suspected ground flashes and fault towers is also analyzed in this work. The distance distribution is show in Fig. 10, where the 66.1% of the detected ground flashes are locate in 1km vicinity of the fault towers and 96.2% of the detected ground flashes are locate in 3km vicinity of the fault towers, which proved the accuracy of the Lightning Location System in Zhejiang province.

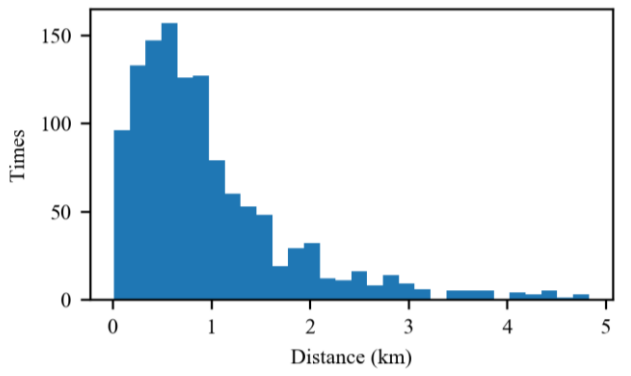

Fig. 11. Distance between ground flash to fault towers.

V. Conclusion

The temporal distribution, spatial distributions and other characteristics are analyzed in this work, and the following conclusions can be drawn

(1) The annual variation of lightning faults is highly correlated with amount of ground flashes. The monthly variation of lightning faults is mainly determined by the monsoon, while the hourly variation of lighting faults is mainly determined by sea land wind circulation.

(2) The altitude of the lightning faults towers are generally higher than that of average tower altitude due to the more turbulent air and higher footing impedance in mountain area.

(3) The span of the lightning faults towers is larger than average span of towers. The transmission lines in coastal area are not more vulnerable to lightning strikes than that in inner land.

(4) The majority of the lightning flashovers in 220 kV and above transmission lines are caused by shielding failure while the majority of the double circuit flashovers are caused by back flashover.

References

[1] Z. S. Jin, W. T. Hu, J. G. G et al. "Analysis of the Measures to reduce the Lightning Flashover rate of high voltage transmission lines in Zhejiang Power Prid", *Zhejiang Electric Power*, 2010, pp 1-5. (in Chinese)

[2] J. C. Das, "Transients in Electrical Systems Analysis, Recognition and Mitigation". *McGraw-Hill Company*, 2010, pp. 91–122.

[3] "IEEE Guide for Improving the Lightning Performance of Transmission Lines", *IEEE Standard* 1243-1997.

[4] CIGRÉ WG 33-01, "Guide to Procedures for Estimating the Lightning Performance of Transmission Lines", *CIGRÉ Technical Brochure*, Nr. 63, October 1991.

[5] C. A. Nucci,. "A survey on Cigré and IEEE procedures for the estimation of the lightning performance of overhead transmission and distribution lines.", *IEEE 2010 Asia-Pacific Symposium on Electromagnetic Compatibility (APEMC)*, 2010.

[6] W Sima, Y Li, V. A. Rakov, et al. "An Analytical Method for Estimation of Lightning Performance of Transmission Lines Based on a Leader Progression Mode.". IEEE Transactions on Electromagnetic Compatibility, 2014, pp. 1530-1539.

[7] A. Ametani, T. Kawamura. A method of a lightning surge analysis recommended in Japan using EMTP. *IEEE Transactions on Power Delivery*, 2005, pp. 867-875.

[8] H. R. Armstrong, and E.R.Whitehead, "Field and analytical studies of transmission line shielding". *IEEE Transactions on Power Apparatus and Systems* , 1968, pp.270-281.

[9] E. B. Shim, J. W. Woo, S. O. Han, and J. D. Moon. "Lightning characteristics in Korea and lightning performance of power systems.", *IEEE/PES Transmission and Distribution Conference and Exhibition*, vol. 1, IEEE, 2002, pp. 534-539.

[10] X. Li, C. Jiahong, G. Shanqiang, and T Xue, "November. Statistics and analysis of lightning flashovers of transmission lines during 2000~ 2007", *2008 International Conference on High Voltage Engineering and Application* , 2008, pp. 53-55.

[11] "East Asian Monsoon," *Wikipedia*, 05-Dec-2018. [Online]. Available: https://en.wikipedia.org/wiki/East_Asian_Monsoon. [Accessed: 03-Apr-2019].

[12] Q. H. Zhou, X. G. Liu, Y. H. Qi and X. Q. Ke. "A preliminary Study on Characteristic Features of Sea-land Breeze Circulation over Zhejiang Coast". *Journal of Hangzhou University*, 1987, pp. 109-20.

[13] X. Zhou, S. Wang, W. Tong et al. "Investigation of Transmission Line Grounding Fault caused by Multiple Terminated Lightning", Electric Porcelain and Surge Arresters, 2018, pp:33-36.(in Chinese)

[14] J.H. Chen, Q. Zhang, W. X. Feng, and Y. H. FANG. “Lightning location system and lightning detection network of China power grid”. *High Voltage Engineering*. 2008,Mar;pp:425-31.

[15] X. Zhou, X. Sun, J. Jin. “Simulation and Analysis of Transformer Neutral Overvoltage during Overhead Transmission Lines Single Phase Grounding Fault”, *Zhejiang Electric Power*, 2015, pp 1-5. (in Chinese)

A compact width-tunable high-voltage nanosecond pulse generator for nanoelectroablation

Xin Rao
School *of Electronic Science and Engineering*
University of Electronic Science and Technology of China
Chengdu, China
raoxinuestc@gmail.com

Xiaodong Chen
School of Electronic Engineering and Computer Science
Queen Mary University of London
London, United Kingdom
xiaodong.chen@qmul.ac.uk

Jun Zhou
School *of Electronic Science and Engineering*
University of Electronic Science and Technology of China
Chengdu, China
zhoujun123@uestc.edu.cn

***Abstract*—Nanosecond pulsed electric fields (nsPEF) have been shown to induce cancerous cell death and cause the remission of tumors in animals. In most of these studies, a fixed pulse width generator is adopted, but not suitable for studying the effect of pulse width. Due to the difference of the cell structures, the optimal pulse width for different tumors may be different. We have designed a compact width-tunable high-voltage nanosecond pulse generator and validated its feasibility in simulation and experiment.**

Keywords—width-tunable, high-voltage, nanosecond pulse, nanoelectroablation

I. INTRODUCTION

Pulsed electric fields have been employed in several different types of cancer therapy[1-2]. The nanosecond pulsed electric fields (nsPEF) has low energy that leads to very little heat production and an ability to penetrate into the cell to permeabilize nucleus membrane and intracellular organelles[3-4]. It has been demonstrated that the nsPEF is a physical modality that can trigger immunogenic tumor cell death[5]. The pulse width affects these peculiar biological properties markedly, though the pulse width of nanosecond high-voltage generators is fixed in most of these studies. To mitigate this problem, we have developed a digital controlled ns pulse generator based on the capacitor discharging system driven by a silicon carbide MOSFET switching array controlled by a FPGA circuit through an optic coupler. The developed pulse generator is proved to be stable when applied to various low impedance loads and capable of adjusting the pulse width between 100ns to 2us, the voltage between 0 to 2KV, and the repeat rate between 0.1Hz to 0.1MHz.

II. METHOD

A. Circuit modelling

The simplified circuit of the proposed pulse generator is modelled by using Multisim circuit simulator, as shown in Fig. 1. In the in-vivo/in-vitro experiments, the biological load can be represented with a parallel connection of the resistor and capacitor. For in-vitro test, the capacitance normally has little variation, which can be treated as a fixed capacitance . On the contrast, the resistance has a wide range of variation. The structure of cell chamber as well as culture properties could affect the magnitude of load resistance. To examine the influence, the resistance value was tuned from 5 Ohm to 100Ohm in the simulation. The energy storage capacitor has the magnitude of 2 μF. The pulse from the MOSFET driver module was with the width of 100ns. The DC supply provides a high voltage of 2 kV. The two protection resistors have a value of 1000Ohm.

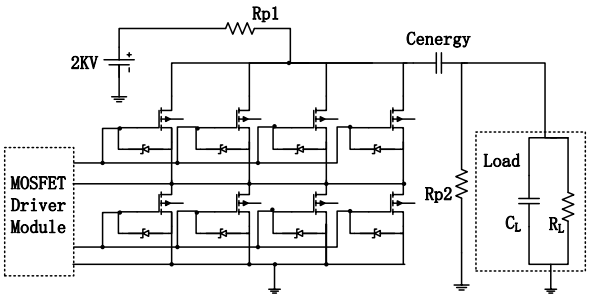

Fig. 1. Diagram of the simplified circuit of the pulse generator with the load

B. Description of the generator set-up

The system is further outlined with mainly six blocks: low voltage digital signal generator, optic-coupler driver block, SiC MOSFET array, high voltage/power supplier, energy storage component and in vivo/vitro load. A digital block incorporating the microcontroller, Digilent BASYS2 FPGA board, is implemented as low voltage signal generator. Since the FPGA board used here has the oscillation frequency of 50 MHz, it can feed out the digital signals with a variable width and a minimum width of 20 ns.The FPGA board is controlled by VHDL (VHSIC Hardware Description Language) program, which is firstly written and debugged in ISE design suite 14.1.

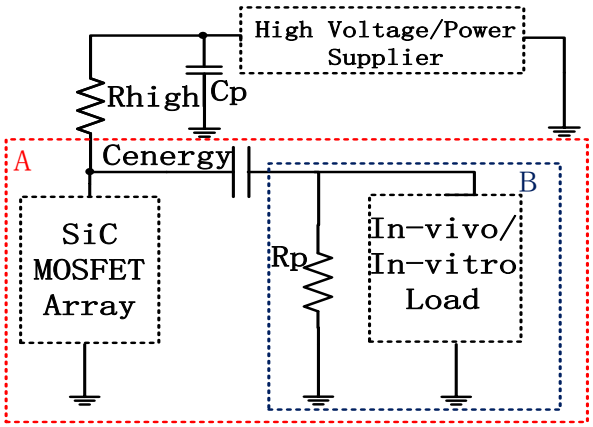

Fig. 2. Schematic diagram of energy storage component.

This work is supported by the National Natural Science Foundation of China (61505022, 61871003), the Sichuan Province Science and Technology Support Program (2016JY0197, 2016JY0076), the National Key Research and Development Program of China (2017YFA0701000), and the National Key Scientific Instrument and Equipment Development Project (2018YFF0101300).

SiC MOSFET array is arranged with silicon carbide MOSFETs and transient voltage suppressor diodes. The power MOSFET is normally used as the core of switching block in the pulse generators because of its sophisticated power handling capabilities. The conduction of the drain-source channel in MOSFET leads to the pulse at the load with desirable width and amplitude. Compared with the traditional silicon MOSFET, the silicon carbide one has good performance under high voltage with low on-state resistance, excellent switching performance, and stable temperature behaviors. The deployed MOSFET has high breakdown voltage of 1200 V between the drain and source, and current rating of 14 A. The turn-on or turn-off delay time is 19 ns or 47 ns respectively. Based on these criteria and the consideration of redundant design, MOSFET configuration is designed and implemented as two stages in series while four in parallel.

Energy storage component connects with high voltage/power supplier, SiC MOSFET array and biological load. A high voltage DC source, the core of high voltage/power supplier, is TD2200 made by Dalian Teslaman Tech. Co., Ltd., with the output DC voltage from 0 to 5 kV and current to 60 mA maximum. The load is the cuvettes with biological samples in-vitro or body tissues in-vivo. The capacitor Cenergy with a large capacitance and a high voltage rating is set as 2uF. The capacitance needs to be carefully balanced with rapid raise/fall edges and enough stored energy supporting the pulse train with desired amplitude, width and repetition rates. The high voltage rating ensures the stability of the capacitor. The bypass capacitor Cp filters out the high frequency noise from DC voltage source and the resistor Rhigh depresses the voltage ripple efficient.

The high voltage supplier initially charges the energy storage component without biological load during the MOSFET switch is close, then load the required load. When MOSFET array triggered by the digital signal pulse, the circuit A is turned on and the load charges rapidly to the desirable amplitude. The voltage of the load is hold on until the control pulse finished. The close drain-source channel in MOSFET turns on Loop B instead of A and the load quick discharge, which leads to the pulse at the load with appropriate width. The appropriate resistor Rp is 1000 Ohm.

III. Results and Discussion

A. *Simulation results on the various load*

The voltage of different loads with various pulse width differs greatly, as shown in the Figure. 3. When the same When the resistance is less than 20 Ohm, the peak voltages decrease and falling edges steepen with the increasing load resistances, caused by the voltage dividing with drain-source resistance of the silicon carbide MOSFET. When the resistance is increased, the pulse takes less time to fall and more time to raise, especially the raising edge is more affected. It is because of the different charge/discharge circuit prior introduced. The pulse generator with different loads, whose resistance range from 20 Ohm to 100 Ohm, can output pulses with the time width, which is 100ns.

B. *Measured data of the novel generator*

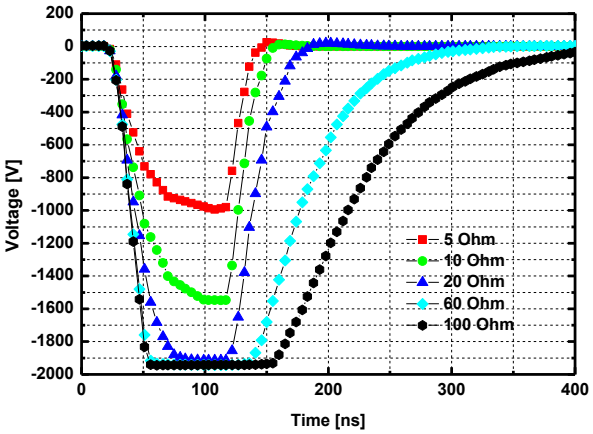

Fig. 3. Pulses of the loads with various resistances. The resistances are 5 Ohm (red rectangle), 10 Ohm (green hexagon),20 Ohm (blue upper triangular), 60 Ohm(cyan diamond) and 100 Ohm (black dot)

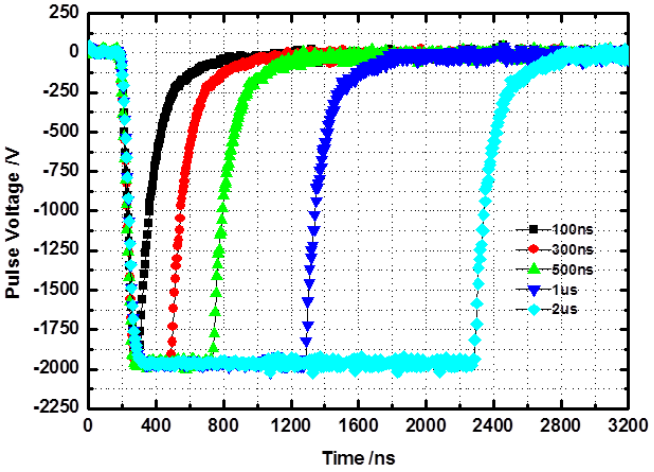

Fig. 4. Pulses with different widths at the in-vivo load were probed with DPO5204B. The pulse widths are 100ns (black rectangle), 300ns (red dot), 500ns (green upper triangular) , 1μs (blue lower triangular) and 2μs (cyan diamond). The in-vivo load is the fresh swine tissue clamped with plant electrodes whose gap is 3mm.

The novel generator implemented as previously introduced description is tested with the in-vitro load. The load, fed by the pulses whose width is 100ns, 300ns, 500ns 1us or 2us and amplitude is 2kV, is the fresh swine tissue clamped with plant electrodes whose gap is 3mm. The results in Figure 4 show that the pulses could satisfy the requirements from 100 ns to 1us. The widths of falling edge and raising edge are 90ns and 480ns approximately, while the rise time and fall time of silicon carbide MOSFET is 19ns and 29ns typically. The time during the pulse raising from -2kV to -1kV is 70ns roughly, because the raising edge is extremely steep at first but flatten fast with time. The different widths of rising edge and falling edge are come from the different charge/discharge circuit prior introduced and the characters of the silicon carbide MOSFET. According to these parameters, the pulse generator process the adjustable time width (100ns-2us), flexible voltage (0-2KV) and stable outputs with in-vivo load.

IV. Conclusion

A compact width tunable high voltage ns pulse generator is designed and implemented. The pulse generator is verified in simulation and experiment. .

REFERENCES

[1] Nuccitelli R , Pliquett U , Chen XH, et al." Nanosecond pulsed electric fields cause melanomas to self-destruct" BIOCHEMICAL AND BIOPHYSICAL RESEARCH COMMUNICATIONS Vol.343 pp351-360 2006

[2] M. Breton and L. M. Mir, "Microsecond and nanosecond electric pulses in cancer treatments," Bioelectromagnetics, Aug 3 2011.

[3] E.S. Buescher, K.H. Schoenbach, Effects of submicrosecond, high intensity pulsed electric fields on living cells-intracellular electromanipulation, IEEE Trans. Dielect. El. In. 10 (2003) 788–794.

[4] S.J. Beebe, P.F. Blackmore, J. White, R.P. Joshi, K.H. Schoenbach, Nanosecond pulsed electric fields modulate cell function through intracellular signal transduction mechanisms, Physiol. Meas. 25 (2004) 1077–1093.

[5] Nuccitelli R, McDaniel A, Anand S et al."Nano-Pulse Stimulation is a physical modality that can trigger immunogenic tumor cell death," Journal for ImmunoTherapy of Cancer, vol5, pp32, 2017

Steady-state security region of power system based on hyper-plane under the influence of geomagnetic storms*

Xinjie Li
School of Electrical and Electronics Engineering
North China Electric Power University
Beijing, China
lixinjie0908@126.com

Chunming Liu
School of Electrical and Electronics Engineering
North China Electric Power University
Beijing, China
liuchunming@ncepu.edu.cn

***Abstract*— Geomagnetic storms are violent disturbances of the geomagnetic field around the world, which produce geomagnetic induced currents(GIC) in power system. Power transformer enters the half-wave saturation state under the influence of GIC. The harmonics and reactive power loss produced by transformer affect the voltage stability of power system and cause the maloperation of relay protection devices in power system. With the increase of voltage level and the expansion of power grid scale, geomagnetic storms will seriously threaten the safe operation of power grid. The security region attracts increasing attention because it provides a wealth of global information to secure power system's operation. The method of using a set of hyperplanes to approximate the boundary of a security region under the problem of geomagnetic storms has accuracy and engineering practicability. In this paper, the nodal power injection equations are linearized to establish a linear relationship between nodal voltages' magnitudes and angles and nodal power injections, and then hyperplanes of nodal power injection security region representing operational constraints are obtained. The security and margin of and the hyper-cube security region for operational point are studied based on the obtained hyperplanes.**

Keywords— geomagnetic induced currents, steady-state security, boundary of security region, nodal power injection, hyper-plane

I. INTRODUCTION

Geomagnetic storm is a violent geomagnetic disturbance (GMD) phenomenon, which generates geomagnetically induced currents (GIC) in the power grid to affect the safe operation of the power system. In addition to the overheating damage caused by the DC bias of the transformer, the GIC causes the DC bias of the whole network transformer to be simultaneous. The time difference between different locations in the world does not exceed 2 min [1]. When the whole network transformers generate harmonic and reactive losses at the same time, it will cause a fluctuation on the reactive power of the system, which may cause system voltage fluctuations or even voltage instability. The North American Reliability Council (NERC) released a reliability assessment report for geomagnetic storm disturbances in 2012 that the geomagnetic induction current poses two major risks to the power system: First, the risk of potential damage to system equipment such as transformers. Second, the risk of grid voltage collapse after the loss of reactive power loss.

Security domain provides rich security information. So as E. Hnyilicza etc. proposing this concept, it has received a lot of attention. Literatures [2] and [3] give implicit and explicit expressions of static security domains, respectively. On the basis of the literature [3], the literature [4] groups the system security constraints, and proposes that the active power tends to the maximum security domain. Generally speaking, most of the current research methods of static security domain are based on the power flow equation, while the large power flow equation has the characteristics of high dimensionality and strong nonlinearity, and the boundary expression of the security domain is not intuitive enough. Based on this feature, literature [4] proposes a method for obtaining a static security domain hyperplane group. The method linearizes the node power injection equation to obtain a hyperplane group that approximates the boundary of the real node power injection security region.

Based on the above methods, this paper analyzes the static security region of power system under the influence of geomagnetic storm, and obtains the security region boundary hyperplane group represented by node power injection, and analyzes the influence of geomagnetic storm on the safety margin of power system operation.

II. STEADY-STATE SECURITY REGION

A. Node injection Power Equation Linearization

For a power network with n nodes, the node power injection equation is:

$$\begin{cases} P_i = V_i \sum_{j\in i} \left(G_{ij}\cos\theta_{ij} + B_{ij}\sin\theta_{ij} \right) \\ Q_i = V_i \sum_{j\in i} \left(G_{ij}\sin\theta_{ij} - B_{ij}\cos\theta_{ij} \right) \end{cases}_{i,j=1,2,\ldots,n} \quad (1)$$

Where G and B are $n \times n$ order node admittance matrices.

The calculation formula of the line current is:

$$\begin{cases} P_{ij} = V_i V_j \left(G_{ij}\cos\theta_{ij} + B_{ij}\sin\theta_{ij} \right) - V_i^2 G_{ij} \\ Q_{ij} = V_i V_j \left(G_{ij}\sin\theta_{ij} - B_{ij}\cos\theta_{ij} \right) + V_i^2 B_{ij} \end{cases}_{i,j=1,2,\ldots,n} \quad (2)$$

where P_{ij} and Q_{ij} are active power and reactive power of branch ij respectivly.

The power system generally operates near the area of point(v=1, θ=0). Therefore, Equation(1) has been simplified as:

$$\begin{cases} P_{ij} = G_{ij}\left(V_j - V_i \right) + B_{ij}\left(\theta_i - \theta_j \right) \\ Q_{ij} = -B_{ij}\left(V_j - V_i \right) + G_{ij}\left(\theta_i - \theta_j \right) \end{cases}_{i,j=1,2,\ldots,n} \quad (3)$$

Applying Kirchhoff's Law to node i can be obtained:

$$\begin{cases} P_i = \mathring{a}_{j\hat{I}i} P_{ij} = \sum_{j\hat{I}i} \left[G_{ij}\left(V_j - V_i\right) + B_{ij}\left(q_i - q_j\right) \right] \\ Q_i = \sum_{j\hat{I}i} Q_{ij} = \sum_{j\hat{I}i} \left[-B_{ij}\left(V_j - V_i\right) + G_{ij}\left(q_i - q_j\right) \right] \end{cases}^{i,j=1,2,\ldots,n} \quad (4)$$

Let node 0 be the reference node, then the power injection and the relationship between the voltage amplitude and the phase angle of other nodes besides the reference node can be written in matrix form:

$$\begin{pmatrix} V' \\ q' \end{pmatrix} = \begin{pmatrix} G' & -B' \\ -B' & -G' \end{pmatrix}^{-1} \begin{pmatrix} P' - G_0 \\ Q' + B_0 \end{pmatrix} \quad (5)$$

Equation (5) gives the voltage amplitude and phase angle equations expressed by the node power injection, which is a linear map of the obtained state quantity space to the node power injection space after linearization.

B. Node power injection security region

According to literature [3], the static security constraints of the power network are:

- *PQ node voltage amplitude constraint:*

$$V_m \le V \le V_M \quad (6)$$

- *Power flow constraint:*

$$-d \le A^T q \le d \quad (7)$$

Substituting voltage amplitude and phase angle constraints into the linearized node power injection equation to obtain a hyper planar group representing the subdomain of the safety region.

C. Analyzing the security region

Determine the safety of the operating point according to the sign of d by calculating the distance d from the operating point to the boundary of the security region. Using the minimum value of the projection of the space vector d at each coordinate, the power variation limit of each node is formed, and the ultra-cuboid security domain of the system at the operating point o is formed.

III. Case Analysis

Uiuc 150 bus system [5] is taken as an example to obtain the reactive power injection safety domain under the influence of geomagnetic storms.

We calculate Node power injections at the operating point of the system in three cases of 0V/Km, 6V/Km, and 12V/Km eastward geoelectric fields. Only the stations with higher GIC values in 98 substations were selected for research. Then the distance d from operation points to hyper-planes is calculated through the static security constraints. The hyper-cube for operation points can be obtained through decomposing d in all directions.

When the eastward geoelectric field in 0V/Km, 6V/Km and 12V/Km, the voltage level of the substation nodes is shown in Table I.

TABLE I. Voltage Level of the Substation Nodes(baseKVA=100MVA)

Node	0V/Km	6V/Km	12V/Km
27	1.0297	0.9863	0.9345
43	1.0231	0.9324	0.7589
45	1.0244	0.9327	0.7586
79	1.0080	0.9509	0.8611

References

[1] Liu Lianguang, Liu Chunming, Zhang Bing. Effects of Geomagnetic Storm on UHV Power Grids in China[J]. Power System Technology, 2009, 33(11): 1-5.

[2] J. A. Demaio, Fischl R. Fast identification of the steady-state security regions for power system security enhancement[J]. IEEE PES Winter Meeting, NY, US, 1976:25-30.

[3] F. F. Wu, S. Kumagal. Steady-state security regions of power systems[J]. IEEE Transaction on Circus and systems, 1982, 29(11):703-711.

[4] Wu Yingjun. Practical approximation static security domain of power system based on hyperplane and its solving method[J]. Transactions of China Electrotechnical Society, 2014, 29(sup.1):374-383

[5] A. B. Birchfield, K. M. Gegner, T. Xu, K. S. Shetye and T. J. Overbye. Statistical Considerations in the Creation of Realistic Synthetic Power Grids for Geomagnetic Disturbance Studies[J]. IEEE Transactions on Power Systems, 2017, 32(2):1502-1510.

Two Scenarios of Positive Lightning Leader Channel Branching *

Xiushu Qie
LAGEO, Institute of Atmospheric Science, Chinese Academy of Science, Beijing, China
qiex@mail.iap.ac.cn

Shanfeng Yuan
LAGEO, Institute of Atmospheric Science, Chinese Academy of Science, Beijing, China
yuanshanfeng@mail.iap.ac.cn

Rubin Jiang
LAGEO, Institute of Atmospheric Science, Chinese Academy of Science, Beijing, China
jiangrubin@mail.iap.ac.cn

Zhuling Sun
LAGEO, Institute of Atmospheric Science, Chinese Academy of Science, Beijing, China
sunzhuling@mail.iap.ac.cn

Dongfang Wang
LAGEO, Institute of Atmospheric Science, Chinese Academy of Science, Beijing, China
wangdongfang@mail.iap.ac.cn

Abhay Srivastava
LAGEO, Institute of Atmospheric Science, Chinese Academy of Science, Beijing, China
abhaysrivastava2313@gmail.com

***Abstract*— We report two scenarios causing the positive leader branches with the fine time-resolved high speed video images. For the first scenario, floating bidirectional leaders initiating near a progressing positive leader was observed. The bileaders tended to originate at a radial distance of about 200 m from a progressing positive leader channel, propagating more or less radially toward and away from the main channel. Significant asymmetrical channel extensions at opposite ends were clearly recognized. The bidirectional leaders eventually connected to the existing main positive leader, resulting in the formation of new branches to the lateral side of the main positive leader channel. Another scenario for positive leader branching was the head splitting directly at its head and developing into different branches synchronously, which were sometimes invisible but were revealed by recoil leaders. This process was sometimes invisible, but could be revealed clearly by subsequent.**

Keywords—Positive leader, Channel branching, Side bidirectional leaders, Head splitting

I. INTRODUCTION

A fundamental issue of lightning physics concerns the generation and propagation of leaders that eventually establish the channels of a lightning discharge. Recent research has arrived at a common understanding of the considerable differences of lightning leaders of positive and negative polarities. However, the details of positive leader development are still not well understood.

Recently, a few cases of bidirectional breakdown initiating close to the channels of developing positive leader were observed [1-3]. Opposite ends of the bidirectional leaders exhibited obvious asymmetric characteristics. The positive ends formed single channels, while the negative ends developed into multiple branches with obvious stepping features. Bidirectional propagation was also found in subprocess of lightning leader development, such as the space leader formation during an individual step of negative leader [4-8] and in the preconditional lightning channel [9], which was regarded as a kind of polarity inverted recoil leader [10].

In this paper, we present observations of two scenarios causing the positive leader branches with the fine time-resolved high speed video images. The first scenario is associated with initial development of side bileaders, and another scenario was caused by the head splitting directly.

The research was supported by the National Natural Science Foundation of China (grant 41630425 and 41761144074).

II. EXPERIMENT AND DATA

The data used in this work are from “Storm973 (Dynamic-microphysical-electrical processes in severe thunderstorms and lightning hazards)” summer campaign in the Beijing area in 2017. An upward positive leader initiated from the 405 m a CRT Tower at local time (UT + 8:00) of 23:31:22 on 7 July 2017. A high-speed monochrome camera (v711) with a 16 mm/2.8 lens captured the entire development of the upward flash. The camera was located on the ninth floor of the Institute of Atmospheric Science, CAS, at a distance of 9.5 km from the upward flash. The sampling rate for the lightning images was 9,501 frames per second with exposure time of 100 μs and a resolution of 1,024×768 pixels. The Beijing Lightning Network (BLNET) documented high time-resolved data of electric field changes and VHF radiation associate with the development of the bileaders. The electromagnetic signals were observed at one BLNET site 8.9 km northwest of the flash.

III. RESULTS

Within the field of view of the camera, three bileaders occurred during an upward positive leader development from the CRT Tower. Here we just present the development of the first bileader to show its effect on the leader channel branching.

The first bileader (BL1) initiated at an altitude of about 2 km, with a 2D radial distance of 157m from the main channel of the progressing upward positive leader. Rather than starting immediately as the upward positive leader propagated close to the initiation region, the bileader appeared after the upward positive leader had turned horizontally and developed for a distance of 650 m in 9.3 ms. As shown in Figures 1a-g, BL1 kept growing in opposite directions after its formation. The polarity of the leader end propagating toward the existing upward positive leader is negative (determined by the general understanding of opposite charges attract, and meanwhile, the different propagation manners at opposite ends of the bileader and the extinguishment of those unconnected branches toward the

original main channel, as described hereafter, additionally verified the polarity classification). This negative end started to bifurcate at 0.53 ms after its first appearance. The end of BL1, which propagated away from the parent positive leader, was positive and maintained a single channel during the entire time of the bidirectional development. The branching negative end attached to the main upward positive channel at 1.05 ms, as shown in Figure 1h. As shown in Figures 1e and 1f, the approaching negative branches (NBs) induced several connecting leader segments from the existing positive channel. One of these branches made the connection to the side of the main leader channel. This led to an abrupt luminous enhancement, as the high potential differences between the leaders with opposite polarities transiently equilibrated. Thereafter, the channel formed by the BL1 became a new branch of the parent positive leader, and its outward positive end continued to develop.

The 2D speeds of the opposite ends of the bileaders exhibit considerable differences, with the positive end of the bileader propagating slower than the corresponding negative ends, even though the negative ends involve multiple branches. The average partial speed for the positive end was 8.6×10^4 m/s, and that was 2.3×10^5 m/s for the negative end.

It is obvious, from the observations above, that by inducing side bidirectional discharges, the progressing positive leader actually produced its branched channels. To illustrate clearly, three particular areas are marked in the integrated image of the upward flash, as shown in Figure 2a. The first bileader and other 2 bileaders and their junctions to the original main channel occurred in area 1. Their further development made them parts of the principal channel of the flash.

Area 3 in Figure 2a illustrates another mode of positive leader branching. For more detailed information, some selected frames are shown in Figure 2b. The leader directly split at the head during its development, as shown in frames 1003-1011. Although this behavior is infrequent, it does occur during the upward propagation of positive leaders, generally when a leader has propagated to several kilometers high. It is possible that the electric field ahead of the leader facilitate the direct branching at the channel head by simultaneously intensifying positive streamers in different directions. Some of these splitting attempts survived, growing into branched channels with sustained extensions, while the others extinguished shortly after initiation. As pointed out by the ellipses in Figure 2b, the extinguished branching segments may reactivate in some situations, although the leader had already propagated to a higher altitude. Since the branching segments here share similarities with those connecting segments during the junction of bileaders to the main channel (as shown in Figure 1f), the possible relationships between the two is worth further investigation.

In area 2, the positive leader branching is also illustrated, with branched channel structures being illuminated by negative recoil events. An outstanding feature here is that it exhibits the most obvious and intensive branching morphologically among the whole flash region. The broom-like channel structure in this area is due to weak preconditioning processes (namely, weak outward positive breakdown) and negative recoil events retracing those preconditioned routes. The branches here are somewhat short. The outward ends of the recoil leaders are also the extremities of lightning channels to this direction, without further extension thereafter. In essence, this branching can be the head-splitting type, which appears to occur more frequently (and be more successful) when the positive breakdown enters a region of net negative charge. Since the weak preconditioning processes were invisible, the occurrence of recoil leaders makes them hot and visible.

IV. CONCLUSIONS

The initiation and propagation of one bileader excited by a nearby progressing positive leader have been analyzed utilizing detailed time-resolved images of the channel structure captured by a high speed video camera. The positive end propagated in single paths with bright tips, while the negative end propagated in a stepping and branching pattern. By propagating more or less radially toward the main channel, the negative end of the bileader eventually connected to the existing main positive leader channel. The bileader generation, extension, and the subsequent connection made the bileaders into nearly formed branches. The 2D propagation speeds for the positive end and negative end of the bileaders was 8.6×10^4 m/s and 2.3×10^5 m/s, respectively. The positive partial speeds remained relatively stable, while the negative partial speeds varied with time.

Based on our observations, there are two scenarios, which can lead to the branching of a positive leader: (1) the direct splitting at the channel head under an appropriate electric field and the possible reactivation of the extinguished branching segments, which was weak sometimes and revealed by the negative recoil leaders retracing the preconditioned routes, and (2) the development of side bileaders in the trailing wake behind the progressing leader head and the connection to the main positive leader channel.

REFERENCES

[1] Montanyà, J., van der Velde, O., & Williams, E. R. The start of lightning: Evidence of bidirectional lightning initiation. Scientific Reports, 2015,, 15180. https://doi.org/10.1038/srep15180

[2] Warner, T., M. Saba, C. Schumann, J. Helsdon, R. Orville, Observations of bidirectional lightning leader initiation and development near positive leader channels. J. Geophys. Res. Atmos., 2016, 121, 9251−9260. https://doi.org/10.1002/2016JD025365

[3] Yuan, S., Jiang, R., Qie, X., Sun, Z., Wang, D., & Srivastava, A.. Development of side bidirectional leader and its effect on channel branching of the progressing positive leader of lightning. Geophys. Res. Lett., 2019, https://doi.org/10.1029/2018GL080718

[4] Biagi, C. J., Uman, M. A., Hill, J. D., Jordan, D. M., Rakov, V. A., & Dwyer, J.. Observations of stepping mechanisms in a rocket‐and ire triggered lightning flash. J. Geophys. Res., 2010, 5, D23215. https://doi.org/10.1029/2010JD014616.

[5] Gamerota, W., V. Idone, M. Uman, T. Ngin, J. Pilkey, D. Jordan, Dart-stepped-leader step formation in triggered lightning. Geophys. Res. Lett., 2014, 41, 2204-2211. https://doi.org/10.1002/2014GL059627

[6] Hill, J. D., Uman, M. A., & Jordan, D. M.. High‐speed video observations of a lightning stepped leader. J. Geophys. Res., 2011,116, D16117. https://doi.org/10.1029/2011JD015818

[7] Qi Q., W. Lu, Y. Ma, L. Chen, Y. Zhang, and V. A. Rakov. High-speed video observations of the fine structure of a natural negative stepped leader at close distance. Atmos. Res., 2016, 178-179, 260-267.

[8] Jiang R., X. Qie, H. Zhang, M. Liu, Z. Sun, G. Lu, Z. Wang, Y. Wang, 2017: Channel branching and zigzagging in negative cloud-to-ground lightning. Sci Rep, 2017, doi:10.1038/s41598-017-03686-w, SREP-16-50830

[9] Jiang R., Z. Wu, X. Qie, D. Wang, and M. Liu. High-speed video evidence of a dart leader with bidirectional development. Geophys. Res. Lett., 2014, 41, doi: 10.1002/2014GL060585.

[10] Qie X., Y. Pu, R. Jiang, Z. Sun, M. Liu, H. Zhang, X. Li, G. Lu, and Y. Tian. Bi-directional leader development in a preexisting channel as observed in rocket-triggered lightning flashes. J. Geophys. Res. Atmos., 2017, 2, 86–599, doi:10.1002/2016JD025224.

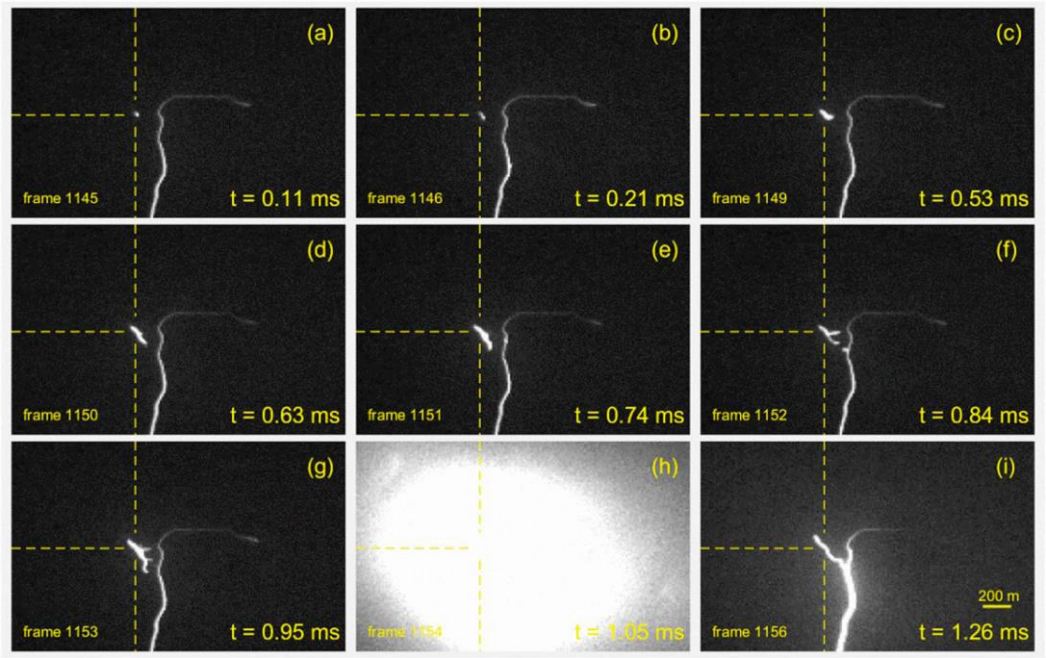

Fig. 1. The development of the first bidirectional leader (BL1): (a) luminous spot at the initiation point, (b – g) bidirectional propagation of the leader from the initiation point, (h) intense brightness caused by the negative end of BL1 connecting with the existing main upward positive channel, and (i) positive leader branch formed by the bidirectional leader after the connection. Note that the first frame with recognizable luminosity at the initiation point is set as the reference time.

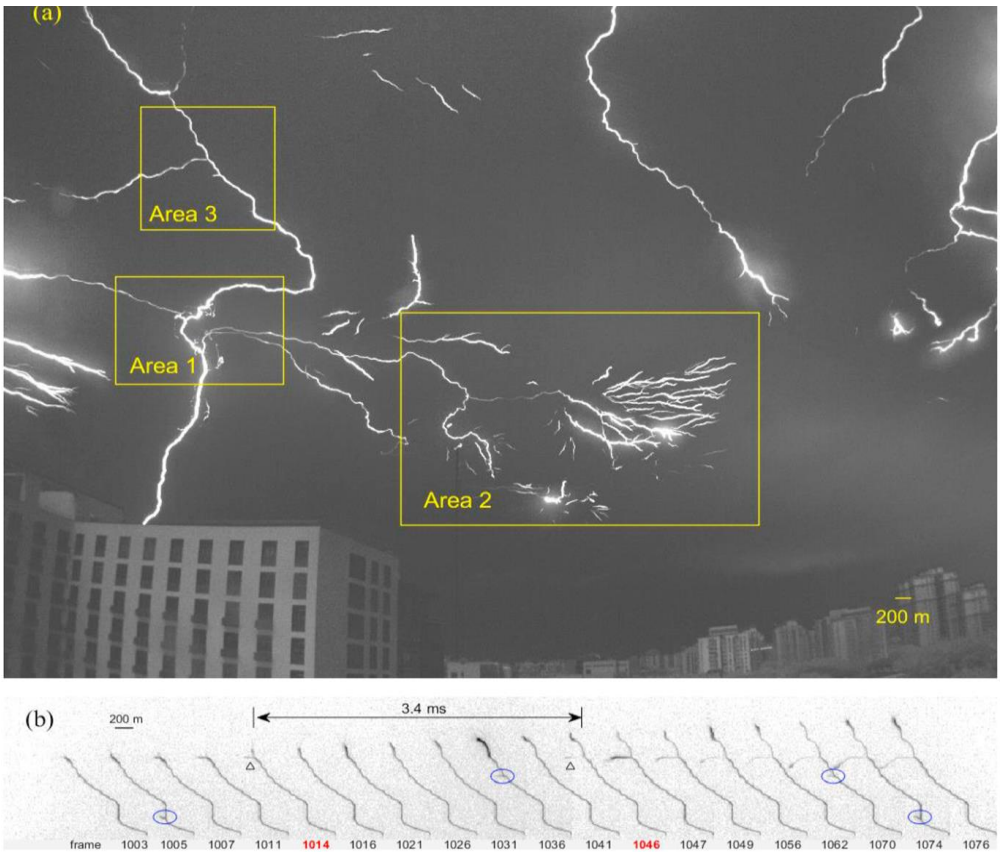

Fig. 2. (a) Integrated image of the entire upward flash with bidirectional leaders induced in area 1 and abundant recoil leaders occurred in area 2; (b) details of leader development in area 3.

Study on Electromagnetic Coupling Characteristics of Fuselage Cavity Cover Irradiated by HEMP

Xuefeng Qi
Aviation Key Laboratory of Science and Technology on Electromagnetic Environmental Effects
Shenyang Aircraft Design and Research Institute, AVIC
Shenyang, China
qixuefeng08@sina.com

Yan Wang
Aviation Key Laboratory of Science and Technology on Electromagnetic Environmental Effects
Shenyang Aircraft Design and Research Institute, AVIC
Shenyang, China
sy601wangyan@163.com

Guoshuai Zhen
Aviation Key Laboratory of Science and Technology on Electromagnetic Environmental Effects
Shenyang Aircraft Design and Research Institute, AVIC
Shenyang, China
lanyun0@163.com

Yu Mao
Aviation Key Laboratory of Science and Technology on Electromagnetic Environmental Effects
Shenyang Aircraft Design and Research Institute, AVIC
Shenyang, China
maoyu0807@163.com

Baihan Liu
College of Electronic and Information Engineering
Shenyang Aerospace University
Shenyang, China
liubaihan59@163.com

Tao Zhang
Aviation Key Laboratory of Science and Technology on Electromagnetic Environmental Effects
Shenyang Aircraft Design and Research Institute, AVIC
Shenyang, China
zhangtaowf86@163.com

Abstract **In this paper, commercial electromagnetic simulation software CST 2016 is used to study the coupling due to the gap between the cover and the cavity surface and also used to establish four types of fuselage cover cavities with the same circumference and different shapes, they are namely circular cavity cover, square cavity cover, rectangle cavity cover and serrated cavity cover, and to explore the electric field intensity induced by them in the cavities under HEMP irradiation. It is found that when the perimeter of the fuselage cover is fixed, the electric field inside the circular cavity is the strongest, the electric field inside the serrated cavity cover is the smallest, and the peak electric field appears after the time deviation.**

Keywords —HEMP, electromagnetic simulation software, fuselage cavity cover, electric field

I. INTRODUCTION

The fuselage cavity cover is the bridge connecting the exterior of the aircraft with the important equipment inside the aircraft, the fuselage cavity cover serves as a passageway for personnel access and equipment maintenance, it involves the maintenance of the aircraft by the user. Electromagnetic isolation measures shall be taken for the fuselage cavity cover with electromagnetic protection requirements to prevent unintentional or intentional electromagnetic interference from unnecessary performance degradation of sensitive equipment and sensitive wire harness area under the body cover. In addition, strategic nuclear weapons are the main force of nuclear deterrence in modern war, among which the important high-altitude nuclear electromagnetic pulse (HEMP) releases a large number of γ rays, X rays and other radioactive particles in the nuclear explosion. When these radioactive particles radiate outward at the speed of light, they interact with molecules or other media in the atmosphere to produce a Compton current that stimulates the electromagnetic pulse of outward radiation.

At present, the HEMP has the characteristics of high field intensity, wide frequency band and wide range of action. With the high integration of electronic equipment carried on aircraft platforms in war and the increasing sensitivity to electromagnetic pulse, the threat and damage effect of HEMP on electronic facilities should be paid special attention. Therefore, it is of great significance to study the electromagnetic coupling characteristics of the fuselage cavity cover irradiated by HEMP and its survival ability in HEMP environment.

This paper, by using the method of electromagnetic numerical simulation calculation, attached to the airframe of circumference of different shape cover cavity in HEMP irradiation. It guide the rational layout of the fuselage cover cavity and improve fuselage cover cavity in the field of electromagnetic spectrum wars and other related professional design efficiency.

II. HEMP ENVIRONMENT

HEMP can produce a strong transient electromagnetic field, energy can be radiation, coupling and conduction in a moment to a large number of electronic equipment and systems paralysis or even destroyed. HEMP has the characteristics of high pulse amplitude, rich spectrum components, fast rising speed, short duration and large coverage radius. According to the time-domain expression of the standard GJB3622-99 HEMP is:

$$E(t) = E_0(e^{-\alpha t} - e^{-\beta t}) \tag{1}$$

E_0 is the electric field constant, α and β are the attenuation coefficient. With reference to standard GJB3622-99, the motion-picture HEMP waveform is modeled in commercial electromagnetic simulation software, as shown in figure 1.

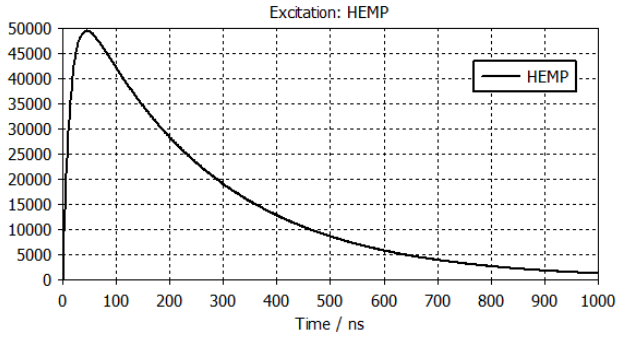

Fig. 1. HEMP waveform

III. THE CAVITY OF THE FUSELAGE COVER AND ITS SIMULATION MODEL

In order to explore the law of the electromagnetic field inside the cavity under the HEMP irradiation of the fuselage cover, a 1m × 1m × 1m cavity was built in the electromagnetic simulation software. The cavity material was selected as the perfect electric conductor, and the electric field probe was set up in the geometric center of the cavity. On the upper surface of the cavity body are placed four kinds of different shapes, which are made of the same perfect electric conductor material. They are round, square, rectangle and serrated. The mounting gap between the cover and the fuselage is set as 1 millimeter, the circumference of the cavity of different cover is fixed for 500 millimeter. The plane wave of HEMP is irradiated 5 meters from the upper surface of the cavity, and the polarization direction is consistent with the direction of the long side of the cover. The air inside and outside the cavity is treated as a lossless material, and the specific setting of the model in the electromagnetic software is shown in fig 2 to fig 5. The simulation calculation time is 1000 nanoseconds, the simulation frequency band was 0 to 1000MHz, and the electric field intensity value induced by the electric field probe inside the cavity was observed.

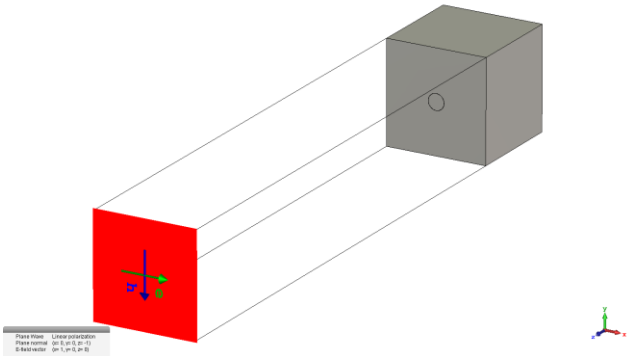

Fig. 2. Circular shape of the cavity cover model

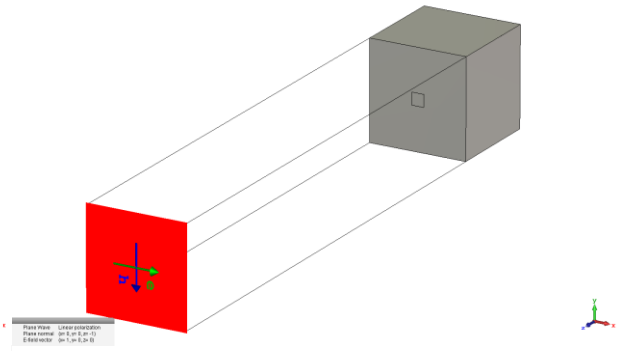

Fig. 3. Square shape of the cavity cover model

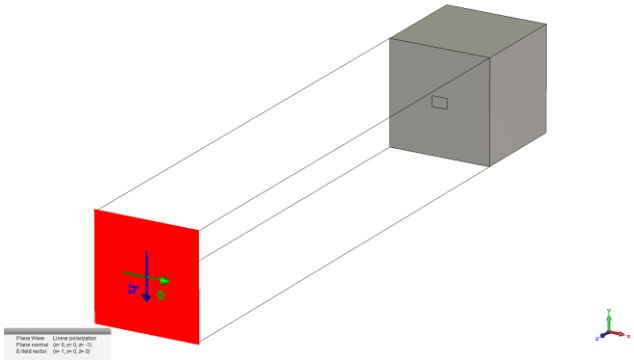

Fig. 4. Rectangle shape of the cavity cover model

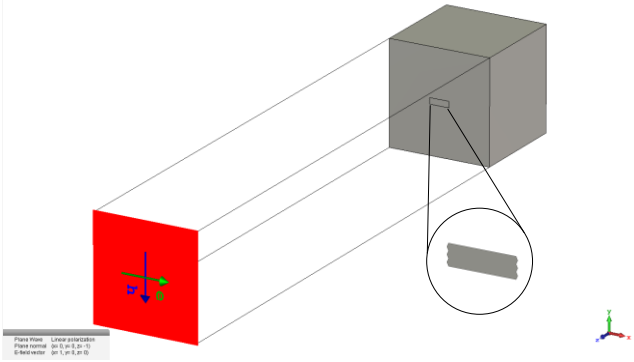

Fig. 5. Serrated shape of the cavity cover model

IV. SUMMARIZING AND ANALYZING THE SIMULATION RESULTS

Due to the resonant characteristics of the cavity, the plane wave of HEMP is coupled into the cavity through the gap between the cover and the skin of the fuselage and forms resonance. The time-domain waveform of the electric field probe shows multiple oscillation peaks. In the electromagnetic simulation engineering file of this paper, the energy decays below -30dB, indicating that 1000 nanoseconds calculation time can be accepted. The electric field probe values of different shapes of the cavity cover with a fixed circumference of 500 millimeter are shown in fig 6 to fig 9. The electric field distribution inside the cavity cover with a typical frequency point is shown in fig 10.

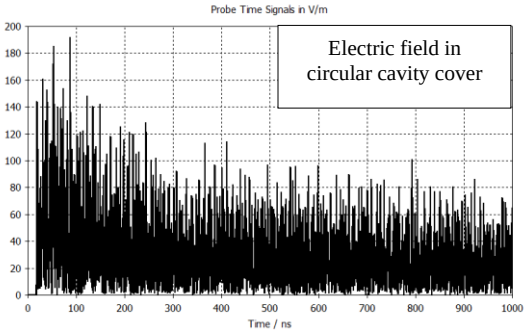

Fig. 6. The probe value inside the fixed circumferential circular cavity cover

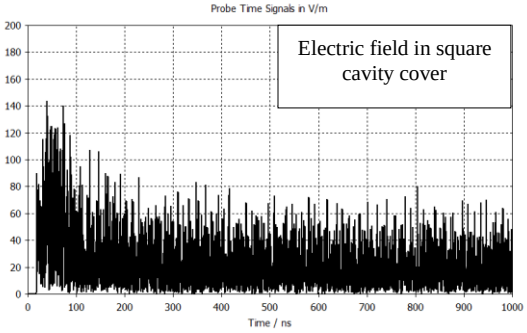

Fig. 7. The probe value inside the fixed circumferential square cavity cover

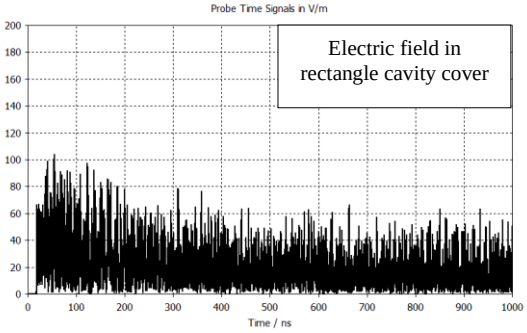

Fig. 8. The probe value inside the fixed circumferential rectangle cavity cover

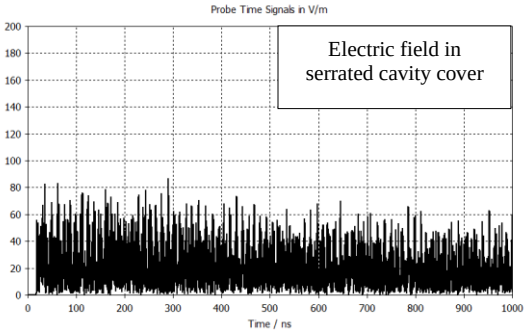

Fig. 9. The probe value inside the fixed circumferential serrated cavity cover

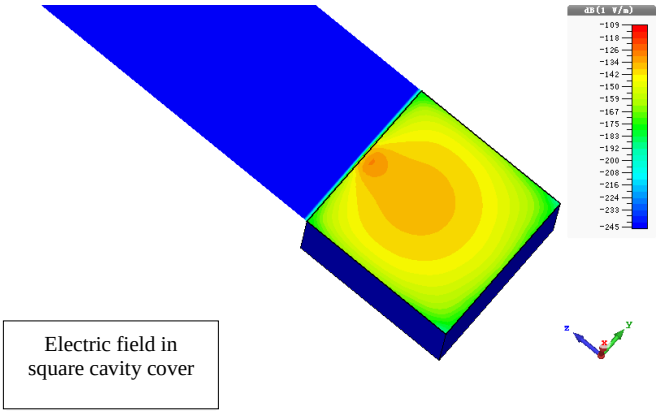

Fig. 10. The distribution of electric field in the cavity under typical frequency

It can be seen from fig 6 to fig 9 that the coupling of electric field intensity inside the cavity changes with the change of the shape of the cover. As can be clearly seen from fig 10, the plane wave of the HEMP is coupled into the cavity by the gap between the cover and the fuselage, and the resonance phenomenon occurs. The resonance center is generated in the geometric center of the cavity. Table 1 shows the peak electric field of coupling inside the cavities with different covers.

TABLE I. PEAK OF COUPLING ELECTRIC FIELD IN DIFFERENT CAVITIES

Cover type	***Electric field peak***	***Peak time***
Circular cover	191 V/m	87 ns
Square cover	143 V/m	39 ns
Rectangle cover	104 V/m	54 ns
Serrated cover	87 V/m	289 ns

By comparing the value of different shape cavity cover inter electric field probe, it can be seen in the case of fixed cover circumference, circular cover inside the cavity of the electric field intensity is the largest. The square cavity cover internal electric field intensity is smaller than the circular, the rectangle cavity cover and the serrated cavity cover are similar, but the serrated cavity cover internal electric field intensity is minimal. With the passage of time, the probe values inside the cavities all presented a oscillatory decline, which was also consistent with the electromagnetic pulse excitation waveform of HEMP. Rectangle cavity cover and the serrated cavity cover internal probe induced electric field value although similar, but the interior of the serrated cavity cover induced electric field peak time backwards, this is because the special shape of serrated occurs when the incident plane wave through the aperture coupling polarization matching and phase cancellation in complicated conditions, make the inside of the cavity of induced electric field value.

V. CONCLUSIONS

The electromagnetic coupling characteristics of the fuselage cavity cover irradiated by HEMP are studied in this paper. According to the results of electromagnetic simulation, the following conclusions can be drawn:

- Generally speaking, the geometric center of the symmetrical cavity is the resonance center, where the resonance effect is the strongest.

- The resonant characteristics of the cavity change with the change of the shape of the cavity cover. The intensity of the induced electric field inside the cavity cover of the serrated is the least under the condition of the same perimeter.
- The induced electric field inside the rectangle cavity is slightly stronger than that inside the serrated cavity. Due to the complex situation such as polarization matching and phase cancellation on the serrated edge, the internal field intensity of the cavity is slightly smaller. Therefore, the design of serrated cavity cover can be considered in the actual electromagnetic design of aircraft.

It should be noted that, it is a bit surprising that a time domain illumination of a covered cavity would resonate for such a long period of time, due to the lack of any absorbing materials that would actually be present inside of a normal aircraft. Therefore, this paper only provides guidance for HEMP protection. In the subsequent practice, digital modeling and simulation calculation should be done according to different real conditions in an aircraft.

REFERENCES

[1] Umashankar K R and Taflove A, A novel method of analyzing electromagnetic scattering of complex objects, IEEE Trans. Electromagn. Compat. Nov. 1982, EMC-24(4):397~405.

[2] Mei K K, Cangellaris A C and Angelakos D J, Conformal time domain finite difference method. Radio Science, 1984, 19(5):1145~1147.

[3] E. Van Keuren, Dr J.Knighten. Implicaions Of The High-Power Microwave Weapon Threat In Electric System Design. IEEE International Symposium on Electromagnetic Compatibility, 1991, 370~371.

[4] Ricketts L W, Bridges J E, Miletta J. EMP radiation and protective techniques. [M]. New York: Wiley, 1976.

[5] Murphy Tim. Electromagnetic pulse from surface burst [R]. LA-11060-MS. LANL. August 1987.11.

[6] Karzas WJ, Latter R. Detection of the Electromagnetic Radiation from Nuclear Explosions in Space [J]. Phys Rev, 1965, 137(5B):1369.

ASIAEM 2019- Development of EMP Survivability Test Equipment for Conductive Gaskets

Ya Li
Electromagnetic Compatibility Laboratory
Southeast University
Nanjing, China
ly1994seu@foxmail.com

Zhongyuan Zhou
Electromagnetic Compatibility Laboratory
Southeast University
Nanjing, China
zyzhou@seu.edu.cn

***Abstract*—In order to study the electromagnetic pulse (EMP) survivability of conductive gaskets, the EMP current injection simulator was developed based on the study of EMP survivability test method in the U.S. military standard MIL-DTL-83528F, which can output a 9-kiloampere peak-to-peak dampened sinusoidal current pulse with a frequency of 1 to 1.5 megahertz and a decay time of 500 to 1,300 nanoseconds. The working principle, the design of circuit parameters, switch and device structure of the device were introduced in this paper. The output pulse current waveform of the device meets the relevant requirements of MIL-DTL-83528F.**

Keywords—EMP survivability of conductive gasket, EMP current, MIL-DTL-83528F

I. INTRODUCTION

Transient EMP generated by nuclear explosion will cause damage to military electronic equipment [1]. Electromagnetic shielding is a common and effective method in EMP protection. In order to ensure the integrity of shielding, conductive gaskets are often used to improve the continuity of electrical conductivity in the holes of the cabinet. When the conductive gaskets are irradiated by strong EMP, the resistance will increase, which will affect the overall shielding performance of the system. According to the American military standard MIL-DTL-83528F, the EMP survivability standard compliance test of conductive gaskets is required [2]. The test equipment is an EMP current injection simulator, which is required to output damping sine waves with a peak to peak value of 9kA±10%, a frequency of 1MHz to 1.5MHz, and an attenuation time of 500ns to 1300ns. However, at present, there is no relevant test standard and test device in China. In order to study the EMP survivability of conductive gaskets and provide preliminary research work for the establishment of relevant standards in China, an EMP current injection simulator meeting the requirements of MIL-DTL-83528F is required to be developed.

II. SYSTEM COMPOSITION AND WORKING PRINCIPLE

The pulse waveform generation principle of EMP current injection simulator is to generate damped sine wave waveform by using the transient response of RLC series circuit [3].System composition block diagram is shown in Fig. 1. The system works as follows： The capacitor is charged by a High-voltage DC power supply through a charging circuit. After the capacitor voltage reaches the preset charging voltage, The switch is conducted by triggering circuit, and then the capacitor is discharged by the switch to output the damped sinusoidal pulse current. The current detection module is used to detect output current.

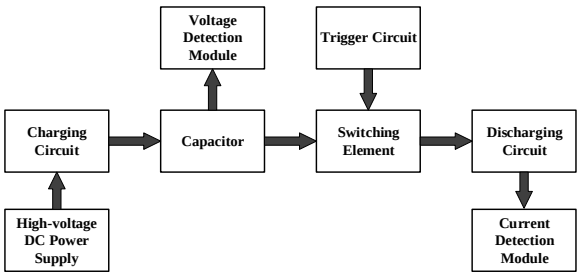

Fig. 1. System composition block diagram

III. DESIGN OF EMP CURRENT INJECTION SIMULATOR

A. Design of circuit parameters

According to the U.S. military standard MIL-DTL-83528F, waveform functions and waveform index are shown in (1) and (2) respectively.

$$I(t) = I_0 \sin(2\pi f t) e^{-t/\tau} \tag{1}$$

$$\begin{cases} 1\text{MHz} \le f \le 1.5\text{MHz} \\ 0.5\text{us} \le \tau \le 1.3\text{us} \\ I_{P-P} = 9\text{kA} \pm 10\% \end{cases} \tag{2}$$

where $I(t)$ is instantaneous current in the circuit; I_0 is current amplitude factor； f is frequency; τ is decay time.

Schematic diagram of the circuit is shown in Fig. 2. C is an ideal capacitor, and the initial voltage is $U_0 \le 20$kV; L is the total inductance in the discharge circuit, including capacitor parasitic inductance, switch discharge inductance, load inductance and connection line inductance; R is the total resistance in the discharge circuit, including load resistance, wave regulating resistance, and other parasitic resistance.

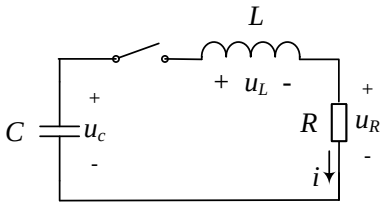

Fig. 2. Schematic diagram

According to Kirchhoff's voltage law, the following equation can be obtained[4]:

$$i = I_0 e^{-\alpha t} \sin \omega_d t \tag{3}$$

$$I_0 = \frac{U_0}{\omega_d L} \tag{4}$$

Where $\omega_d = \sqrt{\omega_0^2 - \alpha^2}$ is the natural angular frequency; $\omega_0 = \frac{1}{\sqrt{LC}}$ is the resonant angular frequency; $\alpha = \frac{R}{2L} = \frac{1}{\tau}$ is damping constant; R is the total resistance in the circuit.

The formula for calculating the peak to peak value of current is

$$I_{\text{p-p}} = I_0 e^{-\frac{\alpha T}{4}} + I_0 e^{-\frac{3\alpha T}{4}} = \frac{U_0}{\omega L}\left(e^{-\frac{\alpha}{4f}} + e^{-\frac{3\alpha}{4f}} \right) \tag{5}$$

Thus

$$L = \frac{U_0}{\omega I_{\text{p-p}}}\left(e^{-\frac{\alpha}{4f}} + e^{-\frac{3\alpha}{4f}} \right) \tag{6}$$

$$R = 2\alpha L = \frac{2L}{\tau} \tag{7}$$

$$C = \frac{1}{L}\frac{1}{4\pi^2 f^2 + \alpha^2} \tag{8}$$

From (3)(5)(6)(7)(8), the value of R, L, C would be calculated.

B. Design of switch

A three-electrode gas spark switch is selected, the main electrode of which is a ball structure, and the trigger electrode is a needle-like structure.

The self breakdown voltage of the main electrode is[5][6]

$$U_{\text{B}} = \frac{24.22\,pd + 6.08\sqrt{pd}}{f} \tag{9}$$

$$f = \frac{q + \sqrt{q^2 + 8}}{4} \tag{10}$$

where q=1+d/r; p, atm, is the gas pressure; d, cm, is the distance of the main electrode; r, cm, radius of the main electrode; U_{B}, kV; f is the field inhomogeneity coefficient.

The ratio of the operating voltage to the self-breakdown voltage is written as β which typically ranges from 70% to 80%.

According to (9)(10) and the range of U_0 and β , the distance between the main electrodes is designed to be 12.5mm.

C. Design of trigger circuit

The trigger circuit schematic is shown in Fig. 3. Thyristor is used as a switching element for the trigger circuit. When the thyristor is turned on, the storage capacitor discharges to generate a low-voltage double-index pulse, which would be boosted into a high-voltage double-exponential pulse by a pulse transformer. And then the high-voltage double-exponential pulse output to the trigger electrode to control the conduction of the two main electrodes of the three-electrode switch.

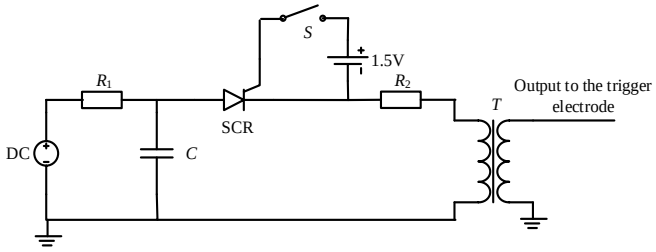

Fig. 3. Schematic diagram of trigger circuit

The output waveform of the trigger circuit is shown in Fig. 4. The output waveform has an amplitude of 1.97kV, a rise time of 490ns, and a half-pulse width of 1.8us. It is experimentally verified that the trigger pulse can turn on the three-electrode switch.

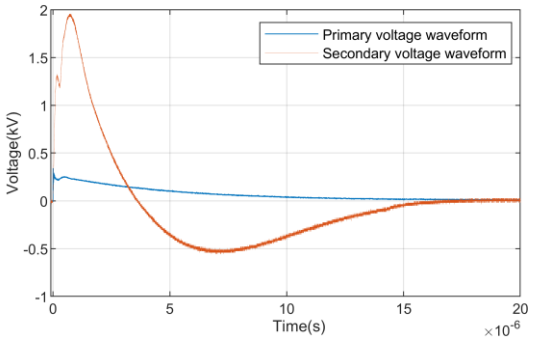

Fig. 4. Output waveform of the trigger circuit

D. Design of device structure

The coaxial monolithic structure is used in the EMP current injection simulator. Place the three-electrode gas spark switch together with the resistor in the shield shell. The current detecting resistor is connected to the main body section of the device through a coaxial connector. The storage capacitor is placed outside the body section of the device because it is too bulky. The schematic diagram of the EMP current injection simulator is shown in Fig. 5.

In order to facilitate the debugging and switching test under different working voltages, the switch anode is designed as a movable structure. As shown in Fig. 5, the switch anode is connected to the anode stud to move in the

axial direction. The trigger electrodes can be placed in different slots, which can be easily adjusted according to different working voltages and trigger pulses. The divice body section and the current measuring resistor section are connected by a coaxial connector, which is convenient for assembly and disassembly on the one hand, and the conductive gaskets test clamp is conveniently mounted between the main body portion of the device and the current measuring resistor portion on the other hand.

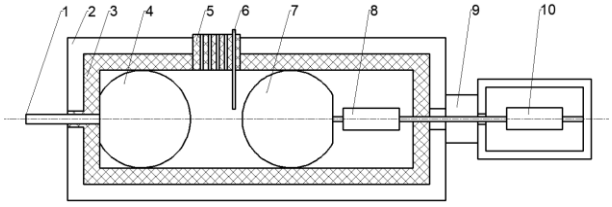

Fig. 5. Structure diagram of EMP current injection simulator. 1- input connector; 2- shield shell; 3,5- insulated medium; 4- anode; 6- trigger electrode; 7- cathode; 8- resistance; 9- coaxial connector; 10- current measuring resistor.

IV. Experiment Results and Analysis

A total of four sets of tests were carried out. The charging voltages of the storage capacitors were 12.5 kV, 13.8 kV, 17.6 kV and 20 kV, respectively. The voltage waveform measured across the current-measuring resistor during discharge is shown in Fig. 6. The current-measuring resistor was selected from a 25mΩ thick film resistor with a rated power of 100W, and its parasitic inductance was 3.95nH measured by a vector network analyzer.

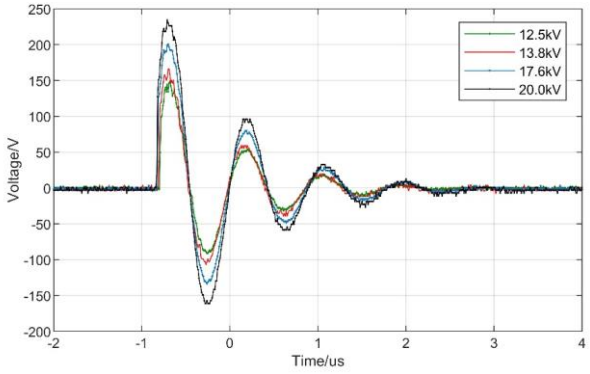

Fig. 6. Voltage waveform of current measuring resistor

Combined with the waveform and current resistance parameters, the pulse current waveform parameters would be calculated, as shown in Table I.

TABLE I. Four sets of pulse current waveform parameters

Group	Charging voltage (V)	Frequency of Waveform (MHz)	Decay Time (us)	Peak-to-peak Value of Current (kA)
1	12.5	1.136	870	5.956
2	13.8	1.136	992	6.84
3	17.6	1.136	1052	8.461
4	20.3	1.136	1105	9.833

It can be seen from Table 1 that the frequency and decay time of the pulse current waveform in the four sets of tests are in compliance with the relevant requirements of the US military standard MIL-DTL-83528F. When the storage capacitor charging voltage is 17.6kV and 20.0kV, the current Peak-to-peak values meet the standard requirements.

V. CONCLUSIONS

The EMP current injection simulator was designed according to the requirements of the US military standard MIL-DTL-83528F for the conductive gasket EMP survivability test equipment. The design of the circuit parameters, switch and the structure were discussed in detail. The pulse current of the test equipment was measured and its parameters are in accordance with MIL-DTL-83528F. The development of this equipment provides the basis for the development of China's conductive gaskets electromagnetic pulse survivability test standards.

References

[1] American National Standard Dictionary of Electromagnetic Compatibility (EMC) including Electromagnetic Environmental Effects (E3) [S]. ANSI PC63.14/D15, 2014.

[2] MIL-DTL-83528F (2015). Gasketing material, conducive, shielding gasket electronic, Elastomer, EMI/RFI general specification for[S].

[3] C. F. M. Carobbi and A. Bonci. “Elementary and ideal equivalent circuit model of the 1, 2/50-8/20 μs combination wave generator,” IEEE Electromagnetic Compatibility Magazine, 2013, 2(4): 51-57.

[4] T. Haryono, K. T. Sirait, Tumiran and H. Berahim, “The Design of a High Amplitude Impulse Current Generator,” 2008 International Conference on High Voltage Engineering and Application, Chongqing, 2008, pp. 339-343.

[5] L. Tianxue et al., “200kV Multi-gap Multi-channel Gas Spark Switch for Fast Linear Transformer Driver,” 2008 International Conference on High Voltage Engineering and Application, Chongqing, 2008, pp. 474-476.

[6] C. Lei, “420kv High Voltage Pulse Power Supply and Research of its Trigger Switch,” Lanzhou: Lanzhou University, 2016

Coupling Path Visualization for Automotive Intentional Electromagnetic Interference

Yang Zhong[1], Woncheol Song[1], Cheolhan Kim[2], Changyul Park[3] and Chulsoon Hwang[1]

[1]*EMC Laboratory*
Missouri Univ. of Sci. & Tech.
4000 Enterprise Drive, Rolla, MO
65401, USA
hwangc@mst.edu

[2]*Hyundai Motor Company*
150 Hyundaiyeonguso-ro,
Hwaseong-si, Gyeonggi-do,
18280, Korea

[3]*Korea Testing Laboratory*
10 Chunggui-ro, Jinju-si,
Gyeongsangnam-do,
52852, Korea

***Abstract*—Coupling paths from a high power electromagnetic source (HPEM) to the victim electric system inside an automobile are visualized. Based on the automotive intentional electromagnetic interference (IEMI) experiments, an accurate IEMI simulation is used to investigate the coupling mechanism. The coupling path visualization based on reciprocity is applied on the simulation. The visualized 3D coupling path can help determine the protection approaches.**

Keywords—high power electromagnetic source (HPEM), automobile, intentional electromagnetic interference (IEMI), coupling path visualization, reciprocity theorem

I. INTRODUCTION

The threat of intentional electromagnetic interference (IEMI) on automobiles is increasing as the operation of modern cars are largely depends on electric systems. Also, the rapid development of the high power electromagnetic source (HPEM) in recent years stimulates the public aware of the IEMI threats on automobiles. According to report [1], among 37 cars tested in an electromagnetic pulse (EMP) environment, 3 cars stopped at field strength of 30kV/m, 25 automobiles exhibited malfunctions. Besides, the car stopper which can stop a moving car by emitting high power electromagnetic pulse has been demonstrated in [2]. To characterize the vulnerability of a car, several automotive IEMI experiments were conducted [3][4]. However, these investigations on the automotive IEMI were totally based on the measurement. To understand the coupling mechanisms and propose solutions to eliminate the IEMI attack, an accurate automotive simulation model and theoretical analysis methods will be needed.

In this paper, the automotive IEMI simulation is used to reproduce the measurement results. Applying the coupling path visualization method on the simulation model, the coupling paths from the attacker to the victim location inside of the car are visualized.

II. IEMI MEASUREMENT AND SIMULATION

To investigate the vulnerability of a car to IEMI attacks, automotive experiments on a real car running at 30 km/h were conducted by authors. As shown in Fig. 1, a HPEM source and a vehicle with a D-dot sensor in it were used in the measurements which characterize the effect of IEMI attacks. The dipole shape HPEM source is a standard mesoband source made by Replex [5][6]. The D-dot sensor was placed close to the pedal to measure the vertical electric field component at where surrounded with important electronic systems.

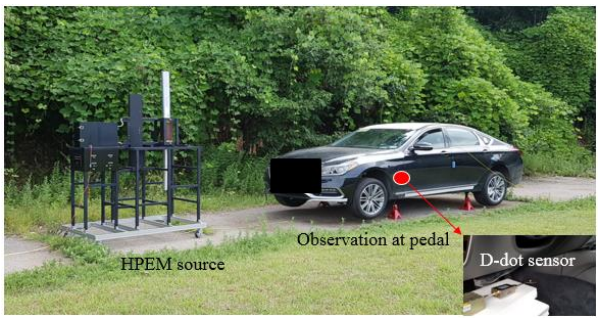

Fig. 1. Automotive IEMI measurement set-up

The D-dot sensor was located in the far-field range of the dipole antenna and almost in its maximum radiation direction. Also, the dipole antenna and infinitesimal vertical electric dipole moment have the similar expressions on calculating the radiated fields in the maximum radiation direction. Therefore, the dipole shape HPEM source can be replaced by an equivalent dipole moment. In [7][8], the source reconstruction method was proposed and validated. A vertical electric dipole P_z at the attack location can accurately represent the HPEM source. As shown in Fig. 2, the IEMI simulation model consists of the equivalent dipole moment and a full size vehicle model. Actually, a more precision vehicle model was used but not shown here due to the confidential issue.

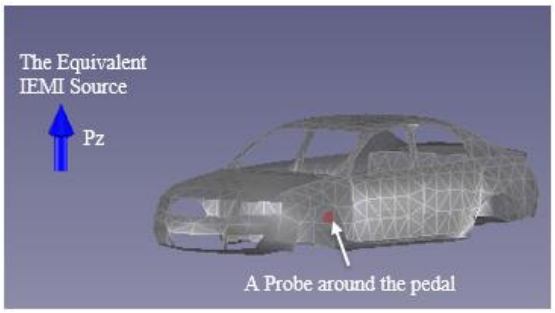

Fig. 2. The equivalent simulation model

To check accuracy of the equivalent source and the vehicle model, the simulation results were compared to the

measurement data. The good match in Fig. 3 indicates that the IEMI simulation is reliable.

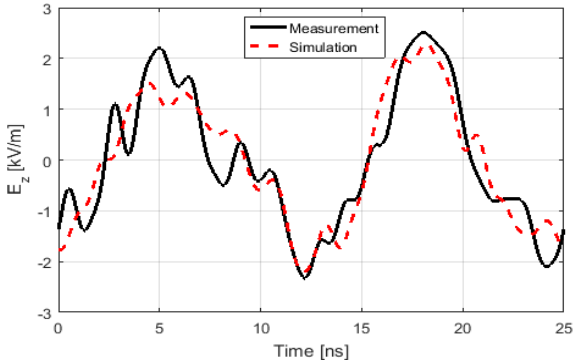

Fig. 3. Measurement and simulation comparison when source is 5 m in front

III. Coupling Path Visualization

A. Visualization Based on Reciprocity

Assume that within a linear, isotropic medium, there are two sets of sources $\vec{J}_1,\vec{M}_1$ and $\vec{J}_2,\vec{M}_2$ that produce fields $\vec{E}_1,\vec{H}_1$ and $\vec{E}_2,\vec{H}_2$, respectively. For the fields to be valid, they must satisfy the following equation:

$$-\oiint_S\left(\vec{E}_1\times\vec{H}_2-\vec{E}_2\times\vec{H}_1\right)\cdot d\hat{s} = \iiint_V\left(\vec{E}_1\cdot\vec{J}_2+\vec{H}_2\cdot\vec{M}_1-\vec{E}_2\cdot\vec{J}_1-\vec{H}_1\cdot\vec{M}_2\right)dv \quad , \qquad (1)$$

which is known as the Lorentz reciprocity theorem in integral form [9]. It is directly derived from Maxwell's equation without other assumptions [10]. In (1), V is the space enclosed by a surface S. There is no limitation on this closed surface. As shown in Fig. 4, the surface S is selected to separates the aggressor and victim. Only victim is included in the volume V.

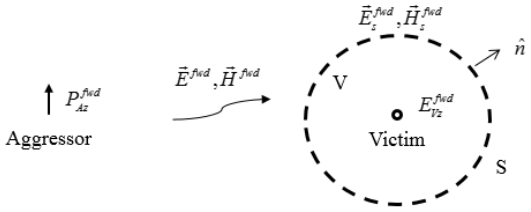

(a) Forward problem

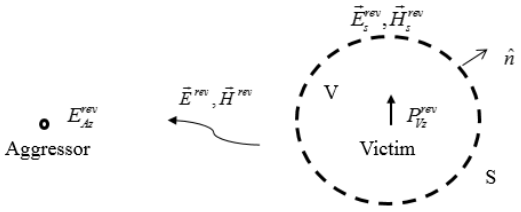

(b) Reverse problem

Fig. 4. Illustration of the dipole-based reciprocity

In Fig. 4, the sources in forward problem and reverse problem are two vertical electric dipole moments P_{Az}^{fwd} and P_{Vz}^{rev}, respectively. The fields on the surface S are represented by $\vec{E}_s^{fwd},\vec{H}_s^{fwd}$ and $\vec{E}_s^{rev},\vec{H}_s^{rev}$. Using the definition of dipole moment, the reciprocity of (1) can be rewritten as

$$\oiint_S\left(\vec{E}_s^{rev}\times\vec{H}_s^{fwd}-\vec{E}_s^{fwd}\times\vec{H}_s^{rev}\right)\cdot\hat{n}ds = E_{Vz}^{fwd}P_{Vz}^{rev} \quad , \qquad (2)$$

where $\hat{n}$ is the normal vector of surface S. The right side term in (2) is the production of forward vertical E-field component and the reverse vertical dipole moment. The unit of this production is W. It has the physical insight of coupled power from the aggressor to the victim. Therefore, the term inside of the closed surface integral in (2) has the physical meaning of surface coupled power density which is comparable to the definition of surface current density.

If the closed surface is a spherical surface whose center is the victim location, the normal vector of the closed surface will become the radial vector $\hat{r}$ in the spherical coordinates. Also using the forward and reverse fields in the spherical coordinates, the coupling coefficient that indicates the coupled power distribution on the spherical surface can be defined as

$$CC \triangleq \left(\vec{E}_s^{rev}\times\vec{H}_s^{fwd}-\vec{E}_s^{fwd}\times\vec{H}_s^{rev}\right)\cdot\hat{r} \quad . \qquad (3)$$

The defined CC is a complex scalar at each point over the space. By properly adjusting the excitation phase, the surface integral of imaginary part of CC can be zero [11]. For these spherical surfaces, the surface integrals of CC are equal to the forward E-fields by setting the unit excitation in the reverse problem. The coupling path can be tracked by plotting the real part of CC on the spherical surfaces. Fig. 5 illustrates the steps of the proposed coupling path visualization method. Since the closed surface has to separate the aggressor and victim, the radius of valid spherical surface ranges from 0 to d, where d is the distance between aggressor and victim.

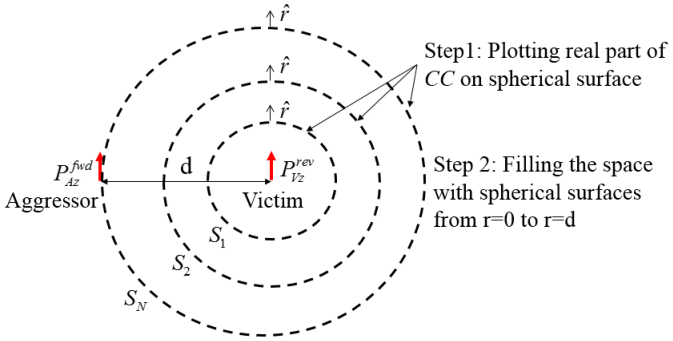

Fig. 5. Procedures of the coupling path visualization

B. Application on Automotive IEMI Simulation

Based on the automotive IEMI simulation model, the proposed coupling path visualization method can be applied on it to help determine the coupling mechanism. Fig. 6 shows the model for coupling path visualization. An unit vertical electric dipole P_{Vz}^{rev} was added at the victim location in the reverse problem. All fields were obtained in the spherical coordinates which origin is the victim location. The coupling coefficient can be calculated and plotted on the spherical surfaces.

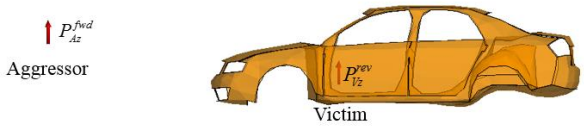

Fig. 6. Simulation model for coupling path visualization

Following the procedures in Fig. 5, the 3D coupling path visualization result at 100 MHz is shown in Fig. 7. For better visualization, logarithm scale was used.

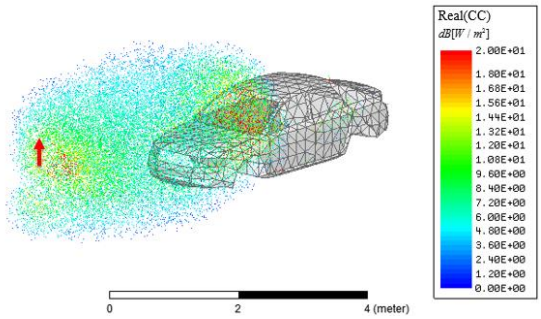

Fig. 7. 3D coupling path visualization when the attacker is in front

When the attacker was placed in front of the car, the fields mainly coupled from the front windshield. The coupling path may relate to the attack location. Fig. 8 and Fig. 9 exhibit the 3D coupling path when the attacker is in the rear and on the left side, respectively.

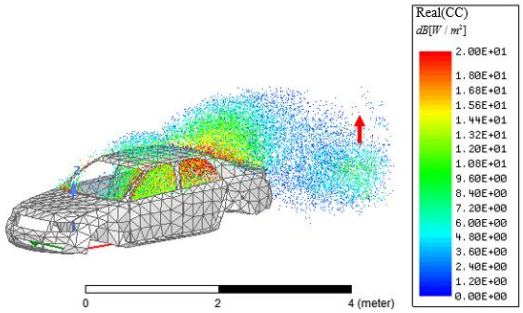

Fig. 8. 3D coupling path visualization when the attacker is in rear

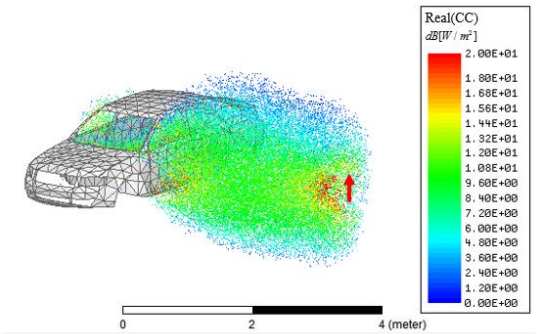

Fig. 9. 3D coupling path visualization when the attacker is on the left side

In Fig. 8, it is observed that the dominant coupling path is from the rear windshield. In Fig. 9, there are two coupling paths. One is from the left side window and another is from the gap under the left side front door. As shown in Fig. 10, a plane close to the left side door is selected to quantify the coupling ratios of the different coupling paths. Here, the coupling coefficient is calculated in the rectangular coordinates, and the normal vector is perpendicular to the large plane. The patterns in Fig. 10 can be divided into path 1 and path 2. The surface integrals of CC over the two coupling path regions are 1.89 kW and 0.61 kW. Since the coupled vertical electric field component is 2.5 kV/m and the unit reverse dipole is 1 Am. Equation (2) is validated. Therefore, the coupling path 1 contributes 75.6% of the total coupling, and the path 2 contributes the rest 24.4%.

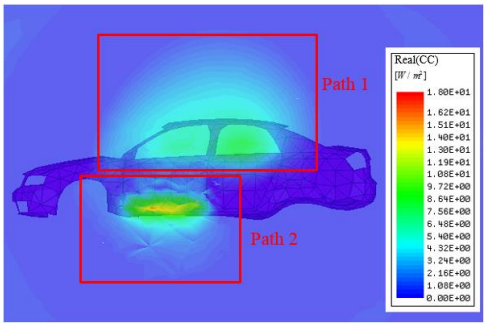

Fig. 10. Coupling path ratio quantification when attacker is on the left side

Also, the D-dot sensor can be placed in the car's trunk. When the aggressor is placed on the left side, the 3D coupling path visualization result is shown in Fig. 11. The top view result is shown in Fig. 12.

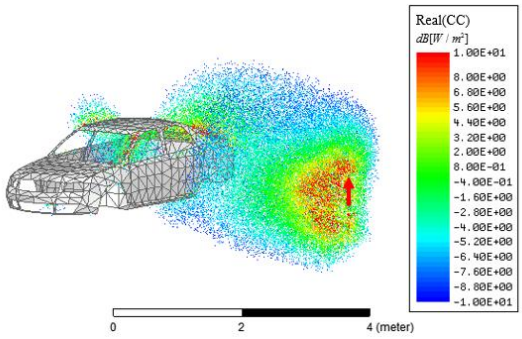

Fig. 11. 3D coupling path visualization when the attacker is on the left

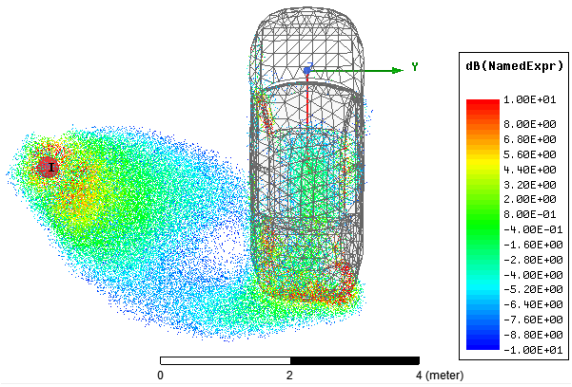

Fig. 12. Top view of the coupling path

For the coupling from the source on the left side to the victim in the trunk, the coupling path is mainly from the gap

between the trunk door and car body. Also, there is a part of coupling from the side window and the back seat.

IV. Conclusion

For the automotive IEMI testing, the HPEM source were modeled as an equivalent dipole moment which generated the same fields in the specific far field region. The simulation model consists of the reconstructed dipole and the car model was proposed. The comparison of simulation results and measurement data indicates that the IEMI simulation model is accurate and reliable. With the automotive IEMI simulation model, the coupling mechanism can be studied more conveniently. A coupling path visualization based on the reciprocity is applied on the IEMI simulation. The coupling coefficient is defined to characterize the coupled power density on spherical surfaces which separate the aggressor and victim. By plotting the real part of the coupling coefficient with proper scale, the 3D coupling path can be visualized on top of the simulation model. The visualization results can help understand the coupling mechanism and propose mitigation methods.

Acknowledgment

This work was supported in part by the National Science Foundation under Grant No. IIP-1440110.

References

[1] Critical National Infrastructures, "Report of the Commission to Assess the Threat to the US from Electromagnetic Pulse (EMP) Attack," 2004

[2] Pocket-lint, "Pulse gun stops cars using smart radio frequency system,"2013.Available:https://www.pocketlint.com/cars/news/125573-pulse-gun-stops-cars-dead-using-smart-radio-frequency-system.

[3] M. Bäckström, "HPM testing of a Car: A Representative Example of the Susceptibility of Civil Systems", *13th International Zurich Symposium Supplement*, February 1999, pp. 189-190.

[4] Sabath, F., "What can be learned from documented Intentional Electromagnetic Interference (IEMI) attacks?" *2011 XXXth URSI General Assembly and Scientific Symposium*, pp.1-4, 13-20 Aug. 2011.

[5] IEC 61000-4-36. Available: https://www.iec.ch/.

[6] Replex HPEM-DMS-120KV. Available: http://www.replex.co.kr/

[7] Y. Zhong, W. Song, C. Kim, C. Park and C. Hwang, "Intentional Electromagnetic Interference Source Reconstruction for Automotive Simulation" accepted by the *IEEE Asia-Pac. EMC Symp, 2019*.

[8] Y. Zhong, W. Song, C. Kim, C. Park and C. Hwang, "Efficient Automotive Simulation Using Reciprocity for Intentional Electromagnetic Interference" accepted by the *IEEE EMC Symp, 2019*.

[9] J.R.Carson, "Reciprocal Theorems in Radio Communication," *Proc. IRE*, vol. 17, pp. 952 – 956; June, 1929.

[10] C. A. Balanis, Advanced Engineering Electromagnetics. Hoboken, NJ, USA: Wiley, 1989.

[11] Y. Zhong and C. Hwang, "Coupling Path Visualization Based on the Reciprocity Theorem" submitted to the *Transaction on EMC*.

ASIAEM 2019−Analysis of Active Surge Protection Gap Impulse Breakdown Voltage *

1st Yangjing Le
Xi'an Jiaotong University
School of Electrical Engineering
Xi'an, China
leyangjing@stu.xjtu.edu.cn

2nd Xueling Yao
Xi'an Jiaotong University
School of Electrical Engineering
Xi'an, China
xlyao@mail.xjtu.edu.cn

3rd Jinru Sun
Xi'an Jiaotong University
School of Electrical Engineering
Xi'an, China
jinru2014sun@163.com

4th Tianquan Li
Xi'an Jiaotong University
School of Electrical Engineering
Xi'an, China
litianquan@stu.xjtu.edu.cn

5th Wenjun Xu
Xi'an Jiaotong University
School of Electrical Engineering
Xi'an, China
702289443@qq.com

6th Jingliang Chen
Xi'an Jiaotong University
School of Electrical Engineering
Xi'an, China
cjl@mail.xjtu.edu.cn

***Abstract*—In the electronic information system, there are some problems with the commonly used Class I protection device, passive sure protection gap (SPG), such as high pulse breakdown voltage, large dispersion and long response time. So we designed an active SPG and constructed an active coupling trigger circuit in this paper. Comparing the impulse breakdown voltages of active SPG and passive SPG, the influence of active trigger circuit on SPG impulse breakdown voltage is analyzed. And the voltage distribution of the active coupling circuit components is obtained through the simulation and experimental comparison. It provides a theoretical and experimental basis for further improving the protection characteristics of SPG.**

Keywords—active coupling trigger circuit, surge protection gap, impulse breakdown voltage, voltage distribution

I. INTRODUCTION

In recent years, the losses caused by lightning strikes in information systems have increased, and lightning surge protection is important for system safety [1, 2].

In the information system, the commonly used Class I protection device, passive SPG [3], has the disadvantages of high impulse breakdown voltage, large dispersion, long response time and unstable protection characteristics [4]. To solve these problems, researchers have proposed to use the external trigger to breakdown the SPG by coupling the surge energy. It can reduce the impulse breakdown voltage, reduce the response time, and improve the stability of protection characteristics of the passive SPG [5, 6].

Therefore, we constructed an active SPG and tested the active SPG and the passive SPG with 1.2/50μs lightning voltage impulse. Comparing the active SPG and passive SPG impulse breakdown voltage, the influence of the active coupling circuit on the SPG impulse breakdown voltage is analyzed. Through the analysis and simulation, the voltage distribution of the active coupling circuit components in the impulse process is obtained, which provides a theoretical and experimental basis for further improving the protection characteristics of SPG.

II. ACTIVE SURGE PROTECTION GAP DESIGN

A. Surge Protection Gap Structure

The three-electrode SPG structure designed in this paper is shown in Figure 1.

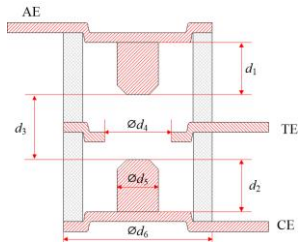

Fig. 1. Schematic diagram of the active SPG

In Figure 1, AE, CE, and TE are the anode, cathode, and trigger electrode of the SPG, respectively. The electrode lengths d_1 and d_2 are both 7.9 mm; the distance between main electrodes d_3 is 1.5 mm; the spacer thickness d_4 is 2.0 mm; the trigger hole diameter is d_5; the main electrode diameter is d_6; the ceramic tube diameter is d_7, and the ceramic tube thickness is 2mm. The gas composition in the gap is 15% H2 mixed air.

B. Active Coupling Trigger Circuit Design

In the active SPG, the active coupling trigger circuit needs to couple the lightning strike energy to form a trigger pulse, which breaks the trigger gap and generates a large number of carriers to cause the main gap breakdown in advance. Therefore, the active trigger circuit is composed of a coupling varistor VDR, a coupling capacitor C, a coupling GDT, and a boost pulse transformer T as shown in Fig. 2.

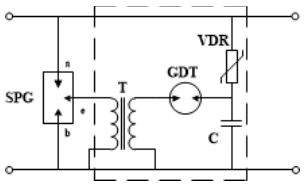

Fig. 2. Schematic diagram of the active coupling trigger circuit

III. INFLUENCE OF ACTIVE TRIGGER CIRCUIT ON SPG BREAKDOWN VOLTAGE

The active and passive SPGs are tested with the 1.2/50μs lightning voltage impulse, and the test results are as follows.

A. Impulse breakdown voltage comparison

The 1.2/50μs impulse breakdown voltage curve of the passive SPG is as shown in Fig. 3. The 1.2/50μs impulse voltage curve of the SPG is shown in Fig. 4.

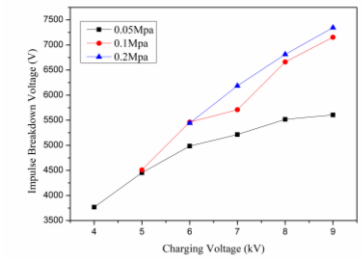

Fig. 3. Passive SPG impulse breakdown voltage

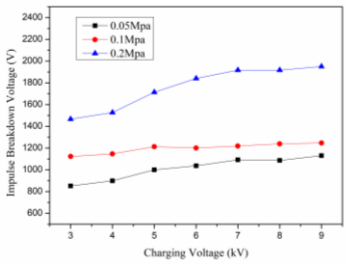

Fig. 4. Active SPG impulse breakdown voltage

Comparing Fig. 3 with Fig. 4, it can be found that the impulse breakdown voltage of the active SPG is significantly reduced with the same charging voltage. When the charging voltage rises, the impulse breakdown voltage of the active SPG tends to be more stable.

B. Impulse breakdown waveform comparison

The passive SPG impulse breakdown waveform is shown in Fig. 5; the active SPG impulse breakdown waveform is shown in Fig. 6.

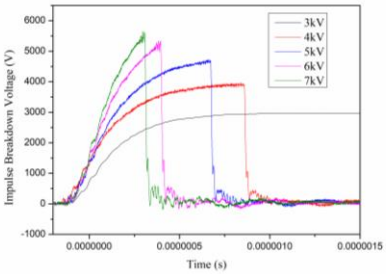

Fig. 5. 1.2/50μs breakdown waveform of passive SPG

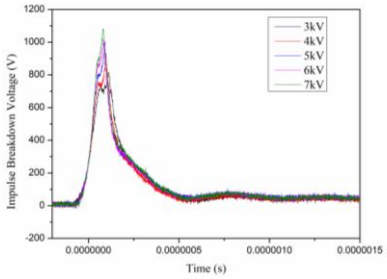

Fig. 6. 1.2/50μs breakdown waveform of active SPG

Comparing Fig. 5 with Fig. 6, it can be found that the passive SPG operating time is significantly larger than the active SPG. As the charging voltage rises, the operating time of the passive SPG is greatly reduced, and the operating time of the active SPG is almost constant. This is caused by the active trigger circuit. With the different charging voltage, the active trigger circuit couples the lightning energy; the voltage of the varistor and the capacitor rise quickly, and the coupling GDT breakdowns. With the boost transformer, a high-voltage pulse is applied to the trigger gap and the main gap is triggered in advance.

IV. VOLTAGE DISTRIBUTION OF THE ACTIVE TRIGGER CIRCUIT COMPONENTS

To analyze the operation of the active coupling trigger circuit, the simulation analysis and experiments are carried out to obtain the voltage distribution of the coupling circuit components with lightning voltage impulse injected.

A. Equivalent Circuit Model

The transient voltage and current of the coupling circuit components are analyzed. When the varistor voltage does not reach U_{1mA}, the main current of the coupling circuit is mainly capacitive current, as shown in Fig.7. When the varistor voltage is more than U_{1mA}, the main current is different from the capacitive current. The transient currents are shown in Fig. 8.

Therefore, the RC parallel circuit is used as the equivalent model of the coupling varistor for simulation [7, 8].

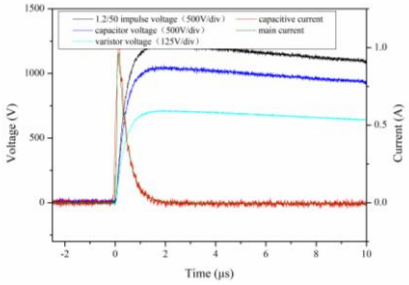

Fig. 7. Transient voltage and current when the varistor is in high impedance state

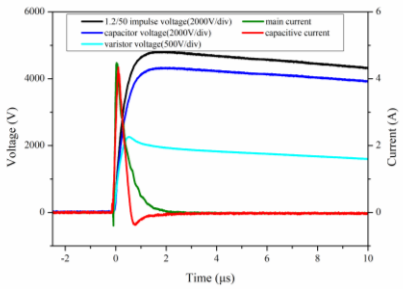

Fig. 8. Transient voltage and current when the varistor is in low impedance state

B. *Simulation and Analysis*

The equivalent model of active coupling circuit is shown in Fig. 9. C_0 is the equivalent capacitor of the varistor. R is a nonlinear resistor reflecting the volt-ampere characteristic.

When the varistor voltage is less than U1mA, R is always in a high-impedance state, and its equivalent impedance is much larger than the capacitor C. The main current of the coupling circuit is approximately the same as the current on capacitor, and the current on the nonlinear resistor is negligible. The varistor voltage and the coupling capacitor voltage are distributed according to their capacitance.

When the varistor voltage exceeds U1mA, the impedance of R decreases rapidly, the current on the capacitor drops rapidly, and the varistor voltage rises slowly. When the varistor voltage reaches a maximum, the capacitive current on the varistor drops to zero. As the equivalent impedance of the varistor decreases, the varistor voltage begins to gradually decrease [9].

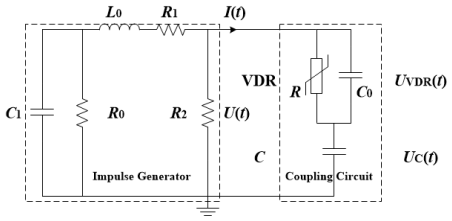

Fig. 9. Equivalent circuit model

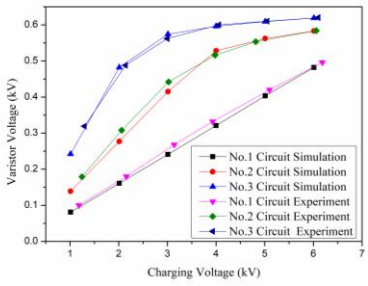

Fig. 10. Simulated varistor voltage and measured varistor voltage

The simulation model is used to obtain the varistor voltage when the coupling circuits with the different parameters operate. The comparison between the simulated voltage and the measured voltage is shown in Fig. 10. It can be found that the simulation and the measured results basically coincide.

V. Conclusion

In this paper, an active coupling trigger circuit is constructed, and an active surge protection gap is designed. Comparing the impulse breakdown voltage and waveform of the active SPG and the passive SPG, it can be found that the impulse breakdown voltage of the active SPG is obvious lower than passive SPG due to the operation of the active coupling circuit. And the dispersion is significantly reduced.

To further analyze the active coupling trigger circuit operation, an equivalent model is established based on the transient voltage and current of the trigger circuit components. In the simulation and experiments, the changes of transient voltage and current in the coupling circuit under the lightning voltage impulse are analyzed, and the voltage distribution of the coupling varistor and the coupling capacitor in the impulse process is obtained.

Acknowledgment

The study was supported by the National Natural Science Foundation of China (No. 51577151), the Fundamental Research Funds for the Central Universities and the Scientific and Technological Innovation Team of Shaanxi Province (No. 2012kct-07)

References

[1] Paul D. Low-voltage power system surge overvoltage protection[J]. IEEE Transactions on Industry Applications, 2001, 37(1):223-229.

[2] Paul D. Low voltage power system surge overvoltage protection[C]// Industrial and Commercial Power Systems Technical Conference, 2000. Conference Record. Papers Presented at the 2000 Meeting. IEEE, 2000:21-29.

[3] Protection of Structures Against Lightning, Part 1: General Principles, IEC61024[S]. Geneva, Switzerland: IEC. 1990.

[4] Martzloff, F. D. (1980). Coordination of surge protectors in low-voltage ac power circuits. IEEE Transactions on Power Apparatus & Systems, PAS-99(1), 129-133.

[5] YAO Xueling, Chen Jingliang, Chen Antong. Research of Surge Protective Gap With Active-Energy-Coupling-Triggered Circuit[J]. IEEE Transactions on Plasma Science, 2011, 39(11): 3222-3226.

[6] Sun W, Yao X, Chen J. Study on Gas Discharge Characteristics for Gap Type Surge Protective Device under Low Atmospheric Pressure[J]. Low Voltage Apparatus, 2011.

[7] Jones R A, Clifton P R, Grotz G, et al. Modeling of metal oxide surge arresters[J]. Power Delivery IEEE Transactions on, 1992, 7(1):302-309.

[8] Zadeh M K, Abniki H, Akmal A A S. The modeling of metal-oxide surge arrester applied to improve surge protection[C]// International Conference on Power Electronics and Intelligent Transportation System. IEEE, 2010:238-243.

[9] Lee B H, Kang S M. Properties of ZnO varistor blocks under multiple lightning impulse voltages[J]. Current Applied Physics, 2006, 6(5):844-851..

An UWB Radiation System and Its Electromagnetic Interference Effect on UAV System

Yangxin Qiu , Yanzhao Xie, Mingxiang Gao, Shaofei Wang, Siqi Wang, Yuchen Lai, Yuhao Gu
State Key Laboratory of Electrical Insulation and Power Equipment
School of Electrical Engineering, Xi'an Jiaotong University
Xi'an, China
yxinqiu@163.com, yzxie@mail.xjtu.edu.cn

***Abstract*—In this paper, an ultra-wideband(UWB) radiation system based on avalanche transistor pulse generator and combined antenna(CA) is fabricated, which consists of 18 identical small radiation modules. Based on the spatial synthesis method, the effective potential rE_p in far field of the radiation system could reach to 100 kV and the system can operate stably with the repetition frequency rate 1 kHz. Based on the system, electromagnetic interference effect experiment was carried out on the small civilian UAV system. Datalink system of UAV system is most susceptible for front door coupling. And repetition frequency rate is a key parameter for the electromagnetic effect of UAV systems.**

Keywords—ultra-wideband radiation system, avalanche transistor, spatial synthesis, UAV system

I. INTRODUCTION

The full-solid UWB high-power pulse generator based on switching devices is widely used for full-solid state, ultra-wideband, high reliability, and high repetition rate in various fields such as ultra-wideband radar, ultra-wideband communication, and cell medical and so on [1-2]. However, the solid-state switching devices are limited by power capacity, it is difficult for a single solid-state pulse generator to produce pulse with several tens of MW power. Spatial synthesis technology and circuit synthesis technology are main technical methods to obtain higher-power pulse for solid-state generator [3].

The avalanche transistor is a common switching device with the advantages of easy cascading, fast switching response and high stability [4]. When certain conditions are met, the transistor will avalanche breakdown. Since the avalanche effect is as short as a hundred picoseconds, the avalanche effect can be used to generate fast leading edge short pulses.

II. DESIGN OF UWB SYSTEM

A. Design of Pulse Generator

The generation of high amplitude pulse is often achieved by using the Marx circuit principle, which can be summarized as "capacitor charging in parallel and then series discharging." Increasing the number of Marx circuit stages is an effective measure to increase the amplitude of the output pulse. So we designed a 100-stage Marx circuit. When the peak current of avalanche transistor exceeds the rated current, the avalanche transistor is easy to be destroyed. Therefore, we need to design the avalanche transistor in parallel to function as a shunt. In this condition, the Marx circuit is an electrically large circuit, so it is necessary to consider the traveling-wave in the pulse forming process [5]. As the avalanche process progresses, the charge stored in the charging capacitor is sequentially released, so that the pulse amplitude is continuously increased. The current flowing through the rear stage of the Marx circuit is different with the current flowing through the previous stage. The waveform of the pulse generator on 50 Ω is shown in the Fig.1. The pulse rise time is about 150 ps. The full width at half maximum is about 300 ps. The amplitude of pulse is about 6 kV. The pulse generator can operate stably with the repetition frequency rate 1 kHz and it can operate at 2 kHz in a short time.

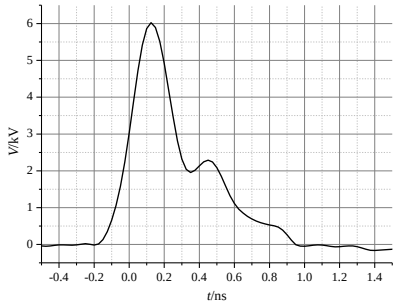

Fig.1. Waveform of the pulse generator

B. Design of Antenna

CA is a kind of ultra-wideband antenna, which introduces a magnetic dipole on the basis of the horn antenna to improve its low-frequency radiation characteristics. It is compact and easy to assemble. In order to enhance radiation field strength under the finite aperture area, the compacted combined antenna is designed. Replacing a large-diameter antenna with a 2×2 compacted antenna array of the same aperture can increase the electric field by 22%. Detailed design method was introduced in [6].

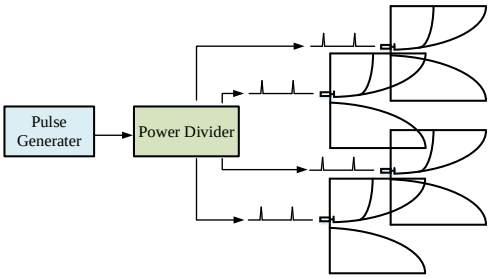

Fig.2. The schematic diagram of the module

A radiation module consists of a pulse generator, a 1 split 4 power divider, and a 2×2 antenna array. The schematic diagram of the module is as shown as Fig.2. Measured electric field waveform of the generator in Fig.1. at the point which is 6 m (far field) from the transmitting antenna is as shown in the Fig.3. So the electric field gain of the module

$\frac{rE_p}{V_p} = 1.2$. As we can see, the width of the waveform is about 1 ns. According to frequency domain analysis, the central frequency of the electric field is 1 GHz.

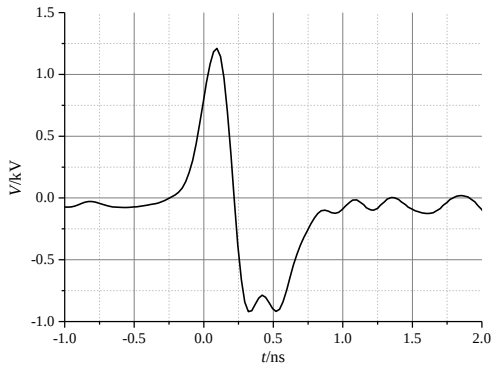

Fig.3. Waveform of E-field

III. Spatial Synthesis of the Radiation System

The radiation system consists of 18 identical radiation modules and its size is $1.3\text{m}\times1.2\text{m}\times1\text{m}$ .Picture of the radiation system is shown as Fig.4. In order to avoid the additional jitter caused by the difference of the trigger signals, the pulses provided by a high-amplitude pulse connected with a 1 split 18 power divider are used as the trigger signals of the 18 generators respectively. To achieve good spatial synthesis, the key points are the adjustment of the trigger delay and the control of the pulse jitter.

Fig.4. Picture of the fabricated UWB system

A. *Time Delay Adjustment*

Although the parameters of devices (resistor, capacitor, transistor) of the 18 pulse generators are the same, the outputs of the pulse generators are inevitably different in time because of the individual performance difference of the avalanche transistors. So we adjust the time of trigger signals to make sure the time delays of generators are same. The time of the trigger signal is controlled by changing the length of the trigger connection cable. Of course we need to measure the relative delay time of every generator firstly.

B. *Jitter Control*

Jitter in time is resulted from the uncertainty of the avalanche transistor transition from "off" state to "on" state. The main reason for this is 1) the voltage level resulting in the state change of avalanche transistor is a range value rather than a constant value. 2) the random thermal noise in the circuit also makes the switch level jitter at random [7]. Studies have shown that trigger signal stability has a large impact on pulse jitter. Pulse jitter can be effectively reduced by increasing the amplitude of the trigger pulse and decreasing the leading edge of the trigger pulse. The output of the generator based on avalanche transistor is used as a trigger signal. To improve stability of the generator output under the premise of ensuring the pulse amplitude is sufficiently high, we designed multi-stage trigger pulse generator with small charging capacitor C and small charging resistor R, which allows the charging capacitor to be fully charged. So the stability of trigger pulse will be improved. The trigger signal with amplitude of 2.1 kV, leading edge of 150 ps and pulse width of 1 ns is obtained. After 1 split 18 power divider, the trigger signal amplitude of each generator is about 320 V. The jitter of generator is approximately 100 ps according to measured result.

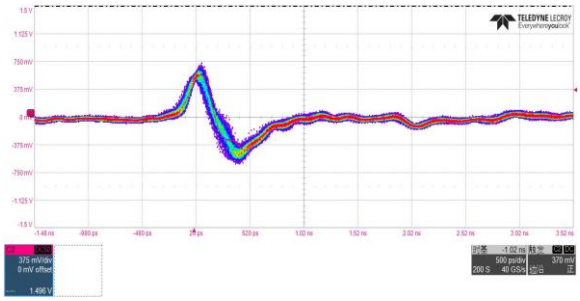

Fig.5. The electric field waveform of the system

The electric field waveform of the system is shown in Fig.5., from which we can see the synthesis of the waveform is good enough to proceed effect experiment. The waveform is measured at the distance R=9.5 m (far field) from the antenna. After calculation, the effective potential rE_p of the radiation system is 99.75 kV.

IV. Electromagnetic Effect on UAV System

The small civilian UAV system we used in the experiment is composed of four main subsystems, which are flight control system, power system, datalink system and GPS system. The flight control system is the key component of the whole UAV, which receives data from various types of sensors and gives orders to control propeller and flight mode. Brushless motor and Electronic speed controller can convert electricity into flight power. The GPS system locates UAV by communicating with GNSS (Global Satellite Navigation System), and the communication frequency of GPS is 1575 MHz. In order to communicate with the ground base station, data transmission module and image transmitter are necessary. Data transmission module usually works in 433 MHz or 915 MHz. Image transmitter usually works in 2.56 GHz, 1.2 GHz or 5.8 GHz. UAV system is complicated. It is difficult to study the effect phenomenon of the whole UAV system. So we study interference effect of the subsystems respectively.

According to the experiment result, there are no obvious effect phenomena when power system, GPS system, flight control system are exposed to electric field. We can see obvious phenomena when datalink system is radiated. The effect phenomena of image transmitter and data transmission module are shown respectively as bellows.

Fig.6. is the picture of the image transmitter. The transmitting antenna transmits the image information, which is received by the receiving antenna and displayed on the

monitor. The module we used in the experiment works at 2.56 GHz.

Fig.6. Picture of the image transmitter

The specific electromagnetic effect results are shown in table I. We can obtain from the table I that repetition frequency rate has a strong influence on the suppression of the signal. The higher is the repetition frequency, the worse is the signal quality of the image. However, the image transmitter is not damaged. If the electric field is cancelled, the picture transmitter will be back to normal instantly.

TABLE I. EFFECT RESULTS OF THE IMAGE TRANSMITTER

Amplitude of electric field/(kV/m)	***Repetition frequency rate/Hz***	***phenomenon***
30	200	Jitter on the screen
30	1k	Jitter becomes intense and the picture changes from color to black and white.
30	2k	Jitter becomes more intense and the picture changes from color to black and white.

The data transmission module we use works at 915 MHz. It is shown in Fig.7. It is connected to the flight system directly. The way it works just like the image transmitter's.

Fig.7. Picture of the data transmission module

We can see from the Table II that the higher are the amplitude of the E-field and repetition frequency rate of the pulse, the more obvious is the interference effect. What's more, when the antenna is parallel to the polarization direction of electric field, the effect is most obvious and when the antenna is vertical to the polarization direction of electric field, the effect is weakest. It demonstrates that the interference is coupled through the antenna.

TABLE II. EFFECT RESULTS OF THE DATA TRANSMISSION MODULE

Amplitude of electric field/(kV/m)	***Repetition frequency rate/Hz***	***phenomenon***
30	200	Data transmission module stops working. Soft fault appears.
15	200	No obvious change
15	1k	Signal strength reduced from 84% to 75%
15	2k	Signal strength reduced from 84% to 60%

V. CONCLUSION

In this paper, an UWB radiation system based on avalanche transistor and CA antenna was introduced. We obtain E-field pulse with rE_p >100 kV, repetition frequency rate >1 kHz by use of spatial synthesis technology. Firstly, this paper introduces design of the generator based on transistor and CA antenna. The key points to achieve spatial synthesis are the adjustment of the trigger delay and the control of the pulse jitter. Then methods of adjusting of the trigger delay and controlling of the pulse jitter are introduced. Finally, effect experiment of the small civilian UAV system is presented. Because of front door coupling, datalink system of UAV system is most susceptible. And repetition frequency rate is a key parameter for the electromagnetic interference of UAV system. Further study of electromagnetic interference effect of UAV system will be done in the future.

REFERENCES

[1] Q. J. Liang, X. Y. Shi, and S. Y. Feng, "Application of high power solid state switch DSRD in UWB radar," Modern Radar, 2005, pp. 69-71.

[2] Q. J. Liang, X. Y. Shi, and Y. F. Wei, "Design of carrier free ultra wideband radar transmission signal waveform," Modern Radar, 2003, pp. 45-50.

[3] Q. J. Liang, X. Y. Shi, and Y. Y. Cao," Design of new style 50MW Full solid-state high amplitude nanosecond pulse," Modern Radar, 2010, pp. 80-83.

[4] B. G. Liang, G. F. Zhang, and W. J. Zhang," Synchronization of full-solid high-stability nanosecond pulse sources," High Power Laser and Particle Beams, 2006, pp. 1043-1045.

[5] M. Gao, Y. Xie, Y. Qiu, Y. Hu and K. Li, "Performance improvement for sub-nanosecond Marx generator based on avalanche transistors by considering the traveling wave process," 2018 IEEE International Symposium on Electromagnetic Compatibility and 2018 IEEE Asia-Pacific Symposium on Electromagnetic Compatibility (EMC/APEMC), Singapore, 2018, pp. 925-927

[6] S. Wang, Y. Xie, M. Gao, Y. Qiu and Y. A. Andreev, "Optimizing High-Power Ultra-Wideband Combined Antennas for Maximum Radiation Within Finite Aperture Area," in IEEE Transactions on Antennas and Propagation, vol. 67, no. 2, pp. 834-842, Feb. 2019

[7] X. L. Yuan, H. Q. Qiao, Q. S. Hao," Effect of trigger pulse on avalanche tube pulse source," High Power Laser and Particle Beams, 2016, 28(3).

Circuit Modeling of Capacitive and Inductive Couplers of Pulsed Current Injection Tests

Yi Zhou
School of Electrical Engineering
Xi'an Jiaotong University
Xi'an, China
zhouyi4080@stu.xjtu.edu.cn

Yan-zhao Xie
School of Electrical Engineering
Xi'an Jiaotong University
Xi'an, China
yzxie@xjtu.edu.cn

Dao-zhong Zhang
School of Electrical Engineering
Xi'an Jiaotong University
Xi'an, China
cnsdxtzdz@stu.xjtu.edu.cn

***Abstract*—In standards related to PCI tests, the pulse generator is well characterized while coupling method is unspecified. To study the response in circuit under test and effect of DUT, two widely used couplers, capacitive couplers and inductive couplers, are modeled in this paper.**

Keywords—PCI, HEMP, coupler

I. INTRODUCTION

Pulsed current injection test was firstly applied in MIL-STD-188-125 Appendix B, which is a test method for measuring performance of a device under test (DUT) against pulsed current caused by HEMP.

The pulse generator used in PCI tests (short pulse) is characterized with a short-circuit current with a double exponential waveform with peak current up to 5 kA, rise time no longer than 20 ns, and pulse width from 500 ns to 550 ns, while source impedance is at least 60 Ω.

The coupling method is not specified in MIL-STD-188-125 except that introduction of a coupler must not interfere with normal circuit operation. Further research on response and effect of the circuit under test is still needed to be developed. In this paper, two widely used couplers, capacitive couplers and inductive couplers of PCI test are modeled and analyzed.

II. MODELING OF CAPACITIVE COUPLERS

Typically, a capacitive coupler includes 60 Ω resistors and non-linear components such as metal oxide varistors (MOV) and gas discharge tubes (GDT), which is often used to isolate the circuit under test and pulse generator. To improve the performance in high frequency, capacitors are applied in parallel to MOV and GDT. The rated voltage of varistors and the DC breakdown voltage of GDT shall be higher than the operating voltage of circuit under test. A typical capacitive coupler's circuit is shown in Fig. 1.

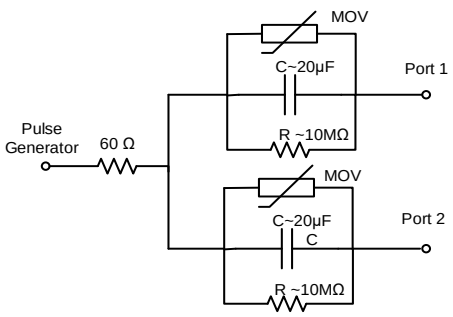

Fig. 1 Circuit of a capacitive coupler using in PCI test for two-port devices

The parameters of MOV are usually tested under DC, 8/20 μs pulse and etc. The switching voltage V_0 of MOV under pulse with rise time 20 ns is observably higher than V_{1mA}, and linearly related to V_{1mA}. Thus, the residual voltage behavior, the impedance behavior, and the response behavior of MOV when excited by HEMP need to be investigated.

According to our experiment results, the model of MOV for HEMP is developed, as shown in Fig. 2. Based on this model, the injected current waveform at the port of DUT can be analyzed.

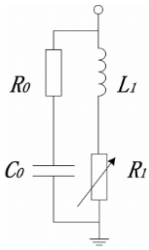

Fig. 2 Model of MOV when excited by HEMP

III. MODELING OF INDUCTIVE COUPLERS

Inductive coupling technique based on ferrite cores can be applied without interrupting the cable bundle to test. Unlike a current injection clamp for BCI test, an inductive coupler is much larger and heavier since the magnetic core is more likely to be saturated. Due to the big size and frequency characteristics of the magnetic core, inductive couplers usually perform under 30 MHz. The introduction of inductance also leads to a slower rise time.

An inductive coupler behaves like a RF transformer. Its primary winding, fed by the pulse generator, is wound onto the ferrite core and runs parallel to the inner surface of the coupler frame. Its secondary winding is the clamped wire bundle. The coupler behavior is mainly determined by frequency-dependent lossy magnetic coupling, and conditioned by some additional capacitive/ inductive phenomena.

A inductive coupler when a single wire is clamped is modeled as shown in Fig. 3. R_{wd}, L_{wd} and C_{wd} denote winding resistance, capacitance and inductance between primary winding and coupler frame. Self-inductance $L_1(\omega)$ relates to the complex permeability of the ferrite core. Leakage Inductance L_{2d} can be approximated by the inductance of an imaginary coaxial transmission line whose cross section from the clamped wire to the inner surface of ferrite core.

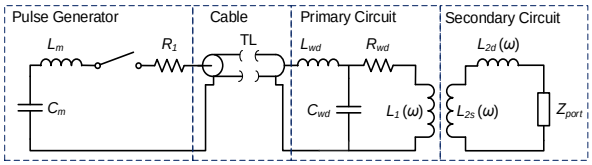

Fig. 3 Model of the inductive coupling circuit

Circuit modeling of the inductive coupler when a wire bundle is clamped is more complex and needed to be study in the future.

REFERENCES

[1] MIL-STD-188-125-1"High-Altitude Electromagnetic Pulse (HEMP) Protection for Ground Based C4I Facilities Performing Critical, Time-Urgent Missions, Part 1 Fixed Facilities", July 1998

[2] J. Chen et al., "Behavior Comparison of Metal Oxide Arrester Blocks When Excited by VFTO and Lightning," in IEEE Transactions on Electromagnetic Compatibility, vol. 57, no. 6, pp. 1608-1615, Dec. 2015.

[3] F. Grassi, F. Marliani and S. A. Pignari, "Circuit Modeling of Injection Probes for Bulk Current Injection," vol. 49, pp. 563 - 576, 2007.

[4] F. Grassi, F. Marliani and S. A. Pignari, "SPICE Modeling of BCI Probes Accounting for the Frequency-Dependent Behavior of the Ferrite Core," in XIXth General Assembly of International Union of Radio Science (URSI) Chicago, IL, USA, 2008.

[5] Z. Cui, F. Grassi, S. A. Pignari, and B. Wei, "Pulsed Current Injection Setup and Procedure to Reproduce Intense Transient Electromagnetic Disturbances," IEEE Transactions on Electromagnetic Compatibility, vol. 60, pp. 2065-2068, 2018.

[6] Y. Zhou and Y. Xie, "Comparison and Circuit Modeling of Coupling Techniques of Pulsed Current Injection Tests," in 23rd International Conference on American Electromagnetics (AMEREM 2018) Santa Barbara, USA, 2018.

Accumulative Effects of Multiple Pulse on Microcontroller

Yinghui Zhou
National Key Laboratory on Electromagnetic Environmental Effects and Electro-optical Engineering
Nanjing, China
nowaiting@163.com

Lihua Shi
National Key Laboratory on Electromagnetic Environmental Effects and Electro-optical Engineering
Nanjing, China
lihuashi@aliyun.com

Shangchen Fu
National Key Laboratory on Electromagnetic Environmental Effects and Electro-optical Engineering
Nanjing, China
fshangchen@hotmail.com

***Abstract*—In order to investigate the interference effect of multiple pulse on microelectronic device, the microcontroller module based on CAN bus technique for communicating module is designed. About 100 modules are tested under series electromagnetic pulse (EMP). The interference and damage effects on experiments are investigated by the electromagnetic pulse injection experimental system. Accumulative effects of multiple pulses with different pulse amount and different time interval are discussed.**

Keywords—Microcontroller, electromagnetic pulse, threshold value, multiple pulse, accumulative effect.

I. INTRODUCTION

Microcontrollers are widely used in both industry control and civil engineering. In the same time of improving control efficiency, the application of microcontrollers also raises the sensitivity to electromagnetic interference (EMI). The coupling paths into the microcontrollers are various. Cable conducted coupling is the highest energy coupling way, it is also the main way leading to EMI. The study of the anti-interference ability of microelectronic devices is necessary.

At present, the research of immunity mainly aimed at the following conditions: the theory analysis, the damage threshold analysis, damage device failure mechanism analysis, etc. M. Camp and H. Gerth proposed a concept of failure rate to describe the interference effect of the integrated circuit under EMP and ultra-wide band (UWB) pulses[1-2]. L. H. Shi, X. Y. Chen and A. B. Zhai also reported their experimental results on the EMP sensitivity of single-chip systems[3-4]. F. Sabath and M. Fernandez. systematically classified the effects of electromagnetic pulses, and evaluate the uncertainty under large current injection[5-6]. However, most of the conclusions are derived from limited number of test samples. The variation of threshold with different samples needs to be further investigated.

In this paper, a test module based on CAN bus technique is designed and large number of modules are tested. The influence of pulses amount and time intervals between multiple repeated pulses are studied.

II. TEST SETUP

The designed test module consists of the CPU circuit, power supply circuit, debug interface circuit, reset circuit and CAN bus interface circuit. The microcontroller with on-chip of CAN controller sent preset digital signal to the CAN transceiver through the TX pin. The CAN transceiver convert digital signal and sent to the cable via CANH and CANL bus. Another CAN transceiver receives and converts it to digital signal through the RX pin. Pulse injection to the module is provided by EFT61004B pulse generator. The voltage is from 100V to 4500V and the rise time is 2.5 ns, the half width is 25ns. The test setup is shown in Fig. 1.

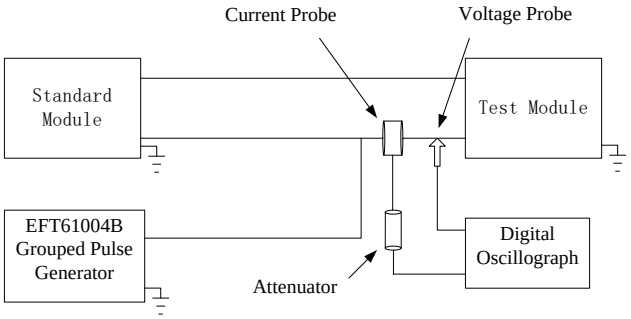

Fig. 1. Microcontroller test setup

The data is transmitted by two parallel cables with length of 3m between the two modules. The positive electrode of pulse generator is connected with CANH data line, and the negative electrode is connected to ground of the testing circuit. A voltage probe is used to measure the input voltage on CANH data line in vicinity of the receiving port, and a current probe is used to measure the coupling current on CANH data line.

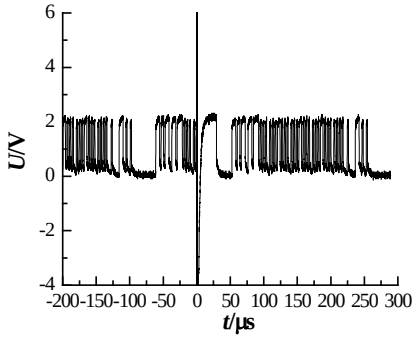

Fig. 2. Voltage waveform when the communication is disturbed.

The judgment of the interference and damage phenomenon is performed automatically by the embedded program in the tested module. This program monitors the accuracy of the received data and gives a LED indication when the received data is not exactly same as the known one. Fig. 2 shows the waveform when the communication is disturbed.

III. TEST RESULT AND ANALYSIS

The influences of multiple pulses with different number and with different time interval were investigated: (a) Influence of pulse amount. The amount of pulse is selected as 1, 5, 10 and 20, and for each pulse amount we use 10 modules to observe the variation of threshold versus different samples. The time interval between each pulse is 30s. If the module does not show any interference effect, the test module is removed from data records and a new module will be adopted. (b) Influence of the time intervals. Three kinds of intervals are used, which is 1s, 10s and 1min, with the upper limit of pulse amount being 10.

A. Influence of pulse amounts

Fig. 3 shows the distribution of interference and damage threshold under different pulse amounts. In the figure the horizontal axis is the serial number of the test module, their sequence is of no meaning. The number on x axis just show different sample. The vertical axis is the threshold voltage/current. Each dot represents a separate sample module. From Fig. 4(a) we can see that all lines are without intersection and they are distributed in different voltage levels. The accumulative effect is reflected clearly. The more pulse amounts lead to the lower threshold voltage. The average interference threshold difference between each group is about 20V, and the damage threshold difference between each group is about 200V.

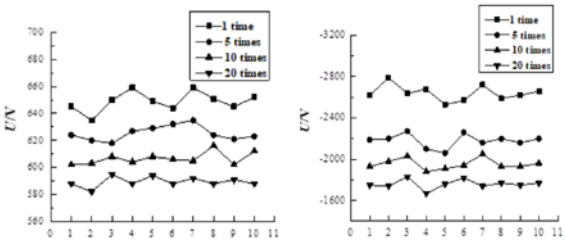

（a） (b)

Fig. 3. Distribution of threshold with applied pulse amount and test sample. (a) interference threshold voltage, (b) damage threshold voltage.

B. Influence of time intervals

Fig. 4 shows the distribution of interference and damage threshold with pulse interval. Three kinds of intervals are used, which is 1s, 10s and 1min, with the upper limit of pulse amount 10. We can see from Fig. 4 that the threshold voltage of three cases are different, there are obvious boundaries and no intersections among these three lines. This indicates that we can find the accumulative effect of time intervals in this test. The shorter time intervals lead to the lower threshold voltage. The difference of interference threshold is about 30V.

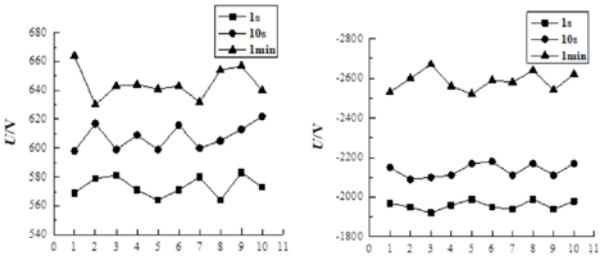

(a) (b)

Fig. 4. Distribution of threshold with applied pulse amount and test sample. (a) interference threshold voltage, (b) damage threshold voltage.

IV. CONCLUSION

Pulse injection test is carried out to investigate the variation of interference threshold under electromagnetic pulse. The threshold voltages under two situations, multiple pulses with different amount and with different time interval are measured from a relative large number of test samples. Accumulative effects of multiple pulses are observed and discussed. The results show that the accumulative effects are obvious on pulse numbers and time intervals situation in our test setup.

REFERENCES

[1] M Nitsch D, Camp M and Sabath F. Susceptibility of Some Electronic Equipment to HPEM Threats[J]. IEEE Trans. EMC, 2004, 46(3): 380-389.

[2] Camp M, Gerth H, and Garbe H. Predicting the Breakdown Behavior of Microcontrollers Under EMP/UWB Impact Using a Statistical Analysis[J]. IEEE Trans. EMC, 2004, 46(3): 368-379.

[3] Wang Zezhong, Lu Binxian, Li Chengrong. The Susceptibility of the Microprocessor-Based Relay of High Voltage Substations to EMP[C]. IEEE Trans. EMC, 2003: 517-520.

[4] Shi Lihua, Chen Bin, Gao Cheng. Experiments on the Susceptibility of the Direct Digital Control System to EMP in Intelligent Buildings[C]. Proc. Asia-Pasific CEEM, Guangzhou, China, 2003: 350-353.

[5] Sabath F. Classification of electromagnetic effects on system level. Ultra-Wideband, Short Pulse Electromngnetics. New York, USA, 2010: 325-332.

[6] Genender E, Garbe H. Probabilistic Risk Analysis Technique of Intentional Electromagnetic Interference at System Level[J]. IEEE Trans. EMC, 2014, 56(1): 200-207.

High Power Microwave Waveguide Slot Array Antenna with grooves

Yong Liao, Fanbao Meng , Ping Xie,Hongge Ma

Institute of Applied Electronics,CAEP
Mianyang Sichuan China
liaoyongmail@163.com

***Abstract*—In this paper, a subwavelength choke groove structure is symmetrically loaded at both sides of each longitudinal slot of the HPM waveguide array. The choke grooves not only reducing the mutual coupling between the rectangular waveguide but also improve the capability of wide-angle scanning of array by modulation of the surface wave propagation of array. The effectiveness of the proposed surface grooves is verified by numerical simulation and experiment. It is found that the scanning angle with the gain of array decreased 3dB without choke groove structure is only 24° , and it is 37° for the array with surface groove structure. The influences of groove parameters on the mutual coupling and wide-angle scanning performance are discussed. The physical mechanism of the corrugated structure is investigated.**

Keywords—high power microwave(HPM), waveguide slot array，wide angler scanning, choke groove, dielectric window .

I. INTRODUCTION

In recent years, the high power microwave(HPM) technology has developed into application period which need the antenna to satisfy special requirements, such as high power-handling capacity, high gain radiation ,compactness and low profile [1]. The high power microwave slotted waveguide array is one promising candidate of these antennas. One virtue of the slotted waveguide array is that the radiation beam can be steered by adjusting the phase of feeding microwave in different waveguide of array[2]. Unfortunately, the capacity of wide-angle scanning of radiation beam of array is deteriorated by the surface wave generated by the element mutual coupling in array [3].Some effective technologies have been developed to suppress the element mutual coupling in array design, such as using electromagnetic band-gap(EBG) structure[4], baffle structure[5],and periodic corrugated structure[6].

The surface-wave suppression was demonstrated by placing an EBG arrays over the ground plane of a linear 1 ×4 waveguide-slot-array antenna, up to 10 dB reduction of mutual coupling was observed[4]. But the EBG structure is not fit to HPM antenna for its lower capacity of power. The baffle structure with the high of a quarter of a wavelength can make the input resistance do not vary by more than ±3 percent when scan angel no more than 60° [5].The gain of the antenna with periodic grooves can be improved by 11dB and the mechanism for the improvement of the radiation has been explained by the resonance excitation of the surface EM wave and coherent superposition of power radiated from the grooves and central slits[6].

In this paper, The wide angle scanning capability of an L-band HPM waveguide array is analyzed and improved by the choke grooves structure. The result of simulation and experiment verified that the choke grooves structure can reduce the mutual coupling of array and improve the capability of wide-angle scanning of array. It is groove cavity resonance and coupling between grooves and slots can determine the distribution of surface electromagnetic resonance mode[7,8].Simulation and experiment results both show that the scanning angle with the gain of array decreased 3 dB can improved by 13° with the introduction of choke groove structure.

II. A HIGH POWER MICROWAVE ARRY ANTENNA

The L-Band HPM waveguide array of longitudinal shunt slots was shown in figure 1. Array consist of four waveguides and a planar dielectric window. The distance between antenna window and waveguides is 20 mm, antenna working frequency is 1.6 GHz, The sizes of broad wall and narrow wall of waveguide are 120 mm and 40 mm respectively .Each waveguide consists of seven slots which width is 20 mm. The whole array size is 1050 mm × 490 mm. The spacing distance of adjacent slots alone the propagation direction is half of wavelength of the waveguide.

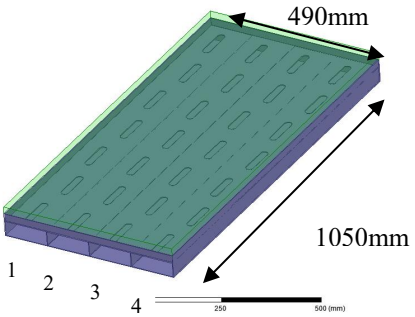

Fig. 1. Structure of HPM waveguide array

III. WIDE ANGLE SCANNING ANALYSIS OF ARRAY WITH CHOKE GROOVES

In order to improve the wide angle scanning capacity of array and suppress the mutual coupling of slots between different waveguide, choke grooves of waveguide slots array were designed as shown in figure 3. After the optimization of array structure, depth of groove is 32mm(0.17λ),width of groove is 13.5mm(0.07λ).The wide angle scanning property is shown in figure 4. Although the gain of array with groove structure slightly decline of 0.3 dB compared to that without choke groove, the wide angle scanning capacity was improved obviously. After scanning

angle of 15° ,there is no steep falling of gain of array. The scanning angle at which the gain of array with groove structure drop 3dB is 37° .The gain of array with scanning angle of 30° only drop 1.7 dB compared to max gain radiated in normal direction of array. The active VSWR of waveguide slots array with choke grooves with scanning angle of 0° and 30° are shown in Figure 5 and Figure 6 . The bandwidth of VSWR ≤ 3 is 8.0%. For the array with choke grooves, when scanning angle change from 0° to 30° ,the reflection bandwidth of VSWR ≤3 keep stabilization.

The effects of grooves parameters on the radiation of array are studied. The active of S_{31} of array are showed in Fig.7. The minimum S_{31} occurs at depth of 32mm(0.17 λ). Fig.8 shows the gain of array versus depth of groove at scanning angle of 30° .The maximum gain is located at depth of groove of 32 mm(0.17λ). Fig. 9 show the gain of array versus width of groove at scanning angle of 0° . When the width of groove is bigger than 10 mm(0.05λ),the gain of array keep nearly consistent.

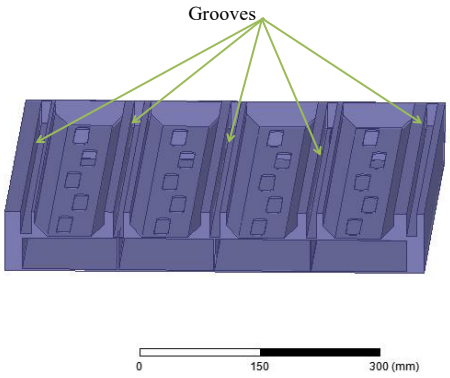

Figure.2. Waveguide slots array with choke grooves

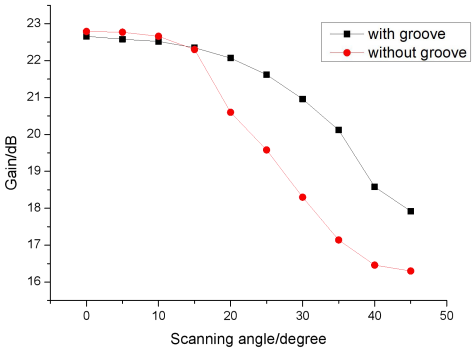

Figure.3. Gain of Array antenna with grooves

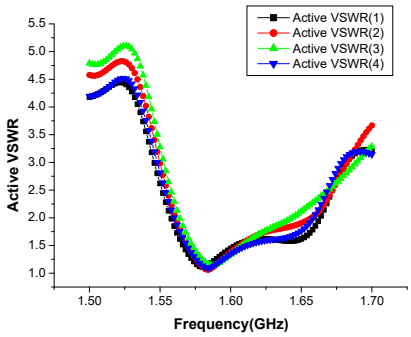

Figure. 4. Active VSWR of choke groove array with scanning angle of 0°

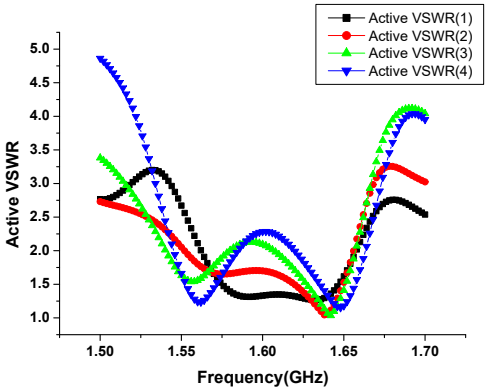

Figure. 5. Active VSWR of choke groove array with scanning angle of 30°

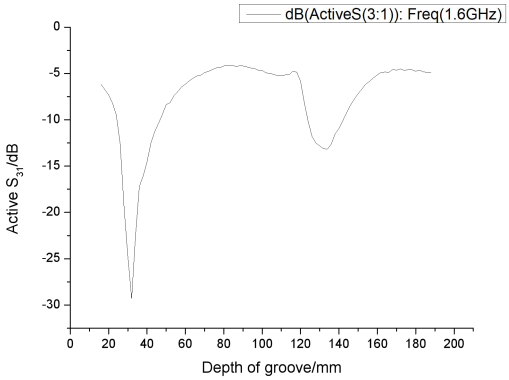

Figure. 6. Active S_{31} of array versus depth of groove at scanning angle 30°

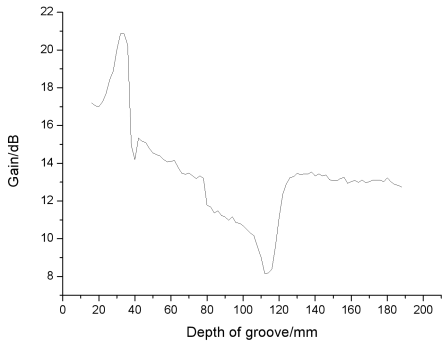

Figure. 7. Gain of array versus depth of groove at scanning angle 30°

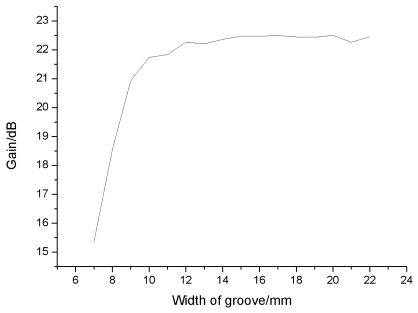

Figure. 8. Gain of array with width of groove at scanning angle 0°

The periodic grooves not only reduce mutual coupling between adjacent waveguides of array but also improve the gain of array by modulating the surface wave propagation of array [7].The mechanism for improvement of the gain of array has been explain by the resonance excitation of surface electromagnetic wave and coherent superposition of power radiated from the grooves and slits of array[8].The periodic modulated field can be expressed as a superposing of a set of harmonic waves. If the period of grooves $1/2 < d/\lambda < 1$ (in my paper the period of groove is 122 mm(0.65λ),there exists only one harmonic wave with $\beta_1 = \beta_0 - 2\pi/d$ which represents a plane wave with a direction angle determined by $\sin\theta = \beta_1/\beta_0$ [8],The direction of grooves diffraction from both sides of slit coincide to each other, such as $d=\lambda$ at 0° （direction normal to the surface of array) and $d=0.65\lambda$ at ±32°.This implies that the radiation at the angle nearby ±32° will be reinforced by the diffraction from grooves. In Ref.[8], for period of groove $d=0.625\lambda$ and width of groove $w=0.1\lambda$， as the depth of groove is about 0.18λ, the attainable diffraction efficiency which indicates the portion of energy being excited to surface electromagnetic wave reaches maximum. The results of simulation in my paper(Fig.7-Fig.8) are good agreement with the research result in Ref. [8].

IV. CONCLUSION

This paper analyzes the wide angle scanning of an L-band waveguide slot array, and the influence of the mutual coupling of the slots between adjacent waveguides to wide angle scanning property. Choke grooves are proposed loaded in waveguide array of longitudinal shunt slots to improve the ability of wide angle scanning. The result of numerical simulation and experiment show that the scanning angle of array with the gain of array drop of 3 dB increases from 24° to 37° with the introduction of the groove structure .

References:

[1] Benford J. ,Swegl J. A. e, Schamiloglu, E. High Power Microwaves,2nd ed. Taylor & Francis, New York, 2007.

[2] YangY , Yuan C.W , Qia B.L., “A beam steering antenna for X-band high power applications,” *Int. J. Electron. Communications*., 2014.68:763-766.

[3] R.J.Mailloux,*phased array antenna handbook*,2nd ed.Boston,MA:Artech House,2005,pp.306-316.

[4] H.Farahani,M.Veysi,M.Kamyab and A.Tadjalli,"Mutual coupling reduction in patch antenna arrays using a UC-EGB superstrate,*"IEEE Antenna Wireless Progag.Lett.*,vol.9,pp.57-59 2010.

[5] S.Edelberg and A.A.Oliner,"Mutual Coupling Effects in Large Antenna Arrays Ⅱ:Compensation Effects", *IRE Transaction on antennas and Propagation*,AP-8,4,July 1960,pp.360-367.

[6] C. Huang, C. Du,and X. Luo,”A waveguide slit array antenna fabricated with subwavelength periodic grooves”,*Appl.phys.lett.*,vol.91,pp.143512-1-143512-3,Oct.2007.

[7] C. Wang,C. Du,Y. Iv,and X. Luo,”Surface electromagnetic wave excitation and diffraction by subwavelength slit with periodically patterned metallic grooves,” *Opt.express*,vol.14,no.12,pp.5671-5681,Jun.2006.

[8] C. Chang,G. Z. Liu, C. X. Tang, etc, “Review of recent theories and experiments for improving high-power microwave window breakdown thresholds,”*Physics plasma*,2011.18:05702.

Research on HEMP Front-door Coupling Evaluation

Yu Mao[1,3], Yan Wang[1], Xuefeng Qi[1], Guoshuai Zhen[1], Lin Wang[2]
[1]*Aviation Key Laboratory of Science and Technology on Electromagnetic Environmental Effects*
[2]*Department of Avionics*
Shenyang Aircraft Design and Research Institute, AVIC
Shenyang, China
[3]maoyu0807@163.com

***Abstract*—The front-door coupling of high altitude electromagnetic pulse (HEMP) is very harmful to electronic equipment, and the front-door coupling evaluation of HEMP is an important prerequisite for the research on the front-door coupling protection technology. In this paper, the front-door coupling of high altitude electromagnetic pulse is evaluated from three approaches, which are theoretical calculation of transient energy transfer, electromagnetic simulation and electromagnetic pulse test. The results show that the theoretical calculation result is 2.3dB larger than the electromagnetic simulation result, and the electromagnetic simulation result is 4.9dB larger than the test result. The more ideal the front-door coupling condition is, the greater the coupling power will be. The research shows that the final evaluation value of front-door coupling should be between the simulation result and the test result.**

Keywords— high altitude electromagnetic pulse (HEMP), front-door coupling, transient energy transfer, electromagnetic pulse test

I. INTRODUCTION

Strong electromagnetic pulse (EMP) is an electromagnetic effect produced by the explosion of nuclear weapons or EMP bombs. It is a transient electromagnetic wave with directional propagation at the speed of light, wide spectrum and slow attenuation. Strong electromagnetic pulse can cause functional disorder or permanent damage to electronic systems [1]. With the improvement of the performance of electronic devices, the sensitivity and vulnerability to EMP are also enhanced. The energy of the EMP can be applied to sensitive devices through various coupling pathways, thus damaging electronic devices. From the perspective of the coupling path of EMP, front-door coupling and back door coupling are two main kinds of coupling pathways. EMP energy coupled by the front-door coupling is larger, which has a greater impact on electronics. Therefore, the front-door coupling protection of EMP is very important, and the front-door coupling evaluation of EMP is an important prerequisite for the research on the front-door coupling protection technology.

II. HIGH ALTITUDE ELECTROMAGNETIC PULSE

Nuclear explosion can be divided into deep-space nuclear explosion, high-altitude nuclear explosion, ground nuclear explosion and underground nuclear explosion. The electromagnetic pulse generated by the upper air nuclear explosion is the most harmful, which is mostly used to intercept aircraft groups or to produce electromagnetic interference to a wide range of ground facilities. HEMP generally consists of three parts, namely the early stage ($0 \le t \le 1\mu s$), the middle stage ($1\mu s < t \le 1s$), and the late stage ($t > 1s$). The standard and public publications on HEMP generally describe the typical HEMP waveform with double exponential function [2-4]. The time-domain expression of HEMP electric field waveform is:

$$E(t) = kE_0(e^{-\alpha t} - e^{-\beta t}) \tag{1}$$

Where k is the correction coefficient, E_0 is the peak electric field, generally 50kV/m, and α and β are the parameters representing the front and rear edges of the pulse. Due to the EMP front-door coupling test, the EMP waveform used in this paper shown in Fig. 1 refers to the EMP waveform emitted by the generator in the experiment, so k=1.34, E_0=37000V/m, α=0.045/ns, β=0.599/ns.

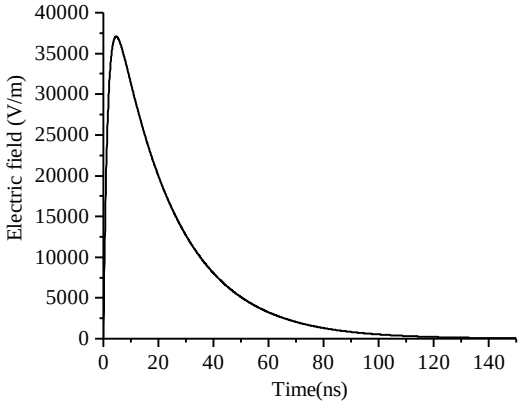

Fig. 1. The EMP waveform used in this paper.

III. FRONT-DOOR COUPLING EVALUATION

A. Theoretical Calculation

In this section, the front-door coupling of a monopole antenna with EMP is calculated and analyzed. The antenna is mounted on a metal shell, as shown in the figure below.

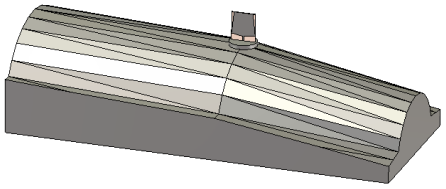

Fig. 2. The monopole antenna.

The power distribution of the EMP in the frequency domain as shown in figure 1 is shown below.

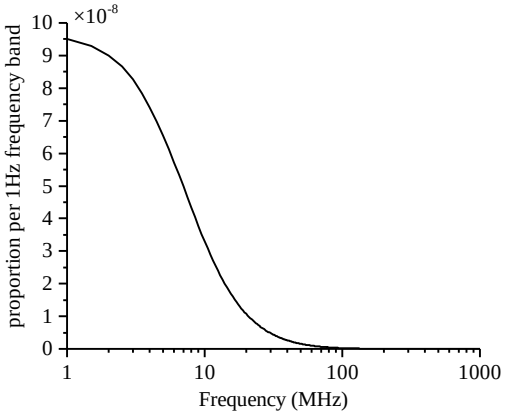

Fig. 3. The power distribution of the EMP in the frequency domain.

The time-domain waveform of the EMP shown in figure 1 can be regarded as the superposition of cosine waves of different frequencies and phases. Figure 3 shows the power distribution of the EMP in the frequency domain. It can be seen that the energy of the EMP is mainly concentrated below 30MHz. Take its integral in the whole frequency domain as 1, and the vertical axis k_i is the proportion of frequency domain components in each 1Hz frequency band, where i is the right boundary frequency of each 1Hz frequency band.

The reflection coefficient of the monopole antenna is shown in figure 4.

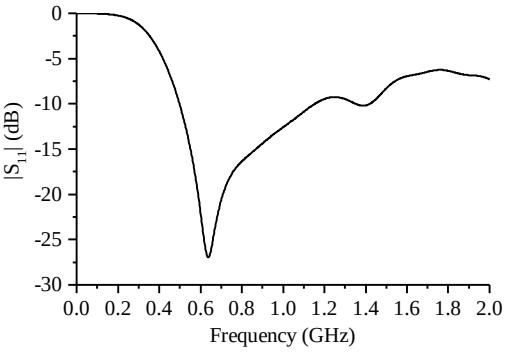

Fig. 4. The reflection coefficient of the monopole antenna.

When the polarization is matched and the antenna radiation efficiency is 1, the receiving power of the antenna is:

$$P_r = P_{in\rho} S_e e_z \tag{2}$$

Where P_r is the antenna receiving power, $P_{in\rho}$ is the power flow density, S_e is the effective area of the antenna, and e_z is impedance matching efficiency of the receiving antenna.

$$P_{in\rho} = \frac{|E|^2}{2\eta_0} \tag{3}$$

$$S_e = G_r \frac{\lambda^2}{4\pi} \tag{4}$$

$$e_z = 1 - |S_{11}|^2 \tag{5}$$

Where E is the electric field at the antenna, η_0 is the free space wave impedance, G_r is the gain of the antenna, and λ is wave length. Take the maximum transient electric field of the EMP, E=37kV/m. Since the frequency band where the EMP energy is concentrated is much lower than the operating frequency band of the antenna, the gain of the antenna is taken as the gain of the short dipole antenna, G_r=1.5. Take the bandwidth of each narrow band as 2MHz, the front-door coupling power is:

$$P_r = \sum_j \frac{|E|^2}{2\eta_0} \cdot \frac{G_r}{4\pi} \cdot (\frac{c}{f_j})^2 \cdot (1 - |S_{11}|^2) \cdot k_j \tag{6}$$

$$\sum_j k_j = 1 \tag{7}$$

Through the calculation, the front-door coupling power is 13736W.

B. Electromagnetic Simulation

The HEMP front-door coupling is simulated by CST Microwave Studio Transient solver, which is based on the Finite Integration Technique (FIT). The simulation uses EMP plane wave to radiate the antenna, and the plane wave matches the antenna polarization, as shown in the figure below.

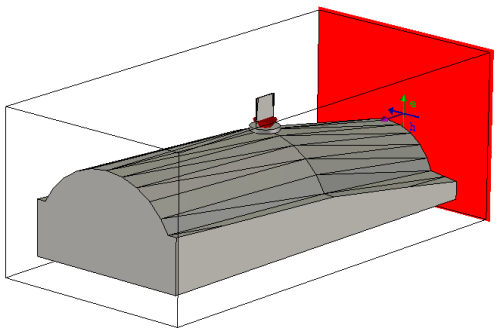

Fig. 5. Front-door coupling simulation model.

The simulation results of the front-door coupling are shown in the figures below.

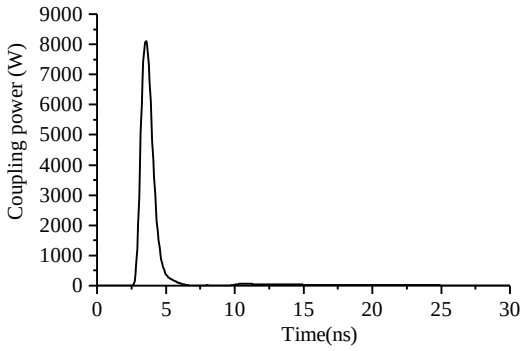

Fig. 6. Simulation result of the front-door coupling power.

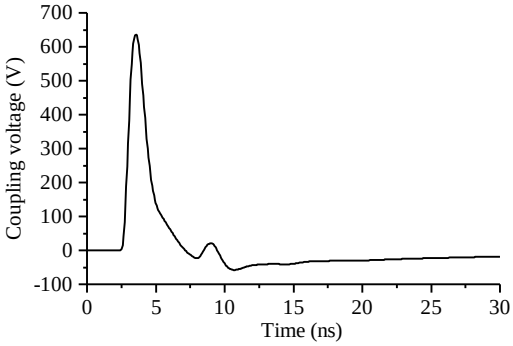

Fig. 7. Simulation result of the front-door coupling voltage.

It can be seen that the maximum value of the simulation result of the front-door coupling power is 8108W, the maximum front-door coupling voltage is 636V.

C. EMP Test

The front-door coupling of the monopole antenna was tested in the anechoic chamber, as shown in the figure 8. The EMP matches the antenna polarization. A 20dB attenuator is installed on the receiving side. The monopole antenna used in the test is equipped with an antenna cover, and loss caused by other factors will result in lower test results. The measured result of the coupling level of the monopole antenna is 362V.

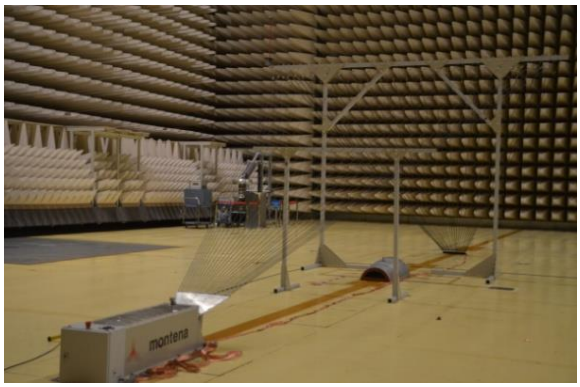

Fig. 8. EMP front-door coupling test.

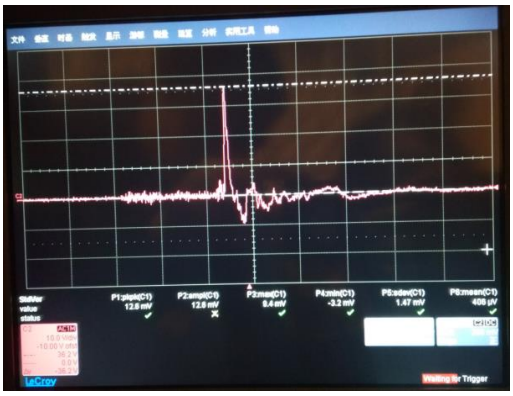

Fig. 9. Measured result of EMP front-door coupling.

IV. CONCLUSION

The results of HEMP front-door coupling from theoretical calculation of transient energy transfer, electromagnetic simulation and EMP test are listed in table 1.

TABLE I. THE RESULTS OF HEMP FRONT-DOOR COUPLING

Evaluated method	**Coupling power**	**Coupling voltage**
Theoretical Calculation	41.4dBW	-
Electromagnetic Simulation	39.1dBW	56.1dBV
EMP Test	-	51.2dBV
Compare	2.3dB	4.9dB

It can be seen in the table 1 that the theoretical calculation result is 2.3dB larger than the electromagnetic simulation result, which shows that the simulation result is quite reliable. The electromagnetic simulation result is 4.9dB larger than the test result. The more ideal the front-door coupling condition is, the greater the coupling power will be. The research shows that the final evaluation value of front-door coupling should be between the simulation result and the test result.

REFERENCES

[1] Radasky, W. A. , C. E. Baum and M. W. Wik, “Introduction to the Special Issue on High-Power Eletromagnetics (HPEM) and Intentional Electromagnetic Interference (IEMI)”, IEEE Transactions on Electromagnetic Compatibility, Volume 46, No. 3, August 2004, pp. 314-321.

[2] Ianoz M, Nicoara B I C, Radasky W A. Modeling of an EMP conducted environment [J]. IEEE Trans on EMC, 1996,38 (3): 400-413.

[3] MIL-STD-461E Requirements for the control of electromagnetic interference characteristic of subsystems and equipment[S].

[4] IEC 61000-2-9 Description of HEMP Environment Radiation Disturbance Basic EMC Publication[S].

Modeling of HEMP Conducted Responses Using State-Space System Identification Method

Yu-hao Chen
State Key Laboratory of Electrical Insulation and Power Equipment
Xi'an Jiaotong University
Xi'an, China
chenyuhao@stu.xjtu.edu.cn

Ke-jie Li
State Key Laboratory of Electrical Insulation and Power Equipment
Xi'an Jiaotong University
Xi'an, China
kejie.li@hotmail.com

Yan-zhao Xie
State Key Laboratory of Electrical Insulation and Power Equipment
Xi'an Jiaotong University
Xi'an, China
yzxie@xjtu.edu.cn

***Abstract*—This paper presents a system identification method based on state-space model to extrapolate the responses of conduction path excited by high altitude electromagnetic (HEMP) environments. A subspace algorithm is adopted to derive state matrices and system dynamics and a normal information criterion (NIC) is proposed to determine the order of state space model. The simulation of a conducted case is carried out by Spice program and state-space model is built using input and output data obtained from Spice simulation. Compared with simulated results, state-space system identification (SSSI) validates its capacity to accurately extrapolate the response of conduction path with other transient input signals.**

Keywords—HEMP, conduction path, state space system identification, order determination

I. INTRODUCTION

In the last decades, vulnerability assessments of electrical and electronic components under HEMP environments have received increasing attention [1]-[4]. As most critical infrastructures are generally grouped with many components in complex networks, threatening currents or voltages generally have been transformed when getting to the ports of target components. So In general, real transients threatening target components through conduction path should be obtained.

In this respect, the characteristics of conducted paths should be modeled so that extrapolation responses can be predicted. However, most systems with complex configurations and unknown characteristics are normally impossible to be modeled with physical analysis. Generally, only some rough qualitative descriptions, such as linguistic terms, are adopted [5]-[7]. To deal with this problem in quantitative description, a system identification method is proposed to model conduction path using input and output data obtained in experiments.

The state-space models, which are discrete time, linear and time-invariant, are adopted in this paper. They seem like a highly restricted class of models, especially the fact they are linear, but many industrial processes have been described very accurately by this type of models [8]. State space model not only describe the relationship between input and output, but also the internal characteristics of system. So that it is generally regarded as a complete description of the system. For conduction system, the input are generally HEMP environments with different waveform parameters, output are responses at the port of target components and internal influences come from intermediate components.

In this paper, a subspace method is adopted to derive state matrices and system dynamics of state-space models. As traditional criterion in state-space model order determination needs to compute likelihood function via complex Kalman filtering algorithm, a new efficient criterion is proposed. Finally a simulation study of a conduction case is carried out, and the results predicted by identified state-space models are well identical with simulation results by Spice program.

II. STATE SPACE SYSTEM IDENTIFICATION ALGORITHM

A. State Space Equation

State space model builds a relationship between observable variables and internal states, which is a complete description of the system. The discrete linear time invariant state space equation with single input and single output is described as:

$$\boldsymbol{x}_{k+1} = \boldsymbol{A}\boldsymbol{x}_k + \boldsymbol{B}\boldsymbol{u}_k + \boldsymbol{w}_k \tag{1}$$

$$\boldsymbol{y}_k = \boldsymbol{C}\boldsymbol{x}_k + D\boldsymbol{u}_k + \boldsymbol{v}_k \tag{2}$$

in the meantime:

$$E\left[\begin{pmatrix}\boldsymbol{w}(i)\\ \boldsymbol{v}(i)\end{pmatrix}\left(\boldsymbol{w}(j)^T\ \boldsymbol{v}(j)^T\right)\right] = \begin{bmatrix}\boldsymbol{Q} & \boldsymbol{S}\\ \boldsymbol{S}^T & R\end{bmatrix}\delta_{ij} \tag{3}$$

In this model, $\boldsymbol{u}_k \in \mathbb{R}$ is the measured input signal, $\boldsymbol{x}_k \in \mathbb{R}^n$ is the state variable, $\boldsymbol{y}_k \in \mathbb{R}$ is the measured output signal; $\boldsymbol{w}_k \in \mathbb{R}^n$ is process noise, $\boldsymbol{v}_k \in \mathbb{R}$ is measured noise, and $\boldsymbol{w}$ and $\boldsymbol{v}$ are both zero-mean white Gaussian noise; $\boldsymbol{A} \in \mathbb{R}^{n\times n}$ is state matrix, which describe the dynamics of system; $\boldsymbol{B} \in \mathbb{R}^n$ is the input matrix, which represents the influence of input signal on the state at next moment; $\boldsymbol{C} \in \mathbb{R}^n$ is output matrix, which represents the influence of intermediate state on the measured output; $D \in \mathbb{R}$ is feedforward value, which represent the direct influence of input signal on the measured output; $\boldsymbol{Q} \in \mathbb{R}^{n\times n}$, $\boldsymbol{S} \in \mathbb{R}^n$ and $R \in \mathbb{R}$ form the covariance matrix of $\boldsymbol{w}_k$ and $\boldsymbol{v}_k$; δ_{ij} is the Kronecker symbol.

In this way, the identification problem of state space model can be summarized as: determination of parameters matrices $\boldsymbol{A}$, $\boldsymbol{B}$, $\boldsymbol{C}$ and D by knowing the input and output sequences.

B. MOESP Identification Algorithm

MOESP as one of the subspace identification algorithm has several advantages: 1) no problems brought by parameter iterative optimization because only model order is the only parameter to be determined; 2) no convergence problems and high arithmetic speed based on reliable linear algebra methods, such as singular value decomposition (SVD); 3) computation efficiency can be increased by model order reduction. The specific implementation steps are introduced as follow.

1) Extended State Space Equation

The extended state space equation is composed of Hankel matrices, in which subscript *f* denotes the future moment and subscript *p* denotes the past moment.

$$\boldsymbol{Y}_p = \boldsymbol{\Gamma}_i \boldsymbol{X}_p + \boldsymbol{H}_i \boldsymbol{U}_p + \boldsymbol{G}_i \boldsymbol{W}_p + \boldsymbol{V}_p \tag{4}$$

$$\boldsymbol{Y}_f = \boldsymbol{\Gamma}_i \boldsymbol{X}_f + \boldsymbol{H}_i \boldsymbol{U}_f + \boldsymbol{G}_i \boldsymbol{W}_f + \boldsymbol{V}_f \tag{5}$$

where $\boldsymbol{V}_p$ and $\boldsymbol{V}_f$ are past and future noise Hankel matrices.

The augmented observation matrix $\boldsymbol{\Gamma}_i$ is represented as:

$$\boldsymbol{\Gamma}_i \triangleq \begin{pmatrix} \boldsymbol{C} \\ \boldsymbol{CA} \\ \boldsymbol{CA}^2 \\ \vdots \\ \boldsymbol{CA}^{i-1} \end{pmatrix} \tag{6}$$

The Toeplitz matrix $\boldsymbol{H}_i$ and $\boldsymbol{G}_i$ are presented as:

$$\boldsymbol{H}_i \triangleq \begin{pmatrix} D & 0 & 0 & \cdots & 0 \\ \boldsymbol{CB} & D & 0 & \cdots & 0 \\ \boldsymbol{CAB} & \boldsymbol{CB} & D & \cdots & 0 \\ \cdots & \cdots & \cdots & \cdots & \cdots \\ \boldsymbol{CA}^{i-2}\boldsymbol{B} & \boldsymbol{CA}^{i-3}\boldsymbol{B} & \boldsymbol{CA}^{i-4}\boldsymbol{B} & \cdots & D \end{pmatrix} \tag{7}$$

$$\boldsymbol{G}_i \triangleq \begin{pmatrix} 0 & 0 & 0 & \cdots & 0 \\ \boldsymbol{C} & 0 & 0 & \cdots & 0 \\ \boldsymbol{CA} & \boldsymbol{C} & 0 & \cdots & 0 \\ \cdots & \cdots & \cdots & \cdots & \cdots \\ \boldsymbol{CA}^{i-2} & \boldsymbol{CA}^{i-3} & \boldsymbol{CA}^{i-4} & \cdots & 0 \end{pmatrix} \tag{8}$$

2) Calculation of Model Matrices

The MOESP algorithm, which can identify the model parameters without estimating the state sequence, includes two steps. The first step is to calculate state matrix $\boldsymbol{A}$ and output matrix $\boldsymbol{C}$ by estimating augmented observation matrix $\boldsymbol{\Gamma}_i$; the second step is to calculate input matrix $\boldsymbol{B}$ and feedforward value *D* by constructing least square problem of Toeplitz matrix.

B. NIC Order Determination Method

For state space model, model order is the only parameter to be determined. So estimating the model order accurately has important significance for MOESP algorithm. On one hand, fitting precision can be enhanced by increasing model complexity; on the other hand, probability of overfitting problem increased simultaneously. In this way, the balance between model complexity and degree of fitting should be controlled.

Likelihood function is usually required for traditional information criterions of order determination, such as Bayesian information criterion (BIC). But for state space model, unobserved state matrix $\boldsymbol{x}_k (k = 1,2,\ldots,N)$ is included in likelihood function, where Kalman filtering algorithm is usually used to obtain optimal estimator of state matrix. To avoid relatively complex computation process, a reforming information criterion is proposed in this section.

Assuming there exist an output distribution interval around measured output, which obey normal distribution with $\mu = y_k$ and $\sigma = 0.025(y_{\max} - y_{\min})$ ($y_{\max}$ and $y_{\min}$ are maximum and minimum of output signal). Then we denote the ratio of probability of model predicted value y_{pk} and probability of y_k as normal prediction accuracy:

$$np_k = \frac{N(y_{pk} \mid \mu = y_k, \sigma = 0.025 y_{\max})}{N(y_k \mid \mu = y_k, \sigma = 0.025 y_{\max})} \tag{9}$$

To multiply the normal prediction accuracy of all output signal and replace the likelihood function in BIC, the NIC can be defined:

$$NIC = m\ln(N) - 2\ln\left(\prod_{k=1}^{N} np_k\right) \tag{10}$$

where *m* is the number of parameters in model, *N* is the sampling size.

For (10) we can realize that the smaller NIC is the better identified model is. At the same time, the sampling size is a very identical factor to balance NIC, which appears in both two parts of (10).

III. Simulation Illustration

In this section, a conduction system excited by HEMP is built in Spice simulation environment. Based on the measured input and output signal, the MOESP algorithm is adopted to construct state space models of the system.

A. Spice Simulation

The conduction system is shown in Fig. 1. The parameters of the system are: the height of transmission line is 3m, the radius is 5mm and the earth is lossless; the length is 300m where a simplified transformer model is located at 100m distance; the earth capacitance of transformer model is 300pF, the equivalent resistance and inductance of winding are 5Ω and 2μH respectively; load located at the terminal of the system is a 100Ω resistance.

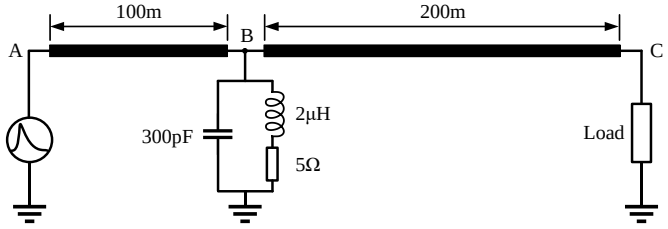

Fig. 1. The sketch of simulated conduction system.

The impulse signal adopts a double-exponential voltage source with amplitude of 100kV, rise time 19.33ns and pulse width 518.7ns, which conform to the requirement of MIL-STD-188-125.

In the simulation, the currents at injected port A and load port C are measured, which are adopted as the input and output signals for state space model identification. The sampling rate is 100M/s which is enough to cover the bandwidth of injected signal. The first 100μs signal are collected for identification without considering the influence

of reflection. In addition, the first 1μs output signal is eliminated as the transmission time of signal from injected port to load port is $t_0 = 300/c = 1\mu s$, which is regarded as zero-input response.

B. State Space System Identification

To identify the state space model of the system, the NIC is adopted to determine the order. The normalized NIC changing curves of the systems is shown in Fig. 2 and the minimum NICs are selected as 5.

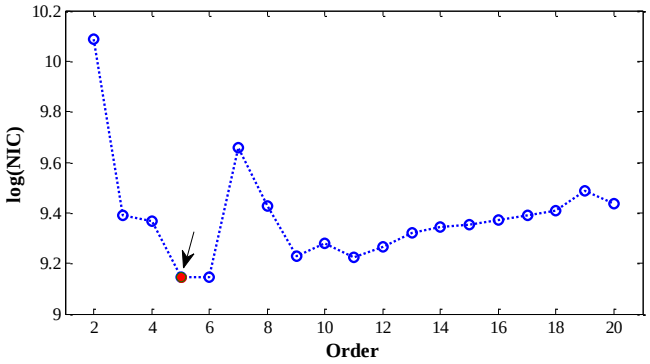

Fig. 2. Normalized NIC changing curves of the system with 100Ω resistance.

Based on the order determined, the waveforms of SSSI prediction and Spice simulation are compared in Fig. 3. In the figure, state space models can be basically equivalent to the system performances, the root-mean-square errors (RMSE) is $RMSE_R = 0.0357$.

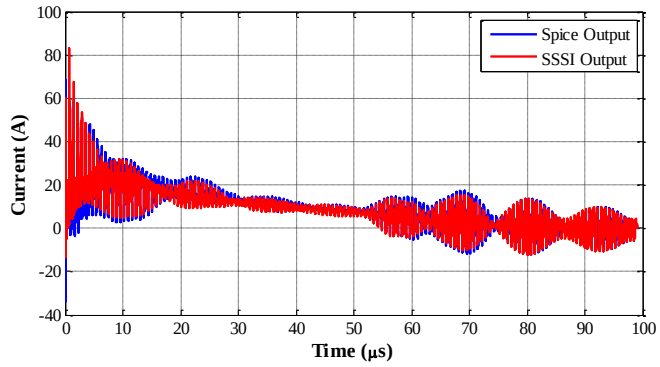

(a)

Fig. 3. Comparison of SSSI prediction and Spice simulation excited by HEMP.

To verify the effectiveness of the identified models, a lightning voltage with amplitude 100kV, rise time 1.2μs and pulse width 50μs is injected as exciting signal.

The sampling rate is 100M/s and the first 200μs signal is selected for system identification. The compared waveforms of SSSI prediction and Spice simulation are shown in Fig. 4 for system with resistive load. The RMSE of the model is 0.0298.

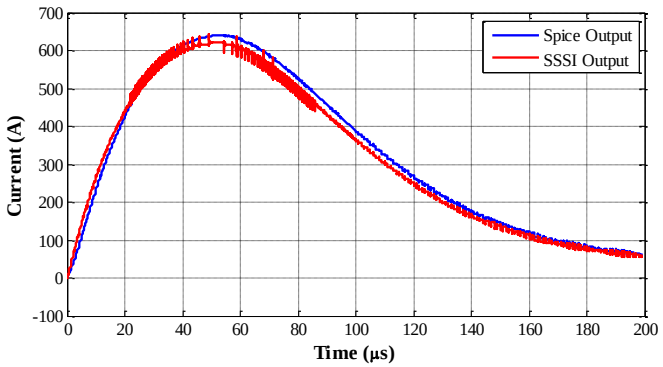

Fig. 4. Comparison of SSSI prediction and Spice simulation excited by lightning pulse.

IV. CONCLUSION

In this paper, SSSI method is proposed to model the HEMP conducted responses and MOESP algorithm is adopted to derive state matrices and system dynamics of state-space models. To avoid complex Kalman filtering algorithm in traditional order determination criterion, a new efficient criterion NIC is proposed. Finally, a simulation study of a conducted case is carried out by Spice program and state-space model is built using input and output data obtained from Spice simulation. The result predicted by SSSI is well identical with simulation result by Spice program.

REFERENCES

[1] D. Nitsch M. Camp, F. Sabath J. L. Haseborg and H. Harbe, "Susceptibility of some electronic equipment to HPEM threats," IEEE Trans. Electromagn. Compat., vol. 46, no. 3, pp. 380-389, Aug. 2004.

[2] M. Camp, H. Gerth, H. Garbe and H. Haase, "Predicting the breakdown behavior of microcontrollers under EMP/UWB impact using a statistical analysis," IEEE Trans. Electromagn. Compat., vol. 46, no. 3, pp. 368-379, Aug. 2004.

[3] D. Mänsson, R. Thottappillil, T. Nilsson, O. Lundén and M. Bäckström, "Susceptibility of civilian GPS receivers to electromagnetic radiation," IEEE Trans. Electromagn. Compat., vol. 50, no. 2, pp. 434-437, May 2008.

[4] J. Xu, W. Yin, J. Mao and L. Li, "Thermal transient response of GaAs FETs under intentional electromagnetic interference (IEMI)," IEEE Trans. Electromagn. Compat., vol. 50, no. 2, pp. 340-346, May 2008.

[5] F. M. Tesche, "Topological concepts for internal EMP interaction," IEEE Trans. Antennas Propagat., vol. AP-26, no. 1, pp. 60-64, Jan. 1978.

[6] Y. V. Parfenov, L. N. Zdoukhov, W. A. Radasky and M. Ianoz, "Conducted IEMI threats for commercial buildings," IEEE Trans. Electromagn. Compat., vol. 46, no. 3, pp. 404-411, Aug. 2004.

[7] B. J. A. M. van Leersum, F. J. K. Buesink, J. G. Bergsma and F. B. J. Leferink, "Ethernet susceptibility to electric fast transients," in Proc. 2013 Int. Symp. Electromagn. Compat. (EMC Europe), Brugge, Belgium, Sep. 2-6, 2013, pp. 29-33.

[8] P. V. Overschee and B. D. Moor, Subspace Identification for Linear System, Kluwer Academic Publishers, 1996.

The Computational Model of Deep Transcranial Magnetic Stimulation and Induced Electric Field Optimization

YuQiao LI
School of Electrical Automation and Information Engineering
Tianjin University
Tianjin, China
yuqiaoli@tju.edu.cn

Jiang Wang
School of Electrical Automation and Information Engineering
Tianjin University
Tianjin, China
jiangwang@tju.edu.cn

XiLe Wei
School of Electrical Automation and Information Engineering
Tianjin University
Tianjin, China
xilewei@tju.edu.cn

Bin Deng
School of Electrical Automation and Information Engineering
Tianjin University
Tianjin, China
dengbin@tju.edu.cn

***Abstract*—Transcranial magnetic stimulation (TMS) is a non-invasive stimulation technique which can induce neural excitation and modulate brain functions. For the treatment of neurological and mental disorders, it is necessary to induce a deep and focused electric field by TMS on the target regions. Previous studies on the induced electric fields were limited to mature coil patterns but few considerations about coil attributes. In this paper, we focus on how to improve the effects of TMS by optimizing different coil attributes. We propose twelve different coils based on three attributes which are the loop offset distance on 2-D plane, the eccentric angle in 3-D space, and the independent loop number of coil array. We use the finite element method to calculate the electric field distributions in an isotropic human brain model and choose penetration depth and stimulation focality as the two most important indicators. We find that the loop offset distance can influence the stimulation focality and penetration depth at the same time, the increasing of the eccentric angle can significantly improve stimulation focality, and the increasing of the loop numbers can distinctly improve the penetration depth. Although a tradeoff between penetration depth and focality was found in almost all attributes, there still is adequate possibility to optimize coils with significant improvement of one indicator but a slight decrease in performance of the other.**

Keywords—Transcranial Magnetic Stimulation, Electric field, Coil attributes, Optimization, Depth, Focality.

I. INTRODUCTION (*HEADING 1*)

As a painless brain modulation technology, transcranial magnetic stimulation (TMS) is becoming an important tool for the treatment of drug-resistant brain disorders, such as Alzheimer's disease (AD), major depressive disorder and Parkinson's disease (PD) [1-6]. TMS stimulator can generate time-varying magnetic fields to induce electric fields via Faraday's Law [7, 8]. Under the influence of specific electric fields, the cortical neurons would be activated via depolarization or hyperpolarization of the membrane potentials [9]. To understand the biologic effects of TMS, the assessment of the induced electric field distribution in the human brain is necessary. Recent studies have proved that neuropsychiatric disorders are also involved in deep brain regions [10-14]. It has led to the optimization of TMS coil, for the purpose of finding a deep and focused electric field induced by TMS.

In this study, we design 14 TMS coils and investigate the effects of main coil attributes on the induced electric fields. We consider three main attributes, 2-D plane loop offset distance, 3-D space eccentric angle, and independent loop number of coil array, which are three important aspects of coil configurations. Except two reference coils, the other 12 coils are separated into three groups with four coils each. To evaluate the performance of the coils, we use a spherical human brain model with realistic geometric dimension in this study, which provides a standard platform without individual difference.

We first describe the characteristics of electric field distribution over the surface of cortex. Then we quantify the penetration depth and focality of the induced electric field [12, 13, 15]. Finally, different electric field characteristics induced by TMS with different transition states of the coil attributes are summarized to provide more detailed guide information for optimizing coil configurations.

II. MODELLING OF COILS AND HUMAN HEAD

In order to examine the electric fields induced by different coils based on three attributes, three kinds of models for human head, air and coils respectively were simulated using ANSYS (version mechanical APDL 15.0, ANSYS, the USA). Among them, the human head model is a homogeneous isotropic sphere of 85 mm radius which is about the average size of a real head. Its electrical conductivity is 0.33 S/m and relative magnetic conductivity is 1. Outside the head and coils is free space with full of air. Then a 300mm × 300mm × 300mm cuboid air model was created with electric conductivity of 0 and relative magnetic conductivity of 1. For the further calculation, all the models were separated into millions of 3-D tetrahedral elements by the software package Hypermesh (Altair Hyperworks, version11.0.0.39, the USA) and each element contained twenty nodes. After grid division, the models were not only electromagnetic solids, but also 3-D impedance networks.

Fig.1 gives the schematic diagram of the simulation models. The excitation coil carrying a known current is placed above the human head model. The material of coil is copper, and its electric conductivity was set to 5.9 × 107 S/m. A sinusoidal current wave with amplitude of I = 5 kA and working angular frequency of ω = 2π * 3 kHz was fed into each loop of coils. A conventional circular coil and a figure-8 coil are regarded as a reference group (Fig. 1, Group 1). Four coil configurations in group 2 are modeled based on different offset distance (d) between two loops of figure-8 coil (coil1: d = 20 mm, coil2: d = 40 mm, coil3: d = 60 mm, coil4: d = 80 mm). Group 3 consists of four different coil configurations based on eccentric angle (a) of butterfly coil (coil1: a = 0°, coil2: a = 30°, coil3: a = 60°, coil4: a = 90°). All coils in group 2 and group 3 consist of two loops with the outer diameter of 86 mm and the inner diameter of 56 mm. Different loop number (n) of coil array are divided into four coil configurations in group 4 (coil1: n = 2, coil2: n = 3, coil3: n = 5, coil4: n = 7). The loop sizes of all coils are the same, with inner diameter of 40 mm and outer of diameter of 44 mm.

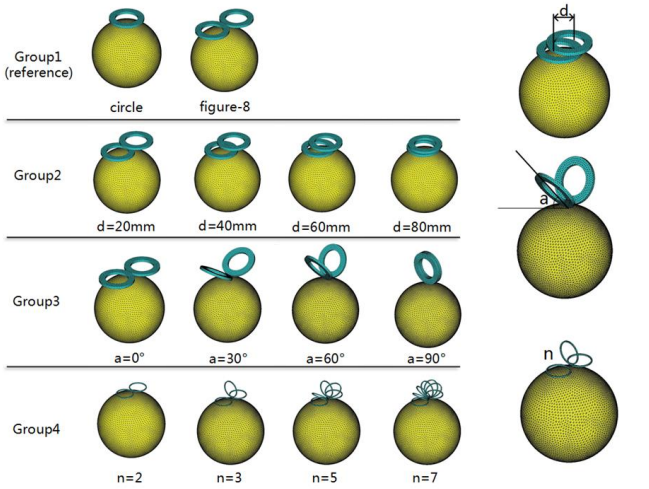

Figure 1. Schematic diagram of the simulation model. Four group coil configurations placed on the spherical head model. The symbols d, a and n represent offset distance between two loops, eccentric angle and loop numbers, respectively.

III. RESULTS

A. *Electric field distribution*

Fig. 2 illustrates color intensity maps of the electric field distributions on the brain surface induced by fourteen coils with different configurations. The warmer colors represent areas with bigger electric field amplitudes, while the cooler colors represent areas with smaller ones. The electric fields induced by the single-circular coil and the figure-8 coil belong to group 1 as shown in the first line of Fig. 2. Similar to previous studies, it is evident that the electric field induced by the figure-8 coil has better focality than the conventional single-circular coil and involves more brain regions.

Group 2 in Fig. 2 shows the effects of offset distance (d) between two loops of figure-8 coil on the induced electric field distributions. As d is increased from 20mm to 80mm, the distribution area with maximal electric field amplitude (red area) gets larger and the entire stimulated area (except blue area) becomes smaller. And it is worth mentioning that the maximum of electric field amplitude distribution gets scattered when d = 80 mm. It means that this coil does not have the ability to stimulate focused.

In group 3, the eccentric angle is changed from 0° to 90°, the whole electric field induced by these coils are evidently distributed in the brain area below the center of the two loops. The variety mainly concentrates on the green area. As the increase in angle, the green area is changed from a circular to a dumbbell-shaped distribution and become smaller. Compare to the group 2, the coils in group 3 have stronger focality. If the simulation threshold is selected as 50% of $E_{\max}$, the area of dumbbell-shaped distribution is less than initial circular distribution. It shows that increasing eccentric angle of TMS coils in 3-D space can significantly improve the focality of electric fields.

Group 4 is the decomposition of coil array, which contains four coils with different numbers of loops. All the electric field distributions in this group are similar, and just have a little growth in area. As the number of loops increases, the stimulation area (except blue area) shows a tendency to slowly expand. It shows that the independent loop number of coil array in the same space has a weak influence on the focality of electric fields.

From the perspective of stimulated area size, comparing four group coils, we can find that all the coils in the groups 1, 2 and 3 have better characteristics than the single- circular coil in group 1, and all the coils in the groups 2 and 3 have better characteristics than the figure-8 coil in group1.

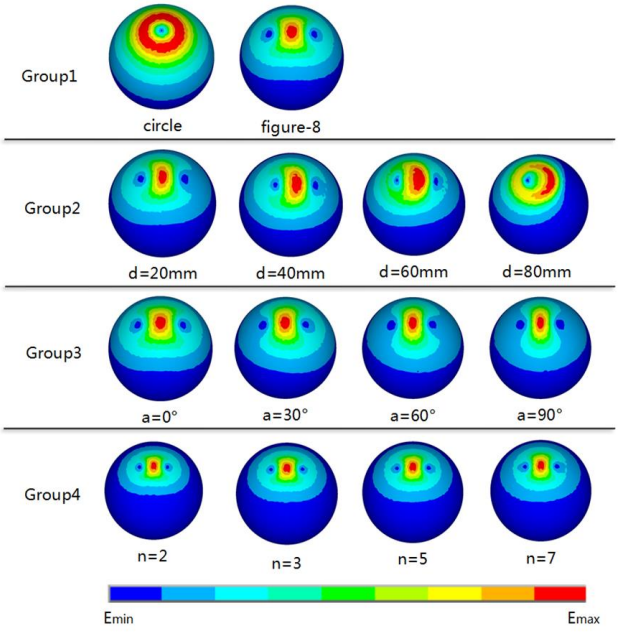

Figure 2. Electric field distributions on the surface of the brain model induced by fourteen different coils with different configurations. The electric field amplitudes are normalized respect to the maximum electric field amplitude for each coil configuration.

B. *Identify the Headings*

Similarly, to better quantify the spread of these electric field amplitude distributions in the brain, we calculate the half volume percentage， which is the percentage of brain volume exposed to an electric field amplitude equal to or

greater than 50% of $E_{\max}$. It is very apparent that the single-circular coil in reference group has a large value of half volume and even five times more than that in group 4. Variation trends are evident in all other group. In the group 2, the values of half volume increase with the increasing of d, and it means that more loop offset distance in coils, less focality the electric field can achieve. When d = 20 mm, the half volume is the smallest and the electric field induced by this coil configuration get best focality among this group. As the eccentric angle of coils in the group 3 changes from 0° to 90°, the half volumes show a marked decreasing trend, which means the increase of the coil eccentric angle can strengthen the focality to make less side effects. The half volumes in the group 4 show very low values and a very weak increasing trend as the number of loops increases. It is shown that the coil with more loop numbers will stimulate more brain regions but cause just a little side effect.

REFERENCES

[1] *Gideon Vardi MD MPH, Joav Merrick M D. Neurological Disorders. Public Health Challenges[J]. Journal of Policy & Practice in Intellectual Disabilities, 2010,5(1):75-75.*

[2] *Walsh V, Rushworth M. A primer of magnetic stimulation as a tool for neuropsychology.[J]. Neuropsychologia, 1999, 37(2):125-35.*

[3] *Fridley J, Thomas J G, Navarro J C, et al. Brain stimulation for the treatment of epilepsy.[J]. Neurosurgical Focus, 2012, 32(3):E13*

[4] *Fitzgerald P B , Daskalakis Z J . The effects of repetitive transcranial magnetic stimulation in the treatment of depression.[J]. Expert Review of Medical Devices, 2011, 8(1):85-95.*

[5] *Polanía R, Nitsche M A, Ruff C C. Studying and modifying brain function with non-invasive brain stimulation.[J]. Nature Neuroscience, 2018.*

[6] *Hallett M. Transcranial magnetic stimulation and the human brain[J]. Nature, 2000, 406(6792):147-150.*

[7] Barker A T, Jalinous R, Freeston I L. "Non-invasive magnetic stimulation of human motor cortex." Lancet, 325(8437):1106-1107, 1985.

[8] Parazzini M, Fiocchi S, Chiaramello E, et al. Electric field estimation of deep transcranial magnetic stimulation clinically used for the treatment of neuropsychiatric disorders in anatomical head models.[J]. Medical Engineering & Physics, 2017, 43:30–38.

[9] Pashut T, Wolfus S, Friedman A, et al. Mechanisms of Magnetic Stimulation of Central Nervous System Neurons[J]. Plos Computational Biology, 2011, 7(3):e1002022.

[10] Lu M, Ueno S, Dong X W. Deep transcranial magnetic stimulation using the semi-Halo coil[C], Progress in Electromagnetic Research Symposium. IEEE, 2016:4644-4647.

[11] Bersani F S, Minichino A, Enticott P G, et al. Deep transcranial magnetic stimulation as a treatment for psychiatric disorders: a comprehensive review[J]. Eur Psychiatry, 2013, 28(1):30-39.

[12] V. Guadagnin, M. Parazzini and S. Fiocchi, et al., Deep transcranial magnetic stimulation: modeling of different coil configurations[J], IEEE Transactions on Biomedical Engineering, 2016, 63(1):1543-1550.

[13] Lu M, Ueno S. Comparison of the induced fields using different coil configurations during deep transcranial magnetic stimulation.[J]. Plos One, 2017, 12(6):e0178422.

[14] Meng Y, Hadimani R L, Crowther L J, et al. Deep brain transcranial magnetic stimulation using variable “Halo coil” system[J]. Journal of Applied Physics, 2015, 117(17):1106-128.

[15] Peterchev A V, Wagner T A, Miranda P C, et al. Fundamentals of Transcranial Electric and Magnetic Stimulation Dose: Definition, Selection, and Reporting Practices[J]. Brain Stimulation, 2012, 5(4):435-453.

Investigation of power loss caused by the antenna connected to a gyromagnetic nonlinear transmission line

Yuwei Wang
College of Advanced Interdisciplinary Studies
National University of Defense Technology
Changsha 410073, P. R. China
ywei_wang@163.com

Dongqun Chen
College of Advanced Interdisciplinary Studies
National University of Defense Technology
Changsha 410073, P. R. China
csycdq@163.com

Zicheng Zhang
College of Advanced Interdisciplinary Studies
National University of Defense Technology
Changsha 410073, P. R. China
successchang@163.com

Shengguang Cao
College of Advanced Interdisciplinary Studies
National University of Defense Technology
Changsha 410073, P. R. China
csg_7005@sina.com

Da Li
College of Advanced Interdisciplinary Studies
National University of Defense Technology
Changsha 410073, P. R. China
xuannudt@163.com

***Abstract*—Gyromagnetic nonlinear transmission line (NLTL) is generally implemented by a transmission line filled with saturated ferrite. It has been proved to have the ability of generating high power RF oscillation without relativistic electron beam. After the interaction with the gyromagnetic NLTL, the incident pulse is directly modulated. A high power RF source based on a gyromagnetic NLTL has been developed at National University of Defense Technology (NUDT) recently. In this system, a patch array antenna was employed as the radiating antenna, while a band-pass filter was connected between the gyromagnetic NLTL and the antenna to filter the low frequency component and extract the high power RF oscillation. The output signal of the filter and the radiated electric field measured at a distance of 13 m is shown in Fig. 1 and Fig. 2, respectively. The peak power of the signal as shown in Fig. 1 exceeded 100 MW. However, the radiated peak power was only less than 50 MW. It means significant power loss has been brought by the antenna. To understand the reason of this power loss, the transient response of the antenna was investigated. As analyzed, it can be attributed to the relatively narrow bandwidth of the antenna. To reduce the power loss, the low frequency radiating efficiency of the antenna should be improved. This is proved by the simulation of another antenna.**

Keywords—gyromagnetic, nonlinear transmission line, antenna, power loss, transient response

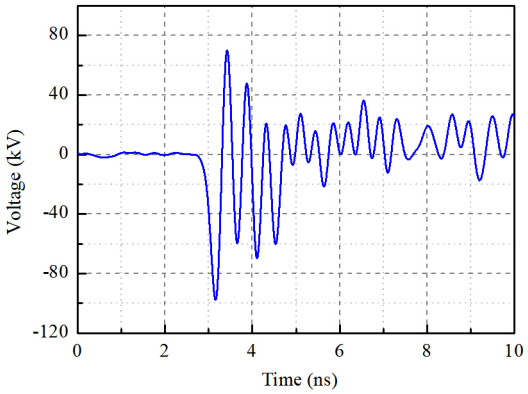

Fig. 1 High power RF oscillation extracted by the band-pass filter from the output pulse of the gyromagnetic nonlinear transmission line

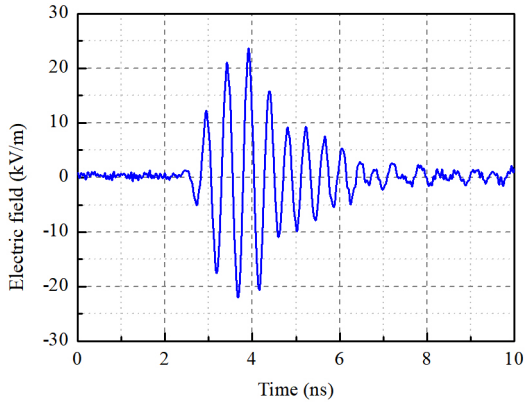

Fig. 2 Radiated electric field at a distance of 13 m

The circuit model of linear-mode, vertical SiC PCSS

Zhao, Yuxin
National University of Defense Technology
College of Advanced Interdisciplinary Studies
Changsha, Country
447452531@qq.com

Wu, Qilin
National University of Defense Technology
College of Advanced Interdisciplinary Studies
Changsha, Country
Kylinwu570@163.com

Yang, Hanwu
National University of Defense Technology
College of Advanced Interdisciplinary Studies
Changsha, Country
yanghw@nudt.edu.cn

***Abstract*—At present, the generation method of High Power Microwave (HPM) is making a transition from the generation of electric vacuum devices to solid state devices. Under the excitation of modulated light, a pulsed power source based on the light-switching technology can generate a radio frequency signal to realize the synchronous conversion of the light to the microwave signal, and finally generate high-power microwave [1] [2]. The HPM solid-state amplification generation method based on the SiC linear operation mode is expected to modulate the pulse width and frequency to improve the operating voltage and amplification efficiency. In this paper, PSpice software was used to construct a 6H-SiC photoconductive switch circuit model with V-doped positive electrode structure. The light absorption process of SiC material, the photocarrier concentration, on-resistance expression, and the light saturation condition were analyzed. The optical saturation model was established by limiting the concentration of impurities to the concentration of photogenerated electrons. In addition, factors such as the dependence of carrier mobility on the electric field and parasitic capacitance of the switch were incorporated into the model. The results calculated using the variable electronic lifetime expressions in the model are consistent with the literature data, and the simulated waveforms are in good agreement with the experimental results. This model converts the SiC photoconductive switch into a PSpice circuit component, which fits its working characteristics, and provides an effective reference for the experiment and design of the optical waveguide microwave system.**

Keywords—circuit model, SiC PCSS, photoconducting devices, PSpice

I. INTRODUCTION

As a representative of the third-generation wide bandgap semiconductor materials, silicon carbide (SiC) photoconductive semiconductor materials operating in a linear mode have many advantages: high breakdown electric field strength, large dark state resistance, high carrier drift rate, and heat. High-conductivity, the light-conducting switch with its core material has the advantages of small volume, low jitter (ps), fast response speed (ps), high repetition frequency and long working life, which can meet the compactness of pulse power device [3] [4] [5]. The demand for all-solid-state and high-repetition frequency operation has broad room for development in terms of high repetition rate and power capacity.

In this paper, a PSpice circuit model suitable for the electrode structure SiC-PCSS is established, which mainly considers the light absorption process in the photoconductive switch, the electron mobility changes with the field strength, the number of photogenerated carriers under the saturated light intensity, and the capacitance. The influence of inductance and other factors on the on-resistance of SiC provides a reference for predictive analysis of the working characteristics of SiC photoconductive switches.

II. PSPICE MODEL OF SIC PHOTOCONDUCTIVE SWITCH

The PSpice model of SiC material on-resistance in linear operation mode is constructed, which mainly includes the following parts: photoconductive switch working circuit and electron mobility simulation, carrier concentration simulation and on-resistance simulation.

The working circuit of the photoconductive switch and the electron mobility μn simulation are shown in Fig. 1. We consider it as an ideal varistor in parallel with the ideal capacitor.

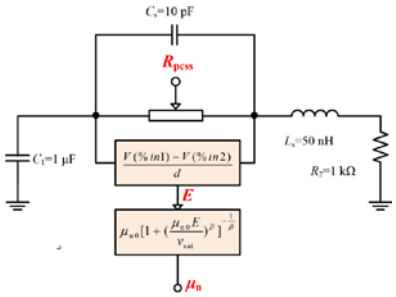

Fig. 1 SiC photoconductive switch working circuit and electron mobility simulation

In addition to the electron mobility, the carrier concentration $n(t)$ is also an important factor affecting the on-resistance of the switch. With the idea of analog computing technology, we solve the expression (1) of $n(t)$ in PSpice, as shown in Figure 2.

$$\frac{dn(t)}{dt} = N_T K\sigma_{op} I(t) - \sigma_n v_{th} n(t)[\frac{K\sigma_{op} I(t)}{\sigma_n v_{th}} + N_V - N_T] - \sigma_n v_{th}[n(t)]^2 \quad (1)$$

The model parameter is set to: photon energy $h\nu$=1.874×10^{-19} J, linear absorption rate of the semiconductor material α=80 m^{-1}, the thickness of the semiconductor wafer d=400 μm, incident light cross-sectional area S_1=0.04 cm^2, electron mobility of 6H-SiC along the C axis of crystal μ_{n0}=415 cm^2·V^{-1}·s^{-1}, quantum efficiency η=0.1, element charge q=1.6×10^{-19} C, surface reflectance of SiC r=0.205, peak optical power I_{max}=1.8×10^6 W, constant b=17 ns, constant c=1.98554 ns, empirical parameter β=1.7, V acceptor level optical transition cross section σ_{op}=1×10^{-17} cm^2, V acceptor level electron capture cross section σ_n=5.77×10^{-16} cm^2, electron thermal velocity

v_{th}=1.16796×10^{7} cm/s, difference between N and B concentration N_t=2.05×1016 cm^{-3}, V density N_v=1.75×10^{17} cm^{-3}. The electron lifetime was calculated to be 948 ps using equation (2), which is in good agreement with the results of 960 ps in the literature [6], with a relative error of 1.3%.

$$\tau = (\sigma_n v_{th})^{-1}[N_V - N_T + n(t) + \frac{K\sigma_{op} I(t)}{\sigma_n v_{th}}]^{-1} \quad (2)$$

Figure 3 compares the carrier concentration simulation results with the light pulse waveforms, where the light pulses are normalized. It can be seen that the electron concentration peak time lags the optical power peak time by 920 ps, and its half-height pulse width is increased by 340 ps compared to the latter, which can be attributed to the influence of electronic lifetime and external circuit parameters. As an example, take N_v=1×10^{17} cm^{-3}, N_t=9×10^{15} cm^{-3}, and the calculated electronic lifetime is 158 ps, which is close to the measurement result of 140 ps in the literature [7]. The error comes from ignoring the existence of electron traps, which can lead to a reduction in electron lifetime. The above results preliminarily verified the validity of the model.

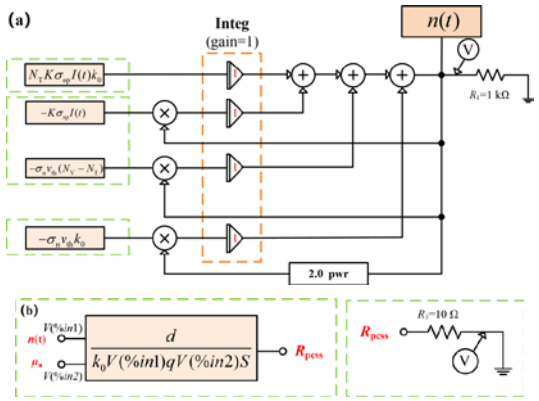

Fig. 2 (a) PSpice solution to the differential equation with n(t); (b) Simulation of the on-resistance of SiC photoconductive switch

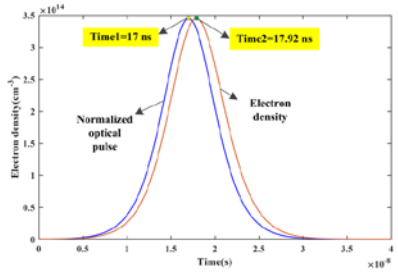

Fig. 3 Comparison of carrier concentration analog value with optical pulse signal

III. EXPERIMENTAL VERIFICATION

The SiC photoconductive switch used in the experiment belongs to the V-doped semi-insulating type, which is mainly composed of V, N and B doping, and adopts a positive electrode-type structure. Figure 4 shows an epoxy-encapsulated SiC photoconductive switch with a thickness of 200 μm and a side length of 1 cm in the "a" plane. Tested 532 nm pulsed laser with a single pulse output with a maximum energy of 1.2 mJ, a half-height width of approximately 1.7 ns, and a repetitive frequency of 20 Hz.

Fig. 4 SiC-PCSS packaged epoxy

The measurement experiment layout is shown in Figure 5. The laser light pulse is modulated into a two-pulse laser signal that is input to the interior of the switch in a manner perpendicular to the plane of the electrode. The optical signal is detected by a photodiode and passed to the oscilloscope. At the bias voltage, SiC operates in a linear mode and outputs the amplified oscillating electrical signal. The circuit uses a high-voltage DC power supply, and a current-limiting resistor and a load resistor are connected in series with the switch. The functions of the circuit are respectively to protect the circuit and facilitate the measurement of the voltage. The pulse capacitor is connected in parallel with the switch and discharged through the switch and the load resistor. In order to meet the needs of pulse high current measurement, the current through the load is simultaneously measured by a CVR detector with a resistance of 0.05 Ω and a 8585C Rogowski coil with a sensitivity of 1 V/A.

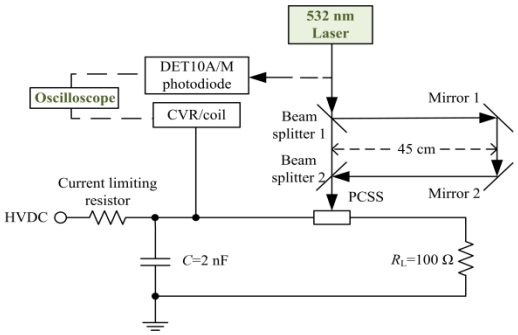

Fig. 5 Experimental layout

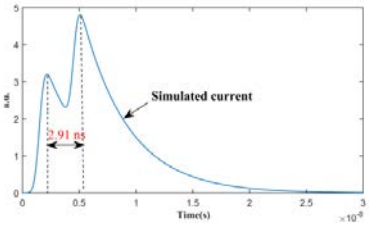

(a) Simulation waveform

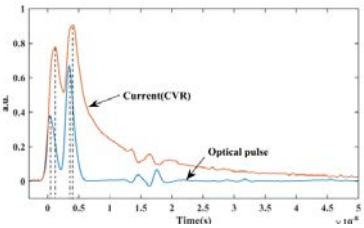

(b) Experimental waveform

Fig. 6 Comparison of simulated waveforms and experimental waveforms

The simulated waveform and the experimental waveform are shown in Fig. 6(a) and (b), respectively, and the two

basically match. In the current simulation waveform, the double pulse peaks differ by 2.91 ns, and the tail is about 25 ns. In the current experiment waveform, the double pulse peaks differ by 3.1 ns, and the first peak is 0.9 ns behind the peak time of the optical pulse, and 0.6 ns behind the second time, which is basically consistent with the simulation. It can be seen from Fig. 6(b) that the current experiment waveform tailing is relatively long, because when the loop inductance begins to release the energy storage, the partial pressure across the switch appears an instantaneous high voltage; during the phase of the light pulse annihilation, the switch still continues. There is a higher voltage and the voltage gradually decays, forming a tail. The experimental waveform has a slight oscillation phenomenon, which is mainly caused by the influence of the capacitance between the switches, and can effectively solve this problem by adjusting the load resistance. The minimum on-resistance simulation value is about 1.56 kΩ, and it is estimated to be several thousand ohms according to the current value in the experiment, but both moments appear at 0.5 - 0.6 ns after the second peak, which is consistent.

IV. Conclusion

In this paper, PSpice software was used to construct a 6H-SiC photoconductive switch circuit model with V-doped positive electrode structure. The light absorption process of SiC material was considered, and the photocarrier concentration and on-resistance expression were obtained. The light saturation condition was analyzed, and the optical saturation model was established by limiting the concentration of impurities to the concentration of photogenerated electrons. In addition, factors such as the dependence of carrier mobility on the electric field and the capacitance between the switches were incorporated into the model. The results calculated using the variable electronic lifetime expressions in the model are consistent with the literature data, and the simulated waveforms are in good agreement with the experimental results. This model converts the SiC photoconductive switch into a PSpice circuit component, which fits its working characteristics, and provides an effective reference for the experiment and design of the optical waveguide microwave system. Further refinement of the model can be carried out in consideration of factors such as electron traps and two-photon absorption.

References

[1] A. Karabegovic and R. M. O'Connell, “Photoswitch-controlled class e RF power amplifier,” in Conference Record of the 2006 Twenty-Seventh International Power Modulator Symposium. IEEE, may 2006, pp. 150–152, DOI: 10.1109/modsym.2006.365204.

[2] C.-J. Huang and R. M. O'Connell, “Optoelectronic class AB microwave power amplifier,” in Conference Record of the 2006 Twenty-Seventh International Power Modulator Symposium. IEEE, may 2006, pp. 146–149, DOI: 10.1109/modsym.2006.365203.

[3] M. Pocha and R. Druce, “35-kV GaAs subnanosecond photoconductive switches,” IEEE Transactions on Electron Devices, vol. 37, no. 12, pp. 2486–2492, Dec 1990, DOI: 10.1109/16.64522

[4] W. Nunnally and M. Mazzola, "Opportunities for employing silicon carbide in high power photo-switches," Digest of Technical Papers. PPC-2003. 14th IEEE International Pulsed Power Conference (IEEE Cat. No.03CH37472), Dallas, TX, USA, 2003, pp. 823-826 Vol.2. doi: 10.1109/PPC.2003.1277936

[5] J. Y. Tsao, S. Chowdhury, M. A. Hollis, D. Jena, N. M. Johnson, K. A. Jones, R. J. Kaplar, S. Rajan, C. G. V. de Walle, E. Bellotti, C. L. Chua, R. Collazo, M. E. Coltrin, J. A. Cooper, K. R. Evans, S. Graham, T. A. Grotjohn, E. R. Heller, M. Higashiwaki, M. S. Islam, P. W. Juodawlkis, M. A. Khan, A. D. Koehler, J. H. Leach, U. K. Mishra, R. J. Nemanich, R. C. N. Pilawa-Podgurski, J. B. Shealy, Z. Sitar, M. J. Tadjer, A. F. Witulski, M. Wraback, and J. A. Simmons, “Ultrawidebandgap semiconductors: Research opportunities and challenges,” *Advanced Electronic Materials*, vol. 4, no. 1, p. 1600501, dec 2017, DOI: 10.1002/aelm.201600501.

[6] J. S. Sullivan, Wide bandgap extrinsic photoconductive switches, Ph.D.dissertation, Lawrence Livemore National Laboratory, Jul 2013, DOI: 10.2172/1088462.

[7] Tamulaitis, G., Yilmaz, I., Shur, M. S., et al. "Carrier lifetime in conductive and vanadium-doped 6H-SiC substrates." Applied Physics Letters 84.3(2004):335, DOI: 10.1063/1.1641172.

Electromagnetic Transient Simulation and Analysis Caused by 500kV Side Switching of Nuclear Power Plant

Wu Yuying
College of Electrical Engineering, Xi'an Jiaotong University
Xi'an ,China
yywu626@stu.xjtu.edu.cn

Qiu Yunpeng
College of Electrical Engineering, Xi'an Jiaotong University
Xi'an ,China
a04145116@163.com

Guo Jie
College of Electrical Engineering, Xi'an Jiaotong University
Xi'an ,China
jguo0510@xjtu.edu.cn

***Abstract*—In the conventional island of a nuclear power plant, no-load tripping is one of the common operations, but the capacitive current and the inductive current of tripping will have problems of arc re-ignition and current chopping, respectively, resulting in electromagnetic oscillation and the overvoltage of the line, which threats the overall operation and safety of electrical equipment. Therefore, in this paper, the EMTP-RV software is used to construct the electromagnetic transient simulation model. The process of electromagnetic oscillation and the formation mechanism of overvoltage in the process of switching are calculated and analyzed. The results show that the re-ignition of arc switching the capacitive current can lead to a strong electromagnetic oscillation to generate a higher overvoltage, while switching the inductive current, the arc re-ignition is an advantageous factor to reduce the overvoltage.**

Keywords—electromagnetic transient, switching, re-ignite, current chopping

I. INTRODUCTION

The nuclear power plant is composed of nuclear islands, conventional islands, supporting facilities and safety protection measures. The conversion process among thermal energy, mechanical energy and electric energy is basically done in the conventional island. Therefore, this paper deals with the electromagnetic transient process caused by switching of the 500kV side of the conventional island substation.

When the no-load tripping occurs, the continuous conversion, transmission and gathering of electromagnetic energy inside the system produces a high overvoltage amplitude, and the duration on the transmission line side is also long, which will have a large impact on the insulation of the line[1-3]. Up to now, although the level of insulators in China has reached a certain height, the phenomenon of flashover and breakdown of insulators caused by no-load tripping operation has not been completely eliminated, and the circuit breaker may still have re-ignition of the arc. Therefore, the research on the electromagnetic transient process of no-load tripping with the re-ignition of the arc is of great significance[4-6].

In this paper, the EMTP-RV electromagnetic transient software is used to build the simulation model of the nuclear power plant conventional island, and the 500kV side airborne opening and closing situation is calculated and analyzed.

II. SIMULATING AND CALCULATING

A. Switching the Capacitive Current: Cut Off the No-load Line

Switching capacitive current is one of the common operations in the power grid. In the power system, the capacitor current at the fault is often removed due to some situations. Because of the opening and closing of the switch, the re-ignition of the arc may occur, and the re-ignition of the arc may cause electromagnetic oscillation, which may cause an overvoltage at the contact. Taking the no-load line tripping as an example, each component is represented by a simplified single-phase concentration parameter shown as Figure 1 [6-7].

In the figure, the lumped parameter equivalent transmission line is represented by T-type circuit in actual operation, where Ls is the power equivalent inductor, C_T is the line-to-ground capacitance, L_T is the transmission line inductance, and the power supply potential e(t) is set to e(t)=Em·cosωt. Before the QF is disconnected, the line power on the no-load line is $U_C(t)=e(t)$, assuming the first arc-extinguishing occurs (t_1) when the power frequency capacitor current $i_C(t)$ occurs at zero crossing time. As shown in Figure 2, for better analysis, assuming that the leakage of the wire does not occur, then after half a cycle, $U_C(t)$ becomes Em, besides, the voltage between contacts, Ur(t), is as follows:

$$U_r(t) = e(t) - E_m = E_m(cos\omega t - 1) \quad (1)$$

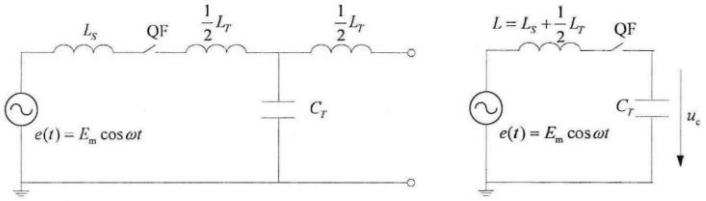

Figure 1. Breaking no-load line equivalent calculation circuit

At this time, e(t) becomes -Em. This is the maximum value that the recovery voltage will reach, 2Em. If the insulation strength between the contacts does not reach the predetermined effect at the time of recovery, then at $t=t_2$, the arc is very likely to re-ignite. At this point, a varying voltage is generated across the line capacitance C_T, and the voltage transitions from +Em to the steady-state voltage -Em. High-frequency vibrations also occur at this time, during which the maximum voltage on the line will change from U_{Cmax} to-3Em. According to the assumptions in the figure, the high-

frequency current will cross zero at $t=t_3$. When the circuit breaker performs the reclosing process, the line loop oscillation angular frequency is greater than ω at the power frequency, and the arc extinguishing phenomenon of the capacitor current will occur when the current first zero crossing. Then $U_C(t)$ is reserved as -3Em. After half the power frequency period ($t=t_4$), the power supply potential e(t) will reach the maximum again. At this time, the maximum voltage $U_C(t)$ between the switch contacts is 4Em. According to this law, any one of the power frequencies in the system will reignite the arc at half the period, a high voltage is generated between the contacts. Only when the insulation strength between the contacts becomes high, does no re-ignition occur between the contacts.

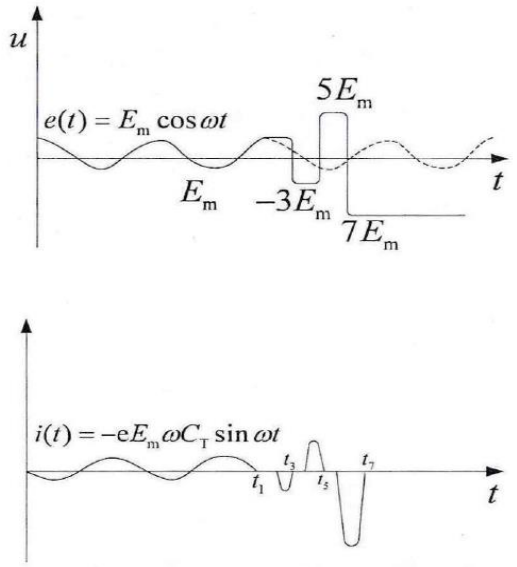

Figure 2. Switching the no-load line overvoltage development process

In the actual situation, when the no-load line is excluded, the over-voltage cannot be infinitely large due to many uncommon factors. For example, when the overvoltage on the line reaches a very high value, a severe corona will appear on the line. The overvoltage wave will carry a lot of energy, and the generated energy will be consumed by the corona, which will cause the voltage wave to attenuate, thus limiting the overvoltage.

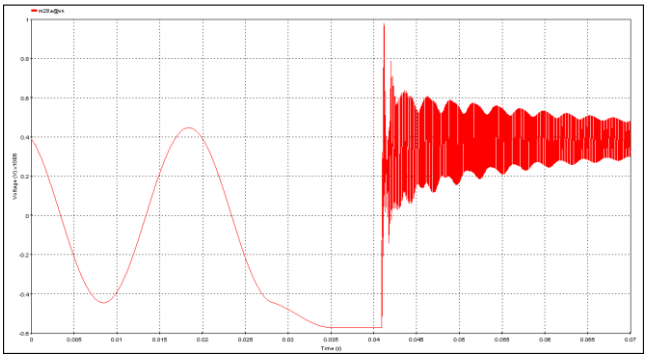

Figure 3. The waveform of voltage on the 500kV side when no-load line is opened and a re-ignition is considered

During the simulation, the 500kV side no-load line is opened and a re-ignition is considered. The simulation results obtained are shown in the figure 3.

The 500kV line side overvoltage reaches 2.282p.u. (base value is $525 \times \frac{\sqrt{2}}{\sqrt{3}}$kV) . According to Q/CSG 1 0011—2005, Electrical technology guide for the 220kV~500kV substation, the relative statistical overvoltage generated on the line of the 500kV system should not be greater than 2.0 p.u. With the existing arrester setting, the overvoltage generated by re-ignition once does not meet the requirements. Therefore, the parameters of the arrester are improved, and the MOA of model Y20W-420/1006 is used to place MOA Y20W-444/1050.

B. Switching the Inductive Current:Cut Off the No-load Transformer

In normal operation, the no-load transformer behaves as an inductive load. When the AC current above 100A is cut off, the arc between the switch contacts is normally extinguished when the power frequency current naturally crosses zero. In this case, the magnetic field energy stored in the inductor is zero, so no overvoltage is generated during the ablation process. However, when the no-load transformer is cut off, the no-load current of the transformer is cut off. The value is very small, which is 0.2%~4% of the rated current of the transformer. The arc-extinguishing capability of the circuit breaker is very strong relative to this current, so that the no-load current is cut off due to forced arc extinction before the zero-crossing current, that is the current chopping. If the no-load current $i=I_0$ is cut off, then the sudden drop of I_0 to zero when the power supply voltage is U_0, the energy stored in the inductor and capacitor at the moment of cutting is :

$$W_L = \frac{1}{2} L I_0^2 \tag{2}$$

$$W_C = \frac{1}{2} C U_0^2 \tag{3}$$

After that, electromagnetic oscillation occurs in the oscillation circuit composed of L and C. At a certain moment, all the electromagnetic energy becomes electric field energy. At this time, the maximum overvoltage Umax appears on the capacitor C, according to the law of conservation of energy, Umax is :

$$U_{max} = \sqrt{\frac{L}{C} I_0^2 + U_0^2} \tag{4}$$

It can be seen that the larger I_0 value of the choipping instant, the larger the magnetizing inductance L of the no-load transformer of the transformer is, the larger the magnetic field energy is. In addition, the smaller the capacitance C is, the smaller the magnetic field energy is converted into the capacitor, and the higher the overvoltage is generated.

During the simulation, the 500kV side no-load line is opened and a re-ignition is considered. The simulation results obtained are shown in the figure 4. The 500kV line side overvoltage reaches 1.350p.u. (base value is $525 \times \frac{\sqrt{2}}{\sqrt{3}}$kV) , which meets the acquirement of the guide book.

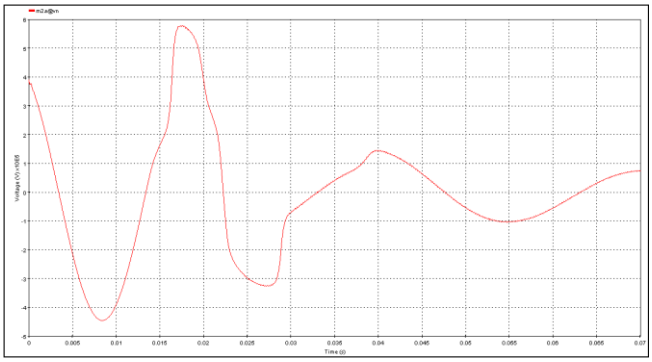

Figure 4. The waveform of voltage on the 500kV side when no-load transformer is opened

In the actual process of cutting off the no-load transformer, multiple arc re-ignition occurs between the contacts of the circuit breaker. This is because the current chopping causes a large recovery voltage between the contacts of the circuit breaker while causing an overvoltage. The recovery voltage rises quickly. Therefore, during the cutting process, when the distance between the contacts is not sufficiently large, re-ignition may occur.

During multiple re-ignitions, the reduction in energy limits the magnitude of the overvoltage. Contrary to the case of removing the no-load line, re-ignition is a favorable factor for reducing the overvoltage. In addition, a considerable part of the magnetic energy will disappear due to the loss of the transformer core and copper wire during the oscillation process, so the actual overvoltage will be much lower than the above-mentioned maximum overvoltage.

III. CONCLUSIONS

Based on the conventional island simulation model, this paper simulates the electromagnetic transient process when tripping and draws the following conclusions:

(1) When the no-load line is cut off, a re-ignition will result in higher amplitude oscillations, resulting in an increase in overvoltage on the line. Improving the parameters of the arrester can suppress the 500kV side overvoltage within a reasonable range.

(2) When the no-load transformer is cut off, current chopping occurs, and the no-load current is forced to extinguish the arc before being cut off. At this time, electromagnetic oscillation occurs in the oscillation circuit composed of L and C, and overvoltage is generated. The larger I_0, the larger the overvoltage. In addition, in this case, multiple arc re-ignition between the contacts of the circuit breaker is an advantageous factor for reducing the overvoltage.

ACKNOWLEDGMENT

I sincerely thank Professor Guo Jie for guide in this project. Besides, my classmate Qiu Yunpeng also helps me a lot in modeling, simulation and analysis of results so that I have learned a lot.

REFERENCES

[1] Zhang Cunzhu. “Simulation analysis of overvoltage of 750kV no-load line under arc reignition”[D]. Anhui University of Science and Technology, 2017.

[2] Zhang Cunzhu, Li Xiang. “Analysis of over-voltage simulation of opening operation under arc reignition of 500kV transmission line based on ATPdraw”[J]. Heilongjiang Science and Technology Information ,2016(33):178.

[3] Wang Yongqiang.“Research on vacuum switch operation overvoltage and its protection” [D]. North China Electric Power University, 2002.

[4] Zhang Ligang. “Suppression Analysis of Cutoff Overvoltage Generated by Vacuum Circuit Breaker Breaking Small Inductor Current”[J]. Electrical Engineering, 2007(12):60-62.

[5] Zhai Shuai, Zhang Peide, Fang Chunen, Li Wei, Chen Chuanjiang, Ren Xiao. “Study on the best switching phase of no-load transformer”[J].Water Power Science, 2018,36(11):178-181+91.

[6] Qi Huaying. “Research on calculation of no-load tripping overvoltage of high voltage transmission lines” [D]. Guangxi University, 2013.

Effect of Penetrating Conductors on Shielding Effectiveness of Metallic Enclosures

Z. Wang, N. Mora*, C. Romero[§], M. Nyffeler[§], F. Rachidi**
**EMC Laboratory, Swiss Federal Institute of Technology (EPFL), Switzerland*
[§] HPE Laboratory, Armasuisse Science and Technology, Switzerland

***Abstract*—In this paper we report a simulation study on the effect of penetrating conductors such as dowels, anchors or cables on the shielding effectiveness of metallic enclosures.**

***Keywords*—** *HPEM environment; metallic enclosure; penetrating conductors; shielding effectiveness.*

I. Introduction

The purpose of this study is to analyze the effect of penetrating conductors such as dowels, anchors or cables on the shielding effectiveness of metallic enclosures [1, 2]. The shielding effectiveness is often analyzed disregarding the presence of penetrations. The penetration of conductors may seriously degrade the shielding effectiveness of the overall shield [2, 3].

This study performs a systematic analysis of the effect of penetrating conductors on the shielding effectiveness of a metallic enclosure. The shielding effectiveness is evaluated using a high-altitude EMP incident field directly illuminating the enclosure. The coupling field inside the enclosure, as well as the induced current along a bare conductor placed above the ground floor (panel), are used to assess the effect of the penetrating conductors. The numerical simulations are conducted using CST microwave studio.

II. Shielding Configuration and Radiated Scenario

As illustrated in Fig. 1, the considered shielding configuration is a 4-m long, 2.5-m wide and 3-m high metallic enclosure with 6 side walls of 80-cm thickness. Five 1-m long perfect electric conductors are considered, one at the center of each side (except for the lower panel), to penetrate the walls. The diameter of each conductor is 10 mm. The penetration is assumed to be through 20-mm diameter apertures.

The radiated interference is assumed to be a 50 kV/m incident plane wave (NEMP) illuminating the shielded enclosure. The shielding effectiveness will be evaluated for the electric field and induced current along the conductor inside the enclosure. The electric field is determined at the center point inside the enclosure. A 2-m long bare conductor is placed above the ground floor (panel) and terminated with 50-ohm resistors at each end.

The simulation results are presented as a function of the external portion of the penetrating conductor L_{ex} (see Fig. 2).

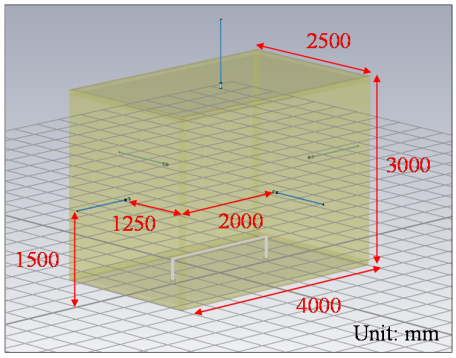

Fig. 1 Schematic diagram of the study case.

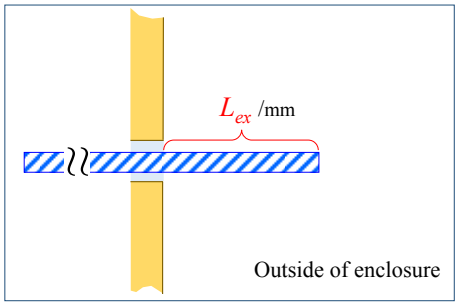

Fig. 2 Penetrating conductor. The overall length of the penetrating conductor is 1 m.

III. Simulation Results

Fig. 3a presents the electric field peak as a function of L_{ex}. It can be seen that, regardless of the field polarization, the electric field reaches its maximum when L_{ex} is 500 mm. In Fig. 3, L_{ex} = 0 mm corresponds to the case when the conductor is fully within the enclosure, while L_{ex} = 1000 mm represents the case when the conductor is fully outside the enclosure. The same conclusion applies to the induced current (see Fig. 3b).

The obtained results show that maximum interference occurs when the length of the exposed conductor is equal to that of the inner section of the conductor.

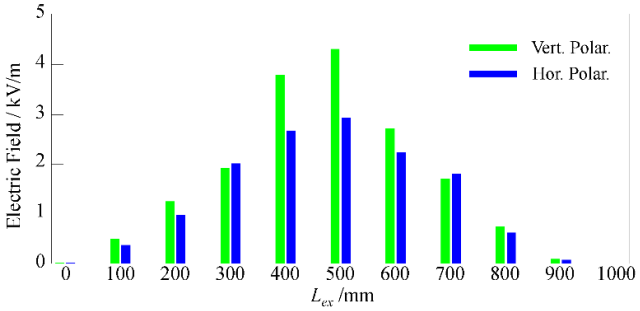

(a)

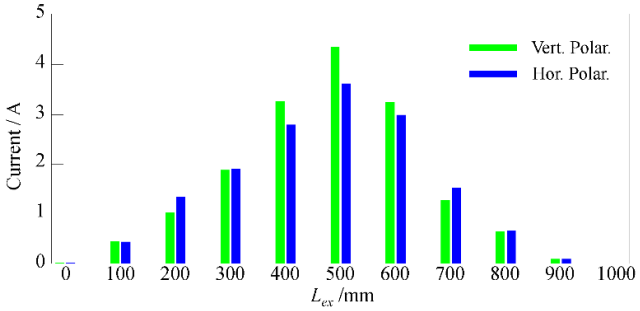

(b)

Fig. 3 Electric field (a) and induced current (b) as a function of the length of the conductor section exposed outside the enclosure.

The situation is analogous, to some extent, to the maximum power transfer theorem, according to which the output power reaches its maximum when the load resistance is equal to the source resistance.

REFERENCES

[1] T. Konefal *et al*., "Electromagnetic coupling between wires inside a rectangular cavity using multiple-mode-analogous-transmission-line circuit theory, *IEEE Transactions on Electromagnetic Compatibility*, vol. 43, no. 3, pp. 273 – 281, Aug. 2001.

[2] D. W. P. Thomas *et al*., "Electromagnetic coupling to an enclosure via wire penetration," 2001 IEEE Intl. Symp. Electromgn. Compat., vol.1, pp. 183– 188, 2001.

[3] R.B. Schulz, V.C. Plantz and D.R. Brush, "Shielding theory and practice," *IEEE Transactions on Electromagnetic Compatibility*, vol. 30, no. 3, pp. 187 – 201, Aug. 1988.

The Effect of Current Intensity and Propagation Distance on Rise-time

Zhigang Lu
National Key Laboratory on Electromagnetic Environmental Effects and Electro-Optical Engineering
Nanjing, China
2965759114@qq.com

Shi Qiu
National Key Laboratory on Electromagnetic Environmental Effects and Electro-Optical Engineering
Nanjing, China
zeustone@yeah.net *(Corresponding Author)*

Shaolei Li
National Key Laboratory on Electromagnetic Environmental Effects and Electro-Optical Engineering
Nanjing, China
289608999@qq.com

***Abstract*— In this work, a lightning return stroke (RS) waveform bank has been built using the single station observation, which contains a vertical component of electric field and two horizontal components of the magnetic field. The effect of propagation distance and current intensity on the rise-time of the RS waveform were studied. The results showed that the propagation distance has little effect on the rise-time of stroke waveform, and the strike current intensity is positively correlated with the rise-time. Rise-time increased linearly with the increase of current intensity. Those findings are important for understanding the waveguide propagation and lightning mechanism.**

Keywords—lightning, waveform, rise-time, propagation distance, current intensity

I. INTRODUCTION

Due to the attenuation of the electromagnetic field propagation on the earth, the inversion of lightning discharge parameters, such as lightning current and charge density, based on remote lightning electromagnetic pulse (LEMP) observations has great uncertainty. Therefore, the research on the RS electromagnetic field propagation along the infinite conductive ground has an important application for lightning detection and lightning physics research. In this paper we have used a statistical method to obtain the propagation effect and lightning current intensity on rise-time of lightning waveforms.

Many studies on the rise-time of lightning RS waveform has been analyzed. Weidman (1980), for example, found that the initial portion of return-stroke fields have 10-90% rise-time ranging from 40 to 200 ns [1]. Ishii (1989) reported that the 0-100% rise-time is 8.6 μs mean for negative and 13.2 μs for positive RS in summer, and it is 21.2 μs mean for positive return-stroke in winter [2]. One of the limitation of those studies is that they don't explain the factors of rise-time (such as the propagation distance and RS strength). Later, Said (2010) developed a new technique for long-range lightning detection and geolocation [3], which estimate the propagation distance by cataloging the dominant variation in expected received waveforms. Zoghzoghy proposed that larger oceanic peak radiated fields result from higher-amplitude RS currents [4], and the weak strokes have shorter rise-times than strong strokes in either ocean or land.

Lightning waveforms can be characterized on the basis of their propagation distance from receivers in order to study radio wave propagation [5]. The ground wave portion of the lightning sferic, which, unlike the sky waves, propagates directly from the source lightning to the receiver without reflecting off of the ionosphere. This paper focuses on the characteristics of the rise-time in ground wave portion. Although numerous studies have simulated the relationship between the waveform and propagation distance, this is a report that the results obtained from actual data statistics. The purpose of this paper is to find the relationship between rise time and propagation distance, current intensity.

II. Observations

We deployed a highly sensitive electromagnetic observation system (HSEOS) in a certain part of northern Jiangsu, to collect nearby lightning waveforms, geolocated using the ADTD network. The receiver consists of a magnetic antenna and an electric field antenna, with a sampling rate of 20 MHz. More than 3000 sets of VLF lightning data had been stored by HSEOS from June 2017 to September 2017.

ADTD uses magnetic direction finding and time-of-arrival methodologies based on multi-station to achieve a location accuracy of 0.5 km. HSEOS is a single-station lightning detection system developed by our team. It can only be used to location the direction of RS. We believe that if the triggering time difference between ADTD and HESDI records is less than 10μs and the orientation angle is less than 1.5 degree, the two records are the same lightning process. Throughout the experiment, HSEOS locally stored more than 200 of ADTD RSs within 300 km radius from the station. In the waveform bank, the propagation distance and the peak current of RS are obtained by ADTD lightning location network. The magnetic field amplitude, electric field amplitude and rise-time are obtained from the data waveforms recorded by HSEOS.

III. Data Analysis

All data used were of lightning RS electromagnetic field waveforms. Fig. 1 is a RS waveforms observed at 142 km distance, which records a magnetic field and electric field signal of 200 μs. The 10~90% rise-time was extracted and marked with two asterisks in the figure.

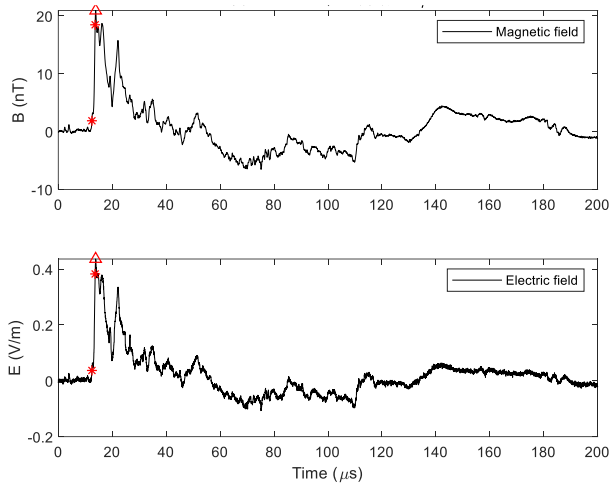

Fig. 1. Example of RS waveforms observed at 142 km distance

Liu (2012) calculated the propagation characteristics of lightning electromagnetic fields under different soil types by using the Cooray-Rubinstein algorithm [6]. It is concluded that poor ground conductivities attenuate the higher-frequency components, smoothing the rising slope of the waveform. When the ground conductivity is constant, the rise-time increases as the propagation distance increases, as shown in Fig. 2.

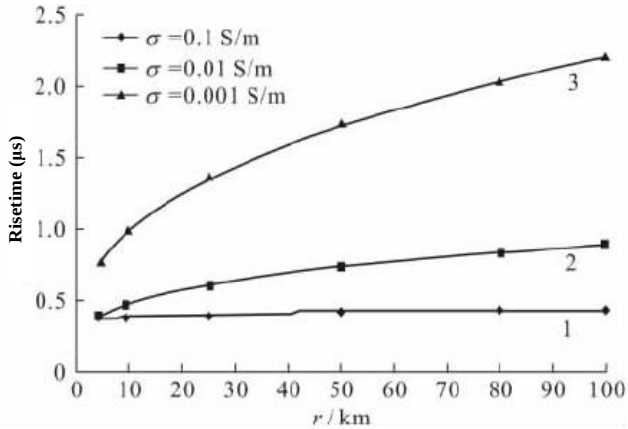

Fig. 2. Variation of electric field rise-time with distance changed by several conductivities [6]

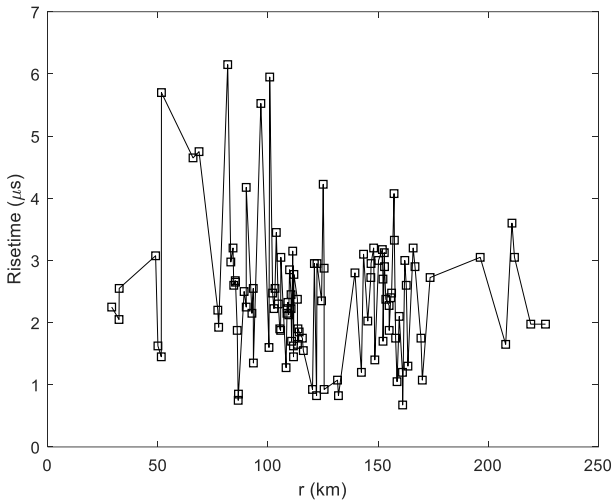

Fig. 3. The relationship between the rise-time and the distance in the experimental observation

In order to further analyze the relationship between rise-time and propagation distance, we use the measured data for statistical analysis. The scatter plot of rise-time and observation distance is shown in Fig. 3. It shows that the rise-times in the range of 1 μs to 6 μs with an average value of 3.1 μs. Our experimental data suggested that the rise-times have an irregular change with the increase of observation distance, which is different with liu's study. We infer that there may be two reasons for this: First, the conductivity of the earth is larger than the commonly considered of 0.001 S/m, which results the VLF waves propagate through the Earth-ionosphere waveguide with relatively low attenuation; Second, when the rise-time of the RS reaches 3 μs, the high frequency component of the signal has been reduced, which caused the effect of propagation distance on the rise-time is to be negligible. The shortcomings of this study are as follows: Fig. 2 is for a given current but the results of Fig. 3 are obtained for different currents, the effect of propagation is mixed up with the effect of variability in the current rise time, which would affect the outcome.

In addition, we also compare the relationship between the rise-time and the peak current. The value of RS peak current is obtained by multi-station lightning location network ADTD, the accuracy of the current value has been verified by comparing the relationship between the amplitude intensity of the observatory and the propagation distance and the peak return current. Fig. 4 shows the relationship between the unit magnetic field strength (B/I) and the propagation distance. The unit magnetic field strength decreases inversely with the increase of propagation distance, which accords with the attenuation relationship of amplitude of long-distance radiation field with distance. Therefore, the results of the return current intensity given by ADTD are reliable.

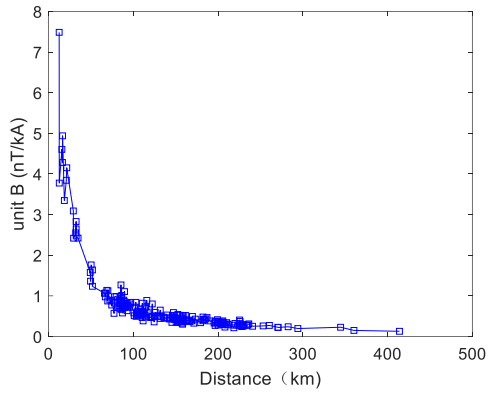

Fig. 4. The relationship between the unit magnetic field strength (B/I) and the propagation distance

The relationship between the stroke current intensity and the rise-time is shown in Fig. 5. The scatter represents the real data, and the solid line represents the fitted curve of the scatter. The correlation coefficient between the original data and the fitted data is 0.53. Interestingly, it can be seen from the figure that weak strokes have shorter rise-times than strong strokes, which corresponds to [4]. However, since the correlation coefficient between the fitting curve and the actual data is only 0.53, it is not feasible to estimate the lightning current intensity by the magnitude of the rise-time, which would cause a large error.

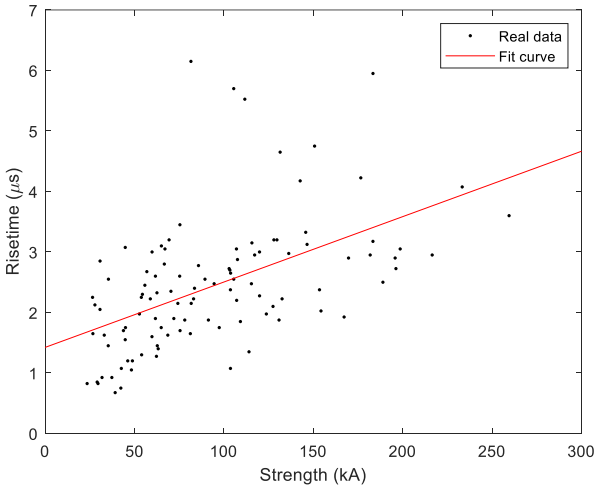

Fig. 5. The relationship between the stroke current intensity and the rise-time

IV. Summary

In this paper, statistical tools were introduced to process the collected VLF waveforms from single station. On the one hand, the relationship between the rise-time and the propagation distance studied in this paper is different from the results of previous simulations, which shows that the propagation distance has little effect on the rise-time. On the other hand, the result about rise-time and current intensity agree with Zoghzoghy's study, weak strokes have shorter rise-times than strong strokes. Theoretical calculation fails to fit the facts. On the basis of the experimental results, the following conclusion can be made:

1 The ground conductivity is larger than the commonly considered of 0.001 S/m.

2 A larger strike speed would cause the smaller charge density of the RS channel, resulting in a smaller amplitude of the RS electromagnetic field.

It should be noted that this study has examined only on the statistical data, there is still some uncertainty in the theoretical analysis of this study. The problems about waveguide propagation and lightning mechanism remain to be solved.

References

[1] Weidman C D, Krider E P. Submicrosecond rise-times in lightning return-stroke fields[J]. Geophysical Research Letters, 1980,7(11):955-958.

[2] Ishii M, Hojo J I. Statistics of fine structure of cloud-to-ground lightning field waveforms[J]. Journal of Geophysical Research Atmospheres, 1989, 94(D11): 13267-13274.

[3] Said R K, Inan U S, Cummins K L. Long-range lightning geolocation using a VLF radio atmospheric waveform bank[J]. Journal of Geophysical Research, 2010,115(D23).

[4] Zoghzoghy F G, Cohen M B, Said R K, et al. Shipborne LF‐VLF oceanic lightning observations and modeling[J]. Journal of Geophysical Research: Atmospheres, 2015,120(20):10, 810-890, 902.

[5] Liu Z, Koh K L, Mezentsev A, et al. Lightning Sferics: Analysis of the Instantaneous Phase and Frequency Inferred From Complex Waveforms[J]. Radio Science, 2018,53(4):448-457.

[6] Xiaodong, LIU, Qilin, ZHANG, Xuyu FENG. Effect of Finite Conductivity on Rise Time and Field Strength Amplitude of return stroke Radiation Field of Cloud-ground Flash[J]. High Voltage Engineering 2012, 38(02): 457-463.

Process Analysis for the Insulation Failure of a Peaking Capacitor in an EMP Simulator*

Zhiqiang Chen[1, 2], Wei Jia[1, 2], Junping Tang[1], Junna Li [2], Fan Guo[1, 2], Shengchang Ji[1]

1. State Key Laboratory of Electrical Insulation and Power Equipment, Xi'an Jiaotong University, Xi'an, China, 710049
2. State Key Laboratory of Intense Pulsed Radiation Simulation and Effect (Northwest Institute of Nuclear Technology), Xi'an, China, 710024

***Abstract*—The coaxial peaking capacitor is one of the key components in an EMP (Electromagnetic pulse) simulator, and its insulation strength affects the reliability of the simulators greatly. In this paper, the process of the insulation failure of a damaged peaking capacitor due to the flashover is analyzed. At first, the damaged capacitor is disassembled, and the traces of ablations on the film show that the film layers close to the inner core are generally with darken and denser ablation spots, which indicates that higher current flows on the surface of the inner film layers. Then, the circuit and field simulation are performed and the results show that the earlier the flashover occurs on the film layers, the smaller the flashover current is and the field on the outer film layer would have more parallel component. Lastly, according to the above analysis, the process of the flashover on the peaking capacitor is proposed, that the flashover occurs on the first inner layer due to its shortest insulation length at first, and then the outer film layers with electrical field parallel to the surface of the film, and at last the inner layers with electrical field normal to the surface.**

Keywords—insulation failure, flashover, peaking capacitor, EMP simulator, ablation

I. INTRODUCTION

In the EMP simulators, the compression of the pulse is accomplished by the co-working of the peaking capacitor and the output switch. The peaking capacitor is made with the laminate structure utilizing alternative thin metal electrodes and film layers. The film layers extend the edge of the electrodes at a distance and are supported by its own inflexibility, thus the extension distance of the film layer is limited, or the adjacent layers may droop to connect each other. The peaking performance is affected by the inductance of the peaking capacitor partly, which constrains the diameter and the length of the capacitor. On the other hand, the capacitor could withstand high voltage with more film layers. Therefore, for megavoltage applications, the insulation performance and the equal inductance often contradict each other. In order to meet the requirement of the waveform's risetime, the capacitor often utilizes its insulation performance to the maximum level, which would reduce the operation reliability especially under high voltage.

Compared to the bulk breakdown of the film layers, the flashover on the edge of the film layers is the leading cause of the peaking capacitor's insulation failure. The capacitor consists of many coaxial film layers and electrodes, and the electrical fields on the film layers are different from each other due to the coaxial cone structure. The flashover phenomena on different film layers may have different features. When stressed on a nanosecond pulse, the film layers would break down on the surface in an order. Herein, to master the flashover sequence is very important for the insulation improvement of the capacitor. However, the peaking capacitor locates in the center of the simulator, and no electrical and optical methods are used to monitor the capacitor's status. In this paper, a damaged peaking capacitor is disassembled and analyzed, and according to the ablation traces and simulation results, the flashover sequence of the capacitor is proposed.

II. FLASHOVER TRACES ON AN PEAKING CAPACITOR

Fig.1 illustrates the cross section view of a peaking capacitor. The capacitor consists of 18 PP (polypropylene) film layers, and each film layer along with the 2 attached metal rings form a small coaxial capacitor. The capacitance of the 18 small coaxial capacitors is designed the same, such that the voltage applied at the peaking capacitor would be uniformly. There are 2 sides of the capacitor, namely, Side A and Side B in Fig. 1. The cone angle of Side A is 32°, which is in accordance with the radiation antenna, and the angle with the axis of symmetry of Side B is approximately 90°.

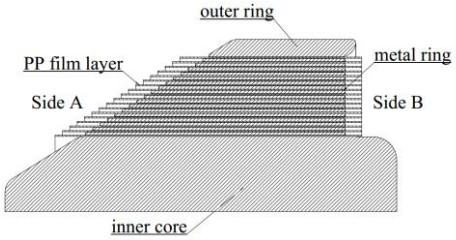

Fig. 1. Section view of a peaking capacitor.

The surrounding insulation gas of the peaking capacitor is high pressure SF_6. The capacitor needs to withstand a nanosecond pulse voltage with the amplitude of megavoltage scale. In the practical operation, the peaking capacitor is usually the weak link of the simulator due to the insulation failure. Fig. 2 illustrates the flashover traces on a damaged peaking capacitor.

Fig. 2. Flashover traces on a peaking capacitor.

The surface of the film layers is full of carbonization channels and spots, and some films are even melt and destroyed. It indicates that serious flashover phenomena have ever occurred before the capacitor lost its insulation ability.

The damaged peaking capacitor is disassembled one layer by one layer, and the flashover traces are recorded carefully. It's found that the traces on the film layers are different from each other. There are mainly 2 types of traces on the film layers as shown in Fig. 3, and one describes the flashover channel between the neighboring 2 metal rings while the other describes the flashover channel jumping from one film layer to the neighboring film layer.

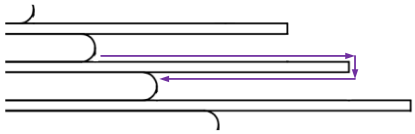

(a) Flashover channel between the neighboring rings

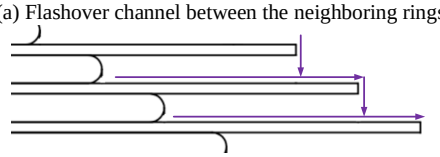

(b) Flashover channel jumping from one film layer to the neighboring one

Fig. 3. The 2 types of the flashover traces.

The film layer close to the inner core is denoted as Layer 1, and the other layers are denoted in order as Layer 2, Layer 3 and so on. The major characteristics of the flashover trace distribution on the film layers are analyzed. There are 4 distinctive characteristics: (a) In Side B, the flashover traces only occur on Layer 1, and there are no traces on other layers; (b) In Side A, the surface of Layer 1 is clean with no carbonization spots. The phenomena in (a) and (b) may be a result of the special structure that Layer 1 in Side B is fit to the inner core with no gas gap, thus the total insulation length in Side B is shorter than that in Side A; (c) In Side A, the film in Layer 2 are damaged the most severely, and the flashover traces are bestrewn on both sides of the layer following the flashover channel type in Fig.3 (a), this phenomenon implies that the flashover occurs frequently on Layer 2 or the flashover current on this layer is larger than that on others; (d) In Side A, the damage degree of Layer 3 to Layer 7 is slightly higher than that of Layer 8 to Layer 18, and the flashover channel type of the 16 layers could be classified to the type in Fig. 3 (b).

III. Electrical Circuit and Field Simulations

A. *Circuit simulation*

The circuit simulation model is established in order to study the flashover characteristics of the peaking capacitor. The model is a two-stage pulse compression circuit, which could output a standard EMP pulse on the load resistor. The peaking capacitor consists of 18 small coaxial capacitors, and each small coaxial capacitor is simulated as a parallel circuit including the small coaxial capacitor and a flashover branch. A self-breakdown switch, an equal resistor and an equal inductor are connected in series in the flashover branch. The regulation of the flashover time is realized by changing the breakdown voltage of the switch. The normal operating voltage U_c and the maximal withstand voltage of the small coaxial capacitor are set to 150 kV and 200 kV, respectively, and the equal resistor and the equal inductor of the flashover branch are set to 0.5 Ω and 10 nH, respectively. The aim of the circuit simulation includes 2 aspects: (a) When the flashover occurs on the small coaxial capacitor, what is its influence on the other small coaxial capacitors and the pulse applied on the load resistor; (b) What is the influence of the flashover time on the flashover current.

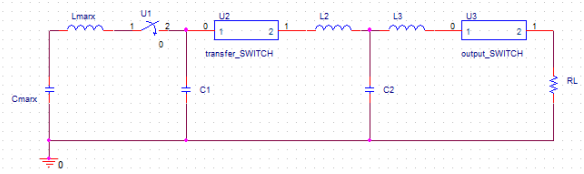

(a) The simulation circuit of an EMP simulator

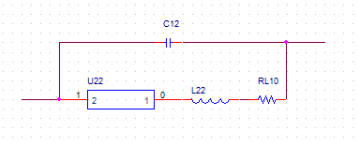

(b) The flashover branch (C2 in Fig.4 (a) includes 18 branches in series)

Fig. 4. The circuit simulation model.

Layer 1 is supposed to break down on the surface at first, and its influence on the applied voltage of the other small coaxial capacitors is studied. The flashover voltage is set to 30 kV (20% U_c), 60 kV (40% U_c), 90 kV (60% U_c) and 120 kV (80% U_c). Fig. 5 illustrates the amplitude of the applied nanosecond pulse on Layer 2. It can be seen from Fig. 5 that if the flashover occurs at the very early stage low than 60% U_c, the change of the applied pulse on Layer 2 is relatively obvious; if the flashover occurs latter, the influence could be neglected.

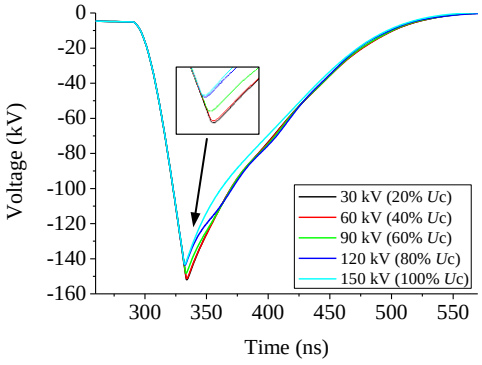

Fig. 5. Influence of the flashover time on the small coaxial capacitor Flashover traces on a peaking capacitor.

The influence of the flashover time on the flashover current is shown in Fig. 6. The latter the flashover occurs, the larger the amplitude of the current is. The results indicate that the flashover on Layer 2 might occur at last in sequence.

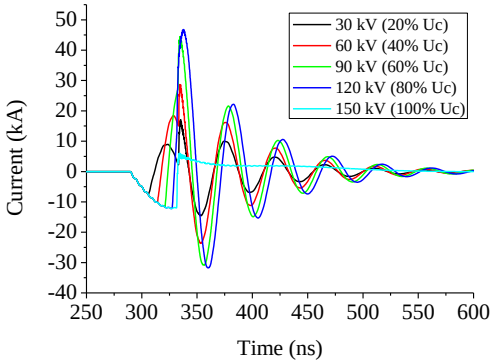

Fig. 6. Influence of the flashover time on the flashover current capacitor Flashover traces on a peaking capacitor.

Fig. 7 shows the influence of the number of small coaxial capacitors occurring surface flashover on the load's applied voltage. The flashover voltage is set to 50% U_c . The simulation results show that if the number of capacitors occurring surface flashover is less than 2, the output pulse voltage on the load could be acceptable; if the flashover occurs in 3 or 4 film layers, the output pulse would change a lot; if the number is 5 or more, flashover would occur on the whole peaking capacitor with the parameter settings in this paper.

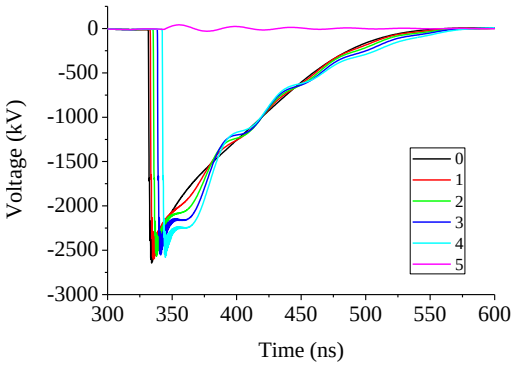

Fig. 7. Influence of the number of flashover film layers on the voltage applied on the load.

B. *Field Analysis*

The electrical field on the film layers of the peaking capacitor is analyzed using static field method. Obviously, most of the flashover channels occur in Side A in Fig.2, thus a typical point located on the film layers in Side A and 7 mm away from the edge is selected to compare the field distribution on the film layers. The comparison results are shown in Fig.9. It can be seen from the figure that: (a) the total field on the film layer decreases with the layer number; (b) on the inner film layers, normal component of the field is much higher than the parallel component; (c) on the outer film layers, the parallel component of the field is dominant.

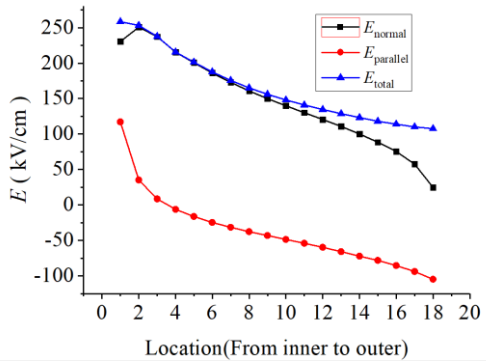

Fig. 8. The field distribution on the typical point of the film layers.

IV. Flashover Process

Based on the above phenomena, analysis and the streamer theory, a model describing the flashover process on the peaking capacitor is proposed as follows. The flashover process could be divided into 4 stages.

(1)As the increase of the applied nanosecond pulse, the surface flashover first occurs on Layer 1 due to its shortest insulation length. The phenomena would slightly enhance the voltage applied on other film layers;

(2)The field on the outer layers is mainly parallel to the film surface, which means that the field has the same direction with the flashover channels. Usually, the propagation of the streamers is along with the electrical line. Therefore, although the total field on the inner layers is higher than the outer layers, the flashover would firstly occur on the outer layers. Other evidence supporting this conclusion is that the earlier the flashover occurs, the smaller the current on the film is in the circuit simulation.

Hence, streamers would initiates on the outer film layer and develop to the edge of the film, leading to the electrical connection of the neighboring electrodes, which would also increase the applied voltage on other layers.

(3)The voltage on the peaking capacitor keeps increasing, and the voltage is applied at the remaining small coaxial capacitors. When the voltage is high enough, the streamers initiating in the triple point would develop to the edge of the film layers with normal electrical field, and the neighboring 2 electrodes are connected electrically. The flashover current in this stage is higher than that in Stage 2, thus the damage of the films is more serious.

(4) The voltage of the metal ring attached to Layer 1 and the inner core has been the same in Stage 1, thus the streamers would not occur on Layer 1 in Side A. The voltage applied on Layer 2 is very high, and the streamers on Layer 2 would develop on both sides of the films and meet at the edge, leading to the complete insulation failure of the peaking capacitor finally . The most severely damaged traces are due to the strongest flashover current in the flashover channels in both sides of the film layer.

V. Conclusion

The flashover traces of a peaking capacitor in an EMP simulator are analyzed and the simulations on electrical circuit and field are performed in this paper, and some conclusions are obtained. Based on the conclusions, the flashover process of the capacitor is proposed. The flashover first occurs on Layer 1, and then from the outer layer to the inner layer via the jumping flashover mode, and at last on Layer 2 with a U shape channel. The results point out the weak spots of the capacitor's insulation and offer references to the insulation improvement.

References

[1] A. C. Qiu. Application of the pulse power technology. Xi`an: Shaanxi Science and Technology Press, 2016

[2] W. Q. Chen, X. P. He, W. Jia, et al, "Development of a 2.5MV fast pulse generator for EMP simulation," in 14th National Conference on Nuclear Electronics & Detection Technology, Beijing, Nuclear Electronics and Detection Technology Branch, China Electronic Academy, 2008: 689-693

[3] C. E. Baum. EMP simulators for various types of nuclear EMP environments: an interim categorization. IEEE Trans Electromagnetic Compatibility, 1978, 20(1): 35-53.

[4] I. D. Smith, The pulse power technology of high altitude EMP simulators. Proc. 5th Symp. Tech. Exhib. Electromagn. Compat., Zurich, Switzerland, Mar. 1983: 8-10.

[5] V. Bailey, V. Carboni, C. Eichenberger, et al. A 6-MV Pulser to Drive Horizontally Polarized EMP Simulators. IEEE Transactions on Plasma Science, 2010, 38(10): 2554-2558.

[6] G. Charles, S. K. Lam, J. T. Naff, et al. Design and performance of the FEMP-2000: A fast risetime, 2 MV EMP pulser. 12th IEEE International Pulsed Power Conference, 1999:1437-1440.

Unified Mechanism of Geo-magnetic Storm and Sub-storm

Zhishan Liang Zuo Xin
Automation Department, College of
Information Science and Engineering.
China University of Petroleum Beijing
–CUPB Beijing city China
Email : lzs1960@cup.edu.cn

***Abstract*—This paper reviews some research achievements and problems for Geo-magnetic Storm, Geo-magnetic Sub-storm and relationships between Geo-magnetic storm and sub-storm, and then points out that there exist some problems and are not clear right conclusions. At last, creative works are given in the paper, that is, (1) New concepts: single-pole magnetic bottle and double-pole magnetic bottle; (2) Neutral current sheet model of the Earth; (3)Disruption mechanism of magnetopause current facing the Sun of the Earth; (4) the unified mechanism, view points and explanations of geo-magnetic storm and sub-storm.**

Keywords—Geo-magnetic Storm, Geo-magnetic Sub-storm, mechanism, Neutral current sheet model, Disruption mechanism of magnetopause current facing the Sun, unified mechanism

I. INTRODUCTION

Generally, a vast of achievements has been made in the scientific researches of Geo-magnetic storm and sub storm. But three important problems are existed in (Xu Wenyao, 2014).

Firstly, Geo-magnetic storm process is composed of initial phase, main phase and recovery phase, initial phase corresponds to F--C current, main phase and recovery phase correspond to symmetric loop current respectively. With the help of these concepts and the current models, much geo-magnetic phenomenon can be explained clearly (Margaret G. Kivelson and Christapher T. Russel, 2002). However, F--C current is so too far away from the surface of the Earth with respect to the symmetric loop current.

Secondly, Geo-magnetic sub-storm is composed of growth phase, expansion phase and recovery phase, growth phase and recovery phase correspond to two whirl type current, expansion phase corresponds to one whirl type current. By scientific researches of many scholars for about half century, Mcpherron thought that six sub-storm models has been made as follows (Mcpherron, 1995), Near-earth neutral-line model (Mcpherron et al., 1973), Driven model (Perreault and Akasofu, 1978), Thermal catastrophe model (Smith 1986), Boundary-layer-dynamics model (Rostoker and Eastman, 1987), Near-Earth current-sheet-disruption model(Lui, 1988), Magnetosphere-ionosphere coupling model (Kan, 1979). Additionally, other models are also important, for example, Unloading instability (Kan, 1991), Ballooning instability model (Roux et al., 1991; Pu et al., 1992), Cross-field current instability (Lui, 1996), Hydrid whirl instability (Voronkov, 1977), Near earth and tail current (Pu Zuyin et al., 1996 and Hong Minghua et al., 1997)and others. It is because so much models that the real mechanism of geo-magnetic sub-storm has not been also found. These models are the results of data distributed in the different places of the Earth, that is to say, “Mang Ren Mo Xiang” in Chinese language. Many discussions are also continued in progress (Xu Wenyao, 2014). So Kan suggested that it is very necessary for us to build a global model of geo-magnetic sub-storm (Kan, 1990).

Thirdly, it is not clear the actual relationships between Geo-magnetic storm and sub-storm and it is hard to say that one is distinguished from another and can’t be give the general conclusions (Iymori and Rao, 1996; Mcpherron, 1997; Maltseve, 2004; Sharm et al., 2004). For the geo-magnetic index, on the whole, the relationships are divided into three modes: (1) when one increases or decreases and meanwhile another increases or decreases; (2) one increases or decreases and another decreases or increases; (3) one has nothing to do with another.

(1) Mode 1: One increases and meanwhile another increases.

Many statistic results have shown that AE index for Geo-magnetic sub-storm has more positive relative properties with Dst index for Geo-magnetic storm (Shen et al., 2002). In other words, they have same variations tends for solar wind phenomena. So Geo-magnetic storm is composed of a series of Geo-magnetic sub-storm (Akasofu, 1981).

(2) Mode 2: One increases and another decreases.

Iymori and Rao had made much statistic researches results for different periods Geo-magnetic sub-storms of a Geo-magnetic storm and came conclusions of “One increases and another decreases” (Iymori and Rao, 1996). Another scholars has also made the same results (Huang C. S. at al., 2004).

(3) Mode 3: One has nothing to do with another.

What Geo-magnetic storm has happened has nothing to do with Geo-magnetic sub-storm seldom. But there were also some exceptions that Geo-magnetic storm has appeared without obvious Geo-magnetic sub-storms (Yahnin et al., 1994; Zhou et al., 2003). Iymori and Rao had also made much statistic researches results for different periods Geo-

This research was supported by the support of National Key R&D Program of China (No. 2016YFC0800100) .

magnetic sub-storms of a Geo-magnetic storm and came conclusions of " One has nothing to do with another" (Iymori and Rao, 1996). Some scholar considered that energy dissipation for Geo-magnetic sub-storms has no effects to Geo-magnetic storm (Grafe and Feldstein, 2000), symmetric loop current and polar electrojet current are independent for each other.

So, there are not clear conclusions in the actual relationship between Geo-magnetic storm and sub-storm

All in all, many kernel problems of Geo-magnetic storm and sub-storm are still not solved at present. The aim of this paper is to establish unified mechanism , view points and explanations of Geo-magnetic storm and sub-storm.

II. BAISIC DEFINATIONS AND THEORY

A. Basic definations

1. Solar wind

It is composed of motion plasmas and magnetic field with solar wind (Margaret G. Kivelson and Christapher T. Russel, 2002).

2. Magnetic bottle

Magnetic bottle is divided into single-pole magnetic bottle and double-pole magnetic bottle corresponding to non-dipole and dipole individually.

B. Baisicelectric and megnetic field theory model of the Earth

1. Dipole magnetic field theory

The ideal geomagnetic field of the Earth is dipole geomagnetic field with position and shape in smallest energy Under the conditions of no influence of non-geomagnetic field.

2. Magnetic field distorsion current theory

The geomagnetic field of the Earth is shaped into non dipole geomagnetic field Under the conditions of influence of any magnetic field. The current is produced in the deformed place.

3. Round neutral current sheet theory

The Earth has round neutral current sheet in the equatorial plane around it as the same as the Sun does as shown in Fig.1.

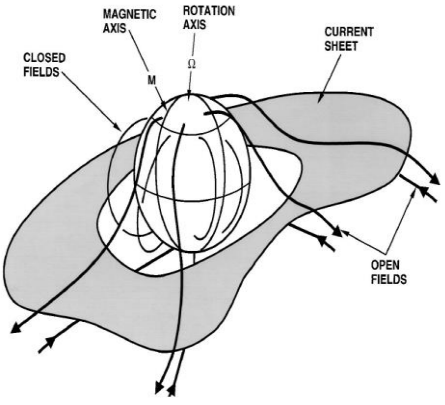

Fig.1 the round neutral current sheet of the Earth

4. Current disruption theory: There exists near-Earth current-sheet-disruption model in the magnetic tail (Lui, 1988), author in this paper think that it is the same as the disruption mechanism of magnetopause current facing the Sun of the Earth as shown in Fig.2.

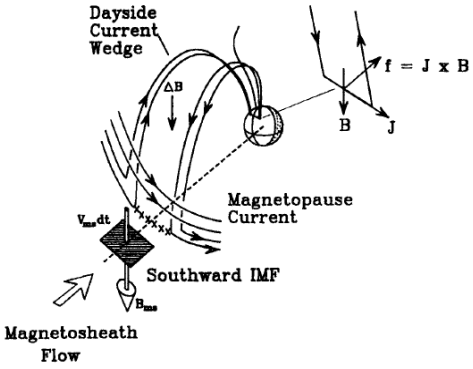

Fig.2 the disruption mechanism of magnetopause current facing the Sun (Xu Wenyao, 2014)

III. UNIFIED MECHANISM OF GEO-MAGNETIC STORM AND SUB-STORM

In traditional observation and researches of the geo-magnetic, Geo-magnetic storm process is composed of initial phase, main phase and recovery phase. Geo-magnetic sub-storm is composed of growth phase, expansion phase and recovery phase. The unified mechanism of geo-magnetic storm and sub-storm is suggested as follows as shown in Fig.3. The unified mechanism of geo-magnetic storm and sub-storm is composed of initial phase, main phase, recovery phase and normal state. R_A, R_B and R_C are the equivalent radius of dipole Earth in the different geo-magnetic storm phase respectively.

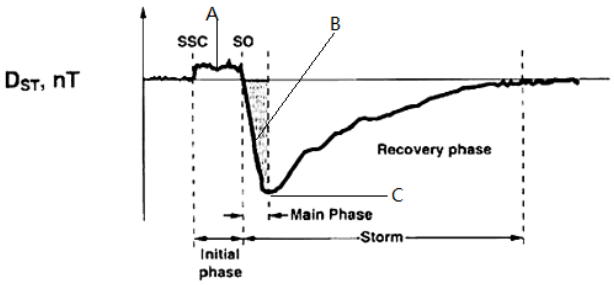

Fig.3 . The unified mechanism of geo-magnetic storm and sub-storm

A. Initial (or Groth) phase

Dipolarization is decreasing gradually.

Tail magnetopause current and magnetopause current facing the Sun are loaded or charged by solar wind.

Double-pole magnetic bottle is changed into single- pole magnetic bottle with decrease of solar wind gradually.

When the equivalent geo-magnetic radius of dipole Earth is the R_A, the magnetic line corresponding to R_A has accessed to meddle to low latitude region from high latitude region.

B. *Main phase(or expansion)*

Dipolarization is increasing gradually.

Symmetric loop current is loaded or charged by charging tail magnetopause current and magnetopause current facing the Sun individually.

Two single-pole magnetic bottle are composed into double-pole magnetic bottle with increase of solar wind gradually.

When the equivalent geo-magnetic radius of dipole Earth is the R_B, the magnetic line corresponding to R_B access to high latitude region from meddle to low latitude region again.

C. *Recovery Phase*

Symmetric loop current is dissipated.

In the recovery phase, the equivalent geo-magnetic radius of dipole Earth is the R_X, the magnetic line corresponding to R_X is located in high latitude region, R_X is greater than anyone of R_A and R_B.

D. *Normal State*

Dipolarization is changable stablely dynamically.

Symmetric loop current is dissipated.

Double-pole magnetic bottle and single-pole magnetic bottle is changed into with increase or decrease of solar wind gradually dynamically reversibly.

In the recovery phase, the equivalent geo-magnetic radius of dipole Earth is the R_X, the magnetic line corresponding to R_X is located in high latitude region, R_X is greater than anyone of R_A and R_B.

IV. EXPLANATION OF RELATION BETWEEN GEO-MAGNETIC STORM AND SUB-STORM

Relationships between Geo-magnetic storm （corresponding to the magnetic lines of meddle to low latitude region） and sub-storm （corresponding to the magnetic lines of high latitude region）can be explained as follows, according to the unified mechanism of geo-magnetic storm and sub-storm.

A. *Mode 1: One increases and meanwhile another increases*

From normal state to R_A region storm and sub-storm may happen at random at the same time.

B. *Mode 2: One increases and another decreases*

From R_B region to normal state, storm happens rarely and sub-storm may offen happen at random.

C. *Mode 3: One has nothing to do with another*

In the region between the equivalent Earth dipole geo-magnetic radius R_A and R_B, the magnetic line is no corresponding to high latitude region. Geo-magnetic storm is corresponding to the magnetic lines of meddle to low latitude region） and sub-storm is corresponding to the magnetic lines of high latitude region.

Dynamic solar wind offen happens. In this way, main phase and recovery phase appear one after another repeatedly. In this way, “One has nothing to do with another” mode maybe show up.

V. CONCLUSIONS

The following is a list of the main points discussed in this paper.

(1) New concepts: single-pole magnetic bottle and double-pole magnetic bottle;

(2) New model: Neutral current sheet model of the Earth;

(3) New view point: Disruption mechanism of magnetopause current facing the Sun of the Earth is the same as tail current;

(4) New unified mechanism: The unified mechanism, new view points and explanations of geo-magnetic storm and sub-storm.

Research results in this paper is only initial main ideas of framework due to the limitation of paper length, the further details results about Geo-magnetic Storm, Geo-magnetic Sub-storm will be published in other papers.

Acknowledgment

Author thanks my graduate students and PhD students for the related discussion with especially Huang Yong and Zhai Weifeng. This research was supported by the support of National Key R&D Program of China (No. 2016YFC0800100) .

REFERENCES

[1] Akasofu S I. Energy coupling between the solar wind and the magnetosphere [J]. Space Science Reviews, 1981, 28(2):121-190.

[2] Grafe A, Feldstein Y I. About the relationship between auroral electrojets and ring currents [J]. Annales Geophysic ae, 2000, 18(8):874-886.

[3] Hong Minghua et al.A substorm expansion model based on canfiguration instability of the near-Earth magnetotail: the relation between plasma flow in the midtail and substorm activity in the near-Earth magnetotail [J]. Acta Geophysica Sinica, 1997,3(40):154-163

[4] Huang C S , Foster J C , Goncharenko L P , et al. Variations of low-latitude geomagnetic fields and Dst index caused by magnetospheric substorms [J]. Journal of Geophysical Research Space Physics, 2004, 109(A5)

[5] Iyemori T, Rao D R K. Decay of the Dst field of geomagnetic disturbance after substorm onset and its implication to storm-substorm relation [J]. Annales Geophysicae, 1996, 14(6):608-618.

[6] Kan J R, Lee L C. Energy coupling function and solar wind - magnetosphere dynamo [J]. Geophysical Research Letters, 1979, 6(7):577-580.

[7] Kan J R. Developing a global model of magnetospheric sub-storms [J]. Eos Transactions American Geophysical Union, 1991, 71(38):1083-1087.

[8] Lui A T Y, Lopez R E, Krimigis S M, et al. A case study of magnetotail current sheet disruption and diversion [J]. Geophysical Research Letters, 1988, 15(7):721-724.

[9] Lui A T Y. Current disruption in the Earth's magnetosphere: Observations and models [J]. Journal of Geophysical Research Space Physics, 1996, 101(A6):13067-13088.

[10] Mcpherron R L, Russell C T, Aubry M P. Satellite studies of magnetospheric substorms on August 15, 1968: 9. Phenomenological model for substorms [J]. Journal of Geophysical Research, 1973, 78(16):3131-3149.

[11] Mcpherron R L, Magnetospheric dynamics [M]. Kivelson M G ,Russell C T ed. Introduction to space physics. New York: Cambridge University Press, 1995:593-739

[12] Mcpherron R L. The role of substorms in the generation of magnetic storms [M] Tsurutani B T, Gonzalez W D, Kamide Y, Arballo J K ed. Magnetic Storms, Geophys. Monograph 98. Washington D C: American Geophysical Union, 1997:131-148.

[13] Maltsev Y P. Points of controversy in the study of magnetic storms [J]. Space Science Reviews, 2004, 110(3-4):227-267.

[14] Margaret G. Kivelson and Christapher T. Russel (translated by Cao Jinbin et al), Introduction to Space Physics, China Science Press, 2002.

[15] Perreault P, Akasodu S-I. A study of geomagnetic storms [J]. Geophys.j.r.astron.soc, 1978, 54(3):547-573.

[16] Pu Z Y, Hong M H, Wang X M, et al. A substorm expansion model based on configuration instability of the near-Earth magnetotail: I. Configuration instability in the near-Earth magnetotail[J]. Chinese Journal of Geophysics, 1996, 52(10):2566-2574.

[17] Pu Z Y, Korth A, Kremser G. Plasma and magnetic field parameters at substorm onsets derived from GEOS 2 observations[J]. Journal of Geophysical Research Space Physics, 1992, 97(A12):19341-19349.

[18] Rostoker G, Eastman T E. A boundary layer model for magnetospheric substorms [J]. Journal of Geophysical Research Space Physics, 1987, 92(A11):12187-12201.

[19] Roux et al., Plasma sheet instability related to the westward travelling surge. J. Geophys. Res., 96,17697-17714, 1991.

[20] Smith R A, Goertz C K, Grossman W. Thermal catastrophe in the plasma sheet boundary layer [J]. Geophysical Research Letters, 2013, 13(13):1380-1383.

[21] Shen C, Liu Z, Kamei T. A physics-based study of the Dst - AL relationship [J]. Journal of Geophysical Research Space Physics, 2002, 107(A1):SMP-1-SMP 4-10.

[22] Sharma A S, Kamide Y, Lakhina G S. Disturbances in Geospace: The Storm-Substorm Relationship[M]. Geophys. Monogr. Ser., vol. 142,2004, Washington D C: American Geophysical Union

[23] Voronkov I, Rankin R, Frycz P, et al. Coupling of shear flow and pressure gradient instabilities[J]. Journal of Geophysical Research, 1997, 102(A5):9639-9650.

[24] Xu Wenyao, Introduction to Geomagnetic Activity [M], China Science Press. 2014

[25] Yahnin et al., Features of steady magnetospheric convections [J]. Res. 99. 4039-4052. 1994.

[26] Zhou X-Y, Tsurutani B T, Reeves G, et al. Ring current intensification and convection‐driven negative bays: Multisatellite studies [J]. Journal of Geophysical Research, 2003, 108(A11):SMP 13-1.

Study on the Characterization of Shielding Effectiveness under Narrow Band High Power Microwave

Yan Zhiyang
Key Laboratory of Science and Technology on Complex Electromagnetic Environment , CAEP
Institute of Applied Electronics, CAEP
Mianyang, China
ms_hit_yzy@163.com

Qin Feng
Key Laboratory of Science and Technology on Complex Electromagnetic Environment , CAEP
Institute of Applied Electronics, CAEP
Mianyang, China
qinfeng@caep.cn

Cai Jinliang
Key Laboratory of Science and Technology on Complex Electromagnetic Environment , CAEP
Institute of Applied Electronics, CAEP
Mianyang, China
caijl@caep.cn

***Abstract*—Shielding effectiveness is the most important technical indicator of electromagnetic shielding materials, accurate characterization and calculation of shielding effectiveness are crucial to the correct use of shielding materials. However, the characterization of shielding effectiveness under high power microwave has not been unified. Moreover, whether the shielding characteristics of shielding material will change or not is not clear. In this paper, the differences and similarities of shielding effectiveness calculated by 'peak ratio', 'Fourier transform' and 'energy attenuation' for different types of electromagnetic shielding materials under the condition of narrow band high power microwave are studied. The results show that 'peak ratio' is a simple and accurate method to calculate shielding effectiveness under the condition of narrow band high power microwave. On this basis, the effects of pulse width, repetition frequency and power density on the shielding characteristic of shielding materials are studied.**

Keywords—shielding effectiveness, narrow band high power microwave, characterization, the ratio of peak value, shielding property

I. INTRODUCTION

In modern wars, frequency devices are widely used. The power of these devices is higher and higher, and more and more frequency bands are occupied[1]. This phenomenon makes the electromagnetic environment of wars increasingly complex especially with the emergence of strong electromagnetic pulses represented by high-power microwave, it poses a great threat to the normal use of military electronic systems. So protecting and reinforce the military electronic systems under strong electromagnetic pulse become especially important for improving its survivability. Using electromagnetic shielding materials to isolate the electronic system from the complex electromagnetic environment in space is an important protection method to reduce the influence of electromagnetic fields on equipment and systems[2]. For electromagnetic shielding materials, shielding effectiveness is the key parameter. It has been a key problem that how the shielding effectiveness is characterized and whether the shielding property will change under strong electromagnetic pulse, and has been essential to select correct protective materials to improve the viability of the electronic equipment under complex electromagnetic environment.

Researchers have done lots of study on shielding effectiveness based on characteristic parameters, frequency domain characterization and time domain characterization[3-9]. But it is not clear to describe the protecting properties underr strong electromagnetic pulse that may occurred in actual wars such as narrow band HPM, wide band HPM, and HEMP.

In this paper, the characterization of shielding effectiveness including 'peak ratio', 'Fourier transform' and 'energy attenuation' under narrow-band high-power microwave is studied. Based on above works, the change of the protective properties of typical electromagnetic shielding materials under narrow-band high-power microwave conditions are studied, and corresponding explanations are given.

II. EXPERIMENTAL SYSTEM AND PRINCIPLE

A. Experimental System

The experiment was completed on the self-developed shielding effectiveness test platform, as shown in Figure 1. In order to ensure the test results are universal and persuasive, carbon based foam, shielding metal mesh, shielding glass and shielding coating are used, testing are finished under the condition of 20ns, 50ns, 100ns, 200ns and 500ns.

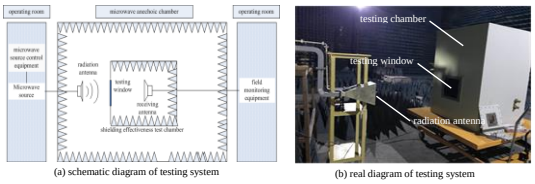

(a) schematic diagram of testing system (b) real diagram of testing system

Fig. 1. Sketch map of testing system and experimental device

B. Experimental Principle

According to the peak voltage of the time domain waveform obtained by the oscilloscope before and after the shielding material is placed, and the attenuation value of the signal receiving loop under two states, the peak shielding effectiveness can be calculated. The calculation formula is:

$$SE_p = 20\lg\frac{v_0}{v_1} + (R_0 - R_1) \quad (1)$$

SE_p is the peak shielding effectiveness. V_0 and R_0 are the voltage peak readings and path attenuation values when the shielding material is not placed in the test window. v_1 and R_1 are the voltage peak readings and path attenuation values after the shielding material is placed in the test window.

By integrating the time domain waveform obtained before and after the shielding material is placed. Then energy attenuation shielding effectiveness can be calculated according to the path attenuation value and the matching impedance. The calculation formula is:

$$SE_E = 20\lg\frac{W_0}{W_1} + (R_0 - R_1) \tag{2}$$

W_0 and R_0 are the energy and path attenuation values when the shielding material is not placed in the test window, and W_1 and R_1 are the energy and path attenuation values after the shielding material is placed in the test window. Wherein, the energy W is obtained by integrating the time domain waveform voltage component ΔV and the matching impedance R.

The Fourier transform shielding performance is mainly obtained by extracting the corresponding information from the transformed amplitude-frequency curve, and then combing the path attenuation before and after the shielding material is placed in the test window. In general, by taking the logarithm of ratio of amplitude to frequency curves and then combining the channel attenuation value, shielding performance curves can be gotten. While when the spectral components of the domain signal are concentrated at a certain frequency (time domain signals of narrowband high-power microwave have this feature), the shielding effectiveness can be calculated by combing the peak value at the center frequency and path attenuation value. The calculation formula is:

$$SE_F = 20\lg\frac{V_{c,0}}{V_{c,1}} + (R_0 - R_1) \tag{4}$$

SE_F is the shielding effectiveness. $v_{c,0}$ and R_0 are the voltage peak value at the center frequency and channel attenuation value of the amplitude-frequency curve when the shielding material is not placed in the test window. $v_{c,1}$ and R_1 are the voltage peak value at the center frequency and channel attenuation value of the amplitude-frequency curve after the shielding material is placed in the test window.

III. CHARACTERIZAION OF SHIELDING EFFECTIVENESS

Under different pulse width of narrow band HPM microwave, three shielding effectiveness calculation results based on ‘peak ratio’, ‘Fourier transform’ and ‘energy attenuation’ is shown in Fig. 2. Fig. 3 shows the results of subtracting the Fourier transform calculation result and the energy attenuation calculation result from the time domain waveform peak ratio calculation result. As can be seen from the Fig. 3, for narrowband HPM, under different pulse width conditions, the deviation of the shielding effectiveness value obtained by the three calculation results does not exceed 3dB, and the results are basically the same. Considering that it can be directly calculated from the waveform peak and path attenuation, the ‘peak ratio’ characterization is the easiest and quickest way to calculate the SE. Therefore, the following conclusions can be drawn: Using time-domain waveform peak ratio to calculate the shielding performance can obtain accurate results. At the same time, it can reflect the shielding performance of materials under narrow-band HPM conditions.

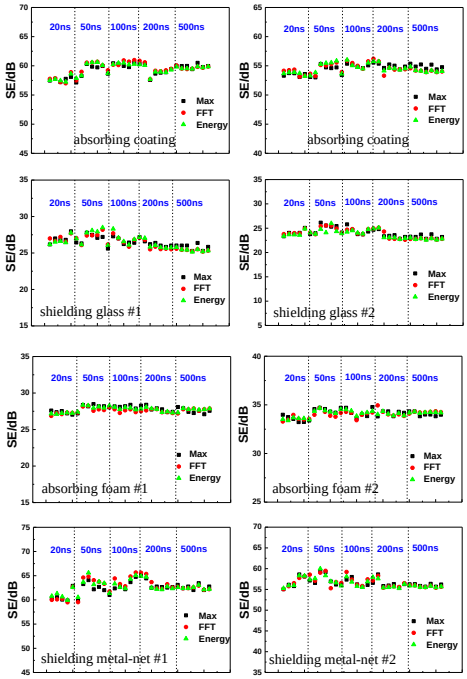

Fig. 2. Results of 8 groups of shielding materials based on three characterization methods of shielding effectiveness

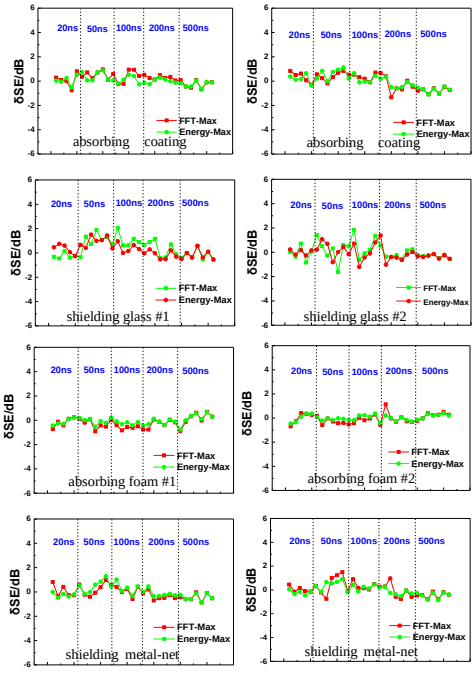

Fig. 3. Difference curves of 8 groups of shielding materials based on three characterization methods of shielding effectiveness

Compared with the continuous small microwave signal, the narrow band high power microwave signal has a relatively simple frequency. Although the single pulse power is large, the duty ratio is extremely small (usually less than 0.01%), so it is still a regular periodic signal. Therefore, using the same characterization method as the continuous wave small signal test, the shielding effectiveness under

narrow-band high-power microwave conditions can be accurately calculated.

IV. SHIELDING PROPERTIES UNDER HPM

Based on the above conclusion, the 'peak ratio' of waveform in time domain is used to characterize the shielding effectiveness. Then the effects of pulse repetition frequency, pulse width and power density on test results were studied. Figure 4 shows the test results of eight groups of materials under different repetition frequency and pulse width. It can be seen that the repetition frequency and pulse width have little effect on the shielding effectiveness of materials.

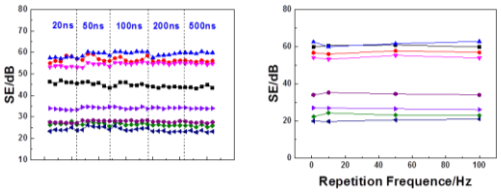

Fig. 4. Testing results of shielding effectiveness under different pulse width and repetition frequency

Figure 5 shows the results of shielding effectiveness at power density of 1 W/cm^2, 10 W/cm^2, 50 W/cm^2, 100 W/cm^2, and 200 W/cm^2 under a single repetition frequency. From the figure, it can be seen that between 1W/cm^2 and 50W/cm^2, the shielding effectiveness of the four materials increases with the increasing of power density, and when the power density is greater than 50 W/cm^2, the shielding effectiveness of the materials become stable.

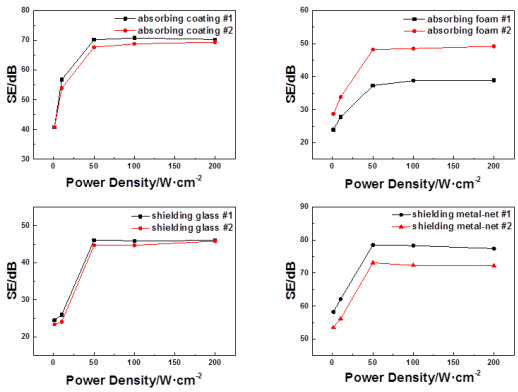

Fig. 5. Results of shielding effectiveness under different power density

Under the electromagnetic field, the fibers of the tested material are polarized and tend to be ordered. When the electromagnetic field reaches a certain value, the intensity of the polarization becomes stronger, so that the conductive interconnection between the fibers occurred and produces more conductive meshes, thereby increasing the electrical conductivity of the material and increasing the shielding efficiency. When the field increases to a certain value, the polarization interconnection becomes saturated, the number of conductive grids no longer increases with the increase of the field strength, and the material conductivity reaches the extreme value, so the shielding efficiency no longer increases.

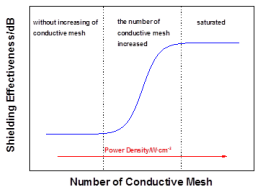

Fig. 6. The relationship between the shielding effectiveness of materials and the number of conductive mesh

V. CONCLUSION

For narrow-band high-power microwave shielding effectiveness, when using the 'peak ratio', 'Fourier transform' and 'energy attenuation' as characterization methods respectively, the calculated shielding effectiveness value does not exceed 2dB. Considering the test is simple and the calculation is fast, it is most suitable to use the 'peak ratio' for the calculation of the shielding effectiveness under narrow-band high-power microwave. Under narrow-band high-power microwave, the repetition frequency and pulse width have no effect on the shielding performance, while the pulse field power density has a great influence on the shielding effectiveness. Preliminary analysis of the effect of power density on shielding effectiveness is that the microscopic fibers of the shielding material are polarized to produce micro stress under strong electromagnetic field, which tends to be ordered, thereby increasing the conductive interconnection, and then increasing the conductivity and shielding efficiency. When the field strength reaches a certain value, the conductive interconnection has been saturated, and the shielding performance no longer increases as the power density increases.

REFERENCES

[1] Lai Zuwu. Damage effect and protection of strong magnetic pulse. Electronic Technology Guide, 1997,11(4):32-34.

[2] Liu Peiguo, Liu Chenxi, Tan Jianfeng, et al. Research progress of strong electromagnetic protection technology. Chinese Ship Research, 2015, 10(2): 2-6.

[3] S.A. Schelkunoff. Microwaves and mathematics[J]. IRE Transactions on Microwave Theory and Techniques,1957,3(6):173-176.

[4] GJB 6190-2008,Measurement methods for shielding effectiveness of electromagnetic shielding materials[S],2008.

[5] Li Yanxin, Chen Bin, Shi Lihua, et al. Pulse electric field shielding effectiveness measurement system, High Power Laser and Particle Beams, 2006, 18(6):972-976.

[6] Wang Yan, Ma Hongge, Cao Xuejun, et al. Attenuation characteristics of microwave pulse penetrating walls, High Power Laser and Particle Beams, 2005, 17(8):1277-1280.

[7] Long Zhang, Xiaofeng Hu, Xinfu Lu, et al.Simulation analysis for the materials shielding effectiveness of EMP. 2011 Cross Strait Quad-Regional Radio Science and Wireless Technology Conference,2011.

[8] Peng Chen, Congguang Mao, Gang Wu. Shielding effectiveness assessment of enclosure by means of EMP excitation. 7th Asia Pacific International Symposium on Electromagnetic Compatibility,2016.

[9] Chen Xiang, Chen Yongguang, Wei Ming, et al. Time domain testing methods of material' s shielding effectiveness of electromagnetic pulse using flange coaxial, High Voltage Engineering,2012,38(3):594-600.

Compact Small-Sized Pulsed Power Sources ARC-01/02 and Their Applications *

Zicheng Zhang, Hanwu Yang, Shifei Liu, Yuwei Wang, Jiande Zhang
College of Advanced Interdisciplinary Studies
National University of Defense Technology
Changsha, 410073, China
zczhang@nudt.edu.cn

***Abstract*—Development of pulsed power technology is high power density, compactness and high reliabilities. Liquid dielectric, because of its high insulation, easy flow, fast recovery and good heat dispersion, is widely used in the pulse power source based on liquid pulse forming line as energy storage medium. Research focuses are put emphases on the key techniques of the ARC series of pulse power sources. And studies are carried out on pulsed breakdown characteristics, system development and its application. The results are shown as follows. Firstly, through the research on the pulsed insulation characteristics of liquid dielectric in the microsecond regime, the database is established by statistical analysis method. And then, by using the ultrafast camera optical diagnosis method, based on the images of generation, propagation, cut-off for shock wave, sub-microscopic fracture surface, a liquid dielectric breakdown model is presented, combined with amorphous energy band and Griffith tension theory. Secondly, it is proposed for a pulse formation line based on high-energy-density-storage liquid dielectric and slow wave structure. By using the method of electromagnetic field uniformity and insulation technology to solve the high-voltage insulation problems, the compact pulse power sources ARC-01/02 are developed. They can output 1-2 GW power, 5-30 ns duration, 1-100 Hz rep-rate. And their maximum compact level is increased by 6 times than the international advanced similar devices. Finally, the compact pulse power sources are used in the fields of high-power microwave generation, high voltage generator for dielectric breakdown and novel high-quality cathode material test. These efforts set solid foundation and show a prospect future for the development of the compact pulse power sources and their applications.**

***Index Termss*—pulsed power source; pulse power technology; compactness; small-sized; liquid dielectric**

I. INTRODUCTION

PULSED power source can be used to drive particle beams, electromagnetic pulses, high power microwaves, ultra wide-bands, high power lasers, and industrial applications, and so on [1]-[8]. Development of pulsed power technology is towards high average power, compact structure and high reliability. A capacitive-energy-storage-type pulsed power source uses a pulse forming line as an energy storage element, which has advantages of good output waveform, repetitive operation [9]-[14]. And its key technique is energy storage. Liquid dielectric, due to its great permittivity, high insulation strength, good self-healing, and easy shaping, has a good potential in compact pulsed power source as the energy storage medium of pulse forming line. And its technical problems are the improvement of the insulation strength and the optimization of the insulation structure.

General liquid dielectric as an energy storage medium includes oil dielectric, water dielectric and water-based mixtures. Here oil dielectric is mineral oil, such as transformer oil and capacitor oil. And water dielectric is deionized water and water-based mixtures include ethylene glycol / deionized water mixture, methanol / deionized water mixture, and ethanol / deionized water mixture. Moreover, propylene carbonate (PC) has a wide-range of temperature with a freezing point of -50˚C. And its energy-storage characteristic can be improved by the additive of the ethylene carbonate (EC).

In this paper, focusing on the technical problems of compactness for ARC series of pulsed power sources, the studies are carried out on key technique, system development and its application. Firstly, based on the operation principal of the pulsed power source, the pulsed insulation characteristics of liquid dielectric are investigated in the microsecond regime for transformer oil, castor oil, glycerin and propylene carbonate. And then the database is established by statistical analysis method. Furthermore, by using the ultrafast camera optical diagnosis method, based on the images of generation, propagation, cut-off for shock wave, sub-microscopic fracture surface, a liquid dielectric breakdown model is presented, combined with amorphous energy band and Griffith tension theory. Secondly, it is proposed for a pulse formation line based on high-energy-density-storage liquid dielectric and slow wave structure. By using the method of electromagnetic field uniformity and insulation technology to solve the high-voltage insulation problems, the compact pulse power sources are developed. Finally, the applications of compact pulse power sources are carried out.

II. PULSE INSULATION OF LIQUID DIELECTRIC

Firstly, the pulsed insulation characteristics of liquid dielectric are investigated in the microsecond regime. Based on the breakdown experimental setup, shown as Fig. 1 and Fig.

This work was supported by the National Natural Science Foundation of China under Grant No.51677190 and the Hunan Provincial Natural Science Foundation of China under Grant No. 2017JJ1005.

2, breakdown database for liquid dielectric is established. Through the statistical analysis method, the energy storage density is compared for different liquid dielectric in the microsecond regime. And the energy storage density can be significantly improved by the additive and pressurization, illustrated in Fig. 3 and Table I.

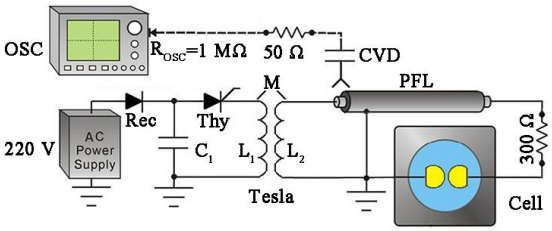

Fig. 1. Schematic of breakdown setup for liquid dielectric.

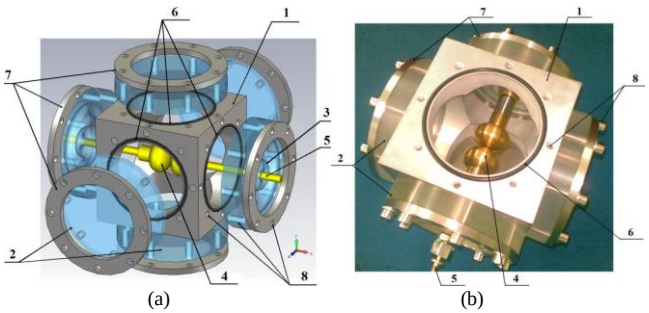

(a) (b)

Fig. 2. Schematic (a) and facility (b) of test cell.

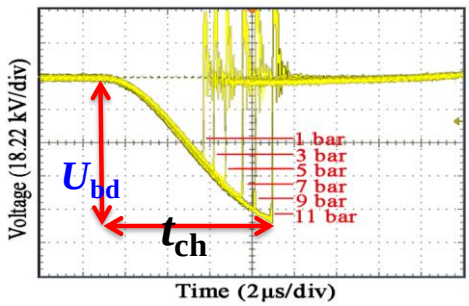

Fig. 3. Typical breakdown voltage waveform for pressurized liquid dielectric.

Table I. Methods to improve the energy storage density of the liquid dielectric and their comparison

No.	Effect	Method	Energy storage
1	Surface roughness level	Electrode polished	1.2-1.4
2	Gas content	Degased	1.69
3	Additive	Additive (EC)	1.23
4	Pressure	Pressurization (p=1 MPa)	1.69

III. Physical Mechanism of Pulsed Breakdown

As an accurate type of non-contact diagnostic technology, optics diagnosis is widely applied to the test of transient physical quantity. Optical diagnosis experiment setup is built and the synchronization problem is solved. And then the breakdown images for the propagation process of the initiation, development and conduction are captured by the high-speed camera, shown as Fig. 4. For needle positive, the streamer is filamentary and dense liking an umbrella. For needle negative, the streamer is less branched and sparse liking a leafless treetop. The small point circled is corresponding to the bubble in the propylene carbonate (PC). According to the optical diagnosis images, the breakdown process is analyzed and the breakdown mechanism is explored. And then the breakdown model is improved and the breakdown experimental phenomena are physically explained to improve the insulation strength for the method of pressurization, degas, additive, electrode polish and nano-particle modification.

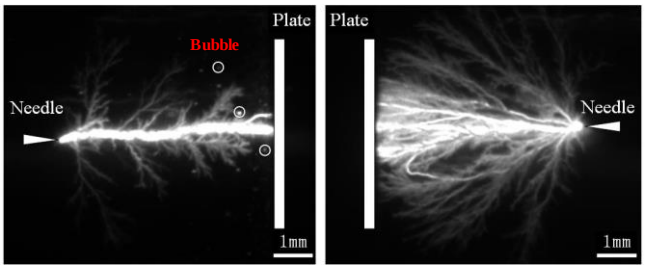

(a) (b)

Fig. 4. Comparison of positive (a) and negative (b) breakdown for high-energy-storage liquid dielectric.

IV. Develeopment of Pulsed Power Sources

It is proposed for a pulse formation line based on high-energy-density-storage liquid dielectric and slow wave structure. By using the method of electromagnetic field uniformity and insulation technology to solve the high-voltage insulation problems, the compact pulse power sources are developed, shown as Fig. 5. The typical output waveforms of voltage, current and power are shown as Fig. 6. Across 10 Ω load, it can output 1 GW power, 30 ns duration, 100 Hz rep-rate. When the energy storage medium adopts transformer oil, castor oil and glycerin, the output parameters of the compact small-sized pulsed power sources are shown as Table II. They can output 1-2 GW power, 5-30 ns duration, 1-100 Hz rep-rate.

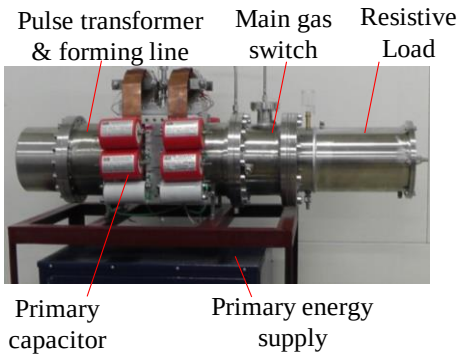

Fig. 5. Compact pulsed power source ARC-02.

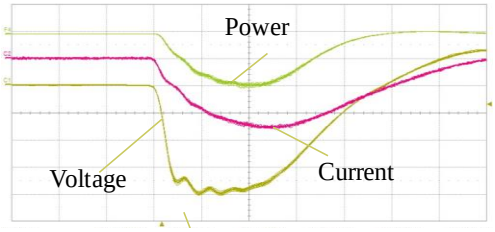

Fig. 6. Output waveforms of compact pulsed power source ARC-02 in 100 Hz mode.

Table II. Output parameters of compact pulse power source ARC-01/02.

No.	Source	Dielectric	Power (GW)	Duration (ns)	Impedance (Ω)	Rep-rate /Hz
1	ARC-01	Trans. oil	1	5	30	100
2	ARC-01	Castor oil	1-2	10	20	100
3	ARC-02	Glycerin	1	30	10	100

V. Applications of Compact Pulsed Power Sources

Finally, the compact pulse power sources are used in the fields of high-power microwave generation, high voltage generator for dielectric breakdown and novel high-quality cathode material test.

A. Microwave Generation

The compact small-sized pulsed power sources are used to drive backward wave oscillator (BWO) to produce narrow-band microwave, to drive non-linear transmission line (NLTL) to produce wide-band microwave.

B. Dielectric Breakdown

The microsecond pulse generation part of compact small-sized pulsed power source ARC-01 is used to be a pulsed high-voltage generator, shown as Fig. 1. It is applied to investigate the pulsed breakdown and optical diagnosis for propylene carbonate and nono-fluids in the microsecond regime.

C. Novel High-Quality Cathode Material Test

The compact small-sized pulsed power source ARC-02 is applied to drive radial vacuum diode to produce radial electron beam. And it is used to test the operation stability and life-time for the carbon-fiber cathode material.

VI. Conclusion

Research focuses are put emphases on the key techniques of the ARC series of pulse power sources. And studies are carried out on key technique, system development and its application. The results are shown as follows. Firstly, through the research on the pulsed insulation characteristics of liquid dielectric in the microsecond regime, the database is established by statistical analysis method to obtain high reliabilities with the small cost. And then, by using the ultrafast camera optical diagnosis method, based on the images of generation, propagation, cut-off for shock wave, sub-microscopic fracture surface, a liquid dielectric breakdown model is presented to explain some experimental phenomena, combined with amorphous energy band and Griffith tension theory. Secondly, it is proposed for a pulse formation line based on high-energy-density-storage liquid dielectric and slow wave structure. By using the method of electromagnetic field uniformity and insulation technology to solve the high-voltage insulation problems, the compact pulse power sources ARC-01/02 are developed. They can output 1-2 GW power, 5-30 ns duration, 1-100 Hz rep-rate. Finally, the compact pulse power sources are used in the fields of high-power microwave generation, high voltage generator for dielectric breakdown and novel high-quality cathode material test. These efforts set solid foundation and show a prospect future for the development of the compact pulse power sources and their applications.

Acknowledgment

The authors wish to thank Prof. Huihuang Zhong, Prof. Jun Zhang, Prof. Baoliang Oian, Prof. Ting Shu, and Prof. Jianhua Yang for their encouragement and valuable suggestions.

References

[1] Martin J C. The pre-history of pulsed power[C]. 1995.

[2] Martin J C. Nanosecond pulse techniques[J]. Proceedings of the IEEE. 1992, 80(6): 934-945.

[3] Schamiloglu E, Barker R J, Gundersen M, et al. Modern Pulsed Power: Charlie Martin and Beyond[J]. Proceedings of the IEEE. 2004, 92(7): 1014-1020.

[4] Mesyats G. A., Pulsed power, New York: Kluwer Academic/Plenum Publishers, 2005

[5] Bluhm H. Pulsed Power Systems[M]. Verlag Berlin Heidelberg, 2006.

[6] Pai S T, Zhang Q. Introduction to High Power Pulse Technology[M]. World Scientific, 1995.

[7] T. H. Martin, A. H. Guenther and M. Kristiansen. J. C. Martin on pulsed power[M]. New York: Plenum, vol.3, 1996: 1-35.

[8] J. C. Martin. Nanosecond pulse techniques SSWA/TCM/704/49, AWRE England, 1970.

[9] V. P. Gubanov, S. D. Korovin, I. V. Pegel, et al. Compact 1000 PPS high-voltage nanosecond pulse generator[J]. IEEE Transactions on Plasma Science, 1997, 25(2):258-265.

[10] V. P. Gubanov, A. V. Gunin, S. D. Korovin, et al. Periodically pulsed high voltage generator based on Tesla transformer and spiral forming line[C]. Pulsed Power Plasma Science. IEEE, 2001:336.

[11] S. D. Korovin, V. P. Gubanov, A. V. Gunin, et al. Repetitive nanosecond high-voltage generator based on spiral forming line[C]. Pulsed Power Plasma Science, 2001. PPPS-2001. Digest of Technical Papers. IEEE, 2001:1249-1251.

[12] G. A. Mesyats, S. D. Korovin, A. V. Gunin, et a1. Repetitively pulsed high-current accelerators with transformer charging of forming lines[J]. Laser and Particle Beams, 2003, 21 (2): 197-209.

[13] M. Kristiansen, L. L. Hatfield. High voltage water breakdown studies[R]. Lubbock, TX: Defense Special Weapons Agency, 1998.

[14] J. Mankowski, J. Dickens, M. Kristiansen. High voltage subnanosecond breakdown[J]. IEEE Trans on Plasma Science, 1 998, 26 (3) 874-881.

A Measurement System for Detonation-Generated Plasma Density

1th Ziqi Yang
ZNDY of Ministerial Key Laboratory
Nanjing University of Science and Technology
Nanjing, China
657438347@qq.com

2nd Yong He
ZNDY of Ministerial Key Laboratory
Nanjing University of Science and Technology
Nanjing, China
yhe1964@mail.njust.edu.cn

3rd Xuchao Pan
ZNDY of Ministerial Key Laboratory
Nanjing University of Science and Technology
Nanjing, China
pxchxc@njust.edu.cn

4th Hong Chen
ZNDY of Ministerial Key Laboratory
Nanjing University of Science and Technology
Nanjing, China
1012702581@qq.com

5st Jiangnan Zhang
ZNDY of Ministerial Key Laboratory
Nanjing University of Science and Technology
Nanjing, China
117101010261@njust.edu.cn

6th Yu Zhou
ZNDY of Ministerial Key Laboratory
Nanjing University of Science and Technology
Nanjing, China
839634568@qq.com

***Abstract*—In this paper, based on microwave reflection method, a measurement system for density of plasma generated by explosion was built. The measure principle is that microwaves of different frequencies injected into the plasma will be reflected on different cutoff layer, and the distribution law of the detonation-generated plasma density can obtained by analyzing the reflection characteristics of microwaves by plasma. The measurement system is mainly composed of microwave generation source, microwave transmission system, phase measurement system, and data acquisition system. And because the system works in an explosive environment, shielding measures and vibration isolation measures were taken. The experimental method was also designed.**

Keywords—measurement system, microwave reflection method, detonation-generated plasma density

I. INTRODUCTION

The plasma is composed of a large number of free electrons or negative ions, positive ions and neutral atoms and molecules, and is generally an electrically neutral macroscopic system. The plasma generated by the explosion was first discovered by Cook and his colleagues from the conductivity measurements of the reaction zones of various solid explosives [1]. Studies have shown that the number of free electrons in the explosive plasma is at least $10^{17}/cm^3$, and in some cases, the number of free electrons can exceed $10^{19}/cm^3$. The initial moment of the interaction between the detonation product and the air, the transmission speed of detonation product can reach 7-9km/s due to the action of the detonation air shock wave, and the wavefront pressure can reach 0.07-0.09Gpa [2]. The plasma emitted from the surface of the explosive explosion is metastable and can last for more than $250\mu s$ when propagating in the air. It is rapidly attenuated into a normal explosive product after being stirred or after a certain time even without agitation. Due to the existence of such explosive plasma clouds, it has a certain influence in the relevant application fields of explosives. And to study the plasma generated by the explosion to determine its properties and possible effects in the occurrence and development of the reaction, the process can be controlled by applying an electromagnetic field to change the characteristics of the explosion.

At present, more mature plasma diagnostic methods include electrostatic probe method, microwave interference method, microwave reflection method. Due to the high temperature, high pressure and shock wave caused by the explosion, the electrostatic probe method as an intrusive measure method will generate some impurity ions in the test process that affects the purity of the plasma to be measured [3]. The microwave interferometry method obtains the dielectric constant of the plasma by measuring the phase shift of the incident wave propagating in the plasma, thereby obtaining the plasma density information. The measurement system is relatively complex, and when subjected to the shock and vibration caused by the explosion, the accuracy will be greatly affected. Microwave reflection method is to use the total reflection phenomenon that occurs when electromagnetic waves propagate in the plasma for density diagnosis. It does not interfere with the plasma to be measured, and the system composition is relatively simple. Based on the above, this paper designs a density measurement system for plasma generated by explosion based on microwave reflection method.

Based on the principle of microwave reflection method, a measurement system for plasma density generated by explosion is designed. The system can be used to obtain the time-frequency curve of the detonation-generated plasma development process and the density distribution at a certain time. It avoids the interference of shock, vibration, high temperature and other factors that may affect the result during the explosion, and does not introduce impurities to affect the test results. In this paper, the testing principle of microwave reflection method is introduces, then it gives the specific method of system construction, and the experimental method is given. Langmuir probe system is also used to serve as a contrast.

II. PRINCIPLE OF MICROWAVE REFLECTION METHOD

A. Plasma reflection characteristics

From a macroscopic point of view, the plasma is electrically neutral and satisfies Maxwell's equation. According to Maxwell's equation, the wave equation can be obtained and solved,

$$\vec{E} = \vec{E}_0 \cdot \exp(j\omega t - j\vec{k} \cdot \vec{r}) \tag{1}$$

$$k^2 = \frac{\omega^2}{c^2}\varepsilon_r \tag{2}$$

The above formula determines the propagation characteristics of electromagnetic waves in the plasma. The expression of the relative permittivity ε_r in the formula is:

$$\varepsilon_r = 1 - \frac{\omega_p^2}{\omega^2 + \upsilon_e^2} - j\frac{\upsilon_e}{\omega}\frac{\omega_p^2}{\omega^2 + \upsilon_e^2} \tag{3}$$

Where ω is the microwave angular frequency, ω_p is the plasma characteristic frequency, and υ_e is the collision frequency.

Let $\vec{k} = \beta - j\alpha$, β be the phase constant, α be the decay constant, and let $k_0 = \omega/c$ be the wave vector in the vacuum. Combine equations (1), (2) and (3) to obtain:

$$\beta = k_0 \left\{ \frac{1}{2}\left(1 - \frac{\omega_p^2}{\omega^2 + \upsilon_e^2}\right) + \frac{1}{2}\left[\left(1 - \frac{\omega_p^2}{\omega^2 + \upsilon_e^2}\right)^2 + \left(\frac{\omega_p^2}{\omega^2 + \upsilon_e^2}\frac{\upsilon_e}{\omega}\right)^2\right]^{\frac{1}{2}} \right\}^{\frac{1}{2}} \tag{4}$$

$$\alpha = k_0 \left\{ -\frac{1}{2}\left(1 - \frac{\omega_p^2}{\omega^2 + \upsilon_e^2}\right) + \frac{1}{2}\left[\left(1 - \frac{\omega_p^2}{\omega^2 + \upsilon_e^2}\right)^2 + \left(\frac{\omega_p^2}{\omega^2 + \upsilon_e^2}\frac{\upsilon_e}{\omega}\right)^2\right]^{\frac{1}{2}} \right\}^{\frac{1}{2}} \tag{5}$$

In the case where the collision frequency of the plasma is much smaller than the frequency of the electromagnetic wave, it can be regarded as a collision-free plasma, so that:

$$\varepsilon_r = 1 - \frac{\omega_p^2}{\omega^2} \tag{6}$$

$$\beta = k_0\sqrt{1 - \frac{\omega_p^2}{\omega^2}} \tag{7}$$

When the incident electromagnetic wave frequency ω is smaller than the plasma characteristic frequency ω_{pe}, the phase constant β is a pure imaginary number, thus the wave vector k is a pure imaginary number, indicating that the electromagnetic wave incident on the plasma cannot propagate and total reflection occurs.

When the incident electromagnetic wave frequency ω is greater than the plasma characteristic frequency ω_{pe}, the electromagnetic wave can pass through the plasma.

When the incident electromagnetic wave frequency ω is equal to the plasma characteristic frequency ω_{pe}, the incident wave just cannot continue to propagate in the plasma, and total reflection occurs. At this time, the microwave frequency at this time is the cutoff frequency corresponding to the plasma frequency here. The plasma location is referred to as the cutoff layer.

B. Density measurement principle

The microwave reflection method can measure the plasma electron density in space and time, that is, the spatial distribution and density disturbance of the electron density can be measured, and the system does not interfere with the result.

Microwave reflection method is a density diagnosis using the total reflection phenomenon that occurs when electromagnetic waves propagate in a plasma. According to the principle that the critical plane of the incident wave reflected at different frequencies is different in the plasma, the refractive index tends to zero at the plasma cut-off layer, and the probing wave is reflected. The electron density can be calculated by measuring the critical plane position. In the test, the most basic measurement is the delay time or phase shift of the reflected wave. The delay time of a wave in a plasma is generally on the order of nanoseconds, and it is obviously difficult to obtain the result directly, so we measure the phase difference due to the delay time instead.

For the non-uniform plasma with a monotonous rise in density profile, microwaves of different frequencies are injected into the plasma, and the time delay of the corresponding reflected wave is measured. The electron density and its distribution can be obtained by Abel transform.

For electromagnetic waves perpendicular to the magnetic field propagating O-mode (the electric field of the wave is parallel to the magnetic field in the plasma), the refractive index can be written as:

$$\mu(r) = \sqrt{1 - \frac{\omega_p^2}{\omega^2}} = \sqrt{1 - \frac{n_e e^2}{\varepsilon_0 m_e (2\pi f)^2}} \tag{8}$$

e and n_e is the electronic charge and density, ε_0 is vacuum dielectric constant. $f = \omega/2\pi$ is the frequency of detecting electromagnetic waves. When the plasma frequency is equal to the detection frequency, the refractive index becomes zero and the wave is reflected. Therefore, the relationship between the density of the cutoff layer and the corresponding frequency of the detected electromagnetic wave is:

$$n_e = \frac{m\varepsilon_0 (2\pi f)^2}{e^2} \tag{9}$$

The phase change of the reflected wave relative to the incident wave is:

$$\varphi(f) = \frac{4\pi f}{c}\int_{r_c}^{r_1} \mu(r)dr - \frac{\pi}{2} \tag{10}$$

In (10), r_c is the cutoff layer position corresponding to frequency f, r_1 is the plasma boundary position. Deriving (10) gives the time delay in which the signal propagates:

$$\tau(f) = \frac{1}{2\pi}\frac{d\varphi}{df} \tag{11}$$

The Abel inverse transform is performed on the measured swept signal delay to obtain the cutoff layer position:

$$r_c(f_c) = \frac{c}{\pi}\int_0^{f_c} \tau(f)\frac{df}{\sqrt{f_c^2 - f^2}} \tag{12}$$

It should be pointed out that due to the limited frequency range of the reflection method signal source, the time delay must be extrapolated during the Abel transform, and the

extrapolated values are mostly based on the density profile data measured by other diagnostic tools.

III. Design of the Measurement System

The measurement system is mainly composed of microwave generation source, microwave transmission system, phase measurement system, and data acquisition system (shown in fig.1). The main system design method is given below according to the test requirements of the plasma cloud density generated by the explosion.

A. Microwave generation source

The microwave generation source adopts an improved wideband frequency modulation continuous wave system, which has been well applied in devices such as ASDEX-U [4]. The microwave source signal is obtained by a steady-state HTO oscillator and frequency multiplier. The system frequency range can cover 16-100 GHz and repeat ultra-fast sweep (10μs or more) [5]. The ultra-fast sweep frequency of the microwave source can ensure that the plasma is almost frozen during the frequency sweeping process, and the influence of the fluctuation is greatly reduced.

B. Microwave transmission system

The transmission, emission and reception of microwaves from the microwave source requires the microwave transmission system. The microwave transmission system includes waveguide and antenna. In order to avoid stray reflection inside the waveguide and affect the accuracy, two sets of discrete microwave transmission systems are used for transmitting and receiving respectively, symmetrically distributed with the upper and lower sides of the central plane of the plasma with a angle less than 5°. Since the system does not require microwaves for long-distance transmission in the waveguide, according to the national standard, a fundamental mode rectangular waveguide is used. The antenna adopts a horn antenna with a simple structure and a large bandwidth. In order to ensure that the incident wave has a certain directionality, and at the same time avoiding an increase in the antenna aperture, the horn antenna with a small aperture and a good gain is used, which size is 28mm×30mm×100mm.

C. Phase measurement system

The phase measurement system uses a heterodyne frequency conversion method to measure. It is very difficult to directly measure the phase difference of the incident wave. The heterodyne frequency conversion can transfer the phase information to a lower frequency, and can perform effective measurement even in the case where the amplitude disturbance is strong or the reflected signal is weak. The phase measure is approximately the comparison of the two signals. The phase of the detected signal is compared with the reference signal. The magnitude of the output signal voltage directly reflects the phase difference between the two input signals. The polarity of this voltage reflects the reference signal. The relative phase relationship, that is, the detection signal leads or lags behind the reference signal.

D. Acquisition system

In terms of data acquisition, the plasma generated by the explosion has a strong disturbance, that is, the reflecting surface of the microwave is not static. Therefore, to overcome the effect of the disturbance on the measurement, the sweep time must be fast enough that the plasma appears to be stationary during a sweep. This requires the acquisition speed of the data acquisition card to be relatively fast. In order to meet the above requirements, the PCI-8521 data acquisition card is used.

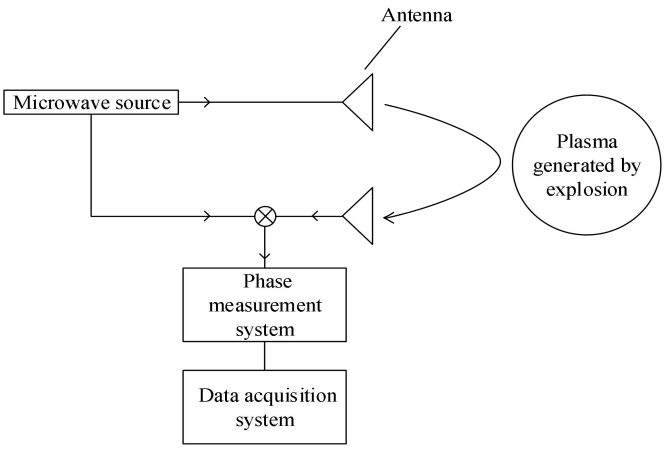

Fig. 1. System composition diagram

E. System protection

In terms of system protection, the explosion is accompanied by a complex electromagnetic environment, the electromagnetic pulse spectrum generated by different types of chemical explosions is very wide, the amplitude varies widely, and due to the persistence of the explosion and the unevenness of the charge. The electromagnetic pulses radiated are random. Shielding measures are taken to eliminate or reduce electromagnetic interference to get a more accurate result. In addition, during the explosion process, the shock wave will directly act on the measurement system or act on the system through the ground, causing vibration and generating additional signals and affecting the results. In order to avoid or reduce vibration interference, the system is reinforced by taking vibration isolation measures.

IV. Experiment

A. Experimental propose

- Reflection coefficient change curve. The microwave source emits a frequency-swept microwave, which requires the sweep speed to be in the microsecond range. The plasma can be regarded as static during one sweep. The microwaves of each frequency are totally reflected at the corresponding plasma cut-off layer to be tested until the frequency of the sweep microwave is greater than the characteristic frequency corresponding to the plasma cut-off layer, and no total reflection occurs. That is, the maximum density of the plasma at this time can be obtained by each sweeping, and the maximum density variation law during the development of the explosive plasma can be obtained by continuous frequency sweeping.
- The phase difference or time delay of the reflected wave. In the total reflection part, the phase cut-off layer position can be obtained by phase difference or time delay analysis, and the density distribution of the plasma at this time can be obtained combining the relationship between the cut-off layer density and the frequency.

B. Experimental method

- The test object is a plasma generated by explosives. Several different kinds of explosives in different dosages are used and for each dosage the measurement is done for 5 times to reduce random deviation. The explosive types include: TNT, TNT with Al, RDX, RDX with Al. The dosage includes: 10g, 15g, 20g. The detonation method uses electric detonator detonation, and the test is carried out in a free space without wind. In order to prevent the explosive from tumbling during the detonation process, it is fixed on the designed bracket to ensure the relative stability of the position during plasma generation.

- When constructing the test system, measures are taken to reduce the impact on the characteristics of the impact and vibration of the explosive environment. The equipment is arranged according to the safe distance of the explosion shock wave: $R = K\sqrt{m_T}\,(50 \le K \le 150)$, m_T is the TNT equivalent of the explosive used. At the same time, the antenna arrangement is supposed to satisfies the far field measurement conditions:

$$R \ge 2\frac{d^2}{\lambda} \tag{13}$$

According to the dose that is used, calculate the required safety distance between the shock wave and the measurement system, and at the same time make sure that the far field measurement condition is satisfied.

- In view of the possible effects of the shock wave and vibration that directly exert on the measurement system and transimit through the ground to affect the system, measures such as fixing the microwave source and the antenna and attaching the cushioning pad are adopted.

After the system is set up, it needs to be checked and calibrated first. In the condition that no plasma have been generated, the metal plate is placed in the predicted plasma generation position to test the microwave reflection signal reception, and then the metal plate is removed in order to test the environmental reflection in the absence of plasma. It can eliminate the interference caused by environmental factors.

- During the test, the test system starts scanning a few seconds before the plasma starts, and the system stabilizes after a few hundred milliseconds to ensure the timing of the collected data stability. At the beginning of the explosion, the frequency scanning microwave generated by the microwave generating device enters the explosive plasma through the transmitting antenna, the reflection occurs at the cut-off layer, the reflected wave enters the receiving antenna, and the phase measurement system obtains the phase difference between the original and the reflected wave, which is recorded by the data acquisition system. At the same time, Langmuir probe system is also used to serve as a contrast.

- Data processing and error analysis are performed to observe the consistency of the two diagnostic methods.

C. Source of error

- The unevenness of the charge and the influence of fluctuations in the measurement points.

- The plasma density changes too fast, the sweep frequency is not fast enough, and the plasma cannot be regarded as static.

- If the plasma collision frequency is large, the reflection coefficient will be reduced and the density calculation will be affected. In the collision plasma, as the electron collision frequency increases, the reflectance and transmittance of the electromagnetic wave will decrease, and the energy of the electromagnetic wave will be absorbed by plasma.

- The uneven distribution of the plasma reduces the reflection coefficient. The change of plasma density gradient means that there is no obvious interface between plasma and vacuum. At this time, there is no sudden change in intensity between electric field and magnetic field. The energy of electromagnetic wave below the cutoff frequency is lost due to resonance absorption, so that the reflection coefficient is reduced.

- The low-frequency partial density distribution in the calculation formula of the cutoff layer position requires artificial assumptions and may introduce errors.

ACKNOWLEDGMENT

We would like to acknowledge the guidance of Yong He and Xuchao Pan. And we are very grateful for the support of all the people who helped us during writing this paper.

REFERENCES

[1] Bauer A, Cook M A, Keyes R T. Detonation-Generated Plasmas[J]. Proceedings of the Royal Society A Mathematical Physical& Engineering Sciences, 1961, 259(259):508-517.

[2] Cook M A, Keyes R T, Udy L L. Propagation Characteristics of Detonation-generated Plasmas[J]. Journal of Applied Physics, 1960, 30(12):1881-1892.

[3] Fang M T, Zhang J L, Yan J D. On the use of Langmuir probes for the diagnosis of atmospheric thermal plasmas[J]. IEEE Transactions on Plasma Science. 2005, 33(4): 43l-442

[4] Silva A, Cupido L, Manso M. Microwave reflectometry diagnostic for density profile and fluctuation measurements on ASDEX Upgrade[J]. Review of Scientific Instruments, 1999, 70(1):1072.

[5] Yang Zhoujun. Development of microwave reflectometer on HL-2A tokamak device[D]. Huazhong University of Science and Technology, 2006.

[6] Laviron C, Millot P and Prentice R, First experiments of pulse compression radar reflectometry for density measurements on JET plasmas Plasma Phys. Control. Fusion 37, 975(1995).

[7] Fu Hongjun, Ding Xuantong, Liu Zetian. Design of HL-2A Swept Microwave Reflection System[J]. Science Technology and Engineering, 2004, vol. 4: 272-274.

[8] Cappelli M, Hermann W, Kodiak M. A 90 GHz phasebridge interferometer for plasma density measurements in the near field of a hall thruster[C]. 40th AIAA/ASME/SAE/ASEE Joint Propulsion Conference and Exhibit, Florida, 2004(AIAA-2004-3775): 1-8

[9] Moreau P H, Clairet F, Chareau J M. Ultrafast frequency sweep heterodyne reflectometer on the Tore Supra tokamak[J]. Review of Scientific Instruments. 2000, 71(1): 74-81

[10] Sabot R,Clairet F,honore C.Advances of reflectometry on tore-supra:from edge density profile to core density fluctuations[J]. International Journal of Infrared and Millimeter Waves, 2004,25(2):229-246.

[11] Shneidera M N,Miles R B.Microwave diagnostics of small plasma objects[J].Journal of Applied Physics.2005,98(033301):l-3.

[12] Li Bin. Research on plasma microwave characteristics and microwave diagnostic methods [D]. Hefei: University of Science and Technology of China, 2010.

[13] Jiang Yuanjun. Study on plasma characteristics based on microwave reflection method [D]. Chengdu: University of Electronic Science and Technology, 2016

[14] Bulanin V V, Lebedev S V, Levin L S. Study of plasma fluctuations in the Tuman-3M tokamak using microwaver reflectometry with an obliquely incident probing beam[J]. Plasma Physics Reports, 2000, 26(10):813-819.

[15] Bulyginskiy D G, Gurchenko A D, Gusakov E Z,et gal. Radar upper hybrid resonance scattering diagnostics of small-scale fluctuations and waves in tokamak plasmas[J]. Physics of Plasmas, 2001, 8(5): 2224-2231.

[16] Huang Jiarong, Wang Xing, Sun Guijuan. Influence of electromagnetic pulse on test signal in explosion test[C]. National Conference on Structural Engineering, 2009

[17] Wang Wei, Ding Yonghong, You Wenbin. Study on anti-electromagnetic interference of explosion field parameter detection head[J]. Computer Measurement & Control,2014,22(2):486-488.

[18] Jeong S H, Kim I Y,Hwang C K. Design of a heterodyne electron cyclotron emission system on KSTAR[J]. Review of Scientific Instruments, 2003, 74(3):l433-1436.